Faradaic and Adsorption-Mediated Depolarization of Electric Double Layers in Colloids

Promotor:	Prof. dr. M. A. Cohen Stuart hoogleraar Fysische Chemie, met bijzondere aandacht voor de Kolloïdchemie
Co-promotor:	Prof. dr. H. P. van Leeuwen universitair hoofddocent bij de Leerstoelgroep Fysische Chemie en Kolloïdkunde en buitengewoon hoogleraar Fysische Milieuchemie bij de Universiteit van Genève

Samenstelling promotiecommissie:

Prof. dr. D. C. Prieve, Carnegie Mellon University, Pittsburgh, USA.
Prof. dr. A. A. Foissy, Université de Franche-Comté, Besançon, France.
Prof. dr. J. J. Kelly, Debye Instituut, Universiteit Utrecht, The Netherlands.
Prof. dr. R. M. Boom, Wageningen Universiteit, The Netherlands.
Prof. dr. J. Lyklema, Wageningen Universiteit, The Netherlands.

Jérôme Duval

Faradaic and Adsorption-Mediated Depolarization of Electric Double Layers in Colloids

Proefschrift
ter verkrijging van de graad van doctor
op gezag van de rector magnificus
van Wageningen Universiteit,
Prof. dr. ir. L. Speelman,
in het openbaar te verdedigen
op maandag 20 oktober 2003
des namiddags te vier uur in de Aula

Duval, Jérôme F. L.

Faradaic and Adsorption-Mediated Depolarization of Electric Double Layers in Colloids
Proefschrift Wageningen Universiteit
Met samenvatting in het Nederlands.

ISBN 90-5808-940-1
Subject headings: Double Layers/Electrokinetics/Faradaic Depolarization/Colloidal Interactions

“La poésie peut plaire encore, mais le combat, lorsque la vie est l’enjeu, ne se livre qu’en prose.”

Czeslaw Milosz, Prix Nobel de Littérature 1980.

“Poëzie kan blijven behagen, maar de strijd om het naakte bestaan wordt slechts in proza gevoerd.”

Czeslaw Milosz, Nobel Prijs voor de Literatuur 1980.

A la mémoire de Marijke
Ter herinnering aan Marijke

TABLE OF CONTENTS

Chapter 1. Introduction ………………………………………………………………………… 1

Chapter 2. Amphifunctionally Electrified Interfaces: Coupling of Electronic and Ionic Surface Charging-Processes ………………………………………………………………… 9

Chapter 3. Double Layer of a Gold Electrode Probed by AFM Force Measurements ……….. 19

Chapter 4. Double Layers at Amphifunctionally Electrified Interfaces in the Presence of Electrolytes containing Specifically Adsorbing Ions …………………………... 27

Chapter 5. Bipolar Electrode Behaviour of the Aluminium Surface in a Lateral Electric Field ………………………………………………………………………………………… 43

Chapter 6. Faradaic Depolarization in the Electrokinetics of the Metal|Electrolyte Solution Interface ……………………………………………………………………………… 55

Chapter 7. Coupling of Lateral Electric Field and Transversal Faradaic Processes at the Conductor|Electrolyte Solution Interface …………………………………………. 67

Chapter 8. Rigorous Analysis of Reversible Faradaic Depolarization Processes in the Electrokinetics of the Metal|Electrolyte Solution Interface ……………………….…81

Chapter 9. Electrokinetics of the Amphifunctional Metal|Electrolyte Solution Interface in the Presence of a Redox Couple …………………………………………………... 119

Chapter 10. Interaction Between Electric Double Layers: Regulation. Its Chemical and Electrostatic Aspects ………………………………………………………... 145

Chapter 11. Electrostatic Interactions between Double Layers: Influence of Surface Roughness, Regulation and Chemical Heterogeneities ………………………………………. 195

Chapter 12. Conclusions, Perspectives …………………………………………………….. 221

Samenvatting ……………………………………………………………………………. 229
List of Pulications ……………………………………………………………………….. 231
Curriculum Vitae ………………………………………………………………………….. 233
Dankwoord ……………………………………………………………………………………. 235

CHAPTER 1

INTRODUCTION

Hydrophobic surfaces in contact with an aqueous solution often carry a charge. This charge, generally located at the surface, is compensated by an equivalent ionic countercharge diffusely distributed in the adjacent medium. The interfacial region encompassing the surface charge and the diffuse countercharge is called electric double layer or *double layer*, in short. The charging mechanisms underlying the spontaneous formation of ionic double layers at surfaces are chemical in nature, the double layer being the result of preferential adsorption of ions on the surface. Equilibrium double layers at insulated interfaces are said to be *relaxed* or *reversible*, their Gibbs energy of formation being negative. Knowledge of the double layer charging mechanisms is a mandatory prerequisite in understanding the interface and colloid science involved in such subjects as electrokinetics, ionic and macromolecular adsorption at phase boundaries, colloid stability, etc.

If the substrate material is an electronic conductor, the double layer may be controlled by an externally applied potential. As long as the medium does not contain electroactive species, i.e. species that may undergo (faradaic) electron transfer reactions, the interface is said to be *polarizable*. The classical representative of this category is the interface between liquid mercury and an aqueous solution of a so-called background (that is, electroinactive) electrolyte. If the ions present in the solution have no chemical affinity for the surface, that is, if they do not specifically interact with the surface, then the driving force for the double layer formation is of purely *electrostatic* nature. In the more general case, the double layer arises from the interplay between *electronic* and *ionic charging processes*. If the medium contains electroactive species, a faradaic current may flow. This current generally depends on the magnitude of the potential difference applied across the interface and the thermodynamic/kinetic characteristics of the electron transfer reaction.[1] The interface then undergoes *faradaic depolarization*. The external source provides the initial Gibbs energy required to create an excess or deficit of electrons on the surface, that is, to generate a potential difference between the substrate and the solution. The understanding of these systems has been and is still an important research area in interfacial electrochemistry. Much attention is being devoted to the generation of physical insight into the charge/potential relationships obtained under conditions leading or not to faradaic double layer depolarization in the presence or absence of specific adsorption of ions. Within the framework of electrochemistry, knowledge of the structure of the interfacial double layer is crucial in relation to its implications for electrode kinetics and electrochemical measurements.[2]

The parallel between interfacial double layers as considered in electrochemistry and colloid chemistry underlines the different primary interests of the two chemical disciplines. Colloid chemists tend to concentrate on non-conducting materials or rather, on double layers without electronic charge components, whereas electrochemists focus on controllable electronic charge at the surface of conducting electrodes. Some substrates, however, combine polarizable and reversible double layer features. Partially oxidized metals and semiconducting oxides are illustrative examples. Within the scope of fundamental research, the topic is challenging because it necessarily integrates the ‘reversible’ (colloid chemical) and ‘polarizable’ (electrochemical) features of an interfacial double layer. On a more practical level, such double layer knowledge opens the perspective of optimizing industrial processes that apply these amphifunctional interfacial systems. Electrophoretic deposition of colloidal particles onto conducting substrates is an illustrative example of such a process.[3-6]

Context of this study

In the electrophoretic deposition process (EPD), an electric field is applied across a suspension containing charged colloidal particles. These particles migrate towards a deposition electrode, at the surface of which a deposit of the particle material is formed. EPD comprises two basic steps: the migration of charged particles in the applied electric field (electrophoresis) and the settling of the particles to form an adherent layer on the electrode (deposition). The main objective is the generation of well structured patterns of deposited particle layers, that could be manipulated at will by variation of the external electric variable. Practical rates of migration of the particles require a sufficiently strong electric field, which can only be maintained if there is an ongoing interfacial current, i.e. if electrochemical reactions occur. Mostly, reduction/oxidation of water will ensure the passage of this faradaic current. Unfortunately, under certain deposition conditions, the resulting gas formation at the surface may strongly influence the ability of the particles to adhere at the electrode and thus may give rise to heterogeneous deposits.[7]

An alternative solution to the above problem would be the addition of a suitable reversible redox couple to the aqueous suspension. The choice of an appropriate couple requires careful consideration: its standard potential should be located at such a position with respect to the p.z.c. of the electrode that (while the faradaic current is flowing) the actual electrodic charge has the appropriate sign and magnitude to warrant the right level of interaction with the incoming particles. In the absence of an externally applied field (no faradaic current flows), the redox couple fixes the potential difference across the interfacial region at a value $\div\pi_{\text{redox}}$ given by the

Nernst relation. Generally, this potential differs from the total potential drop $\div\pi_{\text{pzc}}$ established across the interface in the absence of electroactive species in the dispersion. When applying an external field $\div\pi_{\text{ext}}$, the reversibility of the ensuing faradaic processes taking place prevents electrolysis of water from interfering with the particle adhesion process. The difference $\div\pi_{\text{redox}}\ 4\ \div\pi_{\text{pzc}}$ fixes the electronic charge at the electrode under open circuit conditions. Variation of $\div\pi_{\text{ext}}\ 4\ \div\pi_{\text{redox}}$ (in sign as well as in magnitude) allows control of the strength of the electric field in the solution and the magnitude of the interfacial faradaic current. Supposing that the particle does not influence the surface properties of the deposition electrode (which is true only if the particle is sufficiently far from the electrode surface), the polarization/depolarization state of the electrode then depends on its chemical surface properties, on the respective magnitudes of the potential differences $\div\pi_{\text{redox}}$, $\div\pi_{\text{pzc}}$, $\div\pi_{\text{ext}}$ and on the characteristics of the redox couple (standard potential, reversibility of the electron transfer reaction at the surface of interest, diffusive transport properties, etc). The combination of all these variables determines the double layer structure at the electrode⁄suspension interface and fixes the ′-potential, i.e. the potential at the electrokinetic slip plane. In the bulk solution, outside the interfacial double layer region, the propensity for the particle to migrate is determined by the charge it carries and the strength of the electric field. In the vicinity of the electrode, that is, within the spatial range corresponding to significant overlap of the particle and electrode double layers, migration and subsequent adhesion of the particle are governed by (i) the surface properties of the particle as well as the strength of the local electric fields experienced by the particle (these fields are the strongest at the electrode surface), (ii) the ′-potential at the deposition electrode, and (iii) the possibility of regulation mechanisms of the electric properties of the interacting surfaces upon overlap of the double layers. These latter mechanisms may be electrical, chemical and/or faradaic in nature. Realizing that these considerations are far from exhaustive (e.g. induced hydrodynamic fields, particle-particle interactions at the electrode surface[8-10] were not mentioned), it is clear that EPD results from a subtle combination of electrochemical *and* colloidal phenomena, both of which play a determining role in the two basic steps of the deposition process.

Though much attention is rightly paid to the colloidal properties of the particles to be deposited (surface charge, electrophoretic mobility), those of the deposition electrode together with the electrochemical characteristics of the ongoing faradaic reactions, are generally given less attention. The work reported in this thesis therefore focuses on the double layer charging mechanisms at the conducting substrate⁄aqueous solution interface under conditions leading to polarization, whether or not followed by faradaic depolarization. Double layer properties of insulating surfaces are classically studied by electrokinetics and atomic force microscopy (AFM). These two techniques will be considered under the conditions underlined above, from both theoretical and experimental points of view.

Electrokinetics

Electrokinetic phenomena are characterized by the tangential motion of liquid with respect to an adjacent charged surface. The measured electrokinetic quantities reflect the double layer properties of the surface⁄solution interface, in particular the ˊ-potential.[11] Streaming potential is by far the most widely used experimental quantity to probe double layer properties of flat surfaces. It is the steady state potential difference generated by the flow of liquid along the charged surface in a capillary or thin-layer cell. Other techniques such as potentiometric and conductometric titration commonly adopted for electrical characterization of dispersed colloidal systems are useless since the surface area for macroscopic substrates is too low. The streaming potential technique has gained a prominent position in probing double layer properties of dielectric solid surfaces. The feasibility of the technique for conducting surfaces like metals has been questioned because the strong electronic conduction in the bulk substrate is often believed to annihilate the generation of any measurable streaming potential. As early as in the 1930's, work from the Overbeek school of colloid chemistry already highlighted the necessity of electron transfer between substrate and medium before any impact of such conduction needs to be considered.[12-14] Streaming potential data for metals can be found in the literature.[15] Conversion of these into ˊ-potentials is performed following the route usually employed for dielectric substrates,[16,17] implying that the electronic conduction of the metals is believed to be insignificant, or simply ignored. Nowadays, with the current insight into surface conduction effects on electrokinetic parameters[11] and a well-developed state of electrodic chemistry of faradaic processes,[1] it seems timely to get back to the subject and aim for a rigorous analysis. It is pertinent to add here that at the onset of the current age of micro- and nanochemistry, the kinetics of surface reactions in small channels with flowing reaction mixtures call for a comprehensive physicochemical analysis. Thus, the electrokinetic field of research as emerging from the context of electrophoretic deposition may well also provide the general basis for such new fields.

Atomic Force Microscopy (AFM)

Atomic Force Microscopy constitutes a young and powerful tool for measuring interaction forces between charged colloids.[18] A particle with known double layer properties, the so-called colloidal probe, is attached to a cantilever and made to approach the target surface with unknown double layer features.[19,20] The deviations of the cantilever due to the interactions between the surfaces are converted into a force/separation curve by means of Hooke's law. The origin of this force may be multiple. At short separation (typically in the nm scale), Van der Waals forces prevail whereas in the range of larger separation, electrical forces dominate. The total force is subjected to theoretical analysis so as to derive the surface properties of the substrate studied. As far as the electrostatic contribution is concerned, typically, trial and error is used to determine which model provides the best fit of the experimental data: i.e., either a surface charge that does not adjust during interaction (interaction at constant charge), or a surface charge that is completely relaxed during encounter (interaction at constant potential). In practice, however, chemical ion adsorption equilibria at the interfaces may lead to regulation of the double layers upon encounter.[21] This thesis presents a new approach to electrostatic interactions between two charged colloids, allowing inclusion of surface roughness and/or chemical heterogeneity. The importance of considering the exact surface topology and/or nonuniformity of the charges at the surface is justified by a plethora of experimental evidence revealing huge discrepancies between predicted and observed behaviour in coagulation analysis,[22] interaction forces,[23-25] particle depositions,[26] etc.

Outline of the thesis

The structure of the thesis is as follows. A first part treats the basic characteristics of double layers at conductor⁄solution interfaces responding to electronic and ionic surface charging processes (chapters 2-4). A second part deals with the electrokinetics of such interfacial systems (chapters 5-9) and a third part is devoted to regulation and surface roughness aspects in double layers interaction (chapters 10-11).

In **chapter 2**, a theoretical analysis is given for the double layer properties at the conductor⁄solution interface where electronic and ionic charges simultaneously govern the double layer features. We have termed such interfaces as amphifunctional since they are controlled by solution properties (pH, ionic composition, etc) as well as by an external electrical source. In **chapter 3**, the amphifunctional model is applied to the interpretation of diffuse double layer potentials as derived from atomic force data on a gold electrode using a silica colloidal probe. In **chapter 4**, the model is extended to the case where background ions contribute to the charging processes at the amphifunctional electrode surface. The case of semi-conducting electrodes is also tackled. On the basis of the modelling of the interfacial region, both adsorption properties of ions as a function of pH and externally applied potential and atomic force data on the titanium oxide surface are re-examined and interpreted. **Chapter 5** qualitatively describes the electrodic behaviour of the aluminium surface in a thin-layer cell usually employed for electrokinetic measurements. In the analysis, the electrokinetics is mimicked by a lateral electric field applied in the solution so as to highlight the possibility of interfering faradaic electron transfer between the substrate and the solution. A first-order theory based on the assumption of a linear potential distribution in the electrolyte solution exploits the monopolar electrochemical properties of the metallic substrate for interpreting the measured polarization curves. In **chapter 6**, the electrokinetics is examined for gold and aluminium surfaces in the absence or presence of a redox couple in the electrolyte solution. It is shown that electrokinetic experiments on conducting substrates are indeed feasible provided that the occurrence of faradaic depolarization is properly taken into account. **Chapter 7** proposes a theory for quantifying transversal faradaic depolarization processes induced by a lateral field applied in the thin-layer chamber of an electrokinetic cell. The analysis is carried out for the two limiting cases of irreversible and reversible electron transfer and quantifies the deviation of the potential distribution from linearity, as assumed earlier in chapter 5. **Chapter 8** analyzes the reversible faradaic processes occurring at metallic surfaces as generated by hydrodynamic tangential flow applied through a thin-layer cell. Rigorous theoretical analysis, taking into account the coupled diffusion, convection and conduction processes, results in a comprehensive description including full-scale concentration profiles of the relevant species. On the basis of this theory, streaming potentials for gold surfaces in the presence of the redox couple $\mathrm{Fe(CN)}_6^{34} / \mathrm{Fe(CN)}_6^{44}$ are analyzed in **chapter 9**. A procedure is developed for converting the measured streaming potentials into the underlying ζ-potentials. The peculiar nature of the computed ζ-potentials is discussed in terms of the chemical/electrochemical properties of the redox compounds. **Chapter 10** deals with regulation mechanisms that are effective upon approach of two interacting interfaces. The corresponding double layers are systematically described on the Gouy-Stern level, which allows transparent consideration of ionic specificity. The ensuing Gibbs energy of interaction deviates significantly from that predicted on the basis of the DLVO theory, even at relatively large separation corresponding to weak overlap of the double layers. **Chapter 11** treats interactions between heterogeneous surfaces. Using a two-gradient mean-field lattice theory, it is shown how the topology of the surfaces may be critical in determining the anisotropic electrostatics and the chemical regulation of the double layers, which together govern both the amplitude and the sign of the net interaction force. Finally, **chapter 12** summarizes the main overall conclusions from the foregoing chapters and suggests promising lines of future expansion of the field of research covered by this thesis.

In line with the importance of EPD in industrial processes, this work was part of a joint project with Philips Research Laboratories, Eindhoven, The Netherlands.

References

(1) Bard, A. J.; Faulkner, L. R. “Electrochemical Methods: Fundamentals and Applications”, John Wiley & Sons, Second Edition, New York, 2001.

(2) Delahay, P. “Double layer and electrode kinetics”, John Wiley & Sons, New York, 1965.

(3) Sarkar, P.; Nicholson, P. S. *J. Am. Ceram. Soc.* **79 (8)**, 1897 (1996).

(4) Gani, M. S. J. *J. Industrial Ceramics* **14 (4)**, 163 (1994).

(5) Sasaki, K. Y.; Tablot, J. B. *Adv. Mater.* **11**, 91 (1999).

(6) Narisawa, T.; Arato, T.; Koganezawa, N.; Shibata, M.; Nonaka, Y. *J. Ceramic Soc. Jpn.* **103**, 54 (1995).

(7) Duval, J.; de Beer, E.; Meulenkamp, E. A., Internal Report, Philips Research Eindhoven, The Netherlands, 1999.

(8) Trau, M.; Saville, D. A.; Aksay, I. A. *Langmuir* **13**, 6375 (1997).

(9) Solomentsev, Y.; Böhmer, M.; Anderson, J. L. *Langmuir* **13**, 6058 (1997).

(10) Solomentsev, Y.; Guelcher, S. A.; Bevan, M.; Anderson, J. L. *Langmuir* **16**, 9208 (2000).

(11) Lyklema, J. “Fundamentals of Interface and Colloid Science: Solid Liquid Interfaces”, Vol. II, Chapter 4, Academic Press, London, 1995.

(12) Oosterman, J., Thesis, University of Utrecht, The Netherlands, 1937.

(13) Overbeek, J. Th. G., Thesis, University of Utrecht, The Netherlands, 1941.

(14) Overbeek, J. Th. G. *Kolloidchem. Beih.* **54**, 287 (1943).

(15) Giesbers, M., Thesis, University of Wageningen, The Netherlands, 2001.

(16) Von Helmholtz, H. *Ann Phys.* **7**, 337 (1879**)**.

(17) Von Smoluchowski, M. *Bull. Int. Acad. Sci. Cracovie* 184 (1903**)**. Von Smoluchowski, M. “Handbuch der Electrizität und des Magnismus”, W. Graetz, Ed., Vol. II, Barth Leipzig, 1914, p. 366; *Z. Physik. Chem.* **92**, 129 (1918).

(18) Binnig, G.; Quate, C. F.; Gerber, C. *Phys. Rev. Lett.* **56**, 930 (1986).

(19) Ducker, W. A.; Senden, T. J.; Pashley, R. M. *Nature* **353**, 239 (1991).

(20) Ducker, W. A.; Senden, T. J.; Pashley, R. M. *Langmuir* **8**, 1831 (1992).

(21) Lyklema, J.; Duval, J. To be submitted (chapter 10 of this thesis).

(22) Vreeker, R.; Kuin, A. J.; den Boer, D. C.; Hoekstra, L. L.; Agterof, W. G. M. *J. Colloid Interface Sci.* **154**, 138 (1992).

(23) Tsao, Y.-H.; Evans, D. F.; Wennerström, H. *Science* **262**, 547 (1993).

(24) Velegol, D.; Anderson, J. L.; Garoff, S. *Langmuir* **12**, 675 (1996).

(25) Velegol, D.; Anderson, J. L.; Garoff, S. *Langmuir* **12**, 4103 (1996).

(26) Elimelech, M.; Gregory, J.; Jia, X.; Williams, R. A. “Particle Deposition and Aggregation: Measurement, Modeling, and Simulation”, Butterworth: Oxford, 1995.

Langmuir **2001,** *17,* 7573−7581

Amphifunctionally Electrified Interfaces: Coupling of Electronic and Ionic Surface-Charging Processes

Jérôme Duval,* Johannes Lyklema, J. Mieke Kleijn, and
Herman P. van Leeuwen

Department of Physical Chemistry and Colloid Science, Wageningen University, Dreijenplein 6, 6703 HB Wageningen, The Netherlands

Received June 5, 2001. In Final Form: August 13, 2001

Solid/liquid interfaces can acquire a charge by two principally different processes, i.e., by charging the interface via an external electric source or by specific adsorption/desorption of ionic species from/to the liquid. Here, we analyze the properties of electric double layers (DL) that are governed by the simultaneous functioning and coupling of these two charging mechanisms. For such interfaces, which we will denote as amphifunctional, the quantitative dependencies of the DL parameters on the electric variables and bulk composition are computed. The interface between a partially oxidized metal and an electrolyte solution is an example of an amphifunctional interface. Particular situations occur at the point of zero charge (pzc) and at the isoelectric point, which refer to specific values of the electrode potential and the pH of the solution. Limiting cases of the amphifunctional model correspond to the familiar DL behavior of either fully polarized metal/electrolyte interfaces or fully relaxed oxide/electrolyte interfaces. Our analysis can successfully be applied in the interpretation of recent atomic force microscopy force measurements on the gold/solution interface. It also allows a new approach in the understanding of the dependence on pH of the potential of zero charge of metals and the dependence on the potential of pzc (pH value) of oxide surfaces.

Introduction

For solid/solution interfaces, generally, two principally different charging processes can be distinguished.

(i) A double layer (DL) can be imposed externally. Over the range of potentials applied across the interface where no faradaic current flows, the interface is called “polarizable”. The classical representative is the mercury/aqueous solution interface. The interfacial tension or the differential DL capacitance can be measured as a function of an externally applied potential. Electrocapillary curves are obtained, which upon differentiation yield the surface charge density.[1,2] It is characteristic for such interfaces that the externally supplied electric energy gives rise to an independent term in the Gibbs adsorption equation.[3]

(ii) A DL can form spontaneously by preferential adsorption/desorption of certain types of ions. Such DLs, denoted as electrically “relaxed” or “reversible”, involve ion exchange equilibria between the surface and the medium. Typical examples are insoluble oxides, which exchange protons with the aqueous medium.[4−6] For these interfaces, the ion excess and the electric components of charge are coupled in the Gibbs equation.[7]

The difference in behavior between electrically relaxed and electrically polarized interfaces is not absolute. Mercury electrodes can become reversible at potentials where a faradaic current flows: that is, when a “depolarizer” is present. On the other hand, relaxed interfaces such as at AgI electrodes can be polarized by working at sufficiently high frequencies.[8] The present paper is concerned with interfaces at zero frequency where the two operative processes described in (i) and (ii) jointly determine DL formation. In this case, the surface charge depends on both the pH and the external potential. Our attention will be focused on systems allowing for the coupling of (i) and (ii), the interface between an oxidized metal and an aqueous electrolyte being one of them. This latter interface is often encountered in electrochemistry in fields as disparate as electrocatalysis,[9−12] electrodeposition,[13,14] corrosion,[15,16] and kinetic studies of electroactive species.[17,18] Colloid scientists encounter the full range of metal to metal oxide surfaces in contact with electrolytes. A rigorous analysis of the DL under conditions where both the metallic character and the ion exchange function are included is most timely. Recent atomic force microscopy (AFM) force measurements on such interfaces[19−22] are calling for quantitative interpretation of the DL properties.

---

[1] Gouy, G. *Ann. Chim. Phys.* **1903**, *29*, 145; *Ann. Chim. Phys.* **1906**, *8*, 291; *Ann. Chim. Phys.* **1906**, *9*, 75; *Ann. Phys.* **1916**, *6*, 3.

[2] Lippmann, G. *Ann. Phys.* **1873**, *149*, 546; *Ann. Chim. Phys.* **1875**, *5* (5), 494; **1877**, *12*, 265; *Wied. Ann.* **1880**, *11*, 316.

[3] Lyklema, J. *Fundamentals of Interface and Colloid Science*; Academic Press: London, 1991; Vol. 1, Chapter 5, p 5.94.

[4] Sears, G. W. *Anal. Chem.* **1956**, *28*, 1981.

[5] Bolt, G. H. *J. Phys. Chem.* **1957**, *61*, 1166.

[6] Heston, W. M., Jr.; Iler, R. K.; Sears, G. W. *J. Phys. Chem.* **1960**, *64*, 147.

[7] Lyklema, J. *Fundamentals of Interface and Colloid Science*; Academic Press: London, 1991; Vol. 1, Chapter 5, p 5.91.

[8] Bard, A. J.; Faulkner, L. R. *Electrochemical Methods*; Wiley: New York, 1980; Chapter 9, p 316.

[9] Raj, C. R.; Gobi, K. V.; Ohsaka, T. *Bioelectrochem. Bioenerg.* **2000**, *51* (2), 181.

[10] De Battisti, A.; Ferro, S.; Dal Colle, M. *J. Phys. Chem. B* **2001**, *105* (9), 1679.

[11] Ronconi, C. M.; Pereira, E. C. *J. Appl. Electrochem.* **2001**, *31* (3), 319.

[12] Burke, L. D.; Nugent, P. F. *Electrochim. Acta* **1997**, *42* (3), 399.

[13] Ishihara, T.; Sato, K.; Takita, Y. *J. Am. Ceram. Soc.* **1996**, *79* (4), 913.

[14] Negishi, H.; Sakai, N.; Yamaji, K.; Horita, T.; Yokokawa, H. *J. Electrochem. Soc.* **2000**, *147* (5), 1682.

[15] Kuznetsova, A.; Yates, J. T.; Zhou, G.; Yang, J. C.; Chen, X. D. *Langmuir* **2001**, *17* (7), 2146.

[16] Shih, C. C.; Lin, S. J.; Chung, K. H.; Chen, Y. L.; Su, Y. Y. *J. Biomed. Mater. Res.* **2000**, *52* (2), 323.

[17] Yukari, S.; Fujita, M.; Mizutani, F.; Uosaki, K. *J. Electroanal. Chem.* **1996**, *409*, 145.

[18] Bailey, S. I.; Ritchie, I. M.; Hewgill, F. R. *J. Chem. Soc., Perkin Trans. 2* **1983**, 645.

2. Double Layer Properties of Amphifunctional Interfaces

2.1. Description of the Amphifunctionality of the Systems Considered. The oxidized metal/electrolyte interface combines features of both relaxed and polarized interfaces, for which we shall now summarize the functional properties. Studies of relaxed oxide/electrolyte interfaces have been carried out in great detail by many authors (e.g., see refs 23−27). The charging processes for such interfaces take place via uptake or release of protons. The substrate exhibits a surface hydration leading to the formation of amphoteric hydroxyl surface groups (−MOH). The resulting surface charge (σ^0), which we shall call the protonic surface charge, derives from the acid−base interactions of the solution components with these surface groups. The relevant protolytic reactions of the −MOH groups are

$$-\mathrm{MOH}_2^+ \Leftrightarrow -\mathrm{MOH} + \mathrm{H}_\mathrm{s}^+ \quad (K_{\mathrm{a}_1}) \tag{1a}$$

$$-\mathrm{MOH} \Leftrightarrow -\mathrm{MO}^- + \mathrm{H}_\mathrm{s}^+ \quad (K_{\mathrm{a}_2}) \tag{1b}$$

for which the constants K_{a_1} and K_{a_2} ($K_{\mathrm{a}_1} > K_{\mathrm{a}_2}$) are the measures of their acidity and alkalinity. H_s^+ denotes a proton close to the surface. If we write the surface concentrations of the various species as [−MOH], [$-\mathrm{MO}^-$], and [$-\mathrm{MOH}_2^+$] in terms of molecules per unit area, σ^0 is given by

$$\sigma^0 = e([-\mathrm{MOH}_2^+] - [-\mathrm{MO}^-]) \quad (\mathrm{C\ m}^{-2}) \tag{2}$$

with e as the elementary charge.

We can define N_s, the total number of sites per unit surface area, as

$$N_\mathrm{s} = [-\mathrm{MOH}] + [-\mathrm{MOH}_2^+] + [-\mathrm{MO}^-] \quad (\mathrm{m}^{-2}) \tag{3}$$

The ensuing formulation of the variation of σ^0 with pH is known as the site-binding model.[28,29] Protons (H^+) and hydroxyl ions (OH^-) may be considered as “charge-determining”. Consequently, the pH of the solution is the primary externally adjustable variable, which together with the electrolyte concentration determines the sign and the magnitude of σ^0. Important characteristics of the amphoteric surface are the isoelectric point (iep) and the point of zero charge (pzc). In the absence of specific adsorption of ions, the iep and the pzc are equal and this pzc is sometimes called the “pristine point of zero charge” (ppzc). For that point, we have

$$\mathrm{iep} = \mathrm{pzc} = \mathrm{ppzc} = (1/2)\,(\mathrm{p}K_{\mathrm{a}_1} + \mathrm{p}K_{\mathrm{a}_2}) \tag{4}$$

In practice, the DL at the oxide/solution interface is commonly studied by titration and electrokinetics. From these data, one can estimate the parameters K_{a_1} and K_{a_2} as well as N_s by using some extrapolation procedure mentioned in the literature.[30,31]

For the nonoxidized parts of the metal surface, the surface potential does not depend on pH and is only externally applied. The surface charge depends on this potential and on the presence of specifically adsorbing ions. In practice, potentials are always given with respect to a reference state; therefore, a point of zero potential (pzp) cannot be defined. As for a relaxed interface, one speaks in terms of pzc as a reference state for the electrode surface. This common terminology used for both types of interfaces might induce some confusion since the pzc for a polarized interface refers to a potential, whereas the pzc for a relaxed oxide/solution interface is a pH value. The numerous data reported in the literature and related to the DL at the mercury electrode[32] are mostly derived from the surface tension (γ) as a function of the applied potential ($\Delta\varphi$). The $\gamma(\Delta\varphi)$ plots are called electrocapillary curves, which upon differentiation yield the excess charge on the metal σ^e. Electrocapillary curves have a pseudoparabolic shape with a maximum, known as the electrocapillary maximum. At this maximum, $\sigma^\mathrm{e} = 0$, so that automatically the pzc is obtained.

For amphifunctional interfaces, we allow the solution side of the DL to be determined by the combination of both charge-determining processes mentioned previously. This combination of electric and electrolytic surface-charging elements generates the amphifunctionality. Experimentally, investigation of the amphifunctionality can be achieved either by applying a given potential across the interface (potentiostatic experiments)[19] or by supplying to the conducting phase a known electronic charge (galvanostatic experiment) at constant bulk composition. Once equilibrium is reached, the relationships between electric and electrolytic parameters remain independent of the type of experiments used to build up the DL; that is, the state is independent of the history. The interface acquires amphifunctional behavior provided certain conditions related to the solid substrate are satisfied. These conditions are explicitly outlined below.

2.2. Nature of the Systems under Modeling. Only one of the charging processes directly depends on pH and indirectly depends on the applied potential. The protolytic sites are formed by the localized amphoteric groups (−MOH). The second type of charging is of an electronic nature, the electrons being withdrawn (or supplied) from (to) the conducting surface by an external source. This process is only indirectly dependent on pH. Therefore, for an interface to behave amphifunctionally, the solid side should either consist of (i) a metallic conductor or semiconductor partially covered with a layer of binding sites, e.g., an oxidized metal[19] or an oxidized semiconductor[33,34] (type 1), or (ii) a conductive or semiconductive phase with intrinsic surface ion binding sites, e.g., an oxide with

---

[19] Barten, D.; Kleijn, J. M.; Duval, J.; van Leeuwen, H. P.; Lyklema, J.; Cohen, S. Manuscript in preparation.

[20] Raiteri, R.; Grattarola, M.; Butt, H. J. *J. Phys. Chem.* **1996**, *100*, 16700.

[21] Döppenschmidt, A.; Butt, H. J. *Colloids Surf., A* **1999**, *149*, 145.

[22] Hu, K.; Fan, F. R. F.; Bard, A. J.; Hillier, A. C. *J. Phys. Chem. B* **1997**, *101*, 8298.

[23] Yates, D. E.; Levine, S.; Healy, T. W. *J. Chem. Soc., Faraday Trans.* **1974**, *1* (70), 8361.

[24] Healy, T. W.; White, L. R. *Adv. Colloid Interface Sci.* **1978**, *9*, 303.

[25] Bousse, L.; Bergveld, P. *J. Electroanal. Chem.* **1983**, *152*, 25.

[26] Hunter, R. J. *Foundations of Colloid Science*; Clarandon Press: Oxford, 1987; Vol. 1.

[27] Trasatti, S. *Electrodes of Conductive Metallic Oxides*; Trasatti, S., Ed.; Elsevier: Amsterdam, 1981; Vol. 11, part B.

[28] Yates, D. E.; Levine, S.; Healy, T. W. *J. Chem. Soc., Faraday Trans.* **1974**, *1* (70), 1807.

[29] Davids, J. A.; James, R. O.; Leckie, J. O. *J. Colloid Interface Sci.* **1978**, *63*, 180.

[30] Sprycha, R.; Szczypa, J. *J. Colloid Interface Sci.* **1984**, *102*, 288.

[31] Sprycha, R.; Szczypa, J. *J. Colloid Interface Sci.* **1987**, *115*, 590.

[32] Lyklema, J.; Parsons, R. *Electrical Properties of Interfaces: Compilations of Data on the Electrical Double Layer on Mercury Electrodes*; Office of Standard, Reference Data, National Bureau of Standards, U.S. Department of Commerce: Washington, DC, 1983.

[33] Gerischer, H. *Electrochim. Acta* **1989**, *34* (8), 1005.

[34] Memmimg, R. *Semiconductor Electrochemistry*; Wiley-VCH: Weinheim, 2001; Chapter 5.3.

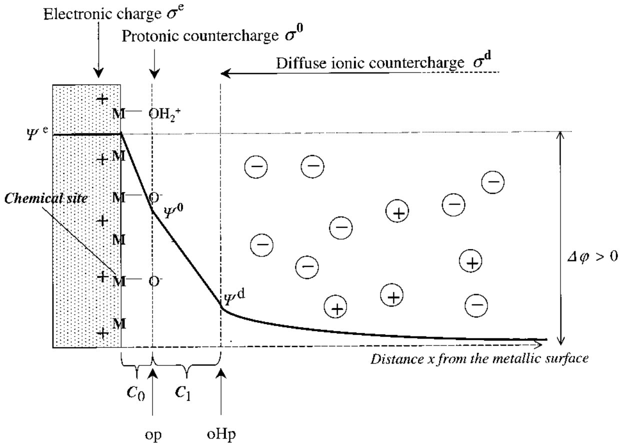
Electronic charge σ^e
Protonic countercharge σ^0
Diffuse ionic countercharge σ^d
Ψ^e
M
OH_2^+
Chemical site
O^-
Ψ^0
Ψ^d
$\Delta\varphi > 0$
Distance x from the metallic surface
C_0
C_1
op
oHp

Figure 1. Schematic representation of the DL model used to describe an amphifunctional interface between a partially oxidized metal and an aqueous electrolyte. The situation is depicted for an external potential $\Delta\varphi > 0$.

metallic conductivity or a semiconductive oxide[35] (type 2). In the frame of this paper and for the sake of illustration, the amphifunctionality potential/pH will be accounted for on the basis of a model describing the simplest situation where the amphifunctional analysis is not becoming more complex because of the occurrence of other phenomena made explicit later. Our model can be extended by taking into account the equations accounting for these phenomena.

2.3. DL Model for an Amphifunctional Interface. Figure 1 depicts a schematic representation of the structure of the DL at an amphifunctionally electrified interface between an oxidized metal and an electrolyte solution (type 1) in the case where no other ionic species than protons specifically interact with the amphifunctional surface. This latter situation will be explicitly reported in more detail subsequently[36] in connection with papers from the Russian school, which so far have been the first to point out the issue of a double mechanism of charging, albeit in the restricted context of specific adsorption of anions.[37−41] The total charge at the interface consists of the protonic charge (σ^0) and the electronic charge (σ^e), the latter supplied by the external electric source. Considering the oxidic groups as part of the substrate, in accordance with the GCS model,[42−44] the solution side of the DL is subdivided into two parts: (i) an inner part, the Stern layer, including the amphoteric sites and (ii) a diffuse layer extending from the plane of closest approach for indifferent ions (outer Helmholtz plane, oHp) into bulk solution. To avoid any confusion with the traditional meaning of the inner Helmholtz plane in the Grahame or triple layer model[45] accounting for the occurrence of specific adsorption of ions on a relaxed oxide surface, here we shall call the plane where the oxidic groups reside the oxide plane (op).

A necessary, but still not sufficient, condition for amphifunctionality is the presence of a spatial separation between the bare surface of the conducting material and the op. For interfaces of type 1, the capacitance of the layer situated between σ^0 and σ^e should be sufficiently high (thin layer of oxide) so that a significant fraction of the potential applied is operational at the solution side of the interface to allow for amphifunctionality. Thus, in that case, the amphifunctional character of the interface is defined by a submonolayer of oxide. For interfaces of type 2, one would rather speak of a metallic or semiconductive oxide layer. A further surface characteristic relevant for amphifunctionally electrified interfaces is the way in which the chemical sites are distributed over the surface. We shall assume the surface to be flat and homogeneous with the functional groups randomly distributed. Diffuse DL calculations on the basis of smeared-out charges are allowed if the potential profile is essentially independent of the position on the surface. This is the case for systems that obey

$$\ell\kappa \ll 1 \qquad (5)$$

where ℓ is the average separation between chemical sites and κ is the reciprocal screening Debye length defined by

$$\kappa = (2F^2 I/\epsilon_0\epsilon_{r_w} RT)^{1/2} \qquad (6)$$

where ϵ_0 is the dielectric permittivity of vacuum, ϵ_{r_w} is the relative permittivity of water, I is the ionic strength of the solution, F is the Faraday constant, R is the gas constant, and T is the temperature. For $\ell\kappa \geq 1$, the relevance of an equipotential op, defined by the loci of the oxygen atoms, becomes disputable and so does the monodimensionality of the DL. We shall not consider this situation.

In the following, it will be assumed that no charge transfer phenomena take place in the range of potentials investigated and that only charging/discharging of the DL occurs. Consequently, neither formation nor disappearance of oxide sites is taken into account and the parameter N_s is supposed to remain constant. This assumption is reasonable for interfaces of type 2 since the coverage rate of oxide surface is relatively high and the range of potentials where the DL is studied narrow. Some authors have summarized measured values for the surface density of protolytic sites (N_s) of surfaces densely covered by oxide groups and reported values between 2×10^{14} and 9×10^{14} sites cm^{-2}.[46] On the contrary, the lower number of oxidic sites found for interfaces of type 1[19] renders the assumption in that case more pragmatic than realistic. Indeed, one expects the surface oxidation and, hence, the oxide coverage to be in that case very sensitive to pH and to the applied potential. The interface becomes therefore reversible and polarizable with a ratio depending on the two charging parameters. The function N_s(pH, $\Delta\varphi$), $\Delta\varphi$ being the total potential difference applied across the metal/solution interphase, can be inferred from the experimental investigation of the electrochemical properties of the substrate immersed in the medium of given pH and salt concentration. We shall not discuss this complication.

---

(35) Ardizzone, S.; Trasatti, S. *Adv. Colloid Interface Sci.* **1996**, *64*, 173.

(36) Duval, J.; Kleijn, J. M.; Lyklema, J.; van Leeuwen, H. P. Manuscript in preparation.

(37) Kazarinov, V. E.; Andreev, V. N. *Elektrokhimiya* **1977**, *13*, 685; *Elektrokhimiya* **1978**, *14*, 577.

(38) Safonova, T. Ya.; Petrii, O. A.; Gudkova, E. A. *Elektrokhimiya* **1980**, *16*, 1607.

(39) Andreev, V. N.; Kazarinov, V. E.; Kokoulina, D. V.; Krishtalik, L. I. *Elektrokhimiya* **1978**, *14*, 1271.

(40) Kokarev, G. A.; Kolesnikov, V. A.; Gubin, A. F.; Korobanov, A. A. *Elektrokhimiya* **1981**, *18*, 407.

(41) Kazarinov, V. E.; Andreev, V. N.; Mayorov, A. P. *J. Electroanal. Chem.* **1981**, *130*, 277.

(42) Gouy, G. *Compt. Rend.* **1909**, *149*, 654; *J. Phys.* **1910**, *4* (9), 457; *Ann. Phys.* **1917**, *7* (9), 129.

(43) Chapman, D. L. *Philos. Mag.* **1913**, *6* (25), 475.

(44) Stern, O. *Z. Elektrochem.* **1924**, *30*, 508.

(45) Grahame, D. C. *Chem. Rev.* **1947**, *41*, 441.

(46) James, R. O.; Parks, G. A. Characterization of Aqueous Colloids by Their Electrical Double-Layer and Intrinsic Surface Chemical Properties. In *Surface and Colloid Science*; Matijevic, E., Ed.; Plenum: New York, 1982; Vol. 12, p 119.

For amphifunctional substrates exhibiting semiconducting properties, a potential drop occurs in the bulk of the material so that there are potential and charge distributions within the space charge region. We shall neglect this solid diffuse layer in the following.

In usual DL analyses, it is assumed that ions remain fully charged during the adsorption process, that is, the full ionic charges are supposed to be localized at the op. In reality, however, because of covalency involved in O−H and M−O bonds,[47] the spatial electronic density distribution is altered, which effectively means that some charge separation is generated. This notion of partial charge transfer was first suggested by Lorentz[48] in the context of specifically adsorbed halide ions at the mercury surface and further developed by Vetter and Schultze.[49] As suggested by these authors, the partial charge transfer generally depends on the externally applied potential. As a first approach, we will here construct the modeling of the DL on the basis of full ionic charges of $-MO^-$ and $-MOH_2^+$. Details of the real spatial distribution are then subsumed into the formal inner layer capacitance (C_0), which models the decay of the potential between the bare surface of the substrate and the op and also accounts for the interfacial potential jump (χ). For the sake of simplicity, we will exclusively focus on an ideally flat surface for which the potential decay is one-dimensional and where C_0 is estimated by

$$C_0 = \epsilon_0 \epsilon_{r_i}/d \quad (\mathrm{F\ m^{-2}}) \tag{7}$$

Here ϵ_{r_i} is the relative permittivity of the layer between the bare surface of the conducting substrate and the op, and d is the length of the chemical bond M−O. Equation 7 should be seen within the frame of the above modeling features. C_0 is of the order 5−10 μF cm^{-2}, roughly corresponding to a molecular condenser with a relative dielectric permittivity close to unity and a distance between the parallel planes delimiting the charge-free space of O (0.5 nm).

The total potential drop across the interface ($\Delta\varphi = RT\Delta y/F$) is given by the relation

$$\Delta\varphi = \psi^{e} - \psi^{\infty} \tag{8}$$

where ψ^{∞} is the potential of the bulk solution that is taken as the reference potential. ψ^{e} is the potential inside the bulk of the conducting phase. It is identical to the potential at the first layer of metallic atoms located in the close vicinity of the first layer of water molecules. Any deviations caused by orientation of water dipoles on the metal as well as on the solution side of the interface or induced by solid phase polarization of electronic or ionic origin are neglected. The contributions to the interfacial potentials (χ) are subsumed in C_0 taken constant, and its probable dependencies on pH and potential are therefore not taken into account.

2.4. Equations Describing the Potential and Charge Distributions at the Amphifunctional Interface. It is assumed that the capacitance (C_0) and the density of chemical sites (N_s) do not vary with the position on the surface and that eq 5 is satisfied. Then, we may consider that the electric charge and potentials are smeared-out and write the equation of electroneutrality of the complete interphase as

$$\sigma^{e} + \sigma^{0} + \sigma^{d} = 0 \tag{9}$$

where σ^{d} is the diffuse ionic charge as derived from the Gouy−Chapman theory for a 1:1 electrolyte[42,43]

$$\sigma^{d} = -(8I\epsilon_0\epsilon_{r_w}RT)^{1/2}\sinh(y^{d}/2) \tag{10}$$

with y^{d} the normalized dimensionless potential defined as

$$y^{d} = F\psi^{d}/RT \tag{11}$$

and ψ^{d} the potential at the oHp (generally approximated to the electrokinetic potential (ζ) at low ionic strength). For convenience, we shall use y^{0} for $F\psi^{0}/RT$ and y^{e} for $F\psi^{e}/RT$, with ψ^{0} being the potential at the op.

The charge-free Stern layer acts as a molecular condenser represented by a capacitance (C_1). Vorotyntsev[50] summarized results obtained by different authors concerning DL properties of "uniform" gold metal/electrolyte interfaces. For C_1, also called the Helmholtz capacitance, values between 15 and 50 μF cm^{-2} are reported, depending on the surface roughness, the degree of polycrystallinity, and the crystallographic nature of the surface considered. C_1 is generally obtained as a fit parameter of the so-called Parsons−Zobel plots derived from capacity measurements performed for different electrolyte concentrations at a given electrode charge density.[51] For an amphifunctional interface of type 1, C_1 should therefore be written as a function of pH and the applied potential, these two variables determining σ^{e}. Taking into account such a dependence does not affect the general conclusions presented here, and consequently, as a first approximation, C_1 will be considered as a constant parameter later. For interfaces of type 2, C_1 is generally found to be substantially higher (100−140 μF cm^{-2}).[52] In this latter case, C_1 is commonly also supposed constant.

The activity coefficients of the bound ionic species and protons are assumed to be independent of σ^{0}.[53] Designating x as the distance counted from the bare surface of the metal, the concentration of unbound protons beyond the oHp noted c_{H^+} is, according to the Boltzmann law, given by

$$x > x_{\mathrm{oHp}}:\ c_{H^+} = c_{H^+}^{\infty}\exp(-y(x)) \tag{12}$$

with $c_{H^+}^{\infty}$ the concentration of protons in the bulk. Equation 12 is valid for the diffuse part of the DL where the work required to bring a proton from the bulk to the position x is of a purely electrostatic nature. To adapt eq 12 to the situation of chemisorption of protons at the op, one should realize that the driving force in such a case has two contributions: an electric component that brings the proton from the bulk to the oHp and a chemical component that binds the proton at the op. The chemical work is actually expressed by the corresponding constants (K_{a_1} and K_{a_2}), which do not contain the electric contribution. Therefore, we can describe the chemisorption process via the two pertaining dissociation constants (K_{a_1} and K_{a_2}) by considering eq 12 for $y(x) = y^{0}$ as follows

---

(47) Pauling, L. *The Nature of the Chemical Bond*, 3rd ed.; Cornell University Press: Ithaca, NY, 1960; Chapter 3, p 64.

(48) Lorenz, W. *Z. Phys. Chem.* **1962**, *219*, 421.

(49) Vetter, K. J.; Schultze, J. W. *Ber. Bunsen-Ges. Phys. Chem.* **1972**, *76*, 920.

(50) Vorotyntsev, M. A. In *Modern Aspects of Electrochemistry*; Bockris, J. O'M., Conway, B. E., White, R. E., Eds.; Plenum Press: New York, 1986; Vol. 17, Chapter 2, p 177.

(51) Hamelin, A.; Foresti, M. L.; Guidelli, R. *J. Electroanal. Chem.* **1993**, *346*, 251.

(52) Yates, D. E.; Healy, T. W. *J. Chem. Soc., Faraday. Trans. 1* **1980**, *76*, 9.

(53) Chan, D.; Perram, J. W.; White, L. B.; Healey, T. W. *J. Chem. Soc., Faraday Trans. 1* **1975**, *71* (6), 1046.

$$K_{a_1} = [-\mathrm{MOH}]c^{\infty}_{\mathrm{H}^+}\exp(-y^0)/[-\mathrm{MOH}_2^+] \qquad (13)$$

$$K_{a_2} = [-\mathrm{MO}^-]c^{\infty}_{\mathrm{H}^+}\exp(-y^0)/[-\mathrm{MOH}] \qquad (14)$$

The potentials ψ^e, ψ^0, and ψ^d and the surface charges σ^e and σ^d are related via the capacitances[54] by

$$C_0 = \mathrm{d}\sigma^e/\mathrm{d}(\psi^e - \psi^0) \qquad (15)$$

$$C_1 = -\,\mathrm{d}\sigma^d/\mathrm{d}(\psi^0 - \psi^d) \qquad (16)$$

The complete set of equations (2, 3, 9, 10, and 13−16) for the potential and charge distributions at the amphifunctionally electrified interface can be rewritten in terms of one independent variable, ψ^d, for example. In the following, the notation $X(Y)$ means "X function of Y", with X a charge or a potential and Y the parameter ψ^d or $\Delta\varphi$. With constant capacitances C_0 and C_1, the transformed system of equations is

$$\psi^0(\psi^d) = \psi^d + ((8I\epsilon_0\epsilon_{r_w}RT)^{1/2}/C_1)\sinh(y^d/2) \qquad (17)$$

$$\sigma^0(\psi^d) = eN_s\frac{(c^{\infty}_{\mathrm{H}^+}/K_{a_1})\exp(-y^0(\psi^d)) - (K_{a_2}/c^{\infty}_{\mathrm{H}^+})\exp(y^0(\psi^d))}{1 + (c^{\infty}_{\mathrm{H}^+}/K_{a_1})\exp(-y^0(\psi^d)) + (K_{a_2}/c^{\infty}_{\mathrm{H}^+})\exp(y^0(\psi^d))} \qquad (18)$$

$$\sigma^d(\psi^d) = -C_1(\psi^0(\psi^d) - \psi^d) \qquad (19)$$

$$\sigma^e(\psi^d, \Delta\varphi) = C_0(\Delta\varphi - \psi^0(\psi^d)) \qquad (20)$$

from which ψ^d is found as the solution of the following transcendental equation

$$\sigma^e(\psi^d, \Delta\varphi) + \sigma^0(\psi^d) + \sigma^d(\psi^d) = 0 \qquad (21)$$

Once the relation $\psi^d(\Delta\varphi)$ is known, all of the other parameters describing the DL can be computed as a function of $\Delta\varphi$.

At this stage of the discussion, it has to be stressed that the equations established above are written in forms suitable to analyze cases where $\Delta\varphi$ is the independent electric parameter that can be fixed via an external potentiostatic source. The mathematical treatment of the galvanostatic situation would require rewriting of the equations describing the potential and charge distributions so as to obtain the relationship $\psi^d(\sigma^e)$.

For potentiostatic experiments, starting from the situation where the interface is relaxed (no external potential applied), one could conceive the influence of the applied potential on the DL formation in the following way: development of a potential difference across the interface, charging of the metallic phase by flow of electrons in the external circuit, accumulation of charge at the two sides of the interface, displacement of the adsorption equilibria, and redistribution of ions at the electrolyte side of the interface. In reality, these processes occur almost simultaneously. There is a functional relationship between the charges σ^e, σ^0, and σ^d (or the potential difference across the interface) and the structure of the interfacial region. The difficulty is to unravel this functional relationship. In the following, we shall discuss the case of a DL resulting from an externally applied potential difference, keeping in mind that the description of charging of the DL in separate steps is only relevant for explanatory purposes.

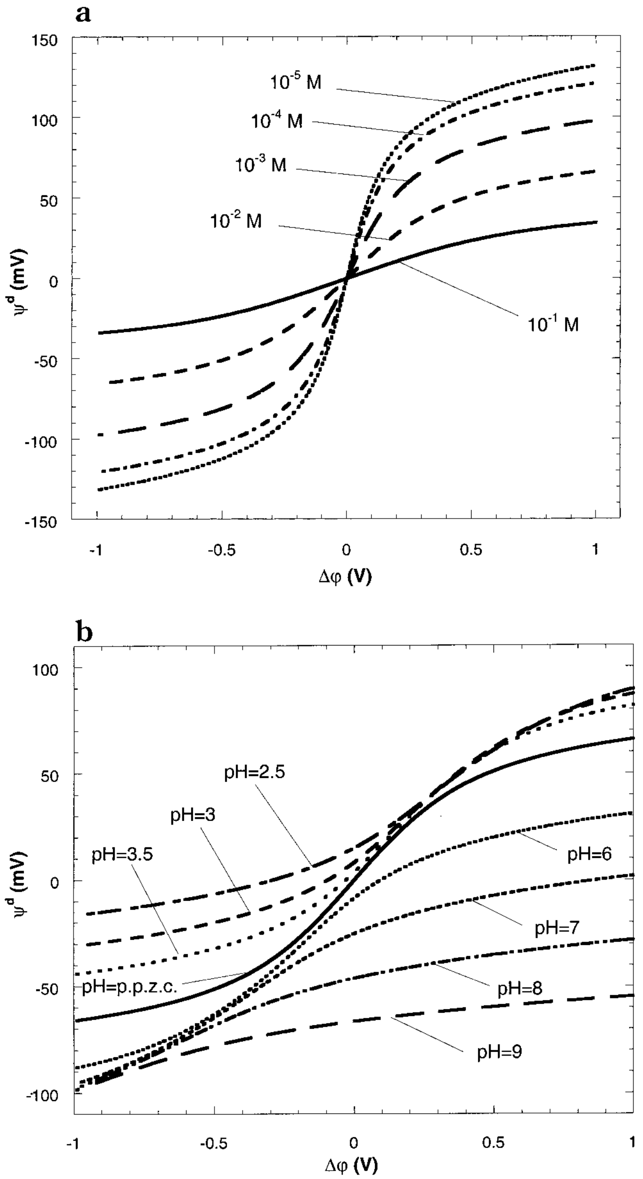

Figure 2. (a) DL potential as a function of the externally applied potential for various concentrations of indifferent electrolyte at a given pH = ppzc = 4.5. Parameters used for calculations: $\mathrm{p}K_{a_1} = 1$, $\mathrm{p}K_{a_2} = 8$, $C_0 = 5\ \mu\mathrm{F\ cm^{-2}}$, $C_1 = 30\ \mu\mathrm{F\ cm^{-2}}$, $N_s = 3 \times 10^{14}$ sites cm^{-2}. (b) Dependence on the external applied potential for various pH values at a given electrolyte concentration 10^{-2} M; ppzc = 4.5. Parameters used for calculations: same as in panel a.

2.5. Dependencies of the DL Properties on $\Delta\varphi$ and pH. Figure 2a represents ψ^d as a function of $\Delta\varphi$ for different electrolyte concentrations and at pH = ppzc. All curves are symmetrical with respect to the origin. This is so because the equations derived in section 2.4 are invariant with respect to the signs of potentials and charges when replacing the ratio $c^{\infty}_{\mathrm{H}^+}/K_{a_1}$ by $K_{a_2}/c^{\infty}_{\mathrm{H}^+}$, the latter condition resulting from our setting pH = ppzc. At a given $\Delta\varphi$, ψ^d decreases with increasing ionic strength. This is a consequence of screening of the surface charge by counterions accumulating close to the surface. For a given concentration of electrolyte, starting from the situation at $\psi^d = 0$, an increase of $\Delta\varphi$ renders the potentials ψ^d and ψ^0 positive. By externally bringing the potential

---

[54] Lyklema J. *Fundamentals of Interface and Colloid Science*; Academic Press: London, 1995; Vol. 2, Chapter 3, p 3.61.

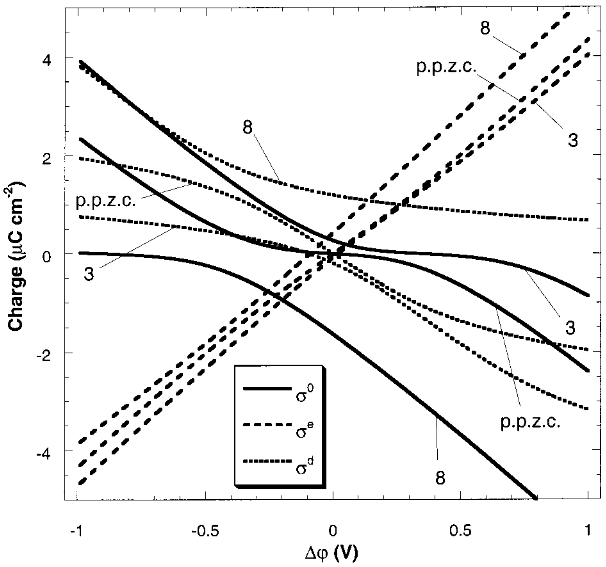

Figure 3. Dependence of the protolytic charge σ^0 (—), the electronic charge σ^e (– –), and the diffuse charge σ^d (· · ·) on the external applied potential for three pH values at 10^{-2} M; ppzc = 4.5. Parameters: same as in Figure 2.

of the metallic phase at positive values, one withdraws electrons from the conducting phase. The electronic charge therefore increases. The protolytic equilibria (a and b), which depend on $\Delta\varphi$ via the potential ψ^0, are displaced toward the formation of $-MO^-$ sites, and consequently, σ^0 decreases. In accordance with eq 10 and the dependence of ψ^d on $\Delta\varphi$, the diffuse charge σ^d becomes negative. Throughout, the electroneutrality condition (eq 21) applies. A similar reasoning can be given for $\Delta\varphi < 0$. Figures 2b and 3 show the dependencies of ψ^d and of the charges σ^d, σ^0, and σ^e on the applied potential ($\Delta\varphi$) at given interfacial adsorption conditions, electrolyte concentration, and various values of pH. As expected, the curves for pH ≠ ppzc are not symmetrical with respect to the origin. The more negative the difference (pH − ppzc) is, the more the $\psi^d(\Delta\varphi)$ curves are shifted toward positive values. Indeed, by adding charge-determining H^+ ions while maintaining a certain potential difference across the interface, the potential (ψ^0) and the protonic charge (σ^0) increase, ψ^d becomes more positive, and σ^d becomes more negative. At the given $\Delta\varphi$, the total charge $\sigma^d + \sigma^0$ is positive (if $\Delta\varphi < 0$) or negative (if $\Delta\varphi > 0$) since the inducing protonic charge (σ^0) is always larger than the resulting diffuse charge (σ^d). As a consequence, to compensate the charge $\sigma^d + \sigma^0$, the higher the pH of the solution is, the more positive the electronic charge (σ^e) is rendered. The trends of the zero-charge and zero-ψ^d points as a function of pH are analyzed in the next section.

2.6. Relationships between $\Delta\varphi$ and pH at the iep and pzc Values. For an amphifunctional interface, the situations encountered at the iep ($\psi^d = 0$) and pzc values ($\sigma^0 = 0$ and $\sigma^e = 0$) are not described by one sole parameter such as the pH for a relaxed oxide/electrolyte interface[46] or the metallic potential for a mercury/electrolyte interface[45,55] but typically by the two charge-determining variables, viz., $\Delta\varphi$ and pH.

2.6.1. Situation at the iep. Given the approximation $\psi^d = \zeta$, the condition of the iep, and the absence of specific adsorption of background electrolyte ions, it follows from eqs 18−21 that

$$\Delta\varphi_{\text{iep}}(\text{pH}) = -\frac{eN_s}{C_0}\left(\frac{(c^{\infty}_{H^+}/K_{a_1}) - (K_{a_2}/c^{\infty}_{H^+})}{1 + (c^{\infty}_{H}/K_{a_1}) + (K_{a_2}/c^{\infty}_{H^+})}\right) \qquad (22)$$

Figure 4 shows a plot of $\Delta\varphi_{\text{iep}}(\text{pH})$ for selected values of pK_{a_1} and pK_{a_2}. If the pH of the solution is brought to the value of the ppzc, the potential to apply across the interface to fulfill the condition $\psi^d = 0$ is zero. For pH < ppzc, $\Delta\varphi_{\text{iep}} < 0$; for pH > ppzc, $\Delta\varphi_{\text{iep}} > 0$. Let us define the pair ($\Delta\varphi = 0$, pH = ppzc) as the pristine starting condition for further discussion. Starting from this condition (situation A in Figure 5), when charge-determining anions are added (pH > ppzc), σ^0 as well as ψ^d become negative and the resulting σ^e becomes positive, compensating the total countercharge $\sigma^0 + \sigma^d$. In this case, one can say that σ^e is protonically induced. This is situation B given in Figure 5, where the condition $\psi^d = 0$ is no longer met. To reestablish the isoelectric situation, $\Delta\varphi$ has to be brought to positive values (situation C). At the newly reached iep, the charge at the metallic layer is more positive than in situation B since some electrons had to be withdrawn to increase ψ^e. To retain electroneutrality, σ^0 is more negative than in situation B. Similar interpretations can be given for pH < ppzc and for the situations that consist in changing $\Delta\varphi$ while keeping the pH constant. For amphifunctional surfaces characterized by K_{a_1} and K_{a_2} values of the same order of magnitude (but still obeying $pK_{a_1} < pK_{a_2}$), the pattern of the $\Delta\varphi_{\text{iep}}(\text{pH})$ plot is somewhat different from the one presented in Figure 4: the plateau region situated around the ppzc disappears and the potential $\Delta\varphi_{\text{iep}}$ changes drastically around the ppzc to reach the values $-eN_s/C_0$ and eN_s/C_0 for pH < ppzc and pH > ppzc, respectively. Further comments related to the DL at such surfaces will be given in section 2.7.1 when examining the conditions giving rise to asymptotic behavior of amphifunctional interfaces.

2.6.2. Situation at the pzc$_1$. The pzc$_1$ is defined as the condition where σ^e is zero. In this particular situation, resolution of the equations presented in section 2.5 allows us to obtain the dependence $\Delta\varphi_{\text{pzc}_1}(\text{pH})$. On the basis of the reasoning used in the previous section, the trend of the curve $\Delta\varphi_{\text{pzc}_1}(\text{pH})$ (Figure 4) can be qualitatively explained. For pH = ppzc, the situations at the iep and pzc$_1$ are similar. These correspond to the pristine condition. Situation D in Figure 5 illustrates that because of the adsorption of H^+ the dependence of pzc$_1$ on pH is opposite to that of the iep. Such a difference of behavior between pzc and iep is also encountered for relaxed oxide/electrolyte interfaces in the presence of specific adsorption.[56] In the terminology used by electrochemists, $\Delta\varphi_{\text{pzc}_1}$ is also called the "open-circuit potential". When the conducting substrate exhibits a substantial surface oxidation ($N_s > 10^{14}$ cm^{-2}), $\Delta\varphi_{\text{pzc}_1}$ tends to a Nernstian behavior with pH. The bulk properties of the material are then more oxidic than metallic, and consequently, the coupling pH/external potential is lost (see section 2.7). Most of the potential applied to the substrate decays in the insulating oxide layer so that only a small fraction of this potential remains at the op. One consequence of such a behavior is the independence of the parameter pH$_{\text{iep}}$ on $\Delta\varphi$. This was observed for a number of "metals" such as Pt.[57,58] On the contrary, metals such as gold, for which N_s is experimentally found to be lower, show a coupling pH/external

---

(55) Baradas, R. G.; Conway, B. E. *Electrochim. Acta* **1961**, *5*, 349.

(56) Lyklema J. *Fundamentals of Interface and Colloid Science*; Academic Press: London, 1995; Vol. 2, Chapter 3, p 3.107.

(57) Gileadi, E.; Argade, S. D.; Bockris J. O'M. *J. Phys. Chem.* **1966**, *70*, 2044.

(58) Kallay, N.; Torbic, Z.; Golic, M.; Matijevic, E. *J. Phys. Chem.* **1991**, *95*, 7028.

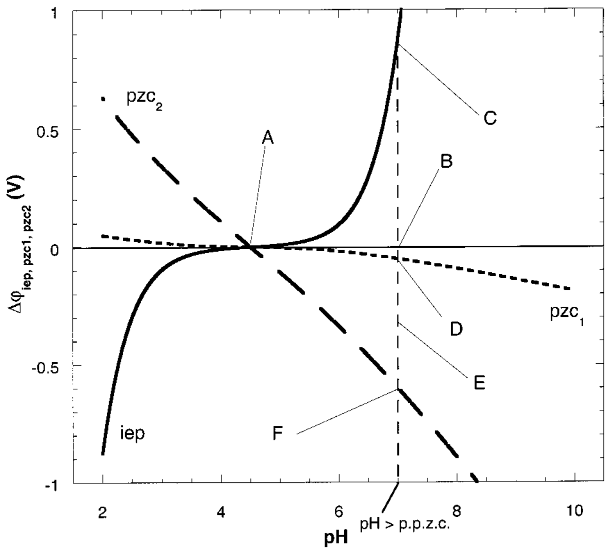

Figure 4. Plot of the potential necessary to apply across the interface to reach the iep, pzc$_1$, and pzc$_2$ as a function of pH at 10^{-2} M; ppzc = 4.5. Model parameters: same as in Figure 2. The points A–F refer to the schemes presented in Figure 5.

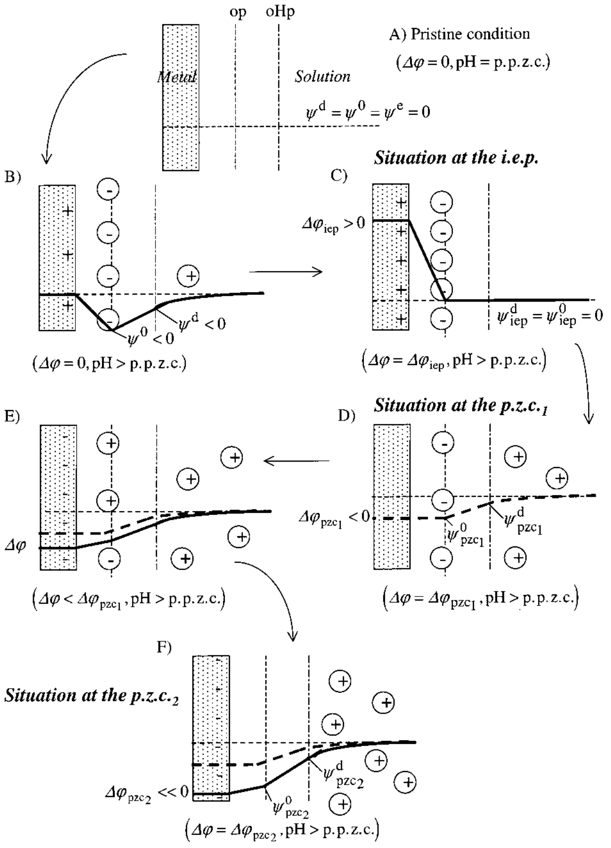
op
oHp
A) Pristine condition
($\Delta\varphi = 0$, pH = p.p.z.c.)
Metal
Solution
$\psi^d = \psi^0 = \psi^e = 0$
Situation at the i.e.p.
B)
C)
$\psi^0 < 0$
$\psi^d < 0$
($\Delta\varphi = 0$, pH > p.p.z.c.)
$\Delta\varphi_{\text{iep}} > 0$
$\psi^d_{\text{iep}} = \psi^0_{\text{iep}} = 0$
($\Delta\varphi = \Delta\varphi_{\text{iep}}$, pH > p.p.z.c.)
E)
D)
Situation at the p.z.c.$_1$
$\Delta\varphi$
($\Delta\varphi < \Delta\varphi_{\text{pzc}_1}$, pH > p.p.z.c.)
$\Delta\varphi_{\text{pzc}_1} < 0$
$\psi^0_{\text{pzc}_1}$
$\psi^d_{\text{pzc}_1}$
($\Delta\varphi = \Delta\varphi_{\text{pzc}_1}$, pH > p.p.z.c.)
F)
Situation at the p.z.c.$_2$
$\Delta\varphi_{\text{pzc}_2} << 0$
$\psi^0_{\text{pzc}_2}$
$\psi^d_{\text{pzc}_2}$
($\Delta\varphi = \Delta\varphi_{\text{pzc}_2}$, pH > p.p.z.c.)

Figure 5. Sketches representing the potential and charge distributions at the iep, pzc$_1$, and pzc$_2$ configurations. The potential profile drawn with a dashed line represents the pzc$_1$ situation.

potential, as manifest in a nonlinear behavior of $\Delta\varphi_{\text{pzc}_1}$(pH) and in a dependence $\psi^d(\Delta\varphi, \text{pH})$.[19]

2.6.3. Situation at the pzc$_2$. The relationship $\Delta\varphi_{\text{pzc}_2}$(pH) corresponding to pzc$_2$ is given by resolution of the equations describing the potential and charge distributions with $\sigma^0 = 0$. As expected, the curve $\Delta\varphi_{\text{pzc}_2}$(pH) (Figure 4) has a common intersection point with $\Delta\varphi_{\text{pzc}_1}$(pH) and $\Delta\varphi_{\text{iep}}$(pH) for pH = ppzc (pristine condition). The trend of the curve $\Delta\varphi_{\text{pzc}_2}$(pH) is similar to that for $\Delta\varphi_{\text{pzc}_1}$(pH). At a given pH, the inequality $|\Delta\varphi_{\text{pzc}_2}| \geq |\Delta\varphi_{\text{pzc}_1}|$ always applies. Indeed, starting from scheme D in Figure 5 and representing the situation occurring at the pzc$_1$ for pH > ppzc, it turns out that pzc$_2$ can only be reached by decreasing $\Delta\varphi_{\text{pzc}_1}$. This requires a decrease of σ^e, which renders ψ^d more negative and σ^d more positive. In response to the change of σ^e, the countercharge located at the op (protonic charge σ^0) becomes more positive, as can be seen in situation E. At some point, the metallic potential ψ^e is such that $\sigma^0 = 0$: at that potential, the condition defining the pzc$_2$ is fulfilled (situation F). Similar reasoning can be given for pH < ppzc. The trend of the relationship $\Delta\varphi_{\text{pzc}_2}$(pH) predicted by the model is experimentally confirmed in ref 59 for the IrO$_x$/Ti/electrolyte interface.

2.7. Limiting Behavior of the Amphifunctionally Electrified DL: Loss of the Amphifunctional Character. For conducting substrates fully covered by a layer of a nonconducting oxide, the thicker the layer is, the more $\Delta\varphi$ will be dominated by the potential drop across the oxide layer. In the limit, the potential at the op is no longer affected by $\Delta\varphi$ and the coupling between the electronic-charging and the ionic-charging mechanisms is lost.[60] This situation is generated for $C_0 \to 0$. For a purely metallic conductor, which constitutes the other known limit of the amphifunctional model ($C_0 \to \infty$), the electronic surface charge, controlled by an external source, prevails over any ionic charge-determining processes as long as no depolarizers are present. The purpose of this section is to examine these two limiting conditions where the surface is basically amphifunctional (section 2.2) but approaches monofunctionality.

2.7.1. Influence of the Acidic/Basic Character of the Surface on the Dependence $\psi^d(\Delta\varphi, pH)$. The surface has a relatively strong potential-buffering propensity when the two pK values defining the proton binding reactions are close together. This can be inferred from the influence of the pK values on the shape of the titration curves σ^0(pH, $\Delta\varphi$). In the case of an amphifunctional interface, titration of the protolytic surface groups can be performed in two ways. One may vary the pH of the solution while maintaining a constant $\Delta\varphi$. This option constitutes the pendant of the titration curve σ^0(pH) obtained for the relaxed case. It is also possible to keep the pH constant while varying $\Delta\varphi$. We will consider this latter situation for further reasoning. For a chosen set of two different pK values, the computed $\sigma^0(\Delta\varphi)$ plots exhibit two waves corresponding to the successive titrations of the $-\text{MOH}_2^+$ and $-$MOH surface species at $\Delta\varphi < \Delta\varphi_{\text{pzc}_2}$ and $\Delta\varphi > \Delta\varphi_{\text{pzc}_2}$, respectively. The range of the external potential corresponding to the plateau situated between these two waves is the more extended when the difference ($\Delta pK = pK_{a_2} - pK_{a_1}$) is larger. In the plateau regime, σ^0 is practically insensitive to variations of the external potential. Then, the countercharge required to compensate the potential-induced σ^e is mainly located in the diffuse layer. In this plateau region, ψ^d (or σ^d) is mainly affected by $\Delta\varphi$. In other words, the DL potential is badly buffered. Outside the plateau region, the large variations of σ^0 indicate that a substantial fraction of the countercharge is situated at the op. Then, variation of $\Delta\varphi$ generates only moderate change of ψ^d (or σ^d): the DL potential is buffered. Therefore, for the case where ΔpK is low and within the situation where the protonic charge is not saturated (see next section), the protolytic surface groups play the role of potential buffer: the pH at the op is practically constant

---

(59) Petrii, O. A.; Vitins, A. U. *Elektrokhimiya* **1991**, *27*, 461.

(60) Ghowsi, K.; Naghshineh, S.; Houlne, M. P. *Russ. J. Electrochem.* **1995**, *31* (12), 1259.

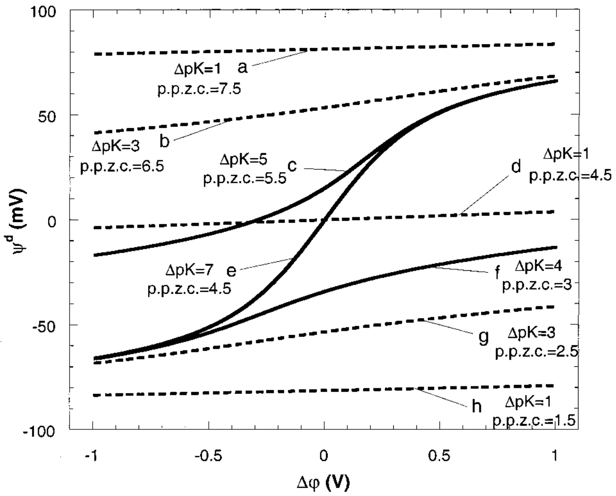

Figure 6. Dependence of the DL potential on $\Delta\varphi$ at given pH = 4.5 and salt concentration (10^{-2} M) for surfaces characterized by different ppzc. Illustration of monofunctional behavior (dashed lines) of the interface of which the DL, under certain conditions ($\mathrm{p}K_{\mathrm{a}_1}$, $\mathrm{p}K_{\mathrm{a}_2}$), is only governed by the ionic-charging process. The plain lines refer to an amphifunctional behavior of the DL. $C_0 = 5\,\mu\mathrm{F\,cm^{-2}}$, $C_1 = 30\,\mu\mathrm{F\,cm^{-2}}$, $N_s = 3 \times 10^{14}$ sites cm^{-2}. (a) $\mathrm{p}K_{\mathrm{a}_1} = 7$, $\mathrm{p}K_{\mathrm{a}_2} = 8$. (b) $\mathrm{p}K_{\mathrm{a}_1} = 5$, $\mathrm{p}K_{\mathrm{a}_2} = 8$. (c) $\mathrm{p}K_{\mathrm{a}_1} = 3$, $\mathrm{p}K_{\mathrm{a}_2} = 8$. (d) $\mathrm{p}K_{\mathrm{a}_1} = 5$, $\mathrm{p}K_{\mathrm{a}_2} = 5$. (e) $\mathrm{p}K_{\mathrm{a}_1} = 1$, $\mathrm{p}K_{\mathrm{a}_2} = 8$. (f) $\mathrm{p}K_{\mathrm{a}_1} = 1$, $\mathrm{p}K_{\mathrm{a}_2} = 5$. (g) $\mathrm{p}K_{\mathrm{a}_1} = 1$, $\mathrm{p}K_{\mathrm{a}_2} = 4$. (h) $\mathrm{p}K_{\mathrm{a}_1} = 1$, $\mathrm{p}K_{\mathrm{a}_2} = 2$.

and independent of the potential applied. The S shape of the curves $\psi^{\mathrm{d}}(\Delta\varphi)$, which is characteristic of amphifunctional behavior (Figure 2b), then tends to a horizontal line, which by changing the pH (or ppzc) at constant ppzc (pH) is shifted as explained in section 2.5 (Figure 6). For these cases where the interface loses its amphifunctional character, the absolute value of the potential-induced charge (σ^{e}) is practically equal to the induced protonic charge (σ^0). One may speak of image-inducing and/or induced charges since

$$\mathrm{d}\sigma^{\mathrm{e}}/\mathrm{d}\Delta\varphi = -\,\mathrm{d}\sigma^0/\mathrm{d}\Delta\varphi \approx C_0 \qquad (23)$$

2.7.2. Relationship $\psi^{\mathrm{d}}(\Delta\varphi, pH)$ at Saturated Surface Protonic Charge. σ^0 cannot exceed the saturation values $\sigma^0_{\mathrm{sat}} = \pm eN_{\mathrm{s}}$ whatever the conditions ($\Delta\varphi$, pH). Saturation of σ^0 can occur (i) at a given pH, when $|\Delta\varphi| \gg |\Delta\varphi_{\mathrm{pzc}_2}|$ and (ii) at a given potential $\Delta\varphi$, when pH $\gg \mathrm{pH}_{\mathrm{pzc}_2}$ or pH $\ll \mathrm{pH}_{\mathrm{pzc}_2}$. Let us, for example, examine situation (i).

DL parameters become independent of pH at extreme $\Delta\varphi$. This is illustrated by Figure 7a,b. In practice, for surfaces with relatively high N_{s}, the saturation can only be reached for $\Delta\varphi$ values that are so high that faradaic processes such as electrolysis of water and dissolution of the metal already depolarize the interface. However, for surfaces with relatively low N_{s}, saturation of the protonic charge occurs for potentials (or pH values) that do not generate per se such extreme electrochemical reactions and that therefore can be encountered experimentally. Then, $\Delta\varphi$ remains the only charge-determining parameter and for all practical purposes the interface behaves monofunctionally. The saturation values of σ^0 can be written $\sigma^0_{\mathrm{sat}} = \beta eN_{\mathrm{s}}$, with $\beta = 1$ referring to $\Delta\varphi \ll \Delta\varphi_{\mathrm{pzc}_2}$(pH) and $\beta = -1$ referring to $\Delta\varphi \gg \Delta\varphi_{\mathrm{pzc}_2}$(pH). Assuming that $\psi^0_{\mathrm{sat}}(\Delta\varphi) \gg \psi^{\mathrm{d}}_{\mathrm{sat}}(\Delta\varphi)$, a simple explicit expression for $\psi^{\mathrm{d}}_{\mathrm{sat}}(\Delta\varphi)$ can be derived:

$$y^{\mathrm{d}}_{\mathrm{sat}}(\Delta\varphi) \approx 2\,\sinh^{-1}\!\left(\frac{\kappa C_1}{4FI}\,\frac{C_0\Delta\varphi + \beta eN_{\mathrm{s}}}{C_0 + C_1}\right) \qquad (24)$$

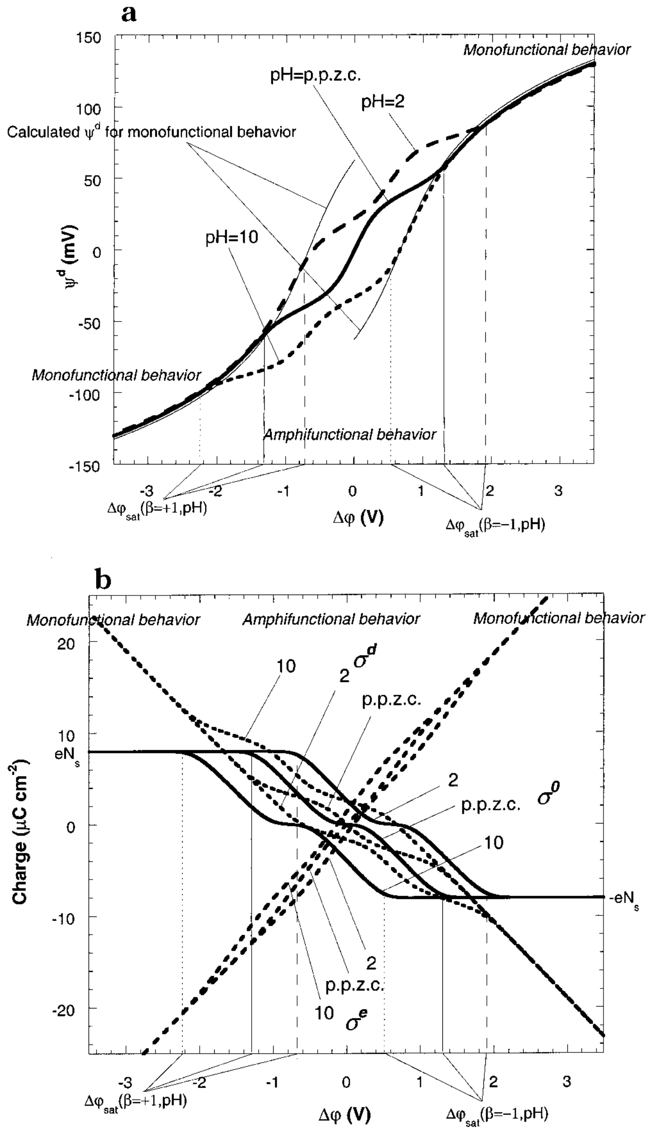

Figure 7. Representation of the potential regimes where the profile of the interface is determined by both types of charging processes (amphifunctional behavior) and where the DL is only controlled by the electric parameter (saturation regimes, monofunctional behavior). ppzc = 5.5, 10^{-1} M. (a) DL potential as a function of $\Delta\varphi$. (b) Charges as a function of $\Delta\varphi$ (same symbols as for Figure 3). Model parameters: $\mathrm{p}K_{\mathrm{a}_1} = 3$, $\mathrm{p}K_{\mathrm{a}_2} = 8$, $C_0 = 12\,\mu\mathrm{F\,cm^{-2}}$, $C_1 = 30\,\mu\mathrm{F\,cm^{-2}}$, $N_{\mathrm{s}} = 5 \times 10^{13}$ sites cm^{-2}.

The curves corresponding to eq 24 ($\beta = \pm1$) are plotted in Figure 7a. For the types of surfaces described in section 2.7.1 and for pH > ppzc or pH < ppzc, the iep situation is reached within the saturation regime of the protonic charge. Equation 24 provides $\Delta\varphi_{\mathrm{iep,sat}} = -\beta eN_{\mathrm{s}}/C_0$: this value is in accordance with eq 22. The potentials $\Delta\varphi_{\mathrm{sat}}$ ($\beta = \pm1$) required to reach the saturations of the protonic charge are equal in absolute value only for pH = ppzc and do not depend on the ionic strength.

In the domains of charge saturation, $\sigma^{\mathrm{e}}_{\mathrm{sat}}$ and $\sigma^{\mathrm{d}}_{\mathrm{sat}}$ vary linearly with $\Delta\varphi$ (see Figure 7b). One can show that

$$\mathrm{d}\sigma^{\mathrm{e}}_{\mathrm{sat}}/\mathrm{d}\Delta\varphi = -\,\mathrm{d}\sigma^{\mathrm{d}}_{\mathrm{sat}}/\mathrm{d}\Delta\varphi \approx C_0C_1/(C_0 + C_1) \qquad (25)$$

In parallel to the situation reported in section 2.7.1 (eq 23), one then may use for $\sigma^{\mathrm{e}}_{\mathrm{sat}}$ and $\sigma^{\mathrm{d}}_{\mathrm{sat}}$ the terms image-induced and/or inducing charges.

3. Conclusions

A model is proposed for a quantitative description of the DL at interfaces of which the electric properties are governed by the coupling between ionic-charging and electronic-charging mechanisms. The dependencies of the DL properties on the electric and chemical state variables (externally applied potential, pH, and salt concentration) are analyzed. Particular attention is paid to situations occurring at the iep and pzc. Under certain limiting experimental potential/pH conditions, the coupling between the two charging processes is lost. In one of these limits, the electrostatic interactions resulting from the externally applied potential outweigh the ionic-charging function. On the other hand, the latter mechanism becomes predominant when the amphifunctional surface contains protolytic surface groups that bind protons and release protons in not too different pH (and potential) ranges. From the model presented in this paper, the DL profiles at a polarized metal electrode and at relaxed oxide/electrolyte interfaces are derived as limiting cases.

The theoretical formalism described in this paper successfully interprets AFM data on the DL at a gold/solution interface examined at various externally applied potentials and various pH values.[19] Furthermore, it allows interpretation of data relating to the dependencies on pH and potential of pzc of metals and oxide surfaces, respectively. A paper currently in preparation[36] focuses on the situation of an amphifunctional interface that specifically interacts with electrolyte ions or polyions.

Glossary of Symbols

ℓ	Average separation between the chemical sites
C_0	Capacitance of the layer between the bare surface of the metal and the op
C_1	Capacitance of the Stern layer (between the op and the oHp)
$c_{\mathrm{H}^+}^{\infty}$	Concentration of protons in the bulk solution
c_{H^+}	Concentration of protons in the diffuse DL
β	Constant equal to ± 1
ϵ_0	Dielectric permittivity of vacuum
σ^{d}	Diffuse charge density
x	Distance counted from the bare surface of the metal
ζ	Electrokinetic potential
σ^{e}	Electronic charge density
e	Elementary charge
F	Faraday
R	Gas constant
χ	Interfacial potential jump
I	Ionic strength
d	Length of the chemical bond M−O
$\mathrm{p}K_{\mathrm{a}_1}$	Logarithm of the first dissociation constant K_{a_1}
$\mathrm{p}K_{\mathrm{a}_2}$	Logarithm of the second dissociation constant K_{a_2}
y^{d}	Normalized oHp potential
y^0	Normalized op potential
Δy	Normalized potential difference
y^{e}	Normalized potential of the metallic phase
ψ^{d}	Potential at the oHp
ψ^0	Potential at the op
$\Delta\varphi$	Potential difference between the bulk solid substrate and the bulk solution
ψ^{e}	Potential in the bulk metallic phase
ψ^{∞}	Potential of the bulk solution taken as a reference
σ^0	Protonic charge density
$\epsilon_{\mathrm{r_i}}$	Relative permittivity of the layer modeled by C_0
$\epsilon_{\mathrm{r_w}}$	Relative permittivity of water
κ	Screening Debye parameter
γ	Surface tension
T	Temperature
N_{s}	Total number of surface oxidic sites

Abbreviations

iep	Isoelectric point
pzc	Point of zero charge
pzp	Point of zero potential
ppzc	Pristine point of zero charge

Subscripts

sat	Pertaining to the regimes where the saturation of σ^0 is reached
iep	Pertaining to the situation $\psi^{\mathrm{d}} = 0$
pzc_1	Pertaining to the situation $\sigma^{\mathrm{e}} = 0$
pzc_2	Pertaining to the situation $\sigma^0 = 0$

Acknowledgment. Prof. Martien Cohen Stuart is acknowledged for his advice concerning the elaboration of the paper as well as for stimulating discussions. This work was carried out within the frame of a project entitled "Electrophoretic Particle Deposition", a cooperation with Philips Research Laboratories (Eindhove, The Netherlands) with financial support from SENTER (Dutch ministry of Economic Affairs).

Langmuir **2003,** *19,* 1133−1139

Double Layer of a Gold Electrode Probed by AFM Force Measurements

D. Barten,* J. M. Kleijn, J. Duval, H. P. v. Leeuwen, J. Lyklema, and M. A. Cohen Stuart

Laboratory of Physical Chemistry and Colloid Science, Wageningen University, P. O. Box 8038, 6700 EK Wageningen, The Netherlands

Received November 26, 2001. In Final Form: October 17, 2002

Colloidal probe atomic force microscopy was used to determine the electric double layer interactions between a gold electrode and a spherical silica probe. The double layer properties of the gold/solution interface were varied through the pH and salt concentration of the electrolyte, as well as by externally applying an electric potential. The double layer potentials ψ^d of the gold surface were obtained by fitting the force−distance curves according to the DLVO (Derjaguin−Landau−Verwey−Overbeek) theory, using earlier obtained values for the double layer potential of the silica probe as input parameter. It was found that the gold electrode combines the features of reversible and polarizable interfaces; i.e., its charge and potential are determined by both the solution pH and the external potential. The pH dependence is attributed to proton adsorption and desorption from oxidic groups on the gold surface. In the potential range studied, ψ^d varies linearly with the applied potential; the variation in ψ^d is roughly 10% of that in the applied potential. The potential of zero force (the external potential at which $\psi^d = 0$) varies with pH. The various features of the gold/electrolyte interface are described well by an amphifunctional double layer model. The results of this study form the basis of the interpretation of adsorption studies on gold as a function of pH and externally applied potential.

Introduction

The adsorption from aqueous solution of charged molecules such as ionic surfactants, polyelectrolytes, and proteins is commonly found to be influenced by the solution pH and background electrolyte concentration.[1−4] This is generally explained by the effect of the solution properties on the potential of the sorbent surface on one hand and, for (weak) polyelectrolytes and proteins, by changes in the charge, structure, and structure stability of the adsorbing molecules on the other hand. To discriminate between these effects, Bos et al.[5] have studied the adsorption of several proteins on indium tin oxide (ITO) as a function of an *externally* applied potential at the adsorbing interface, while keeping the solution properties constant. It was found that variation of the external potential has little or no effect on protein adsorption at ITO, in contrast to the pronounced influence of the pH.

This observation can be explained in two different ways: (1) the large effect of the solution pH on the adsorption behavior of the studied proteins stems mainly from conformational changes within the protein or changes in the protein charge as a result of the solution pH and not so much from changes in the potential of the sorbent surface, or (2) the major part of the externally applied potential difference over the electrode/solution interface is not felt by molecules in solution. Indeed, Hu et al.[6] showed that for TiO_2, like ITO a semiconducting oxide, the influence of an applied potential on the diffuse double layer potential is very limited, typically less than 10% of the applied potential. It is clear that for interpretation of the adsorption as a function of externally applied potential additional information on the double layer in solution as a function of applied potential is required.

For further adsorption studies we have chosen gold as the sorbent because it is a metallic conductor and over a relatively large potential range no electrochemical surface reactions occur in contact with an aqueous solution. Earlier studies[7,8] have shown that the double layer potential of gold is dependent on the pH of the electrolyte solution. For a pristine metal surface, one would not expect this. In the case of gold it is probably due to adsorption and partial discharge of hydroxyl ions upon contact with aqueous solution, resulting in oxidic surface sites on the gold.[8,9] The protolytic activity of these sites is responsible for the pH dependency of the double layer potential.

In this paper we present results concerning the double layer properties of the gold/electrolyte interface as a function of both solution properties and externally applied potentials. Our goal is to elucidate the mechanism that determines the double layer charge and potential when a potential is externally imposed as compared to the situation in which the double layer is reversibly built up by spontaneous exchange of ions with the solution. This allows a better understanding of the role of electrostatics in adsorption phenomena and the possibilities for manipulating the adsorption of charged macromolecules by applying an external potential to the interface.

A way of studying the effect of externally applied potentials on the solution part of the double layer is to

---

* Correspondimg author. Telephone: +31-317-482189. Fax: +31-317-483777. E-mail: desiree.barten@fenk.wag-ur.nl.

(1) Haynes, C. A.; Norde, W. *Colloids Surf., B* **1994**, *2*, 517.

(2) Kleijn, J. M.; Norde, W. *Heterogeneous Chem. Rev.* **1995**, *2*, 157.

(3) Burns, N. L.; Holmberg, K.; Brink, C. *J. Colloid Interface Sci.* **1996**, *178*, 116.

(4) Giacomelli, C. E.; Avena, M. J.; Depauli, C. P. *J. Colloid Interface Sci.* **1997**, *188*, 387.

(5) Bos, M. A.; Shervani, Z.; Anusiem, A. C. I.; Norde, W.; Kleijn, J. M. *Colloids Surf., B* **1994**, *3*, 91.

(6) Hu, K.; Fan, F. F.; Bard, A. J.; Hillier, A. C. *J. Phys. Chem. B* **1997**, *101*, 8298.

(7) Giesbers, M.; Kleijn, J. M.; Cohen Stuart, M. A. *J. Colloid Interface Sci.* **2002**, *248*, 88.

(8) Thompson, D. W.; Collins, I. R. *J. Colloid Interface Sci.* **1992**, *152*, 197.

(9) Angerstein-Kozlowska, H.; Conway, B. E.; Hamelin, A.; Stoicoviciu, L. *J. Electroanal. Chem.* **1987**, *228*, 429.

perform force measurements between the electrode and a reference surface in aqueous solution. Hieda et al.[10] used an atomic force microscope (AFM) to measure the interactions between a gold-coated microsphere tip and an oxidized silicon sample with their interfacial potentials independently controlled using a bipotentiostat. Bard and co-workers[6,11,12] characterized the double layer properties of gold and TiO_2 electrodes in aqueous electrolyte by using a spherical silica particle attached to an AFM cantilever to probe the electric double layer interactions. Recently, Fréchette and Vanderlick[13] designed a gold electrode for use in the surface force apparatus (SFA) and studied the forces between mica and gold under potentiostatic control. Here, we have applied the same method as Bard and co-workers: the interaction between a gold substrate and a silica probe has been measured using an AFM, and from the force−distance curves the double layer potential of the gold surface was obtained by fitting these according to DLVO theory (Derjaguin and Landau[14a−c] and Verwey and Overbeek[14d]). The double layer potential of the silica probe was used as an input parameter, for which we used values determined by Giesbers et al.[7,15] from silica−silica interactions as a function of pH. For practical reasons in the present study the gold substrate is a gold wire. In our adsorption studies, measurements are performed on a reflectometer in which gold-coated silicon wafers are used as the substrate.

As an extension to the work of Hillier et al.,[11] which focused on specific adsorption of halide ions on gold as a function of applied potential, we have measured the interactions as a function of both the applied potential and the pH of the solution. As background electrolyte we used KNO_3, which is considered to be indifferent in this system. The double layer potentials determined from fitting the force curves are quantitatively interpreted in terms of an amphifunctional double layer model developed in our group.[16] This model considers the simultaneous effects of the electronic charge and the protolytic charge, and has recently been extended to also account for specific adsorption.[17] Earlier, Hu et al.[6] have measured the pH dependence of double layer interactions between a TiO_2 electrode and a silica probe, but this was only done at the open circuit potential. Here we provide a two-dimensional data set, i.e., plots of the double layer potential as a function of applied potential over a wide range of pH values. Finally, it is shown that the roughness of the gold surface (on the dimensional scale of the diffuse double layer thickness) is an important factor in the experimental determination of the double layer potential.

In a forthcoming paper we will report on the adsorption of a cationic polyelectrolyte (polyvinylpyridinium, PVP^+) on gold as a function of pH and applied potential, using the results obtained here concerning the variations in double layer potential to interpret the changes in adsorption kinetics and adsorbed amounts.

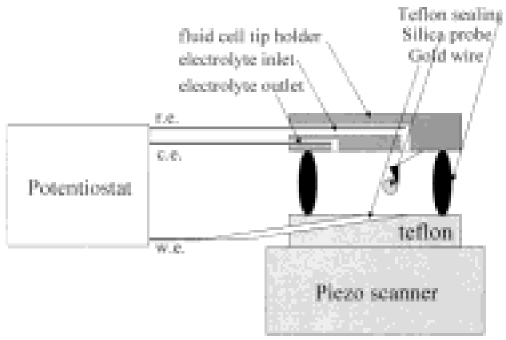

Figure 1. Schematic representation of the experimental setup. c.e. = counter electrode; r.e. = reference electrode; w.e. = working electrode.

Experimental Section

Materials and Methods. The force−distance measurements in this study were performed using a DI (Digital Instruments Inc., Santa Barbara, CA) Nanoscope III atomic force microscope equipped with a standard fluid cell and a piezo scanner "E" (x, y range 12.5 μm × 12.5 μm).

Silica spheres of 6 μm diameter, which were a gift from Philips Research Laboratories (Eindhoven, The Netherlands), were glued to the "wide-legged" 200 μm long standard contact mode cantilevers with integrated tip (Digital Instruments Inc., Santa Barbara, CA). The glue used for this purpose was an epoxy resin, Epikote 1004 (Shell Amsterdam, The Netherlands) which has a melting point of about 100 °C and is highly insoluble in water. The method used to glue the particles to the cantilever tips has been described by Hillier[11] and Giesbers.[15] Just prior to the experiments the cantilevers with attached silica spheres were cleaned in a plasma cleaner (Model pdc 32G, Harrick Scientific, New York) for 30 s.

After each series of measurements the cantilever spring constant was determined. Calibration of the cantilevers was performed following the Cleveland method.[18] According to this procedure, particles of known size and density are attached to the free end of the cantilever and the spring constant k is determined from the resulting shift of the cantilever's resonance frequency.

Flat gold electrode surfaces were obtained by polishing one end of a gold wire with a cross section of 2 mm^2, held in a Teflon sample holder, with a slurry of 40 nm silica particles in water (OP-U suspension, Struers bv, Denmark). After polishing, the surface was ultrasonically cleaned in ultrapure water (EASYpure UV (Richard van Seenus Technologies bv, Almere, The Netherlands), specific resistance 18.3 MΩ cm) to remove the silica particles left by the polishing treatment. This resulted in relatively flat gold surfaces containing areas with a peak-to-valley distance of less than 5 nm over an area of 0.1 μm^2, as determined by AFM imaging in the contact mode with a standard nitride tip. Force measurements were performed at selected positions where the gold surface was relatively flat. To select such positions, the gold surface was scanned with the silica probe.

The other end of the gold wire was connected to a potentiostat (Model 2059, AMEL s.r.l., Milan, Italy). A platinum counter electrode and a Ag/AgCl (in 3 M KCl) reference microelectrode were put into the inlet and outlet of the AFM fluid cell and connected to the potentiostat. A schematic representation of the experimental setup is shown in Figure 1.

Aqueous electrolyte solutions were prepared from analytical grade KNO_3 in ultrapure water. Prior to each experiment nitrogen was bubbled through the solution for at least 30 min to deaerate the solution and to remove dissolved CO_2 which would decrease the pH. Approximately 10 mL of the solution was rinsed through the AFM cell, after which the inlet and outlet of the cell were closed. Three types of measurements were performed: double layer interactions between the silica probe and the gold substrate (1) as a function of salt concentration, (2) as a function of the

---

(10) Hieda, H.; Ishino, T.; Tanaka, K.; Gemma, N. *Jpn. J. Appl. Phys.* **1995**, *34*, 595.

(11) Hillier, A. C.; Kim, S.; Bard, A. J. *J. Phys. Chem.* **1996**, *100*, 18808.

(12) Wang, J.; Bard, A. J. *J. Phys. Chem. B* **2001**, *105*, 5217.

(13) Fréchette, J.; Vanderlick, T. K. *Langmuir* **2001**, *17*, 7620.

(14) (a) Derjaguin, B. *Trans. Faraday Soc.* **1940**, *36*, 203. (b) Derjaguin, B. V.; Landau, L. D. *Acta Phys. Iochim.* **1941**, *14*, 633. (c) Derjaguin, B. V.; Landau, L. D. *J. Exp. Theor. Phys.* **1941**, *11*, 802. (d) Verwey, E. J. W.; Overbeek, J. T. G. *Theory of the Stability of Lyophobic Colloids*; Elsevier: New York, 1948.

(15) Giesbers, M. Thesis Wageningen, The Netherlands, 2001.

(16) Duval, J.; Lyklema, J.; Kleijn, J. M.; van Leeuwen, H. P. *Langmuir* **2001**, *17*, 7573.

(17) Duval, J.; Kleijn, J. M.; Lyklema, J.; van Leeuwen, H. P. *J. Electroanal. Chem.* **2002**, *532*, 337.

(18) Cleveland, J. P.; Manne, S.; Bocek, D.; Hansma, P. K. *Rev. Sci. Instrum.* **1993**, 403.

solution pH [(1) and (2) were under open circuit conditions]; and (3) as a function of the applied potential, for several fixed pH values.

In the first series of measurements, the potential of the gold surface is determined by its equilibrium with the solution (open circuit potential). The pH was not adjusted; after deaeration for at least 30 min with nitrogen the pH was between 6.1 and 6.4. The series were started at the lowest salt concentration. After percolating the KNO_3 solution through the AFM cell and equilibration for 15 min, continuous force measurements with a measuring frequency of 1 Hz were started.

In the second series of measurements the sample and electrodes were connected to a voltmeter to measure the open circuit potential (OCP) as a function of the pH. In these measurements the pH was adjusted by adding aliquots of aqueous solutions of KOH or HNO_3. The experiments were performed as described above. At low pH, the system did not reach equilibrium until after about 1 h; the OCP of the gold slowly changed from +100 mV to a value of +220 mV (vs Ag/AgCl reference electrode). We waited until it shifted by less than 1 mV in 15 min.

Several series of measurements of the double layer interaction as a function of the applied potential were performed in 1 mM KNO_3 solution, each at a fixed pH. After rinsing the cell with the solution, and closing it, the sample, reference electrode, and counter electrode were connected to the potentiostat. A voltammogram of the system was recorded to check the electric circuit and the functionality of the gold electrode. Subsequently an external potential was applied, and after 10−15 min continuous force curves were measured with a measuring frequency of 1 Hz.

Determination of the Double Layer Potential of the Gold Surface from the Force Curves. During the acquisition of a force curve, the measured experimental parameters are the output signal of the photodiode (in volts) which is directly related to the tip deflection. This can be calibrated by comparing the detector signal to the piezo displacement in the constant compliance region and the substrate displacement in nanometers. These data are converted into a normalized force (F/R) vs separation curve by use of the cantilever spring constant and the probe radius R. The onset of the constant compliance region is taken as the point of first contact and the point of zero separation ($r = 0$) in the DLVO fits.

According to DLVO theory the Gibbs interaction energy between two surfaces is given by the sum of the van der Waals and electrostatic interaction Gibbs energies. In the present work the electrostatic interaction between two parallel dissimilar surfaces is calculated using the nonlinear Poisson−Boltzmann equation for the diffuse double layer in a symmetrical (z:z) electrolyte solution (see, e.g., refs 11, 19, and 20). Since this equation is one-dimensional, it applies to flat surfaces or relatively large colloidal particles only ($\kappa R \gg 1$, κ^{-1} being the Debye length and R the radius of the particle). In our system κR varies from about 100 to 1000 for electrolyte concentrations between 1×10^{-4} and 1×10^{-2} M, so this condition is satisfied. The nonretarded equation according to Hamaker has been used to calculate the van der Waals interaction. For a detailed treatment of van der Waals forces between two macrobodies, see, e.g., ref 21.

Interaction curves were solved numerically for the boundary conditions of both surfaces at constant potential as well as for both surfaces at constant charge, using a computing program of Hillier.[11] From the total Gibbs energy G_{tot} as a function of the separation distance r between two flat plates, the normalized interaction force $F(r)/R$ was obtained for a sphere of radius R and a flat plate using Derjaguin's approximation:[22]

$$\frac{F(r)}{R} = 2\pi G_{tot}(r) \tag{1}$$

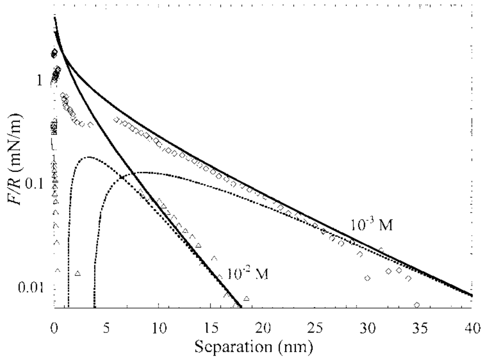

Figure 2. Force−distance curves for a silica sphere (6 μm diameter) interacting with a gold electrode in KNO_3 solutions of concentrations as indicated at room temperature and pH ~6.4, at the open circuit potential. Data points correspond to the measurements. The dotted lines denote the numerical solutions of the nonlinear Poisson−Boltzmann equation under the condition of both surfaces at constant surface potential. The solid lines are the fits for both surfaces at constant surface charge.

The calculated force curves were fitted to the experimental ones choosing the double layer potential (ψ^d) of the gold substrate and the Debye length (κ^{-1}) as the fit parameters. Generally, the resulting Debye length agreed with the value calculated from the bulk electrolyte concentration. The double layer potential of the silica probe at various salt concentrations and pH values was taken from Giesbers et al.[7,15] and used as an input parameter in the fitting of the double layer potential of the gold.

From previous measurements in our laboratory on symmetric systems (silica−silica and gold−gold), it is known that both silica and gold surfaces exhibit a certain degree of charge regulation; i.e., interaction curves are between the two limiting cases of constant diffuse charge and constant diffuse potential surfaces. Here, the *measured double layer potential* $\psi^{d}_{measured}$ was taken as an average value of the two double layer potentials calculated for these two limiting cases, which never differ more than 5 mV.

Generally, fits were performed using a Hamaker constant for the gold−water−silica system of 5.7×10^{-20} J.[21] However, van der Waals forces may be obscured by hydration forces and surface roughness as discussed by Giesbers et al.[7] It should be noted that the surface roughness was not necessarily constant, because the gold sample was polished anew before every series of measurements. van der Waals forces are most pronounced at a distance of a few nanometers from the surface. At a salt concentration of 10^{-3} M, the fitting of the force curve on the basis of DLVO theory mostly refers to the region at 10−40 nm from the surface, where the contribution of van der Waals forces is very small. At the higher salt concentrations, however, the Debye length is so small that a large part of the potential drop takes place in the first 10 nm where the van der Waals forces do count. Especially here it is evident that van der Waals forces are considerably less than expected on the basis of the Hamaker constant for the ideally planar gold/water/silica system. Therefore, those force curves were fitted without the van der Waals contribution to the total Gibbs energy. At the lower salt concentrations, fitting with or without van der Waals forces was found not to be crucial for the resulting value of the double layer potential, the differences being on the order of a few millivolts.

Results and Discussion

Double layer interactions of the gold electrode with the silica probe were measured at various salt concentrations. Figure 2 gives representative examples of the force/distance curves obtained at two KNO_3 concentrations, at neutral pH and without external potential. Only the approach curves are shown, since upon retraction the double layer interactions are somewhat obscured due to adhesion, which makes the corresponding force curves less suitable for fitting with double layer theory. The double layer potential at zero separation ($\psi^{d}_{measured}$) cal-

---

(19) Hiemenz, P. C. In *Principles of Colloid and Surface Chemistry*; Lagowski, J. J., Ed.; Marcel Dekker: New York and Basel, 1986; Vol. 4, Chapter 12.

(20) Hunter, R. J. In *Foundations of Colloid Science*; Oxford University Press: Oxford, 1987.

(21) Lyklema, J. In *Fundamentals of Interface and Colloid Science*; Academic Press: London, 1991; Vol. I, sections 4.6 and 4.7.

(22) Derjaguin, B. V. *Kolloid-Z.* **1934**, *69*, 155.

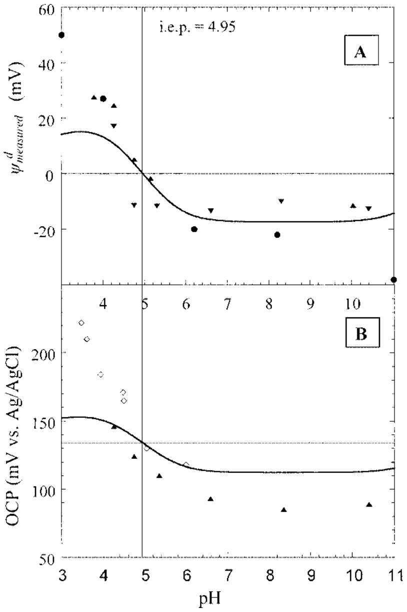

Figure 3. (A) Double layer potentials ($\psi^{d}_{\mathrm{measured}}$) of the gold/electrolyte interface in 1 mM KNO_3 with respect to the solution as calculated from DLVO theory and the measured AFM force−distance curves. The isoelectric point is at pH 4.95 ± 0.15. ▼ = $\psi^{d}_{\mathrm{measured}}$, measured in a series from pH 10 to pH 4. ▲ = $\psi^{d}_{\mathrm{measured}}$, measured from pH 3.5 to pH 10. ■ = data of Giesbers et al. for a gold-coated silicon wafer in 1 mM KCl.[7] The solid curve gives the best fit of the amphifunctional model with $N_s = 0.8 \times 10^{12}$ sites/cm^2. (B) Open circuit potential (OCP) with respect to a Ag/AgCl reference electrode as a function of pH in 1 mM KNO_3. ▼ = OCP measured in a series started at pH 10; ◇ = OCP when started with a fresh surface for each pH.

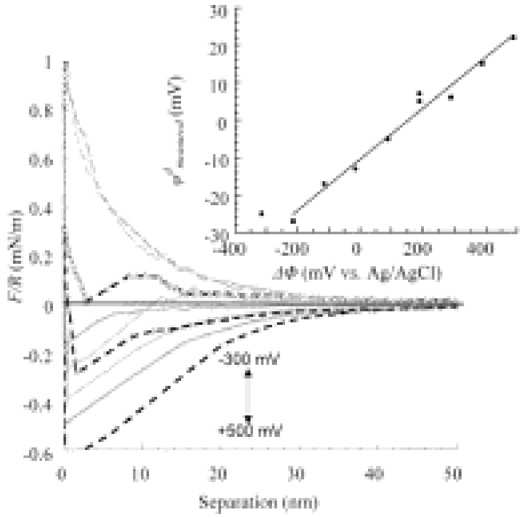

Figure 4. Force curves obtained at different externally applied potentials of gold in 1 mM KNO_3 at pH 4.7. The inset shows the corresponding $\psi^{d}_{\mathrm{measured}}$ values calculated from AFM measurements using DLVO theory. ΔΦ changed in steps of 100 mV.

culated from these fits is −16 mV at 10^{-3} M KNO_3 and −12 mV at 10^{-2} M KNO_3. The decrease in double layer potential with increasing salt concentration is due to screening effects. The fitted values for the Debye length (κ^{-1}) were 9.2 and 3.6 nm, respectively. The Debye lengths calculated from the electrolyte concentrations are 9.6 and 3.0 nm, respectively.

Double Layer Potential of Gold as a Function of pH. For pH values in the range of 3.5−10.5 gold/silica interaction curves and the OCP values of the gold electrode (with respect to a Ag/AgCl reference electrode) were measured simultaneously. The higher salt concentration of the solution due to the adding of HNO_3 or KOH was accounted for in the DLVO fits. The results of the fits are plotted as a function of pH in Figure 3A. This diagram illustrates that ψ^d shows a steep change (30 mV/pH) in the range of pH 3−5. The isoelectric point of the gold surface, i.e., the pH for which $\psi^d = 0$, is at pH 4.95 ± 0.15. At higher pH, ψ^d levels off to a value of −17 mV.

We used solutions of KNO_3, which is generally considered to be an indifferent electrolyte on gold, as supporting electrolyte. Giesbers et al.[7] used solutions of potassium chloride (chloride ions are known to form complexes on the gold surface) to perform similar measurements. The ψ^d values obtained by Giesbers are slightly more negative than those presented in this work. However, the differences between the two data sets (Figure 3A) are so small as to be nearly within experimental error.

The OCP, measured simultaneously with the double layer potential, is given in Figure 3B. Going from high to low pH, the OCP values were approximately the same as those obtained when measurements were started with a fresh surface for every pH. In one case hysteresis was observed, in that upon going from low to high pH OCP values were found to be different from those given in Figure 3B. This observation could not be reproduced in measurements outside the AFM cell and was not considered any further. The trends of Figures 3A and 3B are similar, but quantitatively the variation in the measured ψ^d is much lower than in the OCP. This is because by AFM measurements only a (diffuse) part of the double layer is seen.

Double Layer Potential of Gold at Externally Applied Potential. At various pH values the potential (ΔΦ) applied to the gold/solution interface was varied, keeping the salt concentration and pH constant. Figure 4 shows a typical set of force curves measured at pH 4.7. The inset shows ψ^d, obtained from fitting the force data to double layer theory. An overview of the ψ^d values obtained as a function of ΔΦ at all pH values studied is given in Figure 5A. The lines in this picture are only meant to guide the eye. It can be seen from this picture that ψ^d is determined by both the solution pH and the externally applied potential.

The variations in double layer potential found by either changing the solution pH or applying an external potential are in the same order of magnitude. Both effects are rather small—a change of several tens of millivolts in the potential and pH range studied. This is in line with the results of Hillier et al.[11] and Wang and Bard.[12] Fréchette and Vanderlick,[13] however, have found a larger spread in double layer potential of ca. 150 mV over an external potential range of 400 mV.

With respect to adsorption studies, it should be noted that molecules adsorbing on the surface experience the double layer potential on a much smaller length scale than the radius of the colloidal probe. Since the gold substrate is polycrystalline and has a certain degree of surface roughness, the *local* potential can differ substantially from the smeared-out diffuse double layer potential as experienced by the colloidal probe. The various low index faces of gold crystals exhibit different potentials of zero charge (see, e.g., ref 23 and references therein). The effect of surface roughness is outlined below.

Analysis in Terms of an Amphifunctional Double Layer Model. The dependency of ψ^d on both the pH and

---

[23] Hamelin, A.; Vitanov, T.; Sevastyanov, E. S.; Popov, A. *J. Electroanal. Chem.* **1983**, *138*, 225.

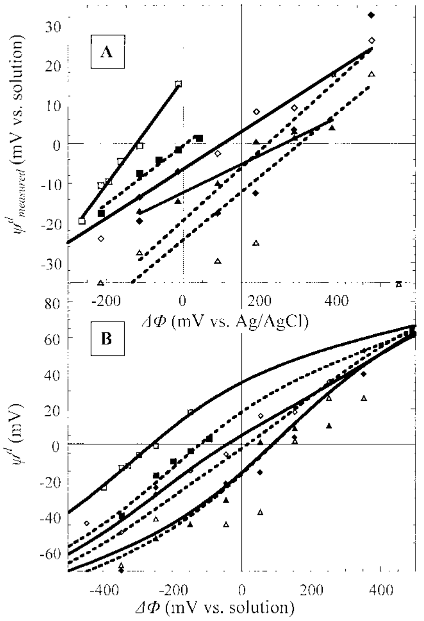

Figure 5. (A) Double layer potential ($\psi^{d}_{\text{measured}}$) as a function of applied potential ($\Delta\Phi$) at different pH values: □, pH 3.5; ■, pH 3.9; ◇, pH 4.7; ◆, pH 5.1; △, pH 6.4; ▲, pH 6.8. The lines are only meant to guide the eye. (B) Identical to (A), here the data are adjusted as described in the text and the curves are fits according to the amphifunctional double layer model.

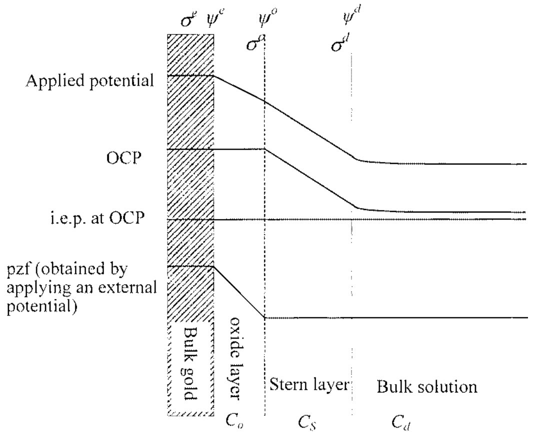

Figure 6. Schematic representation of the potentials and charge distribution at the gold/electrolyte interface used in the amphifunctional double layer model.

the external potential was analyzed using the model developed by Duval et al.[16] This model combines the two charging mechanisms of the electrode/solution interface, i.e., charging by an external electric source and by adsorption/desorption of protons from/to the liquid. A somewhat similar model has been proposed by Smith and White[24] to describe the voltammogram of an electrode covered by a complete monolayer of molecules containing an acid group.

In the model the distribution of charge is assumed to be smeared out over the gold surface. Here, we do not consider specific adsorption of ions from the electrolyte solution onto the gold. Briefly, the electric double layer is modeled to consist of four elements, as schematically represented in Figure 6. The first corresponds to the bulk of the gold substrate. The second is a layer with oxidic binding sites for protons on the gold (referred to as the oxide layer). The third element is the Stern layer, and the fourth is the diffuse part of the double layer. The solution side of the double layer (the Stern layer and the diffuse double layer) is described by classical GCS (Gouy−Chapman−Stern) theory. The pH dependence of the surface charge is described by a two pK site-binding model. Since gold is a metallic conductor, the potential of the gold is constant throughout the entire bulk of the gold, up to the oxide layer. To calculate the potential drop over the oxide layer due to an externally applied potential, this layer is modeled as being a charge-free dielectricum.

We used this so-called amphifunctional model to calculate ψ^d as a function of the solution properties and the externally applied potential. For more details on the model and calculations demonstrating the coupling between the two charging mechanisms and limiting cases, the reader is referred to the original paper of Duval et al.[16]

To fit a series of measurements at different pH values in the absence of a polarizing potential according to the amphifunctional double layer model, the only parameter to be chosen is the capacitance of the Stern layer C_s. In a review on the gold/solution interface, Vorontynsev[25] gives values between 15 and 50 μF/cm^2 for C_s, from which we have chosen 30 μF/cm^2 as an average value. The number of proton binding sites (N_s), which determines the maximum charge density on the surface, and the pK values for the reactions

$$-\mathrm{MOH_2}^+ \overset{K_1}{\rightleftharpoons} -\mathrm{MOH} + \mathrm{H}^+ \tag{2a}$$

$$-\mathrm{MOH} \overset{K_2}{\rightleftharpoons} -\mathrm{MO}^- + \mathrm{H}^+ \tag{2b}$$

which determine the shape of the ψ^d(pH) plot, were obtained by fitting the model to the data of the double layer potential as a function of pH. The solid curve in Figure 3A gives the calculated curve with a value of 4.95 for both pK values (so Δp$K = 0$) and $N_s = 0.8 \times 10^{12}$ sites/cm^2. This number of binding sites would correspond to a coverage of the gold surface with oxidic groups of approximately 0.1%, based upon a density of 1.4×10^{15} gold atoms per cm^2 at the Au$_{111}$ surface. Although the effect of surface roughness has not yet been taken into account in the calculation, the oxide layer seems to be well below full monolayer coverage. Such an observation has been made before[16] and would deserve further study.

In the low pH range, the model does not entirely fit the measured data. To get a better match between experimental data and model calculations, it would be necessary to increase the number of proton binding sites in the model. However, this number is generally believed to decrease with decreasing pH,[8,9] which is at variance with Figure 3A. Hence, it is likely that another double layer property is responsible for the different behavior at low pH.

To fit a series of measurements with an externally imposed potential at the gold surface at a certain pH, we additionally need an estimate for the capacitance of the oxide layer C_o. In contrast to the open circuit situation, there is a potential drop over the oxide layer. C_o is given by the relation

$$C_o = \frac{\epsilon_0 \epsilon_r}{d} \tag{3}$$

in which d is the thickness of the oxide layer. This thickness is determined by the Au−O bond, which is approximately 0.5 nm.

---

(24) Smith, C. P.; White, H. S. *Langmuir* **1993**, *9*, 1.

(25) Vorotynsev, M. A. In *Modern Aspects of Electrochemistry*; Bockris, J. O'M., White, R. E., Conway, B. E., Eds.; Plenum Press: New York, 1986; Chapter 2, p 177.

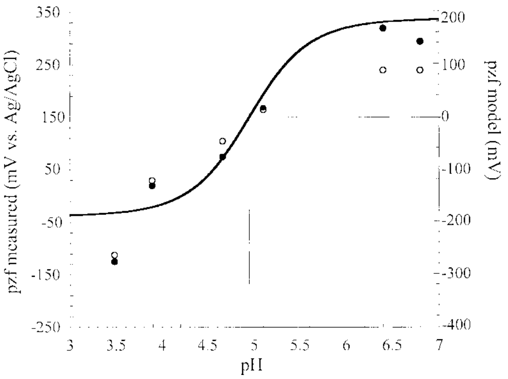

Figure 7. Potential of zero force of gold in 1 mM KNO_3 as a function of pH. The data are taken from Figure 5. ●, pzf determined from Figure 5A; ○, pzf determined from the model curves in Figure 5B. The solid curve gives the fit of the model $N_s = 0.8 \times 10^{12}$ sites/cm^2.

In the model $\Delta\Phi$—like ψ^d—is defined with respect to the potential of the bulk solution ($\Delta\Phi_{\text{Au solution}}$). Of course, in the experiments $\Delta\Phi$ is not applied with respect to the solution but with respect to the Ag/AgCl reference electrode ($\Delta\Phi_{\text{Au ref}}$). By adding the potential difference between the reference electrode and the solution $\{(\Delta\Phi_{\text{Au ref}}) + (\Delta\Phi_{\text{ref-solution}}) = (\Delta\Phi_{\text{Au solution}}) \equiv \Delta\Phi\}$, the applied potential is expressed with respect to the solution. The value of ($\Delta\Phi_{\text{ref solution}}$) can be extracted from comparison of the measured potential of zero force (pzf) with the pzf calculated from the model. The pzf, defined as the applied potential for which the double layer potential equals zero, is a function of the pH and is given in Figure 7. In the point of zero charge, at pH 4.95, the double layer potential equals zero. The measured pzf at this pH is 150 mV (vs Ag/AgCl), which is close to the value of the open circuit potential (135 mV vs Ag/AgCl), as can be seen in Figure 3B. Thus, all potentials applied with respect to the Ag/AgCl reference electrode are shifted by −150 mV to express these with respect to the potential of the bulk solution.

In comparing the measured data with the model, another problem arises. The gold electrode is polycrystalline, and because of surface asperities the probe does not touch the gold surface at every position. The effective double layer potential "felt" by the probe is really an ensemble of different potentials for different separations over an area of about 0.1 μm^2 (the electric interaction area of the probe and the surface). A first-order approximation for the relation between the actual (local) double layer potential ψ^d_{local} and the measured *effective* double layer potential ψ^d_{measured}, which is a smeared-out, average value at the distance of closest approach, is given by

$$\psi^d_{\text{measured}} = \frac{1}{A}\int \psi^d_{\text{local}} e^{-\kappa\delta}\, dA \tag{4}$$

in which A is the interaction area. Since the distance between the surfaces (δ) varies in this interaction area (only the larger surface asperities are touching the opposite surface), the weigh factor $\exp(-\kappa\delta)$ is in the integral.

Equation 4 still assumes a locally undisturbed one-dimensional behavior of the double layer, which is a good approximation provided that there is no significant double layer overlap between the asperities at the gold surface. That is, if the characteristic length λ between the peaks (or valleys) of the surface asperities is much larger than the double layer thickness (characterized by the Debye length κ^{-1}), $\kappa\lambda \gg 1$. From topographic images of the gold surface taken by AFM in the contact mode, it was observed that λ is about 100 nm, so for $\kappa^{-1} = 10$ nm this condition is fairly well satisfied. Unfortunately, eq 4 can only be applied to find the real double layer potential if the roughness profile and characteristics concerning the polycrystallinity of the surface in the interaction area are known. Since such information is not available for our Au surface, we use an even more simplified method, which involves a shift of the plane of charge (i.e., the point of zero separation in the force−distance curves) over a distance Δ. In other words, we consider the distance of closest approach between the probe and gold surface to be Δ, which implies that our ψ^d_{measured} values are related to the average potential at the onset of the diffuse double layer, ψ^d, by

$$\psi^d_{\text{measured}} = \psi^d e^{-\kappa\Delta} \tag{5}$$

Table 1. Values of Δ for the Series of Measurements in Which the Applied Potential Was Varied at a Range of pH Values, at an Electrolyte Concentration of 1 mM KNO_3

pH	Δ (nm)	N_s ($\times 10^{12}$ cm^{-1})
3.5	2	3
3.9	8	1.5
4.7	7	1.2
5.1	2	0.7
6.4	4	1.0
6.8	11	1.0

The significance of Δ is that it replaces the ensemble of all potentials for different separations (summed over A) by a constant potential ψ^d_{measured} at a mean separation Δ. The value of Δ is obtained by comparing ψ^d calculated with the amphifunctional model and the experimental value for ψ^d_{measured}. For one series of measurements Δ should be a constant because the whole series is taken at the same location at the gold surface. For different series, Δ may vary because the measurements refer to another area of interaction at the gold surface. It may be added that any error in determining the spring constant of the cantilever has a proportional effect on the slope of the $\psi^d - \Delta\Phi$ curves, which has an (exponential) impact on the value of Δ. The inaccuracy in the spring constant may be as much as 30% (as a result of inaccuracies in the determination of the radii of the particles used in the Cleveland method of calibration), which adds to the possible error in the estimation of Δ. Each series of measurements was performed with one cantilever.

Figure 5B gives the ψ^d values corrected for roughness as indicated above as well as the curves calculated with the amphifunctional model. It shows that, when the surface roughness is taken into account, the ψ^d values and their pH and $\Delta\Phi$ dependence are fairly well described by the model. In Table 1 the values obtained for Δ are listed. In the third column of Table 1 the fitted values for N_s are shown. Since in the model N_s determines the point of zero force of the curves, whereas Δ determines the slope of the curves, the two parameters are independently obtained from the experimental data.

As can be inferred from Table 1, the value of Δ varies between 2 and 11 nm. Taking into account the large error in this value due to the inaccuracy in determining the spring constant, this agrees fairly well with the observed surface roughness of 5 nm (peak-to-valley distance).

Wang and Bard[12] recently reported a large discrepancy between the electrically induced charge of a gold electrode and its surface charge density calculated from ψ^d values determined with colloidal probe AFM (the latter is in fact the diffuse double layer charge). This discrepancy was mainly attributed to ion correlation and ion condensation effects. However, there is no evidence for counterion condensation from the force curves at different salt concentrations (Figure 2). The analysis presented here shows that the difference between electronic charge and diffuse double layer charge has to be explained in terms of surface roughness, the buffering effect of proton binding sites, and the presence of a very thin dielectric layer at the surface (in our model a very incomplete oxide layer).

Conclusions

The double layer potential of gold can be varied through the solution pH as well as by an externally applied potential. Classical GCS theory alone is inadequate to describe the double layer phenomena of the gold surface. The different fits of the data in Figures 3, 5B, and 7 show that the amphifunctional model proposed by Duval et al.[16] describes very well the charging behavior of the gold/solution interface. This is true in both the presence and absence of a polarizing potential, provided surface roughness is taken into account. It appears that a very low density of proton binding sites at the gold surface causes the pH to have an effect on the double layer potential in a fairly narrow pH range. The total variation in double layer potential is also relatively small due to this small number of oxide sites. The pH dependence correlates with a two-p*K* proton exchange reaction scheme with the same p*K* value of 4.95. The changes in ψ^d as a result of an externally applied potential are small ($\Delta\psi^d/\Delta(\Delta\Phi) \approx 0.1$) due to large potential drops over the oxide layer and the Stern layer. Moreover, due to surface roughness the potential determined with colloidal probe atomic force microscopy is generally lower than the local diffuse double layer potential.

Of course, adsorbing molecules near the gold surface experience the local potential. Therefore, heterogeneity in surface potential due to polycrystallinity of the gold and partial coverage with oxide sites also play a role in adsorption phenomena. As far as electrostatics is important in adsorption, however, we expect to be able to interpret at least the trends in kinetics and adsorbed amounts with pH and applied potential on the basis of the amphifunctional charging mechanism of the gold/solution interface.

Acknowledgment. This work is sponsored by the Dutch government (Ministry of Economic Affairs) and is part of a joint project with Philips Research Laboratories (Eindhoven, The Netherlands). Professor A. J. Bard and Dr. J. Wang at the Laboratory of Electrochemistry in the Department of Chemistry and Biochemistry at The University of Texas at Austin are gratefully acknowledged for helpful suggestions and stimulating discussions.

Journal of Electroanalytical Chemistry 532 (2002) 337–352

Journal of Electroanalytical Chemistry

Double layers at amphifunctionally electrified interfaces in the presence of electrolytes containing specifically adsorbing ions

Jérôme Duval *, J. Mieke Kleijn, Johannes Lyklema, Herman P. van Leeuwen

Department of Physical Chemistry and Colloid Science, Wageningen University, Dreijenplein 6, 6703 HB Wageningen, Netherlands

Received 21 November 2001; received in revised form 18 January 2002; accepted 21 January 2002

Dedicated to Professor Sergio Trasatti on the occasion of his 65th birthday and in recognition of his continuing contributions to interfacial electrochemistry

Abstract

Amphifunctional double layers are defined by the coupling of electronic and ionic surface charging processes. They may be present at interfaces of the type metal | oxide layer | solution or semiconducting oxide | solution. In the present paper, the simultaneous effects of charge-determining ions H^+/OH^- and specifically adsorbing ions from the background electrolyte are analyzed on the basis of the amphifunctional double layer model we developed earlier. Depending on the nature of the substrate the interactions are either or both of the type (i) ions-ionized functional surface groups (ii) ions-metallic surface atoms. For each category, the dependences of the points of zero-charge and the isoelectric point, as defined by potential–pH relationships, on the background electrolyte concentration and the individual ion binding constants are obtained. The analysis of cases (i) and (ii) allows the prediction of the shifts of iep and pzc for relaxed oxide | electrolyte interfaces and the familiar polarized mercury | electrolyte interface in the presence of specifically interacting ions. Attention is paid to the dependences of the ion adsorption isotherms on pH and externally applied potential. The specific adsorption of anions on TiO_2 is treated in some detail: the computations presented here successfully explain experimental data. © 2002 Elsevier Science B.V. All rights reserved.

Keywords: Amphifunctional interface; Electric double layer; Specific adsorption; Point of zero charge; Isoelectric point; Metal oxides

1. Introduction

The charge on a solid oxide electrode in aqueous electrolyte solution generally results from the surface excess of charge-determining ions H^+/OH^-, which is governed by the chemical affinity between ion and surface. Ions of the background electrolyte, which are not primarily charge-determining for a particular type of surface, may be specifically adsorbed on the surface oxidic sites [1]. The non-electrostatic forces involved in this process result in shifts of the point of zero charge (pzc) and the isoelectric point (iep) [2], defined as the pH values where the protonic surface charge and the electrokinetic potential are zero, respectively. For such a *reversible* interface, the amount of specifically adsorbed ions is, for a given concentration and affinity of these ions, determined by the solution parameter pH.

For a completely *polarizable* interface such as between mercury and an electrolyte solution, the double layer parameters depend primarily on the potential externally imposed to the substrate [3]. The occurrence of specific interactions between ions and the bare surface of the electrode is manifested in a modification of the charge density/potential characteristic [4]. The adsorption isotherms of the ions are then dependent on the externally applied potential.

For *amphifunctional* interfaces [5], the double layer (dl) arises from *the combination* between these two charging processes. By way of example, we found that at gold electrodes, the amphifunctionality of the double layer results from the electron-conducting properties of the metal Au and the presence of a submonolayer of oxide at the surface [6]. For conducting (metallic) oxide such as RuO_2 and IrO_2, that the proton mechanism is

---

* Corresponding author. Tel.: +33-317-484-960; fax: +33-317-483-777

operating is evident from the measurable pzc. On the other hand, these electrodes behave according to the laws of electrochemical kinetics for metallic conductors. For semiconducting rutile TiO_2 electrodes, clear dependences of the surface potential (as measured by AFM) on the applied potential and pH have been reported in Ref. [7]. However, adsorption of sulfate and phosphate anions on TiO_2 electrodes have been found to be only pH-dependent, their adsorption at constant pH being insensitive to the applied potential [8]. A priori, these last mentioned results are in contradiction with the amphifunctionality expected for TiO_2 on the basis of the study quoted above. To our knowledge, no quantitative work has been reported so far to explain such behaviour. More generally, the way in which the simultaneous functioning of two disparate dl charging mechanisms affects specific adsorption has not yet been addressed. The present paper proposes models to account for the double layer profiles at such amphifunctional interfaces. These models describe in particular situations where the ions either exclusively interact with the oxidic groups (relevant for semiconducting or metallic oxides) or interact with both metallic surface and oxidized groups (relevant for substrates such as partly oxidized metal surfaces). The ionic specific adsorption on the reversible and polarizable parts of the amphifunctional surface will be treated separately. Understanding the relevant charging mechanisms provides a new route in describing ion adsorption as a function of applied potential and pH. We stress that essentially two types of specific adsorption are involved. The first is that for adsorption of protons and hydroxyls on the reversible sites. This type involves a very high affinity and is responsible for the fact that a surface charge forms at all. The second part is the much weaker specific adsorption of ions other than protons and hydroxyls at the iHp. This second part acts both on the reversible (relaxed) and polarized parts.

2. Specificity of the amphifunctional interfaces under investigation

We consider an amphifunctional interface between a partially oxidized metal, a semiconducting or metallic oxide and an electrolyte solution. In this section, we shall briefly review the main characteristics of such interfaces, of which the double layer properties were analyzed theoretically in Ref. [5]. For such systems, amphifunctionality is warranted by the fulfilment of the following two main conditions.

(i) The presence of amphoteric surface hydroxyl groups –MOH allowing for the release or uptake of protons H^+ to/from the solution via the ionization reactions

$$-MOH_2^+ \Leftrightarrow -MOH + H^+ \tag{1a}$$

$$-MOH \Leftrightarrow -MO^- + H^+ \tag{1b}$$

(ii) Spatial separation of the electric charge density σ^e (brought about via an external source) from the protonic charge σ^0 (resulting from the excess of protons). The charge density σ^e in the substrate may be made up of electrons (in the case of an electronic conductor), of ionic excesses (in the case of doped semiconductors) or of ionic deficits (for example, in the case of oxides submitted to a treatment at high temperature). The layers containing the charges σ^e and σ^0 are separated by a charge-free layer of capacitance C_0. This capacitance must be sufficiently high that a significant fraction of the potential difference applied resides at the electrolyte side of the interface.

In the double layer model developed for such interfaces [5], neither partial charge transfer aspects nor polarization due to, for instance, water dipole orientation were explicitly taken into account. Furthermore, it was assumed that potential and charges are smeared out over a flat interface and specific adsorption was ignored. Electroneutrality for the complete interphase requires

$$\sigma^e + \sigma^0 + \sigma^d = 0 \tag{1}$$

where σ^d is the diffuse double layer charge, given, for a 1:1 electrolyte, by [9,10]

$$\sigma^d = -(8I\varepsilon RT)^{1/2} \sinh(y^d/2) \tag{2}$$

with R the gas constant, T the temperature, I the total ionic strength, ε the dielectric permittivity of the solution. y is the reduced potential defined as

$$y = F\psi/RT \tag{3}$$

Later we shall use $y^d = F\psi^d/RT$, $y^0 = F\psi^0/RT$, $y^\beta = F\psi^\beta/RT$ if ψ^d is the potential at the outer Helmholtz plane (oHp), ψ^0 the potential at the plane where the loci of the oxidic surface groups are assumed to reside (‘op’ plane) and ψ^β the potential at the inner Helmholtz plane (iHp). F is the Faraday constant. As argued in [5], the possible dependences of the extent of surface oxidation and capacitance C_0 on potential and pH were ignored. In the frame of the present study, which focuses on the occurrence of specific adsorption of ions other than protons, we shall also adopt these assumptions.

3. Specific interactions electrolyte ions–oxidic sites

3.1. Potential and charge distributions at the interface

In Fig. 1, specific interactions of ions from the background electrolyte with the functional amphoteric surface groups are accounted for. The plane where these specifically adsorbed ions reside is the iHp. It is assumed that the ions bind to the surface oxidic sites and, for simplicity, that they bind only to sites with opposite charge sign, which is energetically the most favourable option. So, in the case of a 1:1 X^+Y^- electrolyte, the binding of the ions can be expressed as

$$–MOH_2^+ + Y^- \Leftrightarrow –MOH_2Y \qquad (2a)$$

$$–MO^- + X^+ \Leftrightarrow –MOX \qquad (2b)$$

At equilibrium, the (electro)chemical potential of the surface bound ions is equal to that of the corresponding free ions in the bulk of the solution, i.e. for the cations X^+

$$\tilde{\mu}_{X^+,\text{bound}} = \mu^0_{X^+,\text{bound}} + RT\ \ln(\Gamma_{MOX}/\Gamma_{MO^-}) + F\psi^\beta \qquad (4)$$

$$\mu_{X^+,\text{sol}} = \mu^0_{X^+,\text{sol}} + RT\ \ln c^\infty \qquad (5)$$

with Γ_A the surface concentration of A and c^∞ the bulk concentration of X^+Y^-. The term $RT\ \ln(\Gamma_{MOX}/\Gamma_{MO^-})$ stems from the configurational entropy of the bound X^+ ions distributed over the $–MO^-$ binding sites [11]. The above equations can be rearranged into

$$K_X = \left(\frac{\Gamma_{MOX}}{c^\infty \Gamma_{MO-}}\right) \exp(y^\beta) \qquad (6)$$

in which $K_X(= \exp\{-(\mu^0_{X^+,\text{bound}} - \mu^0_{X^+,\text{sol}})/RT\})$ is the intrinsic ('chemical') affinity constant of the X^+ ions for the oxidic sites. In the same way, for anions of type Y^-,

$$K_Y = \left(\frac{\Gamma_{MOH_2Y}}{c^\infty \Gamma_{MOH_2^+}}\right) \exp(-y^\beta) \qquad (7)$$

By the same token, the intrinsic acidity constants can be expressed as

$$K_{a_1} = c^\infty_{H^+}\Gamma_{MOH} \exp(-y^0)/\Gamma_{MOH_2^+} \qquad (8)$$

$$K_{a_2} = c^\infty_{H^+}\Gamma_{MO^-} \exp(-y^0)/\Gamma_{MOH} \qquad (9)$$

where $c_{H^+}{}^\infty$ is the bulk concentration of protons. It is stressed that we have assumed a smeared out potential in the various planes, but of course in the vicinity of charged surface groups, the potential can be much higher (positive or negative) than ψ^0 or ψ^β. However, if the ionized groups are not too close to each other, it is reasonable to consider the difference between the smeared out potential and the local potential as a constant. This local potential difference is then subsumed in the intrinsic binding constants containing a potential contribution apart from the chemical affinity.

The protonic surface charge density σ^0 and the ionic surface charge density σ^β are

$$\sigma^0 = F(\Gamma_{MOH_2^+} - \Gamma_{MO^-} + \Gamma_{MOH_2Y} - \Gamma_{MOX}) \qquad (10)$$

and

$$\sigma^\beta = F(\Gamma_{MOX} - \Gamma_{MOH_2Y}) \qquad (11)$$

respectively. The electroneutrality condition for the interface as a whole is now written

$$\sigma^e + \sigma^\beta + \sigma^0 + \sigma^d = 0 \qquad (12)$$

The total number of surface hydroxyl surface groups is

$$N_s = \Gamma_{MOH} + \Gamma_{MOH_2^+} + \Gamma_{MO^-} + \Gamma_{MOH_2Y} + \Gamma_{MOX} \qquad (13)$$

The potential of the metallic phase ψ^e (reduced potential

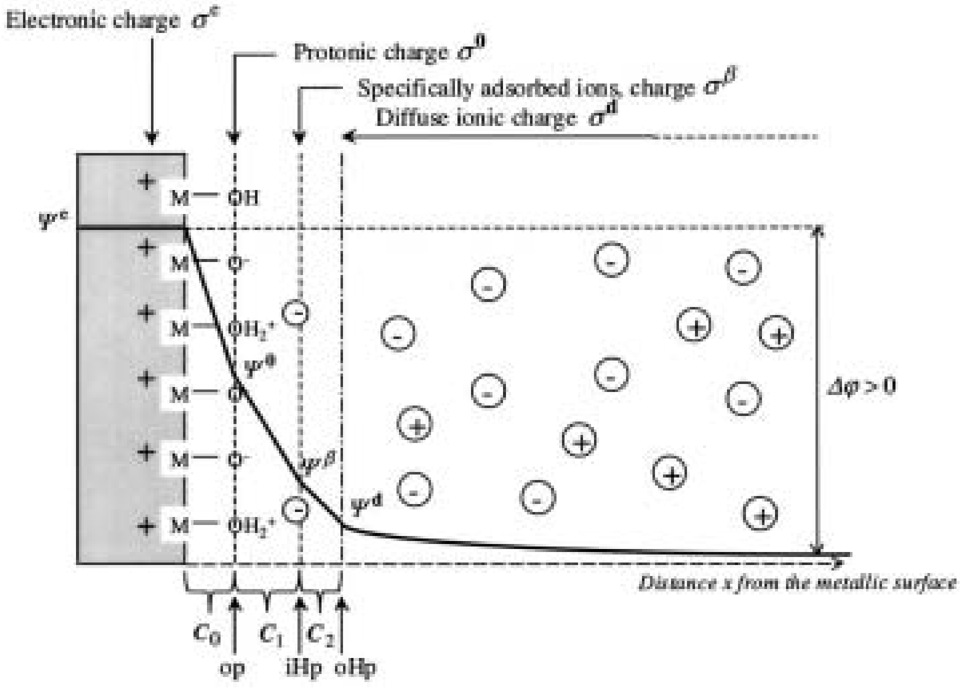
Electronic charge σ^e
Protonic charge σ^0
Specifically adsorbed ions, charge σ^β
Diffuse ionic charge σ^d
ψ^e
M— OH
M— O⁻
M— OH₂⁺
ψ^0
ψ^β
ψ^d
$\Delta\varphi > 0$
Distance x from the metallic surface
C_0
C_1
C_2
op
iHp
oHp

Fig. 1. Double layer model describing an amphifunctional interface between a partially oxidized metal and an aqueous electrolyte in the presence of anions specifically adsorbed on the oxide layer. The situation is depicted for an external potential $\Delta\varphi > 0$.

y^e) is identified to the externally applied potential $\Delta\varphi$ (reduced potential Δy) since the potential of the solution is taken as the reference. The potentials ψ^e, ψ^0, ψ^β, ψ^d are related to the surface charges σ^e, σ^0, σ^d via the capacitance C_0, the inner Helmholtz layer capacitance C_1 and the outer Helmholtz layer capacitance C_2 by

$$C_0 = \mathrm{d}\sigma^e/\mathrm{d}(\psi^e - \psi^0) \qquad (14)$$

$$C_1 = \mathrm{d}(\sigma^e + \sigma^0)/\mathrm{d}(\psi^0 - \psi^\beta) \qquad (15)$$

$$C_2 = -\mathrm{d}\sigma^d/\mathrm{d}(\psi^\beta - \psi^d) \qquad (16)$$

The diffuse layer capacitance C^d is found directly from differentiation of (2) with respect to ψ^d

$$C^d = -\mathrm{d}\sigma^d/\mathrm{d}\psi^d \qquad (17)$$

Eq. (14), relating the electric charge to the applied potential $\psi^e = \Delta\varphi$, is valid when considering an electrode for which the number of charge carriers is very high (such as for metals), i.e. when the potential drop inside the substrate is negligible. In that situation, the electric charge is located in the close vicinity of the surface. For a semiconductor the number of charge carriers is usually much smaller so that the electric charge σ^e can be distributed over a considerable distance behind the interface, i.e. a space charge is formed. To account for this latter situation, the reader is referred to the treatment given in Appendix A, which is similar to the one given for the case of a metallic electrode.

In the case of specific adsorption of anions (cations), $K_Y > 0$ and $K_X = 0$ ($K_X > 0$ and $K_Y = 0$), which renders the surface charge σ^β negative (positive). Eqs. (2), (6)–(16) describing the situation in the interface enable the calculation of the potential and charge distributions at given pH and ionic strength. The model parameters are the three capacitances C_0, C_1, C_2 supposed constant as discussed in Ref. [5], the binding equilibrium constants K_X and K_Y, the acidity constants K_{a_1}, K_{a_2} and the total number of sites per unit area N_s.

3.2. Estimation of the model parameters

Determination of N_s is possible on the basis of experimental data on ψ^d as a function of pH without an externally applied potential. These are obtained from electrokinetic experiments or AFM surface force measurements [6,12–14]. Proton titration experiments yield information on the protonic surface charge and hence the surface oxidation. Given the value of N_s, the constants K_{a_1} and K_{a_2} can be derived from extrapolation procedures used to fit the electrokinetic, AFM or titration data [15,16]. K_X and K_Y can be inferred from the titration data by means of a double extrapolation technique as first introduced by James and Parks [17]. A probable range of values for the capacitance C_0 is 1–10 μF cm^{-2} [5]. The capacitance of the inner layer C_1 can be deduced from two kinds of data sets, of which the availability depends on the total surface area of the system studied. If this area is high (dispersed particles), potentiometric titration data can be obtained and used [18]. Otherwise (metal electrodes), electrochemical experiments can be performed to construct Parsons–Zobel plots [19,20]. Knowing the values of C_0 and assuming no specific adsorption of ions, C_1 may then be estimated with use of the intercept of these plots (straight lines). For oxides, values between 100 and 140 μF cm^{-2} are usually found and generally lower values (15–50 μF cm^{-2}) are reported for metals though values higher than 50 μF cm^{-2} are sometimes reported ($C_1 > 120$ μF cm^{-2} in case of a hydrophilic metal such as Ga). For C_2, a value of 20 μF cm^{-2} has gained some consensus [21].

3.3. Effect of specific ion adsorption on the potential–pH relationships defining the iep and pzcs: limiting case of the relaxed oxide | electrolyte interface

In connection with understanding the electronic and protonic charges in the presence of specific adsorption of ions, it is useful to first consider the conditions where these charges are zero. For amphifunctional interfaces of the type examined here, these conditions are given by the potential–pH relationships $(\Delta\varphi, \mathrm{pH})_{\mathrm{pzc}_1}$ for which $\sigma^e = 0$ and $(\Delta\varphi, \mathrm{pH})_{\mathrm{pzc}_2}$ for which $\sigma^0 = 0$ [5]. At a given pH, the potential $\Delta\varphi_{\mathrm{pzc}_1}$ at the pzc$_1$ condition is sometimes called the open circuit potential and, for a semiconducting substrate, the flat-band potential. The potential of an isolated phase (metal or semiconductor) immersed into a solution corresponds theoretically to the potential of zero charge. The iep $(\Delta\varphi, \mathrm{pH})_{\mathrm{iep}}$ ($\psi^d = 0$) also deserves attention. Here, we shall examine how the characteristic $\Delta\varphi$ values are modified by specific adsorption of ions.

For the sake of simplicity, let us focus on the particular case of specific adsorption of anions at the iHp. Taking into account the relationships defining the pzc$_1$, pzc$_2$ and iep, the set of equations presented in Section 3.1 was solved for the selected set of parameters (Section 3.2) with specifically adsorbing anions and for different electrolyte concentrations c^∞. The corresponding plots $\Delta\varphi_{\mathrm{pzc}_1}(\mathrm{pH})$, $\Delta\varphi_{\mathrm{pzc}_2}(\mathrm{pH})$ and $\Delta\varphi_{\mathrm{iep}}(\mathrm{pH})$ are given in Fig. 2. For low c^∞ ($c^\infty \ll K_Y^{-1}$), specific adsorption is negligible ($\sigma^\beta \approx 0$) and we have

$$\Delta\varphi_{\mathrm{iep}}(\mathrm{ppzc}) = \Delta\varphi_{\mathrm{pzc}_1}(\mathrm{ppzc}) = \Delta\varphi_{\mathrm{pzc}_2}(\mathrm{ppzc}) = 0 \qquad (18)$$

where the pristine point of zero charge (ppzc) is the pH value given by

$$\mathrm{ppzc} = 0.5(\mathrm{p}K_{a_1} + \mathrm{p}K_{a_2}) \qquad (19)$$

Eq. (18) refers to the pristine condition. The trends of the potentials $\Delta\varphi_{\mathrm{pzc}_1}$, $\Delta\varphi_{\mathrm{pzc}_2}$ and $\Delta\varphi_{\mathrm{iep}}$ as a function of pH at low c^∞ are explained in detail in Ref. [5]. At a given pH, the potentials $\Delta\varphi_{\mathrm{pzc}_1}$, $\Delta\varphi_{\mathrm{pzc}_2}$ and $\Delta\varphi_{\mathrm{iep}}$ increase upon specific adsorption of anions. Starting

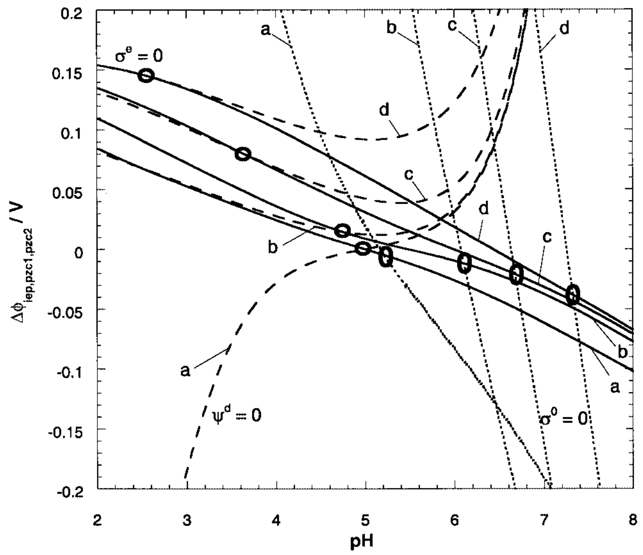

Fig. 2. Combinations of applied potential and pH at which the system is at the iep ($\psi^d = 0$) (– – ·), pzc$_1$ ($\sigma^e = 0$) (—) or pzc$_2$ ($\sigma^0 = 0$) (· · · · · ·) for different electrolyte concentrations c^∞. Electrolyte concentrations $c^\infty = 10^{-4}$ M (a), 10^{-2} M (b), 10^{-1} M (c), 1 M (d). The intersection points of $\Delta\varphi_{\rm iep}$(pH) and $\Delta\varphi_{{\rm pzc}_2}$(pH) with $\Delta\varphi_{{\rm pzc}_1}$(pH) are marked for each c^∞ by the symbols (○) and (0), respectively. Model parameters: p$K_{a_1} = 2$, p$K_{a_2} = 8$, $C_0 = 5$ µF cm^{-2}, $C_1 = 100$ µF cm^{-2}, $C_2 = 20$ µF cm^{-2}, $N_s = 10^{14}$ sites cm^{-2}. $K_Y = 10^4$ mol^{-1} l, $K_X = 0$ mol^{-1} l.

from the pristine condition, ψ^d decreases. The specific anion adsorption leads to a positive induced charge $\sigma^0 + \sigma^e$, which is less than the specifically adsorbed charge. To reestablish the iep, $\Delta\varphi$ must be increased. This is achieved by increasing σ^e since some electrons are withdrawn from the conducting side of the interface, which, in turn, decreases the potential-induced countercharge $\sigma^0 + \sigma^\beta$. Similar reasoning applies to the pzc$_1$ and pzc$_2$ situations and to specific adsorption of cations, for which one obtains a figure (not shown here) which is the mirror image of Fig. 2. Effectively, starting from Eq. (18), the direction of the shift of $\Delta\varphi_{\rm iep}$ ($\Delta\varphi_{{\rm pzc}_1}$ and $\Delta\varphi_{{\rm pzc}_2}$) caused by addition of specifically adsorbing anions is the same (opposite) as that induced by adding charge-determining OH$^-$ ions, i.e. for pH > ppzc. Similar trends are obtained by varying the binding constant K_Y at constant electrolyte concentration c^∞. In the absence of an applied potential, $\Delta\varphi = \psi^e = \psi^0$ is the reversible potential, which depends on pH and on the concentration and nature of the electrolyte via K_X and K_Y. The iep ($\psi^d = 0$) and the pzc ($\sigma^0 = 0$) are then defined by pH values denoted as pH$_{\rm iep}$ and pH$_{\rm pzc}$, respectively. These iep and pzc are indicated in Fig. 2 as the intersection points between the $\Delta\varphi_{{\rm pzc}_1}$–pH and $\Delta\varphi_{\rm iep}$–pH curves, and the $\Delta\varphi_{{\rm pzc}_1}$–pH and $\Delta\varphi_{{\rm pzc}_2}$–pH curves, respectively. pH$_{\rm iep}$ and pH$_{\rm pzc}$ are known to be shifted in opposite directions upon specific adsorption of ions [2], as found by extrapolation of the amphifunctional analysis.

3.4. Characteristics of the ion adsorption isotherms: dependences on pH/potential

In the particular case of specific adsorption of anions Y$^-$, the surface concentration of anions is given by

$$\Gamma_{\rm MOH_2Y} = \Gamma = -\sigma^\beta / F \tag{20}$$

To understand the dependences $\Gamma(\Delta\varphi, \text{pH})$ properly, the composition of the charge $\sigma^0 + \sigma^\beta$ has to be analyzed. Fig. 3 shows anion adsorption isotherms computed for given K_Y ($K_X = 0$) and c^∞ as a function of the applied potential for different values of pH. The characteristic pattern of the isotherm at constant applied potential versus pH is given in the inset. When increasing the pH at constant $\Delta\varphi$, the adsorbed amount Γ decreases since the protonic charge decreases. The negative charges required to counterbalance the shift in σ^e, induced upon increasing the pH, are then preferentially located at the op. At a given pH, Γ reaches a maximum for a potential denoted as $\Delta\varphi_{\max}$. The existence of this maximum is due to the coupling of the proton association process and the specific adsorption of anions (which bind only to –MOH$_2^+$ sites). At extreme positive values of $\Delta\varphi$, all oxidic sites at the surface are in the –MO$^-$ form and anions cannot adsorb. When $\Delta\varphi$ is extremely negative, all sites are in the –MOH$_2^+$ form, but the potential at the interface is too unfavourable for anion adsorption. The electrostatic interactions resulting from the externally applied potential dominate the ion–ion interactions leading to the formation of surface complexes of which the number is in the limit zero. In these extreme potential ranges, the basically amphifunctional interface tends to a monofunctional behaviour [5], the ionic-charging function being ‘blocked’ (saturation situation). This is also the case when the anions adsorb on all the N_s oxidic sites available ($\Delta\varphi = \Delta\varphi_{\rm max,sat}$). Compensation of the potential-induced charge σ^e must then take place by a shift in the diffuse double layer charge σ^d, since the electroneutrality condition (12) always applies. In the intermediate potential range, the interface behaves amphifunctionally. When in this range $\Delta\varphi$ is increased, the total surface charge $\sigma^0 + \sigma^\beta$ decreases to compensate for the positive shift in σ^e. This is achieved according to the two following mechanisms: (i) dissociation of the surface groups –MOH$_2^+$ to –MOH (and further to –MO$^-$), (ii) complexation of the –MOH$_2^+$ groups. The effect of the proton dissociation constant pK_{a_1} is illustrated in Fig. 4. If, for a given type of interface, pK_{a_1} is high (at constant pK_{a_2}), the potential range where –MOH$_2^+$ sites are available for anions is relatively large and compensation for the increasing value of σ^e is primarily achieved by mechanism (ii); the increase in countercharge is then primarily located at the iHp and $\Delta\varphi_{\max}$ corresponds to the potential where the complexes preferably dissociate into $-MO^-$ forms. For lower values of pK_{a_1} (and constant pK_{a_2}, so larger values of ΔpK), both dissociation of surface groups (i) and anion adsorption (ii) contribute to the compensation of the potential-induced change in σ^e. The relative contribution of these mechanisms is governed by the concentrations of protons and anions in solution and their affinity for the $-MOH$ and $-MOH_2^+$ sites, respectively. In that case, $\Delta\varphi_{max}$ is the potential for which the complexes dissociate into $-MOH$ forms. As upon decreasing the pH of the solution, Γ is higher for higher values of pK_{a_1} (keeping pK_{a_2} and pH constant) and $\Delta\varphi_{max}$ is shifted to the right since one renders the surface more acidic (Fig. 4). Γ_{max} increases when increasing the concentration of anions in solution (Fig. 5). The additional adsorption of anions induces an increase in σ^0 (equilibrium (1a) shifts to the left) and a slight decrease in σ^e (at constant $\Delta\varphi$). The potential $\Delta\varphi_{max}$ required to reach the new maximum Γ_{max} is therefore shifted slightly towards the negative direction so as to add electrons to the metallic side of the interface and hence make σ^e more negative (Fig. 5). A plot of the adsorption isotherm at given pH and potential as a function of the bulk concentration c^∞ is shown in the inset of Fig. 5. Comparable results are obtained when increasing the binding constant K_Y, keeping the other parameters constant.

Similar reasoning accounts for specific adsorption of cations. For an insulating substrate, all the applied potential difference resides in the oxide layer ($C_0 \to 0$): the adsorption process is then controlled only by the pH of the solution and c^∞ (monofunctional surface).

4. Specific interactions between background electrolyte ions and the electronically conducting surface

4.1. Potential and charge distributions at the interface

We now consider adsorption of ions from the background electrolyte on the electronically conducting surface (semiconductor or metallic) of which the properties are compatible with an amphifunctional charging of the dl. For this purpose, we assume that the adsorption of the ions takes place at the op, i.e. the plane where the oxidic groups are located (Fig. 6). To avoid confusion with the previous case, we denote the potential at the op

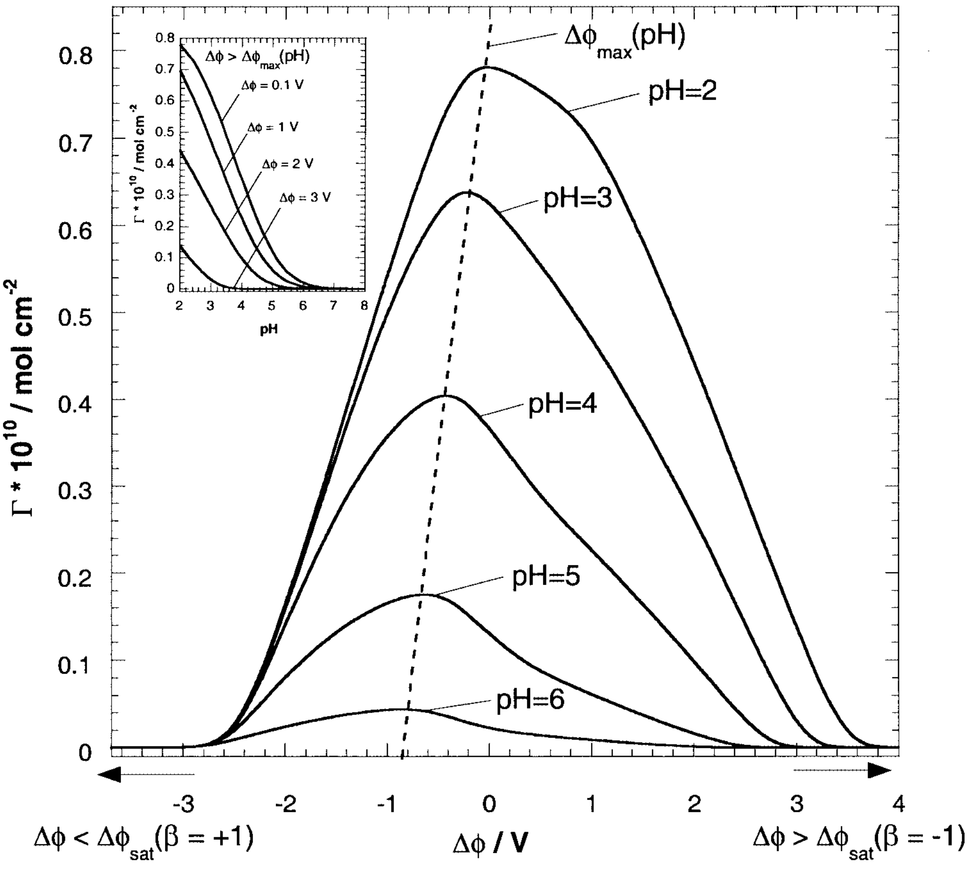

Fig. 3. Adsorption isotherms as a function of potential and pH at constant electrolyte concentration 3×10^{-2} M for anions specifically adsorbed on the oxide layer of the amphifunctional substrate. Model parameters: $pK_{a_1} = 2$, $pK_{a_2} = 8$, $C_0 = 5$ μF cm^{-2}, $C_1 = 100$ μF cm^{-2}, $C_2 = 20$ μF cm^{-2}, $N_s = 5 \times 10^{13}$ sites cm^{-2}. $K_Y = 10^4$ mol^{-1} l. The dashed line sketches the shift of $\Delta\varphi_{max}$ with pH. The potentials $\Delta\varphi_{sat}(\beta = \pm 1)$, depending on pH and c^∞, induce saturations of σ^0 which then equals $\beta F N_s$.

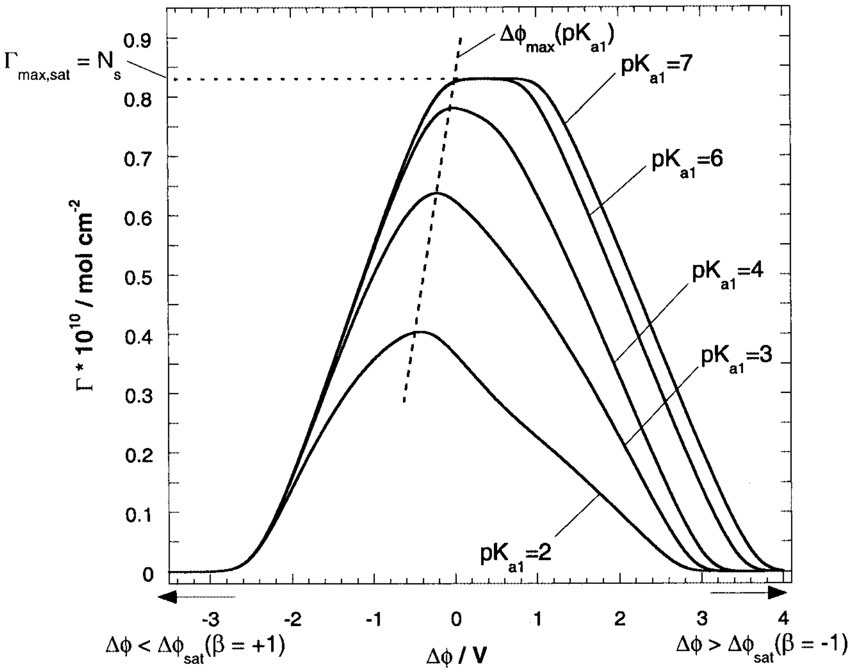

Fig. 4. Adsorption isotherms as a function of potential for surfaces characterized by different pK_{a_1} values at 3×10^{-2} M and pH 4 (adsorption of anions on the oxide layer). $pK_{a_2} = 8$. Other parameters: as in Fig. 3. The dashed line sketches the shift of $\Delta\varphi_{max}$ with pK_{a_1}.

plane as ψ^a. Contrary to the previous situation, we cannot a priori identify localized 'electronic sites' with which the electrolyte ions interact since the electric charge σ^e is smeared out over the surface with a short (metal) or somewhat longer (semiconductor) depth. Nevertheless, the affinity of the ion for the conducting surface finally results in a binding of the ion with an atom surrounded by a sea of electrons assuring the conductivity of the material. Therefore, the interactions of interest can be summarized by the following equilibria now replacing reactions (2a) and (2b)

$$-M + Y^- \Leftrightarrow -MY^- \ (K'_Y) \tag{3a}$$

$$-M + X^+ \Leftrightarrow -MX^+ \ (K'_X) \tag{3b}$$

where K'_Y and K'_X are the binding constants describing the magnitude of the metal–ion interactions. The total adsorbed charge σ^a at the op is given by

$$\sigma^a = \sigma^i + \sigma^0 \tag{21}$$

where σ^0 is the protonic charge as defined by relation (10) after suppressing the charge contributions of the complexes $-MOX$ and $-MOH_2Y$ and replacing the potential ψ^0 (y^0) by ψ^a (y^a). σ^i is the charge resulting from the specific adsorption of electrolyte ions other than H^+/OH^- and can be formulated as

$$\sigma^i = F(N_0 - N_s)(\theta_+ - \theta_-) \tag{22}$$

with N_0 the total amount of atomic sites per unit area ($N_0 \geq N_s$) and $\theta_+ = \Gamma_{MX^+}/(N_0 - N_s)$, $\theta_- = \Gamma_{MY^-}/(N_0 - N_s)$. The fractions θ_+ and θ_- obey

$$\theta_+/(1 - \theta_+) = c^\infty K'_X \exp(-y^a) \tag{23}$$

$$\theta_-/(1 - \theta_-) = c^\infty K'_Y \exp(y^a) \tag{24}$$

The electronic charge and the diffuse charge are now related to the potentials by

$$\sigma^e = C_0(\psi^e - \psi^a) \tag{25}$$

and

$$\sigma^d = -C_1(\psi^a - \psi^d) \tag{26}$$

4.2. Adsorption isotherms; potential of zero charge and isoelectric point

Fig. 7A and B show $\Delta\varphi_{iep}$(pH) and $\Delta\varphi_{pzc_1}(c^\infty)$ for different values of c^∞ and pH, respectively, in the case of specific adsorption of anions. When increasing c^∞ at given pH and constant $\Delta\varphi$ (or increasing the pH at given c^∞ and $\Delta\varphi$), the electronic charge and the diffuse charge become more positive. Since the double layer potential becomes negative, one has to increase $\Delta\varphi$ to come back to the isoelectric conditions. To reach $\sigma^e = 0$, the applied potential $\Delta\varphi$ has to be lowered so as to push electrons to the conducting side of the interface. Contrary to the situation treated in Section 3, upon ionic adsorption $\Delta\varphi_{iep}$ and $\Delta\varphi_{pzc_1}$ shift in opposite directions. This trend was observed experimentally in the case of TiO_2 interacting with the oligomeric anion hexametaphosphate (HMP) [7]. In the limit $N_s \to 0$ where the interface is monofunctional again, the model describes the dl at the mercury | electrolyte interface in the presence of specifically adsorbing ions [4,22–24] (Fig. 8). Assuming $N_0 \gg N_s$ and $\theta_- \ll 1/2$ (Henry region of the Langmuir isotherm), Eq. (22) can then be simplified, for the case of adsorption of anions, into

$$\sigma^i = -Fc^{\infty} N_0 K'_Y \exp(y^a) \tag{27}$$

As shown in Fig. 9A and B representing $\Gamma(\Delta\varphi,\ \text{pH})$ and $\Gamma(\Delta\varphi,\ c^{\infty})$ respectively, the more negative the applied potential, the lower is the adsorption of anions. Upon increasing $\Delta\varphi$, the electronic charge becomes increasingly positive so that the quantity Γ increases till saturation, i.e. $\theta_- \rightarrow 1$. At a given $\Delta\varphi$ and c^{∞}, Γ decreases with increasing pH due to the shift of the equilibria at the oxidic sites, resulting in a decrease in protonic charge. Above a certain value of the pH, the curve $\Delta\varphi_{\text{pzc}_1}(c^{\infty})$ shows a maximum. Indeed, there is a certain concentration regime where the negative charge σ^i resulting from the increase in anion adsorption when increasing c^{∞} is lower in absolute value than the change in the positive diffuse charge. Consequently, to maintain electroneutrality, the electronic charge decreases. The potential $\Delta\varphi_{\text{pzc}_1}$ necessary to recover $\sigma^e = 0$ therefore increases, as can be seen in Fig. 7B. For higher concentrations, the extra specifically adsorbed charge σ^i is larger than the increase in σ^d (in absolute value) so that the induced charge σ^e increases and the corresponding $\Delta\varphi_{\text{pzc}_1}$ decreases. The maximum in the $\Delta\varphi_{\text{pzc}_1}$–$c^{\infty}$ curves would not be observed when an additional supporting electrolyte (which is really indifferent) is present in excess over the adsorbing anions. The dependence of Γ and the other dl parameters on the binding constant K'_Y is of the same kind as the dependence on c^{∞}. Comparable reasoning holds for the case where cations adsorb specifically at the bare surface of the conducting material ($K'_X > 0$, $K'_Y = 0$).

5. Specific adsorption at both oxidic and metallic sites

We consider in this part situations where ions from the background electrolyte can be adsorbed at the

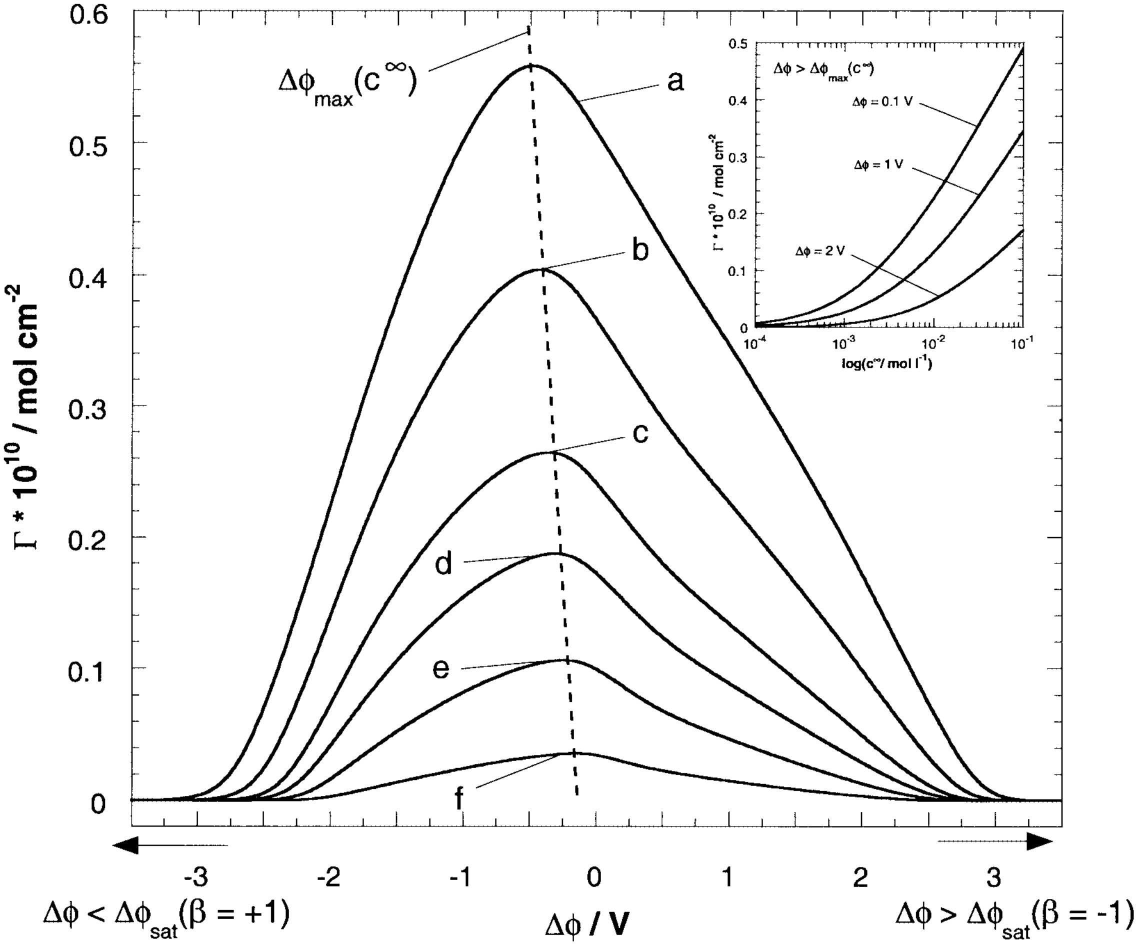

Fig. 5. Adsorption isotherms as a function of potential and electrolyte concentration c^{∞} at pH 4 (adsorption of anions on the oxide layer). $c^{\infty} = 10^{-1}$ M (a), 3×10^{-2} M (b), 10^{-2} M (c), 5×10^{-3} M (d), 2×10^{-3} M (e), 5×10^{-4} M (f). Parameters: as in Fig. 3. The dashed line sketches the shift of $\Delta\varphi_{\max}$ with c^{∞}.

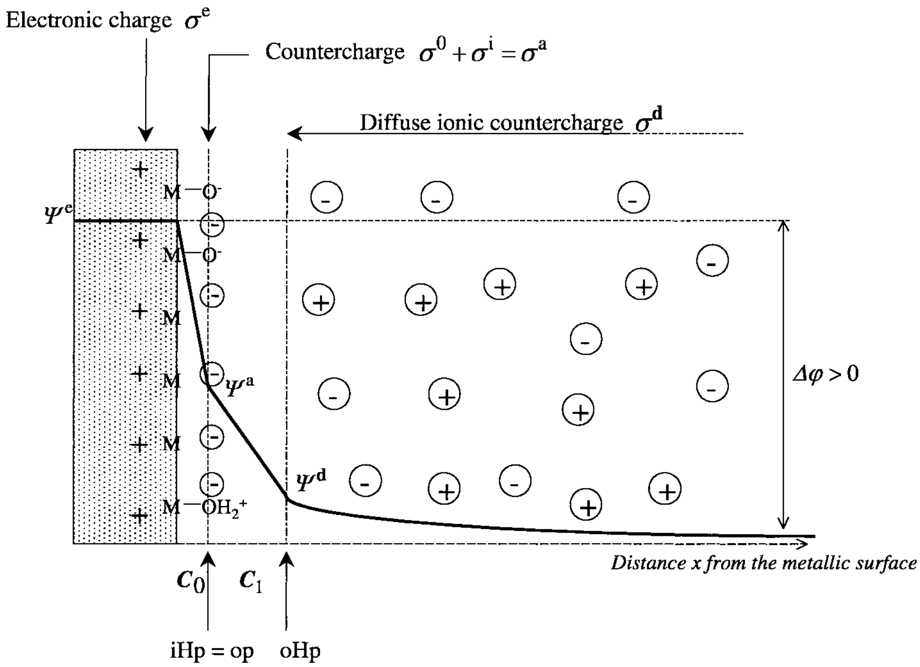
Electronic charge σ^e
Countercharge $\sigma^0 + \sigma^i = \sigma^a$
Diffuse ionic countercharge σ^d
Ψ^e
M–O$^-$
M–O$^-$
M
M
M
M–OH$_2^+$
Ψ^a
Ψ^d
$\Delta\varphi > 0$
Distance x from the metallic surface
C_0
C_1
iHp = op
oHp

Fig. 6. Double layer model describing an amphifunctional interface between a partially oxidized metal and an aqueous electrolyte in the presence of anions specifically adsorbed on the electron-conducting surface. The situation is depicted for an external potential $\Delta\varphi > 0$.

polarizable and at the reversible parts of the amphifunctional substrate. The equations derived in Sections 3 and 4 remain valid. Attention is again focused on the case where only anions specifically interact with the amphifunctional substrate. The adsorption isotherm equation is now given by

$$\Gamma = -(\sigma^i + \sigma^\beta)/F = \Gamma_{\text{polarizable}} + \Gamma_{\text{reversible}} \tag{28}$$

In the situation where $N_0 \gg 2N_s$ (gold electrode [6]) and $K'_Y \gg K_Y$, the interactions described in Section 4 overrule those considered in Section 3 ($\Gamma_{\text{reversible}} < \Gamma_{\text{polarizable}}$). The other limiting case is defined by $N_s/N_0 \approx 1$ and $K'_Y \ll K_Y$ ($\Gamma_{\text{reversible}} > \Gamma_{\text{polarizable}}$). The dependences of Γ on the parameters K_Y, K'_Y, pH, c^∞ and ΔpK have already been discussed in detail in Sections 3 and 4. Depending on the values of these parameters and of the oxide coverage $f = N_s/N_0$, numerous situations (number of adsorption maxima, limiting behaviour at high potentials…) can be considered. For illustration, samples of calculations are shown for a given set of conditions in Fig. 10. These results are relevant when the distribution of the oxidic groups with respect to the metallic surface (or the other way round) allows the occurrence of specific adsorption at two different planes (op and iHp). This is the case when one kind of surface (polarizable or reversible) is organized according to an 'island' structure (still compatible with the assumption of smeared out potentials). If the non-protolytic surface parts are homogeneously 'mixed' with the parts where protons can bind, one may describe specific adsorption using the different adsorption sites previously introduced (metallic –M, –MOH, –MO$^-$ and –MOH$_2^+$) but placed all in the same plane.

6. Application to a real system: adsorption of anions on TiO$_2$ electrode

The literature provides numerous experimental data showing that the adsorption isotherms of a number of oxide electrodes such as titanium oxide are not or only slightly affected by an applied potential [8,25–29]. Nevertheless, a more recent study points at amphifunctional behaviour of TiO$_2$ by showing experimentally a clear dependence of the dl potential ψ^d on $\Delta\varphi$ [7]. On the basis of the results presented so far, we propose a quantitative account for these apparently contradictory features.

As already mentioned in Section 3.2, AFM experiments performed on a solid TiO$_2$ substrate and electrophoresis experiments performed with colloidal dispersion of TiO$_2$ [13,14] can be used to determine the adsorption characteristics (N_s, pK_{a_1}, pK_{a_2}) of the H$^+$ ions at the oxide layer (Fig. 11). The available ψ^d(pH) data refer to different KNO$_3$ concentrations. No significant shifts of pH$_{\text{iep}}$ with electrolyte concentration were observed so that specific adsorption of K$^+$ and NO$_3^-$ ions does not occur. Depending on the electrolyte concentration, the data are fitted with the following set of parameters $N_s = 1–1.9 \times 10^{12}$ cm^{-2}, pK_{a_1} = pK_{a_2} = 5.6–5.7 and pH$_{\text{iep}} \approx 5.6–5.7$. The value of N_s obtained is low compared to the ones commonly reported in the literature for oxide surfaces. When using a more realistic N_s (5×10^{14} cm^{-2} for rutile TiO$_2$ [17]), the fitting procedure described in Refs. [15,16] is in agreement with the experimental data only for $pH<7$. This indicates that, probably due to surface roughness, electrokinetic experiments and colloidal probe AFM measurements give zeta-potentials and ψ^d values that are too low. In fact, only a fraction of the surface charge is probed and therefore a low value for N_s is obtained from a model fit in which the surface is assumed to be flat. By way of illustration, the porous double layer model in which part of the surface charge is distributed in the solid phase (comparable to the effect of surface roughness) adequately describes how, under open circuit conditions, high surface charges can be built up while keeping the electrokinetic double layer potential relatively low [30]. In Ref. [7], TiO$_2$ is treated as an n-type semiconductor of known charge carrier density N_{sc}. In the space-charge layer located inside the substrate, the potential and the charge density vary with distance to the surface as shown in Appendix A. The amphifunctionality of the dl at the semiconductor | electrolyte interface, described in Appendix A, is essentially the same as the one discussed in Ref. [5]. The calculated characteristic applied potential/electric charge for TiO$_2$ is reported in Fig. 12A. The diffuse double layer potentials were determined experimentally for different applied potentials at pH 5.5 by AFM using KCl as the electrolyte [7]. Measurements in the absence of an applied potential reveal that for the surface probed, pH$_{\text{iep}}$ 5.7, which is in agreement with the iep mentioned in Refs. [13,14]. Neglecting specific adsorption of K$^+$ or Cl$^-$ ions [31] at the pH of the experiments, the double layer potentials were computed as a function of the applied potential using the pK parameters obtained from the open circuit measurements and with $N_s=4\times10^{12}$ cm^{-2}. The results are collected in Fig. 12B. The applied potentials in the experimental study are given with respect to the SCE reference electrode and the theoretical potentials are given versus the bulk of the solution: merging of the curves was attained by shifting the calculated φ_{sc}^{b} by 220 mV. The magnitude and the trend of the double layer potential as a function of the applied potential show good overall agreement between experimental data and theory except for high surface potentials. At such potentials corresponding to attractive interactions between the probe (a silica particle

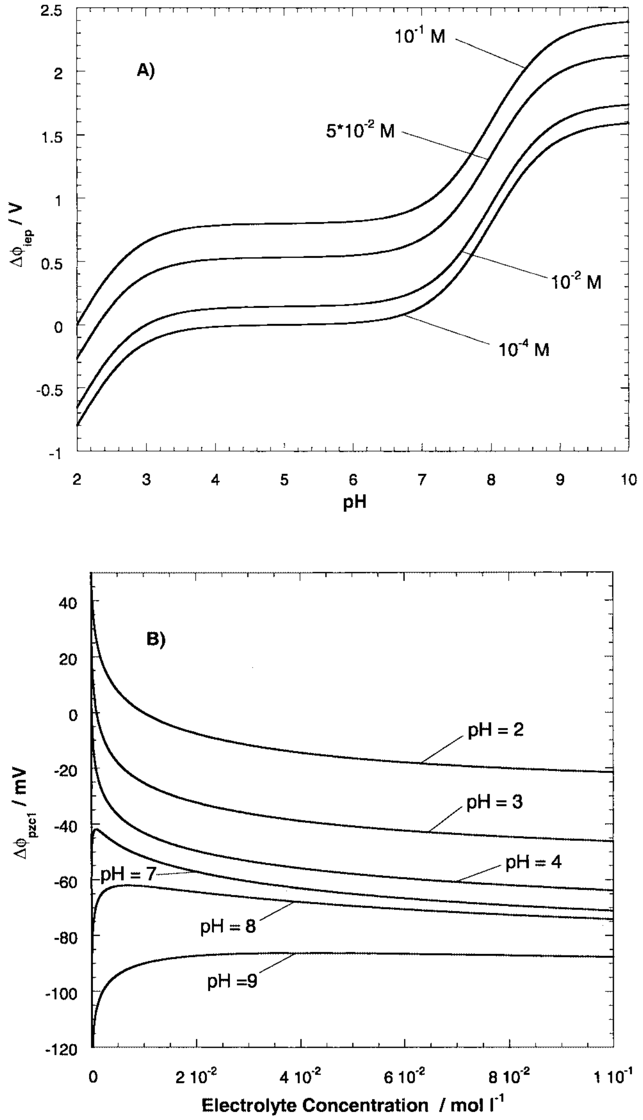

Fig. 7. Potential to be applied across the interface to reach the iep and pzc$_1$ as a function of pH (A) and c^∞ (B), respectively. Parameters: $pK_{a_1}=2$, $pK_{a_2}=8$, $C_0=5$ μF cm^{-2}, $C_1=100$ μF cm^{-2}, $N_0=10^{14}$ atoms cm^{-2}, $N_s=5\times10^{13}$ sites cm^{-2}. $K'_Y=10$ mol^{-1} l, $K'_X=0$ mol^{-1} l (A) $K'_Y=10^2$ mol^{-1} l, $K'_X=0$ mol^{-1} l (B). The calculations refer to adsorption of anions on the electron-conducting surface.

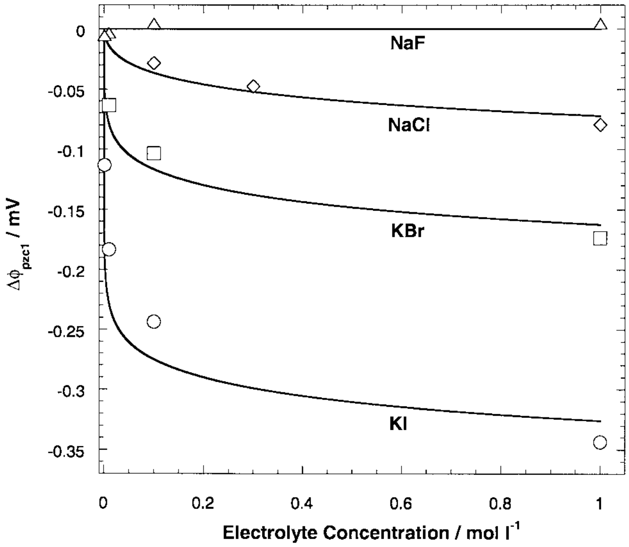

Fig. 8. Shifts of the pzc (potential value) for a mercury electrode upon specific adsorption of anions. Full curves: theory. Points: experiments (taken from Ref. [4]). Parameters: $N_s=0$, $C_1=30$ μF cm^{-2} (pzc independent of C_0). Fit parameter: $K'_Y N_0=0$ (F$^-$), 2×10^{17} (Cl$^-$), 1.5×10^{19} (Br$^-$), 1.75×10^{22} (I$^-$) mol^{-1} cm.

negatively charged) and the surface, the accuracy of the force measurements is questionable because of the instability of the cantilever, which exhibits a characteristic snap-in behaviour. The N_s value used for the fit, which value is in agreement with that derived from the open circuit measurements, remains very low. So, a more detailed analysis would also require inclusion of surface roughness and its consequences for the interpretation of AFM measurements [32].Figs. 11 and 12B show the amphifunctional features of the n-type semiconductor TiO_2. The adsorption of anions of the type SO_4^{2-} or $H_2PO_4^-/HPO_4^{2-}$ (resulting from the ionization of H_2SO_4 and H_3PO_4 initially introduced in the solution in concentration c^∞) on such a TiO_2 surface were studied by the radio-isotope method [8]. These anions are known to interact specifically with the oxide surface

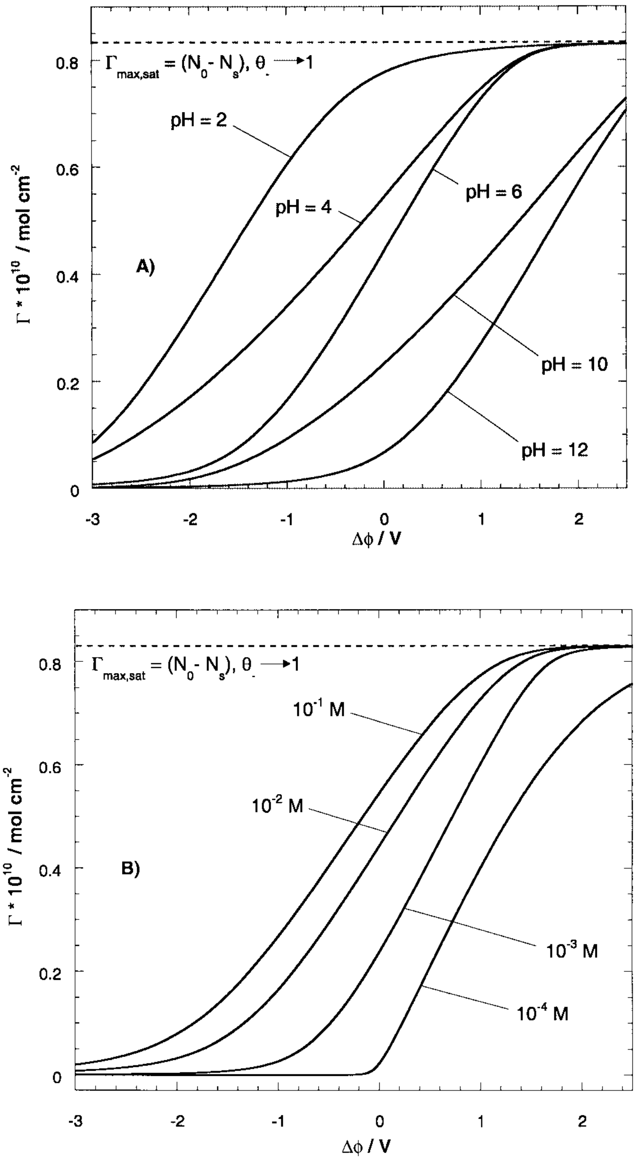

Fig. 9. Adsorption isotherms as a function of potential and pH ($c^\infty = 5 \times 10^{-2}$ M) (A) and as a function of potential and c^∞ (pH 6) (B) in the case of anions adsorbed at the electron-conducting surface of the amphifunctional substrate. Model parameters: $pK_{a_1} = 2$, $pK_{a_2} = 8$, $C_0 = 5$ μF cm^{-2}, $C_1 = 100$ μF cm^{-2}, $N_0 = 10^{14}$ atoms cm^{-2}, $N_s = 5 \times 10^{13}$ sites cm^{-2}. $K'_Y = 10^3$ mol^{-1} l, $K'_X = 0$ mol^{-1} l.

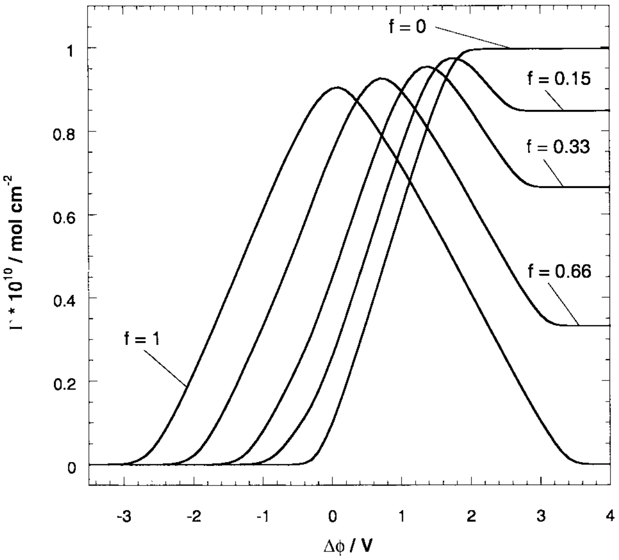

Fig. 10. Adsorption isotherms as a function of potential and oxide coverage $f = N_s/N_0$ in the case of anions interacting with both the polarizable and reversible parts of the amphifunctional electrode. $c^\infty = 10^{-2}$ M, pH 4. Model parameters: $pK_{a_1} = 6$, $pK_{a_2} = 8$, $C_0 = 5$ μF cm^{-2}, $C_1 = 50$ μF cm^{-2}, $C_2 = 20$ μF cm^{-2}, $N_0 = 6 \times 10^{13}$ atoms cm^{-2}, $K_Y = 10^4$ mol^{-1} l, $K'_Y = 10^2$ mol^{-1} l, $K'_X = K_X = 0$ mol^{-1} l.

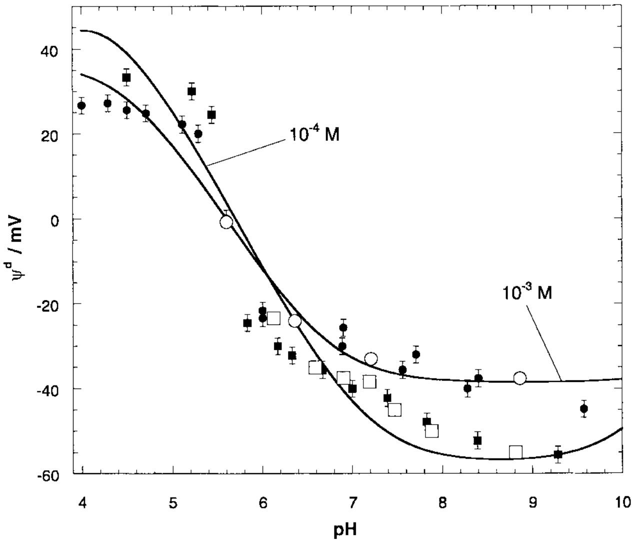

Fig. 11. Diffuse double layer potentials at a TiO_2 electrode as a function of pH (absence of an applied potential) for two (indifferent) electrolyte concentrations of 10^{-3} (circles) and 10^{-4} (squares) KNO_3. The full symbols refer to electrophoresis data performed on colloidal TiO_2 and the open symbols to AFM data [13,14]. The full lines are the computed ψ^d(pH) curves. Model parameters: (10^{-3} M) $pK_{a_1} = pK_{a_2} =$ iep = 5.6, $C_1 = 120$ μF cm^{-2}, $N_s = 1.9 \times 10^{12}$ sites cm^{-2}, (10^{-4} M) $pK_{a_1} = pK_{a_2} =$ iep = 5.7, $C_1 = 120$ μF cm^{-2}, $N_s = 1 \times 10^{12}$ sites cm^{-2}.

[25]. The surface used (treated at high temperature) is reported to essentially consist of anatase for which the iep and N_s are somewhat higher than for the rutile structure [33,17]. In contrast to colloidal probe AFM, all oxidic sites of the surface are probed with the radioisotope method. To fit the data, values of 6.2 for the iep and 6×10^{14} cm^{-2} for N_s were used. The isotherms $\Gamma(\Delta\varphi)$ were computed on the basis of the model presented in Section 3 by replacing the expressions of Γ (Eq. (20)), σ^β (Eq. (11)) and σ^d (Eq. (2)) by the more general expressions accounting for the presence of the different ionized forms of the adsorbing species [34]

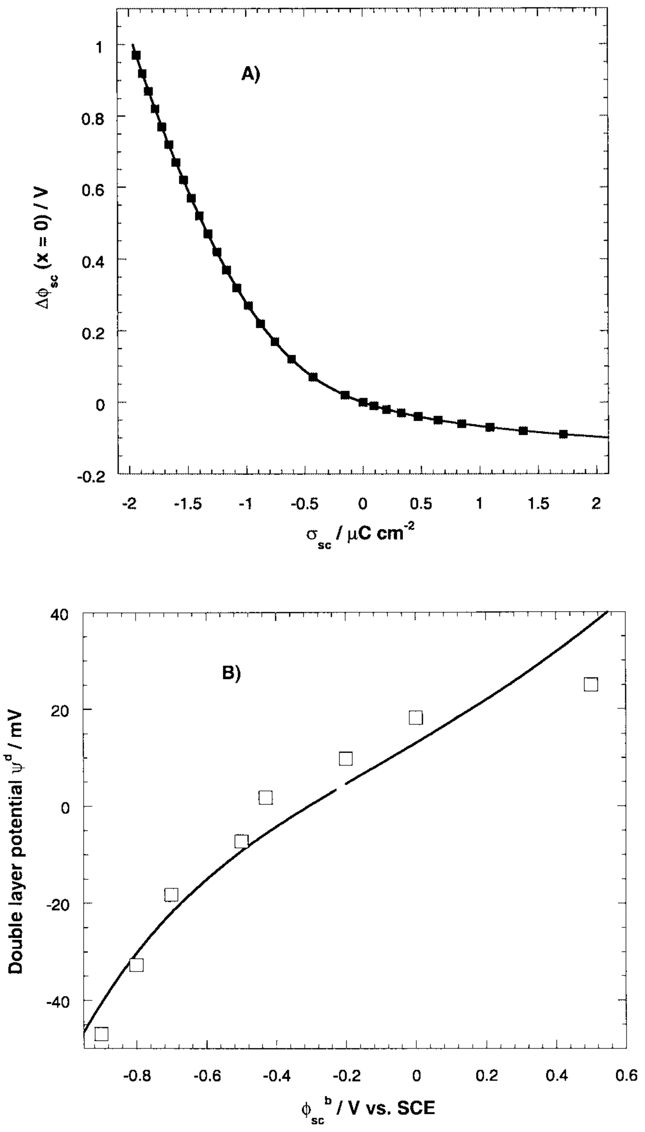

Fig. 12. (A) Potential drop (in the space charge layer)–electric charge relationship for TiO_2 semiconductor (n-type). Model parameters: $N_{sc} = 10^{19}$ cm^{-3}, $\varepsilon_{sc} = 14$. (B) Amphifunctional behaviour of TiO_2. Full line: theory. Points: experiments (redrawn from Ref. [7]). Model parameters: $pK_{a_1} = pK_{a_2} = \text{iep} = 5.6$, $C_0 = 1$ µF cm^{-2}, $C_1 = 120$ µF cm^{-2}, $N_s = 4 \times 10^{12}$ sites cm^{-2}.

$$\Gamma = -\sum_i \sigma_i^\beta / |z_i| F \tag{29}$$

$$\sigma^\beta = \sum_i \sigma_i^\beta = -\sum_i |z_i| F \Gamma_{\mathrm{MOH_2Y_i^{z_i+1}}} \tag{30}$$

$$\sigma^d = -[\mathrm{sign}(y^d)](2I\varepsilon RT)^{1/2} \left| \sum_i c_i^\infty \exp(-z_i y^d) - \sum_i c_i^\infty \right|^{1/2} \tag{31}$$

where the index i refers to the anion $Y_i^{z_i}$ of bulk concentration c_i^∞, valency z_i and binding constant K_{Y_i}. As was observed experimentally in Ref. [8], the computations reveal an apparent absence of effect of the applied potential over a very large potential region because an adsorption plateau is established which does not correspond to saturation (Fig. 13A). The electric charge primarily resulting from the applied potential is totally compensated by the protonic charge σ^0. The oxidic sites present in large numbers at the surface and seen completely by the experiments performed, buffer the double layer potential as well as the adsorption of the anions. The potentials necessary to reach the saturations of the protonic charge, noted $\Delta\varphi_{sat}(\beta = \pm 1)$ in Figs. 3–5, are very high (±100 V). The parameters K_{Y_i}, used as fitting parameters for the experimental data $\Gamma(\Delta\varphi)$, tend to show the following adsorbability sequence $ClO_4^- \approx HSO_4^- \ll SO_4^{2-} \ll H_2PO_4^-$. Using the values of K_{Y_i} derived from the curves $\Gamma(\Delta\varphi)$, the adsorption isotherms $\Gamma(c^\infty)$, obtained at constant pH and potential, and the adsorption isotherms Γ(pH), obtained at constant electrolyte concentration and potential, were computed. The experimental patterns of the pH and concentration dependences of Γ are reproduced well by the model (Fig. 13B and C). These latter data allow the following extension of the adsorbability sequence at TiO_2 as $ClO_4^- \approx HSO_4^- \ll SO_4^{2-} \ll H_2PO_4^- \ll H_2PO_4^{2-}$. Hence, amphifunctional properties of a substrate are compatible with the observations according to which, over certain ranges of conditions, Γ is not affected by $\Delta\varphi$. The common explanation in terms of the 'insulating' properties of TiO_2 is therefore premature and not generally correct. Other studies [25] report that for a substrate consisting of 30% RuO_2 and 70% TiO_2, an adsorption plateau is found for anions over a relatively narrow potential region. The decrease of Γ, expected at positive potentials (see Section 3), occurs at 0.6–0.8 V. The introduction of ruthenium indeed generates a better conductivity of the substrate and hence a higher electric charge. The buffering propensity of the oxidic sites is therefore not as efficient as for TiO_2. Part of the countercharge induced by the potential is present at the iHp, thus leading to the experimentally measurable potential dependence of the anionic adsorption. This reasoning is supported by examining experimental results concerning anion

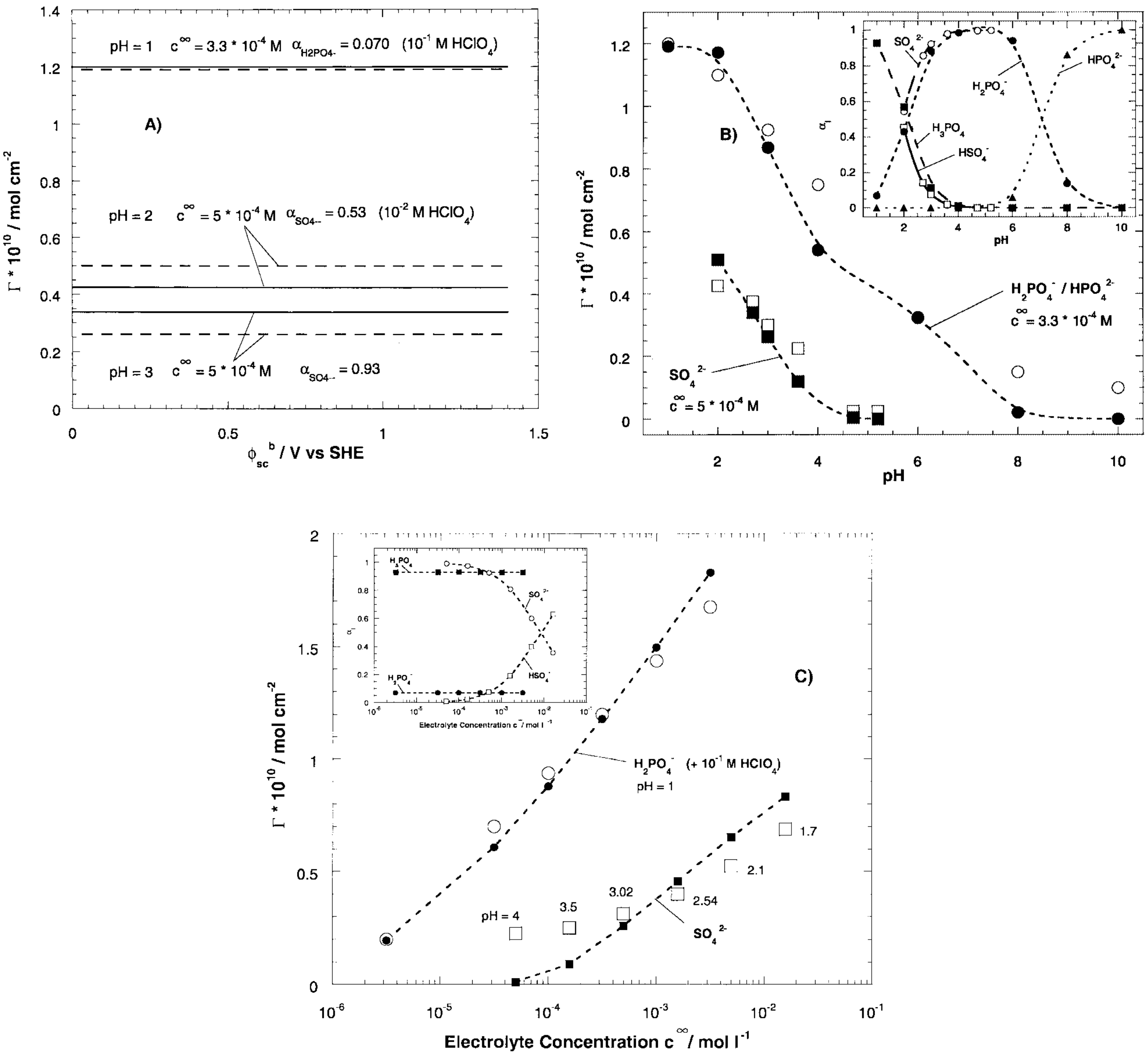

Fig. 13. Computed (dashed lines and/or full symbols) and experimental adsorption isotherms (taken from Ref. [8]) of sulfuric and phosphoric anions on TiO_2 as a function of the applied potential (A), pH (B) and electrolyte concentration (C). In (B) and (C) (applied potential 0.5 V versus SHE), the experimental data are the open symbols and in (A) the full curves. Model parameters: $pK_a = pK_a = \text{iep} = 6.2$, $C_0 = 1$ μF cm^{-2}, $C_1 = 120$ μF cm^{-2}, $C_2 = 20$ μF cm^{-2}, $N_s = 6 \times 10^{14}$ sites cm^{-2}. $K_Y = 5 \times 10^{-3}$ (SO_4^{2-}), 12 ($H_2PO_4^-$), 11.22×10^{42}(HPO_4^{2-}) mol^{-1} l. The mole fractions α_i of the different absorbed species $Y_i^{Z_i}$ ($\alpha_i = c_i^\infty / c^\infty$) are given as a function of pH and the concentration c^∞ of H_3PO_4 or H_2SO_4 in insets.

adsorption on platinum [35], for which the polarizable part dominates the reversible component. The formation of the surface oxide on platinum accounts for the observed Nernstian dependence of the potential of zero charge with pH [36,37]. Two maxima in the adsorption isotherm $\Gamma(\Delta\varphi)$ are observed; they correspond to peaks and not to plateaux (no complete buffering by the 'oxide (sub)monolayer'). The presence of these two maxima indicates that for sulfate ions on platinum the adsorption takes place at sites of different nature (metallic and chemical, Section 5).

7. Conclusions

In a previous paper [5], the double layer potential profiles at amphifunctionally electrified interfaces were examined theoretically. The coupling between electronic and ionic charging processes was considered for the case of charge-determining ions (protons) for the oxidic surface under investigation. The present study describes the situation where in addition the electrolyte ions specifically interact with the amphifunctional surface. The model systems chosen are the interfaces between an electrolyte solution and a partially oxidized metal or semiconducting oxide. The cases where the ions are preferentially adsorbed on the oxide (submono)layer (reversible part of the dl) and on the unoxidized part of the surface (polarizable component of the dl) are examined in detail. The corresponding ion adsorption isotherms as a function of the applied potential, pH, the electrolyte concentration and the parameters describing the adsorption of H^+ ions (pK values and number of oxidic sites) are given. The analysis is extended to the case where the electrolyte ions exhibit affinities for both parts of the amphifunctional electrode surface. The models are consistent with the known limiting dl situations at fully polarizable (mercury) and reversible (oxide) interfaces. The case of specific adsorption of anions on the TiO_2 semiconductor electrode is explicitly analyzed. It is shown how the amphifunctional nature of the dl is compatible, within a certain potential regime, with an apparent independence of Γ on the externally applied potential. The results of the present model computations are in promising agreement with experimental studies. Further refinement of the modelling calls for the inclusion of effects such as roughness of the oxide surface. A paper currently in preparation [32] accounts for the roughness effects in dl measurements (2- or 3-dimensional surface models). This is of particular importance to dl studies by AFM and electrokinetics since these techniques probe only the double layer beyond the surface asperities.

Acknowledgements

This work was carried out within the frame of a project entitled ‘Electrophoretic Particle Deposition’, a cooperation with Philips Research Laboratories (Eindhoven, The Netherlands) with financial support from SENTER (Dutch Ministry of Economic Affairs).

Appendix A: The semiconducting oxide | solution interface

A.1. The potential and charge distributions in the space charge layer

Due to the limited charge carrier density, the charge in a semiconductor electrode is distributed over a space charge layer. The potential and the charge distributions within this layer are described by the Poisson equation:

$$d^2\Delta\phi_{sc}(x)/dx^2 = -\rho(x)/\varepsilon_0\varepsilon_{sc} \tag{A1}$$

where ε_{sc} is the relative permittivity of the semiconductor material, x the distance from the surface and $\Delta\phi_{sc}$ the potential drop in the space charge region defined by

$$\Delta\phi_{sc}(x) = \varphi_{sc}^{b} - \varphi(x) \tag{A2}$$

φ_{SC}^{b} is the potential (externally applied) of the bulk of the semiconductor and $\varphi(x)$ the potential at a distance x from the surface, both with respect to the bulk of the electrolyte solution. In the case of an n-type semiconductor (such as titanium oxide), most of the charge carriers result either from a doping consisting in the injection of electron-donor atoms or from a treatment at high temperature (generating defects in the crystal). Designating the fixed ionized donor density as resulting from one of these operations by N_{sc} and the electron density at a given distance x from the surface by $n(x)$, one can show that $n(x)$ and $\rho(x)$ are given by [38]

$$n(x) = N_{sc}\exp(-\Delta y_{sc}(x)) \tag{A3}$$

$$\rho(x) = eN_{sc}(1-\exp(-\Delta y_{sc}(x))) \tag{A4}$$

where $\Delta y_{sc}(x)$ is the dimensionless potential $(e/k_BT)\Delta\phi_{sc}(x)$, e the elementary charge, k_B the Boltzmann constant and T the temperature. After integration of (A1) and application of the boundary condition $\varphi(x)_{x\to\infty} = \varphi_{sc}^{b}$, the electric field E_s at the surface is found to be

$$\begin{aligned} E_s &= (d\Delta\phi_{sc}(x)/dx)_{x\to 0} \\ &= \frac{(k_BT/e)}{\kappa_{sc}^{-1}}\,[\Delta y_{sc}(x=0) + \exp(-\Delta y_{sc}(x=0)) \\ &\quad -1]^{1/2} \end{aligned} \tag{A5}$$

where κ_{sc}^{-1} is the so-called Debye length (characteristic space charge layer thickness) of the semiconductor defined by

$$\kappa_{sc}^{-1} = (k_BT\varepsilon_0\varepsilon_{sc}/2e^2N_{sc})^{1/2} \tag{A6}$$

Denoting the charge in the space charge region as σ_{sc}, the charge–potential relationship is

$$\sigma_{sc} = \delta\varepsilon_0\varepsilon_{sc}E_s = f(\Delta\phi_{sc}(x=0)) \tag{A7}$$

with $\delta = -1$ for $\Delta\phi_{sc}(x=0) > 0$ and $\delta = +1$ for $\Delta\phi_{sc}(x=0) < 0$. At the flat band potential (equivalent to the potential of zero charge), we have $\varphi(x=0) = \varphi_{sc}^{b} = \varphi_{fb}$ ($\Delta\phi_{sc}(x=0) = 0$) and $\sigma_{sc} = 0$. The differential capacity of the space charge layer is

$$C_{sc} = d\sigma_{sc}/d\Delta\phi_{sc} \tag{A8}$$

Around the flat band potential, the dependence of the interfacial capacitance C_{exp} measured experimentally ($1/C_{exp} = 1/C_{sc} + 1/C_0 + 1/C_1 + 1/C_2 + 1/C^d$) is governed by the space charge capacitance.

A.2. Amphifunctional charging of the dl at a semiconducting oxide | solution interface

In this section, on the basis of the metallic case examined in some detail in Ref. [5], we briefly describe the amphifunctional character of an interface between a

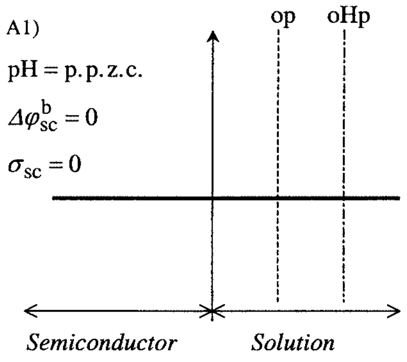
A1)
$pH = p.p.z.c.$
$\Delta\varphi^b_{sc} = 0$
$\sigma_{sc} = 0$
op
oHp
Semiconductor
Solution

Fig. A1.

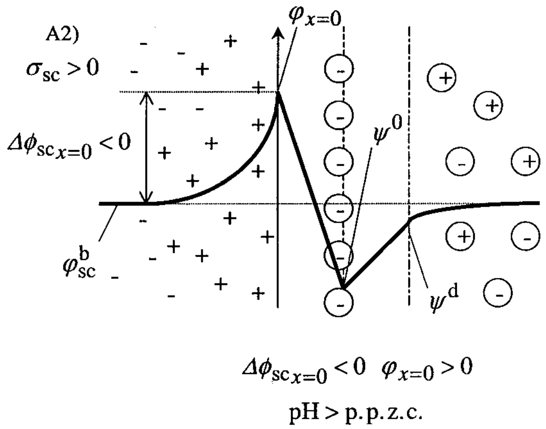
A2)
$\sigma_{sc} > 0$
$\varphi_{x=0}$
$\Delta\phi_{sc\,x=0} < 0$
ψ^0
ψ^d
φ^b_{sc}
$\Delta\phi_{sc\,x=0} < 0 \quad \varphi_{x=0} > 0$
$pH > p.p.z.c.$

Fig. A2.

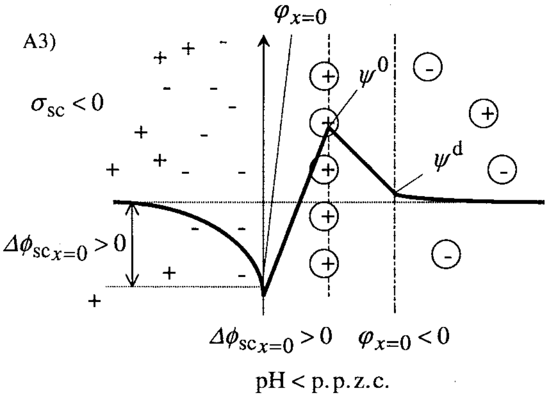
A3)
$\sigma_{sc} < 0$
$\varphi_{x=0}$
ψ^0
ψ^d
$\Delta\phi_{sc\,x=0} > 0$
$\Delta\phi_{sc\,x=0} > 0 \quad \varphi_{x=0} < 0$
$pH < p.p.z.c.$

Fig. A3.

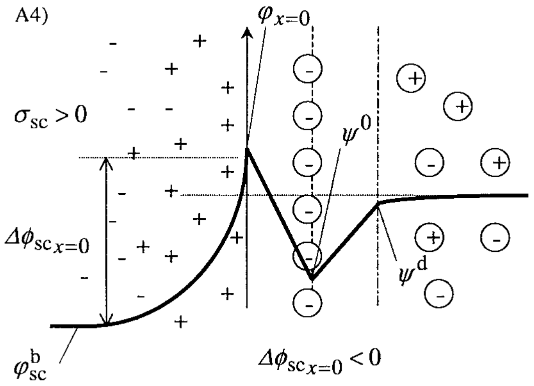
A4)
$\varphi_{x=0}$
$\sigma_{sc} > 0$
ψ^0
$\Delta\phi_{sc\,x=0}$
ψ^d
φ^b_{sc}
$\Delta\phi_{sc\,x=0} < 0$

Fig. A4.

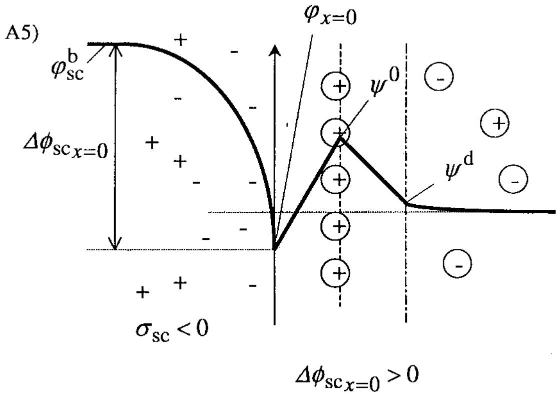
A5)
$\varphi_{x=0}$
φ^b_{sc}
ψ^0
$\Delta\phi_{sc\,x=0}$
ψ^d
$\sigma_{sc} < 0$
$\Delta\phi_{sc\,x=0} > 0$

Fig. A5.

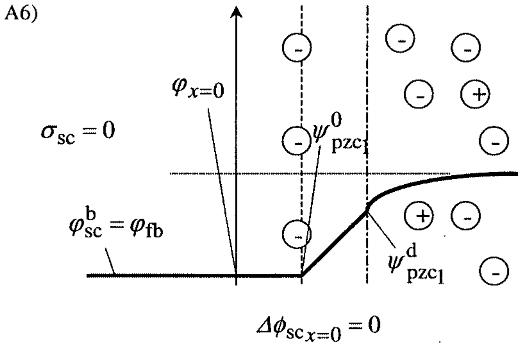
A6)
$\sigma_{sc} = 0$
$\varphi_{x=0}$
$\psi^0_{pzc_1}$
$\varphi^b_{sc} = \varphi_{fb}$
$\psi^d_{pzc_1}$
$\Delta\phi_{sc\,x=0} = 0$

Fig. A6.

semiconductor, of which the bulk properties are oxide-like, and an electrolyte solution. Figs. A1, A2 and A3 sketch the situations where the potential φ^b_{sc} is kept constant and the pH varied. Figs. A4, A5 and A6 picture the dependence of σ_{sc} on the potential φ^b_{sc} at constant pH. Specific adsorption of ions from the background electrolyte can be taken into account by introducing into the double layer model an iHp, as for the metallic case. Effectively, the magnitude of the electric charge necessary to counterbalance the ionic charge is the same in the metallic and semiconductor cases ($\sigma^e = \sigma_{sc}$). The only difference resides in the distribution of this electric countercharge and in the magnitude of the potential to be applied to the bulk of the substrate to generate it. For a given situation ($\Delta\varphi$, pH) with charge σ^e, the corresponding potential φ^b_{sc} for the semiconductor case would be

$$\varphi^b_{sc} = f^{-1}(\sigma_{sc} = \sigma^e(\Delta\varphi,\ \mathrm{pH})) + \Delta\varphi \qquad \text{(A9)}$$

where f^{-1} is the reciprocal function of f introduced in Eq. (A7).

References

[1] J. Lyklema, in: G.D. Parfitt, C.H. Rochester (Eds.), Adsorption of Small Ions, in Adsorption from Solution at the Solid | Liquid Interface (Ch. 5), Academic Press, London, 1983.
[2] J. Lyklema, Fundamentals of Interface and Colloid Science, vol. 2, Solid–Liquid Interfaces. Academic Press, London, 1995, Ch. 3, p. 3.107.
[3] P. Delahay, Double Layer and Electrode Kinetics (Ch. 3–5), Interscience Publishers Wiley and Sons, New York, 1965.
[4] D.C. Grahame, Chem. Rev. 41 (1947) 441.
[5] J. Duval, J. Lyklema, J.M. Kleijn, H.P. v. Leeuwen, Langmuir 17 (2001) 7573.
[6] D. Barten, J.M. Kleijn, J. Duval, H.P. v. Leeuwen, J. Lyklema, M.A. Cohen Stuart, Langmuir, in press.
[7] K. Hu, F.-R.F. Fan, A.J. Bard, A.C. Hillier, J. Phys. Chem. B 101 (1997) 8298.
[8] V.E. Kazarinov, V.N. Andreev, A.P. Mayorov, J. Electroanal. Chem. 130 (1981) 277.
[9] (a) G. Gouy, Compt. Rend. 149 (1909) 654;
(b) G. Gouy, J. Phys. 4 (1910) 457;
(c) G. Gouy, Ann. Phys. 7 (1917) 129.
[10] D.L. Chapman, Phil. Mag. 6 (1913) 475.
[11] T.W. Healy, L.R. White, Adv. Colloid Interface Sci. 9 (1978) 303.
[12] M. Giesbers, Thesis, Wageningen University, the Netherlands, 2001.
[13] I. Larson, C.J. Drummond, D.Y.C. Chan, F. Grieser, J. Am. Chem. Soc. 115 (1993) 11885.
[14] I. Larson, C.J. Drummond, D.Y.C. Chan, F. Grieser, J. Phys. Chem. 99 (1995) 2114.
[15] R. Sprycha, J. Szczypa, J. Colloid Int. Sci. 102 (1984) 288.
[16] R. Sprycha, J. Szczypa, J. Colloid Int. Sci. 115 (1987) 590.
[17] R.O. James, G.A. Parks, Characterization of aqueous colloids by their electrical double layer and intrinsic surface chemical properties, in: E. Matijevic (Ed.), Surface and Colloid Science, vol. 12 (Ch. 2), Plenum Press, New York, 1982.
[18] D.E. Yates, T.W. Healy, J. Chem. Soc. Faraday. Trans. I. 76 (1980) 9.
[19] R. Parsons, F. Zobel, J. Electroanal. Chem. 9 (1965) 333.
[20] M.A. Vorotyntsev, in: J.O'M. Bockris, B.E. Conway, R.E. White (Eds.), Modern Aspects of Electrochemistry, vol. 17 (Ch. 2), Plenum Press, 1986, p. 177.
[21] P.J. Scales, F. Grieser, T.W. Healy, L.R. White, D.Y.C. Chan, Langmuir 8 (1992) 965.
[22] D.C. Grahame, E.M. Coffin, J.I. Cummings, M.A. Poth, J. Am. Chem. Soc. 74 (1952) 1207.
[23] D.C. Grahame, J. Am. Chem. Soc. 80 (1958) 4201.
[24] D.C. Grahame, R. Parsons, J. Am. Chem. Soc. 83 (1961) 1291.
[25] V.E. Kazarinov, V.N. Andreev, Elektrokhimiya 13 (1977) 685.
[26] V.E. Kazarinov, V.N. Andreev, Elektrokhimiya 14 (1978) 577.
[27] T.Ya. Safonova, O.A. Petrii, E.A. Gudkova, Elektrokhimiya 16 (1980) 1607.
[28] G.A. Kokarev, V.A. Kolesnikov, A.F. Gubin, A.A. Korobanov, Elektrokhimiya 18 (1981) 407.
[29] V.N. Andreev, V.E. Kazarinov, D.V. Kokoulina, L.I. Krishtalik, Elektrokhimiya 14 (1978) 1271.
[30] J.M. Kleijn, Colloids Surfaces 51 (1990) 371.
[31] J. Sanchez, J. Augustynski, J. Electroanal. Chem. 103 (1979) 423.
[32] J. Duval, J. Lyklema, J.M. Kleijn, H.P. v. Leeuwen, in preparation.
[33] J. Lyklema, Fundamentals of Interface and Colloid Science, vol. 2, Solid–Liquid Interfaces, Academic Press, London, 1995, Appendix 3.
[34] J. Lyklema, Fundamentals of Interface and Colloid Science, vol. 2, Solid–Liquid Interfaces, Academic Press, London, 1995, Ch. 3, p. 3.32.
[35] N.A. Balashova, Z. Phys. Chem. (Leipzig) 207 (1957) 340.
[36] E. Gileadi, S.D. Argade, J.O'M. Bockris, J. Phys. Chem. 70 (1966) 2044.
[37] N. Kallay, Z. Torbic, M. Golic, E. Matijevic, J. Phys. Chem. 95 (1991) 7028.
[38] R. Memming, Semiconductor Electrochemistry, Ch. 5), Wiley-VCH, Weinheim, 2001.

ELSEVIER

Journal of Electroanalytical Chemistry 505 (2001) 1–11

Journal of Electroanalytical Chemistry

Bipolar electrode behaviour of the aluminium surface in a lateral electric field

Jérôme Duval *, J. Mieke Kleijn, Herman P. van Leeuwen

Department of Physical Chemistry and Colloid Science, Wageningen University, Dreijenplein 6, 6703 HB Wageningen, The Netherlands

Received 10 November 2000; received in revised form 19 February 2001; accepted 20 February 2001

Abstract

This paper reports on the electrochemical processes at the surface of conducting materials such as aluminium in a thin-layer cell usually employed for electrokinetic measurements. The cell contains one or more planar Al wafers in contact with an electrolyte solution, which is subjected to an external electric field parallel to the surfaces of the wafers. Beyond a certain threshold value of the magnitude of the field, the current through the cell increases more than proportionally with the field strength. This is due to faradaic processes occurring at the two ends of the conducting substrates, i.e. reduction at the positive side of the electric field in the solution and oxidation at the negative side. In the case of Al wafers, anodic dissolution of the metal takes place and the progression of the 'corroding' edge can be followed visually. The overall electrolytic process, corresponding with the distributed current along the surface of the wafer, could be explained and modeled on the basis of the conventionally measured Butler–Volmer characteristics of the monopolar Al electrode. © 2001 Elsevier Science B.V. All rights reserved.

Keywords: Bipolar electrode; Electrodissolution; Butler–Volmer equation; Mixed potential; Solution polarization

1. Introduction

Bipolar electrode behaviour of conducting bodies is a phenomenon widely exploited in industrial applications. Examples can be found in such fields as organic electrosynthesis [1,2], elaboration of micro-conductive paths [3–6] and supported catalyst metal particle technology [2]. The phenomenon has been studied extensively for dispersions of conducting particles in so-called bipolar fluidized bed electrodes [2,7–14]. Beyond a critical extent of polarization of such an electrode, i.e. in a sufficiently strong lateral electric field, the overpotentials become sufficiently high to induce noticeable electrolysis: the spatial variation of the particle/solution potential provokes oxidation on one side of the particles, coupled with reduction at the other. Many studies deal with the electrochemical behaviour of such bipolar electrodic particles in a medium with added redox couples [11,12]. The present communication describes a set-up in which the bipolar electrode behaviour is observed for macroscopic planar geometry at aluminium surfaces. At sufficiently high electric fields, the two electrochemical reactions, reduction of water at one side and metallic dissolution at the other, can be observed visually. The theoretical interpretation of the observed faradaic effects is based upon the current–voltage characteristics of the aluminium | solution interface. The anodic and cathodic branches in the voltammogram can be described by exponential Butler–Volmer type relationships, which serve as the basis of further modeling of the overall bipolar current. The analysis explains satisfactorily the variation of the current with the field strength as well as the rate of progression of the corroding edge. This study thus links bipolar electrodic features as reported for conducting particles with macroscopically observable corrosion usually encountered in stray-current situations [15–17].

2. Experimental

The cell is of a type originally designed for electrokinetic measurements [18,19]. It has a well defined geometry and employs two auxiliary electrodes to generate a

---

* Corresponding author. Tel.: +33-317-484960; Fax: +33-317-483777.

dc field in the electrolyte solution parallel to the two wafers to be investigated. Fig. 1 shows a diagram of the parallelepipedic cell with two platinum electrodes placed in the compartments outside the thin-layer chamber. The field effectively experienced by the substrate was estimated by correcting for the potential drop in the auxiliary electrode chambers. The two electrodes used to build up the field across the solution are practically non-polarizable. The measurement of the 'conductivity curve' (i.e. the current–field dependence of the laterally polarized thin-layer cell) was usually performed via a three-electrode arrangement which yielded the most stable current readings. To avoid confusion, the term 'voltammogram' will be used exclusively to designate the current–potential relationship of a defined conducting material, measured by voltammetry. The voltammetric experiments were carried out in a conventional three-electrode cell with Pt as the counter electrode and Ag | Ag | KCl(sat) as the reference electrode (+ 0.222 V vs SHE). Before each experiment, the solution was flushed with oxygen-free nitrogen for 15 min. Measurements were carried out at 25°C.

The experiments were performed on supported Al layers with thicknesses of 200 nm or 500 nm. To warrant proper adhesion, the glass support was first covered with a 10 nm Cr layer. The layers were prepared via vapour evaporation from heated Cr and Al sources directly onto the glass support. Prior to any measurement, the samples were subjected to 15/20 min UV/ozone treatment and extensive cleaning with demineralized water. The solutions were prepared with KNO_3 background electrolyte and demineralized water as the solvent. Monitoring of the applied potential and measurement of the response of the cell were performed with a PGSTAT10 potentiostat controlled by Autolab software (Eco Chemie). Before each measurement, the electrokinetic cell was rinsed extensively with demineralized water by applying a pressure difference of 30 cm Hg.

3. Model for bipolar electrolysis in planar geometry controlled by two redox couples

3.1. Relation between current and applied lateral field

We consider bipolar electrolysis for planar substrates in the case that two different redox couples, Ox_a/R_a and Ox_c/R_c, control the anodic and cathodic processes via two irreversible reactions denoted as (a) and (c), respectively:

$$R_a \rightarrow Ox_a + n_a e^- \quad (a)$$
$$Ox_c + n_c e^- \rightarrow R_c \quad (c)$$

with n_a and n_c the number of electrons transferred per molecule for reactions (a) and (c). For the present geometry, the use of cartesian coordinates (x,y) is the most appropriate. We define arbitrarily the origin of the x-axis at the non-corroding cathodic end of the wafer. The position of the boundary between the anodic and cathodic reactions occurring at the two ends of the surface will be designated by x_0 (the analogue of the angle λ in the case of spherical symmetry [2]). Unlike the common situation for electrochemical reactions, the anodic process occurs at the negative side of the field set up in the solution and the cathodic reduction at the positive one. This is a characteristic feature of bipolar electrodes. Contrary to the usual situation in electrochemistry, interfacial potentials are here varied via the solution potential which is the externally controlled variable. The present set-up allows a direct

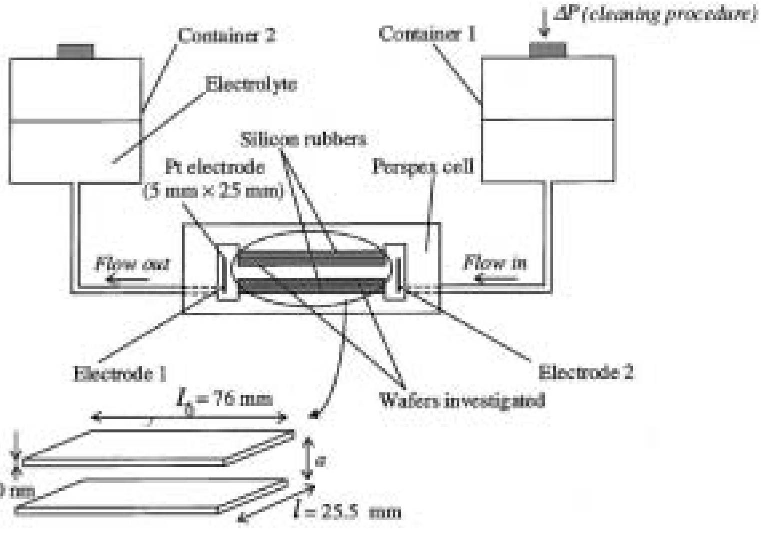

Fig. 1. Cell detail. The cell gap a was 0.15, 0.20 and 2.3 mm (see text). During experiments, no flow was applied.

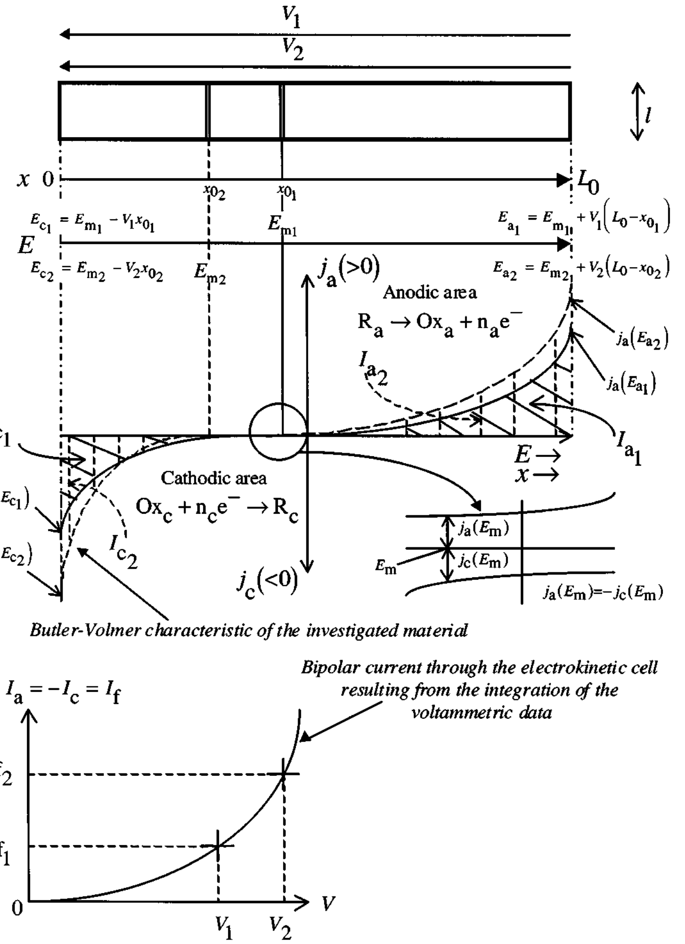
V_1
V_2
l
x 0
x_{0_2}
x_{0_1}
L_0
$E_{c_1} = E_{m_1} - V_1 x_{0_1}$
E_{m1}
$E_{a_1} = E_{m_1} + V_1(L_0 - x_{0_1})$
E
$E_{c_2} = E_{m_2} - V_2 x_{0_2}$
E_{m2}
$E_{a_2} = E_{m_2} + V_2(L_0 - x_{0_2})$
$j_a(>0)$
Anodic area
$R_a \rightarrow Ox_a + n_a e^-$
I_{a_2}
$j_a(E_{a_2})$
$j_a(E_{a_1})$
I_{c_1}
I_{a_1}
$E \rightarrow$
$x \rightarrow$
Cathodic area
$Ox_c + n_c e^- \rightarrow R_c$
$j_c(E_{c_1})$
$j_c(E_{c_2})$
I_{c_2}
$j_c(<0)$
E_m
$j_a(E_m)$
$j_c(E_m)$
$j_a(E_m) = -j_c(E_m)$
Butler-Volmer characteristic of the investigated material
$I_a = -I_c = I_f$
Bipolar current through the electrokinetic cell resulting from the integration of the voltammetric data
I_{f_2}
I_{f_1}
0
V_1
V_2
V

Fig. 2. Reconstruction of the electrolytic processes with varying $\Delta\phi_s$ (or V) from the traditional Butler–Volmer characteristics. Length of the substrate is constant and equal to L_0 (Section 3.1). The subscripts 1 and 2 denote the situations pertaining to V_1 and V_2, respectively ($V_1 < V_2$).

observation of the individual redox reactions occurring at the ends of the conductive substrate in response to the applied field across the solution (see next section).

In analogy with Fleischmann et al.'s treatment for dispersed spherical particles [2], we assume mass transfer polarization to be unimportant. For the electrochemical reactions taking place in our experiments ($H_2O \rightarrow H_2$, $Al \rightarrow Al^{3+}$) this is justified, as will be explained later, on the basis of the current–potential relationships of the substrate. Therefore, the dependence of the anodic and cathodic current densities, j_a and j_c respectively, on the potential E at the substrate | solution interface is given by the Tafel expressions for the two redox couples

$$j_a(E) = j_{0_a}\exp[r_a f(E - E_a^0)] \qquad (1)$$

$$j_c(E) = -j_{0_c}\exp[-r_c f(E - E_c^0)] \qquad (2)$$

with f, r_a and r_c defined by

$$f = \frac{F}{RT} \qquad (3)$$

$$r_a = n_a(1 - \alpha_a) \qquad (4)$$

$$r_c = n_c\alpha_c \qquad (5)$$

where α_a and α_c stand for the transfer coefficients for the oxidation reaction (a) and the cathodic reduction (c), respectively. j_0 is the apparent exchange current density, E_a^0 and E_c^0 the standard potentials of Ox_a/R_a and Ox_c/R_c respectively. F is the Faraday constant, R the gas constant and T the temperature.

The bulk concentrations of the reaction products H_2 and Al^{3+} are zero and the two irreversible processes can be pictured in the polarization curve for the substrate material as outlined in Fig. 2. In the absence of any externally applied electric field, the substrate adopts a mixed potential E_m [20,21] for which the overall current is zero. E_m is defined as the potential for which

$$j_a(E_m) = -j_c(E_m) \qquad (6)$$

and the exponential relationships Eqs. (1) and (2) give immediately

$$E_m = \frac{\ln(j_{0_c}/j_{0_a}) + f[r_c E_c^0 + r_a E_a^0]}{f[r_c + r_a]} \qquad (7)$$

In the absence of mass transfer polarization [14], the surface of the metallic wafer experiences the applied field so that the overpotential at a position x can be generally written as

$$E - E_{\mathrm{m}} = V(x - x_0) \tag{8}$$

where x_0 defines the position at which $E = E_{\mathrm{m}}$. V is the magnitude of the electric field which is related to the potential difference across the solution in the thin-layer compartment $\Delta\phi_{\mathrm{s}}$ and to the total length of the Al substrate L_0 via the simple relation

$$V = \frac{\Delta\phi_{\mathrm{s}}}{L_0} \tag{9}$$

Since there is no accumulation of charge in the bipolar electrode, the total anodic and cathodic currents (I_{a} and I_{c}) must generally obey

$$I_{\mathrm{a}} = -I_{\mathrm{c}} = I_{\mathrm{f}} \tag{10}$$

For the present case of two irreversible reactions, we may neglect the local anodic and cathodic currents for $E < E_{\mathrm{m}}$ and $E > E_{\mathrm{m}}$ respectively, so that the total currents are given by the integrals of j_{a} and j_{c} over the relevant surface areas

$$\begin{aligned} I_{\mathrm{a}} &= \int_{x_0}^{L_0} l j_{\mathrm{a}}(E(x))\mathrm{d}x \\ &= \int_{x_0}^{L_0} l j_{0_{\mathrm{a}}} \exp[r_{\mathrm{a}} f(E_{\mathrm{m}} + V(x - x_0) - E_{\mathrm{a}}^0)]\mathrm{d}x \end{aligned} \tag{11}$$

$$\begin{aligned} I_{\mathrm{c}} &= \int_0^{x_0} l j_{\mathrm{c}}(E(x))\mathrm{d}x \\ &= -\int_0^{x_0} l j_{0_{\mathrm{c}}} \exp[-r_{\mathrm{c}} f(E_{\mathrm{m}} + V(x - x_0) - E_{\mathrm{c}}^0)]\mathrm{d}x \end{aligned} \tag{12}$$

where l is the width of the substrate. After integration, Eqs. (11) and (12) yield

$$I_{\mathrm{a}} = \frac{l j_{0_{\mathrm{a}}}}{r_{\mathrm{a}} f V} \exp[r_{\mathrm{a}} f(E_{\mathrm{m}} - E_{\mathrm{a}}^0)](\exp[r_{\mathrm{a}} f V(L_0 - x_0)] - 1) \tag{13}$$

$$I_{\mathrm{c}} = \frac{l j_{0_{\mathrm{c}}}}{r_{\mathrm{c}} f V} \exp[-r_{\mathrm{c}} f(E_{\mathrm{m}} - E_{\mathrm{c}}^0)](1 - \exp[r_{\mathrm{c}} f V x_0]) \tag{14}$$

Referring to Eq. (6), which defines E_{m}, and using Eqs. (13) and (14), it follows from Eq. (10) that at $E = E_{\mathrm{m}}$

$$\frac{1}{r_{\mathrm{a}}}(\exp[r_{\mathrm{a}} f V(L_0 - x_0)] - 1) = \frac{1}{r_{\mathrm{c}}}(\exp[r_{\mathrm{c}} f V x_0] - 1) \tag{15}$$

This equation defines the position x_0 on the bipolar electrode for which the net faradaic current is zero. Assuming that $V \gg [r_{\mathrm{a}} f(L_0 - x_0)]^{-1}$ and $V \gg (r_{\mathrm{c}} f x_0)^{-1}$, which holds for sufficiently strong fields, x_0 is essentially given by

$$x_0 = \frac{1}{r_{\mathrm{a}} + r_{\mathrm{c}}}\left(\frac{1}{fV}\ln\left(\frac{r_{\mathrm{c}}}{r_{\mathrm{a}}}\right) + r_{\mathrm{a}} L_0\right) \tag{16}$$

For $r_{\mathrm{a}} = r_{\mathrm{c}}$, $x_0 = L_0/2$, the anodic and cathodic surface areas do not depend on V. If $r_{\mathrm{a}} < r_{\mathrm{c}}$, $\mathrm{d}x_0/\mathrm{d}V < 0$ and $x_0 < L_0/2$, while for $r_{\mathrm{a}} > r_{\mathrm{c}}$, x_0 is shifted in the positive direction with increasing electric field ($\mathrm{d}x_0/\mathrm{d}V > 0$).

In the case $r_{\mathrm{a}} \neq r_{\mathrm{c}}$, the position x_0, which defines the border between the anodic and cathodic reactions, is dependent on the field parameter V. For each V, the distribution of the current along the plate will change as pictured in Fig. 2. For low tangential fields, a Taylor-development of the exponential terms in Eq. (15) shows that x_0 approaches $L_0/2$.

The total current I through the thin-layer cell is the sum of the faradaic current I_{f} and the ohmic current I_Ω: the latter is obtained from

$$I_\Omega = g\Delta\phi_{\mathrm{s}} \tag{17}$$

with g the conductance of the cell. Generally, g is linked to the specific conductivity of the bulk electrolyte K^{L} and a possible surface conductance $2K^\sigma l/L_0$ via

$$g = \frac{K^{\mathrm{L}}}{C} + \frac{2K^\sigma l}{L_0} \tag{18}$$

where K^σ is the specific surface conductivity (in Ω^{-1}). C is the cell constant defined by

$$C = \frac{L_0}{al} \tag{19}$$

with a the distance between the two parallel substrates.

Using Eq. (13) and Eqs. (17)–(19), the relation between the total current $I = I_{\mathrm{f}} + I_\Omega$ and the electric field V is

$$\begin{aligned} I &= (aK^{\mathrm{L}} + 2K^\sigma)lV \\ &\quad + \frac{l j_{0_{\mathrm{a}}}}{r_{\mathrm{a}} f V}\exp[r_{\mathrm{a}} f(E_{\mathrm{m}} - E_{\mathrm{a}}^0)](\exp[r_{\mathrm{a}} f V(L_0 - x_0)] - 1) \end{aligned} \tag{20a}$$

A similar expression for I is obtained by considering the cathodic current I_{c} (Eq. (14))

$$\begin{aligned} I &= (aK^{\mathrm{L}} + 2K^\sigma)lV \\ &\quad - \frac{l j_{0_{\mathrm{c}}}}{r_{\mathrm{c}} f V}\exp[-r_{\mathrm{c}} f(E_{\mathrm{m}} - E_{\mathrm{c}}^0)](1 - \exp[r_{\mathrm{c}} f V x_0]) \end{aligned} \tag{20b}$$

3.2. *The anodic dissolution process*

Let us now consider in more detail the electrolytic dissolution of the metal at the anodic side as a function of time t. Our purpose is to give a theoretical expression for $L(t)$, the remaining length of the bipolar electrode, in terms of the evolution of the current during the dissolution process. The fundamental process is the anodic dissolution of the metal and instead of the more general reaction (a), we now write:

$$\mathrm{M} \rightarrow \mathrm{M}^{n_a+} + n_a e^-$$

As expressed by Eq. (8), the interfacial potential E varies linearly with x on the substrate. Consequently, the voltammogram can be projected directly on the length axis of the metal plate (Fig. 3). With decreasing $L(t)$ and constant field strength, the overpotential span along the plate decreases. Therefore, the increase of $\Delta L(t) = L_0 - L(t)$ is accompanied by a lowering of the faradaic current whereas the ohmic contribution is essentially constant. The decrease of the electroactive bipolar area corresponds with a decrease of the current in the anodic and cathodic branches of the voltammogram. During dissolution, the position of x_0 moves towards the cathodic area in order to maintain the balance between anodic and cathodic currents.

The dependence of E on position (Eq. (8)) now becomes time dependent:

$$E(t) - E_m = V(x - x_0(t)) \tag{21}$$

Following the derivation in the previous section (Eqs. (13) and (14)), the total dissolution current I_f depends on $L(t)$ via the expressions

$$I_f(t) = \frac{lj_{0_a}}{r_a f V}\exp[r_a f(E_m - E_a^0)](\exp[r_a fV(L(t) - x_0(t))] - 1) \tag{22a}$$

$$I_f(t) = -\frac{lj_{0_c}}{r_c f V}\exp[-r_c f(E_m - E_c^0)](1 - \exp[r_c fVx_0(t)]) \tag{22b}$$

Providing that the conditions required for the validity of Eq. (16) are fulfilled at each time t, we have

$$x_0(t) = \frac{1}{r_a + r_c}\left(\frac{1}{fV}\ln\left(\frac{r_c}{r_a}\right) + r_a L(t)\right) \tag{23}$$

and $I_f(t)$ can be rewritten as

$$I_f(t) = \frac{lj_{0_a}}{r_a f V}\exp[r_a f(E_m - E_a^0)] \times \left(\exp\left[\frac{r_a}{r_a + r_c}\left(r_c fVL(t) + \ln\left(\frac{r_a}{r_c}\right)\right)\right] - 1\right) \tag{24}$$

Assuming that the front of the corrosion edge corresponds with a step-function of amplitude δ_M (the thickness of the metallic layer), the dissolved mass can be expressed via the density ρ_M of the metal and the total dissolved volume $\Delta L\delta_M l$. This is related to the total faradaic charge Q_f transferred (Faraday's law):

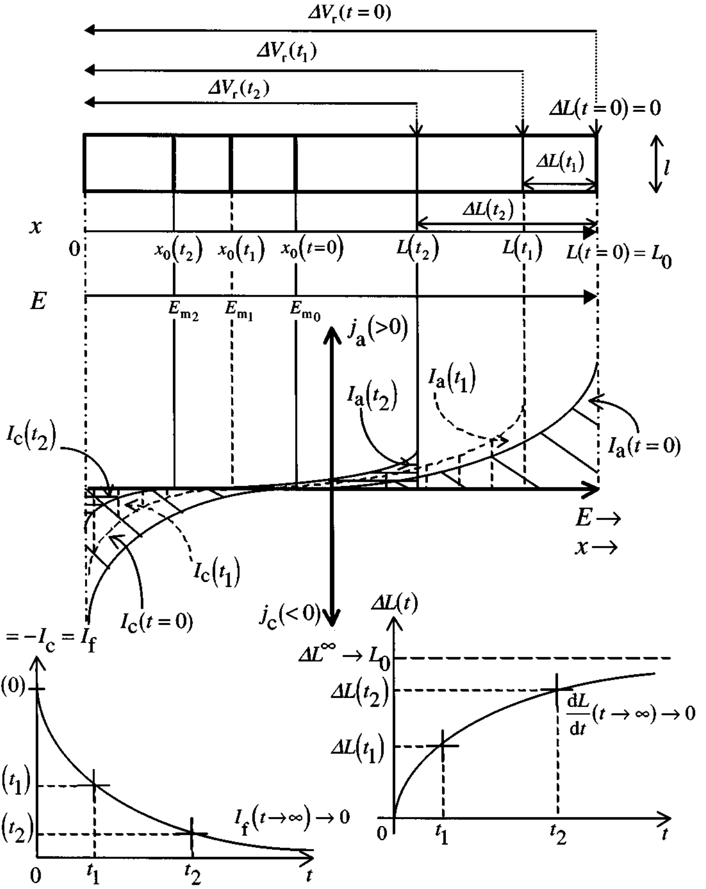

$\Delta V_r(t=0)$
$\Delta V_r(t_1)$
$\Delta V_r(t_2)$
$\Delta L(t=0)=0$
$\Delta L(t_1)$
l
$\Delta L(t_2)$
x
0
$x_0(t_2)$
$x_0(t_1)$
$x_0(t=0)$
$L(t_2)$
$L(t_1)$
$L(t=0)=L_0$
E
E_{m_2}
E_{m_1}
E_{m_0}
$j_a(>0)$
$I_a(t_2)$
$I_a(t_1)$
$I_a(t=0)$
$I_c(t_2)$
$E\rightarrow$
$x\rightarrow$
$I_c(t_1)$
$I_c(t=0)$
$j_c(<0)$
$I_a=-I_c=I_f$
$I_f(0)$
$I_f(t_1)$
$I_f(t_2)$
$I_f(t\rightarrow\infty)\rightarrow 0$
0
t_1
t_2
t
$\Delta L(t)$
$\Delta L^\infty \rightarrow L_0$
$\Delta L(t_2)$
$\Delta L(t_1)$
$\frac{dL}{dt}(t\rightarrow\infty)\rightarrow 0$
0
t_1
t_2
t

Fig. 3. Reconstruction of the anodic dissolution process with time when applying a constant high potential difference $\Delta\phi_s$ across the solution (Section 3.2). $\Delta V_r(t)$ stands for the remaining potential over the plate at t. Three situations at $t = 0$, t_1 and t_2 ($t_1 < t_2$) are considered. On the potential axis, the subscripts 0, 1 and 2 denote the initial situation and the situations at t_1 and t_2, respectively.

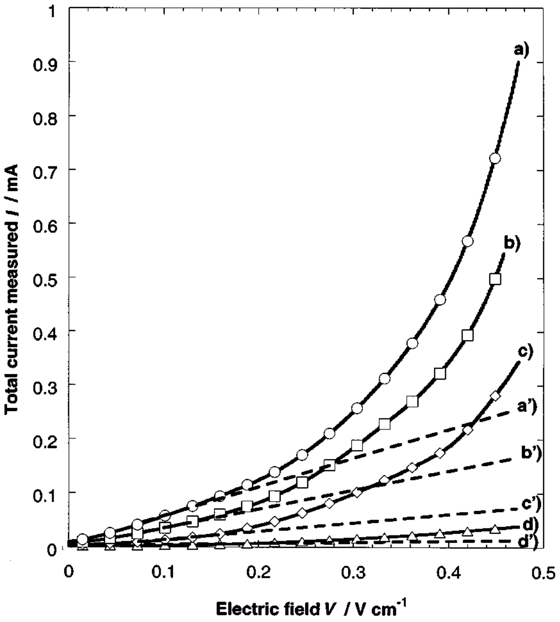

Fig. 4. Conductivity curves for aluminium (plain curves) and silica substrates (dashed curves) for different electrolyte concentrations *c*. Scan rate (increasing potential): 0.03 V s^{-1}. $C = 150$ cm^{-1} ($a = 0.20$ mm). $c = 10^{-1}$ (a, a′), 5×10^{-2} (b, b′), 10^{-2} (c, c′), 2×10^{-4} M (d, d′).

$$I_\mathrm{f}(t) = \frac{\mathrm{d}Q_\mathrm{f}}{\mathrm{d}t} = -n_\mathrm{a}Fl\left(\frac{\rho_\mathrm{M}\delta_\mathrm{M}}{M_\mathrm{M}}\right)\frac{\mathrm{d}L(t)}{\mathrm{d}t} \tag{25}$$

with M_M the molar mass of the metal. In the analysis of the experimental results, the faradaic current resulting from the dissolution of chromium will be considered negligible compared to that of aluminium since the term $\rho_\mathrm{Cr}\delta_\mathrm{Cr}/M_\mathrm{Cr}$ is about 15 times lower than $\rho_\mathrm{Al}\delta_\mathrm{Al}/M_\mathrm{Al}$. The assumption of an infinitely sharp edge is approximate considering the starting point of an exponential j–E relationship (implying a more gradual dissolution profile), but is justified by experimental findings (see Section 4).

Combination of Eqs. (24) and (25) yields

$$-\frac{M_\mathrm{M}j_{0_\mathrm{a}}}{n_\mathrm{a}FfV\rho_\mathrm{M}\delta_\mathrm{M}r_\mathrm{a}}\exp[r_\mathrm{a}f(E_\mathrm{m} - E_\mathrm{a}^0)]\mathrm{d}t = \frac{\mathrm{d}L(t)}{\exp\left[\frac{r_\mathrm{a}}{r_\mathrm{a}+r_\mathrm{c}}\left(r_\mathrm{c}fVL(t) + \ln\left(\frac{r_\mathrm{a}}{r_\mathrm{c}}\right)\right)\right] - 1} \tag{26}$$

Eq. (26) can be solved by integrating over time from $t = 0$ to t and over the spatial variable L from $L(t = 0) = L_0$ to $L(t)$. After some rearrangement, the result is

$$\int_0^t -\frac{1}{\tau}\mathrm{d}t = \int_{L_0}^{L(t)} \frac{fV\left(\frac{r_\mathrm{a}r_\mathrm{c}}{r_\mathrm{a}+r_\mathrm{c}}\right)\exp\left[-\left(\frac{r_\mathrm{a}r_\mathrm{c}}{r_\mathrm{a}+r_\mathrm{c}}\right)fVL\right]}{\exp\left[\left(\frac{r_\mathrm{a}}{r_\mathrm{a}+r_\mathrm{c}}\right)\ln\left(\frac{r_\mathrm{a}}{r_\mathrm{c}}\right)\right] - \exp\left[-\left(\frac{r_\mathrm{a}r_\mathrm{c}}{r_\mathrm{a}+r_\mathrm{c}}\right)fVL\right]}\mathrm{d}L \tag{27}$$

with τ defined by

$$\tau = \left(\frac{r_\mathrm{a}+r_\mathrm{c}}{r_\mathrm{c}}\right)\frac{n_\mathrm{a}F\rho_\mathrm{M}\delta_\mathrm{M}}{M_\mathrm{M}j_{0_\mathrm{a}}}\exp[-r_\mathrm{a}f(E_\mathrm{m} - E_\mathrm{a}^0)] \tag{28}$$

The solution of Eq. (27) can be rearranged to give an explicit expression for $L(t)$:

$$L(t) = \frac{1}{r_\mathrm{c}fV}\ln\left(\frac{r_\mathrm{c}}{r_\mathrm{a}}\right) - \frac{1}{fV}\frac{r_\mathrm{a}+r_\mathrm{c}}{r_\mathrm{a}r_\mathrm{c}}\ln\left\{1 - \exp\left(-\frac{t}{\tau}\right) \times\left[1 - \exp\left[-\frac{r_\mathrm{a}}{r_\mathrm{a}+r_\mathrm{c}}\left(r_\mathrm{c}fVL_0 + \ln\left(\frac{r_\mathrm{a}}{r_\mathrm{c}}\right)\right)\right]\right]\right\} \tag{29}$$

The short-time limit of Eq. (29) is $L(0) \to L_0$. The long-time limit is not provided by Eq. (29) because it is based on the approximate Eq. (23) valid only for sufficiently high potentials $VL(t)$ and hence sufficiently short times.

For $t \ll \tau$, a Taylor-development of the first order in t simplifies Eq. (29) to

$$L(t) = L_0 - \frac{1}{fV}\frac{r_\mathrm{a}+r_\mathrm{c}}{r_\mathrm{a}r_\mathrm{c}}\ln\left\{1 + \frac{t}{\tau}\left[-1 + \exp\left[\frac{r_\mathrm{a}}{r_\mathrm{a}+r_\mathrm{c}}\left(r_\mathrm{c}fVL_0 + \ln\left(\frac{r_\mathrm{a}}{r_\mathrm{c}}\right)\right)\right]\right]\right\} \tag{30}$$

which provides the initial change of the length $\Delta L(t)$ with time.

The expression of the total net current with time $I(t)$ can be derived from Eqs. (17)–(19), (25) and (29):

$$I(t) = (aK^\mathrm{L} + 2K^\sigma)lV + \frac{1}{fV}\frac{r_\mathrm{a}+r_\mathrm{c}}{r_\mathrm{a}r_\mathrm{c}}\frac{n_\mathrm{a}Fl\rho_\mathrm{M}\delta_\mathrm{M}}{M_\mathrm{M}\tau} \left\{\frac{\left[1 - \exp\left[-\frac{r_\mathrm{a}}{r_\mathrm{a}+r_\mathrm{c}}\left(r_\mathrm{c}fVL_0 + \ln\left(\frac{r_\mathrm{a}}{r_\mathrm{c}}\right)\right)\right]\right]\exp\left(-\frac{t}{\tau}\right)}{1 - \left[1 - \exp\left[-\frac{r_\mathrm{a}}{r_\mathrm{a}+r_\mathrm{c}}\left(r_\mathrm{c}fVL_0 + \ln\left(\frac{r_\mathrm{a}}{r_\mathrm{c}}\right)\right)\right]\right]\exp\left(-\frac{t}{\tau}\right)}\right\} \tag{31}$$

4. Results and discussion

4.1. Conductivity curves

Fig. 4 represents the conductivity curves measured in the field strength range 0–0.5 V cm^{-1} for $a = 0.20$ mm and different electrolyte concentrations. The measurements were made using one bare silica plate and one aluminium wafer in the cell. The curves clearly exhibit two regimes. For electric fields lower than approximately 0.2 V cm^{-1} ($\Delta\phi_\mathrm{s} \approx 1.5$ V), current and potential are linked via the linear relationship given by Eq. (17). In this range of potential differences, the current essentially corresponds to the ohmic contribution I_Ω. For each electrolyte concentration, the conductance g was determined from the slope. According to Eq. (18), the plot of g versus K^L allows derivation of the cell constant identified as the inverse of the slope. This yields

$C \approx 135\ \mathrm{cm}^{-1}$, a value in reasonable agreement with the value following from the geometrical parameters of the cell ($150\ \mathrm{cm}^{-1}$), the difference being attributable to stray effects. A similar analysis with $a = 0.15$ mm also provided good correlation between the experimental and geometrical cell constant. The intercept of the linear plot of g as a function of K^{L} is ascribed to surface conductance and is used in the computation of the electrokinetic potential.

For potentials higher than 1.5 V, the interfacial potential difference (solution potential with respect to the conductive substrate) is large enough to cause the cathodic reaction at one side of the plate and the anodic reaction at the other one. The substrate then provides a metallic path for the current, which shunts the electrolyte resistance. Obviously, the simultaneous occurrence of both a cathodic and anodic reaction is required for maintaining the bipolar current.

Under the same experimental conditions as for aluminium (same cell constant and same electrolytic conductivity), the measured conductivity curves for non-conductive substrates such as the silica plate are fully determined by Ohm's law (Eq. (17)) over the whole range of $\Delta\phi_{\mathrm{s}}$ experienced. As expected, the curves for conductive and non-conductive substrates are identical up to the particular value $\Delta\phi_{\mathrm{s}} \approx 1.5$ V (Fig. 4) where for the conductive substrate the contribution from the faradaic current becomes significant. Some experiments were also performed with gold wafers (thickness 50 nm). The same type of conductivity curve was obtained: the threshold value from which the curves deviate significantly from the straight lines calculated via Ohm's law was found to be substantially lower than for aluminium, i.e. about 1 V. When using two conductive plates in the electrokinetic cell instead of one together with a silica wafer, measurements provide similar conductivity curves. For the two situations, the ohmic current is identical and the faradaic current for two conductive substrates is about twice as high as when one is used, which implies that the processes occurring at the two interfaces are largely independent.

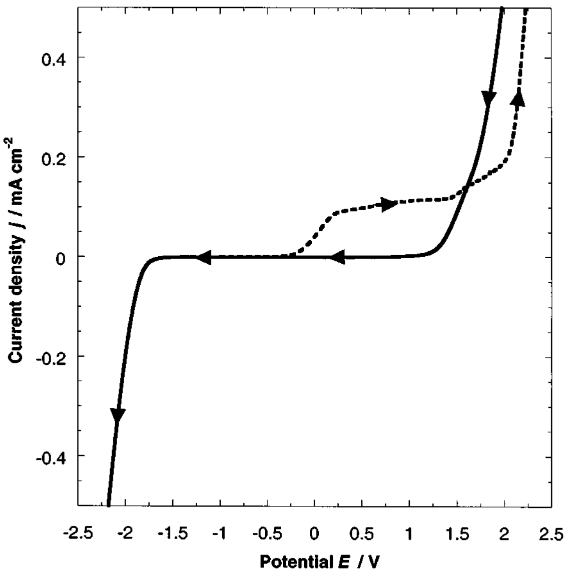

Fig. 5. Voltammogram for monopolar Al wafer in 10^{-2} M $\mathrm{KNO_3}$. Potentials are given with respect to the Ag | Ag | KCl(sat) reference electrode. Scan rate: 0.03 V s^{-1}. The dashed curve shows the influence of the oxide layer formation on the dissolution process (see text).

4.2. *The faradaic processes at the aluminium substrate*

In order to characterize the electrochemical reactions occurring at the aluminium bipolar surface, voltammograms were recorded in 10^{-2} M $\mathrm{KNO_3}$ solution using the substrate as the working electrode. Results are reported in Fig. 5. At potentials below -1.6 V, reduction of water sets in. The resulting onsets of hydrogen formation damaged the surface state of the electrode. For potentials between -0.2 and $+1.3$ V, an oxide layer forms on the aluminium surface [22]. For $c = 2 \times 10^{-4}$–10^{-1} M, the current for this process was found not to exceed $0.2\ \mathrm{mA\ cm}^{-2}$. In the second and subsequent scans, with a sufficiently high scan rate ($100\ \mathrm{mV\ s}^{-1}$), no current is observed in this potential range, indicating that the oxide layer remains intact. For higher potentials ($> +1.3$ V), anodic dissolution of aluminium sets in, resulting in relatively high current densities, e.g. for $c = 10^{-1}$ M, the dissolution current reaches $10\ \mathrm{mA\ cm}^{-2}$ at $+2.5$ V. In the anodic range, the shape of the voltammograms was dependent on the scan direction since the initial states of the electrode surface such as the thickness of the oxide layer are different. This hysteresis is the more pronounced the higher the electrolyte concentration. In order to avoid the effects of passivation, voltammograms were obtained by applying potentials from -1 to -2.5 V to a clean aluminium surface, and potentials from $+2.5$ to -1 V to a second clean Al electrode. The resulting Tafel plots for reduction of water and dissolution of aluminium then allowed determination of the parameters r_{a}, r_{c} and $j_{0_{\mathrm{a}}}$, $j_{0_{\mathrm{c}}}$; values are reported in Table 1. The evaluation of the apparent exchange current densities $j_{0_{\mathrm{a}}}$ and $j_{0_{\mathrm{c}}}$ requires knowledge of the standard potentials. $E^0_{\mathrm{a}} = -1.82$ V vs Ag | Ag | KCl(sat) was taken for the reaction $\mathrm{Al} \rightarrow \mathrm{Al}^{3+} + 3\mathrm{e}^-$ at pH ≈ 5.5 [23] and $E^0_{\mathrm{c}} = -0.55$ V vs Ag | Ag | KCl(sat) for $2\mathrm{H_2O} + 2\mathrm{e}^- \rightarrow \mathrm{H_2} + 2\mathrm{OH}^-$. The quality of the fits of the voltammetric data to Butler–Volmer expressions justifies the assumption that mass transfer is not limiting the rate of the electrodissolution process at all.

4.3. *Comparison with the theoretical model*

According to the previous conclusions, reduction of water and dissolution of aluminium occur in the electrokinetic cell at sufficiently high field strengths. As

Table 1
Kinetic parameters r_a, j_{0_a}, r_c, j_{0_c} determined from the voltammetric data and calculated mixed potentials E_m (Eq. (7)) for different electrolyte concentrations

KNO_3 concentration c/mmol l^{-1}	j_{0_a}/μA cm^{-2}	$r_a \times 10^2$	j_{0_c}/μA cm^{-2}	$r_c \times 10^2$	E_m/V vs Ag | Ag | KCl(sat)
100	0.08	7	2.12	10.7	−0.58
50	0.10	6.5	1.57	10.3	−0.62
10	0.13	5.6	1.16	9.3	−0.65
0.2	5.32	1.6	0.21	6.9	−1.76

expected, the potential range where the aluminium substrate is ideally polarized ($-1.6/-0.2$ V) corresponds approximately to the potential difference $\Delta\phi_s \approx 1.5$ V required for the occurrence of the bipolar regime (Fig. 4). From the slopes and the intercepts of the Tafel plots related to these two processes (Section 4.2), the parameter x_0 was calculated as a function of the electric field V by solving Eq. (15). The mixed potentials E_m for the combination $H_2O \rightarrow H_2$ and $Al \rightarrow Al^{3+}$ were determined from Eq. (7) and are reported in Table 1. Theoretical $I(V)$ curves were then computed for each c (Eqs. (20a) and (20b)) and the resulting values for the bipolar current $I_f(V)$ are presented in Fig. 6. To be directly comparable to the voltammetric data and to minimize the influence of the passivation region, the experimental conductivity curves were obtained for each c by sweeping $\Delta\phi_s$ from high to low values (4.5 to 0 V). The calculated curves are in satisfactory agreement with the experimental data and correctly predict the two experimentally observed regimes of dominant I_f (high V) or dominant I_Ω (low V). The small increase of the bipolar current for $0.2 < V < 0.4$ V cm^{-1} corresponds to the lower part of the j–E exponential relationship where the amplitude is strongly dependent on the electrolyte concentration. From $V \approx 0.4$ V cm^{-1}, I_f increases rapidly with increasing V: the corresponding $\Delta\phi_s$ of about 3 V can be recognized in the voltammogram as the potential difference between the feet of the two exponential functions. This correspondence between conductivity curve and voltammogram was also verified with gold wafers. At low electrolyte concentration (2×10^{-4} M), analysis of the voltammetric data is hampered by the relatively large contribution of the current resulting from the oxide layer formation. This is reflected in the value of the calculated mixed potential (-1.74 V vs Ag | Ag | KCl(sat)) which is high compared to those determined for higher c.

4.4. Dissolution experiments

Two experiments at constant high $\Delta\phi_s$ values of 9 and 6 V, respectively, and high conductance ($a = 2.3$ mm, $c = 10^{-1}$ M) were performed in such a way that the electrochemical reactions could be observed directly: evolution of hydrogen at one side of the substrate and progressive dissolution of aluminium at the other. By reversing the polarity of the applied field, the expected change in the polarization of the substrate and the location of the anodic and cathodic reactions occurs. The position of the dissolution edge could be followed with time (Fig. 7A). The dissolution rate dL/dt decreases with time, corresponding to a decrease of the span potential along the substrate. For very long time, dL/dt tends to zero.

Integration over time of the measured current $I(t)$ (Fig. 7B) allows calculation of the total charge $Q(t)$ passed through the thin-layer cell. This charge can also be evaluated from the experimental data $\Delta L(t)$ and the ohmic current: excellent agreement was obtained (Fig. 7C), confirming that dissolution current and position are satisfactorily correlated via Eq. (25). Kinetic parameters were determined in the previous section for $c = 10^{-1}$ M (Table 1). From Eq. (28), we estimated $\tau \approx 3.9 \times 10^5$ s. The calculated curves $\Delta L(t)$ (Eq. (29)) and $I(t)$ (Eq. (31)) were compared to the experimental data in Fig. 7A and B, respectively. Evolution of $x_0(t)$

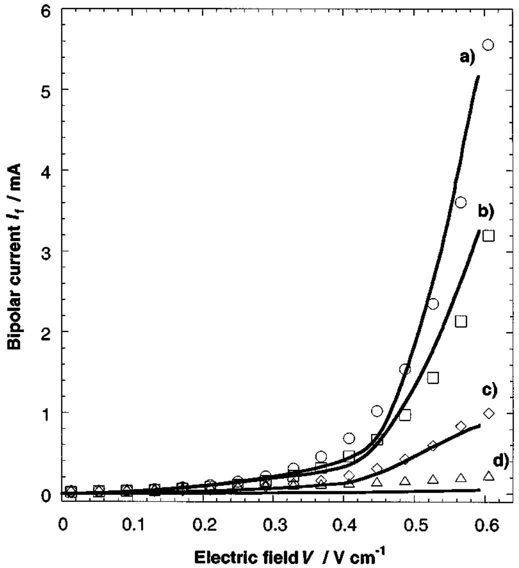

Fig. 6. Comparison between experimental (full curves) and calculated (points) conductivity plots for bipolar Al electrode in different electrolyte concentrations. Only the faradaic contribution I_f is represented. Scan rate (decreasing potential): 0.03 V s^{-1}. $c = 10^{-1}$ (a), 5×10^{-2} (b), 10^{-2} (c), 2×10^{-4} M (d).

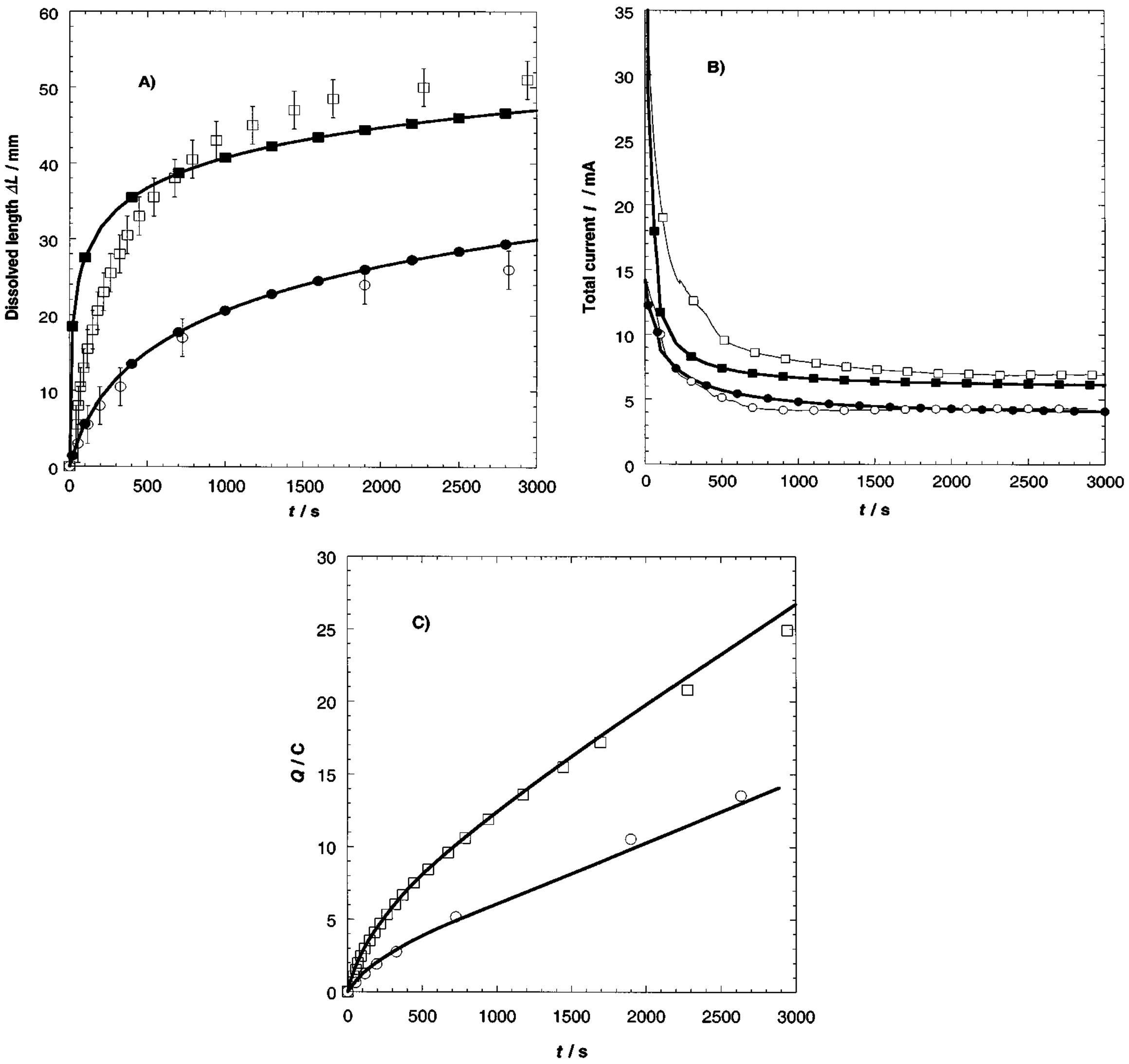

Fig. 7. Evolution of the variables ΔL, I and Q as a function of the dissolution time t for dissolution experiments with $\Delta\phi_s = 6$ (circles) and 9 V (squares). (A) Decrease of length ΔL. Open symbols: experimental data. Filled symbols: calculated points. (B) Decrease of the total current I during the dissolution process. Symbols as for (A). (C) Estimation of the total charge Q passed through the cell from $\Delta L(t)$ (open symbols) and from $I(t)$ (solid curves).

was computed from Eq. (23). The conditions under which Eq. (23) is valid are satisfied in both experiments even at relatively high dissolution times: for the two applied potentials, at $t = 3000$ s, the terms $\exp[r_a fV(L(t) - x_0(t))]$ and $\exp[r_c fVx_0(t)]$ are approximately equal to e^6. Within experimental error, the agreement between experiment and theory was good. For $\Delta\phi_s = 9$ V, reasonable correlation was found for dissolution times longer than about 400 s. For shorter times, the theory overestimates $\Delta L(t)$ due to overestimation of the dissolution current. When calculating a posteriori the potential distributions at different dissolution times, it appears that at short times the overpotential along the substrate for $\Delta\phi_s = 9$ V is far away from the potential window for which the parameters of the model r_a, r_c and j_{0_a}, j_{0_c} were determined. It is possible that at this particular c and for such high potentials, the ohmic drop over the three-electrode cell has to be taken into account, as suggested by the tendency of the j–E curve (voltammogram) to become more linear at high potentials: inclusion of a finite ohmic drop term in the current–potential relation would indeed provide a better estimation of the bipolar current at short dissolution times.

5. Conclusions

The electrochemical behaviour of planar conductive substrates in an electrokinetic cell was investigated.

When applying an electric field across the solution, the bipolar electrodic situation occurring in such a cell is similar to that encountered in fluidized beds of conductive particles. A simple theoretical model based on the concept of mixed potential and Butler–Volmer kinetics was developed to explain quantitatively the bipolar properties of the conductive substrates. The distribution of the current along the substrate was examined for two different situations: (i) the potential across the solution was varied at constant length of the substrate, and (ii) the decrease of the substrate length brought about by anodic dissolution was observed as a function of time at constant solution potential difference. In both cases, the model underlined the narrow link between the conductivity curves of the thin layer cell and the integrated data from the voltammograms for the substrate material. For aluminium wafers, the agreement between theory and experiment was satisfactory. Visual observation of the ongoing bipolar electrolysis process is possible for sufficiently high fields.

Up to now, bipolar faradaic phenomena at flat surfaces subjected to a lateral electric field have been totally ignored in the field of electrokinetic measurements on conductive surfaces. The results presented in this paper provide a way to define properly the electrochemical limitations of zeta-potential measurements on such surfaces.

Acknowledgements

Ab J. van der Linde and Professor Hans Lyklema are thanked for stimulating discussions. Wim Threels is acknowledged for assistance with the voltammetric experiments.

Appendix A. Glossary of symbols

Ox	Oxidized species of a redox couple
R	Reduced species of a redox couple
R	Gas constant (J K^{-1} mol^{-1})
T	Temperature (K)
F	Faraday's constant (C mol^{-1})
f	F/RT (V^{-1})
n	Number of electrons transferred per molecule
α	Transfer coefficient
r	$n\alpha$
a	Distance between the wafers (cm)
l	Width of the wafer (cm)
L_0	Length of the substrate (cm)
C	Cell constant (cm^{-1})
c	Concentration of the electrolyte (mol l^{-1})
K^L	Bulk conductivity (Ω^{-1} cm^{-1})
K^σ	Specific surface conductivity (Ω^{-1})
g	Conductance of the cell (Ω^{-1})
δ	Thickness of the metallic layer (cm)
ρ	Density (g cm^{-3})
M	Molar mass (g mol^{-1})
t	Dissolution time (s)
x	Axial position (cm)
E	Potential at the metal | electrolyte interface (V)
E_m	Mixed potential (V)
x_0	Position (cm) of the substrate for which $E = E_m$
$\Delta\phi$, ΔV	Potential difference (V)
E^0	Standard potential (V)
L	Remaining length of the bipolar electrode (cm)
ΔL	Dissolved length (cm)
j	Current density (A cm^{-2})
I	Current (A)
Q	Charge (C)
V	Electric field (V cm^{-1})
τ	Time characteristic of the electrodissolution process (s)
Subscripts	
a	Anodic
c	Cathodic
f	Denoting the bipolar current
Ω	Denoting the current of conduction
s	Pertaining to the solution
r	Pertaining to the remaining length of the substrate
M	Pertaining to the metal
0	Denoting the exchange current

References

[1] D. Pletcher, Industrial Electrochemistry, Chapman and Hall, London, 1982, p. 162.

[2] M. Fleischmann, J. Ghoroghchian, D. Rolinson, S. Pons, J. Phys. Chem. 90 (1986) 6392 and references to unpublished results by D.R. Rolinson, R.J. Nowak, S. Pons, M. Fleischmann, J. Ghoroghchian, J. Ghoroghchian, S. Pons, M. Fleischmann.

[3] J.-C. Bradley, J. Crawford, K. Ernazarova, M. McGee, S.G. Stephens, Adv. Mater. 9 (1997) 1168.

[4] J.-C. Bradley, H.-M. Chen, J Crawford, J. Eckert, K. Ernazarova, T. Kurzeja, M. Lin, M. Mc Gee, W. Nadler, S.G. Stephens, Nature 389 (1997) 268.

[5] V. Fleury, D. Barkey, Europhys. Lett. 36 (1996) 253.

[6] L. Zeiri, S. Efrima, Langmuir 12 (1996) 5180.

[7] M. Fleischmann, F. Goodridge, J.M. Backhurst, British Patent Application 23070/66.

[8] J.M. Backhurst, Ph.D. Thesis, University of Newcastle upon Tyne, 1967.

[9] M. Fleischmann, F. Goodridge, C.J.H. King, British Patent Application 16765/74.
[10] A.R. Wright, Ph.D. Thesis, University of Newcastle upon Tyne, 1975.
[11] J.N. Hiddleston, A.F. Douglas, Electrochim. Acta 15 (1970) 431.
[12] D.C. Eardley, D. Handley, S.P.S. Andrew, Electrochim. Acta 18 (1973) 839.
[13] F. Goodridge, C.J.H. King, A.R. Wright, Electrochim. Acta 22 (1977) 1087.
[14] M. Fleischmann, J. Ghoroghchian, S. Pons, J. Phys. Chem. 89 (1985) 5530.
[15] I. Kobayashi, T. Ohno, T. Ozaki, Denki-Kagaku 66 (1998) 745.
[16] J.H. Fitzgerald, R. Bosma, F. Paladines, Mater. Performance 38 (1999) 36.
[17] J.L. Maxwell, Mater. Performance 38 (1999) 26.
[18] A.J. Van der Linde, B.H. Bijsterbosch, Colloids Surf. 41 (1989) 345.
[19] W. Norde, E. Rouwendal, J. Colloid Interface Sci. 139 (1990) 169.
[20] C. Wagner, W. Traud, Z. Elektrochem. 44 (1938) 391.
[21] M. Spiro, in: D.V. Fenby, I.D. Watson (Eds.), The Physical Chemistry of Solutions, Massey University, New Zealand, 1983.
[22] A. Charlesby, Proc. Phys. Soc. B 4 (1953) 317.
[23] T. Hagyard, J.H. Williams, Trans. Faraday Soc. 57 (1961) 2288.

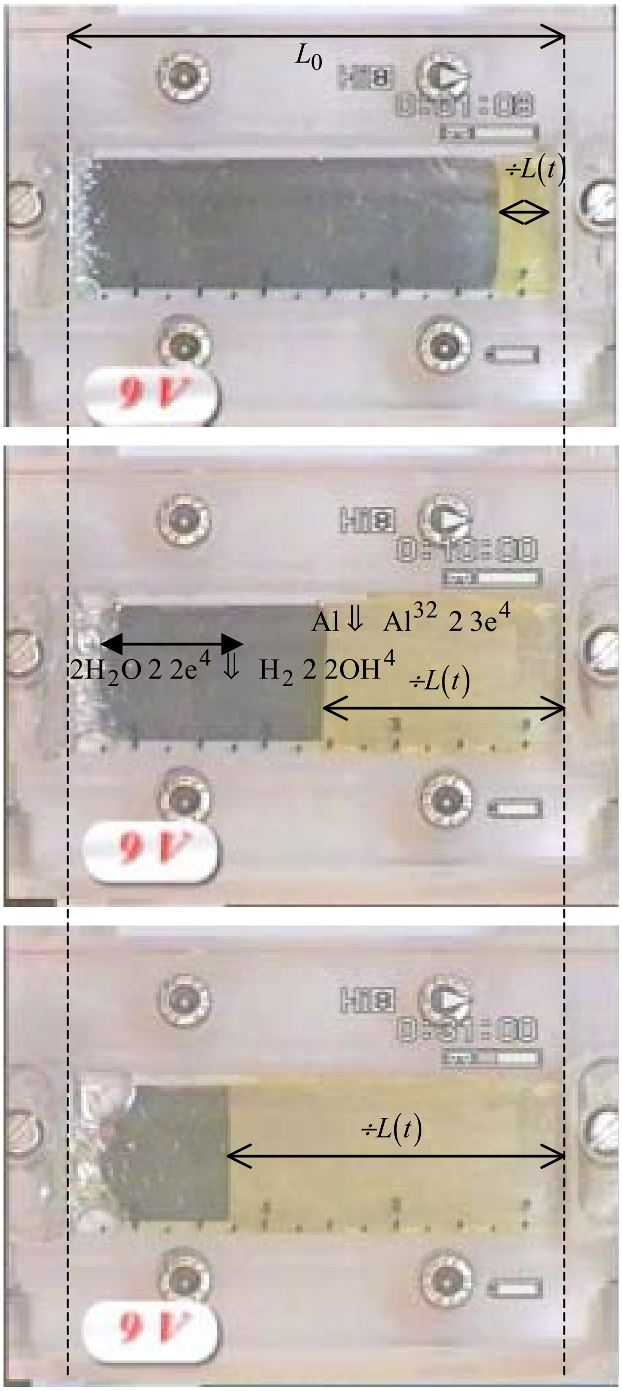

Appendix B.
Bipolar electrodic behaviour of an aluminium surface placed in a thin-layer cell. Progression of the corroding edge with time (see Figure 7). An electric field ($\div\lambda_{\text{S}}$ | 9 V) parallel to the surface is applied in the solution.
Right side of the bipolar electrode: dissolution of Al metal (negative side of the field in solution). Left side of the bipolar electrode: reduction of water (positive side of the field in solution).

ACADEMIC PRESS

Journal of Colloid and Interface Science 260 (2003) 95–106

Journal of Colloid and Interface Science

Faradaic depolarization in the electrokinetics of the metal–electrolyte solution interface

Jérôme F.L. Duval,* Geertje K. Huijs, Wim F. Threels, Johannes Lyklema, and Herman P. van Leeuwen

Department of Physical Chemistry and Colloid Science, Wageningen University, Dreijenplein 6, 6703 HB Wageningen, The Netherlands

Received 9 July 2002; accepted 7 November 2002

Abstract

Streaming potentials (E_{str}) have been measured in a flat thin-layer cell with gold and aluminum surfaces. The conventional relation between E_{str} and the ζ-potential is shown to be applicable only as long as charge transfer reactions at the metal–electrolyte solution interface are insignificant in terms of the ensuing contribution to the overall cell conductivity. Owing to the irreversibility of the reduction/oxidation of water at most metal surfaces, streaming potentials can be obtained over a very broad range of pressure gradients for metallic substrates in electrolytes such as KNO_3. The situation changes drastically in the presence of a reversible redox couple like $Fe(CN)_6^{3-}/Fe(CN)_6^{4-}$. Even small streaming potentials are then greatly diminished due to the extensive conduction that results from the bipolar electrolysis at the metal surface. For gold and aluminum in the presence of various electroinactive and electroactive electrolytes, the measured values for E_{str} are shown to be consistent with their conventional voltammetric characteristics.

© 2003 Elsevier Science (USA). All rights reserved.

Keywords: Streaming potential; Thin-layer cell; Bipolar current; Faradaic depolarization

1. Introduction

It is often presumed that conducting substrates such as metals are not accessible to electrokinetic measurements. The reasoning is that the large overall conductivity would suppress the generation of a measurable streaming potential. However, for the bulk conductivity of the substrate to be operative, charge transfer across the interface between substrate and solution must take place. This mandatory prerequisite was already recognized by the Kruyt school [1] for metallic flat electrodes and later discussed by Overbeek for metallic conducting particles [2,3], well before electrochemists invented the principles of polarography and voltammetry of electroactive (that is, redox active) compounds [4]. The exploratory electrokinetic studies by Oosterman [1] involved metal capillaries which were shown to produce streaming potentials very different from those for glass capillaries. Although the experimental observations for silver and platinum were found to be rather irreproducible (the potential for Pt was said to make "the weirdest jumps"), the tentative explanation correctly referred to the need for controlling the discharge of protons and hydroxyl ions as essential elements in the materialization of substrate conduction.

We have recently investigated the bipolar electrodic behavior of aluminum wafers in KNO_3 solution, exposed to a lateral dc electric field [5]. For sufficiently strong fields the aluminum is anodically dissolved at the negative side of the field and water is reduced at the positive side, thus giving rise to a flow of electrons through the Al substrate. The effective bipolar faradaic current is derived from the spatial integral of either the local cathodic or the local anodic current density, the anodic and cathodic current integrals being necessarily identical. The distribution of the current densities at the anodic and cathodic sides of the Al surface is related to the pattern of the local potential difference between metal and solution, as dictated by the applied field. This has been underscored by the successful modeling of the bipolar current/field strength dependence for aluminum electrode on the basis of the conventionally measured Butler–Volmer electron transfer kinetics [6].

Here we extend our investigations in two directions: (i) the results for aluminum are compared with those for gold, a metal which does not undergo anodic dissolution at

---

* Corresponding author.
E-mail address: jerome.duval@wur.nl (J.F.L. Duval).

moderate potentials, and (ii) the effects of the electrochemically reversible redox couple $Fe(CN)_6^{3-}/Fe(CN)_6^{4-}$ on the streaming potential of gold are set against the voltammetric properties of the couple at a monopolar gold electrode. The study of streaming potentials in the presence of a redox couple is especially interesting because a well-defined Nernstian potential difference [7] between metal and solution is dictated, while the reversible redox couple gives rise to relatively strong bipolar currents. Already at small deviations from the equilibrium potentials (weak lateral fields), the faradaic depolarization of the interface leads to strongly reduced streaming potentials. Such streaming potentials can be properly interpreted only if the Smoluchowski equation is extended with a substrate conductance term which is limited by the faradaic charge transfer reaction at the interface.

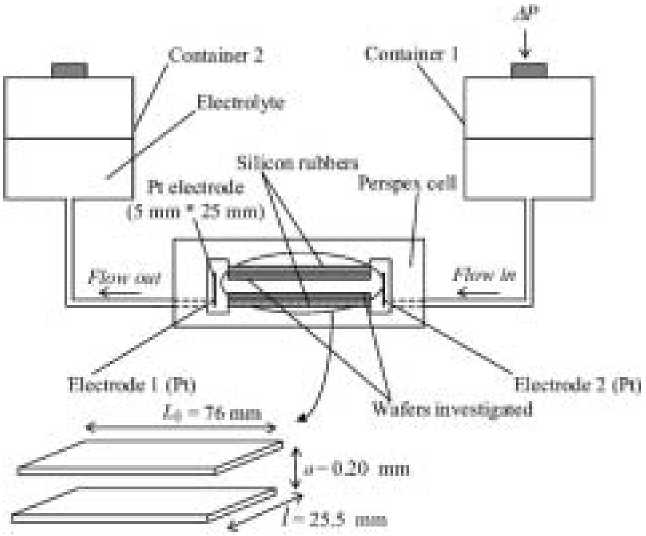

Fig. 1. Cell detail.

2. Materials and methods

2.1. Materials

The metallic surfaces subjected to streaming potential experiments were supported polycrystalline Al layers (200 nm) and Au layers (100 nm). To warrant proper adhesion, the glass support was first covered with a 10-nm Cr layer. The layers were prepared via evaporation from heated Cr, Al, or Au sources directly onto the glass support. The substrates were extensively cleaned with demineralized water. In contrast to Au surfaces, known to be very sensitive to surface oxidation (high energy surface), the Al wafers were subjected to 15/20 min UV/ozone treatment prior to measurement. Aqueous electrolyte solutions were prepared from analytical grade potassium nitrate in ultrapure water as the solvent (specific resistance 18 $M\Omega\,cm^{-1}$). Analytical grade KOH and HNO_3 were used without further purification. The redox couple used ($Fe(CN)_6^{3-}/Fe(CN)_6^{4-}$) was 99% pure. Prior to each measurement (electrochemical or electrokinetic), nitrogen was bubbled for 20 min to remove dissolved oxygen which could interfere with the faradaic reactions.

2.2. Streaming potential measurements

The flat plate streaming potential apparatus is based on the design of Van Wagenen and Andrade [8]. In this setup, a Teflon gasket separates two flat plates to form a flat capillary through which the electrolyte solution is pumped (Fig. 1). A similar type of cell is used by, e.g., Scales et al. [9]. The thickness of the gasket determines the thickness of the gap between the flat plates. For the experiments reported here, the gap was approximately 0.20 mm. The pressure difference was controlled by adjusting the fluid levels in the reservoirs, using nitrogen as the gas. The sensing electrodes were connected to a voltmeter or a conductivity meter, enabling the measurement of the potential difference across the capillary and the conductivity of the cell. The apparatus, fully automated, was connected to a PC, allowing acquisition of the streaming potential as a function of the pressure difference applied across the capillary. The electrokinetic cell was placed in a thermostatted cabinet to maintain the temperature at 25 °C within 0.1 °C.

2.3. Electrochemical experiments

Voltammetric experiments were performed at room temperature in a conventional three-electrode cell with a Pt plate as the counterelectrode (2 cm^2 surface area) and an Ag–AgCl–3 M KCl reference electrode. Single sweep and cyclic voltammetric curves were measured. Before each experiment, the solution was flushed with nitrogen for about 20 min. During the measurements N_2 was passed over the solution. Monitoring the applied potential and measuring the current were performed with a PGSTAT10 potentiostat controlled by Autolab software (Eco Chemie). In the electrokinetic cell, the propensity of the metal–electrolyte interface for depolarization was analyzed by externally applying a tangential potential difference between two platinum electrodes placed outside the thin liquid channel located in between the two flat surfaces [5]. For the investigation of the electrochemical characteristics of the redox couple on gold, a rotating disc electrode (RDE, Metrohm) was also used.

3. Electrokinetics of gold and aluminum in electroinactive electrolyte

3.1. Regime of faradaic depolarization

The possibility of charge transfer between an Al substrate and an aqueous electrolyte solution upon application of a lateral electric field in a thin-layer cell was investigated in a previous study [5]. The overall conductivity of the system is characterized by two regimes. For not too strong fields, with potential differences lower than approximately

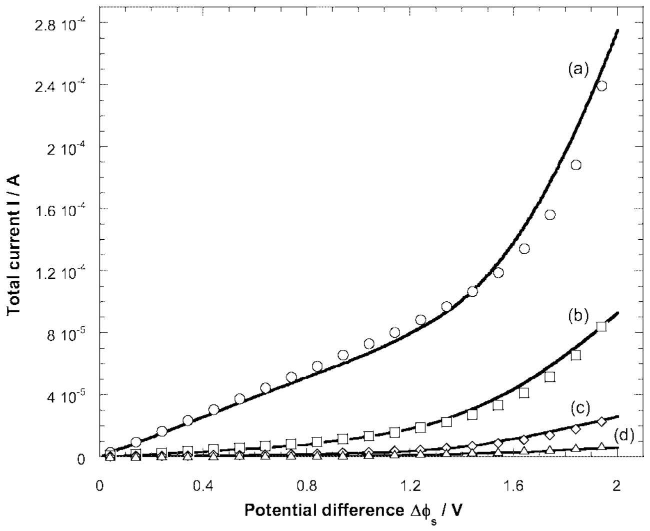

Fig. 2. Experimental (plain curves) and calculated (points) conductivity plots for bipolar gold electrodes at different KNO_3 electrolyte concentrations c^*. (a) $c^* = 10^{-1}$ M; (b) $c^* = 10^{-2}$ M; (c) $c^* = 10^{-3}$ M; (d) $c^* = 10^{-4}$ M. The potential was linearly scanned ($0.03\ \mathrm{V\,s^{-1}}$).

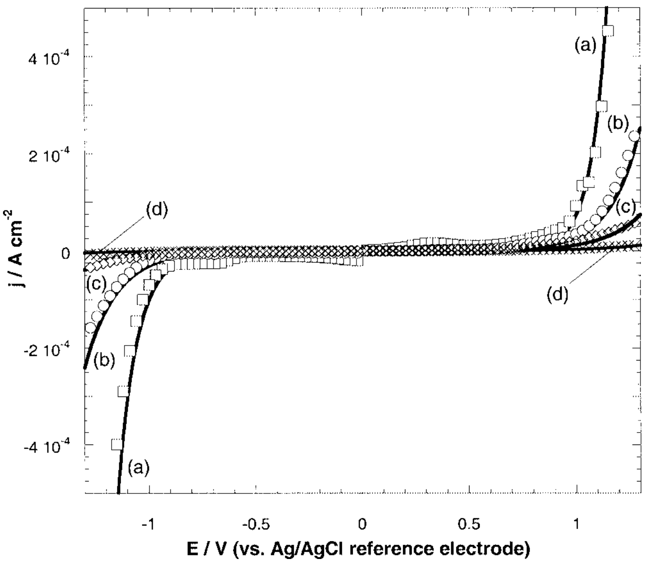

Fig. 3. Measured voltammograms (symbols) of monopolar gold electrode in different KNO_3 electrolyte concentrations c^*. The curves are calculated by means of the Butler–Volmer expression, the kinetic parameters of which are given in Table 1. (a) $c^* = 10^{-1}$ M; (b) $c^* = 10^{-2}$ M; (c) $c^* = 10^{-3}$ M; (d) $c^* = 10^{-4}$ M. The potential was linearly varied with time (scan rate of $0.03\ \mathrm{V\,s^{-1}}$).

1.5 V, the conductance of the cell is the sum of the bulk conductance, as determined by the electrolyte concentration, and any surface conductance, depending on the nature of the electrolyte used. For larger fields, the current through the cell increases more than proportionally with the field strength. The Al substrate then provides a metallic path for the electrons, generated by anodic dissolution of aluminum at one side and consumed by reduction of water at the other side. A similar analysis was performed with gold substrates in the thin-layer cell. The results are shown in Fig. 2. The pattern of the conductivity curves is essentially the same as that for Al. The potential difference beyond which charge transfer takes place is somewhat lower (about 1 V). Voltammograms for a gold plate electrode (Fig. 3) enable the identification of the electrochemical reactions occurring at the two sides of a gold substrate when it operates as a bipolar electrode. Reduction of water at the monopolar gold electrode sets in at potentials below -0.6 V and oxidation of water occurs at potentials beyond $+0.5$ V (with respect to an Ag–AgCl–3 M KCl reference electrode). The analysis of the experimental curves plotted in Fig. 2 was performed using the model developed in [5]. This model exploits the correlation between the kinetic characteristics of the two faradaic reactions and the bipolar current carried by these reactions in the thin-layer cell. Values of the kinetic parameters, as obtained from the voltammograms, are reported in Table 1. As for Al, the analysis on the basis of the Bulter–Volmer characteristics of the monopolar gold electrode and the concept of mixed potentials [10] successfully accounts for the dependence of the bipolar current on the lateral electric field for the different KNO_3 electrolyte concentrations investigated (Fig. 2). For more detail, the reader is referred to [5]. The potential difference of 1 V, beyond which the faradaic bipolar current becomes significant (implying the simultaneous occurrence of the two electrochemical reactions), corresponds very well to the overpotential as determined from Fig. 3.

In a conventional streaming potential experiment, the electrolyte solution is flushed through the capillary between the two charged walls under the influence of an applied

Table 1

Kinetic parameters r_a, j_{0_a}, r_c, j_{0_c} and calculated mixed potentials E_m (see Ref. [5]) estimated for gold from the voltammetric data obtained for different electrolyte concentrations

KNO_3 concentration c^* ($\mathrm{mol\,l^{-1}}$)	j_{0_a} ($\mathrm{\mu A\,cm^{-2}}$)	r_a $\times 10^2$	j_{0_c} ($\mathrm{\mu A\,cm^{-2}}$)	r_c $\times 10^2$	E_m/V vs Ag–AgCl–KCl
10^{-1}	1.26	33.4	0.72	28.2	0.095
10^{-2}	3.05	18.4	1.36	17.7	0.021
10^{-3}	1.85	15.4	0.24	17.5	−0.133
10^{-4}	0.89	10.8	0.07	14.4	−0.286

Note. The voltammograms were fit with the Butler–Volmer expression of the form $j_{0_a} \exp[r_a f (E - E_a^0)]$ (anodic side) and $-j_{0_c} \exp[-r_c f (E - E_c^0)]$ (cathodic side) with E the potential and $f = F/RT$ (Eq. (8)). E_a^0 (0.68 V vs Ag–AgCl–KCl) and E_c^0(-0.55 V vs Ag–AgCl–KCl) are the standard potentials for the oxidation and reduction reactions, respectively (pH 5.5).

pressure ΔP. Due to transport of the mobile part of the countercharge in the interfacial double layer, a potential difference E_{str}, the streaming potential, is built up, which in turn leads to a counter conduction current inside the capillary. This current is generally composed of bulk and surface conduction contributions. Thus, by externally applying a potential difference $\Delta\varphi_s$, one actually mimics the situation encountered in a standard electrokinetic experiment. Usually, E_{str} does not exceed ±100 mV, which is well below the $\Delta\varphi_s$ at which bipolar currents are generated at gold and aluminum in KNO_3 solution. Hence, within the framework of an electrokinetic experiment, the gold and aluminum–KNO_3 interfaces are completely polarized and streaming potential experiments are free from faradaic depolarization effects, as explained in the next section.

3.2. Streaming potential measurements

Within the range of potentials typically encountered in streaming potential experiments, the basic principles of the electrokinetic analysis for dielectric substrates remain valid for the metallic substrates gold and aluminum in electroinactive electrolyte such as KNO_3. The streaming potential E_{str} is thus expected to depend linearly on the applied pressure ΔP as formulated by the Smoluchowski equation [11]

$$E_{\mathrm{str}} = \frac{\varepsilon_0 \varepsilon_r \zeta \Delta P}{\eta(K^L + 2K^\sigma/a)}, \tag{1}$$

where ε_0 is the dielectric permittivity of vacuum, ε_r is the relative dielectric permittivity of the solution, η is the viscosity of the solution, a is the distance between the two flat surfaces, K^L is the specific bulk conductivity ($\Omega^{-1}\,\mathrm{m}^{-1}$), and K^σ is the specific surface conductivity (Ω^{-1}). ζ is the electrokinetic potential, which is usually evaluated from the slope of a plot of E_{str} versus ΔP. Some experimental data were obtained for gold, aluminum, and microscopic glass supports at different KNO_3 concentrations c^* and different pH. Linear relationships between E_{str} and ΔP were found for all three types of surfaces. Typical plots are shown in Fig. 4.

For every experiment, the conduction term written in brackets in the denominator of Eq. (1) was estimated by plotting the conductance g (Ω^{-1}), as determined from the slopes of the measured conductivity curves at low potentials, as a function of K^L. For the thin-layer cell geometry, g is given by

$$g = \frac{K^L}{C} + 2\frac{K^\sigma l}{L_0}, \tag{2}$$

where L_0 and l are the total length and the width of the substrate surface, respectively. C (m^{-1}) is the cell constant defined by

$$C = \frac{L_0}{al}. \tag{3}$$

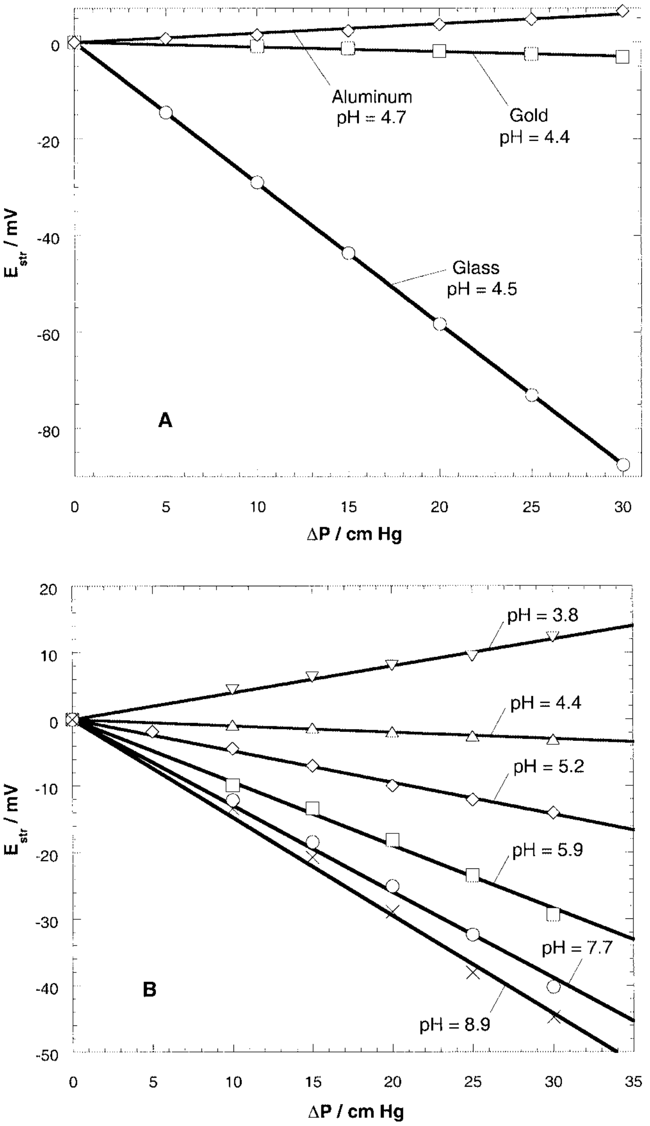

Fig. 4. (A) Streaming potentials obtained with aluminum, gold, and glass wafers placed in the thin-layer cell using KNO_3 as the electrolyte ($c^* = 10^{-3}$ M). (B) Streaming potentials obtained for gold at $c^* = 10^{-3}$ M and various pH. The pH of the KNO_3 solution is indicated.

Hence, the slope of g plotted versus K^L provides C, which was always found to be in good agreement with the value derived from the cell dimensions (Eq. (3)). The intercept yields the surface conductivity K^σ; here we do not consider K^σ in further detail but focus on the analysis of faradaic depolarization effects.

Once the cell conductance and the slopes $E_{\mathrm{str}}/\Delta P$ are known for a given pH and c^*, the ζ-potential can be estimated by means of Eq. (1). In Figs. 5A, 5B, and 5C, results are reported for glass, gold, and aluminum, respectively. The observed dependencies of ζ on pH suggest that H^+ and OH^- are charge-determining ions for all of these three surfaces. Though this is not unexpected for oxides [12–14], it may appear less likely for gold. However, recent studies have shown that the double layer of the gold–solution interface is of amphifunctional nature due to the presence of oxidic sur-

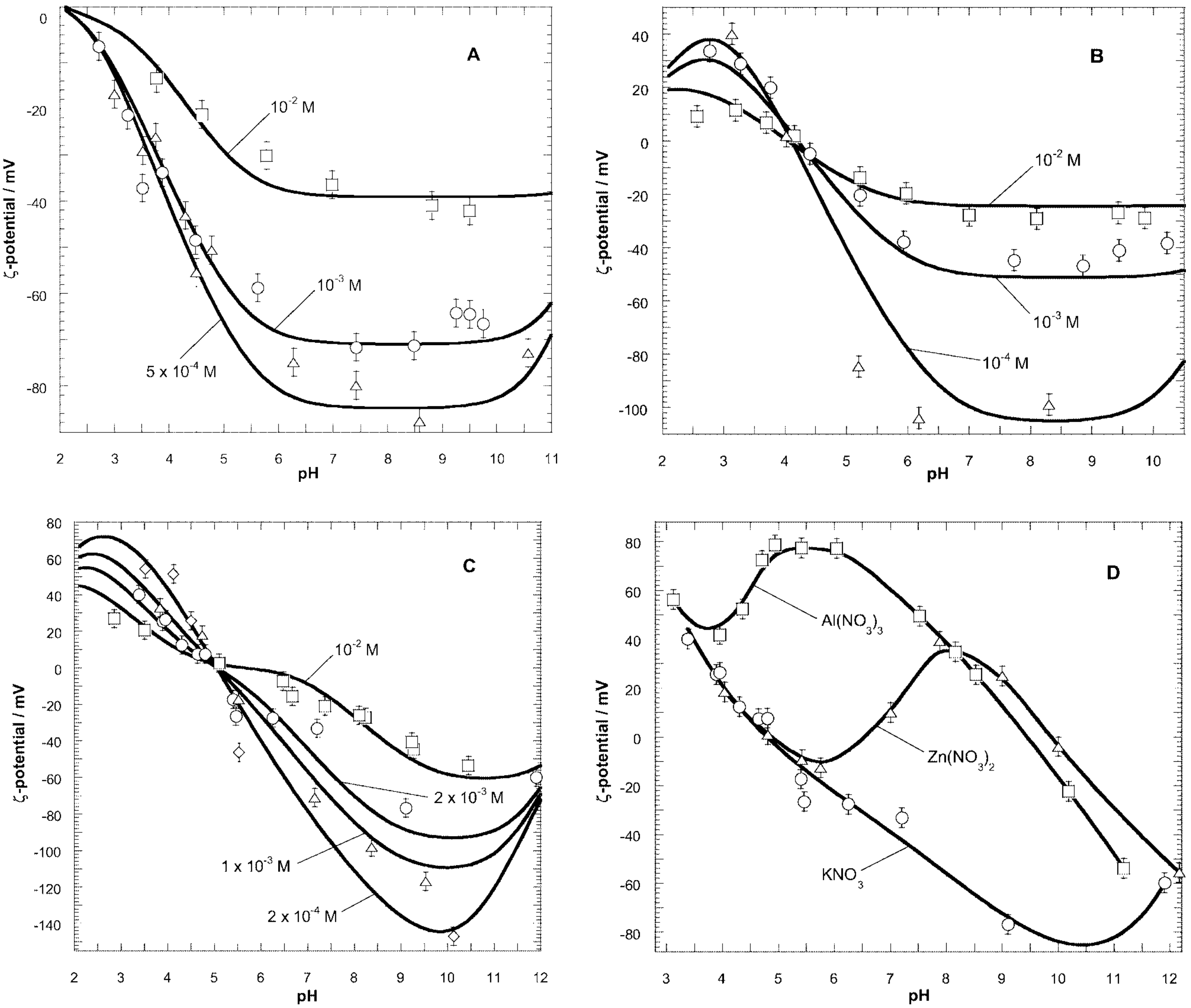

Fig. 5. Measured ζ-potentials (symbols) of glass (A), gold (B), and aluminum (C) wafers in the presence of the indicated concentrations of KNO_3. The curves were calculated as explained in the text (Section 3.2) with the model parameters reported in Table 2. (D) ζ-potentials obtained for aluminum in the presence of 2×10^{-3} solutions of the electrolytes indicated. The curves are only guides for the eye.

face groups that exchange protons with the medium [15–17]. An analysis of the electrokinetic data presented in Fig. 5 was carried out using a 2-pK model [18,19] and the Gouy–Chapman–Stern double layer representation [20–22]. The two pK's used, pK_{a_1} and pK_{a_2}, refer, in this order, to the following surface equilibria:

$$-\mathrm{MOH}_2^+ \Leftrightarrow -\mathrm{MOH} + \mathrm{H}^+, \tag{4a}$$

$$-\mathrm{MOH} \Leftrightarrow -\mathrm{MO}^- + \mathrm{H}^+. \tag{4b}$$

The number of oxidic sites per unit surface area is subsumed in a parameter called N_s. This quantity primarily controls the magnitude of ζ. The difference $\Delta \mathrm{p}K = \mathrm{p}K_{a_2} - \mathrm{p}K_{a_1}$ is a measure of the width of the pH region where the surface groups –MOH are predominant. For a given c^*, it gives information on the relative slope of ζ(pH) around the isoelectric point (iep). The quantity $0.5(\mathrm{p}K_{a_1} + \mathrm{p}K_{a_2})$ is equal to the iep ($\mathrm{pH}_{\zeta=0}$) experimentally determined. Merging of the experimental and theoretical electrokinetic curves was obtained with the model parameters as reported in Table 2 for the three surfaces investigated. In view of these data, several comments can be made.

The order of magnitude of N_s is, even for aluminum and glass, well below the values reported in the literature concerning oxide surfaces [23]. A possible interpretation is that the electrokinetic analysis only probes a fraction of the total surface charge due to binding of counterions in the Stern layer and/or inclusion of counterions in surface asperities. The latter option is supported by the systematic change of N_s with varying c^*. Indeed, the higher the ratio between the Debye length and the characteristic length of the surface roughness, the more efficiently the (real) surface charge is masked. Saturation of the protonic surface charge at high and low pH is observed for gold. This is in agreement with data recently obtained by atomic force microscopy

Table 2
Model parameters $\mathrm{p}K_{a_1}$, $\mathrm{p}K_{a_2}$, and N_s used to fit the electrokinetic curves of Fig. 5

Nature of the surface	KNO_3 concentration c^* ($\mathrm{mol\,l^{-1}}$)	$\mathrm{p}K_{a_1}$ ($\log(\mathrm{mol\,l^{-1}})$)	$\mathrm{p}K_{a_2}$ ($\log(\mathrm{mol\,l^{-1}})$)	$N_s \times 10^{13}$ (sites $\mathrm{cm^{-2}}$)	iep
Gold	10^{-2}	3.95 ± 0.15	4.25 ± 0.15	0.36	4.13 ± 0.08
	10^{-3}			0.27	
	10^{-4}			0.28	
Glass	10^{-2}	1	3.75 ± 0.25	0.61	2.38 ± 0.12
	10^{-3}			0.43	
	5×10^{-4}			0.41	
Aluminum	10^{-2}	3.8 ± 0.2	6.9 ± 0.7	1.1	5.35 ± 0.3
	2×10^{-3}			1.0	
	10^{-3}			1.0	
	2×10^{-4}			1.0	

measurements [15]. The iep, situated between 4 and 4.2, as well as the symmetric character of the curves ζ(pH), agrees with the data of reference [15]. As expected, no saturation is seen for aluminum, which presents a higher degree of surface hydroxylation compared to gold. The iep, located at pH $\approx$ 5.4, is surprisingly low compared to the one obtained from electrokinetic measurements performed on α-alumina powder (iep of approximately pH 9 [24]). This was already mentioned and discussed in [13]. For glass substrates, electrokinetic data extrapolated to low pH show an iep of pH 2.3–2.5, which is typical for silica [25]. The effect of hydrolysable divalent and trivalent metal ions on the electrokinetic data for aluminum was also investigated (Fig. 5D). The patterns of the ζ(pH) curves and especially the different charge reversals can be nicely correlated to the hydrolysis at the aluminum surface of the metal ions chosen, as extensively discussed in [26] for SiO_2 and TiO_2 colloids.

When using an electroinactive electrolyte, the electrokinetic analysis performed on metals yields reliable results in good agreement with their surface chemistry and double layer properties. The conversion of the streaming potential data into ζ-potentials can be carried out following the route usually taken when studying dielectric substrates.

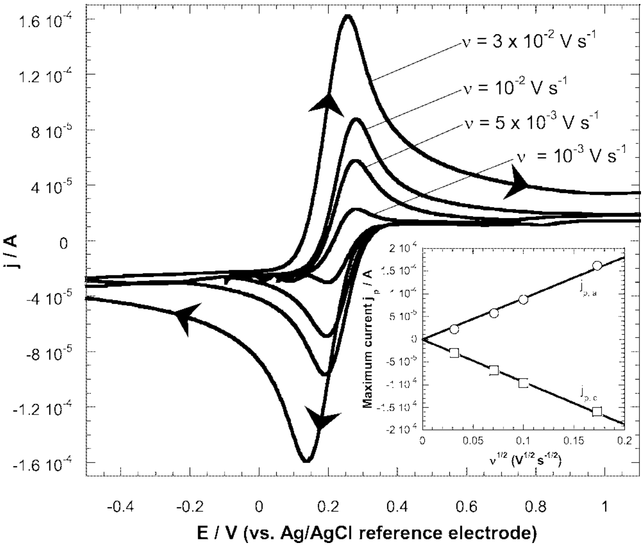

Fig. 6. Cyclic voltammograms of a gold electrode in a 10^{-2} M/10^{-2} M $Fe(CN)_6^{3-}/Fe(CN)_6^{4-}$ solution of pH 5.5 (supporting electrolyte 10^{-1} M KNO_3). The scan rates ν are indicated. Electrode area is 0.18 cm^2. The linear dependence of the maximum currents with $\nu^{1/2}$ is shown in the inset. The arrows indicate the direction of scan.

4. Electrokinetics of gold in electroactive electrolyte

4.1. Reversible character of the $Fe(CN)_6^{3-}/Fe(CN)_6^{4-}$ couple at gold

Cyclic voltammograms for $Fe(CN)_6^{3-}/Fe(CN)_6^{4-}$ at a gold electrode are shown in Fig. 6. A well-defined faradaic response is observed, centered around +0.23 V (versus Ag–AgCl–3 M KCl). The peak potential is practically independent of the scan rate ν. The anodic and cathodic peak currents, $j_{p,a}$ and $j_{p,c}$, respectively, are proportional to $\nu^{1/2}$ (see inset of Fig. 6). These features demonstrate that the charge transfer occurring at the gold surface is electrochemically reversible [27], implying that the overall rate of the electrode reactions is determined by diffusive transport of $Fe(CN)_6^{3-}$ and $Fe(CN)_6^{4-}$ to/from the surface of the electrode. The Nernstian character of the system is confirmed by the current–potential relationship (see Section 4.3.1) measured at a gold RDE for different redox concentrations and different rotation speeds (Fig. 7). The limiting anodic and cathodic currents, denoted as $j_{l,a}$ and $j_{l,c}$, respectively, were indeed found to obey the Levich equation [28], which predicts a linear dependence of the diffusion-controlled limiting current on the concentration and the square root of the rotation speed (inset Fig. 7). For pH > 4, the open circuit potential varies with the $Fe(CN)_6^{3-}/Fe(CN)_6^{4-}$ concentration ratio in accordance with Nernst's law. For lower pH, the basic character of $Fe(CN)_6^{4-}$ leads to deviations. Thus we shall confine ourselves to the range of pH > 4.

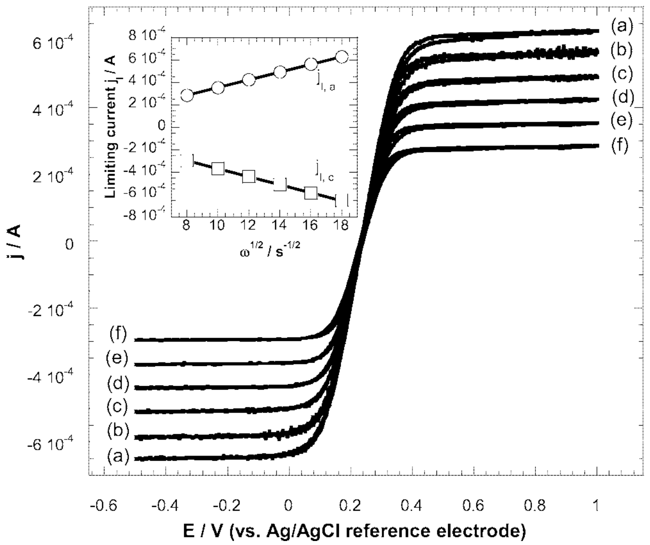

Fig. 7. Current–potential curves measured at a rotating disc electrode for different rotation speeds ω using a 10^{-2} M/10^{-2} M $\mathrm{Fe(CN)_6^{3-}}$/ $\mathrm{Fe(CN)_6^{4-}}$ solution of pH 5.5 (supporting electrolyte 10^{-1} M $\mathrm{KNO_3}$). (a) $\omega = 324\ \mathrm{s^{-1}}$; (b) $\omega = 256\ \mathrm{s^{-1}}$; (c) $\omega = 196\ \mathrm{s^{-1}}$; (d) $\omega = 144\ \mathrm{s^{-1}}$; (e) $\omega = 100\ \mathrm{s^{-1}}$; (f) $\omega = 64\ \mathrm{s^{-1}}$. Electrode area is $0.18\ \mathrm{cm^2}$. The linear dependence of the limiting currents with $\omega^{1/2}$ is shown in the inset. Scan rate used is $0.03\ \mathrm{V\,s^{-1}}$.

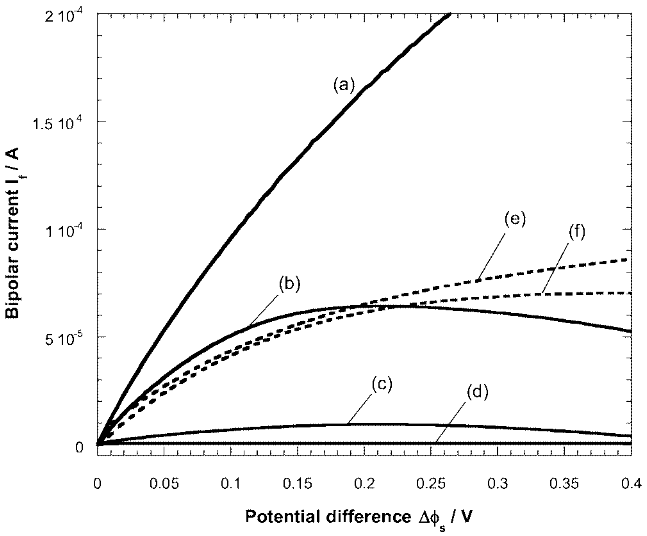

Fig. 8. Conductivity curves for bipolar gold electrodes in the presence of (a) 10^{-3} M/10^{-3} M, (b) 10^{-4} M/10^{-4} M, (c) 10^{-5} M/10^{-5} M, (d) 10^{-6} M/10^{-6} M, (e) 10^{-4} M/10^{-3} M, and (f) 10^{-3} M/10^{-4} M $\mathrm{Fe(CN)_6^{3-}}$/$\mathrm{Fe(CN)_6^{4-}}$ solution. In (a), (e), and (f) supporting electrolyte $\mathrm{KNO_3}$ concentration $c^* = 10^{-1}$ M. In (b), (c), and (d) $c^* = 1$ M. Only the faradaic contribution I_f is represented. The plain (dashed) lines refer to a symmetric (asymmetric) redox system. Scan rate is $0.03\ \mathrm{V\,s^{-1}}$.

4.2. *Conductivity curves for gold in the presence of $\mathrm{Fe(CN)_6^{3-}}$/$\mathrm{Fe(CN)_6^{4-}}$*

Figure 8 shows the bipolar current I_f as a function of the potential difference $\Delta\varphi_s$ externally applied across the electrokinetic cell. I_f was calculated by subtracting the ohmic contribution I_Ω from the total signal, I_Ω simply being the product of the conductance g, as given by Eq. (2), and $\Delta\varphi_s$. The electrolyte solution contains the components of the redox couple $\mathrm{Fe(CN)_6^{3-}}$/$\mathrm{Fe(CN)_6^{4-}}$, the concentrations of which are varied at such low levels that the bulk conductivity of the solution remains dominated by the electroinactive carrier $\mathrm{KNO_3}$.

In contrast to the situation examined in Section 3.1, a significant bipolar current is already measured at very weak fields (low $\Delta\varphi_s$). The bipolar current is carried by the reduction of $\mathrm{Fe(CN)_6^{3-}}$ at one side of the bipolar gold electrode and the oxidation of $\mathrm{Fe(CN)_6^{4-}}$ at the other side. Polarization of the metallic surface with respect to the solution occurs in the same way as for the irreversible bipolar processes examined for Al and Au in $\mathrm{KNO_3}$ solution. Regarding the voltammograms shown in Fig. 6, it is obvious that the electrode processes necessary to carry the bipolar current require only small overpotentials. As soon as the potential difference between the solution and the gold surface deviates from its equilibrium value, a faradaic current starts to flow. The course of the field across the flow cell determines the spatial distribution of the potential of the solution with respect to the gold surface and hence the magnitude of the local faradaic currents. Assuming a linear field, the characteristic pattern of the voltammograms as shown in Fig. 6 can be directly projected on the length axis of the bipolar substrate [5]. The measured bipolar current results from the spatial integration of the local anodic or cathodic current densities over the complete surface areas of oxidation and reduction. Since in the stationary state there is no accumulation of charge in the substrate, these two integrals must be equal. With increasing concentrations of the redox components, the local faradaic currents along the substrate increase and consequently the ensuing bipolar current increases, as shown in Fig. 8. When gradually increasing $\Delta\varphi_s$, the local current densities and hence I_f increase strongly. From a certain value of $\Delta\varphi_s$, the increase of I_f levels off till I_f reaches a constant value or even decreases. This leveling off is related to the transient decrease of the local anodic or cathodic currents (see Fig. 6). Qualitatively, the pattern of the curves $I_f(\Delta\varphi_s)$ is very well predicted by the characteristic Nernstian behavior of the redox couple. However, a more quantitative analysis based on the first-order approximation of a linear field and on the corresponding integration of the voltammograms appears to systematically overestimate the bipolar current. Several reasons may account for the imperfection of such a quantitative approach. In standard voltammetric experiments leading to the voltammograms, one can speak of a bulk concentration for each of the components of the redox couple. In the thin-layer cell, it is likely that depletion/accumulation of the redox components occurs, especially for high $\Delta\varphi_s$, because the thickness of the diffusion layer becomes comparable to the thickness a of the thin-layer cell. This possibility is supported by the experimentally observed decrease of I_f for 10^{-6}/10^{-6} M–10^{-4}/10^{-4} M redox concentrations and $\Delta\varphi_s > 150$–200 mV (Fig. 8). Hence, the semi-infinite diffusion conditions (as met in the voltammetric experiments) are not exactly applicable in quantifying the local faradaic current densities and the corresponding overall bipolar current in the thin-layer cell. Moreover, it appears that even with an excess of electroinactive electrolyte (as is the case in the reported experiments), the bipolar current maintained by the redox processes is significant compared to the ohmic contribution to the total current. Consequently, it is highly probable that even for relatively low concentrations of the redox components, the equipotential planes, perpendicular to the surfaces when assuming a constant field, are considerably perturbed by the electrochemical reactions, thus invalidating the assumption of a linear potential drop across the cell. A rigorous theoretical treatment of the problem would require the simultaneous resolution of diffusion equations and potential distribution in a self-consistent way. Such analysis is currently in preparation [29] and the first results confirm the arguments presented here.

4.3. Streaming potential analysis

4.3.1. Extension of the Smoluchowski relation

In the previous section, it was the externally applied tangential field that induces the bipolar current. In streaming potential experiments, the driving force for the bipolar redox process is the flow of the electrolyte due to an applied pressure ΔP, which creates a potential E_{str} across the thin-layer cell (Fig. 9). Let us consider an experiment where an electrolyte solution, containing the redox couple $\mathrm{Fe(CN)}_6^{3-}/\mathrm{Fe(CN)}_6^{4-}$, is flushed between two gold surfaces in a thin-layer cell under the influence of a pressure gradient ΔP. In the stationary state, the streaming current is balanced by a conductive counter current, which now may contain a contribution from the bulk of the gold phase, as limited by the interfacial electron transfer reaction with the redox couple. This contribution is quantified by the bipolar conductance g^f (Ω^{-1}), which we define, for one bipolar electrode, as

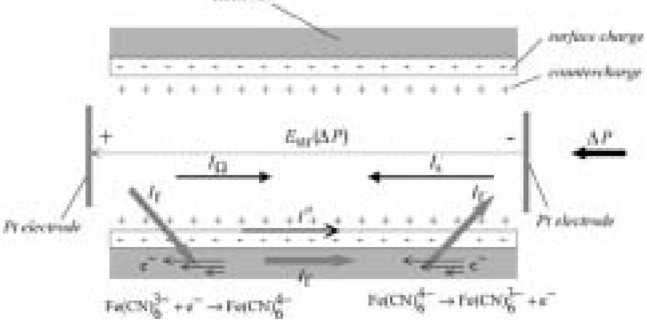
electrode
surface charge
countercharge
+
$E_{\mathrm{str}}(\Delta P)$
-
ΔP
I_Ω
I_s
I_f
I_f
I^σ
I_f
Pt electrode
Pt electrode
e^-
e^-
$\mathrm{FeCN}_6^{3-} + e^- \rightarrow \mathrm{FeCN}_6^{4-}$
$\mathrm{FeCN}_6^{4-} \rightarrow \mathrm{FeCN}_6^{3-} + e^-$

Fig. 9. Schematic representation of the situation typically encountered in a streaming potential experiment in the presence of an electroactive redox couple like $\mathrm{Fe(CN)}_6^{3-}/\mathrm{Fe(CN)}_6^{4-}$ in the solution flushed between the two substrates. The streaming current I_s is counterbalanced by the ohmic current I_Ω, the surface current I^σ, and the bipolar current I_f.

$$g^f = K^f l = \frac{I_f}{E_{\mathrm{str}}}, \tag{5}$$

where K^f is the specific bipolar faradaic conductivity per unit width ($\Omega^{-1}\,\mathrm{m}^{-1}$). K^f represents the integral of the local anodic/cathodic current densities and thus depends on E_{str}, the pressure ΔP, and the bulk concentrations of the oxidized species $\mathrm{Fe(CN)}_6^{3-}$ and reduced species $\mathrm{Fe(CN)}_6^{4-}$, denoted as c_O^* and c_R^*, respectively. For two gold surfaces, each with bipolar conductance g^f, the Smoluchowski Eq. (1) is then expanded to

$$E_{\mathrm{str}} = \frac{\varepsilon_0 \varepsilon_r \zeta \Delta P}{\eta (K^L + 2K^\sigma/a + 2K^f)}. \tag{6}$$

In contrast to the situation of Fig. 8, bulk depletion of the electroactive species does not occur in the case of sufficiently high ΔP. A steady-state convective–diffusion situation is developed, and a parallel with the RDE experiments (Section 4.1), which also refer to conditions of steady-state convective diffusion, can be drawn. This may be used for an estimation of I_f and hence K^f.

The current density–potential relationship $j(E)$ describing the curves in Fig. 7 is given by [30]

$$j = \frac{j_{l,c} + j_{l,a}\exp[nf(E - E_{1/2})]}{1 + \exp[nf(E - E_{1/2})]}, \tag{7}$$

where n is the number of electrons transferred per molecule ($n = 1$ in our case), $j_{l,a}$ and $j_{l,c}$ are the limiting anodic and cathodic current densities, respectively, and

$$f = F/RT, \tag{8}$$

with F the Faraday constant, R the gas constant, and T the temperature. The half-wave potential $E_{1/2}$ is defined by [30]

$$E_{1/2} = E^0 + (nf)^{-1} \ln\left(\frac{D_R}{D_O}\right)^{2/3}, \tag{9}$$

where E^0 is the standard potential of the redox couple and D_R and D_O are the diffusion constants ($\mathrm{m}^2\,\mathrm{s}^{-1}$) of the reduced and oxidized species, respectively. For a symmetric redox system, $c_R^* = c_O^* = c_{\mathrm{redox}}^*$. Assuming $D_R = D_O = D$ (as is the case for the $\mathrm{Fe(CN)}_6^{3-}/\mathrm{Fe(CN)}_6^{4-}$ system), we can write $j_{l,a} = -j_{l,c} = j_l$ (> 0) and $E_{1/2} = E^0$. Equation (7) then becomes

$$j = j_l \tanh\left[\frac{nf}{2}(E - E^0)\right]. \tag{10}$$

In the steady-state diffusion situation, j_l can be formally written as

$$j_l = nF\frac{D}{\delta} c_{\mathrm{redox}}^*, \tag{11}$$

where δ is the thickness of the diffusion layer.

For a flow confined in a flat thin-layer channel, the Reynolds number *Re* is defined by

$$Re = v_0 a/2\upsilon, \tag{12}$$

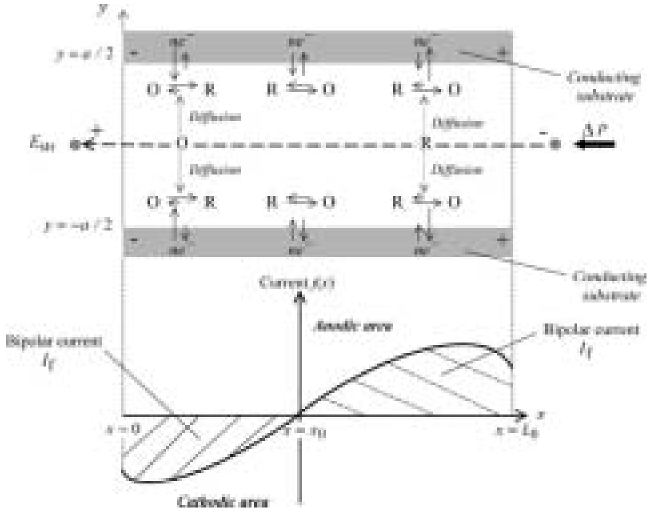

Fig. 10. Schematic representation of the reversible bipolar process occurring in the electrokinetic cell under flow conditions. Diffusion of the redox components *O* (oxidized species) and *R* (reduced species) to/from the surfaces takes place, which in turn generates, along the electrodes, a spatial distribution of the local current $j(x)$, the integration of which provides the bipolar current I_f (see Section 4.3.1). The areas striped in dashed and plain lines are equal.

where υ ($\mathrm{m^2\,s^{-1}}$) is the kinematic viscosity of the medium (the viscosity η divided by the density) and v_0 is the bulk velocity of the fluid expressed by [31]

$$v_0 = \frac{a^2}{8\eta}\frac{\Delta P}{L_0}. \tag{13}$$

For the geometrical characteristics of our cell and the typical range of pressures applied, *Re* is less than 2500, thus validating the hypothesis of a laminar flow. Under such conditions, the component v_y of the velocity vector in the direction perpendicular to the electrodes is zero and the component in the axial direction (Fig. 10) follows a parabolic profile given by

$$v_x = v_0\left(1 - \left(\frac{2y}{a}\right)^2\right). \tag{14}$$

Assuming that the diffusion occurs over small distances from the walls, that is, the concentration profile extends to less than $a/2$, v_x can be linearized and resolution of the resulting convective–diffusion equation provides an expression for the diffusion length δ (see Ref. [31] for further detail). It depends on the position x at the bipolar electrodic surface as

$$\delta(x) = 1.49\left(\frac{Dax}{2v_0}\right)^{1/3}. \tag{15}$$

Therefore, starting from the well-established transport situation encountered in the RDE experiments, the local diffusion-limited current density j_l in the thin-layer cell can be estimated via

$$j_l(x) = nF\frac{D}{\delta(x)}c^*_{\text{redox}}. \tag{16}$$

The potential E introduced in Eq. (7) stands for the potential difference between the metal and the solution. In the thin layer cell, E depends on the position x. The potential profile $E(x)$ is determined by the course of the electric field in the capillary. Within the approximation of a linear field, we have

$$E(x) - E^0 = (x - x_0)E_{\text{str}}/L_0, \tag{17}$$

with x_0 defined as the position at the bipolar electrode where there is no net faradaic current or, equivalently, where the local potential equals the equilibrium potential E^0. For an asymmetric redox system, x_0 may depend on E_{str}, as examined in [5] in the particular case of an irreversible bipolar faradaic process. As for the experiments reported in Section 3, there is a coupling between the local current density $j(x)$, resulting from the diffusion of the electroactive species to/from the electrode surfaces, and the *local* potential. This coupling induced deviations to Eq. (17) which will be analyzed in detail in a separate study [29]. Considering the usual magnitudes of the streaming potential E_{str}, the argument of the tanh function in Eq. (10) remains small for every position on the surface. Combinations of Eqs. (10), (13), and (15)–(17) then provides an expression for the local faradaic current density,

$$j(x) = \frac{nf\beta}{2L_0}c^*_{\text{redox}}(\Delta P)^{1/3}E_{\text{str}}x^{-1/3}(x - x_0), \tag{18}$$

with β given by

$$\beta = 0.42nF\left(\frac{aD^2}{\eta L_0}\right)^{1/3}. \tag{19}$$

For a given streaming potential E_{str}, the bipolar current I_f then follows from the integration of j over either the anodic or the cathodic side (Fig. 10),

$$I_f = -l\int_0^{x_0} j(x)\,dx = l\int_{x_0}^{L_0} j(x)\,dx. \tag{20}$$

From the equality of the two integrals written in Eq. (20), one then obtains $x_0 = 2L_0/5$. Deviation of x_0 from the middle position $L_0/2$ stems from the asymmetric contour of the diffusion layer with the position x. Using Eqs. (18) and (20), the bipolar conductivity K^f can be derived from relation (5). The Smoluchowski Eq. (6) can then be written to explicitly include faradaic depolarization as calculated within the linear field assumption:

$$E_{\text{str}} = \frac{\varepsilon_0\varepsilon_r\zeta\Delta P}{\eta\left(K^L + \frac{2K^\sigma}{a} + \frac{9}{10}\left(\frac{2}{5}\right)^{5/3}nf\beta L_0^{2/3}c^*_{\text{redox}}(\Delta P)^{1/3}\right)}. \tag{21}$$

As discussed in Section 4.1, the validity of the homogeneous field approach and hence of Eq. (21) depends on the magnitude of the ratio I_f/I_Ω [29]. Even at low field strength and low concentrations of redox components, this approach may lead to inappropriate results, as will be discussed in the next section. Nevertheless, it provides a simple analytical

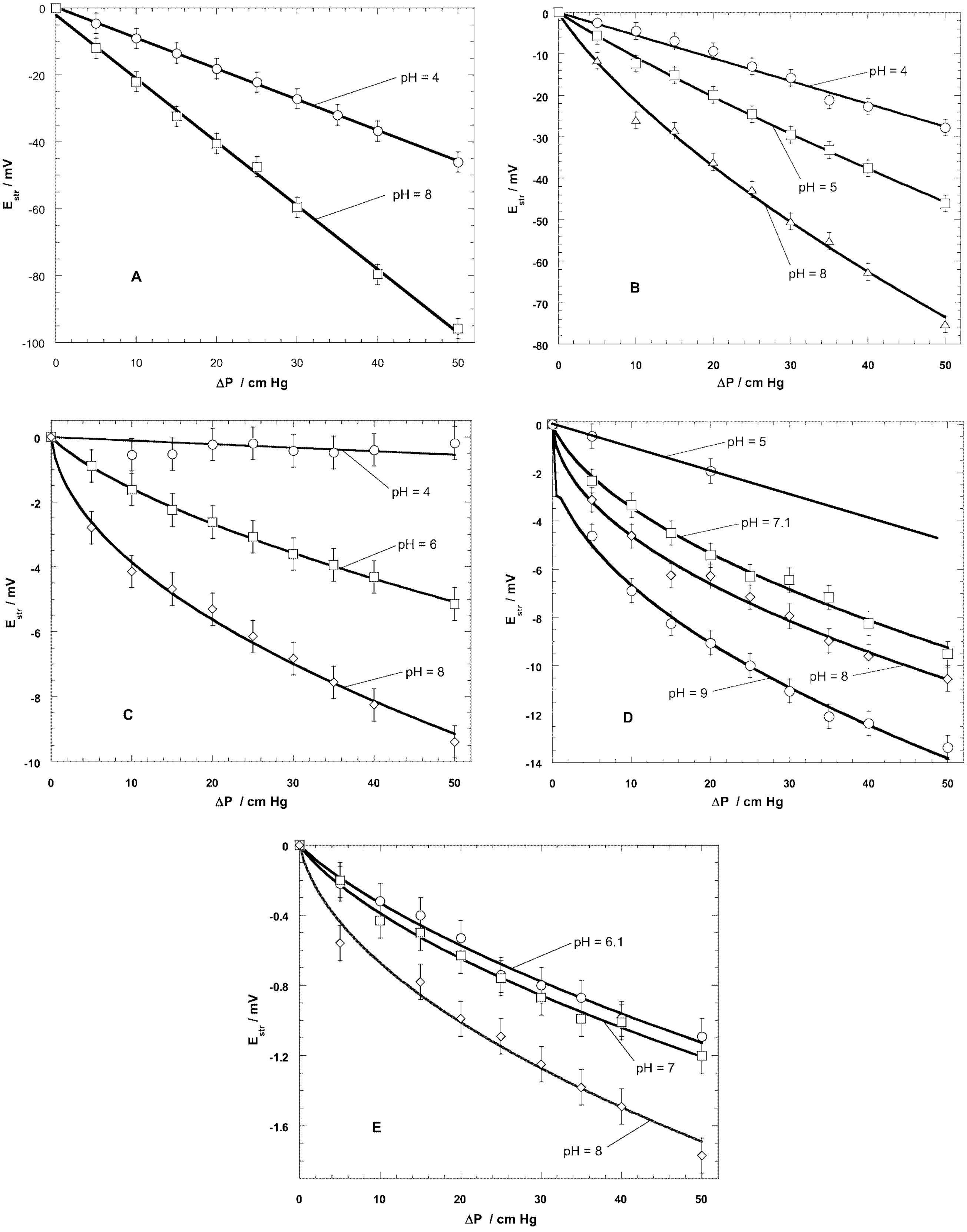

Fig. 11. Streaming potentials measured for gold at different pH in (A) 10^{-3} M KNO_3 and 10^{-5} M/10^{-5} M, (B) 10^{-4} M/10^{-4} M, and (C) 10^{-3} M/10^{-3} M $Fe(CN)_6^{3-}$/$Fe(CN)_6^{4-}$ concentrations. In (D) and (E), 10^{-2} M KNO_3 is used with 10^{-4} M/10^{-4} M and 10^{-3} M/10^{-3} M $Fe(CN)_6^{3-}$/$Fe(CN)_6^{4-}$, respectively. The curves are only guides for the eye.

expression of the bipolar current and the conductance K^f, exhibiting a dependence in $(\Delta P)^{1/3}$, the origin of which is to be found in the nonlinear profile of the diffusion layer thickness (Eq. (15)).

4.3.2. Experimental results

Figure 11 presents a set of experimental data $E_{\text{str}}(\Delta P)$ obtained for flat gold layers under different conditions of pH and concentrations of KNO_3 and redox species. As predicted by the theoretical treatment set forth in Section 4.3.1, the curves significantly deviate from linearity at high c_O^*, c_R^* and relatively high pressure gradients. Under such conditions, the magnitude of the bipolar conductance term becomes significant or even dominant over the bulk solution and surface conductance contributions. The deviation from linearity is particularly pronounced for high pH. Indeed, the driving force for the bipolar current is the streaming potential, which increases with increasing pH above the iep, as illustrated by Fig. 4. It was verified that streaming potential measurements performed on glass (a dielectric substrate) in the presence of the redox couple lead to the same results as the ones presented in Section 3.2, thus ruling out any effects of depolarization at the sensing Pt electrodes. The analysis performed in the previous section (Eq. (21)) explains the experimentally observed nonlinearity of the curves $E_{\text{str}}(\Delta P)$, as generated by the reversible bipolar process.

An attempt was made to evaluate the electrokinetic potential ζ using Eq. (21). The fractional contribution from K^f to the total conductance, noted α $(= 2K^f/(K^L + 2K^f))$, reflects the relative magnitude of the bipolar current. Even at low redox concentrations (10^{-5} M) compared to the indifferent electrolyte concentration (10^{-3} M) and low applied pressures (5 cm Hg), situations a priori favorable for minimizing the bipolar faradaic contribution to the overall conductivity, it is found that $\alpha \approx 0.2$. Such a value already corresponds to significant deviation from a linear potential profile [29], indicating that Eq. (21) generally provides only an estimate of the results. Quantitative interpretation of the streaming potential in terms of the underlying ζ-potential requires a more rigorous analysis based on the coupling between the field in solution and the faradaic conduction processes [29]. Such analysis allows appreciation of the dependence of the electrokinetic potential on the total potential drop across the metal–solution interface, which here is electrochemically manipulated by the redox species in the solution. Though this type of investigation has become common in studies of the interface by atomic force microscopy where the potential of the metallic phase is varied via an external electric circuit [15], it has not yet been envisaged in the field of electrokinetics.

5. Conclusions

We have demonstrated the feasibility of electrokinetic measurements for the investigation of double-layer properties of conducting materials like gold and aluminum on the basis of an analysis of the bipolar faradaic depolarization effects occurring in a thin-layer cell. The explanation includes a comparison between electrokinetic and electrode kinetic features, which correspond to bipolar and monopolar behavior, respectively.

For electroinactive electrolytes, bipolar faradaic depolarization occurs in a potential regime which is irrelevant for standard electrokinetic experiments. The metal–electrolyte interface can then be considered as completely polarized and, from an electrode kinetic point of view, irreversible. Hence, no effective conduction takes place through the bulk metal. The linear dependence of the streaming potential on the applied pressure, as predicted by the Smoluchowski equation for dielectric substrates, has indeed been observed for Au and Al.

In the presence of a redox couple with a reversible electrochemical behavior on the given metal, a significant bipolar current is already detected at very low potential differences in the solution. A first analysis of the dependence of the bipolar current on the pressure indeed shows a nonlinear variation of the streaming potential with the applied pressure. This is in accordance with experimental results, the rigorous interpretation of which requires a theoretical analysis which accounts for the coupling of the bipolar conduction processes with the nonlinear field in solution [29].

Acknowledgment

Dr. J. Mieke Kleijn is acknowledged for her advice and useful remarks concerning the elaboration of the paper.

References

[1] J. Oosterman, Thesis, University of Utrecht, The Netherlands, 1937.

[2] J.Th.G. Overbeek, Thesis, University of Utrecht, The Netherlands, 1941.

[3] J.Th.G. Overbeek, Kolloidchem. Beih. 54 (1943) 287.

[4] J. Heyrovský, J. Kuta, Principles of Polarography, Publishing House of the Czechoslovak Academy of Sciences/Academic Press, Praha/New York, 1966.

[5] J. Duval, J.M. Kleijn, H.P. Van Leeuwen, J. Electroanal. Chem. 505 (2001) 1.

[6] A.J. Bard, L.R. Faulkner, Electrochemical Methods Fundamentals and Applications, Wiley, New York, 1980, p. 103.

[7] A.J. Bard, L.R. Faulkner, Electrochemical Methods Fundamentals and Applications, Wiley, New York, 1980, p. 51.

[8] R.A. Van Wagenen, J.D. Andrade, J. Colloid Interface Sci. 76 (2) (1980) 305.

[9] P.J. Scales, F. Grieser, T.W. Healy, L.R. White, D.Y.C. Chan, Langmuir 8 (1992) 965.

[10] C. Wagner, W. Traud, Z. Elektrochem. 44 (1938) 391;
M. Spiro, in: D.V. Fenby, I.D. Watson (Eds.), The Physical Chemistry of Solutions, Massey University, New Zealand, 1983.

[11] R.J. Hunter, Zeta Potential in Colloid Science, Academic Press, London, 1981, p. 66.

[12] J. Lyklema, in: Fundamentals of Interface and Colloid Science, Vol. 2, Academic Press, London, 1995, Chap. 3, p. 3147.

[13] I. Larson, C.J. Drummond, D.Y.C. Chan, F. Grieser, Langmuir 13 (1997) 2109.
[14] L. Meagher, G.V. Franks, M.L. Gee, P.J. Scales, Colloids Surf. A Physicochem. Eng. Asp. 146 (1999) 123.
[15] D. Barten, J.M. Kleijn, J. Duval, H.P. Van Leeuwen, J. Lyklema, M.A. Cohen Stuart, Langmuir 19 (2002) 1133.
[16] M. Giesbers, J.M. Kleijn, M.A. Cohen Stuart, J. Colloid Interface Sci. 248 (2002) 88.
[17] J. Duval, J. Lyklema, J.M. Kleijn, H.P. Van Leeuwen, Langmuir 17 (2001) 7573.
[18] D.E. Yates, S. Levine, T.W. Healy, J. Chem. Soc. Faraday Trans. 1 70 (1974) 1807.
[19] J.A. Davids, R.O. James, J.O. Leckie, J. Colloid Interface Sci. 63 (1978) 480.
[20] G. Gouy, Compt. Rend. 149 (1909) 654;
G. Gouy, J. Phys. 4 (9) (1910) 457;
G. Gouy, Ann. Phys. 7 (9) (1917) 129.
[21] D.L. Chapman, Philos. Mag. 6 (25) (1913) 475.
[22] O. Stern, Z. Elektrochem. 30 (1924) 508.
[23] R.O. James, G.A. Parks, in: E. Matijevic (Ed.), Surface and Colloid Science, Vol. 12, Plenum, New York, 1982, p. 119.
[24] H.J. Modi, D.W. Fuerstenau, J. Phys. Chem. 61 (1957) 640;
J.A. Yopps, D.W. Fuerstenau, J. Colloid Sci. 19 (1964) 61;
D.A. Griffiths, D.W. Fuerstenau, J. Colloid Interface Sci. 80 (1981) 271;
K.F. Hayes, G. Redden, W. Ela, J.O. Leckie, J. Colloid Interface Sci. 142 (1991) 448.
[25] J. Lyklema, Fundamentals of Interface and Colloid Science, Vol. 2, Academic Press, London, 1995, Appendix 3.
[26] R.O. James, T.W. Healy, J. Colloid Interface Sci. 40 (1) (1972).
[27] A.J. Bard, L.R. Faulkner, Electrochemical Methods: Fundamentals and Applications, Wiley, New York, 1980, p. 215.
[28] A.J. Bard, L.R. Faulkner, Electrochemical Methods: Fundamentals and Applications, Wiley, New York, 1980, p. 288.
[29] J. Duval, M. Minor, J. Cecilia, H.P. Van Leeuwen, J. Phys. Chem., accepted.
[30] A.J. Bard, L.R. Faulkner, Electrochemical Methods: Fundamentals and Applications, Wiley, New York, 1980, p. 290.
[31] V.G. Levich, Physicochemical Hydrodynamics, Prentice–Hall, Englewood Cliffs, NJ, 1962.

ERRATUM

Equations (5) and (21) should be read

$$g^{\mathrm{f}} \mid K^{\mathrm{f}}\frac{al}{L_0} \mid \frac{I_{\mathrm{f}}}{E_{\mathrm{str}}}$$

and

$$E_{\mathrm{str}} \mid \frac{\kappa_0\kappa_{\mathrm{r}}{}' \div P}{\xi \textcircled{R}\textcircled{C}\textcircled{C}\text{™} K^{\mathrm{L}}\, 2\,\frac{2K^{\omega}}{a}\, 2\,\frac{9}{10}\textcircled{R}\textcircled{C}\text{™}\frac{2L_0}{5}\Big|^{5/3}\Big|\, nf\,\frac{\eta}{a}c^{*}_{\mathrm{redox}} / \div P0^{1/3}\Big|}$$

, respectively.

J. Phys. Chem. B **2003,** *107,* 4143−4155

Coupling of Lateral Electric Field and Transversal Faradaic Processes at the Conductor/Electrolyte Solution Interface

J. F. L. Duval,*,† M. Minor,‡ J. Cecilia,§ and H. P. van Leeuwen†

Department of Physical Chemistry and Colloid Science, Wageningen University, Dreijenplein 6,
6703 HB Wageningen, The Netherlands, NIZO Research Institute, Kernhemseweg 2,
6718 ZB Ede, The Netherlands, and Departament de Matematica, Universitat de Lleida,
Rovira Roure 177, 25198 Lleida, Spain

Received: November 20, 2002; In Final Form: February 5, 2003

A quantitative theory is presented for the bipolar behavior of conducting planar surfaces in a thin-layer cell of a type commonly used in electrokinetic studies. The lateral current density distribution in the cell, as dictated by the externally applied field in the solution, is formulated for the situation in which depolarization of the interface arises from transversal electron-transfer processes that occur at the two sides of the conducting surface. The treatment explicitly analyses the two limiting cases of bipolar electrodic behavior, i.e., totally irreversible electron transfer and Nernstian (mass-transfer-limited) electrodics. The spatial distribution of the electric field is calculated by means of Poisson's equation under conditions of a finite current. The results allow for a rigorous estimation of the overall bipolar faradaic current. Analytical expressions are given for the electric parameters (potential, field, local current, and bipolar faradaic current) in the case of irreversible electron transfer, and numerical analysis is performed for the reversible, Nernstian case. Deviations of the conductivity curves from the trend expected on the basis of a linear potential profile are discussed in terms of the local ohmic and faradaic contributions to the total current. The theory is supported and illustrated by experimental data for gold and aluminum surfaces in KNO_3 solution, in the absence and presence of the electroactive species $Fe(CN)_6^{3-}/Fe(CN)_6^{4-}$.

1. Introduction

The bipolar behavior of electroconductive objects isolated between two current feeders and subjected to an external electric field has been discussed extensively in many areas, including the dissolution of nuclear fuel,[1] control of oxide film thickness,[2] organic synthesis,[3−6] corrosion, etc. The bipolar behavior has also been investigated in the specific context of electrochemistry at dispersed microelectrodes.[6,7] The geometry of microsphere electrodes, which allows for the development of spherical diffusion fields in the bulk of the surrounding solution, presents multiple advantages with respect to the electrochemical reaction kinetics[8−11] and the insignificance of the transient electrodic response.[9] The dispersed systems permit an extension of the concepts used in bipolar fluidized bed electrodes[12,13] to the area of microelectrodes. The possibility of carrying out electrochemical reactions at considerable rates in poorly conducting media by means of bipolar electrolysis with dispersions of conducting particles provides motivation for the development of the electrotechnology of dispersed systems. For example, the industrial application of the "superfast electrophoresis" effect,[14] which is based on the specific bipolar behavior of metallic particles[15] or ion-exchanger particles,[16] illustrates the relevance of understanding the bipolar properties of the conducting substrate|electrolyte solution interface. Recently, we have emphasized the fundamental importance of bipolar faradaic depolarization within the new context of streaming potentials generated by metals in electroinactive and electroactive electrolytes.[17] We demonstrated that, in certain circumstances, macroscopic bodies of planar geometry placed in a lateral electric field can behave as bipolar electrodes.[17,18] The propensity of the metallic surface to depolarization under the influence of a lateral electric field in the solution explains the feasibility of electrokinetic measurements for the investigation of double-layer properties of conducting materials. Measurements of the bipolar current have been performed[17,18] for irreversible and reversible systems for which the electron-transfer kinetics and diffusive mass transfer, respectively, govern the faradaic processes. A theoretical treatment based on the first-order approximation of a linear distribution of the potential or, equivalently, on the assumption of a homogeneous field along the bipolar electrode is also available.[17,18] This treatment, though useful for a qualitative understanding of the electrochemical and electrokinetic implications of the bipolar phenomenon, is oversimplified because of the intrinsic coupling between the potential distribution and the position-dependent faradaic current. In this paper, we rigorously tackle the pertinent field−current interrelation that is of importance for both irreversible and reversible electrode processes. We present analytical and numerical approaches to account for the nonlinear potential distribution and for the corresponding bipolar current. The theoretical results for planar symmetry successfully interpret experimental data for gold and aluminum surfaces in the presence and absence of a reversible redox couple. The analysis also provides a rigorous theoretical basis for the quantitative understanding of faradaic depolarization as an interfering element in the study of electrokinetic properties of conducting bodies. In these studies, the bipolar electrodic process arises from enhanced tangential flow

---

* To whom correspondence should be addressed.

† Wageningen University.

‡ NIZO Research Institute.

§ Universitat de Lleida.

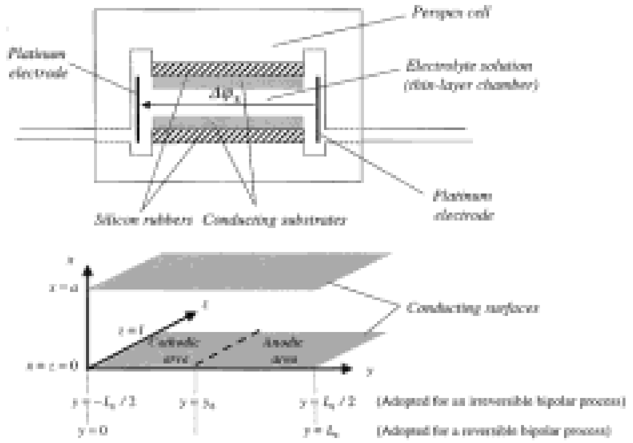

Figure 1. (Top) Schematic representation of the thin-layer cell. (Bottom) Geometric sketch of the coordinate system chosen for the formalism describing the bipolar behavior of the planar surfaces.

of the electrolyte solution along the conducting surface. The implications for the electrophoretic mobility of metallic particles and the collapse of the streaming potential of metallic surfaces in the presence of electroactive species will be discussed in detail elsewhere.

2. Definition of the Coordinate System, Notation

The coordinate system is defined in Figure 1. The distance between the two metallic electrodes in the flat capillary cell is a, the length of the metallic surface is L_0, and its width is l. A potential difference, denoted as $\Delta\varphi_s$, is applied across the long side of the thin-layer cell (y axis) between two auxiliary electrodes placed just outside the thin-layer chamber. In a scanning experiment, the value of $\Delta\varphi_s$ is systematically varied with time t according to the relation

$$\Delta\varphi_s(t) = \nu \times t \tag{1}$$

where ν is the scan rate (V s^{-1}). The bipolar faradaic current I_f at the metal|solution interface is carried by two redox couples denoted as Ox_a/R_a and Ox_c/R_c, where the subscripts a and c pertain to the anodic and cathodic processes, respectively (section 4). In the case where the current is carried by the same redox couple (section 5), the oxidized and reduced forms are denoted as Ox and R, respectively. The solution contains an electrolyte of given concentration c_s assumed to be in excess over the redox species. The solution conductivity in the thin-layer cell is denoted as K^L (Ω^{-1} m^{-1}) and is assumed to be constant with time t. So-called conductivity curves refer to plots of the overall current I, composed of the conduction current I_Ω and the bipolar faradaic current I_f, as a function of $\Delta\varphi_s$.

3. Expression of the Coupling between Electric Field and Faradaic Current

Considering the symmetry of the problem, the electric field and the faradaic current can be considered to be independent of the variable z, i.e., edge effects can be neglected. The explicit expression for the local potential $V(x,y,t)$, which denotes the potential of the solution at the positions x, y and given time t with respect to the (equipotential) metallic surface, is related to the magnitude of the local field, denoted as $E(x,y,t)$ (not to be confused with the common potential notation in electrochemistry)

$$E(x,y,t) = -\left(\frac{\partial V(x,y,t)}{\partial y} + \frac{\partial V(x,y,t)}{\partial x}\right) \tag{2}$$

In the following, we shall neglect the change of potential (and field) and the corresponding ionic charge distribution associated with the interfacial electric double layer (x direction). This assumption is justified provided that the condition $2\kappa^{-1} \ll a$ is fulfilled, where κ^{-1} is the Debye length characterizing the extension of the interfacial double layer. The correctness of this neglect for the systems modeled in this paper is in agreement with the choice made for the electrolyte concentration c_s. For illustration, in the range $c_s = (10^{-4})-1$ M, $2\kappa^{-1}/a \approx (3 \times 10^{-4})-(3 \times 10^{-6})$ ($a = 0.2$ mm). Therefore one can legitimately write the potential and the field as functions of y and t only (the derivative of V with respect to x in eq 2 is not taken into account). To find $E(y,t)$, let us consider an infinitesimally small volume element of the cell as pictured in Figure 2. This volume contains the electrolyte located between the positions y and $y + dy$. An ohmic current enters the considered volume element at y and leaves it at $y + dy$. A faradaic current with density j (A m^{-2}), which results from charge transfer between the solution and the conducting surfaces, enters the volume as a transversal current through the yz plane. In contrast to the common electrochemical situation, the flow of electrons associated with this faradaic current is perpendicular to the direction of the externally applied electric field. For an irreversible process under conditions of relatively weak faradaic depolarization, the chemical composition of the solution between the plates remains essentially constant (section 4). This is also true for the reversible case (section 5), provided that there is an excess of supporting electrolyte over the electroactive compounds. The field is considered to be established instantaneously. The electroneutrality condition for the elementary slice of volume $a \times l \times dy$ is

$$-aK^L \frac{\partial E(y,t)}{\partial y} + 2j(y,t) = 0 \tag{3}$$

Equation 3 defines the *intrinsic* relation between the faradaic current and the electric field at any position y along the surface and any time t. In the situation where $j = 0$ (no depolarization), eq 3, combined with eq 2, reduces to the common one-dimensional Poisson equation for an electroneutral medium

$$\frac{d^2V(y,t)}{dy^2} = 0 \tag{4}$$

Solution of eq 4 leads to a linear profile of the potential, i.e., a constant electric field. Once the dependence of j on the position is known, the electric field distribution, and hence the potential profile along the capillary cell, can be calculated with eq 3. We shall analyze the cases in which (i) the electron-transfer reaction at the bipolar metal|electrolyte interface is very slow compared to mass transport (the totally irreversible case) and (ii) the bipolar electrolytic processes are purely mass-transport-limited, i.e., electrochemically reversible.

4. Irreversible Bipolar Redox Process

4.1. Expressions of the Field Distribution and the Bipolar Current. The spatial variation of the solution potential $V(y,t)$ gives rise to an oxidation reaction at one side of the surface and a concomitant reduction reaction at the other side, as given by

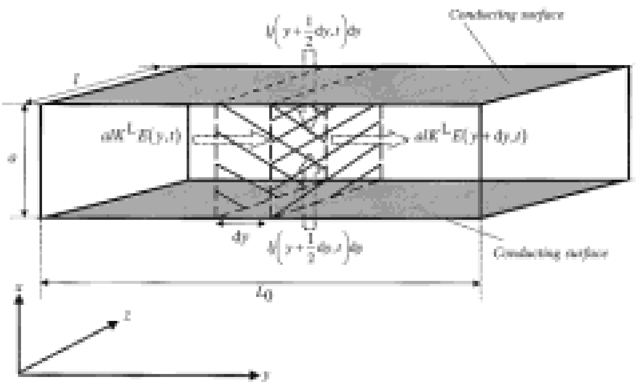

Figure 2. Schematic picture illustrating the coupling (eq 3 in the text) between the electric field E and the transversal faradaic current flow j at a given time t (or given potential $\Delta\varphi_s$) and position y.

$$R_a \rightarrow Ox_a + n_a e^- \tag{5a}$$

$$Ox_c + n_c e^- \rightarrow R_c \tag{5b}$$

with n_a and n_c denoting the numbers of electrons involved in eqs 5a and 5b, respectively. The anodic and cathodic current densities are denoted by j_a and j_c, respectively (A m^{-2}). In the irreversible case with the interfacial charge-transfer kinetics controlling the rates of the reactions, j_a and j_c are usually expressed by the so-called Butler−Volmer expressions[19]

$$j_a(y,t) = j_{0_a} \exp[-r_a f(V(y,t) - V_a^0)] \tag{6}$$

$$j_c(y,t) = -j_{0_c} \exp[r_c f(V(y,t) - V_c^0)] \tag{7}$$

with f, r_a, and r_c defined by

$$f = \frac{F}{RT} \tag{8}$$

$$r_a = n_a(1 - \alpha_a) \tag{9}$$

$$r_c = n_c\alpha_c \tag{10}$$

where α_a and α_c denote the transfer coefficients for the oxidation and the reduction reactions, respectively; j_{0_a} and j_{0_c} are the corresponding apparent exchange current densities; V_a^0 and V_c^0 are the standard potentials of Ox_a/R_a and Ox_c/R_c, respectively, with opposite sign (because here we consider the potential of the solution with respect to the metal surface); F is the Faraday constant; R is the gas constant; and T is the temperature. By analogy with electrochemical convention, the mixed potential V_m[20,21] is the potential at which the net local current ($j_a + j_c$) is zero

$$j_a(V_m) = -j_c(V_m) \tag{11}$$

It follows from eqs 6 and 7 that

$$V_m = \frac{\ln\left(\dfrac{j_{0_a}}{j_{0_c}}\right) + f(r_c V_c^0 + r_a V_a^0)}{f(r_c + r_a)} \tag{12}$$

The position at which V equals V_m is indicated as y_0. For the case of two totally irreversible reactions, we can neglect the local anodic and cathodic currents for $V > V_m$ and $V < V_m$, respectively. Using the properties of the exponential function, differentiation of eq 3 with respect to y and combination of the results with eqs 6 and 7 allows explicit expression of the field distribution for the anodic and cathodic areas by the following nonlinear differential equations of second order

$$y > y_0(t): \qquad \frac{\partial^2 E(y,t)}{\partial y^2} - r_a f \frac{\partial E(y,t)}{\partial y} E(y,t) = 0 \tag{13}$$

$$y < y_0(t): \qquad \frac{\partial^2 E(y,t)}{\partial y^2} + r_c f \frac{\partial E(y,t)}{\partial y} E(y,t) = 0 \tag{14}$$

which we write in concise form as

$$\frac{\partial^2 E(y,t)}{\partial y^2} + \epsilon_{a,c} r_{a,c} f \frac{\partial E(y,t)}{\partial y} E(y,t) = 0 \tag{15}$$

where $\epsilon_a = -1$ for $y > y_0(t)$ (anodic area) and $\epsilon_c = +1$ for $y < y_0(t)$ (cathodic area). Solving eq 15 requires two boundary conditions for the field, or equivalently for the potential (see eq 2). Because the surface of the metallic conductor is an equipotential plane, the total applied potential drop must comply with the condition

$$V(-L_0/2,t) - V(L_0/2,t) = \Delta\varphi_s(t) \tag{16}$$

As a consequence of eq 11, the position $y_0(t)$ is defined by

$$-\int_{-L_0/2}^{y_0(t)} j_c(y,t)\,dy = \int_{y_0(t)}^{L_0/2} j_a(y,t)\,dy \tag{17}$$

which stands for the condition of no charge accumulation in the overall bipolar conducting substrate. Each integral of eq 17 can be expressed as a function of the field by integration of the differential eq 3 so that the second searched boundary condition can be simply rewritten as

$$E(-L_0/2,t) = E(L_0/2,t) \tag{18}$$

Equation 15 can be easily integrated to give

$$\frac{\partial E(y,t)}{\partial y} + \frac{1}{2}\epsilon_{a,c} r_{a,c} f E(y,t)^2 = C(t) \tag{19}$$

where $C(t)$ is a constant (independent of position). $C(t)$ can be calculated at the particular position $y = y_0(t)$

$$C(t) = k_{a,c} + \frac{1}{2}\epsilon_{a,c} r_{a,c} f E(y_0(t),t)^2 \tag{20}$$

where the constant $k_{a,c}$ is defined by

$$k_{a,c} = -\frac{2\epsilon_{a,c} j_{0_{a,c}}}{aK^L} \exp[\epsilon_{a,c} r_{a,c} f(V_m - V_{a,c}^0)] \tag{21}$$

The differential eq 19 can be solved by integrating over the field from $E(y_0(t),t)$ to $E(y,t)$, i.e., over the space from $y_0(t)$ to y. After simple manipulation, it gives

$$\int_{E(y_0(t),t)}^{E(y,t)} \frac{dE(y,t)}{E(y,t)^2 - [E(y_0(t),t)^2 - \Lambda_{a,c}]} = -\frac{1}{2}\epsilon_{a,c} r_{a,c} f \int_{y_0(t)}^{y} dy \tag{22}$$

where $\Lambda_{a,c}$ (positive) is given by

$$\Lambda_{a,c} = \frac{2k}{r_{a,c} f} \tag{23}$$

and $k = |k_{a,c}|$. Let us consider the case where $E(y_0(t),t)^2 > \Lambda_{a,c}$, which typically holds for relatively high electrolyte concentrations (high K^L) and/or relatively low $j_{0_{a,c}}$. Then, the inequality $E(y,t)^2 > [E(y_0(t),t)^2 - \Lambda_{a,c}]$ is always verified, and the solution of eq 22 can be written as

$$E(y,t) = [E(y_0(t),t)^2 - \Lambda_{a,c}]^{1/2}\coth\Big\{\mu_{a,c}(t) + \frac{1}{2}\epsilon_{a,c}r_{a,c}\,f[E(y_0(t),t)^2 - \Lambda_{a,c}]^{1/2}(y - y_0(t))\Big\} \tag{24}$$

with the dimensionless quantity $\mu_{a,c}(t)$ defined by

$$\mu_{a,c}(t) = \coth^{-1}\left\{\frac{E(y_0(t),t)}{[E(y_0(t),t)^2 - \Lambda_{a,c}]^{1/2}}\right\} \tag{25}$$

The potential is then determined by spatial integration of the field from $y_0(t)$ to y (eq 2). The result is

$$V(y,t) - V_m = -\frac{2\epsilon_{a,c}}{r_{a,c}\,f}\ln\left\{\frac{\sinh\Big\{\mu_{a,c}(t) + \frac{1}{2}\epsilon_{a,c}r_{a,c}\,f[E(y_0(t),t)^2 - \Lambda_{a,c}]^{1/2}(y - y_0(t))\Big\}}{\sinh(\mu_{a,c}(t))}\right\} \tag{26}$$

The expression of $j_{a,c}(y,t)$ follows directly from relation 26 because eqs 6 and 7 can be rearranged in the form

$$j_{a,c}(y,t) = -\frac{ka\epsilon_{a,c}K^L}{2}\exp[\epsilon_{a,c}r_{a,c}\,f(V(y,t) - V_m)] \tag{27}$$

The bipolar current I_f equals the integral of the local anodic or cathodic current over the relevant surface area,[17,18] so that the analytical expression of the conductivity curve is given by

$$I_f(\Delta\varphi_s(t)) = lkaK^L\epsilon_{a,c} \times \int_{-\epsilon_{a,c}L_0/2}^{y_0(t)}\left\{\frac{\sinh(\mu_{a,c}(t))}{\sinh\Big\{\mu_{a,c}(t) + \frac{1}{2}\epsilon_{a,c}r_{a,c}\,f[E(y_0(t),t)^2 - \Lambda_{a,c}]^{1/2}(y - y_0(t))\Big\}}\right\}^2 dy \tag{28}$$

To explicitly calculate the potential, field and local current profiles as well as the overall faradaic current, the two parameters $E(y_0,t)$ and $y_0(t)$ remain to be determined as a function of the known input variables. The two additional equations required are provided by the boundary conditions on $\Delta\varphi_s(t)$ and on $y_0(t)$, i.e., eqs 16 and 17/18, respectively.

Equation 26 can be combined with eq 16 to yield

$$\Delta\varphi_s(t) = \frac{2}{r_c\,f}\ln\left\{\frac{\sinh(\mu_c(t))}{\sinh\Big\{\mu_c(t) - \frac{1}{2}r_c\,f[E(y_0(t),t)^2 - \Lambda_c]^{1/2}\Big(\frac{L_0}{2} + y_0(t)\Big)\Big\}}\right\} + \frac{2}{r_a\,f}\ln\left\{\frac{\sinh(\mu_a(t))}{\sinh\Big\{\mu_a(t) - \frac{1}{2}r_a\,f[E(y_0(t),t)^2 - \Lambda_a]^{1/2}\Big(\frac{L_0}{2} - y_0(t)\Big)\Big\}}\right\} \tag{29}$$

and using eq 18, eq 24 can be formulated as

$$\frac{\coth(\mu_c(t))}{\coth(\mu_a(t))} = \frac{\coth\Big\{\mu_c(t) - \frac{1}{2}r_c\,f[E(y_0(t),t)^2 - \Lambda_c]^{1/2}\Big(\frac{L_0}{2} + y_0(t)\Big)\Big\}}{\coth\Big\{\mu_a(t) - \frac{1}{2}r_a\,f[E(y_0(t),t)^2 - \Lambda_a]^{1/2}\Big(\frac{L_0}{2} - y_0(t)\Big)\Big\}} \tag{30}$$

Numeric resolution of the nonlinear system composed of eqs 29 and 30 provides, for different times t, and hence different $\Delta\varphi_s(t)$, the parameters $E(y_0(t),t)$ and $y_0(t)$.

For the cases where, even at high $\Delta\varphi_s$, $E(y_0(t),t)^2 < \Lambda_{a,c}$, the potential and field distributions are given by

$$E(y,t) = [\Lambda_{a,c} - E(y_0(t),t)^2]^{1/2}\tan\Big\{\mu_{a,c}(t) - \frac{1}{2}\epsilon_{a,c}r_{a,c}\,f[\Lambda_{a,c} - E(y_0(t),t)^2]^{1/2}(y - y_0(t))\Big\} \tag{31}$$

$$V(y,t) - V_m = -\frac{2\epsilon_{a,c}}{r_{a,c}\,f}\ln\left\{\frac{\sec(\mu_{a,c}(t))}{\sec\Big\{\mu_{a,c}(t) - \frac{1}{2}\epsilon_{a,c}r_{a,c}\,f[\Lambda_{a,c} - E(y_0(t),t)^2]^{1/2}(y - y_0(t))\Big\}}\right\} \tag{32}$$

with

$$\mu_{a,c}(t) = \tan^{-1}\left\{\frac{E(y_0(t),t)}{[\Lambda_{a,c} - E(y_0(t),t)^2]^{1/2}}\right\} \tag{33}$$

The secant function is defined as $\sec(x) = 1/\cos(x)$, where x is any number. The expression for the bipolar current I_f follows as

$$I_f(\Delta\varphi_s) = lkaK^L\epsilon_{a,c} \times \int_{-\epsilon_{a,c}L_0/2}^{y_0(t)}\left\{\frac{\sec\Big\{\mu_{a,c}(t) - \frac{1}{2}\epsilon_{a,c}r_{a,c}\,f[\Lambda_{a,c} - E(y_0(t),t)^2]^{1/2}(y - y_0(t))\Big\}}{\sec(\mu_{a,c}(t))}\right\}^2 dy \tag{34}$$

Equations 29 and 30, enabling the determination of $E(y_0(t),t)$ and $y_0(t)$, become

$$\Delta\varphi_s(t) = \frac{2}{r_c\,f}\ln\left\{\frac{\sec\Big\{\mu_c(t) + \frac{1}{2}r_c\,f[\Lambda_c - E(y_0(t),t)^2]^{1/2}\Big(\frac{L_0}{2} + y_0(t)\Big)\Big\}}{\sec(\mu_c(t))}\right\} + \frac{2}{r_a\,f}\ln\left\{\frac{\sec\Big\{\mu_a(t) + \frac{1}{2}r_a\,f[\Lambda_a - E(y_0(t),t)^2]^{1/2}\Big(\frac{L_0}{2} - y_0(t)\Big)\Big\}}{\sec(\mu_a(t))}\right\} \tag{35}$$

$$\frac{\tan(\mu_c(t))}{\tan(\mu_a(t))} = \frac{\tan\Big\{\mu_c(t) + \frac{1}{2}r_c\,f[\Lambda_c - E(y_0(t),t)^2]^{1/2}\Big(\frac{L_0}{2} + y_0(t)\Big)\Big\}}{\tan\Big\{\mu_a(t) + \frac{1}{2}r_a\,f[\Lambda_a - E(y_0(t),t)^2]^{1/2}\Big(\frac{L_0}{2} - y_0(t)\Big)\Big\}} \tag{36}$$

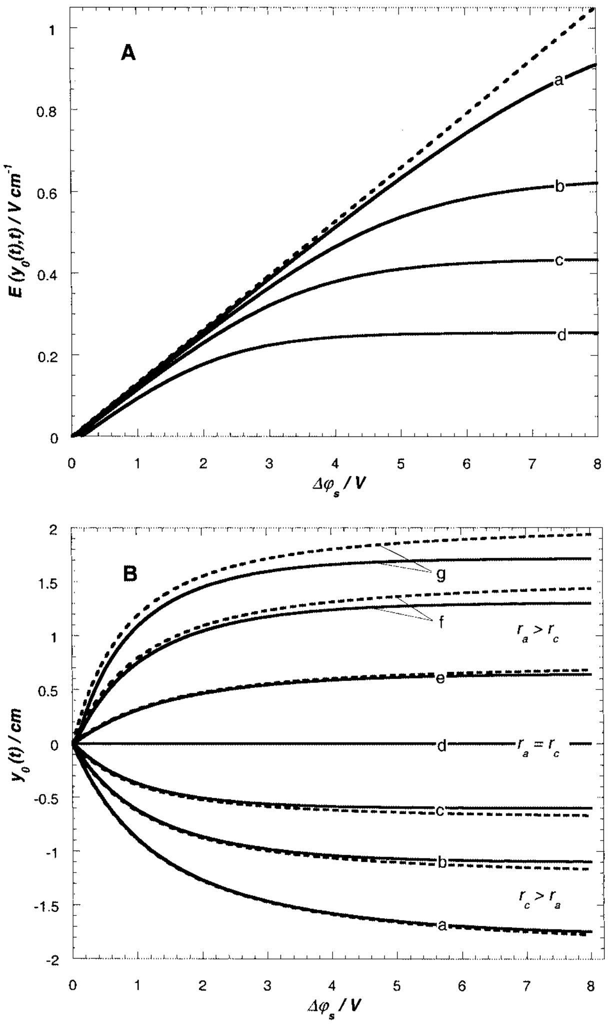

Figure 3. (A) Electric field $E(y_0(t),t)$ and (B) position $y_0(t)$ as a function of the total potential $\Delta\varphi_s$ applied across the thin-layer cell for different sets of kinetic parameters. The dashed lines result from the calculations of these quantities assuming a linear potential distribution (eq 4). Model parameters: $K^L = 10^{-1}\ \Omega^{-1}\ \mathrm{cm}^{-1}$, $a = 0.17$ mm, $V^0_a = 1.82$ V, $V^0_c = 0.55$ V, $j_{0_a} = 10^{-7}$ A cm^{-2}, $j_{0_c} = 3 \times 10^{-6}$ A cm^{-2}. Panel A: $r_c = 1.1 \times 10^{-1}$ and (a) $r_a = 3.5 \times 10^{-2}$, (b) $r_a = 5.5 \times 10^{-2}$, (c) $r_a = 7.5 \times 10^{-2}$, (d) $r_a = 1.1 \times 10^{-1}$. Panel B: curves a−d as in panel A; for the other curves, $r_c = 5 \times 10^{-2}$ and (e) $r_a = 7.5 \times 10^{-2}$, (f) $r_a = 1.2 \times 10^{-1}$, (g) $r_a = 1.7 \times 10^{-1}$.

For the intermediate situations where $\Lambda_c < E(y_0(t),t)^2 < \Lambda_a$ (or $\Lambda_a < E(y_0(t),t)^2 < \Lambda_c$) relevant for bipolar electrodic processes with a strong asymmetry between anodic and cathodic charge transfer, the calculation of the electric parameters is possible by a cross use of the analytical expressions derived in this section for the field and potential position dependences.

4.2. Results and Discussion. Depending on the sign of the quantity $E(y_0(t),t)^2 - \Lambda_{a,c}$, $E(y_0(t),t)$ and $y_0(t)$ were consistently computed using eqs 29 and 30, 35 and 36 (or intermediate) for a few sets of kinetic parameters r_a, r_c, j_{0_a}, and j_{0_c} at constant electrolyte conductivity K^L. Some results are given in Figure 3. The order of magnitude chosen for the kinetic parameters is in agreement with values typical for the bipolar process occurring at aluminum, i.e., reduction of water at the cathodic side and anodic dissolution of the metallic phase at the other.[18] The calculations are shown for $\Delta\varphi_s$ up to 8 V. The choice of such high potentials is motivated by the typical range of electric fields encountered in the context of superfast electrophoresis at conducting particles: for particles of diameter 400 μm, the superfast effect is generated for a total potential difference of about 10 V along a single microsphere electrode.[15] To ensure the balance between the total anodic and cathodic currents, the position $y_0(t)$ at which there is no net current shifts to the anodic (cathodic) side for $r_c < r_a$ ($r_a < r_c$). One easily infers from eqs 30 and 36 that, for a kinetically symmetric system ($r_c = r_a$), y_0 remains independent of the applied potential and equal to 0. Figure 4A and B shows the spatial distributions of the potential and the faradaic current, respectively, along the bipolar electrode surface for a given set of kinetic parameters and for different $\Delta\varphi_s$. The corresponding conductivity curve [$I_f(\Delta\varphi_s)$ plot] calculated by means of the equations derived in the previous section is shown in Figure 4C. The results are also compared with those obtained assuming a linear potential distribution, as detailed in ref 18. The field and potential profile deviate from those obtained using the linear approximation when the bipolar current becomes significant compared to the ohmic current. This is realized by enlarging the kinetic parameters at constant conductivity K^L and/or gradually increasing $\Delta\varphi_s$ (Figures 3 and 4). The linear approximation leads to overestimation of the potentials $V(y,t)$ and, hence, to overestimation of the overall bipolar current I_f. As expected, both analyses correctly show the minimum overpotential (here about 1.5 V) thermodynamically required for the simultaneous occurrence of the anodic and cathodic reactions at the two sides of the surface. Owing to the exponential nature of the bipolar faradaic processes, the magnitudes of the local faradaic currents j_a and j_c grow strongly toward the extremities of the surface. The field (potential)−current correlation, as expressed by eq 3, is therefore the most pronounced at these positions, which results in the typical nonlinear patterns for the field and potential. The inaccuracy of the linear approximation for describing the distribution of the electric parameters at positions situated around y_0 is explained by the deviations of the computed values of $E(y_0(t),t)$ from those estimated on the basis of a linear potential profile.

Using the analytical expressions developed in the previous section, the bipolar current was also calculated for the gold|KNO$_3$ solution interface at different electrolyte concentrations, c_s for which the condition $2\kappa^{-1} \ll a$ is always fulfilled. For the range of applied values of $\Delta\varphi_s$, the bipolar process at gold is carried by the reduction and oxidation of water.[17] The conductivity curves are reported in Figure 5. The results are essentially the same as those obtained for aluminum bipolar electrodes. The higher the conductivity (or c_s), the lower the faradaic contribution to the total current, and the better the merging between the analysis as presented in section 4.1. and the linear approximation based on eq 4. Equations 28 and 34 tend to underestimate the overall measured current at low K^L, whereas the experimental results can still be fitted by the linear analysis. This can be understood by considering that, for moderate potentials, the local currents due to oxidation of the gold surface[22] are not taken into account, even though they probably play a role in the overall bipolar process, especially when the bulk conductivity is low. This is manifested in the difficulty in accurately determining the kinetic parameters at low electrolyte concentration from the measured voltammograms (deviations from the theoretical Tafel plots). Despite this complication, the two types of analysis give an acceptable picture of the conductivity curves. Similar conclusions hold for the irreversible bipolar process observed at aluminum surfaces. The inadequacy of the linear approach is the more apparent at higher $\Delta\varphi_s$. In the particular case where the electrode processes exhibit quasi-reversible behavior, we recognize that

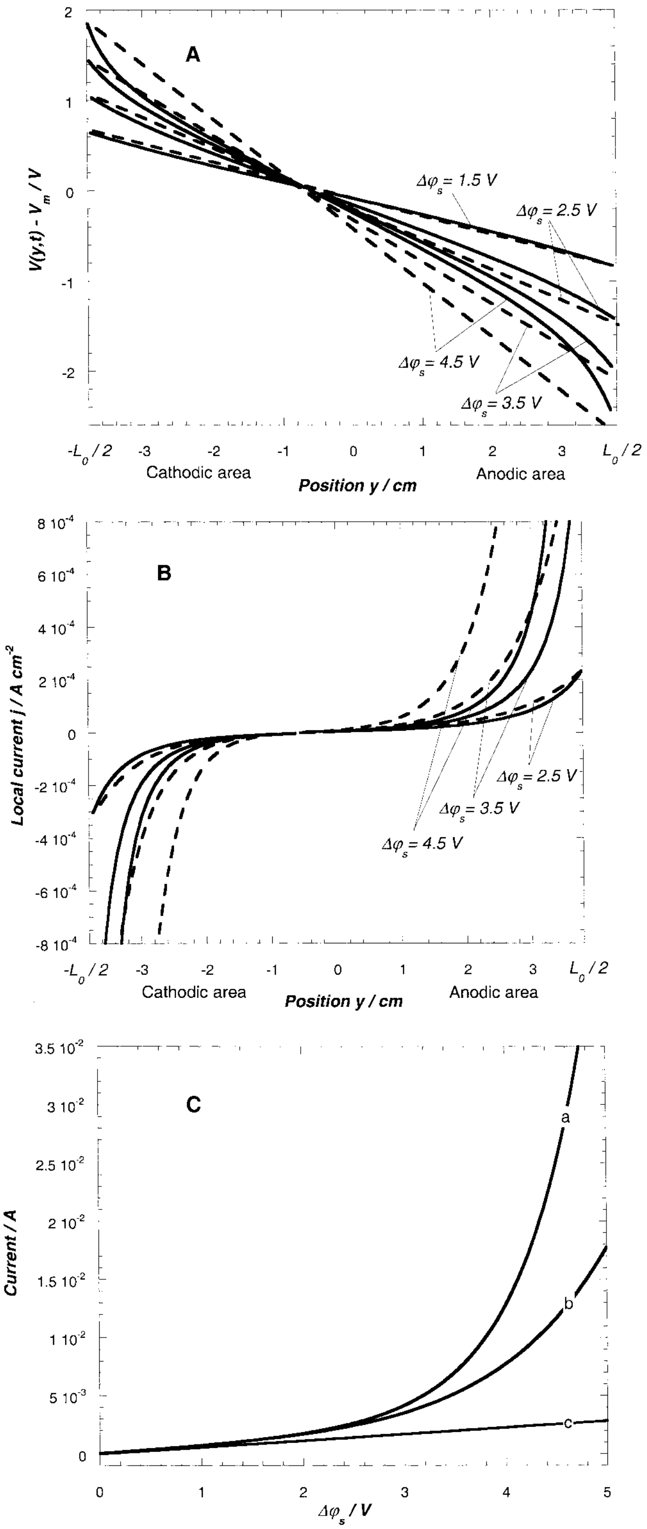

Figure 4. Spatial distributions of the (A) potential and (B) faradaic current at different $\Delta\varphi_s$, as specified in the figures. (C) Representation of the total current (ohmic + faradaic contributions) (a) assuming eq 4 and (b) calculated on the basis of eq 3. Curve c shows only the ohmic contribution to the total current. Model parameters: as in Figure 3 with $r_c = 1.1 \times 10^{-1}$ and $r_a = 7.5 \times 10^{-2}$.

the net current involves appreciable limitation from the finite rates of the forward and reverse charge-transfer processes, meaning that eqs 6 and 7 should be extended with the (smaller) cathodic and anodic terms, respectively. The results related to the potential and field profiles remain qualitatively the same as for the irreversible case.

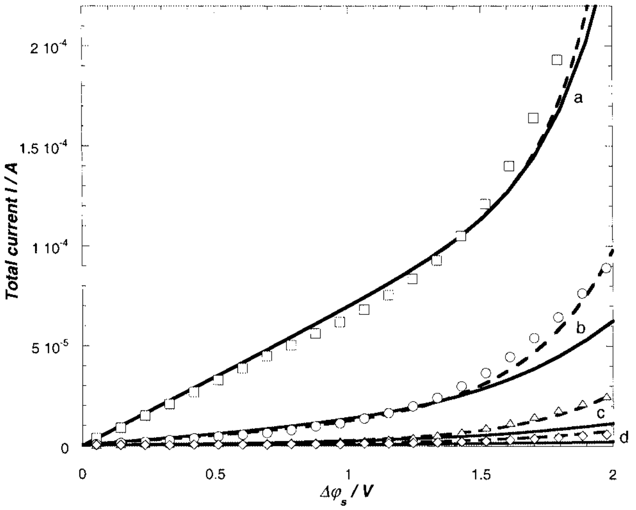

Figure 5. Experimental (points) and theoretical (solid lines) polarization plots for bipolar gold electrodes at different KNO$_3$ electrolyte concentrations, c_s. (a) $c_s = 10^{-1}$ M ($K^L = 11$ mΩ^{-1} cm^{-1}), (b) $c_s = 10^{-2}$ M ($K^L = 1.5$ mΩ^{-1} cm^{-1}), (c) $c_s = 10^{-3}$ M ($K^L = 160$ $\mu\Omega^{-1}$ cm^{-1}), (d) $c_s = 10^{-4}$ M ($K^L = 20$ $\mu\Omega^{-1}$ cm^{-1}). $a \approx 0.20$ mm. The potential was linearly scanned (0.03 V s^{-1}). The dashed lines refer to the theoretical treatment based on eq 4.

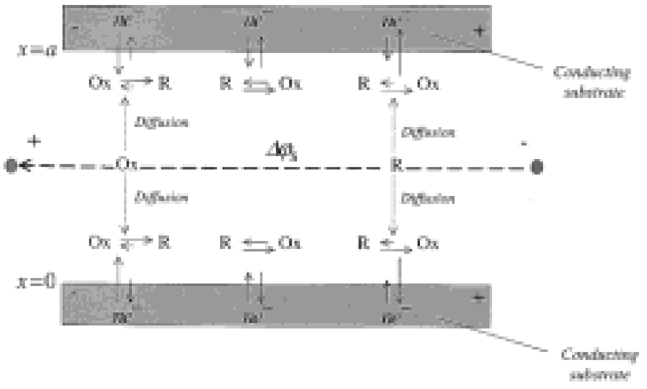

Figure 6. Schematic representation of the reversible bipolar process occurring in the thin-layer cell upon application of a potential drop $\Delta\varphi_s$ across the capillary. Diffusion of the redox components Ox (oxidized species) and R (reduced species) to/from the surfaces governs the faradaic processes.

5. Reversible Bipolar Redox Process

5.1. Expressions for the Local Faradaic Current and the Concentration Profile. If the bipolar current is carried via an electrochemically reversible reaction (fast electron transfer), the local currents along the bipolar surface (y dimension) are controlled by diffusion to/from the surface (x dimension) of the two electroactive species, now denoted as Ox for the oxidized form and R for the reduced form. The electrolyte solution is still assumed to contain an indifferent electrolyte in sufficient excess over the electroactive species. This ensures that diffusive mass transport prevails (migration of the redox species and its contribution to the ohmic current can therefore be neglected). In contrast to section 4, only one redox couple now generates the bipolar depolarization process. Figure 6 schematically depicts the situation typically encountered in the reversible case. Using the same definition for the electric potential as in the previous section (i.e., potentials in solution with respect to the metallic phase), the potential $V(y,t)$ is given by the Nernst relation

$$V(y,t) = V^0 - \frac{1}{nf}\ln\left[\frac{c_{\mathrm{Ox}}(x{=}0,y,t)}{c_{\mathrm{R}}(x{=}0,y,t)}\right] = V^0 - \frac{1}{nf}\ln\left[\frac{c_{\mathrm{Ox}}(x{=}a,y,t)}{c_{\mathrm{R}}(x{=}a,y,t)}\right] \quad (37)$$

where $c_{\mathrm{Ox}}(x,y,t)$ and $c_{\mathrm{R}}(x,y,t)$ stand for the concentrations of the oxidant Ox and reductant R at a given time t and position (x,y) and n is the number of electrons in the reaction Ox + ne$^-$ $\leftrightarrow$ R. V^0 is the negative of the standard potential of the redox couple Ox/R. The potential V^*, identified as the potential drop at the interface at $t = 0$ (before application of $\Delta\varphi_s$) does not depend on y and is related to the bulk concentrations c^*_{Ox}, c^*_{R}, and V^0 by

$$V^* = V^0 - \frac{1}{nf}\ln\left(\frac{c^*_{\mathrm{Ox}}}{c^*_{\mathrm{R}}}\right) \quad (38)$$

Calculation of the local current density $j(y,t)$ along the y axis at time t requires determination of the concentration profiles of the redox species within the capillary cell. Let us examine, e.g., the cathodic reaction and the profile of $c_{\mathrm{Ox}}(x,y,t)$. Considering that, typically, $L_0 \gg a$ and $l \gg a$, the concentration polarization of Ox in the y and z directions can be neglected. Consequently, the faradaic current is limited by the diffusion of the species in the x direction, and $c_{\mathrm{Ox}}(x,y,t)$ can be obtained by solving the diffusion equation

$$\frac{\partial c_{\mathrm{Ox}}(x,y,t)}{\partial t} = D_{\mathrm{Ox}}\frac{\partial^2 c_{\mathrm{Ox}}(x,y,t)}{\partial x^2} \quad (39)$$

where D_{Ox} (m^2 s^{-1}) is the diffusion coefficient of Ox. Resolution of eq 39 requires two spatial boundary conditions related to x (the system is spatially confined by the magnitude of the gap a) and one boundary condition related to the time. The latter is simply the initial condition

$$c_{\mathrm{Ox}}(x,y,0) = c^*_{\mathrm{Ox}} \quad (40)$$

which merely expresses the homogeneity of the solution at the start of the experiment. To define the spatial boundary conditions, we exploit the characteristic feature of reversible electrode reactions, that is, Nernstian equilibrium between the surface concentrations of the redox species and the potential $V(y,t)$. Assuming equal diffusion coefficients of Ox and R, i.e., $D_{\mathrm{Ox}} = D_{\mathrm{R}} = D$, the conservation of matter at the electrode surface $x = 0$ can be written as

$$c_{\mathrm{Ox}}(x{=}0,y,t) + c_{\mathrm{R}}(x{=}0,y,t) = c^*_{\mathrm{Ox}} + c^*_{\mathrm{R}} \quad (41)$$

and a similar expression holds at $x = a$. We note in passing that eq 41 is actually valid for every x because the total concentration of Ox and R at the boundaries is assumed to remain constant (protonation reactions of the redox species at the surfaces and/or in the bulk or other mechanisms likely to modify $c^*_{\mathrm{Ox}} + c^*_{\mathrm{R}}$ are not considered here). Combination of eqs 37 and 41 yields the two spatial boundary conditions

$$c_{\mathrm{Ox}}(0,y,t) = c_{\mathrm{Ox}}(a,y,t) = (c^*_{\mathrm{Ox}} + c^*_{\mathrm{R}})f_{\mathrm{Ox}}(y,t) \quad (42)$$

where the function f_{Ox} is defined by

$$f_{\mathrm{Ox}}(y,t) = \frac{\exp[-nf(V(y,t) - V^0)]}{1 + \exp[-nf(V(y,t) - V^0)]} \quad (43)$$

The symmetry of the problem requires an extremum in the concentration profile of Ox at $x = a/2$. The ensuing condition

$$\partial c_{\mathrm{Ox}}(x,y,t)/\partial x|_{x=a/2} = 0 \quad (44)$$

can be used in combination with eq 42 (at $x = 0$ or at $x = a$) and eq 40 in solving eq 39. The mathematical treatment of the set of eqs 39, 40, 42 and 43 substantially differs from that commonly applied within the semi-infinite planar diffusion approximation. In the present case, the notion of bulk concentration for the redox couple might vanish because of the small volume between the flat plates, and significant depletion might already occur (at $x = a/2$) for relatively short time t. The finite dimension of the capillary is taken into account in eq 42, which depends on one of the variables to be integrated (time t). To solve the problem, we use the Laplace transform with respect to the variable t. Using initial condition (40), eq 39 then becomes

$$s\bar{c}_{\mathrm{Ox}}(x,y,s) - c^*_{\mathrm{Ox}} = D\frac{\partial^2 \bar{c}_{\mathrm{Ox}}(x,y,s)}{\partial x^2} \quad (45)$$

where the super bar denotes the transformed variable. A solution of eq 45 is

$$\bar{c}_{\mathrm{Ox}}(x,y,s) = \frac{c^*_{\mathrm{Ox}}}{s} + A(y,s)\exp(x\sqrt{s/D}) + B(y,s)\exp(-x\sqrt{s/D}) \quad (46)$$

where $A(y,s)$ and $B(y,s)$ are functions that are independent of x. Combination of eq 46, applied to the positions $x = 0$ and $x = a$, and the Laplace transform of eq 43 provides $A(y,s)$ and $B(y,s)$

$$A(y,s) = B(y,s)\exp(-a\sqrt{s/D}) = \frac{(c^*_{\mathrm{Ox}} + c^*_{\mathrm{R}})\bar{f}_{\mathrm{Ox}}(y,s) - c^*_{\mathrm{Ox}}/s}{1 + \exp(a\sqrt{s/D})} \quad (47)$$

Equations 46 and 47 enable the explicit calculation of the local concentration gradients. For the two surfaces ($x = 0$ and $x = a$), we obtain

$$\frac{\partial \bar{c}_{\mathrm{Ox}}(x,y,s)}{\partial x}\Big|_{x=0} = -\frac{\partial \bar{c}_{\mathrm{Ox}}(x,y,s)}{\partial x}\Big|_{x=a} = \left[\frac{c^*_{\mathrm{Ox}}}{s} - (c^*_{\mathrm{Ox}} + c^*_{\mathrm{R}})\bar{f}_{\mathrm{Ox}}(y,s)\right]\sqrt{\frac{s}{D}}\tanh\left(\frac{a}{2}\sqrt{\frac{s}{D}}\right) \quad (48)$$

Dividing by s yields a form for which the inverse Laplace transform is known. Use of the convolution integral[23] and tabulated functions[24] then leads to, e.g., for the surface at $x = 0$

$$\int_0^t \frac{\partial c_{\mathrm{Ox}}(x,y,\tau)}{\partial x}\Big|_{x=0} \mathrm{d}\tau = \frac{4}{a}\int_0^t [c^*_{\mathrm{Ox}} - (c^*_{\mathrm{Ox}} + c^*_{\mathrm{R}})f_{\mathrm{Ox}}(y,\tau)]\left\{\sum_{n=1}^{\infty}\exp\left[-(2n-1)^2\pi^2\frac{D}{a^2}(t-\tau)\right]\right\}\mathrm{d}\tau \quad (49)$$

where τ is a dummy integration variable. Using the Leibniz theorem,[25] the concentration gradient at the surface $x = 0$ follows as

$$\frac{\partial c_{\mathrm{Ox}}(x,y,t)}{\partial x}\Big|_{x=0} = \frac{4}{a}\Bigg\{[c^*_{\mathrm{Ox}} - (c^*_{\mathrm{Ox}} + c^*_{\mathrm{R}})f_{\mathrm{Ox}}(y,0)]\Bigg\{\sum_{n=1}^{\infty} \exp\left[-(2n-1)^2\pi^2\frac{D}{a^2}t\right]\Bigg\} - (c^*_{\mathrm{Ox}} + c^*_{\mathrm{R}})\int_0^t \frac{\partial f_{\mathrm{Ox}}(y,t-\tau)}{\partial t} \Bigg\{\sum_{n=1}^{\infty} \exp\left[-(2n-1)^2\pi^2\frac{D}{a^2}\tau\right]\Bigg\}\,\mathrm{d}\tau\Bigg\} \quad (50)$$

Because we have assumed $D_{\mathrm{Ox}} = D_{\mathrm{R}}$, an expression comparable to eq 50 is obtained for the surface concentration gradient of species R.

The current density $j(y,t)$ for one bipolar electrode is related to the fluxes of Ox and R to/from the capillary surfaces by

$$j(y,t) = -nFD\left[\frac{\partial c_{\mathrm{Ox}}(x,y,t)}{\partial x}\right]_{x=0} = nFD\left[\frac{\partial c_{\mathrm{R}}(x,y,t)}{\partial x}\right]_{x=0} \quad (51)$$

where the sign convention of a negative reduction current is followed. Analytical expressions for the complete profiles of $c_{\mathrm{Ox}}(x,y,t)$ and $c_{\mathrm{R}}(x,y,t)$ can be obtained by following the route employed for solving analogous problems encountered within the context of heat conduction in solids.[26,27] A more straightforward procedure uses Laplace transformation of the concentration, eqs 46 and 47, in the form

$$\bar{c}_{\mathrm{Ox}}(x,y,s) = \frac{c^*_{\mathrm{Ox}}}{s} + \frac{1}{s}\left[s(c^*_{\mathrm{Ox}} + c^*_{\mathrm{R}})\bar{f}_{\mathrm{Ox}}(y,s) - \frac{c^*_{\mathrm{Ox}} + c^*_{\mathrm{R}}}{2} - \frac{c^*_{\mathrm{Ox}} - c^*_{\mathrm{R}}}{2}\right]\frac{\cosh[(x - a/2)\sqrt{s/D}]}{\cosh\left[\frac{a}{2}\sqrt{s/D}\right]} \quad (52)$$

By means of tabulated functions[25] and convolution integral,[24] the inverse transform of eq 52, and hence the concentration profile, is written as

$$c_{\mathrm{Ox}}(x,y,t) = c^*_{\mathrm{Ox}} + \int_0^t\Bigg\{\left[(c^*_{\mathrm{Ox}} + c^*_{\mathrm{R}})\,\frac{\partial f_{\mathrm{Ox}}(y,t-\tau)}{\partial t} - \frac{c^*_{\mathrm{Ox}} - c^*_{\mathrm{R}}}{2}\,\delta(t-\tau)\right] \times \left\{1 + \frac{4}{\pi}\sum_{n=1}^{\infty}\frac{(-1)^n}{2n-1}\exp\left[-(2n-1)^2\pi^2\frac{D}{a^2}\tau\right]\cos\left[(2n-1)\pi\left(\frac{x}{a} - \frac{1}{2}\right)\right]\right\}\Bigg\}\,\mathrm{d}\tau \quad (53)$$

where $\delta(t)$ is the Dirac function. A similar expression can be obtained for $c_{\mathrm{R}}(x,y,t)$.

5.2. Determination of the Field and Potential Distributions. Substitution of the current $j(y,t)$ as defined by eq 51 and eqs 43 and 50 into the differential eq 3 gives an (integro-)differential equation that must be solved to determine the profile of the field/potential across the capillary. In contrast to the irreversible case, which allowed analytical derivation, eq 3 now requires numerical treatment. In the following, we consider the integrodifferential equation written in terms of the potential $V(y,t)$. The methods employed for the discretization and resolution of the current problem are presented in the Appendix. The boundary equations are provided by eqs 16 and 18. With the coordinate system adopted within this section (Figure 1), the latter can also be written as

$$\frac{\partial V(y,t)}{\partial y}\Big|_{y=0} = \frac{\partial V(y,t)}{\partial y}\Big|_{y=L_0} \quad (54)$$

The equivalent of the mixed potential V_{m} for the irreversible case (see eq 12) is the Nernst potential V^* at which, by definition, $j = 0$ (eq 38). The potential−current coupling is subsumed in the function f_{Ox}, indicating that, at the surface, species Ox and R immediately adjust to the potential as dictated by the Nernst equation. For reversible reactions, neglect of double-layer effects is justified for cases where the thickness of the diffusion layer δ is large compared to the typical Debye length κ^{-1}, a condition that is always met in our experiments (sufficiently high salt concentrations).

5.3. Characteristic Features of the Conductivity Curves. Figure 7A and B shows typical curves for the spatial distributions of the faradaic current and potential, respectively, as calculated for different values of $\Delta\varphi_{\mathrm{s}}$ and for a given set of redox concentrations satisfying $c^*_{\mathrm{Ox}} = c^*_{\mathrm{Ox}} = c^*$. For such a symmetric system, the position y_0 is independent of the applied field and is halfway along the surface ($y_0 = L_0/2$). For asymmetric systems ($c^*_{\mathrm{Ox}} \neq c^*_{\mathrm{R}}$), we have $y_0 < L_0/2$ for $c^*_{\mathrm{R}} < c^*_{\mathrm{Ox}}$ and $y_0 > L_0/2$ for $c^*_{\mathrm{Ox}} < c^*_{\mathrm{R}}$ (Figure 8). This is the counterpart of the asymmetry illustrated for the irreversible bipolar process when $r_{\mathrm{c}} \neq r_{\mathrm{a}}$ (see Figure 3B). In contrast to the situation examined in section 4, deviation of the potential distribution from a linear profile is apparent even for very weak applied lateral fields. This is a consequence of the absence of an activation barrier for electron transfer at the interface. As soon as a field is applied, the local potential $V(y,t)$ deviates from the Nernst potential V^* so that a faradaic current starts to flow. To qualitatively explain the dependence of the local current density j on $\Delta\varphi_{\mathrm{s}}$, let us consider a particular position $y_{\mathrm{p}} > L_0/2$ along the electrode (see Figure 7). As the field is gradually increased, the current $j(y_{\mathrm{p}},t)$ first increases because of the increase of the local potential drop $V(y_{\mathrm{p}},t)$ across the interface and the ensuing increase of the flux to the surfaces of the electrodes (Figure 9). This is related to the decrease in the surface concentration of the reduced species (as fixed by eq 37) with respect to the “bulk” value. Simultaneously, depletion of the electroactive species starts (Figure 9), and a diffusion layer (thickness δ) develops for the ongoing reactions at the two surfaces. Bulk depletion typically becomes significant for $\delta(y_{\mathrm{p}},t) \geq a/2$. From a given time t, the concomitant development of the diffuse layers at the two surfaces and the continuous decrease of the surface concentration results in a decrease of the concentration gradient at $y = y_{\mathrm{p}}$, or stated otherwise, the current $j(y_{\mathrm{p}},t)$ passes through a maximum and then decreases to reach 0 in the limit $t \to \infty$ [$c_{\mathrm{R}}(x=a/2,y_{\mathrm{p}},\infty) = 0$].

The *transient nature* of the diffusion process that develops during a linear sweep voltammetry experiment performed at a monopolar electrode leads to a characteristic peak-shaped current−potential curve.[28] The projection of this peak along the bipolar electrode surface, as dictated by the *nonlinear spatial distribution* of the potential/field in the solution, results in the characteristic patterns shown in Figures 7A and 8. For relatively long times t, the potential distribution increasingly tends to linearity owing to the decrease of the faradaic current, as caused by substantial depletion of the electroactive species. The increase of $\Delta\varphi_{\mathrm{s}}$ (or time) at a given scan rate is accompanied by an accelerated compression of the projected voltammograms toward the position y_0 and by a decrease of the local peak currents resulting from depletion. The overall conductivity curves represent the *integration* of the anodic or cathodic current-space waves at varied $\Delta\varphi_{\mathrm{s}}$. As a result of this operation, the curves

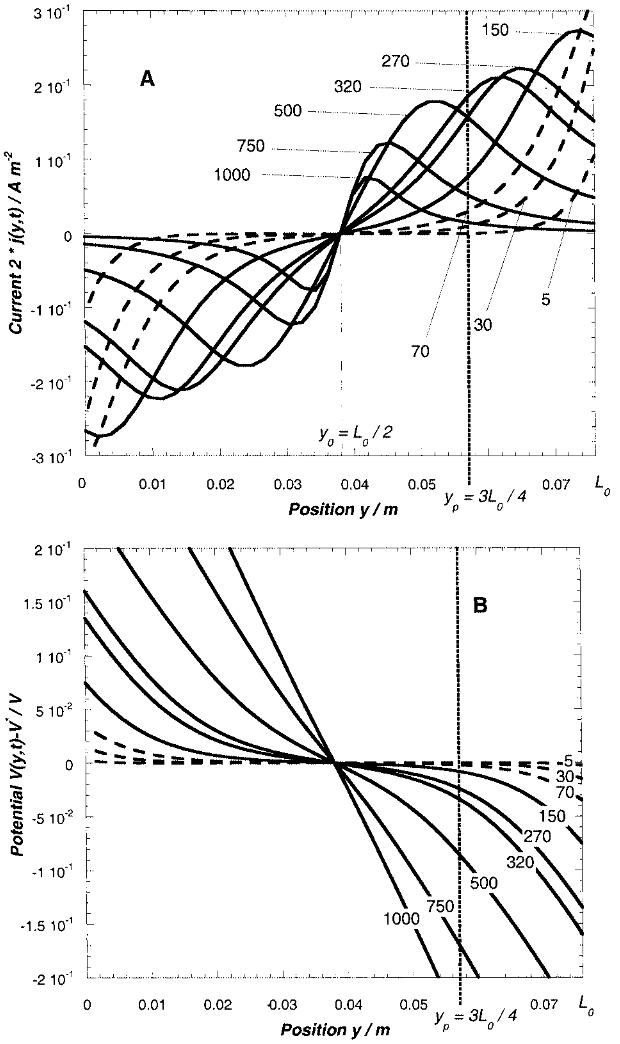

Figure 7. Spatial distribution of the (A) current and (B) potential at varied $\Delta\varphi_s$, as indicated (in mV) in the figures. Model parameters: $K^L = 3 \times 10^{-2}\ \Omega^{-1}\ \mathrm{cm}^{-1}$, $a = 0.20$ mm, $V^0 = -233$ mV, $\nu = 50\ \mathrm{mV\ s}^{-1}$, $D = 10^{-9}\ \mathrm{m}^2\ \mathrm{s}^{-1}$, $n = 1$, $c^* = 10^{-4}$ M. The dashed curves correspond to the potentials where (substantial) depletion of the electroactive species does not occur at any position along the electrode.

exhibit a maximum provided that sufficiently strong lateral fields are applied so as to induce noticeable transversal depletion of the redox species (Figure 10A). The higher the redox concentrations, the more delayed this phenomenon. This differs from monopolar voltammetry characteristics, which show depletion effects scaling with the bulk concentrations of Ox and R.[28] The fundamental difference between mono- and bipolar voltammetry becomes clear if the expression of the local current $j(y,t)$ as predicted from monopolar voltammetry theory is written explicitly with reversible species.[28] For a symmetric system

$$j(y,t) = nFc^*(\pi D\nu)^{1/2}\chi(V(y,t) - V^*) \qquad (55)$$

where χ is a function of position. For monopolar electrode polarization (the driving potential is perpendicular to the electrode surface), determination of χ was carried out both numerically and analytically.[29−33] Using eq 55 and the relation defining I_f, one obtains

$$I_f = 2nFlc^*(\pi D\nu)^{1/2}\int_{L_0/2}^{L_0}\chi(V(y,t) - V^*)\,dy \qquad (56)$$

Equation 56 indicates a linear relationship between I_f and c^*.

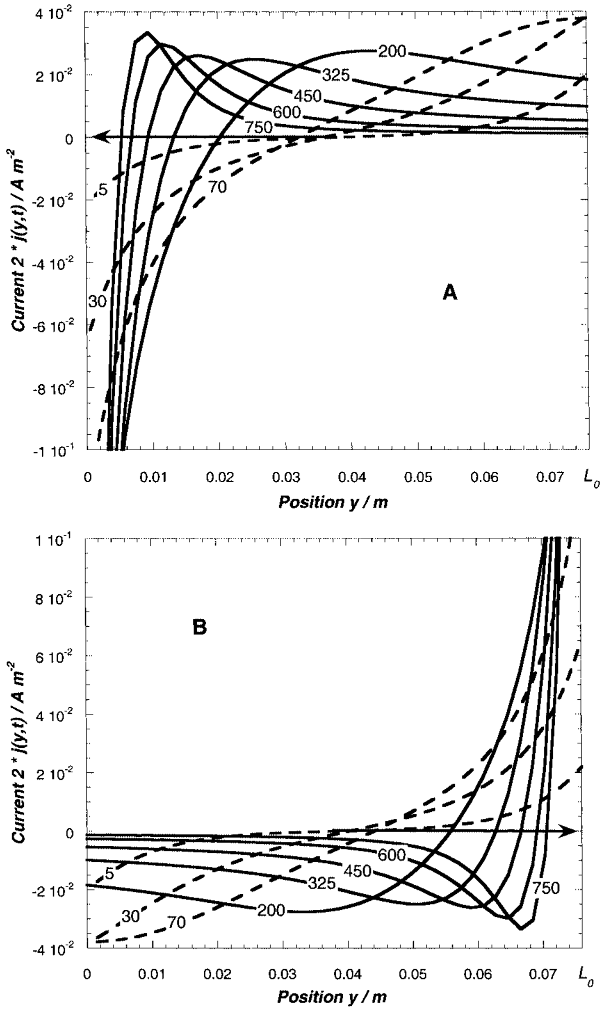

Figure 8. Projection along the bipolar electrode surface of the monopolar reversible waves for asymmetric redox systems at varied $\Delta\varphi_s$, as indicated (in mV) in the figure. Model parameters: as in Figure 7 except for the concentrations (A) $c^*_{\mathrm{Ox}} = 10^{-3}$ M and $c^*_{\mathrm{R}} = 10^{-5}$ M, (B) $c^*_{\mathrm{Ox}} = 10^{-5}$ M and $c^*_{\mathrm{R}} = 10^{-3}$ M. The dashed curves refer to the potentials for which substantial depletion of (A) the reduced species R and (B) the oxidized species Ox does not occur at any position along the electrode [$c_{\mathrm{Ox}}(a/2,y,t) \approx c^*_{\mathrm{Ox}}$]. The two systems lead to identical polarization plots. The arrows indicate the direction of shift of the position y_0 with time.

The absence of linearity in our case (Figure 10B) is explained by the dependence of the potential distribution on the bulk concentration as formulated by eqs 3, 50, and 51. The higher the value of c^*, the more significant the bipolar faradaic current I_f with respect to the ohmic current, and the stronger the nonlinear coupling between the potential profile, as subsumed in the function χ, and the local current or, equivalently, the redox concentrations. Consequently, the error in the results expected on the basis of eq 56 together with a linear potential profile increases as $\Delta\varphi_s$ is increased at constant concentration and/or as the concentrations are increased at fixed $\Delta\varphi_s$, as illustrated in Figure 10B (K^L is kept constant). Similar reasoning holds for the dependence on the parameters D and ν (Figures 11 and 12, respectively). For sufficiently high ν, semi-infinite diffusion applies because the length of the diffusion layer decreases with increasing ν, as the ratio $2\delta/a$ becomes very small in that case. No depletion at $x = a/2$ occurs before the concentration at the conducting surfaces has dropped to 0. Hence, one should complete eq 56 by making the dependence of χ explicit in y, c^*, D, ν, K^L, and a. At every y, this χ function must satisfy the

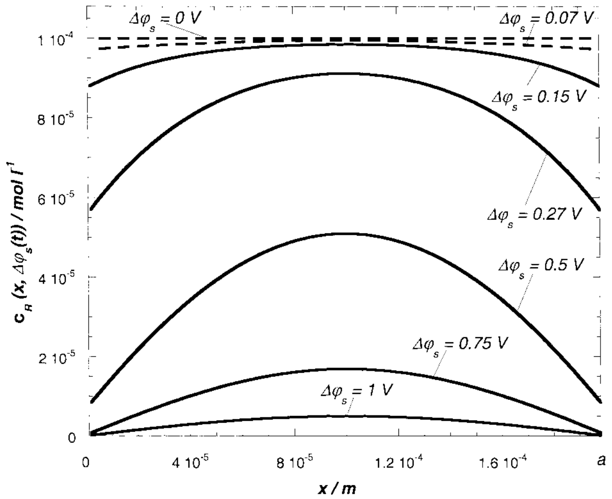

Figure 9. Concentration profile of the reduced species at the position $y = 3L_0/4$ and different applied potentials $\Delta\varphi_s$ (as mentioned in the figure). Model parameters as in Figure 7.

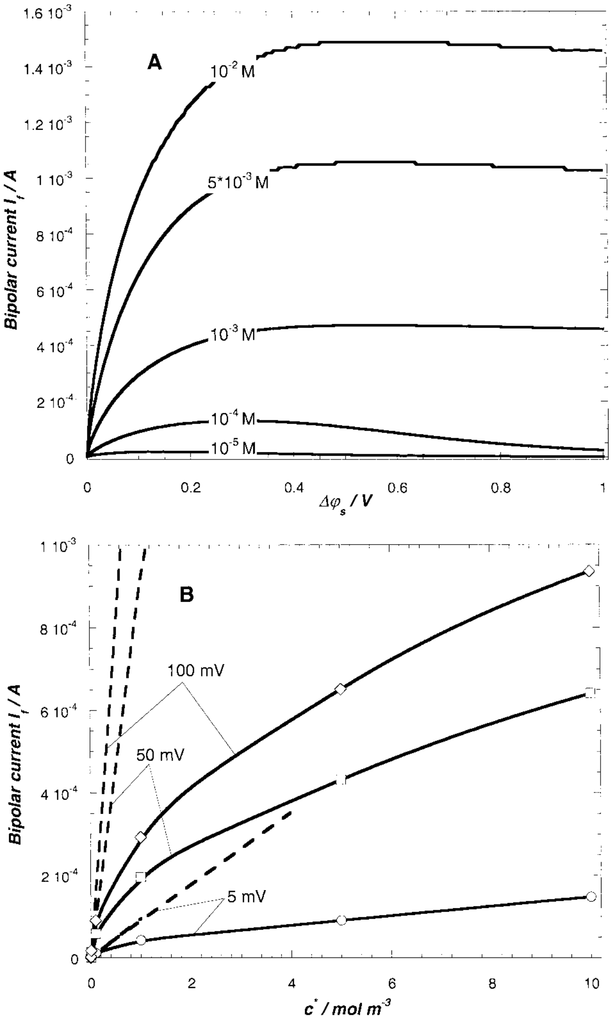

Figure 10. (A) Conductivity curves for different concentrations of the electroactive species c^* (symmetric redox system). c^* is specified in the figure. The other model parameters are the same as in Figure 7. (B) Deviation from the linear predictions (dashed lines) as yielded by eqs 4−56 at three different values of $\Delta\varphi_s$. The solid lines are only guides to the eye.

condition $\chi(V(y,t) - V^*) \leq \chi((y_0 - y)\Delta\varphi_s/L_0)$ because the linear field assumption systematically overestimates the local current and I_f. The extent of depletion depends on the thickness a between the electrodes. The higher a at given Ox and R concentrations, the higher the bipolar current I_f (because of higher local concentration gradients at the surface), and the higher the potential at which depletion appears, as illustrated in Figure 13 (a similar comment holds for Figure 12). For sufficiently high a and/or sufficiently low $\Delta\varphi_s$, the semi-infinite condition (which ascertains that regions sufficiently far from the electrode surfaces remain quasi-unperturbed by the ongoing experiment) is met, and I_f becomes independent of a.

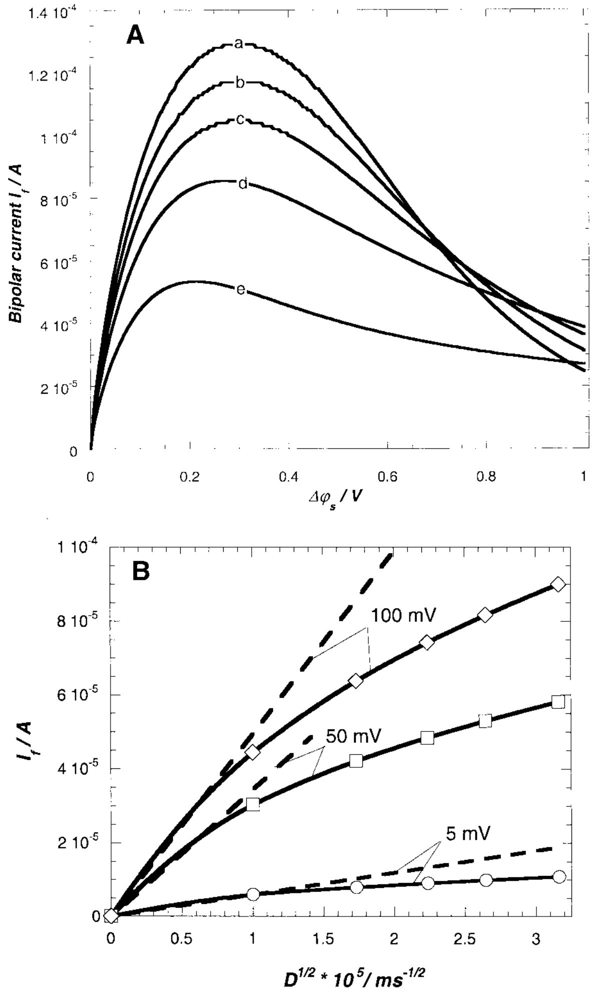

Figure 11. (A) Conductivity curves for different diffusion coefficients D (symmetric redox system). (a) $D = 10^{-9}$ m^2 s^{-1}, (b) $D = 7 \times 10^{-10}$ m^2 s^{-1}, (c) $D = 5 \times 10^{-10}$ m^2 s^{-1}, $D = 3 \times 10^{-10}$ m^2 s^{-1}, (e) $D = 1 \times 10^{-10}$ m^2 s^{-1}. The other model parameters are the same as in Figure 7. (B) Deviation from the linear predictions (dashed lines) as yielded by eqs 4−56 at three different values of $\Delta\varphi_s$. The solid curves are only guides to the eye.

In a previous study,[17] we demonstrated by (monopolar) cyclic voltammetry and electrochemical analysis performed on a gold rotating disk electrode (RDE) that the redox couple $Fe(CN)_6^{3-}$/$Fe(CN)_6^{4-}$ presents Nernstian behavior on gold, that is, the electron transfer is limited purely by diffusion to/from the surface. As such, this system enables validation of the theory presented in section 5. In Figure 14, we present a set of conductivity curves obtained for different redox concentrations and excess KNO_3 electrolyte. The results are in reasonable agreement with theoretical expectation. The difference between the experimental curves obtained for 10^{-3} Fe(III)/10^{-4} Fe(II) and 10^{-4} Fe(III)/10^{-3} Fe(II) is accounted for by a slight increase in the measured conductivity of the solution K^L (due to the difference in valency between the oxidized and reduced species).

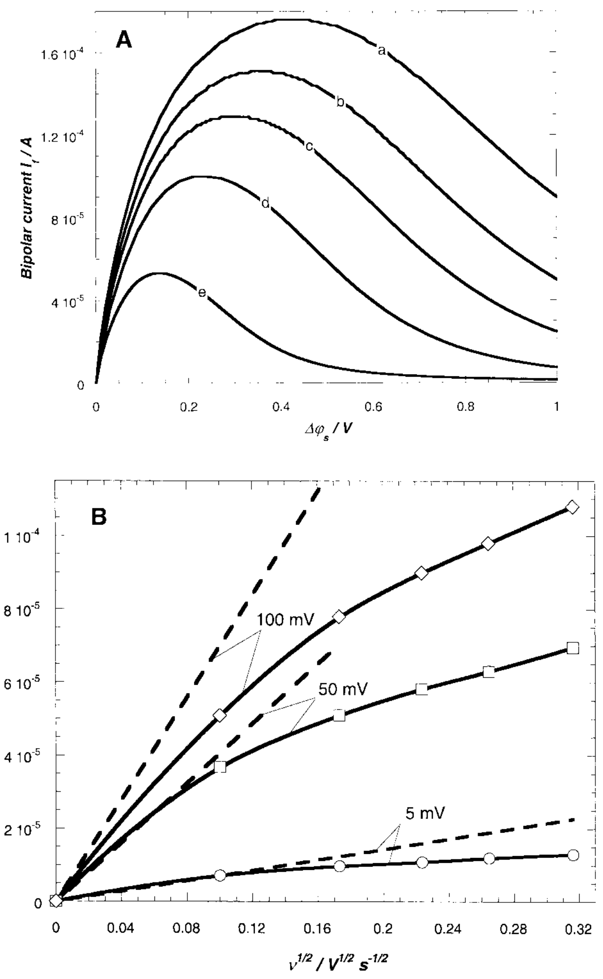

Figure 12. (A) Conductivity curves at different scan rates ν. (a) $\nu = 100$ mV s^{-1}, (b) $\nu = 70$ mV s^{-1}, (c) $\nu = 50$ mV s^{-1}, (d) $\nu = 30$ mV s^{-1}, (e) $\nu = 10$ mV s^{-1}. The other model parameters are the same as in Figure 7. (B) Deviation from the linear predictions (dashed lines) as yielded by eqs 4−56 at three different values of $\Delta\varphi_s$. The solid curves are only guides to the eye.

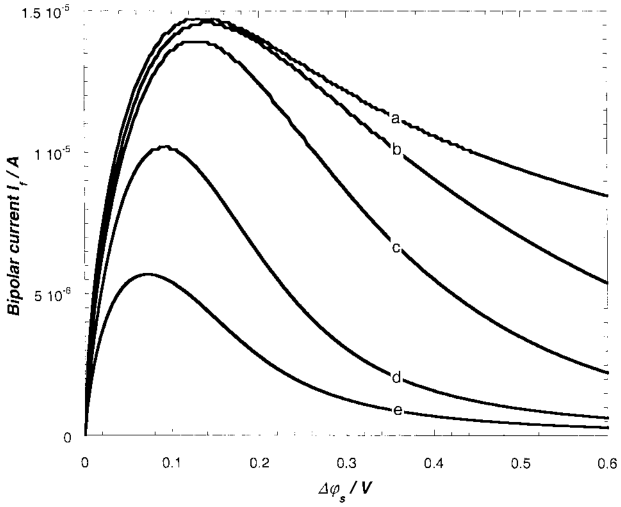

Figure 13. Conductivity curves at different a. (a) $a \geq 600$ μm (semi-infinite diffusion situation reached), (b) $a = 300$ μm, (c) $a = 200$ μm, (d) $a = 100$ μm, (e) $a = 50$ μm. The other model parameters are the same as in Figure 7.

This results in a decrease of the coupling field/current and therefore in an increase of I_f for the system of higher K^L. The trends expected from variation of the scan rate for given redox concentrations (see Figure 12) are also confirmed by experimental findings.

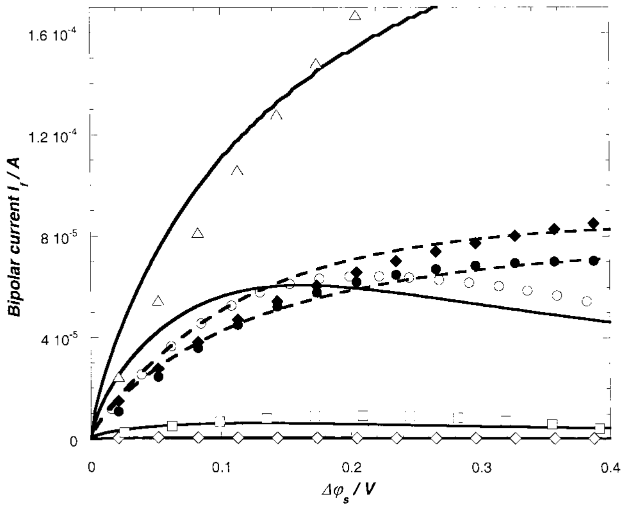

Figure 14. Comparison between experimental (points) and theoretical (curves) conductivity plots for different sets of electroactive concentrations. $V^0 = -233$ mV, $n = 1$, $D = 1.85 \times 10^{-10}$ m^2 s^{-1} [values derived from the rotating disk electrode (RDE) results[17]], $a \approx 0.20$ mm, $\nu = 30$ mV s^{-1}. Meanings of the symbols (1 M KNO_3): (◇) $c^* = 10^{-6}$ M ($K^L = 77$ mΩ^{-1} cm^{-1}), (□) $c^* = 10^{-5}$ M ($K^L = 78$ mΩ^{-1} cm^{-1}), (○) $c^* = 10^{-4}$ M ($K^L = 79$ mΩ^{-1} cm^{-1}); (0.1 M KNO_3) (△) $c^* = 10^{-3}$ M ($K^L = 12.9$ mΩ^{-1} cm^{-1}), (●) $c^*_{Ox} = 10^{-3}$ M and $c^*_R = 10^{-4}$ M ($K^L = 12.3$ mΩ^{-1} cm^{-1}), (♦) $c^*_{Ox} = 10^{-4}$ M and $c^*_R = 10^{-3}$ M ($K^L = 12.5$ mΩ^{-1} cm^{-1}). The theoretical dashed lines refer to the asymmetric redox systems.

6. Conclusions

We have presented a theoretical study for describing the faradaic depolarization effects that occur in a thin-layer cell of the type employed for electrokinetic analysis. A set of analytical equations governing the field distribution and the dependence of the bipolar current on the applied lateral potential difference is developed for the case where the current is carried by slow cathodic and anodic reactions (irreversible case). The case of a reversible bipolar process is also treated in detail. Mass transfer by diffusion of the electroactive species to/from the electrode surfaces is taken into account. Estimation of the ensuing bipolar current requires numerical computation of the intrinsic coupling between the profile of the field, as externally applied in the solution, and the spatial distribution of the faradaic current, in turn related to the local concentration profile of the redox species. The typical characteristics of the overall conductivity curves are described. Theoretical predictions are confirmed by experiments performed on gold electrodes with the electroactive couple $Fe(CN)_6^{3-}/Fe(CN)_6^{4-}$. In particular, transient effects due to development of diffusion layers, depletion of the electroactive species, and nonlinearity between the bipolar current and redox concentrations are well predicted.

The merging between experimental and theoretical results in the framework of the situation where the bipolar current is induced by an externally applied lateral field is promising for the interpretation of streaming potential data obtained on gold in the presence of electroactive compounds.[17] The quantitative interpretation of these electrokinetic results requires a rigorous analysis of the faradaic conduction phenomenon resulting from the interplay between the diffusion process, the field/current coupling, and the convection situation, as determined by hydrodynamic flow applied tangentially to the conducting surfaces. It allows for an appreciation of the dependence of the electrokinetic potential on the total potential drop across the metal|solution interface, which can be electrochemically manipulated by the redox species in the solution. Although this type of investigation has become common in interfacial studies by atomic force microscopy, where the potential of the metallic phase is varied via an external electric circuit,[34−37] it has not yet been envisaged in the field of electrokinetics. The concepts elaborated in this paper are also useful for the quantitative interpretation of faradaic depolarization processes occurring in electrophoretic experiments performed on metallic particles. Rigorous analysis of the so-called superfast electrophoresis of such colloidal particles at low electrolyte concentration is needed. For these systems, the mass-transport-controlled space-charge formation (which is at the origin of the effect) resulting from the bipolar electrolysis requires theoretical analysis.

Acknowledgment. Dr. Josep Galceran and Dr. Jaume Puy from the Department of Chemistry at the University of Lleida (Spain) are acknowledged for their useful advice concerning section 5 of this paper.

Appendix

Descretization of the Reversible Charge-Transfer Problem (Eqs 3, 50, and 51 in the Text). The local faradaic current density (eqs 50 and 51) is written for two bipolar electrodes as

$$2j(y,t) = -\frac{8nFD}{a}\Bigg\{[c^*_{\mathrm{Ox}} - (c^*_{\mathrm{Ox}} + c^*_{\mathrm{R}})f_{\mathrm{Ox}}(y,0)]\sum_{n=1}^{\infty} \exp\left[-(2n-1)^2\pi^2\frac{D}{a^2}t\right] - (c^*_{\mathrm{Ox}} + c^*_{\mathrm{R}})\int_0^t \frac{\partial f_{\mathrm{Ox}}(y,t-\tau)}{\partial t}\left\{\sum_{n=1}^{\infty} \exp\left[-(2n-1)^2\pi^2\frac{D}{a^2}\tau\right]\right\} \mathrm{d}\tau\Bigg\} \quad \text{(A1)}$$

Discretization of the local current density with respect to time was performed by linear piecewise interpolation of the function f_{Ox}. Using the uniform convergence of the integral expression in eq A1, we obtain

$$2j(y,t_N) = -\frac{8nFD}{a}\Bigg\{[c^*_{\mathrm{Ox}} - (c^*_{\mathrm{Ox}} + c^*_{\mathrm{R}})f_{\mathrm{Ox}}(y,0)]\sum_{n=1}^{\infty} \exp\left[-(2n-1)^2\pi^2\frac{D}{a^2}t_N\right] - (c^*_{\mathrm{Ox}} + c^*_{\mathrm{R}})\sum_{k=1}^{N}\frac{f_{\mathrm{Ox}}(y,t_{N-k+1}) - f_{\mathrm{Ox}}(y,t_{N-k})}{h}\sum_{n=1}^{\infty}\int_{t_{k-1}}^{t_k} \exp\left[-(2n-1)^2\pi^2\frac{D}{a^2}\tau\right] \mathrm{d}\tau\Bigg\} \quad \text{(A2)}$$

where $t_k = kh$, k is an integer satisfying $k \in [1, N]$, and h is the time step. After some rearrangement, one obtains

$$2j(y,t_N) = -\frac{8nFD}{a}\Bigg\{(c^*_{\mathrm{Ox}} + c^*_{\mathrm{R}})\frac{\alpha(N,h)}{h} f_{\mathrm{Ox}}(y,0) + [c^*_{\mathrm{Ox}} - (c^*_{\mathrm{Ox}} + c^*_{\mathrm{R}})f_{\mathrm{Ox}}(y,0)]\beta(N,h) + \frac{1}{h}(c^*_{\mathrm{Ox}} + c^*_{\mathrm{R}})\sum_{j=1}^{N-1}[\alpha(N-j,h) - \alpha(N-j+1,h)]f_{\mathrm{Ox}}(y,t_j) - \frac{1}{h}(c^*_{\mathrm{Ox}} + c^*_{\mathrm{R}})\alpha(1,h)f_{\mathrm{Ox}}(y,t_N)\Bigg\} \quad \text{(A3)}$$

where α and β are the functions defined by

$$\alpha(k,h) = \sum_{n=1}^{\infty}\int_{t_{k-1}}^{t_k}\exp\left[-(2n-1)^2\pi^2\frac{D}{a^2}\tau\right]\mathrm{d}\tau \quad \text{(A4)}$$

$$\beta(k,h) = \sum_{n=1}^{\infty}\exp\left[-(2n-1)^2\pi^2\frac{D}{a^2}t_N\right] \quad \text{(A5)}$$

Performing the integration in eq A4, α is rewritten as

$$\alpha(k,h) = \frac{a^2}{D\pi^2}[\gamma(k-1,h) - \gamma(k,h)] \quad \text{(A6)}$$

with γ given by

$$\gamma(k,h) = \sum_{n=1}^{\infty}\frac{1}{(2n-1)^2}\exp[-(2n-1)^2\theta(k,h)] \quad \text{(A7)}$$

and

$$\theta(k,h) = \pi^2\frac{D}{a^2}kh \quad \text{(A8)}$$

For the estimations of $\gamma(k,h)$ [and hence $\alpha(k,h)$] and $\beta(k,h)$, we use the following inequalities as conditions for convergence

$$|\gamma(k,h) - \sum_{n=1}^{L}\frac{1}{(2n-1)^2}\exp[-(2n-1)^2\theta(k,h)]| \le \frac{\exp[-(2L-1)^2\theta(k,h)]}{(2L-1)^2}\,\frac{\exp[-8L\theta(k,h)]}{1-\exp[-8L\theta(k,h)]} \quad \text{(A9)}$$

$$|\beta(k,h) - \sum_{n=1}^{P}\exp[-(2n-1)^2\theta(k,h)]| \le \exp[-(2P-1)^2\theta(k,h)]\,\frac{\exp[-8P\theta(k,h)]}{1-\exp[-8P\theta(k,h)]} \quad \text{(A10)}$$

where L and P are integers satisfying A9 and A10, respectively, and up to which the summations in eqs A7 and A5 are carried out. At this point of the analysis, the discretization in the space dimension remains to be done. For that purpose, we write $y_i = i\Delta y$ ($y_i \in [0,L_0]$), with $i \in [1, M]$ and Δy the space step. For convenience, we define the following quantities

$$\mathrm{term}(i,N) = -\frac{8nFD}{a^2K^{\mathrm{L}}}\sigma(N,h,i)\Delta y^2 \quad \text{(A11)}$$

$$\sigma(N,h,i) = (c^*_{\mathrm{Ox}} + c^*_{\mathrm{R}})\frac{\alpha(N,h)}{h}f_{\mathrm{Ox}}(y_i,0) + [c^*_{\mathrm{Ox}} - (c^*_{\mathrm{Ox}} + c^*_{\mathrm{R}})f_{\mathrm{Ox}}(y_i,0)]\beta(N,h) + \frac{1}{h}(c^*_{\mathrm{Ox}} + c^*_{\mathrm{R}})\sum_{j=1}^{N-1}[\alpha(N-j,h) - \alpha(N-j+1,h)]f_{\mathrm{Ox}}(y_i,t_j) \quad \text{(A12)}$$

$$\mathscr{R} = \frac{8nFD}{a^2hK^{\mathrm{L}}}\alpha(1,h)\Delta y^2 \quad \text{(A13)}$$

Discretization of eq 3 (see text) in space leads to the following system of M nonlinear equations valid at every time t_N with the potentials at y_i as unknown variables

$$V(y_1,t_N) - V(y_M,t_N) - \Delta\varphi_{\mathrm{s}}(t_N) = 0 \quad \text{(A14)}$$

$$i \in [2, M-1]: \quad V(y_{i+1},t_N) - 2V(y_i,t_N) + V(y_{i-1},t_N) + \mathscr{R}(c^*_{\mathrm{Ox}} + c^*_{\mathrm{R}})f_{\mathrm{Ox}}(y_i,t_N) + \mathrm{term}(i,N) = 0 \tag{A15}$$

$$V(y_1,t_N) - V(y_2,t_N) - V(y_{M-1},t_N) + V(y_M,t_N) = 0 \tag{A16}$$

with the relation giving $f_{\mathrm{Ox}}(y_i,t_N)$ as a function of the potential $V(y_i,t_N)$ (eq 43 in the text)

$$i \in [2, M]: \; f_{\mathrm{Ox}}(y_i,t_N) - \frac{\exp[-nf(V(y_i,t_N) - V^0)]}{1 + \exp[-nf(V(y_i,t_N) - V^0)]} = 0 \tag{A17}$$

Equations A14 and A16 are derived from the boundary conditions associated with eq 3, that is, eqs 16−18 and 54. From the definition of the potential V^* (eq 38), one can write the particular relation $V(y_i,0) = V^*$, so that $f_{\mathrm{Ox}}(y_i,0)$ is known. Subsequently, by iterating N from 1 to a chosen value $N_{\max}$ (depending on the potential range desired), resolution of the system A14−A17 enables determination of the potentials $V(y_i,t_N)_{i\in[1,M],N\in[1,N_{\max}]}$ and consequently of the currents $j(y_i,t_N)_{i\in[1,M],N\in[1,N_{\max}]}$ (eq A3). The ensuing bipolar current at a given N [or $\Delta\varphi_{\mathrm{S}}(t_N)$] was then calculated by integrating the local faradaic currents by means of the trapeze method. The solutions of eqs A14−A17 were derived with a Newton−Raphson-type[38] numerical analysis.

References and Notes

(1) Hartland, M. A.; Spencer, A. J. M. *Trans. Inst. Chem. Eng*. **1963**, *41*, 328.

(2) Nadebaum, P. R.; Fahidy, T. Z. *Electrochim. Acta* **1975**, *20*, 715.

(3) King, C. J. H.; Lister, K.; Plimley, R. E. *Trans. Inst. Chem. Eng*. **1975**, *53*, 20.

(4) Goodridge, F.; King, C. J. H.; Wright, A. R. *Electrochim. Acta* **1977**, *22*, 347.

(5) Pletcher, D. *Industrial Electrochemistry*; Chapman and Hall Ltd.: London, 1982; p 162.

(6) Fleischmann, M.; Ghoroghchian, J.; Rolinson, D.; Pons, S. *J. Phys. Chem.* **1986**, *90*, 6392 and the citations of unpublished results by Rolinson, D. R.; Nowak, R. J.; Pons, S.; Fleischmann, M.; Ghoroghchian, J. and Ghoroghchian, J.; Pons, S.; Fleischmann, M.

(7) Fleischmann, M.; Ghoroghchian, J.; Pons, S. *J. Phys. Chem.* **1985**, *89*, 5530.

(8) Wightman, R. M. *Anal. Chem.* **1981**, *53*, 1125A.

(9) Howell, J. O.; Wightman, R. M. *Anal. Chem.* **1984**, *56*, 524.

(10) Bindra, P.; Brown, A. P.; Fleischmann, M.; Pletcher, D. *J. Electroanal. Chem.* **1975**, *58*, 31.

(11) Bindra, P.; Brown, A. P.; Fleischmann, M.; Pletcher, D. *J. Electroanal. Chem.* **1975**, *58*, 39.

(12) Fleischmann, M.; Goodridge, F.; King, C. J. H. Br. Patent Application 16 765, 1974.

(13) Goodridge, F.; King, C. J. H.; Wright, A. B. *Electrochim. Acta* **1977**, *22*, 1087.

(14) Dukhin, S. S. *Adv. Colloid Interface Sci.* **1991**, *35*, 173.

(15) Baran, A. A.; Mishchuk, N. A.; Prieve, D. C. *J. Colloid Interface Sci.* **1998**, *207*, 240.

(16) Baran, A. A.; Babich, Y. A.; Tarovsky, A. A.; Mischuk, N. A. *Colloids Surf.* **1992**, *68*, 141.

(17) Duval, J.; Huijs, G. K.; Threels, W. F.; Lyklema, J.; van Leeuwen, H. P. *J. Colloid Interface Sci.* **2003**, *260*(1), 95.

(18) Duval, J.; Kleijn, J. M.; van Leeuwen, H. P. *J. Electroanal. Chem.* **2001**, *505*, 1.

(19) Bard, A. J.; Faulkner, L. R. *Electrochemical Methods, Fundamentals and Applications*; John Wiley and Sons: New York, 1980; p 103.

(20) Wagner, C.; Traud, W. *Z. Elektrochem.* **1938**, *44*, 391.

(21) Spiro, M. In *The Physical Chemistry of Solutions*; Fenby, D. V., Watson, I. D., Eds.; Massey University: Auckland, New Zealand, 1983.

(22) Schmid, G. M. in *Standard Potentials in Aqueous Solution*; Bard, A. J., Parsons, R., Jordan, J., Eds.; Marcel Dekker: New York, 1985; p 313.

(23) Bard, A. J.; Faulkner, L. R. *Electrochemical Methods, Fundamentals and Applications*; John Wiley and Sons: New York, 1980; p 661.

(24) Churchill, R. V. *Operational Mathematics*, 2nd ed.; McGraw-Hill: New York, 1958.

(25) Kaplan, W. in *Advanced Calculus*, 2nd ed.; Addison-Wesley: Reading, Mass., 1973.

(26) Carslaw, H. S.; Jaeger, J. C. *Conduction of Heat in Solids*, 2nd ed.; Clarendon Press: Oxford, U.K., 1959.

(27) Duhamel in *Mémoire sur la méthode générale relative au mouvement de la chaleur dans les corps solides plongés dans les milieux dont la température varie avec le temps*, cf. *J. Ec. Polytech. (Paris), Cah. 22* **1833**, *14*, 20.

(28) Bard, A. J.; Faulkner, L. R. *Electrochemical Methods, Fundamentals and Applications*; John Wiley and Sons: New York, 1980; Chapter 6, p 213.

(29) Sevcik, A. *Collect. Czech. Chem. Commun*. **1948**, *13*, 349.

(30) Nicholson, R. S.; Shain, I. *Anal. Chem.* **1964**, *36*, 706.

(31) Reinmuth, W. H. *J. Am. Chem. Soc.* **1957**, *79*, 6358.

(32) Matsuda, H.; Ayabe, Y. *Z. Elektrochem.* **1955**, *59*, 494.

(33) Gokhshtein, Y. P. *Dokl. Akad. Nauk SSSR* **1959**, *126*, 598.

(34) Barten, D.; Kleijn, J. M.; Duval, J.; van Leeuwen, H. P.; Lyklema, J.; Cohen Stuart, M. A. *Langmuir* **2003**, *19* (4), 1133.

(35) Raiteri, R.; Grattarola, M.; Butt, H. J. *J. Phys. Chem.* **1996**, *100*, 16700.

(36) Döppenschmidt, A.; Butt, H. J. *Colloids Surf. A: Physicochem. Eng. Aspects* **1999**, *149*, 145.

(37) Hu, K.; Fan, F. R. F.; Bard, A. J.; Hillier, A. C. *J. Phys. Chem. B* **1997**, *101*, 8298.

(38) Press, W. H.; Teukolsky, S. A.; Vetterling, W. T.; Flannery, B. P. in *Numerical Recipes in Fortran, The Art of Scientific Computing*, 2nd ed.; Cambridge University Press: New York, 1986.

Supporting Information

Another derivation of the expression for the y-profile of the concentration gradient (section 5.1)

The solution $c_{\mathrm{Ox}}(x,y,t)$ of the differential eq 39 coupled with the boundary conditions as given by eqs 40, 42-43 can be expressed as the sum of two functions $c_{\mathrm{Ox}}(x,y,t)_1$ and $c_{\mathrm{Ox}}(x,t)_2$

$$c_{\mathrm{Ox}}(x,y,t) \,|\, c_{\mathrm{Ox}}(x,y,t)_1 \; 2 \; c_{\mathrm{Ox}}(x,t)_2 \tag{S1}$$

, defined by

$$\frac{\in c_{\mathrm{Ox}}(x,y,t)_1}{\in t} \,|\, D\frac{\in^2 c_{\mathrm{Ox}}(x,y,t)_1}{\in^2 x} \tag{S2}$$

$$c_{\mathrm{Ox}}(x,y,0)_1 \,|\, 0 \quad \text{(S3)} \quad ; \quad c_{\mathrm{Ox}}(0,y,t)_1 \,|\, c_{\mathrm{Ox}}(a,y,t)_1 \,|\, \left(c^1_{\mathrm{Ox}} \; 2 \; c^1_{\mathrm{R}}\right) f_{\mathrm{Ox}}(y,t) \quad \text{(S4)}$$

and

$$\frac{\in c_{\mathrm{Ox}}(x,t)_2}{\in t} \,|\, D\frac{\in^2 c_{\mathrm{Ox}}(x,t)_2}{\in^2 x} \tag{S5}$$

$$c_{\mathrm{Ox}}(x,0)_2 \,|\, c^1_{\mathrm{Ox}} \quad \text{(S6)} \quad ; \quad c_{\mathrm{Ox}}(0,t)_2 \,|\, c_{\mathrm{Ox}}(a,t)_2 \,|\, 0 \quad \text{(S7)}$$

, respectively. Resolution of eqs S5-S7 in the Laplace domain provides a simple way to obtain $c_{\mathrm{Ox}}(x,t)_2$

$$c_{\mathrm{Ox}}(x,t)_2 = \frac{4c_{\mathrm{Ox}}^{*}}{\pi}\sum_{\mathrm{n}=1}^{\infty}\frac{1}{2\mathrm{n}-1}\sin\left[(2\mathrm{n}-1)\frac{\pi x}{a}\right]\exp\left[-(2\mathrm{n}-1)^2\pi^2\frac{D}{a^2}t\right] \tag{S8}$$

To solve S2-S4, we may use Duhamel's theorem[27] where the solution $c_{\mathrm{Ox}}(x,y,t)_1$ is derived from that of boundary conditions: zero-initial concentration and unit-surface concentration. Calling this latter function $c_{\mathrm{Ox}}(x,t)_3$, $c_{\mathrm{Ox}}(x,y,t)_1$ is then given by

$$c_{\mathrm{Ox}}(x,y,t)_1 = \left(c_{\mathrm{Ox}}^{*}+c_{\mathrm{R}}^{*}\right)\int_0^t f_{\mathrm{Ox}}(y,t)\frac{\partial c_{\mathrm{Ox}}(x,t-\vartheta)_3}{\partial t}\mathrm{d}\vartheta \tag{S9}$$

with ϑ a dummy integration variable over time $\vartheta\in[0,t[$ and $x\in]0,a[$, ranges for which $\partial c_{\mathrm{Ox}}(x,t-\vartheta)_3/\partial t \neq 0$ (see below), or equivalently $c_{\mathrm{Ox}}(x,y,t)_1 \neq 0$ conforming to the condition dictated by eq S4. An expression for $c_{\mathrm{Ox}}(x,t)_3$ is provided by a treatment similar to the one leading to eq S8

$$c_{\mathrm{Ox}}(x,t)_3 = 1-\frac{4}{\pi}\sum_{\mathrm{n}=1}^{\infty}\frac{1}{2\mathrm{n}-1}\sin\left[\frac{(2\mathrm{n}-1)\pi x}{a}\right]\exp\left[-(2\mathrm{n}-1)^2\pi^2\frac{D}{a^2}t\right] \tag{S10}$$

Combination of eqs S8-S10 yields

$$c_{\mathrm{Ox}}(x,y,t) = \frac{4c_{\mathrm{Ox}}^{*}}{\pi}\left\{\sum_{\mathrm{n}=1}^{\infty}\frac{1}{2\mathrm{n}-1}\sin\left[\frac{(2\mathrm{n}-1)\pi x}{a}\right]\exp\left[-(2\mathrm{n}-1)^2\pi^2\frac{D}{a^2}t\right]\right\}+$$

$$\frac{4D\pi}{a^2}\left(c_{\mathrm{Ox}}^{*}+c_{\mathrm{R}}^{*}\right)\int_0^t f_{\mathrm{Ox}}(y,\vartheta)\left\{\sum_{\mathrm{n}=1}^{\infty}(2\mathrm{n}-1)\sin\left[\frac{(2\mathrm{n}-1)\pi x}{a}\right]\exp\left[-(2\mathrm{n}-1)^2\pi^2\frac{D}{a^2}(t-\vartheta)\right]\right\}\mathrm{d}\vartheta \tag{S11}$$

The expression for $c_{\mathrm{R}}(x,y,t)$ is readily obtained from eq S11 after replacing c_{Ox}^{*} and $f_{\mathrm{Ox}}(y,\vartheta)$ by c_{R}^{*} and $f_{\mathrm{R}}(y,\vartheta)$, respectively. Starting from eq S11, the concentration gradient for the oxidized species at the surface is written

$$\left.\frac{\partial c_{\mathrm{Ox}}(x,y,t)}{\partial x}\right|_{x=0} = \frac{4c_{\mathrm{Ox}}^{*}}{a}\left\{\sum_{\mathrm{n}=1}^{\infty}\exp\left[-(2\mathrm{n}-1)^2\pi^2\frac{D}{a^2}t\right]\right\}+$$

$$\frac{4D\pi^2}{a^3}\left(c_{\mathrm{Ox}}^{*}+c_{\mathrm{R}}^{*}\right)\int_0^t f_{\mathrm{Ox}}(y,\vartheta)\left\{\sum_{\mathrm{n}=1}^{\infty}(2\mathrm{n}-1)^2\exp\left[-(2\mathrm{n}-1)^2\pi^2\frac{D}{a^2}(t-\vartheta)\right]\right\}\mathrm{d}\vartheta \tag{S12}$$

The second part of the r.h.s. in eq S12 can be rearranged by partial integration. The resulting expression for the surface concentration gradient is

$$\left.\frac{\partial c_{\mathrm{Ox}}(x,y,t)}{\partial x}\right|_{x=0} = \frac{4}{a}\left[c_{\mathrm{Ox}}^{*}-\left(c_{\mathrm{Ox}}^{*}+c_{\mathrm{R}}^{*}\right)f_{\mathrm{Ox}}(y,0)\right]\left\{\sum_{\mathrm{n}=1}^{\infty}\exp\left[-(2\mathrm{n}-1)^2\pi^2\frac{D}{a^2}t\right]\right\}-$$

$$\frac{4}{a}\left(c_{\mathrm{Ox}}^{*}+c_{\mathrm{R}}^{*}\right)\left[\int_0^t\frac{\partial f_{\mathrm{Ox}}(y,t-\vartheta)}{\partial t}\left\{\sum_{\mathrm{n}=1}^{\infty}\exp\left[-(2\mathrm{n}-1)^2\pi^2\frac{D}{a^2}\vartheta\right]\right\}\mathrm{d}\vartheta-\sum_{\mathrm{n}=1}^{\infty}f_{\mathrm{Ox}}(y,t)\right] \tag{S13}$$

Expression S13 is the same as the one provided by the analysis performed by means of the Laplace transformation (eq 50 in the text) except for the divergent term $\sum_{\mathrm{n}=1}^{\infty}f_{\mathrm{Ox}}(y,t)$. This latter must not be taken into account in the general expression of the current (or concentration) since it concerns the time $\vartheta = t$, where Duhamel's expression S9 is not defined. The same analysis holds for the concentration gradient at the surface of the reduced form R.

Rigorous Analysis of Reversible Faradaic Depolarization Processes in the Electrokinetics of the Metal / Electrolyte Solution Interface[1]

J. F. L. Duval, H. P. van Leeuwen
Department of Physical Chemistry and Colloid Science, Wageningen University,
Dreijenplein 6, 6703 HB Wageningen, The Netherlands.
J. Cecilia
Departament de Matematica, Universitat de Lleida, Rovira Roure 177, 25198 Lleida, Spain.
J. Galceran
Departament de Quimica, ETSEA, Universitat de Lleida, Rovira Roure 177, 25198 Lleida, Spain.

Abstract.

The bipolar faradaic depolarization of the interface metal⁄solution is examined for the situation in which the transversal electron transfer is limited by mass transfer of the components of a reversible redox couple. Transversal diffusion of the electroactive species to and from the surface and lateral convective mass transport, resulting from a pressure gradient applied along the surface, are taken into account. The analysis first focuses on the case where the lateral electric field required for bipolar behavior is externally applied through the solution. Numerical analysis of the intrinsic non-linear coupling between the convective-diffusion equation and the Poisson equation for finite currents allows derivation of the spatial distribution of the potential and the concentration profiles of the electroactive species. The corresponding distribution of the local faradaic current density along the metallic surface and the ensuing overall bipolar current are obtained. Characteristics of the conductivity curves, bipolar current versus applied field, are given for different sets of electric and hydrodynamic parameters. Then, on the basis of these results, the analysis of bipolar faradaic depolarization process is extended to electrokinetic phenomena, in particular streaming potential.

---

[1] Published in *Journal of Physical Chemistry B* **2003**, *107 (28)*, 6782.

Reversible bipolar faradaic depolarization processes: theory

1. Introduction

Electrokinetic phenomena are characterized by tangential motion of liquid with respect to an adjacent charged surface. In electrophoresis, the relative motion between fluid and charged particles is caused by an externally applied electric field.[1,2] In streaming potential experiments, displacement of the mobile part of the diffuse charge, as induced by a lateral applied pressure gradient, generates a potential difference across the cell, the streaming potential.[3] These are examples of so-called electrokinetic phenomena of the first kind. The relationship between the driving force (electric field and pressure) and the resulting measured quantity (velocity and streaming potential, respectively) is linear and at low driving force described by the classical Helmholtz-Smoluchowski (H-S) equation,[4,5] valid for ρa_p }} 1, ρ being the reciprocal Debye length and a_p the particle radius. Theoretical expressions applicable to the case ρa_p {{ 1 also point out linearity.[6,7] Regardless of the complications brought about by possible surface conduction,[8] use of the H-S equation leads to a straightforward estimation of the electrokinetic potential.[9]

In electrokinetic phenomena of the second kind,[10] the linearity between the applied driving force and the measured electrokinetic quantity is lost. For instance, in very strong electric fields (10^2-10^3 V cm^{-1}), the electrophoretic velocities of metallic particles in aqueous electrolyte are reported to be one or two orders of magnitude *higher* than those predicted by the H-S equation.[11] On the other hand, streaming potentials for metals in the presence of electroactive (i.e. redox active) electrolyte are *lower* than the ones expected on the basis of the classical linear H-S equation.[12]

The common basis for the 'superfast' electrophoresis and the collapse of streaming potential for conducting materials is the occurrence of *bipolar faradaic depolarization*. When metallic particles dispersed in an aqueous medium are subjected to sufficiently strong electric fields, the spatial distribution of the potential difference between metal and solution allows bipolar electrolysis of water: at one side of the particle, water reduction generates an anionic cloud, and at the other, water oxidation yields a cationic cloud. As a result, different ionic concentration polarization zones (space charge regions) are electrochemically generated at the two sides of the particle. An additional process that may contribute to the formation of these space charge regions is the behavior of the counterions of the double layer under condition of high applied fields. As observed by means of preliminary Monte Carlo simulations (Lyklema, De Coninck, unpublished results), these ions have the tendency at high electric fields to leave the surface and its vicinity. The modification of the local field due to the induced space charges results in superfast electroosmosis and electrophoresis. Streaming potentials generated by metallic surfaces in electroactive electrolyte are diminished because of the extensive electronic conduction inherent with the bipolar electrolysis process taking place at the metal surface. If these faradaic processes are carried by an electrochemically reversible redox couple, even low streaming potentials (or low pressure gradients) suffice to induce significant bipolar depolarization.

To our knowledge, rigorous analysis of bipolar faradaic depolarization processes interfering with the electrokinetics of the metal/solution interface has not been tackled yet. Baran et al.[11] give a theoretical expression for the velocity of metallic particles in strong electric fields on the basis of the velocity estimated for ion exchanger particles, which may show superfast electrophoresis.[13] The analysis provided[11] basically relies on the assumption of a linear distribution for the potential tangential to the particle surface. The electrophoretic velocity, v_{ef}, is then obtained after replacing the zeta-potential in the classical H-S equation by the local potential drop across the region where the space charge exists. The result is of the form

$$v_{\mathrm{ef}} \; \nabla \left(2E_0 a_{\mathrm{p}} \; 4 \div \pi^{\mathrm{d}}\right)^2 \left(2\nu \, 4 \, 1\right) \tag{1}$$

where E_0 is the undisturbed externally applied field, $\div \pi^{\mathrm{d}}$ the overpotential required for water electrolysis, and ν a coefficient characterizing the fraction of the total potential drop that occurs on either side of the particle. Though eq 1 is reported to satisfactorily explain experimental data, it is based on the approximation of a linear potential distribution around the particle, which is inconsistent with the magnitude of the overall bipolar faradaic current for the typical range of fields applied through the particle. As demonstrated for bipolar planar surfaces[12,14] and bipolar spherical particles,[15,16] there is an intrinsic *non-linear* coupling between the distribution of the current at the particle surface and the spatial course of the electric field. The more significant the electronic bipolar conduction as compared to the bulk solution conduction is, the more the potential distribution deviates from linearity. Besides, no analysis of the mass transport (coupled convective diffusion and conduction) of the induced space charges is explicitly mentioned in ref. 11 and no connection is made with the bipolar electrochemical behavior of dispersions of spherical metallic particles.[17,18] A quantitative understanding of the electrokinetic properties of the metal/electrolyte solution interface under conditions leading to phenomena of the second kind necessarily requires a more advanced investigation of the corresponding bipolar faradaic processes.

In this paper, we propose a theoretical analysis for faradaic depolarization processes occurring at metallic surfaces in an electroactive electrolyte solution. Mass transport of the electroactive species, including transversal diffusion to/from the surface and lateral convection due to the tangential pressure gradient, is considered for the typical streaming potential conditions in which the lateral field is coupled to the applied pressure gradient. Estimation of the substrate bipolar conductance term for given lateral field and mass-transfer conditions allows (i) a quantitative interpretation of the experimentally observed non-linear relationship between streaming potential and applied pressure gradient, and (ii) an estimation of the zeta-potential of the metal/electroactive solution interface. Corresponding interpretation of experimental data for gold in the presence of the $\mathrm{Fe(CN)}_6^{34}$ / $\mathrm{Fe(CN)}_6^{44}$ redox couple illustrates the applicability of the streaming potential technique for probing double layer properties of metals in the presence of reversible redox systems.[19]

2. Mass-transfer limited bipolar faradaic process induced by an externally applied electric field

2.1. Description of the problem

Let us consider two parallel planar conducting surfaces placed in a thin-layer cell as depicted in Figure 1. The distance between the two metallic electrodes in the flat capillary cell is a, the length of the metallic surface L_0 and its width *l*. The electrolyte solution of bulk conductivity K^{L}, relative dielectric permittivity κ_{r} and (dynamic) viscosity ξ, contains a redox couple denoted as Ox / R which exhibits electrochemically reversible behavior for the particular conducting substrates considered. This means that no appreciable activation barrier is observed for the electron-transfer reaction at the metallic surfaces

$$\mathrm{Ox}\ 2\ n\mathrm{e}^4 \ \Diamond\ \ \mathrm{R} \tag{2}$$

where n is the number of electrons e^4 involved. A potential difference, $\div\pi_{\mathrm{s}}$, is applied to the solution in the thin-layer cell across its long side. As shown in Figure 1, the cell is connected to two reservoirs containing the electrolyte solution.[20] A pressure gradient, $\div P$, is applied, which forces the solution to flow from left to right through the thin-layer chamber between the two surfaces. For convenience, the Cartesian coordinate system (x, y, z) is defined such that the origin coincides with the position halfway the conducting surface placed at the bottom of the cell. In a previous analysis,[12] we demonstrated that, because of the absence of activation energy for the electron-transfer reactions (eq 2), anodic and cathodic electrochemical reactions concomitantly occur at the extremities of the two surfaces as soon as a finite $\div\pi_{\mathrm{s}}$ is effective. The two surfaces behave as bipolar electrodes. We arbitrarily locate the *positive* side of the field applied in the left part of the thin-layer chamber, where consequently the *cathodic* reaction takes place. In the following, it will be convenient to use the dimensionless spatial variables X, Y, Z defined as

$$X \,|\, \frac{2}{a}\left(x\,4\,\frac{a}{2}\right) \quad Y \,|\, \frac{1}{L_0}\left(y\,2\,\frac{L_0}{2}\right) \quad Z \,|\, \frac{2}{l}\left(z\,4\,\frac{l}{2}\right) \tag{3}$$

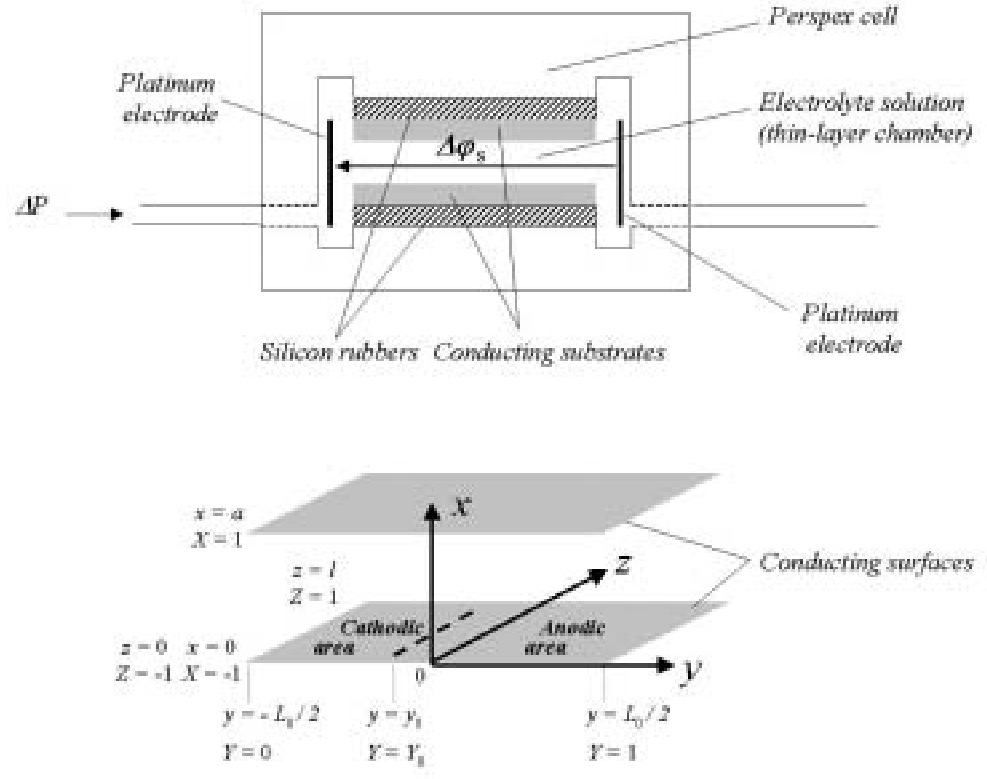
Perspex cell
Platinum electrode
Electrolyte solution (thin-layer chamber)
$\Delta\varphi_s$
ΔP
Platinum electrode
Silicon rubbers
Conducting substrates
x = a
X = 1
x
z = l
Z = 1
z
Conducting surfaces
z = 0 x = 0
Z = -1 X = -1
Cathodic area
Anodic area
0
y
y = - L₀/2
Y = 0
y = y₁
Y = Y₁
y = L₀/2
Y = 1

Figure 1. Schematic representation of the thin flat-layer cell. Notations. Typical dimensions of the cell: L_0 = 7.6 cm, l = 2.6 cm, a = 0.20 mm.

The solution is supposed to contain an excess of supporting electrolyte so that conductive transport of the electroactive compounds is not taken into account. Electron-transfer (eq 2) is then rate-limited by the diffusion to/from the surfaces of the electroactive species Ox and R and by the convective flow due to the imposed ΔP. To derive the overall bipolar current, denoted I_{f}, analysis of the hydrodynamic situation is first required. Then, the set of equations for the calculation of the concentration profile of Ox/R, the spatial distributions of the potential, and the local faradaic current density along the surfaces can be formulated.

2.2. Velocity profile

The direction of the bulk stream of flow is parallel to the surfaces (*y*-direction), and the steady-state velocity profile is represented by $v_Y(X,Z)$, as formulated by the pertaining Navier-Stokes equation

$$\frac{\partial^2 v_Y(X,Z)}{\partial X^2} + \lambda^2 \frac{\partial^2 v_Y(X,Z)}{\partial Z^2} = -\frac{a^2}{4\xi}\frac{\Delta P}{L_0} \tag{4}$$

with $\lambda \mid a/l$. For the pressure domain considered in this paper, the steady state assumption is always valid since the time $\acute{t}_{\mathrm{C}}$ required for the fluid to pass the distance L_0 ($\acute{t}_{\mathrm{C}} \mid L_0 / v_0$) is typically one or two orders of magnitude lower than the measurement time $\acute{t}_{\mathrm{M}}$ of streaming potential ($\acute{t}_{\mathrm{M}} -$20-30 s). At the walls of the parallelepipedic cell, we have the boundary conditions

$$v_Y(X \mid \partial 1, Z) \mid v_Y(X, Z \mid \partial 1) \mid 0 \tag{5}$$

Considering the typical range of applied pressures, the flow is assumed laminar as in agreement with $Re \{ 2500$, where Re is the Reynolds number. The general solution $v_Y(X,Z)$ of eqs 4-5 is written[21]

$$v_Y(X,Z) \mid v^0 \left\{ \left(1 4 X^2\right) 2 \frac{32}{\phi^3} \underset{\mathrm{m} \mid 1}{\leftarrow} \frac{(41)^{\mathrm{m}}}{(2\mathrm{m}\,4\,1)^3} \cos\left[(2\mathrm{m}\,4\,1)\frac{\phi}{2} X\right] \cosh\left[(2\mathrm{m}\,4\,1)\frac{\phi}{2}\frac{Z}{\lambda}\right] \mathrm{sech}\left[(2\mathrm{m}\,4\,1)\frac{\phi}{2}\frac{1}{\lambda}\right] \right\} \tag{6}$$

where v^0 is the characteristic velocity given by

$$v^0 \mid \frac{a^2}{8\xi}\frac{\div P}{L_0} \tag{7}$$

The first term within brackets in eq 6 represents the classical parabolic Poiseuille profile. The second term accounts for the contribution of the walls positioned at $Z \mid \pm 1$ (edge effects). As expected, the magnitude of this latter contribution is correlated to the geometrical factor λ. For intermediate to high λ, the summation term in eq 6 cannot be neglected with respect to the parabolic profile term, whereas for low λ, it is negligible. At a given *Y*, the velocity indeed virtually remains constant over most of the range of Z values: only within a short distance from the walls at $Z \mid \partial 1$, the velocity drops to zero. For the type of thin-layer cell discussed here (Figure 1), λ is not more than 0.01. Hence, in the following, we shall only consider the Poiseuille profile for an infinitely wide channel ($\phi \Downarrow 0$).

2.3. Coupling between the convective-diffusion equation and the Poisson equation

The concentration profiles of the electroactive species, denoted as $c_{\mathrm{Ox}}(X,Y)$ and $c_{\mathrm{R}}(X,Y)$ for the Ox and R species, respectively, are determined by the field and the characteristics of the diffusive and convective mass-transport processes. Symmetry of the problem with respect to the *Z*-dimension follows from the previous discussion and justifies that c_{Ox} and c_{R} are not functions of *Z*. Considering that typically $L_0 \}\} a$ and $l \}\} a$ ($\lambda \{\{ 1$), the concentration polarization of Ox and R in the *Y*- and the *Z*-directions may also be neglected. Transient effects will not be considered here, which is in agreement with $\vartheta_{\mathrm{D}} = \left(\iota^{2} / \phi D\right) \ll \vartheta_{\mathrm{M}}$, ϑ_{D} being the typical time required for building-up a diffusion layer of thickness ι and D the diffusion coefficient. Consequently, the local faradaic currents along the surfaces are limited by diffusion of the species in the *X*-direction and by convection in the *Y*-direction. By way of example, we examine the cathodic reaction and the profile for $c_{\mathrm{Ox}}(X,Y)$. We define the dimensionless concentration difference with respect to the bulk

$$C_{\mathrm{Ox}}(X,Y) = \frac{c_{\mathrm{Ox}}(X,Y) - c_{\mathrm{Ox}}^{\infty}}{c_{\mathrm{Ox}}^{\infty}} \tag{8}$$

where c_{Ox}^{∞} is the bulk concentration of species Ox, that is, the initial homogeneous concentration of Ox. Under the conditions outlined above and with the velocity profile as derived in the previous section, the Nernst-Planck equation reduces to the convective-diffusion equation,

$$v^{0}\left(1 - X^{2}\right)\frac{\partial C_{\mathrm{Ox}}(X,Y)}{\partial Y} = \frac{4D_{\mathrm{Ox}}L_{0}}{a^{2}}\frac{\partial^{2} C_{\mathrm{Ox}}(X,Y)}{\partial X^{2}} \tag{9}$$

where D_{Ox} is the diffusion coefficient of Ox. Resolution of eq 9 requires two boundary conditions with respect to *X* and one related to the *Y*-direction. This latter is simply written

$$C_{\mathrm{Ox}}(X,Y=0) = 0 \tag{10}$$

which expresses that, at the left side of the channel, electroactive species are injected from the reservoir with bulk concentrations c_{Ox}^{∞} and c_{R}^{∞}. The remaining conditions derive from the coupling of the equations expressing the mass balances for Ox and R and the reversible property of the redox couple. If we assume equal diffusion coefficients ($D_{\mathrm{Ox}} = D_{\mathrm{R}} = D$),

$$C_{\mathrm{Ox}}(X=\pm 1,Y) = \frac{c_{\mathrm{Ox}}^{\infty} + c_{\mathrm{R}}^{\infty}}{c_{\mathrm{Ox}}^{\infty}} f_{\mathrm{Ox}}(Y) - 1 \tag{11}$$

which is complementary to the profile $C_{\mathrm{R}}(X,Y)$. f_{Ox} is a function defined by the Nernst-type relationship

$$f_{\mathrm{Ox}}(Y) = \frac{\exp\left[-nf\left(V(Y) - V^{0}\right)\right]}{1 + \exp\left[-nf\left(V(Y) - V^{0}\right)\right]} \tag{12}$$

$V(Y)$ is the potential of the solution at the position *Y* with respect to the (equipotential) metallic surfaces, V^{0} is minus the standard potential of the redox couple Ox / R and *f* is the constant

$$f = \frac{F}{RT} \tag{13}$$

with F the Faraday, R the gas constant, and T the absolute temperature. Relation (12) expresses the equilibrium between the concentrations of the redox species at the surface and the potential $V(Y)$. For further detail, the reader is referred to ref. 14.

To find the profiles of Ox, the spatial course of the potential $V(Y)$ must be known. There is an intrinsic non-linear coupling between $C_{\mathrm{Ox}}(X,Y)$ and $V(Y)$, as subsumed in eqs 11-12. The equation defining $V(Y)$ is provided by the electroneutrality condition written for every *X-Z* slice along the surfaces. In the geometry considered here, the resulting Poisson equation for finite currents is written

$$\frac{aK^{\mathrm{L}}}{L_0{}^2}\frac{\mathrm{d}^2V(Y)}{\mathrm{d}Y^2}\,2\,2\,j(Y)\mid\ 0 \tag{14}$$

where $j(Y)$ is the local faradaic current density at the position Y defined by

$$j(Y)\mid\ \frac{2nFDc^{1}_{\mathrm{Ox}}}{a}\left[\frac{\in C_{\mathrm{Ox}}(X,Y)}{\in X}\right]_{X\mid\ 21}\mid\ 4\,\frac{2nFDc^{1}_{\mathrm{Ox}}}{a}\left[\frac{\in C_{\mathrm{Ox}}(X,Y)}{\in X}\right]_{X\mid\ 41} \tag{15}$$

The derivation of eq 14 is given in detail in ref. 14. Here, we shall only recall the approximations made and the conditions for which these are valid: that is, (i) the potential distribution related to the double layer formation at the two interfaces metal⁄solution is neglected, which is justified provided that the Debye length, ρ^{41}, is much smaller than the position-dependent diffusion layer thickness $\iota(Y)$ and the gap a between the two parallel surfaces; (ii) the electric field across the solution is assumed to be time-independent, and the hydrodynamic and the diffusion processes have reached steady-state conditions; (iii) the chemical composition of the solution remains essentially constant during the experiment (constant K^{L}), which is the case for indifferent ions in sufficient excess over the electroactive species (this also ensures the validity of ρ^{41} {{ $\iota(Y)$). The two boundary conditions related to eq 14 are provided by the potential balance in solution and the condition of no-charge accumulation in the conducting substrates[14]

$$V(Y\mid\ 0)\,4\,V(Y\mid\ 1)\mid\ \div\pi_{\mathrm{s}} \tag{16}$$

$$\left.\frac{\mathrm{d}V(Y)}{\mathrm{d}Y}\right|_{Y\mid\ 0}\mid\ \left.\frac{\mathrm{d}V(Y)}{\mathrm{d}Y}\right|_{Y\mid\ 1} \tag{17}$$

Determination of $C_{\mathrm{Ox}}(X,Y)$, $j(Y)$, and $V(Y)$ requires numerical resolution of the system of coupled eqs 9-12 and 14-17. Details of the computational procedure are reported in the Appendix. Once $j(Y)$ is known for given $\div\pi_{\mathrm{s}}$ and $\div P$, the corresponding overall bipolar current I_{f} is obtained by integration of the local current density $j(Y)$[12,14,22]

$$I_\mathrm{f} \mid 42lL_0 \int_0^{Y_0} j(Y)\mathrm{d}Y \mid 2lL_0 \int_{Y_0}^{1} j(Y)\mathrm{d}Y \tag{18}$$

where Y_0 is the position for which $j(Y \mid Y_0) \mid 0$. The corresponding potential difference between solution and metallic phase, $V(Y \mid Y_0)$, corresponds to the local equilibrium potential, V^1. Combining eqs 14 and 18, I_f may also be expressed as a function of the electric field at the position $Y \mid Y_0$ compared to the front or back edge of the cell ($Y \mid 0$ or $Y \mid 1$),

$$I_\mathrm{f} \mid \frac{alK^\mathrm{L}}{L_0}\left(\left.\frac{\mathrm{d}V(Y)}{\mathrm{d}Y}\right|_{Y \mid Y_0} 4 \left.\frac{\mathrm{d}V(Y)}{\mathrm{d}Y}\right|_{Y \mid 0} \right) \mid \frac{alK^\mathrm{L}}{L_0}\left(\left.\frac{\mathrm{d}V(Y)}{\mathrm{d}Y}\right|_{Y \mid Y_0} 4 \left.\frac{\mathrm{d}V(Y)}{\mathrm{d}Y}\right|_{Y \mid 1} \right) \tag{19}$$

2.4. Results and Discussion

Typical plots of the bipolar current I_f as a function of the lateral field $\div\pi_\mathrm{s}$ are shown in Figure 2 for different values of the applied pressure $\div P$. For low to intermediate $\div\pi_\mathrm{s}$, I_f increases steeply before leveling off. For low $\div P$ ($\Omega 50$ Pa), I_f asymptotically approaches a constant value with increasing $\div\pi_\mathrm{s}$. For larger $\div P$, this limit is reached for larger fields ($\div\pi_\mathrm{s}$ } 1 V, not shown). These characteristic features of the conductivity curves can be interpreted after examination of the concentration profiles upon variation of the hydrodynamic and electric parameters.

2.4.1. Analysis at given pressure gradient $\div P$ and different lateral fields $\div\pi_\mathrm{s}$

The profiles $c_\mathrm{Ox}(X,Y)$ are given in Figure 3 for $\div P \mid 0.5$ kPa and various $\div\pi_\mathrm{s}$. The corresponding spatial distributions of the current density $j(Y)$ and of the potential $V(Y)$ are given in Figure 4. At $\div\pi_\mathrm{s} \mid 0$, the potential drop $V(Y)$ at the interface metal/solution is, for every position Y along the surface, the Nernst potential V^N as defined by

$$V^\mathrm{N} \mid V^0 \, 4 \, \frac{1}{nf} \ln\left(\frac{c_\mathrm{Ox}^1}{c_\mathrm{R}^1} \right) \tag{20}$$

In this case, the local surface concentrations equal their bulk values (Figure 3A), and consequently, $j(Y)$ and I_f are zero. As soon as $\div\pi_\mathrm{s}$ is finite, bipolar conduction takes place in accordance with the slope $\mathrm{d}I_\mathrm{f} / \mathrm{d}(\div\pi_\mathrm{s})$ at $\div\pi_\mathrm{s} \mid 0$ (which is finite for a reversible redox couple). The equilibrium values of the local surface concentrations are dictated by the potential distribution $V(Y)$ (eqs 11-12). When gradually increasing $\div\pi_\mathrm{s}$, one increases the local $V(Y)$, so that the concentration differences, C_{Ox} and C_{R}, and the rates of the local mass transfer for Ox and R become larger in magnitude. Consequently, the surface concentration, i.e. $c_{\mathrm{Ox}}(X \mid \partial 1, Y)$,

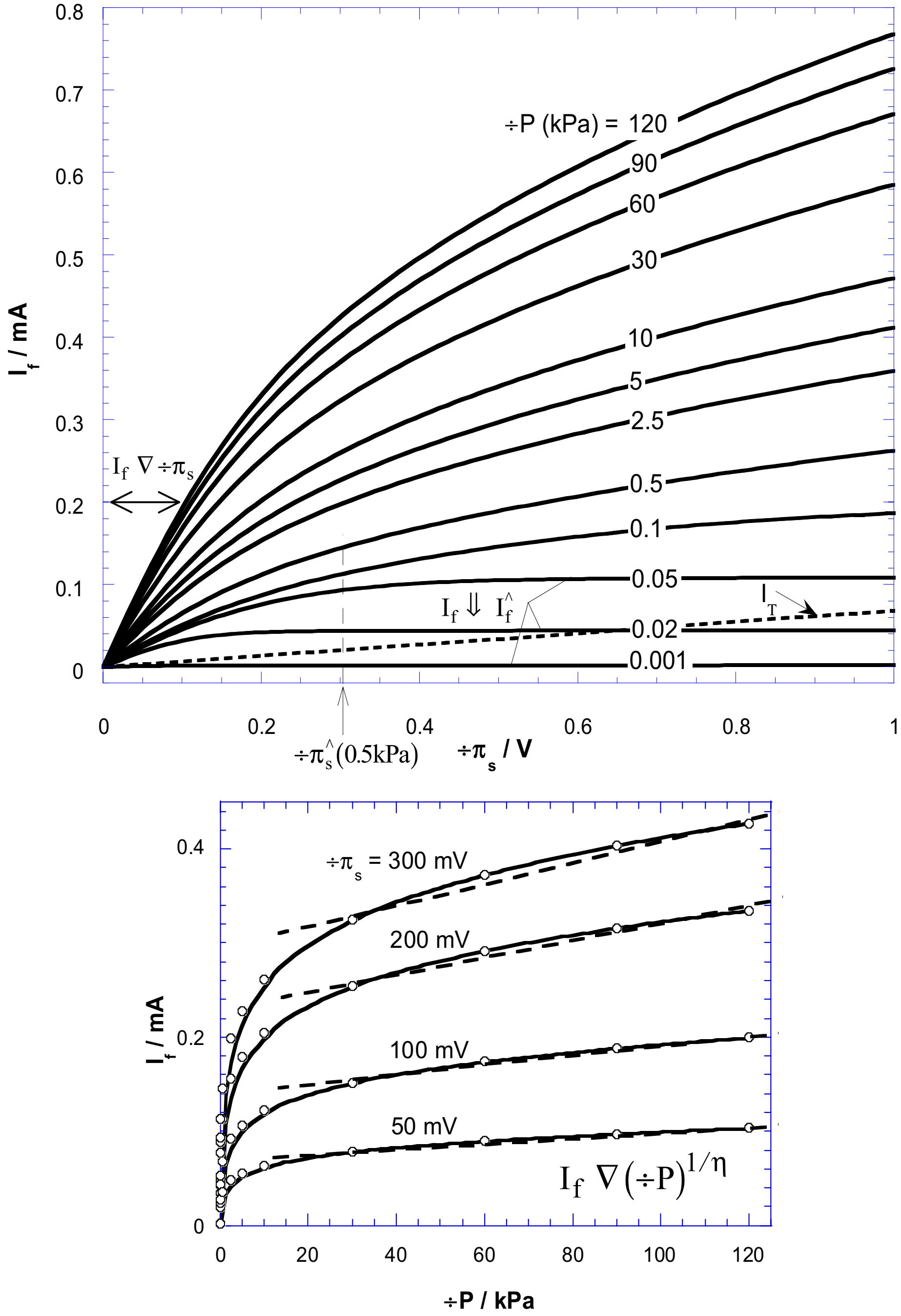

Figure 2. (Top) Bipolar current as a function of the applied lateral field (conductivity curves) at different $\div P$ (indicated in kPa). The ohmic current I_{T} is mentioned for comparison purposes. Model parameters are as follows: $a \mid 0.2$ mm, $L_0 \mid 7.6$ cm, $l \mid 2.6$ cm, $D \mid 10^{49}$ m^2 s^{-1}, $V^0 \mid 4233$ mV, $K^{\mathrm{L}} \mid 1$ T^{-1} m^{-1}, $c^1_{\mathrm{Ox}} \mid c^1_{\mathrm{R}} \mid 0.1$ mM (see section 2.4.1). (Bottom) I_{f} is set against $\div P$ for various $\div\pi_{\mathrm{s}}$ (points). The results are fitted with an expression of the form $(\div P)^{1/\eta}$ with $\eta - 5$ (solid curves). The dashed curves represent linear fits for high $\div P$ (see section 2.4.2).

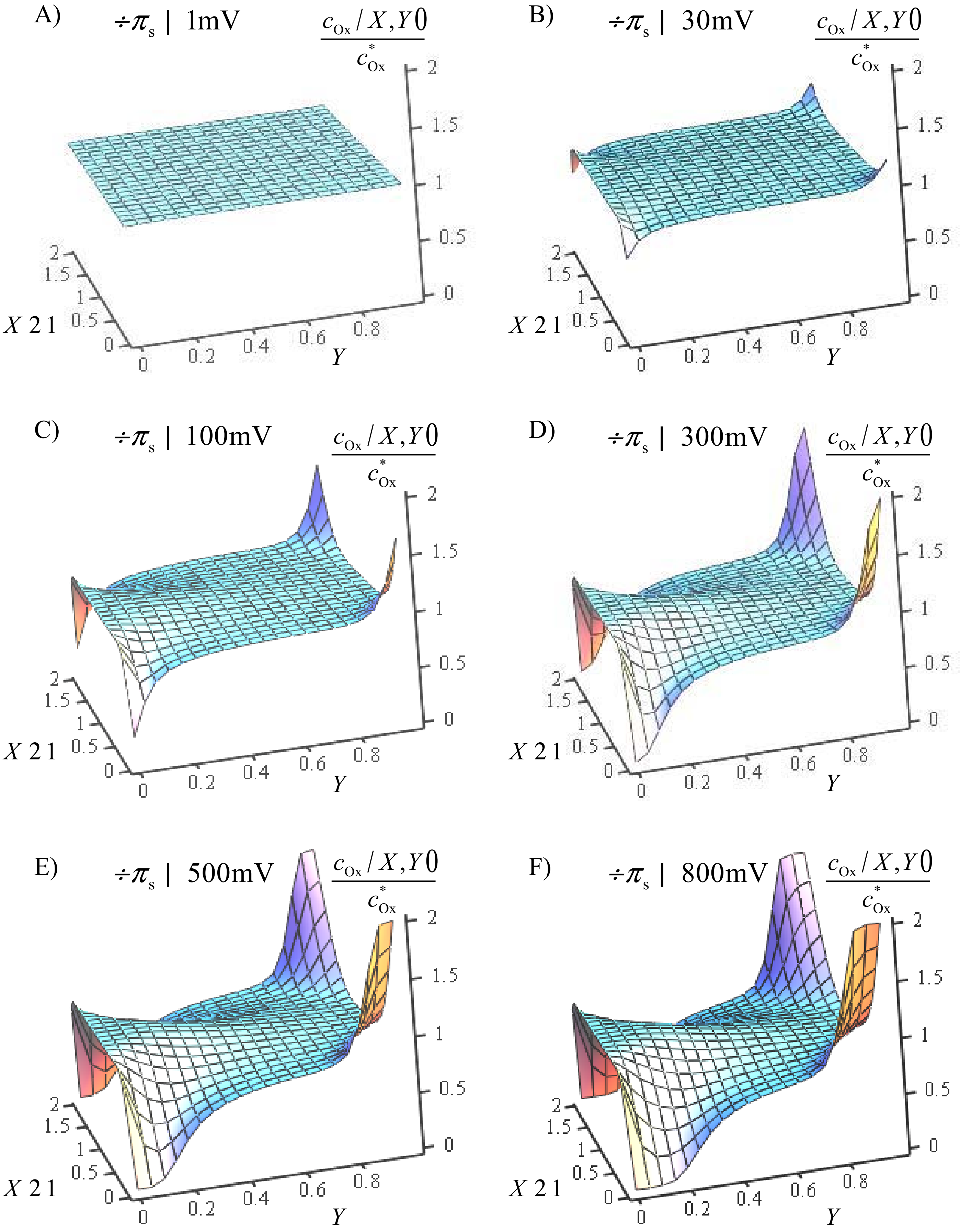
A)
÷π_s | 1mV
c_{Ox} / X, Y 0 / c^*_{Ox}
B)
÷π_s | 30mV
C)
÷π_s | 100mV
D)
÷π_s | 300mV
E)
÷π_s | 500mV
F)
÷π_s | 800mV
0
0.5
1
1.5
2
X 2 1
0
0.2
0.4
0.6
0.8
Y

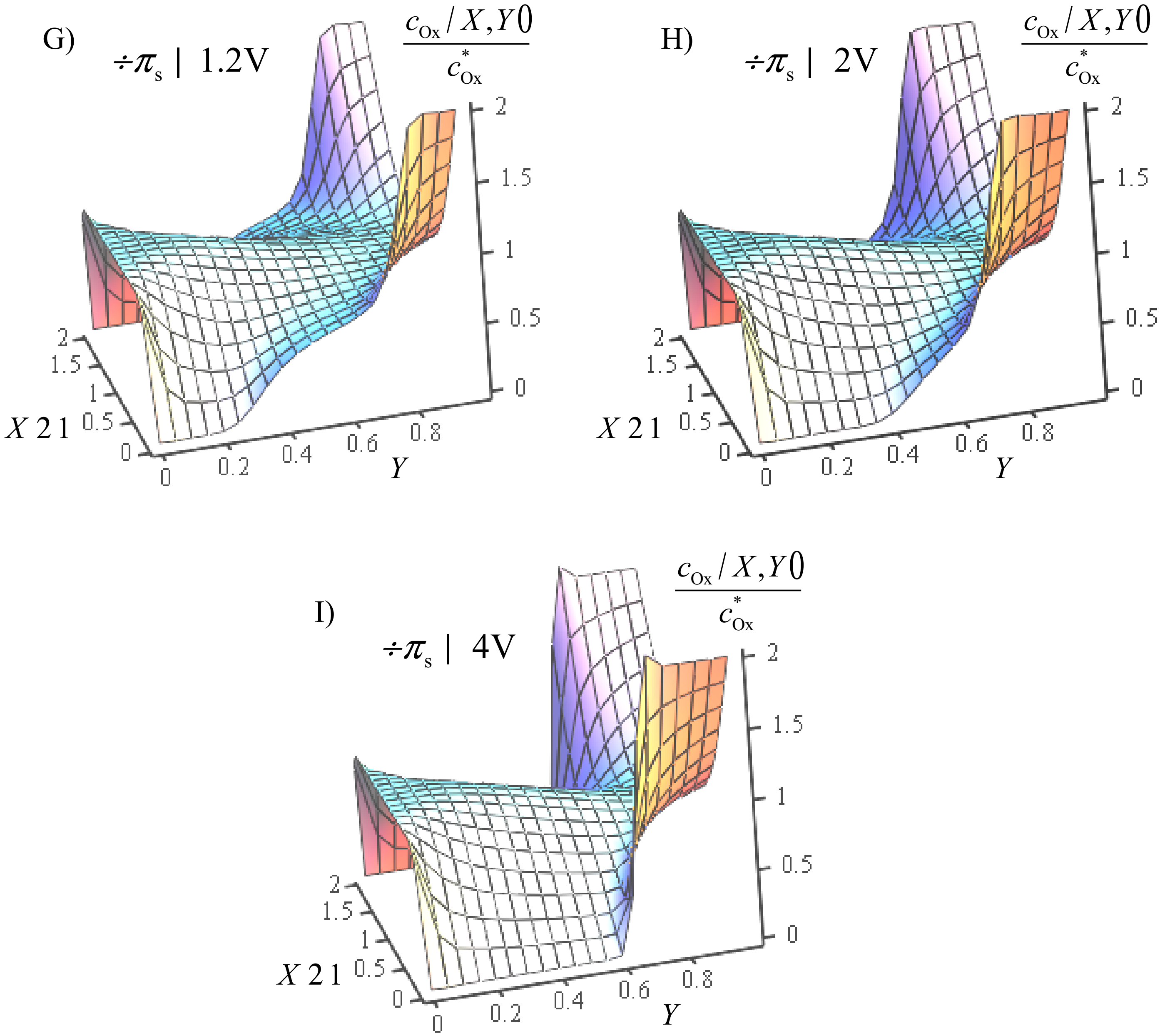

Figure 3. Concentration profiles of the oxidized form of the redox couple at varied applied fields $\div\pi_{\mathrm{s}}$ (indicated) and at the pressure $\div P \mid 0.5$ kPa (section 2.4.1). Same parameters as in Figure 2. The profiles at the injection position $Y \mid 0$ (left extremity of the cell) are not drawn ($c_{\mathrm{Ox}} \mid c^1_{\mathrm{Ox}}$).

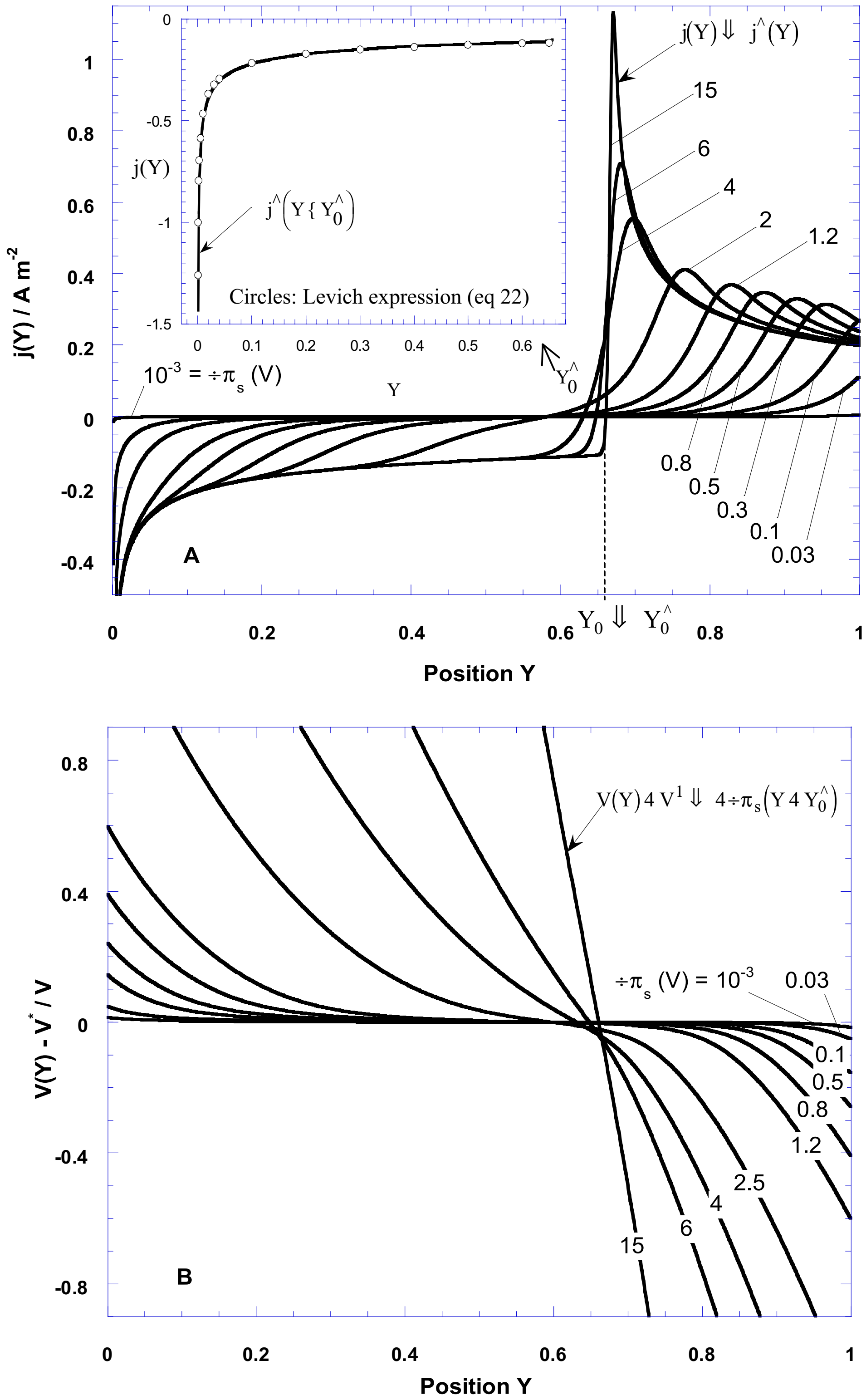

Figure 4. Spatial distributions of (A) the local faradaic current density $j(Y)$ and (B) the local potential $V(Y)$ along the conducting surface at different applied fields $\div\pi_{\mathrm{s}}$ (indicated) and at the pressure $\div P$ | 0.5 kPa. In the inset of panel A, the limiting current $j^{\wedge}(Y)$ pertaining to the cathodic area is plotted (solid line) and compared to the current density calculated with eq 22 (circles). Same parameters as in Figure 2.

progressively decreases (increases) for the left (right) part of the cell (Figures 3A-3C). Changing the sign of $\div\pi_{\mathrm{s}}$ generates the expected permutation of the cathodic and anodic areas. The bulk concentration (at $X \mid 0$) drops due to depletion except for positions *Y* close to the injection point ($Y \mid 0$) where the bulk value is maintained. Steeper transversal depletion occurs when increasing the lateral field. As a result of the decrease of c_{Ox} at the surfaces with increasing the potential $\div\pi_{\mathrm{s}}$ (Figure 5), the concentration gradients at the surfaces, and hence the local faradaic current densities $j(Y)$, increase in size. The overall current I_{f}, resulting from the spatial integration over the relevant surface areas of the current density $j(Y)$, follows the same trend. From a given value of $\div\pi_{\mathrm{s}}$, denoted as $\div\pi_{\mathrm{s}}^{\wedge}$ (the superscript ^ pertains to the diffusion-limiting current condition), the faradaic processes at the extremities of the surfaces ($Y \mid 0$ and 1) are occurring at limiting rate. Ox species are reduced (and R oxidized) as fast as they can be brought to the electrode surfaces. Locally, the *diffusive limiting-current* is reached, and the conductivity curve starts to develop a bend. Because the largest overpotentials $\left(V(Y)\,4\,V^{1}\right)$ are located at $Y \mid 0$ and $Y \mid 1$, the current densities at these positions are the first to be affected by the limiting-current condition (Figure 3D). For $\div\pi_{\mathrm{s}} \varnothing \div\pi_{\mathrm{s}}^{\wedge}$, the limiting-current is reached for larger fractions of the total cathodic and anodic areas (Figures 3D-3I). In the extreme situation where $\div\pi_{\mathrm{s}} \}\} \div\pi_{\mathrm{s}}^{\wedge}$, we have,

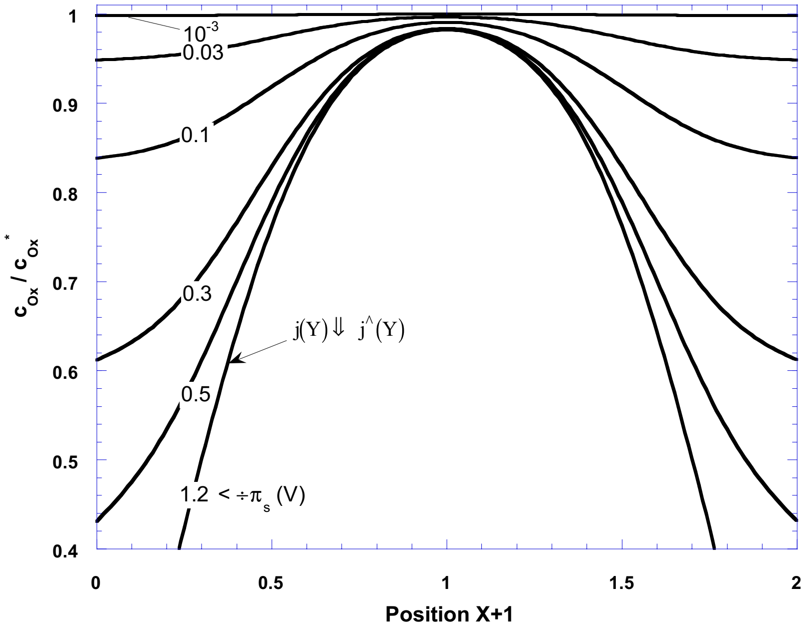

Figure 5. Cross sections of the concentration profiles $c_{\mathrm{Ox}} / c_{\mathrm{Ox}}^{1}$ represented in Figure 3 at the position $Y \mid 0.221$ providing an illustration of the depletion of the electroactive compounds upon increase of $\div\pi_{\mathrm{s}}$ (indicated in V). For the position *Y* chosen, the diffusion-limited flux is reached for $\div\pi_{\mathrm{s}} \varnothing 1.2$ V.

for practically every Y, $j(Y) \mid j^{\wedge}(Y)$. The concentration profile then presents a particular shape, as illustrated in Figure 3I. Applying the Leibnitz rule[23] to the second integral of eq 18, one can show that

$$\frac{\mathrm{d}I_{\mathrm{f}}}{\mathrm{d}\div\pi_{\mathrm{s}}} \mid 2lL_0 \left\{ \int_{Y_0}^{1} \frac{\mathrm{d}j^{\wedge}(Y)}{\mathrm{d}\div\pi_{\mathrm{s}}} \mathrm{d}Y \, 4 \, j^{\wedge}(Y \mid Y_0) \frac{\mathrm{d}Y_0}{\mathrm{d}\div\pi_{\mathrm{s}}} \right\} \tag{21}$$

Since, under the limiting current conditions, the applied pressure maintains $c_{\mathrm{Ox}}(X \mid 0, Y)$ at a constant value, $j^{\wedge}(Y)$ remains independent of $V(Y)$ or, equivalently, $\div\pi_{\mathrm{s}}$. Using the definition adopted for Y_0, one concludes that for $\div\pi_{\mathrm{s}} \}\} \div\pi_{\mathrm{s}}^{\wedge}$, I_{f} is approximately constant with respect to the applied $\div\pi_{\mathrm{s}}$ and equals $I_{\mathrm{f}}^{\wedge}$, as given by eq 18 after replacing $j(Y)$ and Y_0 by $j^{\wedge}(Y)$ and $Y_0^{\wedge}$, respectively. In the analysis, no other electron-transfer reactions than eq 2 are considered. However, in the limit of strong fields, reduction and oxidation of water also come into play,[22] and this would obviously change the whole bipolar process. In the strong field limit ($\div\pi_{\mathrm{s}} \}\} \div\pi_{\mathrm{s}}^{\wedge}$), the potential distribution $V(Y)$ as formulated by eqs 14-17 asymptotically approaches linearity because $I_{\mathrm{T}} / I_{\mathrm{f}}^{\wedge} \}\} 1$, I_{T} being the overall ohmic current. With this assumption, the limiting current density $j^{\wedge}$ is expected to depend on the position according to the expression[12,24]

$$j^{\wedge}(Y) \nabla Y^{41/3} \tanh\left[\frac{nf}{2} \div\pi_{\mathrm{s}}\left(Y \, 4 \, Y_0^{\wedge}\right)\right] \underset{\div\pi_{\mathrm{s}} \}\} \div\pi_{\mathrm{s}}^{\wedge}; Y \{ Y_0^{\wedge}}{\propto \propto \propto \propto \propto \propto \propto\!\!\propto \Downarrow} \, 4 Y^{41/3} \tag{22}$$

This is in very good agreement with the numerical results obtained, as illustrated in the inset of Figure 4A. A similar analysis cannot be straightforwardly performed for the positions $Y_0^{\wedge} \{ Y \,\Omega 1$ (anodic area) because there are no direct monopolar pendants for the corresponding concentration profiles (see below). Sections of various lateral positions Y of three-dimensional concentration profiles corresponding to $\div\pi_{\mathrm{s}} \{ \div\pi_{\mathrm{s}}^{\wedge}$ and $\div\pi_{\mathrm{s}} \} \div\pi_{\mathrm{s}}^{\wedge}$ are represented in panels A and B of Figure 6, respectively. Scanning the bipolar electrodes from their left sides to the position Y_0 (cathodic area), it is clear that the characteristic diffusion length ι increases to reach the value $a/2$ and that subsequently depletion of the oxidized species in the center of the cell occurs. Qualitatively, the observed dependence of ι on Y is in accordance with the trend predicted by Levich[24] in the Leveque approximation[25] for the simple case of a limiting diffusive flux in a laminar flow inside a monopolar circular tube. The dependence of ι on Y justifies that the limiting current density $j^{\wedge}$, though independent of the potential distribution, remains a function of the lateral position Y (eq 22). The situation for $Y_0^{\wedge} \,\Omega Y \,\Omega 1$ is slightly more complicated. For sufficiently high $\div\pi_{\mathrm{s}}$, the current distribution in this Y-range exhibits a peak with an amplitude that grows with the applied potential (Figure 4). The appearance of this peak is linked to the presence of a local minimum (the reasoning is made for $41\,\Omega X\,\Omega 0$) in the concentration profile of Ox (Figure 6), as resulting from the oxidation of R at the surfaces and the overshoot of R (as produced in the cathodic area and introduced by the flow for $Y \} Y_0$) with respect to the position $X \,|\, 0$. The larger $\div\pi_{\mathrm{s}}$ is, the larger the overshoot in R and the Ox concentration at the surfaces becomes, and therefore the larger is the amplitude of the peak. Disappearance of the local minimum coincides with positions Y for which $j(Y)$ decreases. Upon increase of $\div\pi_{\mathrm{s}}$, the peaks are located at positions running from $Y \,|\, 1$ to $\overset{\wedge}{Y_0}$. This is in agreement with the direction according to which the spatial extension of the limiting-current condition takes place in the cathodic and anodic areas with increasing $\div\pi_{\mathrm{s}}$.

For the particular pressure considered, the current and potential distributions present a certain asymmetry with respect to the position halfway the electrode ($Y \,|\, 0.5$). This is directly related to the asymmetrical spatial distribution of the diffusion layer thickness, $\iota(Y)$, which, in turn, gives rise to huge variations of Y_0 with changing $\div P$ (see next section). The amplitude of these variations depends to a minor extent on the electric field (Figure 7). To ensure the balance between the total anodic and cathodic currents, upon increase of $\div\pi_{\mathrm{s}}$, the position Y_0 moves first slightly to lower values and then to higher ones to tend to $\overset{\wedge}{Y_0}$. The initial decrease corresponds to the potential regime in which the growth of the local cathodic currents with the applied field is stronger than that for the local anodic currents. The increase appears at $\div\pi_{\mathrm{s}}$ values for which the cathodic process is critically limited by diffusion in the sense that Y_0 shifts to the anodic area to counterbalance the ongoing increase of the overall oxidation current, as predominantly due to the increasing overshoot of R (current-peak). The values of the potential V^* corresponding to the different positions Y_0 are also indicated. Contrary to the bipolar processes analyzed in ref. 14, V^* is not simply given by the Nernst potential (eq 20) of the original solution with the concentrations c_{Ox}^{1} and c_{R}^{1} but by an increasing function of the electric potential in solution which, as we shall see in the next paragraph, also depends on the mass-transfer conditions.

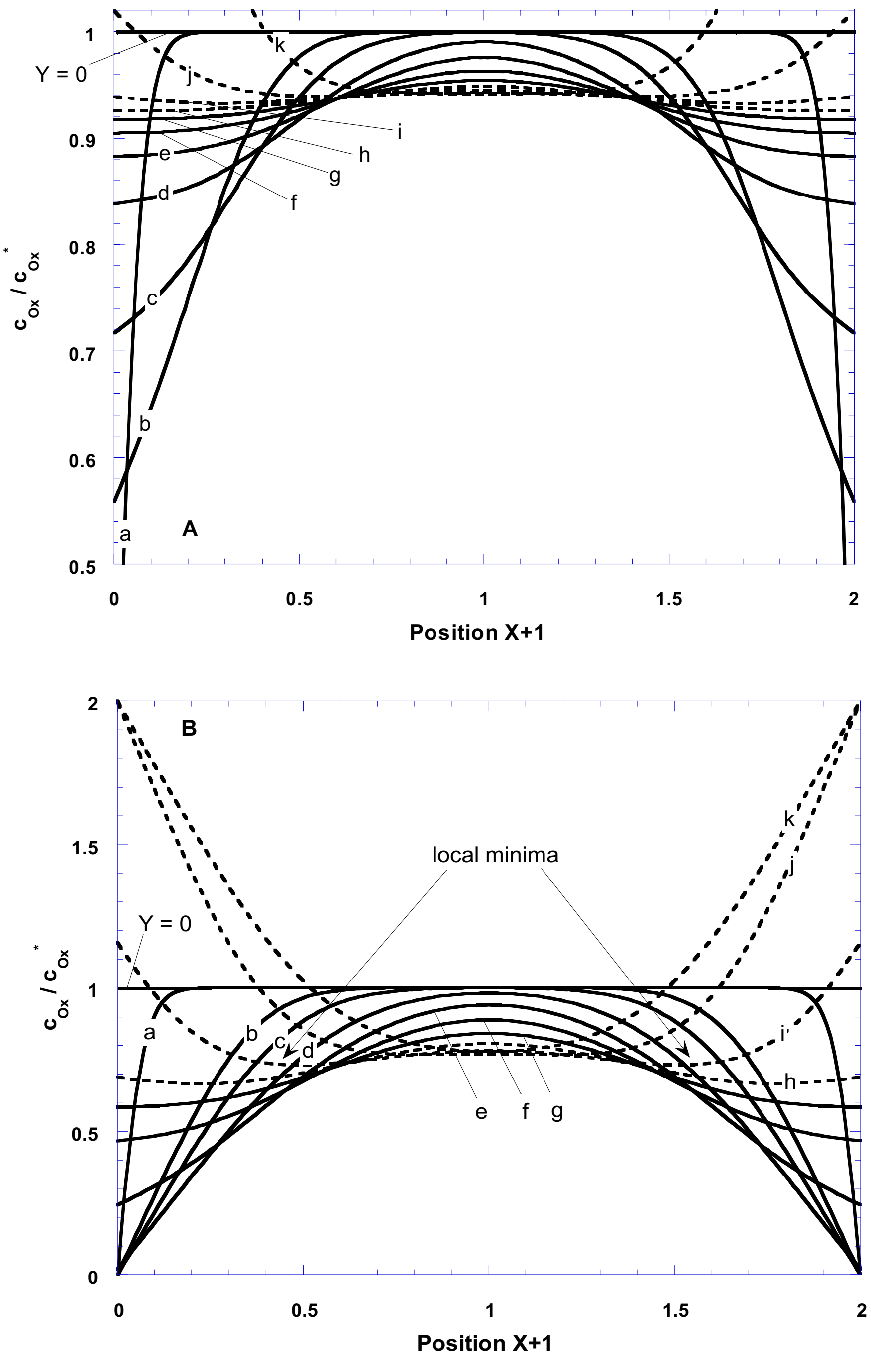

Figure 6. Cross sections at different positions Y of the concentration profiles $c_{\mathrm{Ox}} / c_{\mathrm{Ox}}^{1}$ as pictured in (A) Figure 3C and (B) Figure 3G. Letters a-k refer to the positions $Y\,|\;10^{-3}$, 0.056, 0.111, 0.221, 0.331, 0.441, 0.551, 0.661, 0.771, 0.881 and 0.991. The dashed lines pertain to the positions Y where oxidation reaction takes place.

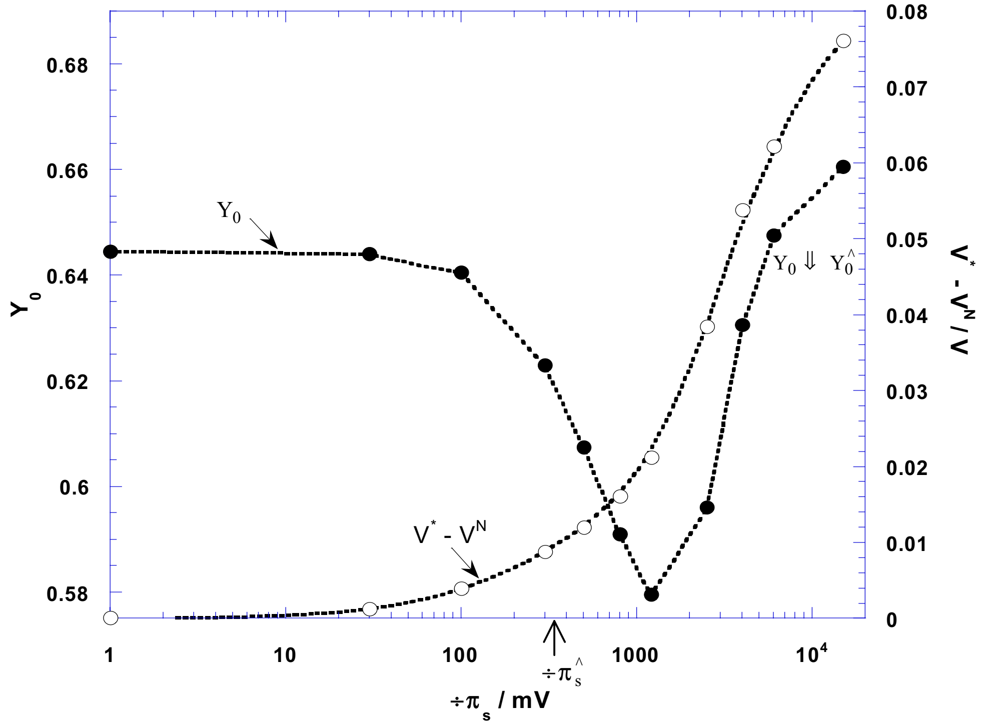

Figure 7. Asymmetry of the bipolar process as induced by the applied field $\div\pi_s$ at constant pressure ($\div P \,|\,$ 0.5 kPa). The other parameters are as in Figure 2.

2.4.2. Analysis at given lateral field $\div\pi_s$ and various pressures $\div P$

Let us analyze more specifically the influence of the applied pressure on the bipolar process. For this purpose, snapshots of the concentration profile for the Ox species are given for different $\div P$ and constant $\div\pi_s$ (Figure 8). The spatial distributions of the local faradaic current and the potential, as well as the characteristic values of Y_0 and V^1, are shown in Figure 9. For every *X*, the velocity at which the electroactive species are transported along the surface is scaled with $\div P$ (eqs 6-7). For very low $\div P$, the lateral convection is so weak that the bulk concentration c^1_{Ox} is only maintained close to the injection point ($Y \,|\,$ 0) and within a certain range of *X*, which also depends on the applied potential (see Figure 5). The cathodic process is confined to the extreme left side of the electrodes ($Y_0 - 0$ and $V^1 - \div\pi_s\, 2\, V^{\mathrm{N}}$), so that oxidation reaction takes place over practically the whole range of *Y* values ($V(Y) \{ V^1$) with a gradual change of c_{Ox} (Figure 8A). The local currents and the corresponding overall bipolar current are so low that the potential distribution is practically linear ($I_{\mathrm{f}} \{\{ I_{\mathrm{T}}$). With increasing $\div P$, the magnitude of the cathodic area increases ($\mathrm{d}Y_0 / \mathrm{d}\div P \} 0$), and the fraction of the total applied potential span along the anodic side of the electrode decreases ($\mathrm{d}V^* / \mathrm{d}\div P \{ 0$). This corresponds to a translation of the spatial distribution of $\left(V(Y)\, 4\, V^1\right)$ toward more positive values, which is combined with a de-

A)

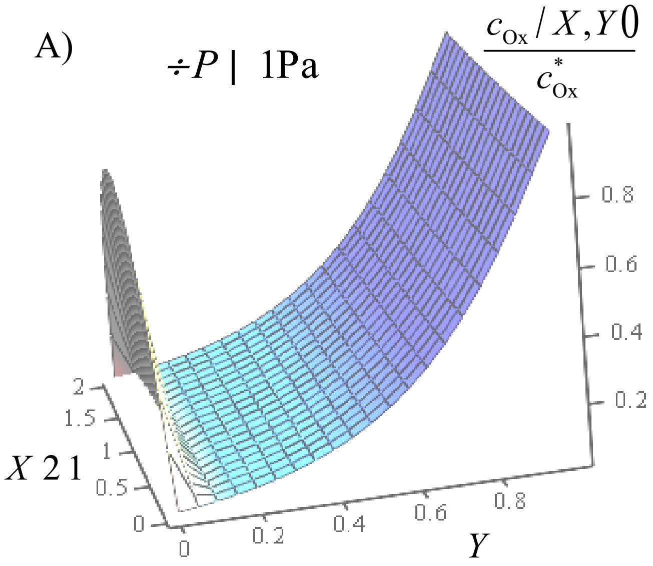
÷P | 1Pa
$\frac{c_{\mathrm{Ox}} / X,Y0}{c_{\mathrm{Ox}}^*}$
0.8
0.6
0.4
0.2
X 2 1
2
1.5
1
0.5
0
0
0.2
0.4
0.6
0.8
Y

B)

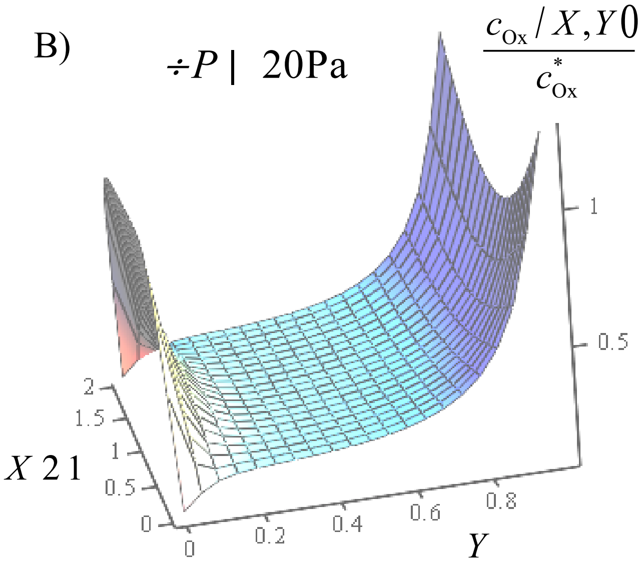
÷P | 20Pa
$\frac{c_{\mathrm{Ox}} / X,Y0}{c_{\mathrm{Ox}}^*}$
1
0.5
X 2 1
2
1.5
1
0.5
0
0
0.2
0.4
0.6
0.8
Y

C)

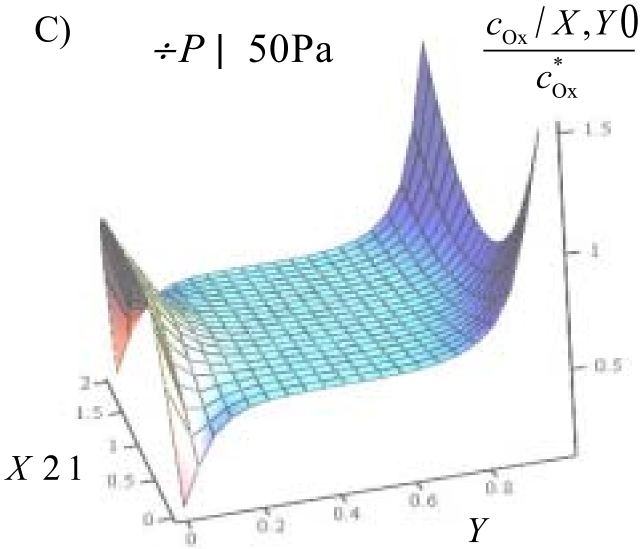
÷P | 50Pa
$\frac{c_{\mathrm{Ox}} / X,Y0}{c_{\mathrm{Ox}}^*}$
1.5
1
0.5
X 2 1
2
1.5
1
0.5
0
0
0.2
0.4
0.6
0.8
Y

D)

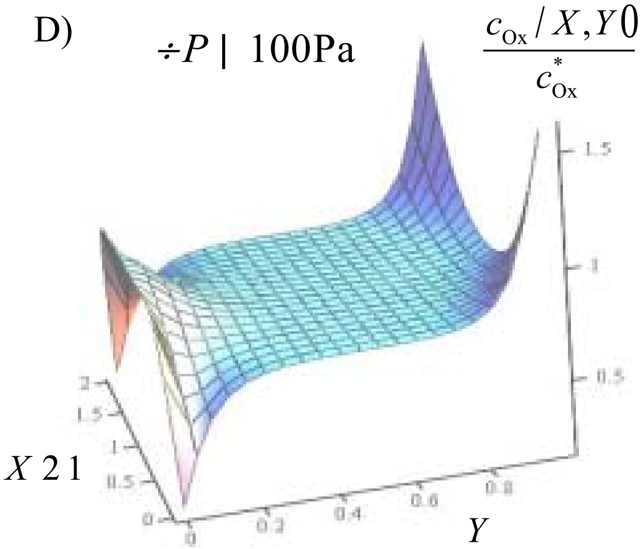
÷P | 100Pa
$\frac{c_{\mathrm{Ox}} / X,Y0}{c_{\mathrm{Ox}}^*}$
1.5
1
0.5
X 2 1
2
1.5
1
0.5
0
0
0.2
0.4
0.6
0.8
Y

E)

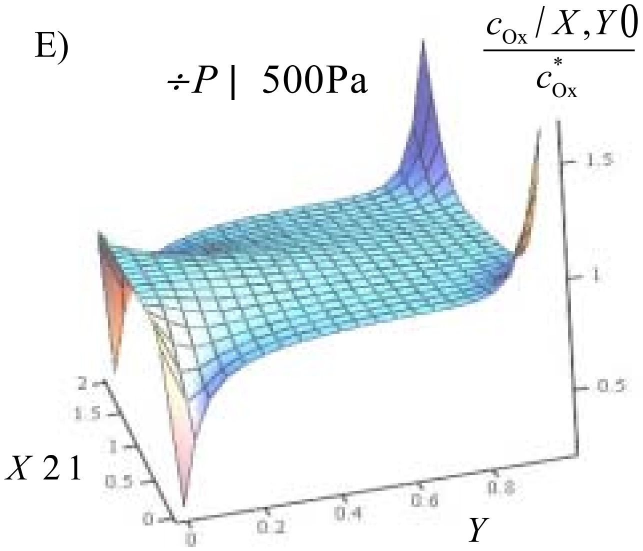
÷P | 500Pa
$\frac{c_{\mathrm{Ox}} / X,Y0}{c_{\mathrm{Ox}}^*}$
1.5
1
0.5
X 2 1
2
1.5
1
0.5
0
0
0.2
0.4
0.6
0.8
Y

F)

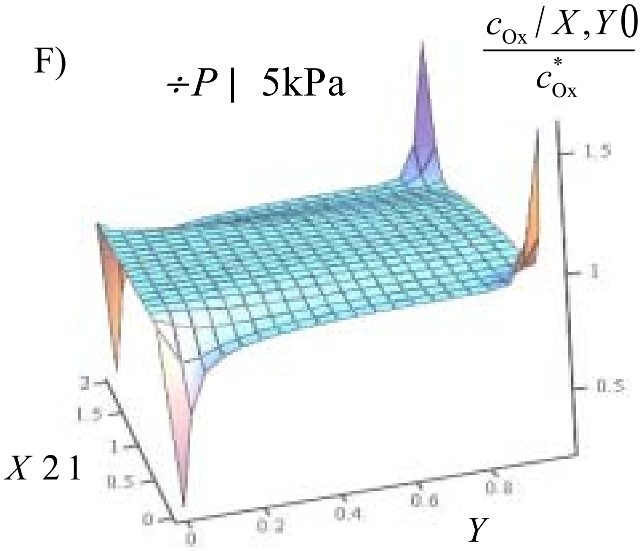
÷P | 5kPa
$\frac{c_{\mathrm{Ox}} / X,Y0}{c_{\mathrm{Ox}}^*}$
1.5
1
0.5
X 2 1
2
1.5
1
0.5
0
0
0.2
0.4
0.6
0.8
Y

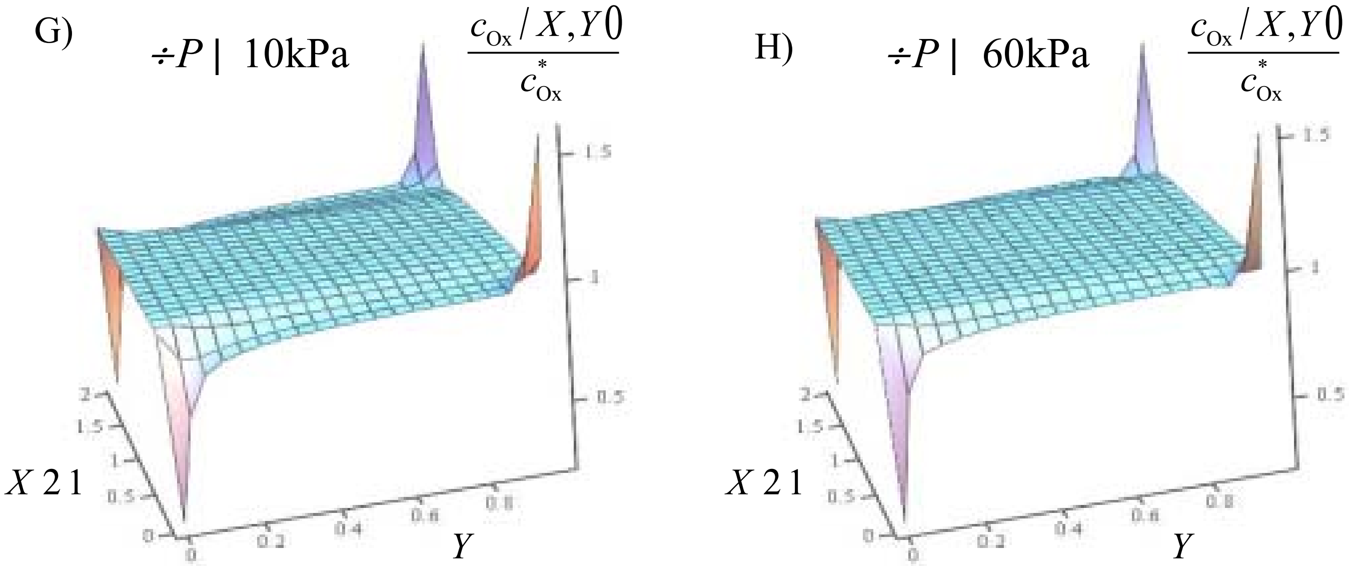

Figure 8. Concentration profiles of the oxidized form of the redox couple at varied applied pressures $\div P$ (indicated) and constant applied field $\div \pi_s \mid 100$ mV (section 2.4.2). Same parameters as in Figure 2. The profiles at the injection position $Y \mid 0$ (left extremity of the cell) are not drawn ($c_{Ox} \mid c^1_{Ox}$).

formation of the profile with respect to linearity (see Figure 9C). Indeed, at both extremities of the cell, the electric field strength increases (eq 17), as can be inferred from the corresponding slopes $\mathrm{d}V(Y)/\mathrm{d}Y$. This is due to the increase of the current $j(Y)$ for $Y \mid 0$ and $Y \mid 1$, as resulting from the decreasing ι (Figures 8B-8F) with $\div P$. In the previous section, the conductivity curve could be interpreted by considering, for a fixed position Y along the electrode and a given $\div P$, the change of $j(Y)$ upon the effect of $V(Y)$ as induced by variation of $\div \pi_s$. In the current analysis, $j(Y)$ is affected not only by the pressure but also by the corresponding significant local variations of the potential $V(Y)$, as resulting from the enhanced spatial asymmetry of the bipolar process. Upon increase of $\div P$, the thickness of the diffusion layer ι for every Y decreases. This means that for any Y, the window of X values where lateral convection prevails becomes wider, with the concentration approaching the value c^1_{Ox} (Figure 10A). The effect of the pressure on $\iota(Y)$ enlarges the concentration gradient at the surface, and hence, the current density $j(Y)$ at the positions where the electric field strength E is the largest, that is, at the left and right sides of the cell. It results in a steep increase of the bipolar current (eq 19), as illustrated in Figure 2. One can verify that, for the (very low) $\div P$ and $\div \pi_s$ ranges corresponding to potential distributions that do not significantly deviate from linearity, I_f varies according to the power law $\div P^{1/3}$, as found in ref. 12. As a result of the concomitant shift of $\left(V\left(Y\right)4\,V^{1}\right)$ and the increase of E at the extremities of the surfaces, the potential gradient flattens in the midrange of Y. The corresponding local E and

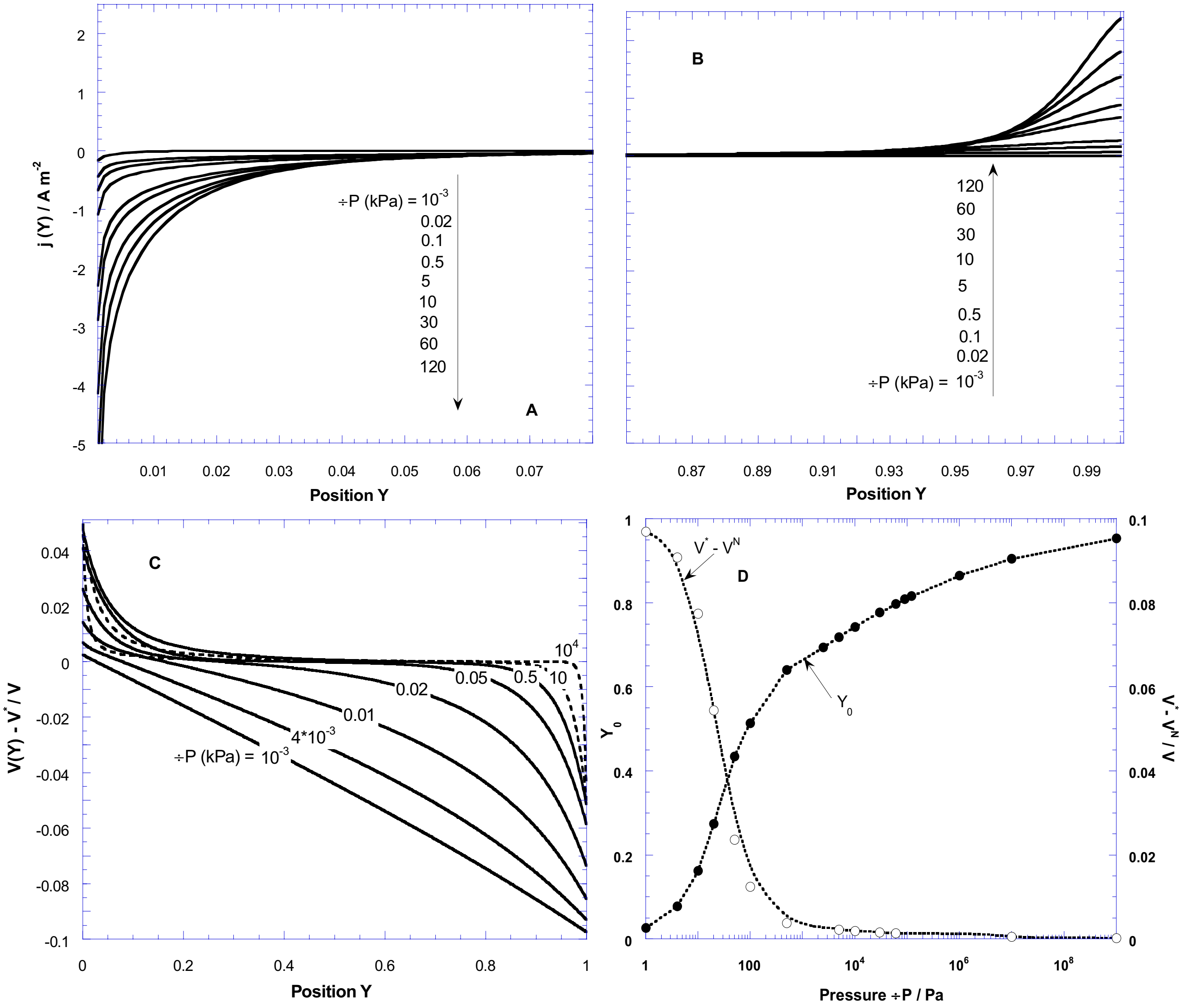

Figure 9. Spatial distributions of the local faradaic current density $j\left(Y\right)$ (panel A, reduction current; panel B, oxidation current) and the local potential $V\left(Y\right)$ (panel C) along the conducting surface at varied $\div P$ (indicated) and constant $\div\pi_{\mathrm{S}}$ | 100 mV. In panel D, the corresponding parameters Y_0 and V^{1} are given. Same model parameters as in Figure 2.

the current density $j\left(Y\right)$ are lowered. The spatial range involved with the suppression of the field increases with the pressure. Quantitatively, the increase of E at the extremities is large enough to compensate for the decreasing $j\left(Y\right)$ in the midrange so that the overall bipolar current I_{f} keeps on growing but to a lesser extent than that for low $\div P$. I_{f} then varies according to the power law $\div P^{1/\eta}$ with $\eta - 5$ (see Figure 2), which is in agreement with the deviation expected on the basis of the assumption of a linear potential distribution (for which $\eta | 3$). The simultaneous dependencies of $j(Y)$ on the hydrodynamic and electric parameters explain the existence of extrema reached by j and by the local E for certain positions Y along the electrode, as shown in Figure 10B. Referring to this figure, in the $\div P$-region (I), $j(Y)$ increases even though the driving

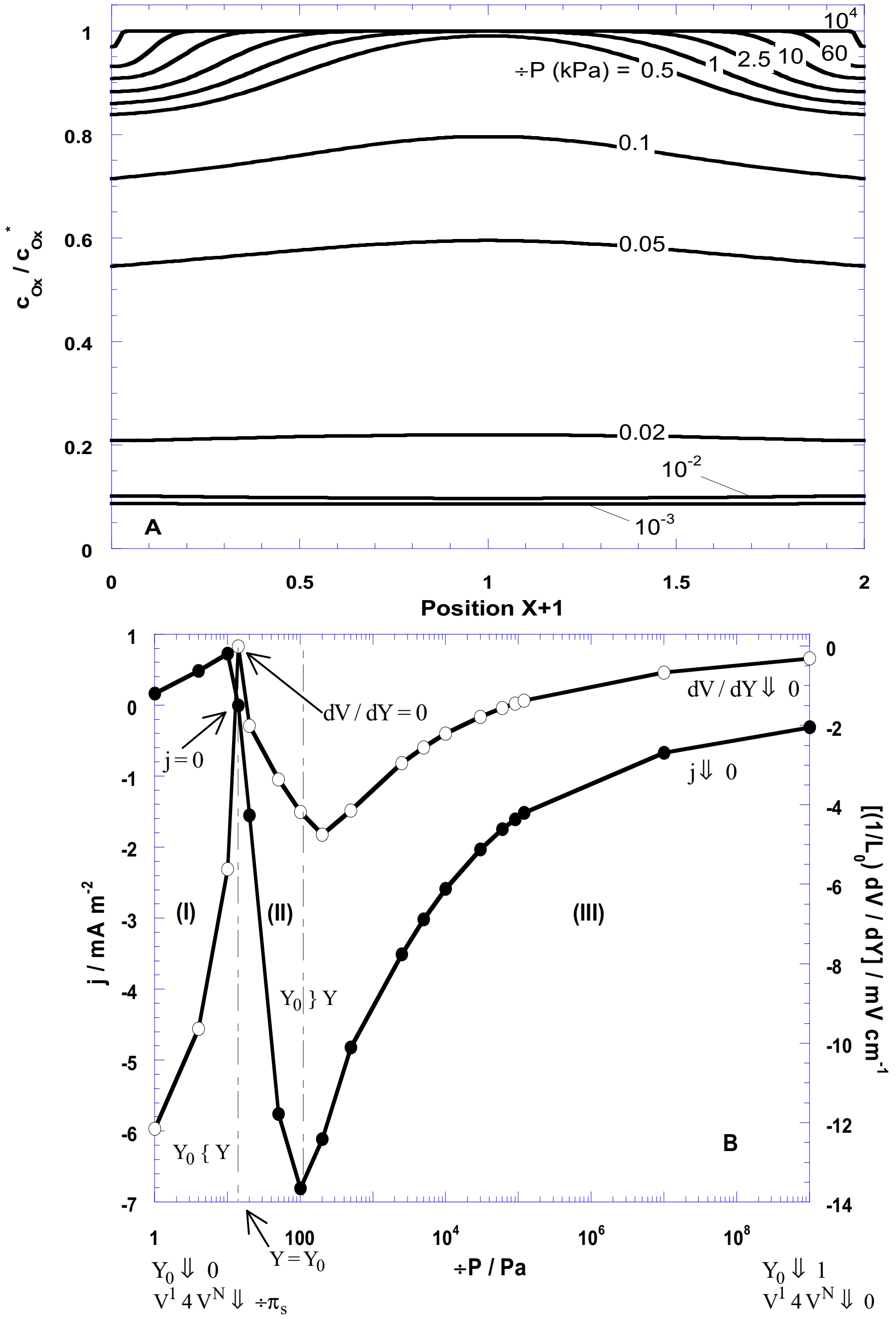

Figure 10. (A) Cross sections of the concentration profiles $c_{\mathrm{Ox}} / c^{1}_{\mathrm{Ox}}$ represented in Figure 8 at the position $Y | 0.221$ providing an illustration of the decrease of the diffusion length ι and of the increase of the concentration $c_{\mathrm{Ox}}(X | 0, Y)$ with increasing $\div P$ (indicated in kPa). (B) Faradaic current density $j(Y | 0.221)$ and local electric field strength $E(Y | 0.221)$ as a function of the pressure (see text). For panel B, the same parameters as for panel A are used.

field decreases (in absolute value): this is mainly attributed to the decrease of $\iota\left(Y\right)$; in region (II), the pressure is such that cathodic reaction now takes place ($Y \{ Y_0$): the increasing field and decreasing $\iota\left(Y\right)$ are both responsible for the increase of the current (in absolute value); in region (III), the decrease of $V \, 4 \, V^1$ results in the decrease of $j(Y)$. In the limit of very high pressure, the anodic reaction is in turn spatially confined at the extreme right side of the electrode ($Y_0 \Downarrow 1$ and $V^1 \Downarrow V^{\mathrm{N}}$), and the cathodic reaction spans over the entire *Y*-range. The effective overpotential $\left(V(Y) \, 4 \, V^1\right)$ and the current $j(Y)$ tend to small values over the whole *Y*-range except at the very edges, where there is a drastic increase of *E* and *j*. The concentration profiles present sharp peaks at the position $Y |\ 0, 1$ and $X |\ 41, 1$ (Figures 8G, 8H).

2.4.3. Dependence of the bipolar current I_{f} on $c_{\mathrm{Ox}}^1/c_{\mathrm{R}}^1$, K^{L} and a

Figure 11A illustrates the effect of the bulk redox concentrations on the conductivity curves. As expected, I_{f} increases with increasing c_{Ox}^1 and/or c_{R}^1 and is limited by the lower of the two concentrations. Because of the non-linear coupling between local current and potential, I_{f} does not depend linearly on the bulk concentrations.[14] A ratio $c_{\mathrm{Ox}}^1 / c_{\mathrm{R}}^1 \prod 1$ induces a spatial asymmetry for the bipolar process and hence a shift of the position Y_0. The potential distribution tends to linearity for low c_{Ox}^1 and/or c_{R}^1, corresponding to low I_{f} with respect to the ohmic current I_{T} (Figure 11B). A comparable picture can be given when varying the bulk conductivity of the solution K^{L} or the cell dimension *a* (Figures 12 and 13). With increasing K^{L} or *a*, the local potential $\left|V(Y)\right|$ and hence the overall current I_{f} increase. In the meantime, the ratio $I_{\mathrm{T}} / I_{\mathrm{f}}$ grows and the potential distribution approaches linearity.

2.4.4. Application to the electrokinetics of the metal ⁄ (electroactive) solution interface

In the frame of streaming potential experiments, a potential difference is built up across the cell upon application of a pressure drop $\div P$ along the surface. This results from the lateral displacement of the mobile part of the counter charge at the interface substrate⁄solution. When the solution contains electroactive species and the surfaces are conducting, this potential, called the streaming potential $\div\pi_{\mathrm{str}}$, induces a bipolar electrodic behavior of the surfaces in the same way as described in section 2.1. In steady-state, the net-current flow in the channel is zero; the streaming current I_{str} caused by the forced convection of solution stripping charge along the double layer is then counterbalanced by the total current *I* flowing in the cell ($I_{\mathrm{str}} \, 2 \, I |\ 0$ with

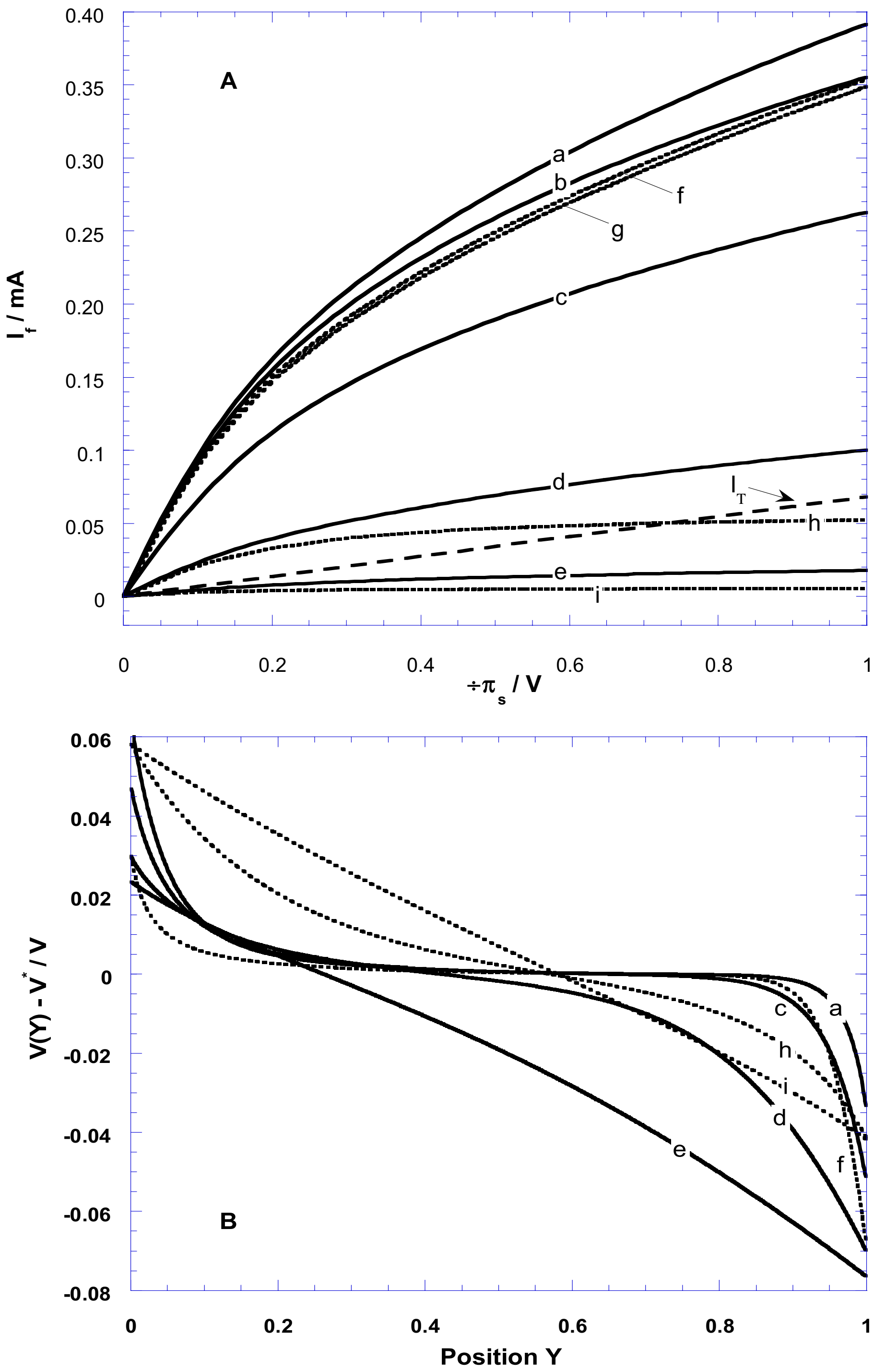

Figure 11. (A) Bipolar current as a function of the applied field for different sets of redox concentrations at constant pressure $\div P \mid 0.5$kPa. The ohmic current I_T is indicated for comparison purposes. (B) Corresponding spatial distributions of the potential at $\div\pi_s \mid 100$ mV. Plain lines: $c^1_{Ox} \mid 10^{-4}$ M / $c^1_R \mid 10^{-2}$ M (a), 10^{-3} M (b), 10^{-4} M (c), 10^{-5} M (d), 10^{-6} M (e). Dashed lines: $c^1_R \mid 10^{-4}$ M / $c^1_{Ox} \mid 10^{-2}$ M (f), 10^{-3} M (g), 10^{-5} M/ (h), 10^{-6} M (i). Other parameters as in Figure 2.

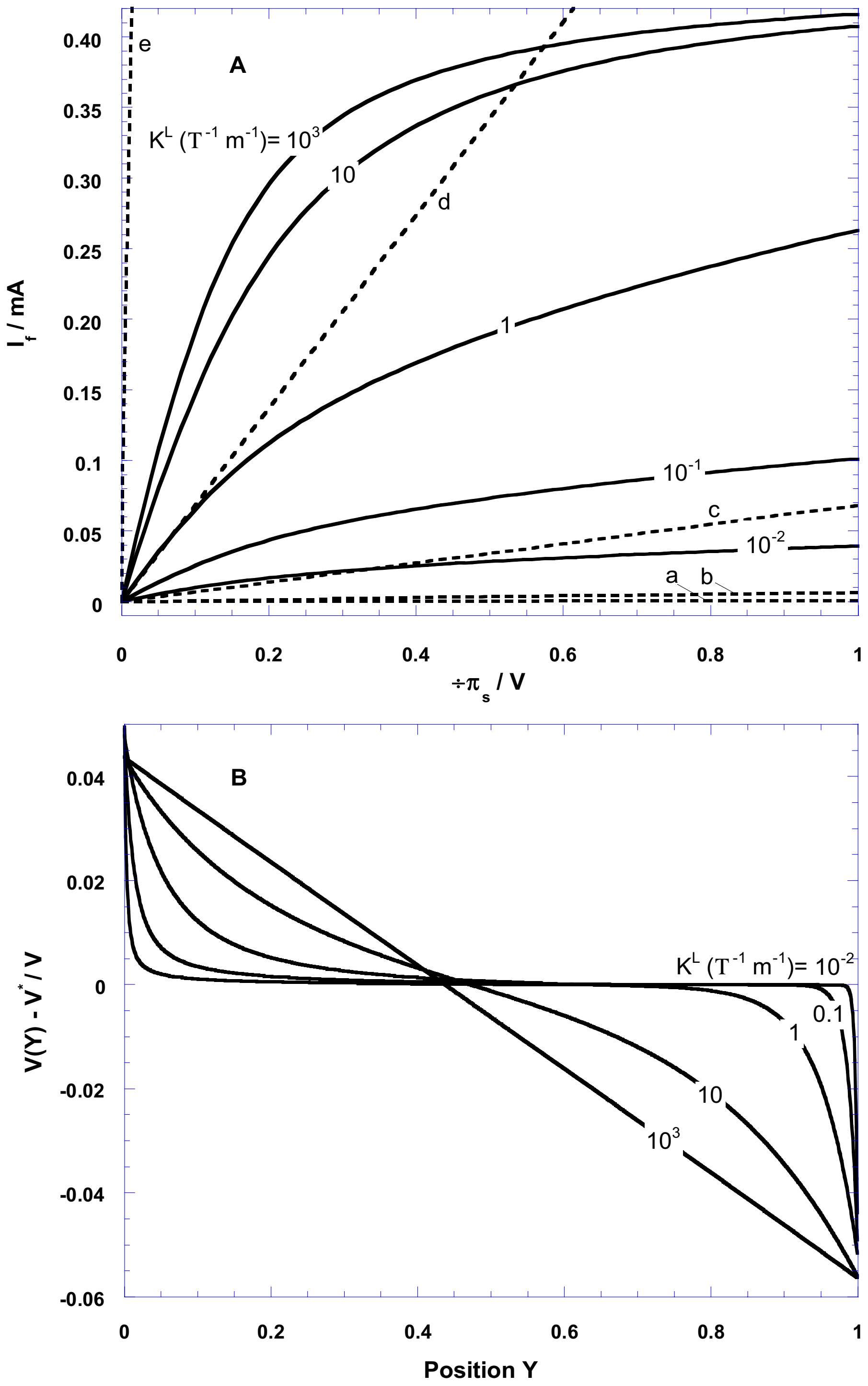

Figure 12. (A) Bipolar current as a function of the applied field for different K^{L} (indicated) at constant pressure $\div P$ | 0.5kPa. The corresponding ohmic currents I_{T} (dashed curves a-e for low to high K^{L}) are given. (B) Corresponding spatial distributions of the potential at $\div \pi_{\mathrm{s}}$ | 100 mV. Other parameters as in Figure 2.

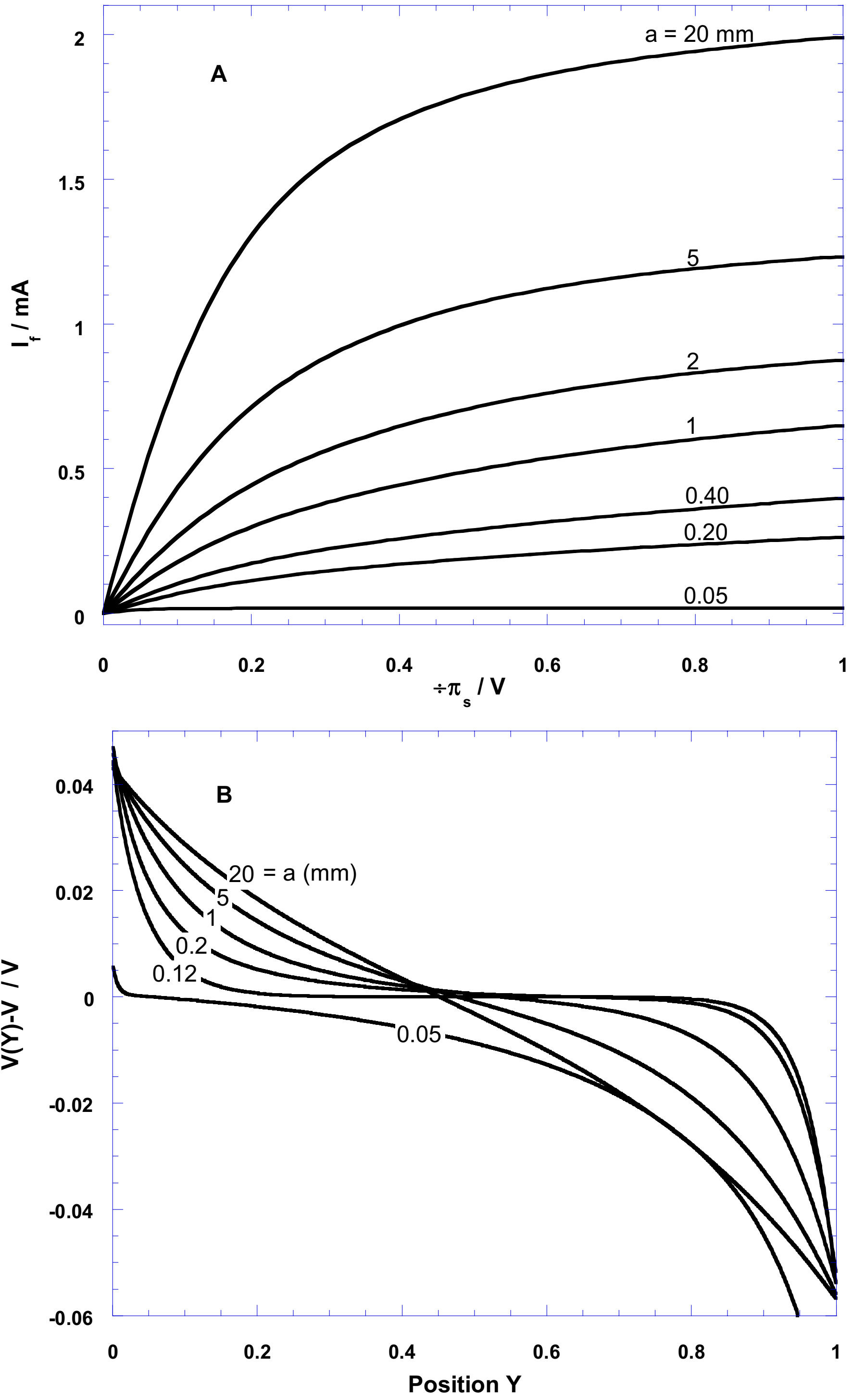

Figure 13. (A) Bipolar current as a function of the applied field for different a (indicated) at constant pressure $\div P \mid$ 0.5kPa. (B) Corresponding spatial distributions of the potential at $\div\pi_s \mid$ 100 mV. Other parameters as in Figure 2.

I_{str} and I algebraic currents). I contains a surface conduction contribution and a bulk contribution depending on the electric field as determined by the coupling between conduction and faradaic currents (see eq 14). For the geometry considered in this paper, I is written

$$I \mid \left(aK^{\mathrm{L}}\ 2\ 2K^{\mathrm{\omega}}\right) l \left.\frac{\in V}{\in y}\right|_{y \mid\ L_0/2} \tag{23}$$

with K^{ω} the surface conductivity. Using eq 19, eq 23 can be rearranged as follows:

$$I \mid\ 4 I_{\mathrm{f}}\left(\div\pi_{\mathrm{str}}, \div P\right) 2\ alK^{\mathrm{L}} \left.\frac{\in V}{\in y}\right|_{y \mid\ y_0} \quad 2\ K^{\omega}\left(4\frac{2I_{\mathrm{f}}\left(\div\pi_{\mathrm{str}}, \div P\right)}{aK^{\mathrm{L}}}\ 2\ 2l\left.\frac{\in V}{\in y}\right|_{y \mid\ y_0}\right) \tag{24}$$

I_{f} is the bipolar current depending on the electric and hydrodynamic variables, $\div\pi_{\mathrm{str}}$ and $\div P$. The streaming current is yielded by[26]

$$I_{\mathrm{str}} \mid\ 2l \int_{a/2}^{a} \psi(x) v(x) \mathrm{d}x \mid\ \frac{al\kappa_0 \kappa_{\mathrm{r}}{}' \div P}{\xi L_0} \tag{25}$$

with $'$ the electrokinetic potential (zeta-potential), κ_0 the dielectric permittivity of vacuum, and $\psi(x)$ the local ionic charge density coupled to the potential distribution at the interface, as expressed by the Poisson-Boltzmann equation. Within the framework of the current study, it is assumed that the surface conduction contribution is either absent or negligible with respect to the other conduction terms so that the condition $I_{\mathrm{str}}\ 2\ I \mid\ 0$ becomes

$$\frac{\kappa_0 \kappa_{\mathrm{r}}{}' \div P}{\xi} \mid\ 4L_0 K^{\mathrm{L}} \left.\frac{\in V\left(y, \div\pi_{\mathrm{str}}, \div P\right)}{\in y}\right|_{y \mid\ y_0} \quad 2\ \frac{L_0}{al} I_{\mathrm{f}}\left(\div\pi_{\mathrm{str}}, \div P\right) \tag{26}$$

One verifies that in the absence of faradaic depolarization (i.e., $I_{\mathrm{f}} \mid 0$ and $\in V / \in y|_{y \mid\ y_0} \mid\ 4 \div\pi_{\mathrm{str}} / L_0$), eq 26 reduces to the classical Helmholtz-Smoluchowski equation. The potential $\div\pi_{\mathrm{s}}$ span along the surfaces is now the potential, as generated by the flow, and related to the double layer properties of the interfaces. For given concentrations of the electroactive species, once steady-state is reached, we have

$$I_{\mathrm{f}}\left(\div\pi_{\mathrm{str}}, \div P\right) \sum I_{\mathrm{f}}\left(\div\pi_{\mathrm{s}} \mid\ \div\pi_{\mathrm{str}}, \div P\right) \tag{27}$$

meaning that, basically, the bipolar current generated by the streaming potential $\div\pi_{\mathrm{str}}$ resulting from the pressure $\div P$ is the same as the one that would be obtained by externally applying the same pressure and a potential difference $\div\pi_{\mathrm{s}} \mid\ \div\pi_{\mathrm{str}}$.

Given some characteristics of the electrolyte solution (K^{L}, c_{Ox}^{1}, c_{R}^{1}), the bipolar current I_{f} was first computed for a given $\div P$ in a potential range $\div\pi_{\mathrm{s}}$ compatible with electrokinetic experiments (0 4 70 mV). The resulting conductivity curve $I_{\mathrm{f}}\left(\div\pi_{\mathrm{s}}, \div P\right)$ was fitted by polynomial regression and use of the least-squares method. Assuming a given $'$-potential, the streaming potential $\div\pi_{\mathrm{str}}$ corresponding to the pressure $\div P$ considered was calculated by solving eqs 26-27 assuming a priori that $\in V / \in y\big|_{y|\ y_0} \mid 0$. It was a posteriori verified that taking into account the first term in the r.h.s. of eq 26 does not change the solution obtained. To reconstruct the $\div\pi_{\mathrm{str}}$-$\div P$ plot, this procedure was repeated for various pressures $\div P$. A graphical illustration is given in Figure 14 (panel B), which also shows typical $\div\pi_{\mathrm{str}}$-$\div P$ plots obtained (panel A). The bipolar faradaic current strongly curbs the generation of the streaming potential, and this is reflected by considerable deviations (also for low pressures) from the results expected on the basis of the linear H-S equation. As a result of the non-linear pressure dependence of I_{f} for the entire $\div P$-range examined, the $\div\pi_{\mathrm{str}}(\div P)$ curves develop a bend (in the example given, at $\div P - 40$ kPa). For higher $\div P$ (> 40 kPa), the $\div\pi_{\mathrm{str}}\ 4\ \div P$ plots progressively reach a linear regime. Indeed, for given (K^{L}, c^{1}_{Ox}, c^{1}_{R}), the magnitude of the lateral field met in electrokinetic experiments is so low that I_{f} depends linearly on $\div\pi_{\mathrm{s}} \sum \div\pi_{\mathrm{str}}$ (see Figure 2). Besides, in the high-pressure range, the bipolar current weakly increases when increasing $\div P$, and the corresponding dependence $I_{\mathrm{f}}\ \nabla\left(\div P\right)^{1/\eta}$ can be legitimately approximated to a straight line (see Figure 2). As a result, the bipolar conductivity remains practically constant in the high-pressure and low-potential ranges. This feature may be particularly useful for the treatment of experimental data.[19] To illustrate the necessity of considering a non-linear spatial distribution for the potential in the determination of I_{f}, $\div\pi_{\mathrm{str}}$-$\div P$ plots were calculated in the condition of Figure 14A with the expression for I_{f} based on the assumption of constant field along the surfaces.[12] As expected, this assumption leads to overestimation of I_{f} and underestimated values for $\div\pi_{\mathrm{str}}$ as compared with those obtained from the rigorous numerical analysis.

A detailed analysis of experimental data for the gold/(Fe(CN)$_6^{34}$ / Fe(CN)$_6^{44}$, KNO$_3$) interface in conjunction with an outline of the nature of the zeta-potential in the presence of a redox couple, is given elsewhere.[19]

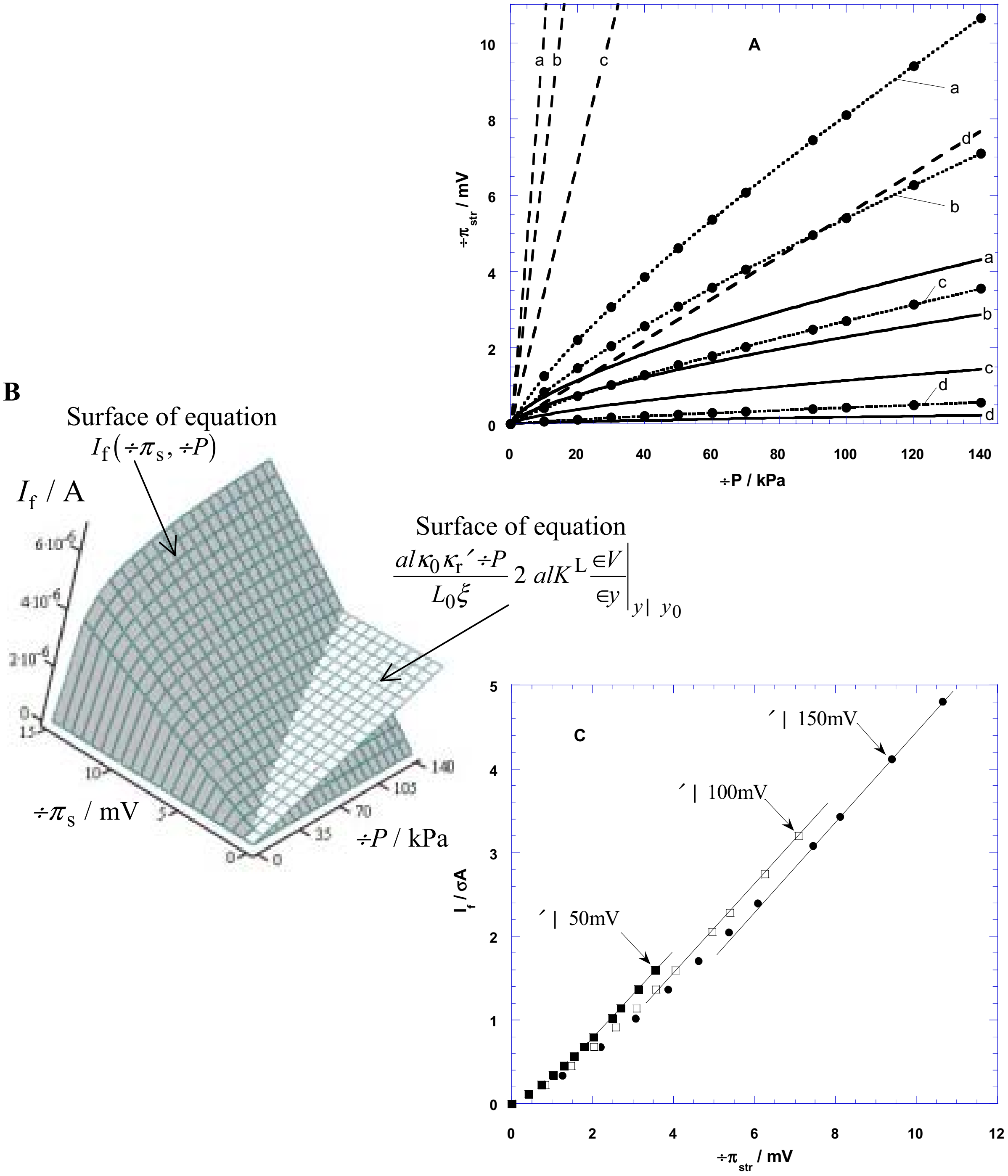

Figure 14. (A) Reconstruction of the $\div\pi_{str}$ 4 $\div P$ plots (points) for ′ | 150 mV (a), 100 mV (b), 50 mV (c) and 8 mV (d). The corresponding curves calculated on the basis of the linear H-S equation (no faradaic depolarization taken into account) and of the assumption of a uniform field[12] are indicated in dashed and plain lines, respectively. (B) Graphical interpretation of the computational procedure followed for the determination of the $\div\pi_{str}$ 4 $\div P$ plots (the example is given for ′ | 100 mV). (C) The points refer to the $(I_f, \div\pi_{str})$ of curves (a), (b), (c) of panel A and computed with the non-uniform field theory. The lines are linear fits in the high-pressure regime (see text). Parameters (common to panels A, B and C): a | 1 mm, L_0 | 7.6 cm, l | 2.6 cm, D | $5\Delta10^{410}$ m^2 s^{-1}, V^0 | 4233 mV, K^L | 0.1 T^{-1} m^{-1}, c^1_{Ox} | c^1_R | 10^{-5} M.

3. Conclusions

The bipolar behavior of metallic surfaces in a thin-layer cell of the type used for electrokinetic experiments is described in the situation in which the faradaic depolarization of the interface is induced by convective diffusion-controlled electron-transfer reactions. The typical pattern of the conductivity curves is interpreted in terms of the corresponding spatial distribution of the concentration polarization of the electroactive species along the conducting surface, the local faradaic current density and the electric field. These were calculated by numerical analysis of the intrinsically coupled Nernst-Planck equation and Poisson equation for finite currents. The bipolar current I_f levels off and asymptotically reaches a constant value at strong lateral fields, as resulting from diffusion-limitation of the local electron transfer. I_f weakly increases at high applied pressure gradients because of the enhanced spatial asymmetry of the bipolar process. The bulk substrate faradaic conduction is more significant with respect to the bulk solution conduction at low applied potential differences and low applied pressure gradients across the cell because these correspond to the steepest variations in I_f. The subtle combination between electric and hydrodynamic variables in the determination of the overall bipolar current yields characteristic non-linear distribution for the local potential along the surface (even at low applied fields). In view of the complexity of the problem, full description of the phenomenon cannot be reduced to a simple analysis based on the assumption of a linear field, which at most provides only a rough estimate of the bipolar current. The steady-state theory developed for the computation of the bipolar faradaic conductivity under given applied field and pressure may be used in the quantitative interpretation of electrokinetic measurements performed on metals in electroactive solution. In such measurements, the electric driving field for faradaic depolarization of the interface is coupled to the pressure, as imposed by the non-linear Helmholtz-Smoluchowski equation. Assuming a given ζ-potential, a computational procedure is proposed to reconstruct the non-linear streaming potential/pressure plots.

This paper shows that it is possible to electrokinetically probe double layer properties of metals in the presence of a reversible redox couple, provided any accompanying bipolar depolarization is well understood and taken into proper account. More specifically, it is shown that electrokinetic experiments may allow assessment of the dependence of the ζ-potential on the total potential drop across the metal|solution interface, which can be electrochemically manipulated via the concentrations of the redox species in the solution. Such type of investigation has not yet been envisaged in the field of electrokinetics, neither experimentally nor theoretically.

Examination of bipolar faradaic depolarization inherent to the electrokinetics of spherical metallic particles submitted to high electric fields will be reported later. It will be shown that a judicious choice of the electrolyte may allow occurrence of superfast electrophoresis at fields commonly applied in standard electrophoresis experiments.

Acknowledgment

This work was carried out within the frame of the project Electrophoretic Particle Deposition with financial support from SENTER (Dutch ministry of Economic Affairs).

Appendix

Computation of the concentration profiles $c_{\mathrm{Ox}}(X,Y)$, the spatial distributions of the potential $V(Y)$ and the local faradaic current density $j(Y)$

Contrary to the study made of the transient characteristics for diffusion-limited bipolar processes,[14] decoupling of the transport equation (eq 9) and the Poisson equation (eq 14) in the current problem cannot be simply performed by analytical means. Therefore, a consistent numerical solution of the complete set of eqs 9-12 and 14-17 must be found.

Discretization of the convective diffusion equation. The problem is symmetrical with respect to $X = 0$, so in the following, the analysis will be restricted to the interval $0 \le X \le 1$. The corresponding boundary conditions, as associated to eq 9 in the text, are

$$C_{\mathrm{Ox}}(X = +1, Y) = Q(Y) \qquad \text{(A1)}$$

, with $Q(Y)$ given by eq 11, and

$$\left.\frac{\partial C_{\mathrm{Ox}}(X,Y)}{\partial X}\right|_{X=0} = 0 \qquad \text{(A2)}$$

The spatial variables X and Y are written

$\mathrm{i} \in [1, \mathrm{M}]$: $$X_{\mathrm{i}} = (\mathrm{i}-1)\Delta X \qquad \text{(A3)}$$

$\mathrm{k} \in [1, \mathrm{N}]$: $$Y_{\mathrm{k}} = (\mathrm{k}-1)\Delta Y \qquad \text{(A4)}$$

where M, N are integers and ΔX and ΔY are the spatial steps for the X and Y directions, respectively. For the sake of simplicity, we write $C_{\mathrm{Ox}}(X_{\mathrm{i}}, Y_{\mathrm{k}}) = C_{\mathrm{i,k}}$ and $Q(Y_{\mathrm{k}}) = Q_{\mathrm{k}}$. To optimize the convergence of the solution and reduce the computation time, the inverse-Euler method[27] was chosen for discretizing eqs 9, A1 and A2. For a given position Y_{k}, this comes to

$\mathrm{i} \in [2, \mathrm{M}-1]$: $$-r_{\mathrm{i}} C_{\mathrm{i}-1,\mathrm{k}-1} + (1+2r_{\mathrm{i}}) C_{\mathrm{i,k}+1} - r_{\mathrm{i}} C_{\mathrm{i}-1,\mathrm{k}+1} = C_{\mathrm{i,k}} \qquad \text{(A5)}$$

$$C_{1,\mathrm{k}+1} - C_{2,\mathrm{k}+1} = 0 \qquad \text{(A6)}$$

$$C_{\mathrm{M,k}+1} - Q_{\mathrm{k}+1} = 0 \qquad \text{(A7)}$$

with r_i the quantity defined by

$$\mathrm{i} \subset [2, \mathrm{M}\,4\,1] : \qquad r_i \;|\; \frac{4DL_0}{v^0 a^2}\,\frac{\div Y}{\left[1\,4\,(\mathrm{i}\,4\,1)^2 \div X^2\right]\div X^2} \qquad \text{(A8)}$$

Equations A5-A8 can be written for every k in the matricial form

$$\mathrm{k} \subset [1, \mathrm{N}] : \qquad T.\overset{ŭ}{C}_{\mathrm{k}+1} \;|\; \overset{ŭ}{C}_{\mathrm{k}} \qquad \text{(A9)}$$

$\overset{ŭ}{C}_{\mathrm{k}+1}$ and $\overset{ŭ}{C}_{\mathrm{k}}$ being the column vectors

$$\overset{\mathrm{d}}{C}_{\mathrm{k}+1} \;|\; \begin{pmatrix} C_{1,\mathrm{k}21} \\ C_{2,\mathrm{k}21} \\ C_{3,\mathrm{k}21} \\ @ \\ @ \\ C_{\mathrm{M},\mathrm{k}21} \end{pmatrix} \qquad \overset{\mathrm{d}}{C}_{\mathrm{k}} \;|\; \begin{pmatrix} 0 \\ C_{2,\mathrm{k}} \\ C_{3,\mathrm{k}} \\ @ \\ C_{\mathrm{M}\text{-}1,\mathrm{k}} \\ Q_{\mathrm{k}+1} \end{pmatrix} \qquad \text{(A10)}$$

and T the trigonal matrix of dimension MΔM

$$T \;|\; \begin{pmatrix} 1 & 41 & 0 & & & & 0 \\ 4r_2 & 1\,2\,2r_2 & 4r_2 & & & & \\ 0 & 4r_3 & 1\,2\,2r_3 & 4r_3 & 0 & & \\ & & & & & & \\ & & & & & & 0 \\ & & & & 4r_{\mathrm{M}41} & 1\,2\,2r_{\mathrm{M}41} & 4r_{\mathrm{M}41} \\ 0 & & & & 0 & 0 & 1 \end{pmatrix} \qquad \text{(A11)}$$

To solve eq A9 for every k, values of the components $(Q_{\mathrm{k}})_{\mathrm{k}\lhd[1,\mathrm{N}]}$ of the column vector $\overset{ŭ}{Q}$ are required. $\overset{ŭ}{Q}$ depends on the potential distribution $\left(V(Y_{\mathrm{k}})\right)_{\mathrm{k}\lhd[1,\mathrm{N}]} \;|\; (V_{\mathrm{k}})_{\mathrm{k}\lhd[1,\mathrm{N}]}$ as formulated by eqs 14-17. The potentials $(V_{\mathrm{k}})_{\mathrm{k}\lhd[1,\mathrm{N}]}$ are coupled to the local concentration profiles via the local faradaic current density $\left(j(Y_{\mathrm{k}})\right)_{\mathrm{k}\lhd[1,\mathrm{N}]} \;|\; (j_{\mathrm{k}})_{\mathrm{k}\lhd[1,\mathrm{N}]}$ defined by

$$\mathrm{k} \subset [1, \mathrm{N}] : \qquad j_{\mathrm{k}} \;|\; \frac{2nFDc^1_{\mathrm{Ox}}}{a\div X}\left(C_{\mathrm{M},\mathrm{k}}\;4\;C_{\mathrm{M}41,\mathrm{k}}\right) \qquad \text{(A12)}$$

For every k, the $C_{\mathrm{i},\mathrm{k}}$ are linear with respect to the Q_{k}. Physically, this means that the concentration profile scales with the surface concentration for every position along the surface (i.e., the shape of the profile does not depend on the actual values of c^1_{Ox} and c^1_{R}). Because the local current density is linearly related to the gradient of the concentration at the surface (eq A12), one infers the existence of a linear relationship between the j_{k} and the Q_{k}. Denoting $\overset{ŭ}{j}$ the column vector of components $\left(j_{\mathrm{k}}\right)_{\mathrm{k}\subset[1,\mathrm{N}]}$, we conclude that there is a matrix *A* of dimension NΔN such that

$$\overset{u}{j} \mid A.\overset{u}{Q} \qquad \text{(A13)}$$

Since the components of the matrix *T* only depend on the index i, the constitutive elements of *A* are independent of k. Because of this property, relation A13 allows decoupling of eqs 9-12 (A9) and eqs 14-17, as we shall demonstrate in the following.

Calculation of the matrix A. Let $\wedge$ be a numerical solver that enables the calculation of the searched $\overset{u}{C}_{\mathrm{k}}$ from a known solution $\overset{u}{C}_{\mathrm{k-1}}$ and a given vector $\overset{u}{Q}$

$$\mathrm{k}\subset\left[1,\mathrm{N}\right]: \qquad \overset{u}{C}_{\mathrm{k}} \mid \wedge\left(\overset{u}{C}_{\mathrm{k\text{-}1}},\overset{u}{Q}\right) \qquad \text{(A14)}$$

Iterating k from 1 to N, with $\overset{u}{C}_0 \mid \overset{u}{0}$ as starting solution, we can obtain the $\left(C_{\mathrm{i,k}}\right)_{\mathrm{i}\subset[1,\mathrm{M}],\mathrm{k}\subset[1,\mathrm{N}]}$ and hence the $\left(j_{\mathrm{k}}\right)_{\mathrm{k}\subset[1,\mathrm{N}]}$. The numerical method as subsumed in $\wedge$ for solving the linear algebraic trigonal system (A9) is based on a simple form taken by the classical Gaussian elimination technique with partial pivoting.[28] Let us consider N sets of solutions $\left(\overset{d}{C}{}^{1(\mathrm{n})}_{\mathrm{k}}\right)_{\mathrm{n}\subset[1,\mathrm{N}]}$ verifying

$$\mathrm{n}\subset\left[1,\mathrm{N}\right]: \qquad \overset{d}{C}{}^{1(\mathrm{n})}_{\mathrm{k}} \mid \wedge\left(\overset{d}{C}{}^{1(\mathrm{n})}_{\mathrm{k\text{-}1}},\overset{d}{e}_{\mathrm{n}}\right) \qquad \text{(A15)}$$

where $\overset{u}{e}_{\mathrm{n}}$ are the vectors of the canonical base of dimension N

$$\overset{d}{e}_{\mathrm{n}} \mid \begin{pmatrix} 0 \\ @ \\ 1 \\ 0 \\ @ \\ 0 \end{pmatrix} \begin{matrix} \\ \\ \longleftarrow \text{nth position} \\ \\ \\ \\ \end{matrix} \qquad \text{(A16)}$$

The asterix denotes that the solutions $\left(\overset{d}{C}{}^{1(\mathrm{n})}_{\mathrm{k}}\right)_{\mathrm{n}\subset[1,\mathrm{N}]}$ considered at this stage are not physically relevant: they are only used for the algebraic determination of the matrix *A*. For every n, the column vectors $\overset{u}{j}{}^{1}_{\mathrm{n}}$, of which the components $j^{1(\mathrm{n})}_{\mathrm{k}}$ are defined by

$$j^{1(\mathrm{n})}_{\mathrm{k}} \mid \frac{2nFDc^{1}_{\mathrm{Ox}}}{a\div X}\left(C^{1(\mathrm{n})}_{\mathrm{M,k}}\ 4\ C^{1(\mathrm{n})}_{\mathrm{M\text{-}1,k}}\right) \qquad \text{(A17)}$$

are calculated. Using A13, we have the matricial relations

$\mathrm{n} \subset [1, \mathrm{N}]$: $$\overset{u}{j}{}^{1}_{\mathrm{n}} \mid A.\overset{d}{e}_{\mathrm{n}} \qquad \text{(A18)}$$

Because of the choice made for the $\overset{u}{e}_{\mathrm{n}}$, the vector $\overset{u}{j}{}^{1}_{\mathrm{n}}$ actually represents the nth column of matrix A. One can show that the components of the vector $\overset{u}{j}{}^{1}_{\mathrm{n}}$ are simply shifted with respect to those of the vector $\overset{u}{j}{}^{1}_{\mathrm{n}41}$ so that computation of (A15) for $\mathrm{n} \mid 1$ suffices to generate all of the elements of A. Consequently, A has the particular following trigonal form:

$$A \mid \begin{pmatrix} j^{1(1)}_{1} & 0 & 0 & ? & 0 \\ j^{1(1)}_{2} & j^{1(1)}_{1} & 0 & & 0 \\ j^{1(1)}_{3} & j^{1(1)}_{2} & j^{1(1)}_{1} & \mathrm{B} & @ \\ @ & @ & @ & \mathrm{B} & 0 \\ j^{1(1)}_{\mathrm{N}} & j^{1(1)}_{\mathrm{N-1}} & j^{1(1)}_{\mathrm{N-2}} & ? & j^{1(1)}_{1} \end{pmatrix} \qquad \text{(A19)}$$

Discretization of the Poisson equation: computation of the potential distribution. Discretization of eqs 14-17 leads to

$\mathrm{k} \subset [2, \mathrm{N}\text{-}1]$: $$V_{\mathrm{k}41} \, 4 \, 2V_{\mathrm{k}} \, 2 \, V_{\mathrm{k}21} \, 2 \, \sigma j_{\mathrm{k}} \mid 0 \qquad \text{(A20)}$$

$$4V_1 \, 2 \, V_2 \, 2 \, V_{\mathrm{N}41} \, 2 \, V_{\mathrm{N}} \mid 0 \qquad \text{(A21)}$$

$$V_1 \, 4 \, V_{\mathrm{N}} \, 4 \div \pi_{\mathrm{s}} \mid 0 \qquad \text{(A22)}$$

with σ the constant given by

$$\sigma \mid \frac{2L_0 \div Y^2}{aK^{\mathrm{L}}} \qquad \text{(A23)}$$

Using eq A13, we write the currents j_{k}

$$j_{\mathrm{k}} \mid \overset{\mathrm{N}}{\underset{\mathrm{p}\mid 1}{\text{——}}} a_{\mathrm{k,p}} Q_{\mathrm{p}} \qquad \text{(A24)}$$

with $\left(a_{\mathrm{k,p}}\right)_{\mathrm{k} \subset [1,\mathrm{N}], \mathrm{p} \subset [1,\mathrm{N}]}$ the components of matrix A as determined in the previous section (eq A19) and Q_{k} the functions of V_{k} defined by

$$Q_{\mathrm{k}} \mid \frac{c^{1}_{\mathrm{Ox}} \, 2 \, c^{1}_{\mathrm{R}}}{c^{1}_{\mathrm{Ox}}} \frac{\exp\left[4nf\left(V_{\mathrm{k}} \, 4 \, V^{0}\right)\right]}{1 2 \exp\left[4nf\left(V_{\mathrm{k}} \, 4 \, V^{0}\right)\right]} 4 1 \qquad \text{(A25)}$$

The non-linear system consisting of the N equations A20-A25 has the potentials V_{k} as the only unknown variables. This system was solved using a Newton-Raphson type method.[28] Once the V_{k} are known, the Q_{k} and j_{k} follow from eqs A25 and A24, respectively. The $\overset{u}{C}_{\mathrm{k}}$ and the local concentration profiles are then calculated using eq A14. The ensuing bipolar current I_{f} was obtained by integrating the local faradaic currents by means of the trapezoid method.

Errors inherent to the discrete analysis of the problem

The error made using the inverse Euler method applied to the convective diffusion equation (eqs A5-A7) is of the order $O\left(\div Y 2 \div X^{2}\right)$ and the one made in the finite difference scheme applied to the local electroneutrality equation (eqs A20-A25) is $O\left(\div Y^{2}\right)$.[27,29] The computations were made with $\mathrm{M} \,|\, 10^{4}$ iterations for the X direction and $\mathrm{N} \,|\, 500\,4\,10^{3}$ iterations for the Y direction, which yields convergence of the results within a satisfactory computation time.

Glossary of Symbols

a	Gap of the thin-layer chamber
a_{p}	Particle radius
c_{Ox}	Local concentration of the Ox species
c_{Ox}^{1}	Bulk concentration of the Ox species
c_{R}	Local concentration of the R species
c_{R}^{1}	Bulk concentration of the R species
C_{Ox}	Dimensionless concentration difference for the Ox species
C_{R}	Dimensionless concentration difference for the R species
D_{Ox}	Diffusion coefficient for the Ox species
D_{R}	Diffusion coefficient for the R species
D	Diffusion coefficient $D \,|\, D_{\mathrm{Ox}} \,|\, D_{\mathrm{R}}$
E	Local electric field strength
E_{0}	Applied field in the solution
f	Defined by F / RT
f_{Ox}	Function of the position Y
F	Faraday number
I_{f}	Overall bipolar current
I_{T}	Overall ohmic current
j	Local current density
K^{L}	Conductivity of the electrolyte solution
l	Width of the metallic substrates
Superscript ^	Pertaining to the diffusion limiting-current condition
L_{0}	Length of the metallic substrates

n	Number of electrons
Ox	Oxidized species
R	Reduced species
R	Gas constant
T	Temperature
v_{ef}	Electrophoretic velocity of a particle
v_Y	Velocity flow according to the Y-axis in the thin-layer channel
v^0	Characteristic velocity of the solution in the thin-layer channel
V	Local potential of the solution with respect to the equipotential metallic phase
V^{N}	Nernst potential
V^0	Standard potential for the redox couple Ox/R
V^1	Potential at $Y \mid Y_0$
x, y, z	Cartesian coordinates
X, Y, Z	Dimensionless Cartesian coordinates
Y_0	Position for which $j(Y \mid Y_0) \mid 0$
$\div\pi_{\mathrm{s}}$	Lateral applied potential difference
$\div\pi^{\mathrm{d}}$	Overpotential required for water electrolysis
$\div\pi_{\mathrm{str}}$	Streaming potential
$\div P$	Tangential applied pressure drop
η	Coefficient in the power law $(\div P)^{1/\eta}$
ν	Fraction of the total overpotential that occurs on either side of a bipolar metallic particle
ι	Thickness of the diffusion layer
κ_0	Dielectric permittivity of vacuum
κ_{r}	Relative dielectric permittivity of water
λ	Ratio a / l
ρ	Inverse of the Debye length
ξ	Dynamic viscosity
$ύ_{\mathrm{C}}$	Characteristic convection time
$ύ_{\mathrm{D}}$	Characteristic diffusion time
$ύ_{\mathrm{M}}$	Characteristic time at which the streaming potential measurements are performed
′	Electrokinetic potential (zeta-potential)

References

(1) Longsworth, L. G. In *Electrophoresis: Theory, Methods, and Applications*; Bier M., Ed.; Academic Press: New-York, 1959.

(2) Lyklema, J. In *Fundamentals of Interface and Colloid Science; Volume II: Solid-Liquid Interfaces*; Academic Press: London, 1995; p 4.9.

(3) Lyklema, J. In *Fundamentals of Interface and Colloid Science; Volume II: Solid-Liquid Interfaces*; Academic Press: London, 1995; p 4.54.

(4) Von Helmholtz, H. *Ann. Phys.* **1879**, *7*, 337.

(5) Von Smoluchowski, M. *Bull. Int. Acad. Sci. Cracovie* **1903**, 184. Von Smoluchowski, M. In *Handbuch der Electrizität und des Magnismus*; Graetz, W., Ed.; Barth Leipzig: **1914**; Vol. II, p 366. Von Smoluchowski, M. *Z. Phys. Chem.* **1918**, *92*, 129.

(6) Hückel, E. *Phys. Z.* **1924**, *25*, 204.

(7) Onsager, L. *Phys. Z.* **1926**, *27*, 388.

(8) Lyklema, J. *The Role of Surface Conduction in the Development of Electrokinetics* in *Interfacial Electrokinetics and Electrophoresis*, Delgado, A. V. Ed.; *Surfactant Science Series*, Vol. 106; Marcel Dekker: New York, 2002; Chapter 3.

(9) Hunter, R. J. In *Zeta Potential in Colloid Science. Principles and Applications*. Academic Press: London, 1981.

(10) Dukhin, S. S. *Adv. Colloid Interface Sci.* **1991**, *35*, 173.

(11) Baran, A. A.; Mishchuk, N. A.; Prieve, D. C. *J. Colloid Interface Sci.* **1998**, *207*, 240.

(12) Duval, J.; Huijs, G. K.; Threels, W. F.; Lyklema, J.; van Leeuwen, H. P. *J. Colloid Interface Sci.* **2003**, *260*, 95 (chapter 6 of this thesis).

(13) Baran, A. A.; Babich, Y. A.; Tarovsky, A. A.; Mischuk, N. A. *Colloids Surf.* **1992**, *68*, 141.

(14) Duval, J.; Minor, M.; Cecilia, J.; van Leeuwen, H. P. *J. Phys. Chem. B* **2003**, *107*, 4143 (chapter 7 of this thesis).

(15) Keh, H. J.; Li, W. J. *J. Electrochem. Soc.* **1994**, *141 (11)*, 3103.

(16) Yen, S.-C.;Yao, C.-Y. *J. Electrochem. Soc.* **1991**, *138 (9)*, 2697.

(17) Fleischmann, M.; Ghoroghchian, J.; Pons, S. *J Phys. Chem.* **1985**, *89*, 5530.

(18) Fleischmann, M.; Ghoroghchian, J.; Rolinson, D.; Pons, S. *J. Phys. Chem.* **1986**, *90***,** 6392.

(19) Duval, J. *J. Colloid Interface Sci.* in press (chapter 9 of this thesis).

(20) Van Wagenen, R. A.; Andrade, J. D. *J. Colloid Interface Sci.* **1980**, *76 (2)*, 305.

(21) White, F. M. In *Fluid Mechanics*, second ed.; McGraw-Hill: New-York, 1986.

(22) Duval, J.; Kleijn, J. M.; van Leeuwen, H. P. *J. Electroanal. Chem.* **2001**, *505*, 1 (chapter 5 of this thesis).

(23) Kaplan, W. In *Advanced Calculus*, 2nd ed.; Addison-Wesley: Reading, MA, 1973.

(24) Levich, V. G. In *Physicochemical Hydrodynamics*; Prentice-Hall: Englewood Cliffs, NJ, 1962; p 114.

(25) Leveque, M. A. *Ann. Mines. Mem. Ser.* **1928**, *12/13*, 201.

(26) Lyklema, J. In *Fundamentals of Interface and Colloid Science; Volume II: Solid-Liquid Interfaces*; Academic Press: London, 1995; p 4.27.

(27) Ames, W. F. In *Numerical Analysis of Partial Differential Equations*, third ed.; Academic Press: New-York, 1992.

(28) Press, W. H.; Teukolsky, S. A.; Vetterling, W. T.; Flannery, B. P. In *Numerical Recipes in Fortran, The art of Scientific Computing*; 2nd ed., Cambridge University Press: Cambridge, U. K., 1986.

(29) Dautray, R.; Lions, J. L. In *Analyse Mathématique et Calcul Numérique pour les Sciences et les Techniques*; Vol. 9, Evolution Numérique; Transport, Edition Masson: 1988.

CHAPTER 9

Electrokinetics of the Amphifunctional Metal/Electrolyte Solution Interface in the Presence of a Redox Couple[1]

Jérôme F. L. Duval
Department of Physical Chemistry and Colloid Science, Wageningen University,
Dreijenplein 6, 6703 HB Wageningen, The Netherlands.

Abstract.

Double layers (DL) at amphifunctionally electrified interfaces, such as that of an oxidized metal in aqueous electrolyte solution, arise from the coupling between ionic and electronic surface charging processes. The electronic component enters the double layer formation in the well-known situation where a potential is externally applied. In that case, the DL is fully or partly polarized depending on the possibility of interfacial electron transfer, that is, a faradaic process. This paper reports on the conjunction of the chemical/electrochemical processes at the interface in the case where the solution contains a redox active couple. This allows to polarize/depolarize a DL without the necessity of invoking any external circuit. Streaming potential data obtained for the gold/(Fe(CN)_6^{34} / Fe(CN)_6^{44}, KNO_3) electrolyte interface are analyzed in terms of a recently developed theory which takes into account reversible bipolar faradaic depolarization, the inherent non-linearity of the lateral field and the effects of flow on the rate of the faradaic reactions. It appears that the theory largely overestimates the bipolar currents leading to physically irrealistic ′-potentials. A careful analysis of monopolar voltammetric data reveals quasi-reversible behavior of the redox couple under the typical convective conditions and electrolyte compositions as met in the electrokinetic experiments. Inclusion of reduced reversibility (the extent of which is position-dependent under the streaming-potential measurement conditions) leads to a consistent set of ′-potentials which compare well to the values for the background electrolyte.

Keywords: Faradaic depolarization, redox couple, streaming potential, amphifunctional interface

---

[1] In press, *Journal of Colloid and Interface Science*

Electrokinetics of gold in the presence of a redox couple

1. Introduction

Recent studies [1-4] have extended the classical Gouy-Chapman-Stern double layer model [5-7] to account for the double layer (DL) structure at amphifunctional interfaces between an aqueous electrolyte solution and a partially oxidized conducting phase. The DL at such interfaces results from two mechanisms: (i) protons are adsorbed/desorbed at the surface and/or ions are specifically adsorbed from the background electrolyte onto the surface, and (ii) electrons are injected/withdrawn to/from the conducting phase so as to reach a fixed electrostatic potential or charge imposed via an external circuit (potentiostatic or galvanostatic experiment, respectively). The coupling between the protonic charge (ionic charging process (i)) and the electrostatic charge (electronic charging process (ii)) is non-linear due to the acid/base equilibria taking place at the conducting surface. In the electric modeling of the interface, this was accounted for by introducing a Stern layer type capacitance C_0 between the bare surface of the metal and the plane where ionic charges are localized. Some of the earlier studies focused on the colloidal aspects [3], namely the effects of the electrode polarization on the diffuse double layer potential ψ^{d}, commonly identified to the electrokinetic potential ζ [8], and others analyzed electrochemical features, e.g. the voltammetric responses of amphifunctional electrodes [1] or the ion adsorption isotherms as a function of the applied potential and pH of solution [4].

The electrostatic potential of a conducting metallic substrate can be fixed without any external circuit. Indeed, with an electrochemically reversible redox couple Ox/R present in the solution (with Ox and R standing for the oxidized and reduced forms, respectively), the potential of the metallic phase is fixed at a defined value, the Nernst redox potential E^{N}, given by [9]

$$E^{\mathrm{N}} = E^0 + \frac{RT}{nF}\ln\left(\frac{c_{\mathrm{Ox}}(y=0)}{c_{\mathrm{R}}(y=0)}\right) \tag{1}$$

with R the gas constant, T the temperature and F the Faraday. $c_{\mathrm{Ox}}(y=0)$ and $c_{\mathrm{R}}(y=0)$ denote the surface concentrations (y is the dimension perpendicular to the electrode surface), n the number of electrons e^- involved in the electron transfer reaction

$$\mathrm{Ox} + n\mathrm{e}^- \rightleftharpoons \mathrm{R} \tag{2}$$

E^0 is the standard potential for the redox couple and E^{N} the potential of the metallic phase set against some reference. Electrochemistry has founded the bases to account for the well-defined voltammetric response generated by redox systems [9]. In [10], the occurrence of faradaic processes in the frame of electrokinetic streaming potential measurements was discussed.

The studies reported in the literature [11-16] which aimed at probing double layer properties of conducting substrates upon electric polarization did not consider the possibility of controlling the potential by means of a redox couple in the medium. Introducing this phenomenon is the incentive of this paper, where DL models as presented in [3,4] are discussed in correlation with the electrochemical characteristics of the redox couple considered.

Recently, we reported electrokinetic measurements on gold surfaces in the presence of the couple $\mathrm{Fe(CN)}_6^{34}$ / $\mathrm{Fe(CN)}_6^{44}$ [10]. Using newly developed, rigorous theory accounting for the non-linearity of the lateral electric field as generated in streaming potential measurements [17], determination of the ′ -potentials corresponding to the data in [10] is carried out. Discussion of the results is made in connection with the validity of the hypothesis of electrochemical reversibility for the redox active species under the convective conditions encountered in the electrokinetic experiments.

2. DL model for the partially oxidized metal⁄electroactive electrolyte interface: charging mechanisms

2.1. Situation at the Nernst potential

We consider an amphifunctional interface of the type described in [3] with double layer properties that depend simultaneously on the potential of the metallic phase, denoted as $\ldots^{\mathrm{e}}$, and the pH of the solution. In Figure 1, a schematic representation of such an interface is given. The ions from the background electrolyte, present at concentration c, are supposed not to specifically interact with the amphifuntional surface. Panel A depicts the situation under conditions of “open-circuit potential”, i.e. when the electronic charge ω^{e} is zero. To follow the symbols of [3], all electric potentials and charges pertaining to this situation are written with the subscript pzc$_1$. There is no potential decay across the first Stern layer represented by the capacitance C_0, so that the potential $\ldots^{0}$ at the plane where the oxide groups reside (denoted as op) is $\ldots^{0}_{\mathrm{pzc}_1} \mid \div\pi_{\mathrm{pzc}_1}$, where $\div\pi_{\mathrm{pzc}_1}$ is the total potential drop across the interface. $\div\pi_{\mathrm{pzc}_1}$ depends on the pH or, for that matter, on the surface charge ω^{0} [3]. In the example given, pH { ppzc (ppzc is the pristine point of zero charge) so that the ionic charge ω^{0} at the op is positive and $\div\pi_{\mathrm{pzc}_1} \} 0$. In panel B, a redox couple Ox/R is present in the solution with bulk concentrations c^{1}_{Ox} and c^{1}_{R}. For the sake of simplicity, we shall assume that the indifferent ions are in excess with respect to the electroactive species and that Ox and R do not undergo any protonation and/or complexation reactions in the bulk and/or at the amphifunctional surface. Taking the bulk solution as the reference for the potentials, the redox couple Ox/R imposes that $\ldots^{\mathrm{e}} \mid E^{\mathrm{N}}$ as given by Eq. (1). The corresponding required electronic charge ω^{e} is given by

$$\omega^{\mathrm{e}} \mid C_0\left(E^{\mathrm{N}}\, 4 \ldots^{0}\right) \tag{3}$$

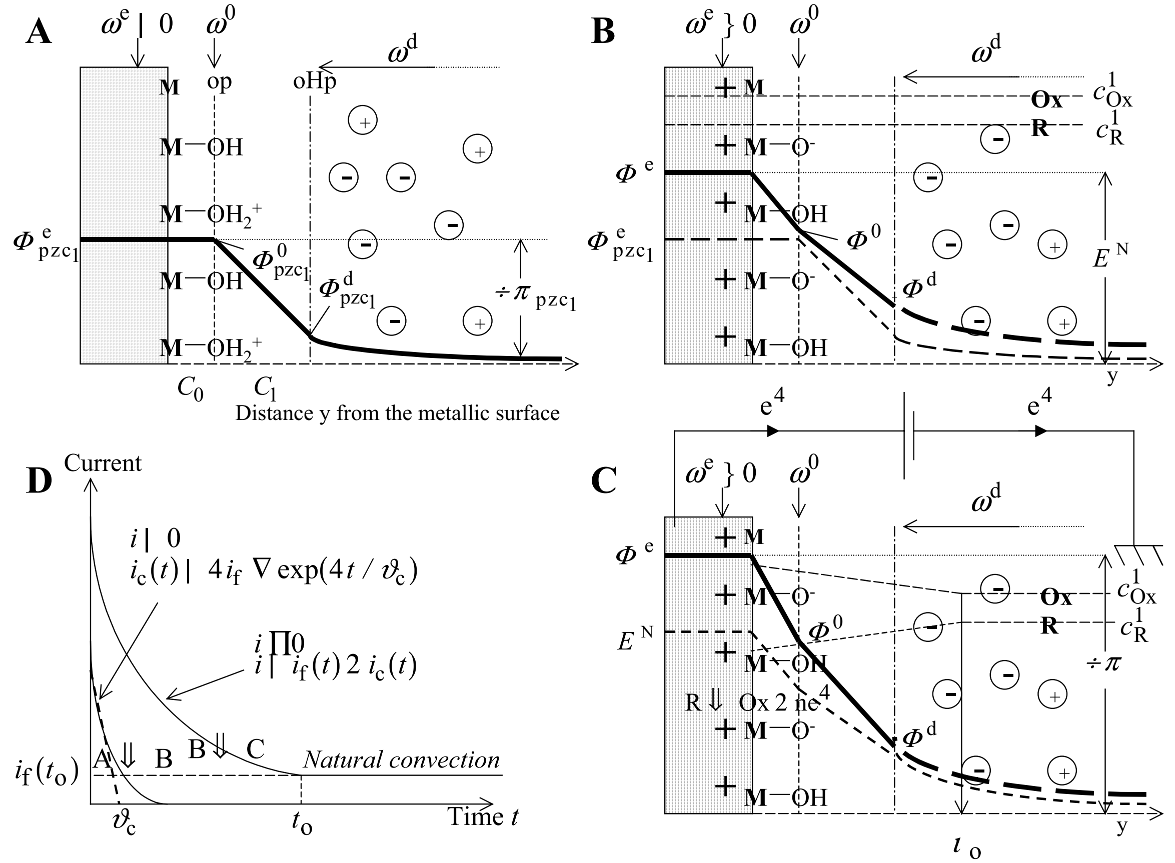
A
$\omega^e \mid 0$
ω^0
ω^d
op
oHp
M
M—OH
M—OH$_2^+$
M—OH
M—OH$_2^+$
$\Phi^e_{\mathrm{pzc}_1}$
$\Phi^0_{\mathrm{pzc}_1}$
$\Phi^d_{\mathrm{pzc}_1}$
$\div\pi_{\mathrm{pzc}_1}$
C_0
C_1
Distance y from the metallic surface
B
$\omega^e \} 0$
ω^0
ω^d
M
M—O$^-$
M—OH
M—O$^-$
M—OH
Ox
R
c^1_{Ox}
c^1_R
Φ^e
$\Phi^e_{\mathrm{pzc}_1}$
Φ^0
Φ^d
E^N
y
e^4
e^4
C
$\omega^e \} 0$
ω^0
ω^d
Φ^e
E^N
Φ^0
Φ^d
R ⇓ Ox 2 ne^4
c^1_{Ox}
c^1_R
$\div\pi$
t_o
y
D
Current
$i \mid 0$
$i_c(t) \mid 4 i_f \nabla \exp(4t/\vartheta_c)$
$i \prod 0$
$i \mid i_f(t)\, 2\, i_c(t)$
$i_f(t_o)$
A ⇓ B
B ⇓ C
Natural convection
ϑ_c
t_o
Time t

Figure 1. Schematic representation of the potential and charge distributions at a partially oxidized metal/electrolyte solution interface. Panel A: absence of a redox couple Ox/R in the solution; Panel B: Ox/R are added in the solution and no external potential is applied across the interface; Panel C: as in B, except that an external potential $\div\pi$ is now applied. For panels B and C, the concentration profiles of Ox and R are sketched. Panel D: capacitive and faradaic currents as a function of time when switching from situation A to B, and from situation B to C. Further information in the text.

We note that in the absence of coupling between the ionic and the electronic charge [2,3] ($C_0 \Downarrow 0$), the potential $..^0$ in Eq. (3) would be replaced by $\div\pi_{\mathrm{pzc}_1}$. For $C_0 \} 0$, variation in ω^e induces changes in ω^0 and hence in the potential $..^0$ at the op, as detailed in [3].

If no redox species are present, the deficit or accumulation of electrons required to charge the DL has to take place externally, usually via an electric circuit. In the situation considered here, the interface is isolated so that the total current i flowing across the interface is zero

$$i \mid i_c\, 2\, i_f \mid 0 \qquad (4)$$

where i_c is the charging (capacitive) current of the double layer and i_f the faradaic current as corresponding to the net rate of electron transfer according to reaction (2). So, in the absence of an external circuit, the faradaic processes are responsible for the DL charging ($i_c \mid 4 i_f$). Considering unstirred solutions and an excess of electroinactive electrolyte ($c \}\} c^1_{Ox}, c^1_R$), transport of the electroactive species Ox and R is controlled by diffusion only. The electron transfer reaction (2) is shifted to the left or to the right when $E^{\mathrm{N}} \} \ldots^{0}$ and $E^{\mathrm{N}} \{ \ldots^{0}$, respectively. For sufficiently long times after adding the redox couple at $t \mid 0$, i.e. for $t \}\} \vartheta_{\mathrm{c}}$ with ϑ_{c} the characteristic time RC_{DL} (R is the charge transfer resistance and C_{DL} the total capacitance of the DL), the DL charging is completed and $i_{\mathrm{f}} \mid 4 i_{\mathrm{c}} \mid 0$. Then, the concentration distributions of Ox and R in the double layer simply follow the Poisson-Boltzmann equation, and diffusion layers vanish. The time scale pertinent to DL charging is in the σs range [18]. The equation of electroneutrality for the complete interphase is then written

$$\omega^{\mathrm{e}}\ 2\ \omega^{0}\ 2\ \omega^{\mathrm{d}} \mid 0 \tag{5}$$

with the diffuse charge ω^{d} given by [8]

$$\omega^{\mathrm{d}} \mid 4\left(8 I \kappa_{0} \kappa_{\mathrm{r}} RT\right)^{1/2} \sinh\left(y^{\mathrm{d}} / 2\right) \mid C_{1}\left(\ldots^{\mathrm{d}}\ 4 \ldots^{0}\right) \tag{6}$$

where C_1 is the capacitance of the outer Helmholtz layer, I the ionic strength, κ_0 and κ_{r} have their usual meaning and y^{d} is the (dimensionless) diffuse double layer potential defined by

$$y^{\mathrm{d}} \mid F \ldots^{\mathrm{d}} / RT \tag{7}$$

ω^{0} is related to the surface potential $\ldots^{0}$ (dimensionless form noted y^{0} defined similarly as in Eq. (7)) by the isotherm

$$\omega^{0}\left(\ldots^{0}\right) \mid eN_{\mathrm{s}} \frac{\left(c^{\leftarrow}_{\mathrm{H}^{2}} / K_{\mathrm{a}_1}\right)\exp\left(4 y^{0}\right) 4 \left(K_{\mathrm{a}_2} / c^{\leftarrow}_{\mathrm{H}^{2}}\right)\exp\left(y^{0}\right)}{1+\left(c^{\leftarrow}_{\mathrm{H}^{2}} / K_{\mathrm{a}_1}\right)\exp\left(4 y^{0}\right) 2 \left(K_{\mathrm{a}_2} / c^{\leftarrow}_{\mathrm{H}^{2}}\right)\exp\left(y^{0}\right)} \tag{8}$$

with e the elementary charge, N_{s} the number of oxide groups per unit area, $c^{\leftarrow}_{\mathrm{H}^{2}}$ the bulk concentration of protons and K_{a_1}, K_{a_2} the constants of the protolytic reactions taking place at the op

$$4\mathrm{MOH}_{2}^{+} \Diamond\ \ 4\mathrm{MOH}\ 2\ \mathrm{H}_{\mathrm{s}}^{2} \qquad (K_{\mathrm{a}_1}) \tag{9a}$$

$$4\mathrm{MOH} \Diamond\ \ 4\mathrm{MO}^{4}\ 2\ \mathrm{H}_{\mathrm{s}}^{2} \qquad (K_{\mathrm{a}_2}) \tag{9b}$$

Equations (1,3,5-9) suffice to describe the potential and charge distributions in the interfacial region. The mechanism according to which the potential $\ldots^{\mathrm{e}}$ is achieved is different from that described in [3] but once the DL is charged, the equations accounting for the double layer properties remain the same. For the sake of illustration, $\ldots^{\mathrm{d}}(\mathrm{pH})$ curves are shown in Figure 2 for different ratios $\chi \mid c^{1}_{\mathrm{Ox}} / c^{1}_{\mathrm{R}}$. With increasing χ, E^{N} increases and the DL potentials are shifted upwards. The electronic charge ω^{e} increases, which induces a shift of the equilibria (9a,b) to the right and hence lowers the surface and diffuse charges ω^{0} and ω^{d} [3]. At given (χ, pH), charge-determining anions (OH^4) have to be added to reach the new isoelectric point (iep) ($\ldots^{d} = 0$). The arrow in Figure 2 illustrates this. The trends for the surface potential $\ldots^{0}$ are similar to those for $\ldots^{d}$ (not shown).

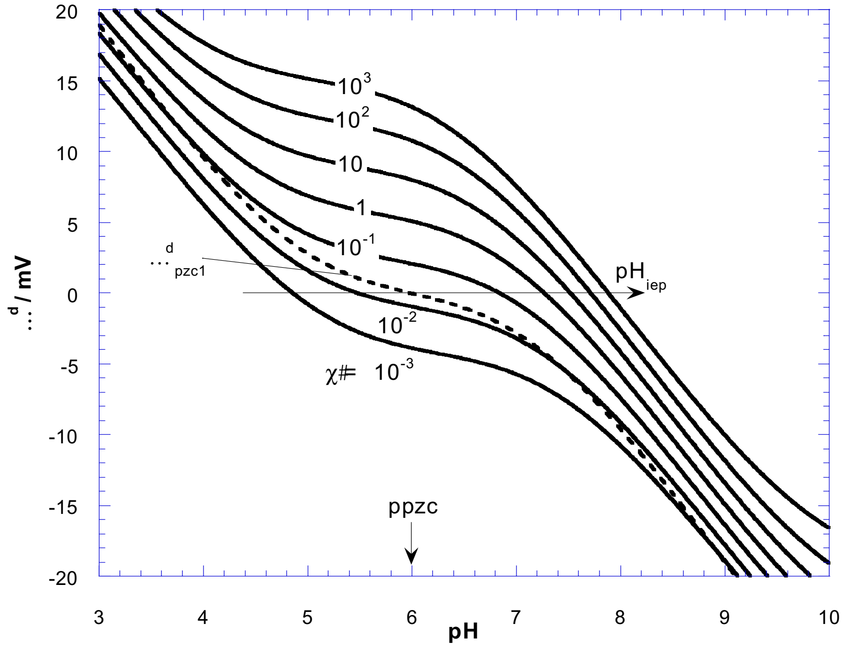

Figure 2. Double layer potential as a function of the pH solution and the ratio $\chi | c^{1}_{\mathrm{Ox}} / c^{1}_{\mathrm{R}}$ calculated according to the DL model represented in Figure 1B. Model parameters are as follows: $\mathrm{p}K_{\mathrm{a}_1} | 4$, $\mathrm{p}K_{\mathrm{a}_2} | 8$, $C_0 | 5\sigma\mathrm{F\ cm}^{-2}$, $C_1 | 30\sigma\mathrm{F\ cm}^{-2}$, $c | 0.1$ M, $N_{\mathrm{s}} | 2\Delta 10^{13}$ sites cm^{-2}, $E^{0} | 100$ mV (versus the bulk solution), $n | 1$.

2.2. Faradaic depolarization

In this section, we consider the situation where the metallic phase is connected to an external circuit and a potential step of amplitude $\div\pi$ is applied with respect to a reference electrode (Figure 1C). Before this application, the potential of the metallic phase, E^{N}, was fixed by the redox couple Ox/R, as discussed in 2.1. Now the total current i is not zero: the charging current i_{c} of the DL decays exponentially with time (time constant ϑ_{c}) and the faradaic current i_{f} varies according to the power law $t^{41/2}$ [9]. Beyond a certain time t_{o} }} ϑ_{c}, corresponding to a significant thickness ι_{o} of the built diffusion layer ($\iota_{\mathrm{o}} | \left(\phi D t_{\mathrm{o}}\right)^{1/2}$), natural convection maintains a given surface concentration gradient for Ox and R, as corresponding to the finite current $i_{\mathrm{f}}\left(t \varnothing t_{\mathrm{o}}\right)$ (Figure 1D). The interface is then depolarized by the ongoing faradaic process (oxidation of R in the example given in Figure 1C). Within the assumptions made in section 2.1, the DL properties still follow Eqs. (1,3,5-9) after replacing E^{N} by $\div\pi$. Provided the usual condition ι_{o} }} ρ^{41} (ρ^{41} is the Debye length) is satisfied, the surface concentrations of Ox and

R are effectively those beyond the DL and are determined by Eq. (1) and the mass balance equation

$$D_{\mathrm{Ox}}\frac{\mathrm{d}c_{\mathrm{Ox}}}{\mathrm{d}y}\bigg|_{y|\,0} \;|\; 4D_{\mathrm{R}}\frac{\mathrm{d}c_{\mathrm{R}}}{\mathrm{d}y}\bigg|_{y|\,0} \qquad (10)$$

where D_{Ox} and D_{R} are the diffusion coefficients for Ox and R, respectively. If convection is imposed, as in the frame of some electrokinetic experiments [10] or voltammetric analyses at rotating disc electrodes [9], the steady-state diffusion profiles of Ox and R are established for shorter t_{o} although $\iota_{\mathrm{o}} \}\} \rho^{41}$ is maintained. The situation where Ox/R may interact with the amphifunctional surface will be discussed in section 4, for the particular case of the interface between gold and an electrolyte solution containing the redox couple $\mathrm{Fe(CN)}_6^{34}/\mathrm{Fe(CN)}_6^{44}$.

3. Streaming potential/pressure dependencies for metal/electrochemically reversible electrolyte solution interfaces

3.1. Reversible faradaic depolarization in electrokinetics: non-linearity of the streaming-potential/pressure plots

The role of faradaic depolarization processes under conditions of electrokinetic experiments performed on conducting surfaces in a thin-layer cell [19] has recently been discussed [10]. For (electrochemically) irreversible interfaces, linearity between streaming potential and applied pressure is found over a limited range of potential differences. Calculation of the corresponding zeta-potential may be performed using the classical linear Helmholtz-Smoluchowski (H-S) equation [20-21]. If the solution between the two conducting surfaces contains a redox couple, and a lateral potential is either externally applied in the solution across the cell [22] or generated by tangential hydrodynamic flow [10,17], faradaic depolarization takes place. The potential distribution in the thin solution layer adjacent to the surfaces leads to reduction of Ox at one side of the surface and oxidation of R at the other. The conducting substrate then behaves as a bipolar electrode [23] and a net faradaic current I_{f} flows, as determined by the interfacial electron transfer reaction (2) of the redox components. The steady state streaming current, generated upon application of a pressure gradient $÷P$, is balanced by the countercurrent, which now contains an electronic contribution. The resulting streaming potential $÷\pi_{\mathrm{str}}$ is defined by the H-S equation, extended with a bipolar conductance term [17]

$$\frac{\kappa_0\kappa_{\mathrm{r}}'\,÷P}{\xi} \;|\; L_0K^{\mathrm{L}}\frac{∈÷\pi(x,÷\pi_{\mathrm{str}},÷P)}{∈x}\bigg|_{x|\,x_0} \;2\frac{L_0}{al}I_{\mathrm{f}}\left(÷\pi_{\mathrm{str}},÷P\right) \qquad (11)$$

where we have ignored any surface conduction. x is the dimension parallel to the surfaces of length L_0 and width l. x_0 is the position at which $\div\pi(x \mid x_0, \div\pi_{\mathrm{str}}, \div P) \mid E^{\mathrm{N}}$, with $\div\pi(x, \div\pi_{\mathrm{str}}, \div P)$ the potential of the conducting surface with respect to the solution at the position x in the electric and hydrodynamic conditions $(\div\pi_{\mathrm{str}}, \div P)$. The distance between the two metallic electrodes in the flat capillary cell is a and K^{L} is the specific bulk conductivity. For a fully reversible redox system, a first order analysis based on the assumption of a linear potential profile along the cell provides an approximate but generally oversimplified analytical expression for I_{f} as a function of $\div\pi_{\mathrm{str}}$ and $\div P$ [10]. Rigorous estimation of I_{f} requires numerical treatment of the coupled Nernst-Planck equation, describing the lateral convective and transversal diffusive transports of the Ox/R species, and the Poisson equation, which relates the potential and local faradaic current distributions in the solution. The theory reported in [17] is valid for steady state situations under the assumption that there is a sufficiently large excess of indifferent ions over the reversible redox species (as assumed in section 2) to render the latter insignificant for the DL composition. I_{f} is a function of a, K^{L} and the redox concentrations c^1_{Ox}, c^1_{R}. Figure 3 shows typical $\div\pi_{\mathrm{str}}$-$\div P$ plots obtained by combining Eq. (11) with the analysis given in [17] for the computation of I_{f}. The results are shown for different redox concentrations $c^1 \mid c^1_{\mathrm{Ox}} \mid c^1_{\mathrm{R}}$ assu-

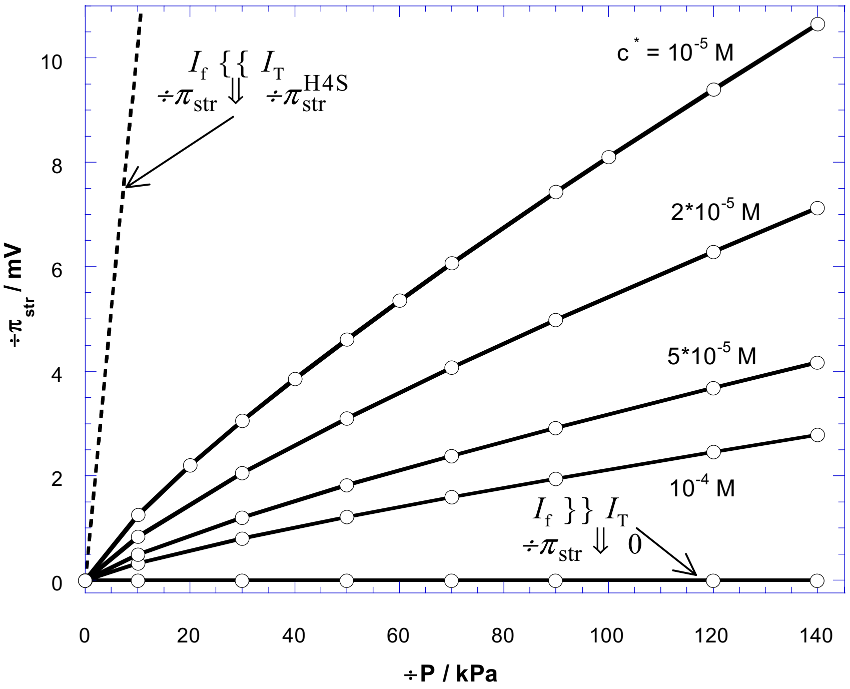

Figure 3. Reconstruction of $\div\pi_{\mathrm{str}}$-$\div P$ plots (points) for different redox concentrations $c^1 \mid c^1_{\mathrm{Ox}} \mid c^1_{\mathrm{R}}$ (indicated) ($K^{\mathrm{L}} \mid 0.1\ \mathrm{T}^{-1}\ \mathrm{m}^{-1}$, $\acute{} \mid 150$ mV). The corresponding curve calculated on the basis of the H-S equation (dashed line) is indicated. Other model parameters used for the computation of I_{f} [17]: $a \mid 1$ mm, $L_0 \mid 7.6$ cm, $l \mid 2.6$ cm, $D_{\mathrm{Ox}} \mid D_{\mathrm{R}} \mid 5\Delta10^{410}\ \mathrm{m}^2\ \mathrm{s}^{-1}$, $E^0 \mid 70$ mV (with respect to bulk solution).

ming a certain value for the ′ -potential. For a given $\div P$, the increase in c^1 results in an increase of the current I_f, which lowers $\div\pi_\mathrm{str}$. Consequently, important deviations from the streaming potential behavior predicted by the linear H-S equation (denoted $\div\pi_\mathrm{str}^\mathrm{H4S}$) in which no faradaic depolarization is taken into account, are observed over the complete pressure range. The two limiting cases are provided by $I_\mathrm{f} \{\{ I_\mathrm{T}$ ($\div\pi_\mathrm{str}(\div P) \Downarrow \div\pi_\mathrm{str}^\mathrm{H4S}(\div P)$) and $I_\mathrm{f} \}\} I_\mathrm{T}$ ($\div\pi_\mathrm{str}(\div P) \Downarrow 0$), where I_T is the ohmic conduction current. Similar conclusions hold when increasing K^L at constant redox concentrations.

3.2. Procedure for the calculation of ′ -potentials from experimental $\div\pi_\mathrm{str}$ - $\div P$ data

In [17], we demonstrated from the rigorous analysis of the potential and pressure dependence of I_f the existence of two distinct pressure regimes for the behavior of the streaming potential $\div\pi_\mathrm{str}$. For low pressures $\div P\,\Omega \div P_0$ (a typical order of magnitude for $\div P_0$ is a few hundreds of Pa), I_f increases steeply upon increase of $\div P$ and obeys the power law

$$I_\mathrm{f} \nabla \div P^{1/3} \tag{12}$$

The potential in the solution then drops linearly along the cell. The inadequacy of Eq. (12) for the pressure-regime $\div P \varnothing \div P_0$ is explained by the reversible nature of the bipolar process which renders the assumption of a constant electric field in the solution invalid. For $\div P \varnothing \div P_0$, the dependence of I_f on $\div P$ becomes

$$I_\mathrm{f} \nabla \div P^{1/\eta} \tag{13}$$

with $\eta \} 3$. Under the conditions of the numerical simulations presented in [17], $\eta - 5$ to 6. There is a pressure range $[\div P_1, \div P_2]$, where $\div P_1, \div P_2 \} \div P_0$ and for which, Eq. (13) can be appropriately approximated by a linear function of $\div P$

$$I_\mathrm{f} \nabla \div P \tag{14}$$

The $\div P$ range commonly applied in streaming potential experiments complies with the condition $\div P \} \div P_0$. Therefore, in the low potential and high-pressure regimes, the bipolar current depends linearly on the streaming potential or, for that matter, on the applied pressure gradient. Hence, the bipolar conductance term and the slope $\div\pi_\mathrm{str} / \div P$ tend to a constant value (see Figure 3). In passing we note that under certain experimental conditions $\left(K^\mathrm{L}, c_\mathrm{Ox}^1, c_\mathrm{R}^1\right)$ leading to faradaic depolarization, the corresponding $\div\pi_\mathrm{str}(\div P)$ plot may be fitted to a straight line for the complete pressure regime (Figure 3). In this situation, which could incorrectly lead to using the linear H-S equation, the pressure $\div P_1$ is so low that the bipolar conductance term, significant with respect to the ohmic and/or surface conductance contributions, appears as constant for the all pressures experimentally considered. Practically, faradaic depolarization is detectable by checking if a linear fit of the measured $\div\pi_{\text{str}}\left(\div P\right)$ curve rigorously yields a non-zero intercept at $\div P \mid 0$.

As a result of the pressure dependencies of I_{f} on $\div P$ (Eqs. (12-14)), the $\div\pi_{\text{str}}\left(\div P\right)$ curves develop a bend for $\div P_0 \;\{\; \div P \;\{\; \div P_1$. Considering the peculiarities of the $\left(\div\pi_{\text{str}}, \div P\right)$ plots outlined above, calculation of the $'$-potential can simply be carried out in the high pressure-regime ($\div P \varnothing \div P_1$) using the relation

$$' \mid \frac{\xi L_0}{\kappa_0 \kappa_{\text{r}}} \left(\frac{K^{\text{L}}}{\div P} \frac{\in \div\pi(x)}{\in x} \bigg|_{x \mid x_0} \quad 2\,\frac{\nu}{al} \right) \tag{15}$$

where the constant $\nu \mid I_{\text{f}} / \div P$ is determined after computation of the current I_{f} for the different $\left(\div\pi_{\text{str}}, \div P\right)$ measured. For $\div P \varnothing \div P_1$, the bipolar current carried by the reversible redox system is that high that the first term into brackets in Eq. (15) can be neglected (see Figure 4, next section). We emphasize that ν does depend on K^{L}: the higher K^{L}, the higher the local potentials $\div\pi(x)$ along the surfaces and the higher I_{f} or ν.

3.3. Spatial distribution of $'$ along the surface

In a thin-layer cell, the local potential $\div\pi$ of the conducting phase with respect to the solution varies along the metallic surface and is therefore a function of the lateral position x (Figure 4). The distribution $\div\pi(x)$ is dictated by the spatial course of the electric field as governed by the local faradaic current density [17], and thus by convective-diffusive mass transport of Ox and R. At given bulk solution composition, the potential distribution is a function of $\div P$ and the total potential span along the electrode, i.e. $\div\pi_{\text{str}}$. One can therefore write the spatial distribution of the potential explicitly as $\div\pi\left(x, \div\pi_{\text{str}}, \div P\right)$ (see Eq. (11)). As discussed in section 2, the potential at the outer Helmholtz plane $y^{\text{d}} \sum F' / RT$ depends on the total potential drop $\div\pi$ applied across the interface. This would suggest that, at given $\left(\div\pi_{\text{str}}, \div P\right)$, there is a spatial distribution of y^{d} and ω^{d} (see Eq. (6)) along the surface and that the electrokinetic potential and electrokinetic charge $\omega^{\text{ek}} - \omega^{\text{d}}$ as yielded by the experiments are averaged over the ensemble of local double layer situations. Starting from the diffusive charge (extensive parameter),

$$\{\; \omega^{\text{d}}\left(\div\pi_{\text{str}}, \div P\right) \;\}\mid \frac{1}{L_0} \int_{4 L_0/2}^{L_0/2} \omega^{\text{d}}\left(\div\pi\left(x, \div\pi_{\text{str}}, \div P\right)\right) \mathrm{d}x \tag{16}$$

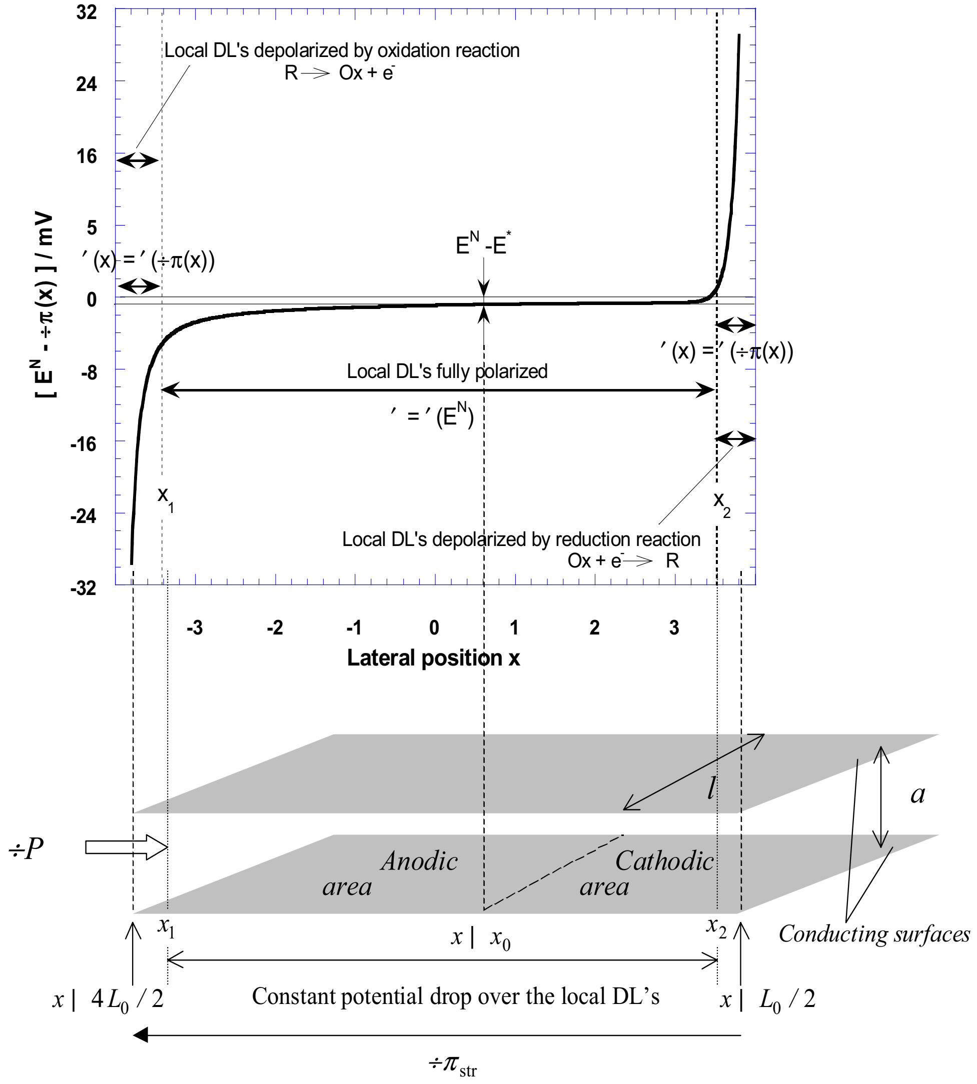

Figure 4. Typical potential distribution calculated from the experimental data of Ref. [10]. Ionic strength $I\,|\,1.2$ mM, $c^{1}_{\mathrm{Ox}}\,|\,c^{1}_{\mathrm{R}}\,|\,0.01$ mM ($K^{\mathrm{L}}\,|\,$ 0.015 T^{-1} m^{-1}), pH | 5.6, $\div P\,|\,30$ cm Hg, $\div\pi_{\mathrm{str}}\,|\,$ 458.7 mV. Other parameters for computing I_{f}: $a\,|\,$ 0.2 mm, $D_{\mathrm{Ox}}\,|\,D_{\mathrm{R}}\,|\,1.85\Delta 10^{410}$ m^2 s^{-1} (value determined in [10]), otherwise as in Figure 3.

In Figure 3, reconstruction of the $\div\pi_{\mathrm{str}}$-$\div P$ plots was carried out by assuming that the ′-potential remains constant for the all potential and pressure ranges considered. A priori, this assumption is in contradiction with Eq. (16). However, a closer look at the spatial potential distribution calculated for the $\div P$-range typically met in electrokinetic experiments (Figure 4) shows that over practically the whole x-range the potential $\div\pi(x)$ remains constant and barely deviates from the potential at which there is no (local) faradaic current, denoted E^{1}. The corresponding position is x_0. E^{1} depends on the hydrodynamic and electric conditions and may differ from E^{N}. Nevertheless, for the pressures and streaming potentials considered, we have here $E^{1} - E^{\mathrm{N}}$ (see [17] for further detail). Only at the extremities, deviations, as caused by significant local faradaic currents, are encountered and the amplitudes of these are predominantly determined by the magnitude of $\div\pi_{\mathrm{str}}$. Using relation (6), the integral of Eq. (16) can therefore be split up as follows

$$\{\,'\left(\div\pi_{\mathrm{str}},\div P\right)\}| \;\frac{2RT}{L_0F}\sinh^{41}\left\{(x_2\,4\,x_1)\sinh\left[\frac{y^{\mathrm{d}}\left(E^{\mathrm{N}}\right)}{2}\right]2\int_{4L_0/2}^{x_1}\sinh\left[\frac{y^{\mathrm{d}}\left(\div\pi\left(x,\div\pi_{\mathrm{str}},\div P\right)\right)}{2}\right]\mathrm{d}x\right.$$

$$\left.2\int_{x_2}^{L_0/2}\sinh\left[\frac{y^{\mathrm{d}}\left(\div\pi\left(x,\div\pi_{\mathrm{str}},\div P\right)\right)}{2}\right]\mathrm{d}x\right\} \qquad (17)$$

where the positions x_1 and x_2 are indicated in Figure 4. The (constant) electrokinetic potential $y^{\mathrm{d}}\left(E^{\mathrm{N}}\right)$ for $x\subset\left[x_1,x_2\right]$ depends on E^{N} according to a DL model as presented in section 2.1 (no faradaic depolarization). The functionality $y^{\mathrm{d}}\left(\div\pi\right)$ at the extremities of the surfaces is determined by a DL model of the type given in section 2.2 (faradaic depolarization). The two integrals of Eq. (17) are insignificant as compared to the first term in the brackets because $x_2\,4\,x_1-L_0$. Depending on the magnitude of the quantity $\mathrm{pH}-\mathrm{pH}_{\mathrm{iep}}$ and/or the potential E^{N} we may additionally have

$$\left|\div\pi\left(x\subset\left[4L_0/2,x_1\right]\right)\right|,\left|\div\pi\left(x\subset\left[x_2,L_0/2\right]\right)\right|\{\;\left|\div\pi_{\mathrm{str}}\right|\{\{\;\left|E^{\mathrm{N}}\right| \qquad (18)$$

which further legitimates the neglection of the two integral terms in Eq. (17).
The presumption of a constant $'$ for different $\left(\div\pi_{\mathrm{str}},\div P\right)$ is therefore justified and one may write

$$\{\,'\left(\div\pi_{\mathrm{str}},\div P\right)\}-\,'\left(E^{\mathrm{N}}\right) \qquad (19)$$

3.4. Validity of the theory for gold/(Fe(CN)$_6^{34}$ / Fe(CN)$_6^{44}$, KNO$_3$) interface

The potential E^{N}, as fixed by the redox species, was measured for given sets of redox concentrations $c_{\mathrm{Ox}}^{1}/c_{\mathrm{R}}^{1}$ (Figure 5) and various pH, and was found to be in good agreement with Eq. (1), with $E^{0}-190\,\partial\,10$ mV with respect to a (Hg$_2$Cl$_2$/ Hg, KCl) reference electrode and $n\,|\;1$. Within experimental error, this value is also in line with potentiometric measurements performed on a rotating gold disc electrode (not shown). Several other redox couples were investigated but $\mathrm{Fe(CN)}_6^{34}/\,\mathrm{Fe(CN)}_6^{44}$ came closest in fulfilling the criterion of reversibility with respect to gold in the time-window of cyclic voltammetric experiments [10]. Figure 5 highlights that protonation of the redox species in the bulk solution is not significant in the range pH > 4-4.2. The open circuit values $\div\pi_{\mathrm{pzc}_1}(\mathrm{pH})$ for gold in the absence of redox compounds are also re-

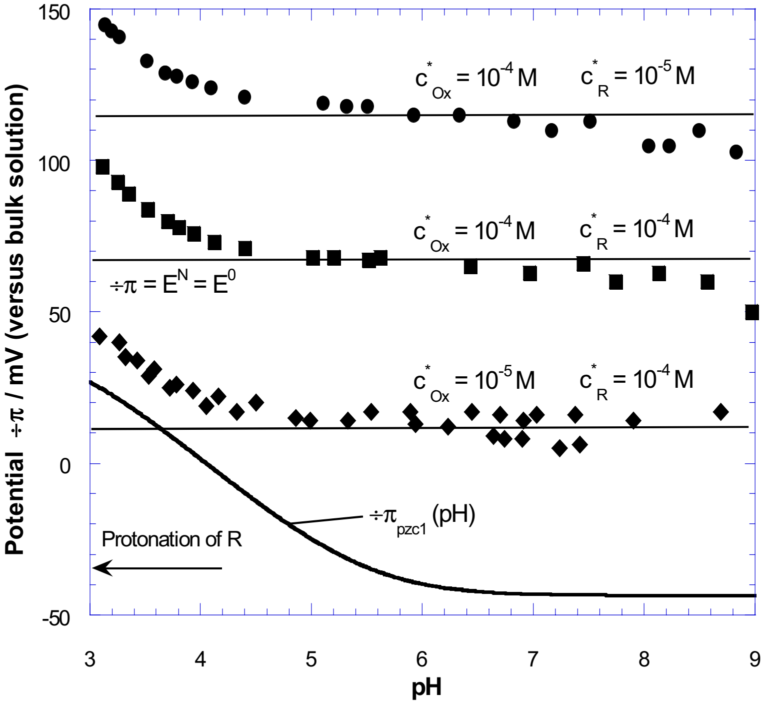

Figure 5. Open circuit potentials for gold in the absence of redox couple (plain curve) and in the presence of redox couple (points).

ported for illustration in Figure 5. These values were calculated as discussed in section 2 $\left(C_0 \Downarrow 0\right)$ on the basis of the parameters $\left(N_\mathrm{s}, \mathrm{p}K_{\mathrm{a}_1}, \mathrm{p}K_{\mathrm{a}_2}\right)$ determined from electrokinetic data obtained in the absence of a redox couple for the same gold surfaces. Experimental evidence for the amphifunctional nature of gold has recently been put forward by atomic force measurements (AFM) [16]. The ensuing double layer potentials as a function of pH solution (and externally applied potentials) are consistent with the data of [10] even though slightly different $\left(N_\mathrm{s}, \mathrm{p}K_{\mathrm{a}_1}, \mathrm{p}K_{\mathrm{a}_2}\right)$ parameters and isoelectric point were found. The different cleaning procedures adopted for the surfaces may account for such discrepancies. Particularly, the potentials $\div\pi_{\mathrm{pzc}_1}(\mathrm{pH})$, as measured by AFM, could be well described, using the corresponding $\left(N_\mathrm{s}, \mathrm{p}K_{\mathrm{a}_1}, \mathrm{p}K_{\mathrm{a}_2}\right)$ values, with the amphifunctional DL model discussed in detail in [3]. For DL calculations, the bulk solution is taken as the reference for the potential. In Ref. [16], the potential of the (Ag⁄AgCl, KCl) reference electrode with respect to the "bulk (10^{-3} M) $\mathrm{KNO_3}$ solution" $\div\pi_{\mathrm{Ag/AgCl4\,bulk}}$ was indirectly determined and estimated $\div\pi_{\mathrm{Ag/AgCl4\,bulk}} - 150$ mV. Assuming $\div\pi_{\mathrm{Ag/AgCl4\,bulk}}$ is not significantly perturbed by the presence of the redox species and the concentration of indifferent ions, one concludes that $E^0(\mathrm{Fe(CN)}_6^{34} / \mathrm{Fe(CN)}_6^{44} \text{at gold}) - 70 \partial 10$ mV with respect to the bulk solution.

Electrokinetics of gold in the presence of a redox couple

From the raw electrokinetic data reported in [10] for the gold/$(\mathrm{Fe(CN)}_6^{34}$/ $\mathrm{Fe(CN)}_6^{44}$, KNO_3) interface, ´-potentials were calculated using Eq. (15). Assuming reversible electron transfer, the pressure above which linearity of the $\div\pi_{\mathrm{str}}(\div P)$ curves is observed is $\div P_1 - 10$ cm Hg (Figure 6). The insignificance of the surface conduction term in the non-linear H-S equation is justified by the low surface area of the gold wafers (7.6 Δ 2.6 cm^{-2}) and the relatively high ionic strength of the electrolyte used. The computed ´-potentials are of the order of several hundreds of mV and values above 1V were found for the higher redox concentrations (c^1 | 10^{43} M). Although the $\div\pi_{\mathrm{str}}(\div P)$ plots present two distinct regimes (low and high pressures) as predicted by the theory, the calculated zeta-potentials are obviously unrealistic, meaning that the bipolar current must have been largely overestimated. The discrepancy between theoretical expectation and experimental observation was found after careful examination of the typical faradaic current density distribution along the surface in terms of the corresponding electrodic reaction rates under the convective conditions in the electrokinetic cell.

4. Impact of $\mathrm{Fe(CN)}_6^{34}$/ $\mathrm{Fe(CN)}_6^{44}$ on electrokinetics at gold

4.1. Reversibility features of the system $\mathrm{Fe(CN)}_6^{34}$/ $\mathrm{Fe(CN)}_6^{44}$ on gold under electrokinetic conditions

In Figure 7, the spatial distribution of the current density $j(x)$ along the laterally polarized gold surface is given for different pressures. The resulting bipolar current I_{f} is given by the integrals of $j(x)$ over the cathodic $(x \} x_0)$ or anodic area $(x \{ x_0)$. So as to comply with the condition of no charge accumulation in the cell, these two integrals must be equal. Roughly speaking, when increasing the pressure drop $\div P$, the thickness of the diffusion layer of the redox species at the position *x*, denoted as $\iota(x)$, decreases and the ensuing local current density $j(x)$ increases. As detailed in [17], one finds the largest j at the entrance of the capillary (x | $4L_0/2$). This position corresponds to the strongest electric field strengths and the lowest ι. Due to the power dependence of ι on *x*, the distribution of $j(x)$ is strongly asymmetric with respect to the position half-way the surface (x | 0). In the context of monopolar cyclic voltammetry, it is well established that systems may yield a reversible response at small scan rate τ, i.e. when the time window of the experiment is large (see Ref. [10]) while at larger scan rates (short times), the finite rate of interfacial electron transfer becomes more and more limiting.

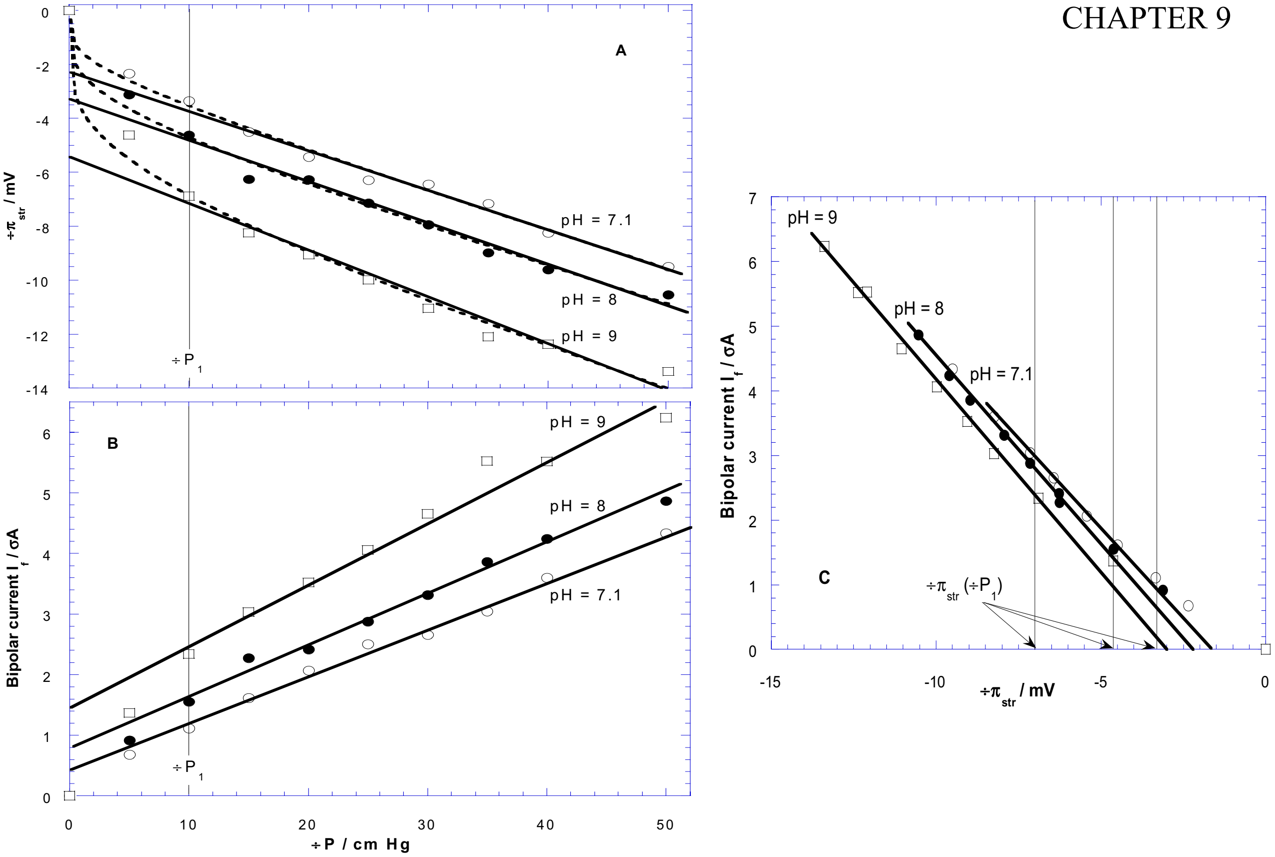

Figure 6. (A) Experimental $\div\pi_{\mathrm{str}}$-$\div P$ plots measured for gold in the presence of Fe(CN)$_6^{34}$/ Fe(CN)$_6^{44}$ redox couple at three different pH [10]. The dashed curves are only guide for the eyes. Ionic strength $I\,|\,12$ mM, $c^1_{\mathrm{Ox}}\,|\,c^1_{\mathrm{R}}\,|\,0.1$ mM ($K^{\mathrm{L}}\,|\;0.15$ T^{-1} m^{-1}). (B) Calculated bipolar current I_{f} (corresponding to the experimental data and conditions of panel A) as a function of the applied pressure $\div P$. (C) I_{f} as a function of the measured streaming potential $\div\pi_{\mathrm{str}}$. Other model parameters for calculating I_{f} [17]: as in Figure 4. In (A), (B) and (C), the solid lines represent linear regressions of the data for $\div P \varnothing 10$ cm Hg (1cm Hg = 1333.22 Pa).

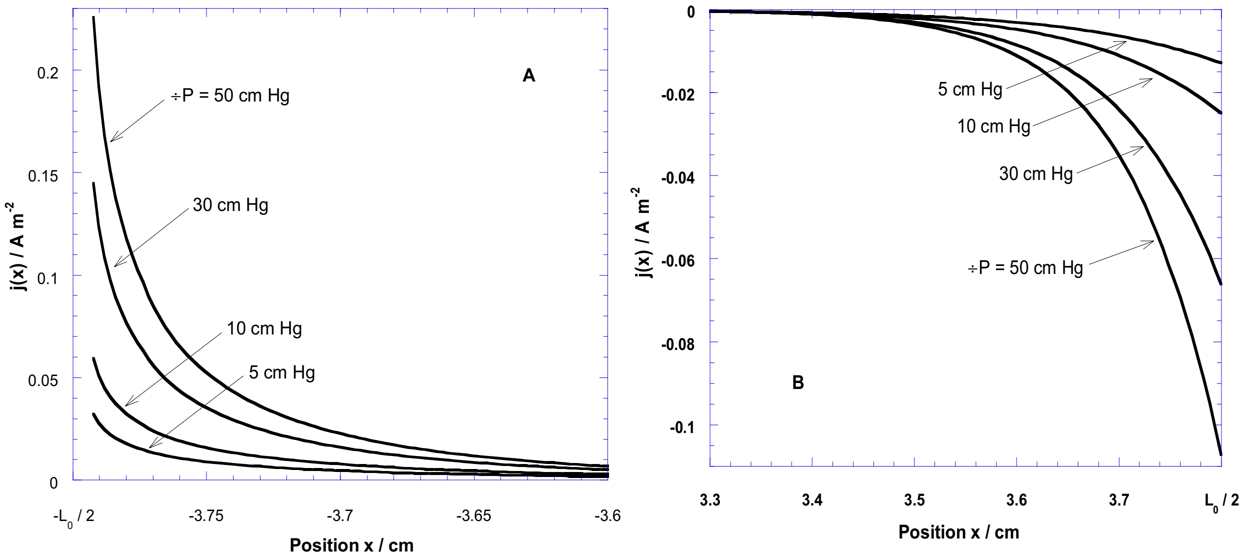

Figure 7. Spatial distribution of the current density $j(x)$ at different pressures $\div P$ as computed within the assumption that the redox system is nernstian. Same parameters as in Figure 6 with $\mathrm{pH}\,|\,8$. Panel A: oxidation current. Panel B: reduction current.

Under the extreme convective conditions in the pressure range $\div P\,|\,$ 5-50 cm Hg, the reversibility criterion is rather severe and we checked whether it is fulfilled by the system $\mathrm{Fe(CN)_6^{34}}$/ $\mathrm{Fe(CN)_6^{44}}$ on gold. For that purpose, cyclic voltammograms were recorded for different sets of concentrations c and c^1 at different τ. Typical results are reported in Figure 8. The difference between the anodic and cathodic peak potentials, denoted as $\div\pi_{\mathrm{p_a}}$ and $\div\pi_{\mathrm{p_c}}$ respectively, is a useful diagnostic test to verify if a reaction is nernstian or not. For a reversible system with $n\,|\,1$, we have $\div\pi_{\mathrm{p}}\,|\,\div\pi_{\mathrm{p_a}}\,4\,\div\pi_{\mathrm{p_c}} - 58$ mV [9]. For very large excess of background electrolyte (Figure 8A), the voltammetric response is nernstian. When decreasing the ionic strength and

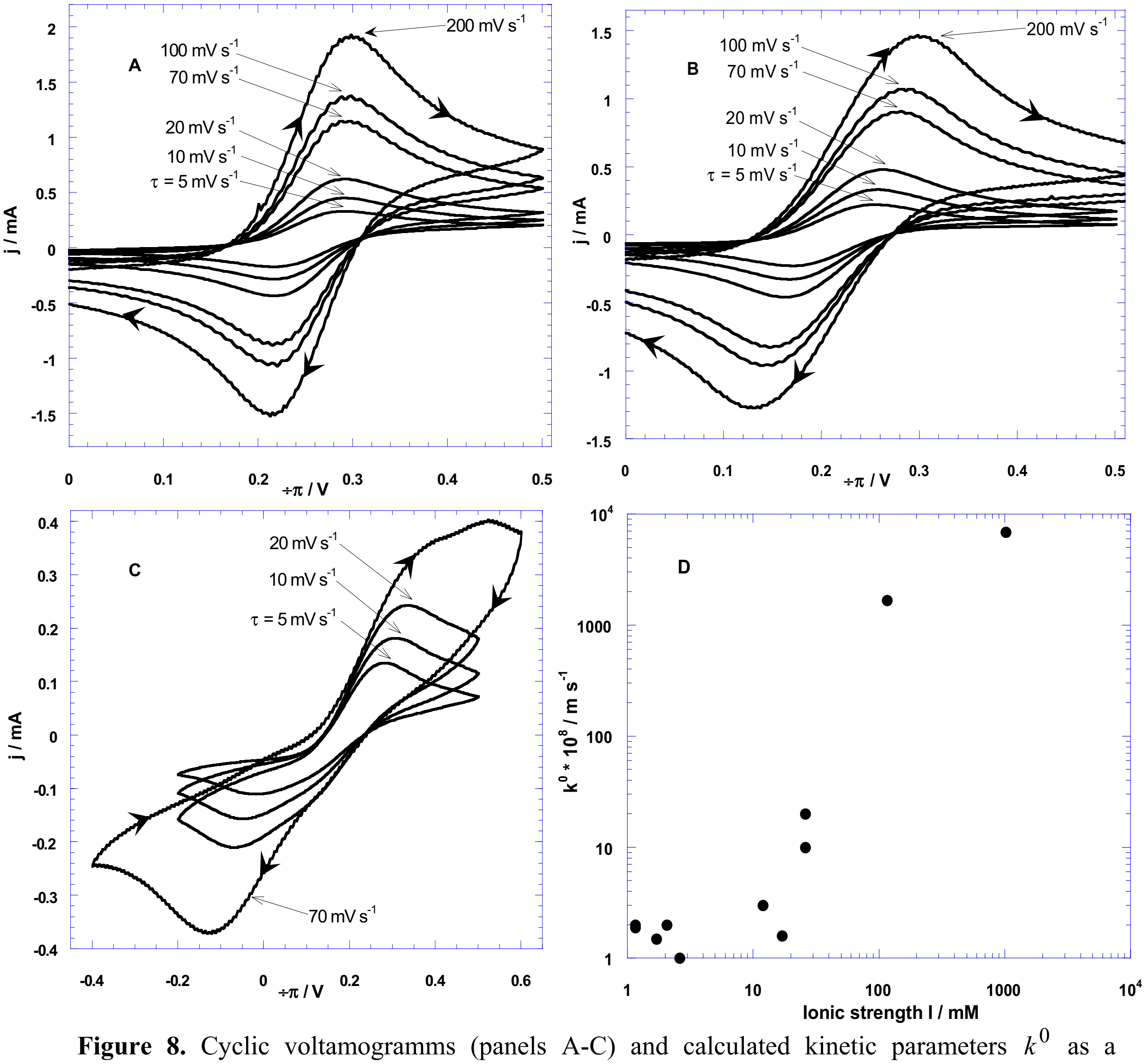

Figure 8. Cyclic voltamogramms (panels A-C) and calculated kinetic parameters k^0 as a function of the ionic strength I (panel D). Electrolyte composition: $c^1\,|\,10^{43}$ M and $c\,|\,1$ M (A), $c\,|\,10^{41}$ M (B) and $c\,|\,10^{42}$ M (C). The potential $\div\pi$ is applied with respect to the Ag/AgCl, KCl reference electrode. Electrode surface Area − 3.1 cm^2 (A and B), 2.3 cm^2 (C).

increasing τ (Figures 8B-8C), substantial deviations from nernstian behavior are observed. The voltammograms clearly show kinetic effects in the evolution of the faradaic current. Quantitatively, the electron-transfer reaction may be characterized by its standard rate constant, denoted as k^0 and expressed in m s^{-1}. For very large k^0, the reaction is mass-transfer limited (nernstian) and for very small k^0, the rate of electron-transfer is controlled by kinetics (irreversible limit). For quasi-reversible systems (intermediate k^0) verifying $D_{\mathrm{Ox}} \mid D_{\mathrm{R}} \mid D$, we have

$$\lambda\left(\div\pi_{\mathrm{p}}\right) \mid \frac{k^0}{\left(\phi D\tau F / RT\right)^{1/2}} \tag{20}$$

where $\lambda\left(\div\pi_{\mathrm{p}}\right)$ is a tabulated function [24]. A plot of $\lambda\left(\div\pi_{\mathrm{p}}\right)$ as a function of $\tau^{41/2}$ yields a straight line of which the slope allows determination of k^0. In Figure 8D, the resulting values of k^0 are set against the ionic strength *I* of the corresponding electrolytic system KNO$_3$, $\mathrm{Fe(CN)}_6^{34}$/ $\mathrm{Fe(CN)}_6^{44}$. For dilute systems (*I* between 1 and 30 mM), which is the range of interest for the electrokinetic analysis (section 4.3), it is found that $k^0 - 2\Delta10^{48}$ - $2\Delta10^{47}$ m s^{-1}. The dependence of k^0 on *I* is the result of the influence of the potential distribution at the interface on the kinetic characteristics of the electron transfer at the electrode. This point will be briefly commented in section 4.3. At this stage of the analysis, it is important to realize that the redox couple $\mathrm{Fe(CN)}_6^{34}$/ $\mathrm{Fe(CN)}_6^{44}$ exhibits reversible properties on gold in the presence of a fairly large excess of background electrolyte ($c - 10^{-1}$-1M) and at moderate time scales. However, at the entrance of the electrokinetic cell, the diffusion layer is very thin (corresponding to extremely short time scale) and the reversibility criterion is very demanding. The values obtained for k^0 lead to kinetically controlled current densities $\left(j_{\mathrm{kin}} \mid nFk^0c^1\right)$ that are well below the diffusion-controlled j_{diff} $\left(\mid D\left[c^1 4\, c_{\mathrm{R}}(y \mid 0)\right]/\iota\right)$. Therefore, we consider the effects of finite rates of the electron transfer on I_{f} in the next section.

4.2. Spatial distribution of the potential, expressions for I_{f} and ′

The current density-potential relationship for a quasi-reversible system with $n \mid 1$ is given by the general relation [9]

$$j(\div\pi) \mid 4Fk^0\left\{c_{\mathrm{Ox}}(y \mid 0)\exp\left(4\zeta F\left(\div\pi 4 E^0\right)/RT\right)4\, c_{\mathrm{R}}(y \mid 0)\exp\left((14\zeta)F\left(\div\pi 4 E^0\right)/RT\right)\right\} \tag{21}$$

and reduction currents are counted negative. ζ is the transfer coefficient. For the system Fe(CN)_6^{34} / Fe(CN)_6^{44}, for which $D_{\text{Ox}} \mid D_{\text{R}}$, it is assumed that $\zeta - 1/2$. One can check that for $\div\pi \mid E^{\text{N}}$, $j \mid 0$. In the frame of bipolar depolarization in a thin layer cell, the potential $\div\pi$ and the current density *j* are functions of *x*. The thickness of the diffusion layer ι also varies along the surface so that, typically, one may have irreversibility at the entrance of the cell (small ι) whereas reversibility still holds at the exit (high ι). To account for the resulting mixed reversibility for the complete electrokinetic cell, a rigorous analysis would require a numerical treatment taking into account the quasi-reversible characteristics of the interfacial electron transfer (Eq. (21)) and the non-linear coupling between the Poisson equation and the convective-diffusion equation.[1] As emphasized above, the reversible properties of the interfacial electron transfer are function of the position *x* and are strongly influenced by the magnitude of the applied pressure $\div P$. Reversibility for the whole spatial range *x* is asymptotically met in the limit of very low $\div P$ (high $\iota(x)$) whereas kinetic effects prevail in the limit of very high $\div P$ (small $\iota(x)$). In section 3.2, we considered the case of a purely diffusion-controlled bipolar current. For the redox system Fe(CN)_6^{34} / Fe(CN)_6^{44} on gold, this analysis is valid for very low $\div P$. In the following, we focus on the regime of high $\div P$ so that the surface concentrations $c_{\text{Ox}}(y \mid 0)$ and $c_{\text{R}}(y \mid 0)$ may be identified to the bulk concentrations, i.e. c_{Ox}^1 and c_{R}^1, respectively. The potential distribution $\div\pi(x)$ is defined by the differential equation expressing electroneutrality [22]

$$aK^{\text{L}} \frac{\text{d}^2 \div\pi(x)}{\text{d}x^2} 4\, 2j(x) \mid 0 \tag{22}$$

The boundary conditions associated to Eq. (22) are given by the relations

$$\div\pi(L_0/2)\, 4 \div\pi(4L_0/2) \mid \div\pi_{\text{str}} \tag{23}$$

$$\int_{4L_0/2}^{L_0/2} j(x)\text{d}x \mid 0 \tag{24}$$

Within the assumption of small overpotenials $\div\pi(x)\, 4\, E^0$, which is consistent with the measured $\div\pi_{\text{str}}$, expression (21) can be linearized and Eq. (22) then becomes

$$\frac{\text{d}^2\left(\div\pi(x)\, 4\, E^0\right)}{\text{d}x^2} 4\, \varpi^2\left(\div\pi(x)\, 4\, E^0\right) \mid \frac{2RT}{F}\varpi^2 \frac{c_{\text{R}}^1\, 4\, c_{\text{Ox}}^1}{c_{\text{Ox}}^1\, 2\, c_{\text{R}}^1} \tag{25}$$

with

$$\varpi^2 \mid \frac{F^2 k^0}{RTaK^{\text{L}}}\left(c_{\text{Ox}}^1\, 2\, c_{\text{R}}^1\right) \tag{26}$$

---

[1] Paper currently in preparation

Using the conditions (23) and (24), the solution of Eq. (25) is written

$$\div\pi(x)\,4\,E^{\mathrm{N}}\;|\;\frac{\div\pi_{\mathrm{str}}}{2\sinh(\varpi L_0/2)}\sinh(\varpi^{*}x) \qquad (27)$$

For $k^0 \Downarrow\ 0$, Eq. (27) reduces to a linear distribution for the potential. After integration of $j(x)$ over the relevant surface area, one finds the following expression for the bipolar current

$$I_{\mathrm{f}}\;|\;\frac{aK^{\mathrm{L}}l\varpi\big(\cosh(\varpi L_0/2)\,4\,1\big)}{2\sinh(\varpi L_0/2)}\div\pi_{\mathrm{str}} \qquad (28)$$

Using Eqs. (11), (27) and (28), the electrokinetic potential can be written in the explicit form

$$\acute{}\;|\;\frac{\xi L_0 K^{\mathrm{L}}\varpi}{2\kappa_0\kappa_{\mathrm{r}}}\coth(\varpi L_0/2)\frac{\div\pi_{\mathrm{str}}}{\div P} \qquad (29)$$

For $k^0 \Downarrow\ 0$, $\coth(\varpi L_0/2)\Downarrow\ (\varpi L_0/2)^{41}$, and Eq. (29) reduces to the classical H-S equation.

4.3. Computation of ´ for the gold/(Fe(CN)$_6^{34}$/ Fe(CN)$_6^{44}$, KNO$_3$) interface

For high $\div P$, the experimental plots $\div\pi_{\mathrm{str}}(\div P)$ are linear (see Figure 6), which is in agreement with Eq. (29). The bend observed at low $\div P$ is attributed to the significant mass-transport contribution in the determination of I_{f} (see section 3.1). We emphasize that the theoretical approaches of sections 3 and 4 both predict two distinct pressure-regimes in the $\div\pi_{\mathrm{str}}\,/\,\div P$ curves but for entirely different reasons.

The computation of ´ (Eq. (29)) requires knowledge of the slope $\div\pi_{\mathrm{str}}\,/\,\div P$ and the kinetic parameter k^0 of which the magnitude was previously determined. The calculated ´ are reported in Figure 9. Small variations of k^0 induce significant deviations of ´ for systems of high redox concentration $c^1\;|\;10^{43}$ M. As such, the corresponding results have to be considered with caution for quantitative interpretation. For redox concentrations corresponding to values of I_{f} which does not overrule I_{T} ($c^1\;|\;10^{44}\,4\,10^{45}$), the ´-potentials are more reliable since the dependence on k^0 is not that strong. The isoelectric point for gold in the only presence of the electroinactive electrolyte KNO$_3$ is $\mathrm{pH_{iep}} - 4.2$. Addition of redox species shifts $\mathrm{pH_{iep}}$ towards acidic values, suggesting that $\mathrm{Fe(CN)_6^{34}}$ and $\mathrm{Fe(CN)_6^{44}}$ adsorb onto the bare gold surface to form negatively charged complexes, as found earlier in the literature [25]. When increasing the pH, the surface potential $\dots^0$ becomes more negative rendering the adsorption of the redox species very unfavorable. This is confirmed by merging at high pH of the electrokinetic data corresponding to relatively low redox concentrations with those obtained in the only presence of the background electrolyte. The specific interaction between these complexes and gold is strong since it overrules the effect expected on the basis of the sign of the quantity $E^{\mathrm{N}}\ 4\ ..^{0}_{\mathrm{pzc}_1}$ $(\}\ 0)$, which would lead to a shift of $\mathrm{pH}_{\mathrm{iep}}$ towards higher values (see Figure 2). The specific adsorption of $\mathrm{Fe(CN)}_6^{34}$ and $\mathrm{Fe(CN)}_6^{44}$ is all the more pronounced when the coverage of gold by oxide sites is low, that is when there is no significant competition between surface protonation and complexation reactions. This is the case for the gold layers used in the present experiments [10].

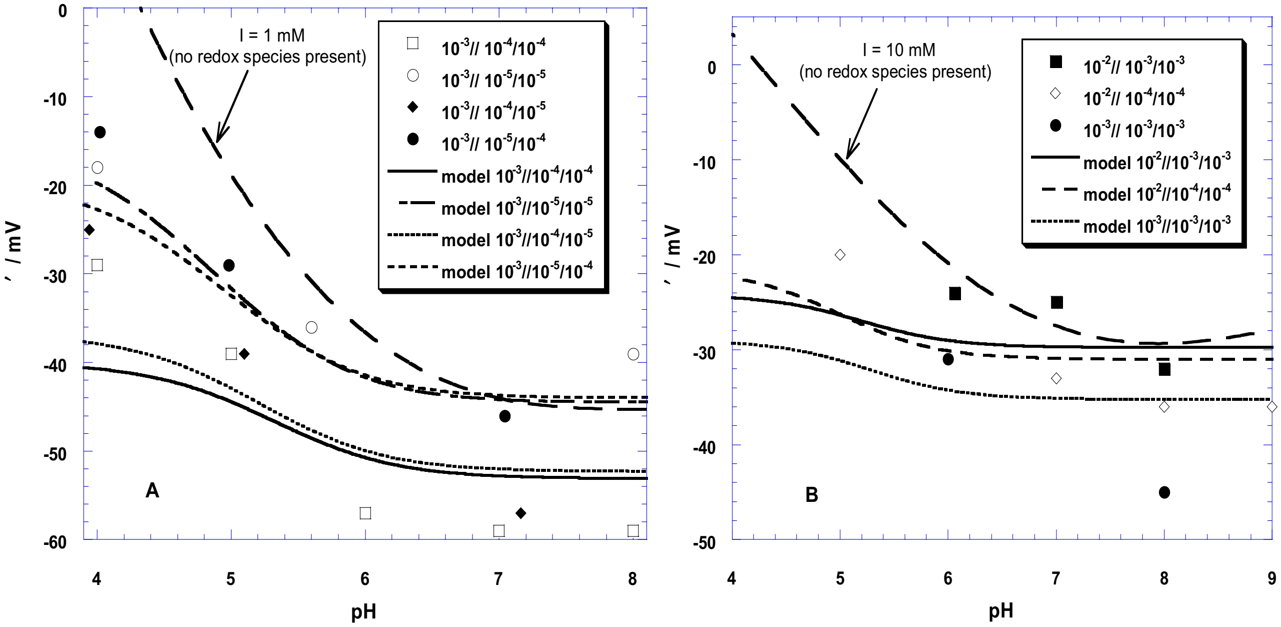

Figure 9. Experimental ´-potentials for gold⁄($\mathrm{KNO_3}$//$\mathrm{Fe(CN)}_6^{34}$ / $\mathrm{Fe(CN)}_6^{44}$) electrolyte interface as a function of the pH solution (points) and calculated with Eq. (29). The lines accompanying the legends $I\,|\,1$ mM and $I\,|\,10$ mM refer to the ´-potentials obtained for gold in the absence of redox species (no faradaic depolarization). The other lines refer to the curves calculated with the DL model presented in section 4.3. The concentrations of the background electrolyte and redox species are indicated.

Based on the aforementioned qualitative observations, a simple DL model is proposed, as pictured in Figure 1B, with the exception that negatively charged species are allowed to adsorb at the bare surface of the metal. Considering the complexity of the adsorption mechanism (charge distribution, complex conformation at the surface, competition between adsorption of Ox and R), the analysis below is only meant to catch the very basic trends of the electrokinetic curves and particularly show the importance of specific adsorption for low pH values. As such, it must be considered as semi-quantitative only. For the sake of simplicity, the adsorbed complexes are supposed to be localized at the op and experience the smeared out potential $..^{0}$. The molar Gibbs adsorption energy $\div_{\mathrm{ads}}G$ is assumed to be identical for the two species Ox and R. The corresponding charge ω^{i} is given by

$$\omega^{\mathrm{i}} \,|\, 4eK\left(f_{\mathrm{Ox}}c^{1}_{\mathrm{Ox}}\;2\;f_{\mathrm{R}}c^{1}_{\mathrm{R}}\right)\left(N_{0}\;4\;N_{\mathrm{s}}\right)\frac{\exp\left(y^{0}\right)}{1\,2\;K\left(f_{\mathrm{Ox}}c^{1}_{\mathrm{Ox}}\;2\;f_{\mathrm{R}}c^{1}_{\mathrm{R}}\right)\exp\left(y^{0}\right)} \tag{30}$$

where N_0 is the total number of atomic sites per unit area, $f_{\mathrm{Ox,R}}$ the activity coefficients of Ox and R as calculated with the Debye-Hückel relation and K is the adsorption constant

$$K \,|\, \exp\left(4\,\div_{\mathrm{ads}}G\,/\,RT\right) \tag{31}$$

Considering the low oxide coverage for the Au surfaces ($N_0\;\}\}\;N_{\mathrm{s}}$, [10,16]) and assuming that we are in the Henry region of the isotherm, Eq. (30) simplifies into

$$\omega^{\mathrm{i}} \,|\, 4e\sigma\exp\left(y^{0}\right) \tag{32}$$

with

$$\sigma \,|\, \left(f_{\mathrm{Ox}}c^{1}_{\mathrm{Ox}}\;2\;f_{\mathrm{R}}c^{1}_{\mathrm{R}}\right)KN_{0} \tag{33}$$

Within the assumptions made, the different potentials and charges can be obtained for every pH by consistently solving Eqs. (1,3,5-9,32) with the charge balance Eq. (5) replaced by

$$\omega^{\mathrm{e}}\;2\;\omega^{0}\;2\;\omega^{\mathrm{i}}\;2\;\omega^{\mathrm{d}} \,|\, 0 \tag{34}$$

The parameters $\left(N_{\mathrm{s}}, \mathrm{p}K_{\mathrm{a}_1}, \mathrm{p}K_{\mathrm{a}_2}\right)$ are known [10] so that σ is the only 'fitting' parameter. The capacitance $C_0 - 1.8$ μF cm^{-2} corresponds to a Stern layer of thickness 0.5 nm (length of the Au-O bond) and a relative dielectric permittivity close to unity. The value $C_1 - 30$ μF cm^{-2} is inferred from [26]. The 'fitting' curves are shown in Figure 9 and the corresponding values of σ are given for illustration in Figure 10. For low concentrations of Ox and R, σ conforms well to Eq. (33) with $KN_0 - 6.4\Delta 10^{14}$ mol^{-1} cm, yielding $\div_{\mathrm{ads}}G - 45$ kJ mol^{-1} with $N_0 - 10^{14}$ cm^{-2}. For high concentrations, σ deviates from Eq. (33). The reason is that adsorption takes place beyond the (linear) Henry regime. The calculated distribution of the charges involved in Eq. (34) reveals that ω^{i} decreases in size upon increasing the pH, as expected, and reaches a small but finite constant value for pH $\}$ 6, as promoted by the positive electronic charge ω^{e}. This latter remains quasi-constant over the whole pH-range, which is explained by the buffering propensity exerted by the adsorption of Ox and R.

No evidence of specific adsorption of the redox species could be found from the monopolar cyclic voltammograms. This is a priori in contradiction with the trends of the $'\left(\mathrm{pH}\right)$ curves. Nevertheless, from the model outlined above, the calculated amount of redox species, denoted as B, is roughly 10^{-12} – 10^{-11} mol cm^{-2} in the conditions of pH and c^{1} of the electrokinetic experiments. The corresponding current that would be observed in a cyclic voltammogram is in the σA m^{-2} range [9] that is 10^{2}-10^{3} times lower than the typical current densities measured. In other words, specific adsorption is not detectable from voltammetric analysis but still comes into play for the determination of the zeta-potential.

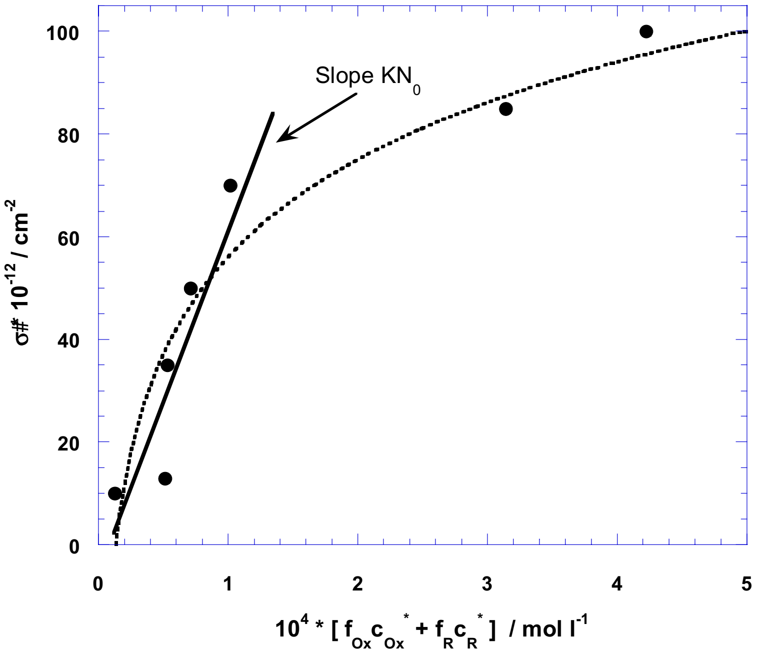

Figure 10. Parameter σ (Eq. (33)) (points) used for the computations of the curves presented in Figure 9. DL model parameters: pK_{a_1} | 3.95 / pK_{a_2} | 4.25 (determined in [10]), C_0 | 1.8σF cm^{-2}, C_1 | 30σF cm^{-2}, N_s | $2.8\Delta 10^{12}$ sites cm^{-2} (determined in [10]), E^0 | 70 mV (versus the bulk solution), n | 1. The plain line is a linear fit of the points corresponding to low redox concentrations, the dashed curve is only a guide for the eyes.

Now that the potential distribution at the interface has been captured, one can give a qualitative explanation for the strong dependence of k^0 on the electrolyte composition. The potential driving the electrode reaction is not $\div\pi\, 4\, E^0$ but instead $\div\pi\, 4\, E^0\, 4\, \ldots^{\mathrm{i}}$ where $\ldots^{\mathrm{i}}$ is the potential of the plane of closet approach for the redox species. For simplicity, we considered in the DL model $\ldots^{\mathrm{i}}\ \Sigma \ldots^0$. Taking into account the actual concentrations of Ox and R at the surface as corrected by the appropriate Boltzmann factor, the true rate constants k_{O}^0 and k_{R}^0 for the oxidation and reduction reactions are defined by

$$k^0 \mid k_{\mathrm{O}}^0 \exp\left(\frac{F\ldots^0}{RT}\left(\zeta\, 4\, z_{\mathrm{Ox}}\right)\right) \qquad k^0 \mid k_{\mathrm{R}}^0 \exp\left(\frac{F\ldots^0}{RT}\left(\left(1\, 4\, \zeta\right) 4\, z_{\mathrm{R}}\right)\right) \tag{35a,b}$$

with $z_{\mathrm{Ox,R}}$ the valency of Ox and R. The correction for DL effects on kinetic parameters is called Frumkin correction [27]. For the redox system we examine, the arguments of the exponentials in relations (35) are negative since z_{Ox} | 43, z_{R} | 44 and $\ldots^0$ { 0. When decreasing I, $\ldots^0$ decreases strongly and therefore k^0 is also expected to do so. In the limit of very high I, we have

$\ldots^{0} \Downarrow 0$ so that $k^{0} \Downarrow k_{\mathrm{O}}^{0}$ or equivalently $k^{0} \Downarrow k_{\mathrm{R}}^{0}$. These trends are in agreement with the experimental results of Figure 8D. To achieve a rigorous quantitative analysis of the dependence $k^{0}(I)$, a more advanced DL model than the one proposed is required.

5. Conclusions

In a previous paper [10], the role of bipolar faradaic depolarization in the electrokinetics of the metal/electroactive electrolyte solution interface was qualitatively discussed and illustrated with streaming potential data for gold surfaces in the presence of the redox couple $\mathrm{Fe(CN)}_6^{34}$/ $\mathrm{Fe(CN)}_6^{44}$. The latter shows nernstian behavior in the typical conditions met in voltammetric experiments, i.e. large excess of background electrolyte and relatively small potential scan rates. A quantitative theory has recently been developed which allows numerical computation of the bipolar conductance term, originating from the faradaic current in the bulk conducting substrate as limited by convective-diffusion transport of the electroactive species in the thin-layer cell. The magnitude of this current depends on the hydrodynamic (applied pressure) and electric (streaming potential) parameters. The ensuing electronic conduction curbs the building up of a streaming potential and requires a correction term in the classical Helmholtz-Smoluchowski equation. The theory however is shown to be inadequate for quantitatively describing the streaming potential curves of the gold/($\mathrm{Fe(CN)}_6^{34}$/ $\mathrm{Fe(CN)}_6^{44}$, $\mathrm{KNO_3}$) electrolyte interface over a wide range of pressures. This is so because the extreme convection conditions in the electrokinetic cell makes extremely high demands on the interfacial electron transfer rates, that is, requires extreme degree of reversibility. The $\mathrm{Fe(CN)}_6^{34}$/ $\mathrm{Fe(CN)}_6^{44}$ system is shown to be unable to meet these demands. We therefore propose an analysis in which kinetic limitation of the local current density along the metallic surface is considered. The resulting calculated zeta-potentials agree well with a first-order DL model taking into account adsorption of the redox pair at the surface. The latter feature hampers the investigation of the amphifunctional character of gold and particularly the influence of the Nernst potential E^{N}, as dictated by the redox couple, on the interfacial properties. A suitable redox couple for this purpose should comply with the conditions that E^{N} largely differs from the open circuit potential of the system in the absence of the redox species and that there is no significant interactions with the surface. With these conditions fulfilled, the streaming potential technique will offer an elegant way to probe interfacial features, and as such, complement studies by Atomic Force Microscopy.

Acknowledgments

The author is grateful to Dr. Herman P. van Leeuwen with whom he discussed the basic elements of this study.

References

[1] C. P. Smith and H. S. White, *Langmuir* **9 (1)**, 1 (1993).

[2] K. Ghowsi, S. Naghshineh and M. P. Houlne, *Russian J. of Electrochem.* **31 (12)**, 1259 (1995).

[3] J. Duval, J. Lyklema, J. M. Kleijn and H. P. van Leeuwen, *Langmuir* **17,** 7573 (2001) (chapter 2 of this thesis).

[4] J. Duval, J. M. Kleijn, J. Lyklema and H. P. van Leeuwen, *J. Electroanal. Chem.* **532**, 337 (2002) (chapter 4 of this thesis).

[5] G. Gouy, *Compt. Rend.* **149**, 654 (1909); *J. Phys.* **4 (9)**, 457 (1910); *Ann. Phys.* **7 (9)**, 129 (1917).

[6] D. L. Chapman, *Phil. Mag.* **6 (25)**, 475 (1913).

[7] O. Stern, *Z. Elektrochem.* **30**, 508 (1924).

[8] J. Lyklema, *Fundamentals of Interface and Colloid Science*, Volume II: *Solid-Liquid Interfaces*, Academic Press 1995, Chapter 3.

[9] A. J. Bard and L. R. Faulkner, *Electrochemical Methods: Fundamentals and Applications*, Eds. John Wiley and Sons, 1980.

[10] J. Duval, G. K. Huijs, W. F. Threels, J. Lyklema and H. P. van Leeuwen, *J. Colloid Interface Sci.* **260 (1)**, 95 (2003) (chapter 6 of this thesis).

[11] A. C. Hillier, S. Kim and A. J. Bard, *J. Phys. Chem.* **100**, 18808 (1996).

[12] R. Raiteri, M. Grattarola and H. J. Butt, *J. Phys. Chem.* **100**, 16700 (1996).

[13] K. Hu, F. R. F. Fan, A. J. Bard and A. C. Hillier, *J. Phys. Chem. B* **101**, 8298 (1997)

[14] A. Döppenschmidt and H. J. Butt, *Colloids and Surfaces A: Physicochemical and Engineering Aspects* **149**, 145 (1999).

[15] J. Fréchette and T. K. Vanderlick, *Langmuir* **17**, 7620 (2001).

[16] D. Barten, J. M. Kleijn, J. Duval, H. P. van Leeuwen, J. Lyklema and M. A. Cohen Stuart, *Langmuir* **19**, 1133 (2003) (chapter 3 of this thesis).

[17] J. Duval, H. P. van Leeuwen, J. Cecilia, J. Galceran, *J. Phys. Chem. B* **107 (28)**, 6782 (2003) (chapter 8 of this thesis).

[18] C. Yarnitzky and F. C. Anson, *J. Phys. Chem.* **74**, 3123 (1970).

[19] R. A. van Wagenen and J. D. Andrade, *J. Colloid Interface Sci.* **76 (2)**, 305 (1980).

[20] H. von Helmholtz, *Ann Phys.* **7**, 337 (1879).

[21] M. von Smoluchowski, *Bull. Int. Acad. Sci. Cracovie* 184 (1903). M. von Smoluchowski, *Handbuch der Electrizität und des Magnismus*, W. Graetz, Ed., Vol. II, Barth Leipzig, 1914, p.366; *Z. Physik. Chem.* **92**, 129 (1918).

[22] J. Duval, M. Minor, J. Cecilia and H. P. van Leeuwen, *J. Phys. Chem. B* **107 (17)**, 4143 (2003) (chapter 7 of this thesis).

[23] J. Duval, J. M. Kleijn and H. P. van Leeuwen, *J. Electroanal. Chem.* **505**, 1 (2001) (chapter 5 of this thesis).

[24] R. S. Nicholson, *Anal. Chem.* **37**, 1351 (1965).

[25] Y. Zhang, Z. H. Fang and M. Muhammed, *Hydrometallurgy* **46 (3)**, 251 (1997).

[26] M. A. Vorotyntsev, In *Modern Aspects of Electrochemistry,* Editors J. O'M. Bockris, B. E. Conway, R. E. White, Plenum Press, 1986; Vol. 17, Chapter 2, p. 177.

[27] B. E. Conway, In *Theory and Principles of Electrode Processes,* Ronald, New-York, 1965, Chapters 4 and 5.

Interaction Between Electric Double layers: Regulation. Its Chemical and Electrostatic Aspects[1]

Johannes Lyklema, Jérôme F. L. Duval,
Laboratory of Physical Chemistry and Colloid Science, Wageningen University,
Dreijenplein 6, 6703 HB Wageningen, The Netherlands.

Abstract. The issue of the adjustment of charges and potentials upon interaction of charged colloids (*regulation*) is revisited and generalized. Distinction is made between purely *electrostatic* and *chemical* phenomena, which allows a more explicit consideration of ionic specificity. To account for the latter, double layers are treated on the Gouy-Stern level. Chemical contributions to the Gibbs energy of interaction occur on the solid surface and/or at the inner Helmholtz plane (iHp). These contributions are determined by the molar Gibbs energies of adsorption of charge-determining ions on the surface and/or of specifically adsorbed ions at the iHp. Purely electrostatic contributions are governed by three capacitances, *viz*. those of the inner Helmholtz layer, the outer Helmholtz layer and the diffuse part of the double layer. Together with the surface charge, these chemical and electrostatic factors determine the extent of *regulation* of a double layer. A set of equations is proposed for the treatment of interactions between identical and dissimilar surfaces (*homo- and hetero-interactions*, respectively). For this latter kind of interactions, a numerical mean-field lattice analysis is performed on the basis of the non-linearized Poisson-Boltzmann equation. The regulation conditions where interaction between two surfaces of the same charge sign leads to attraction (by induction) are elaborated without invoking London-van der Waals forces. The models presented in the paper may be used for interpreting direct force measurements between identical and dissimilar double layers.

---

[1] Part of this chapter will be submitted for publication in *Journal of Colloid and Interface Science* and part for publication in *Langmuir*

Regulation

1. Introduction

Upon overlap of electric double layers, redistribution of charges takes place. This process is known as *charge regulation*. It is always coupled to *potential regulation*. Regulation has chemical and electrical aspects. It is appropriate to distinguish between these two because of the following argument: in sols, double layers form spontaneously by adsorption of charge-determining ions on the particle surface and/or by specific adsorption of ions, i.e. for *chemical* reasons. When charge regulation upon double layer overlap calls for desorption of such chemically bound ions, the Gibbs energy becomes necessarily less negative meaning that repulsion ensues, basically for *chemical* reasons. Isothermal reversible work has to be done against the chemical affinity of ions for the surface. When upon overlap all chemically bound ions remain fixed, the potentials shoot up; in this case repulsion also ensues, but now for purely *electrostatic* reasons. This latter situation refers to the case of *interaction at constant surface charge*. Ad- or de-sorption maintaining equilibrium takes us to the case of *interaction at constant chemical potential*. More generally, in-between situations will occur and this is the theme of the present work.

We shall analyse interaction between two charged hard flat surfaces on the Gouy-Stern level, which is the most transparent model to account for specific adsorption and for the presence of a stagnant layer. In the frame of this model, three charges have to be considered for each surface: a surface charge ω^{o}, an inner Helmholtz plane charge ω^{i} and a diffusely distributed charge ω^{d}. These charges are counted per unit area, i.e. they are surface charge densities. Electroneutrality of a pair of two colloids 1 and 2 as a whole requires

$$\omega_1^{\mathrm{o}}(h)\,2\,\omega_1^{\mathrm{i}}(h)\,2\,\omega_1^{\mathrm{d}}(h)\,2\,\omega_2^{\mathrm{o}}(h)\,2\,\omega_2^{\mathrm{i}}(h)\,2\,\omega_2^{\mathrm{d}}(h)\,|\;0 \tag{1}$$

where h is the distance between the outer Helmholtz planes of the two interacting surfaces. It is realized that for strong overlap it is sometimes difficult to distinguish charges belonging to particle 1 from those pertaining to 2. The accompanying potentials are written as dimensionless quantities $y \sum F\ldots/RT$, where F is the Faraday, R the gas constant and T the absolute temperature. Between surface and iHp, the potential drops linearly from y^{o} to y^{i}, similarly so between the iHp and the outer Helmholtz plane (oHp) from y^{i} to y^{d}. We equate the oHp with the electrokinetic slip plane, for reasons to set forth in section 2. Hence $y^{\mathrm{d}} - F' / RT \,|\; y^{\mathrm{ek}}$, where $'$ is the electrokinetic potential. The position of the slip plane is of a hydrodynamic origin and therefore fixed (i.e. independent of the presence and strength of a double layer). Our task is to determine ω^{o}, ω^{i}, ω^{d}, y^{o}, y^{i} and y^{d} as a function of h, the accompanying Gibbs energy of interaction $G(h)$ and/or the disjoining pressure $M(h)$. We shall only treat flat surfaces at equilibrium, but do include hetero-interaction (section 4). Transient excesses that may occur under dynamic conditions will not be considered here. We note that for isolated particles ($h \Downarrow \leftarrow$) we can determine ω^{o} by potentiometric and/or conductometric titration (or otherwise). Strictly speaking, ω^{d} is not measurable but there are good reasons for identifying ω^{d} with the electrokinetically measured charge ω^{ek} which, in turn, can be derived from the electrokinetic potential ′, using diffuse double layer theory. Once ω^{o} and ω^{d} are known, ω^{i} follows from the charge balance for an isolated particle. If Nernst's law applies y^{o} may also be determined. For y^{i}, a model is needed. Upon overlap, all these parameters are in principle unknown and no unambiguous procedures are available for measuring them. Theories for the various double layer parts (Gouy-Chapman theory, based upon the Poisson-Boltzmann distribution, for the diffuse part,[1,2] and Stern theory[3] or variants of it[4] for the inner layer) remain valid upon overlap, though with changed parameter values. In summary, the new element of the present paper is the systematic introduction of Stern layers to

(i) identify *chemical* contributions to the interaction Gibbs energy, stemming from *ad- and de-sorption of charge-determining ions*, say H^{2} and OH^{4} for oxidic surfaces. Desorption of, say, H^{2} ions from a poly(styrene sulfate) latex also belongs to this category.

(ii) identify *chemical* contributions caused by *specific ion ad- and de-sorption* at the iHp. The ions may be small (like Na^{2} or Cl^{4} ions) or big (like surfactant ions). This contribution underlies *lyotropic* phenomena, both in stability and surface charge.

(iii) identify *electric* contributions, determined by the two capacitances of the inner layer and the diffuse layer.

(iv) locate the oHp, beyond which the distribution is diffuse.

(v) for hetero-interaction, quantify the chemical and electric contributions to regulation, which determines the extent of induction of one double layer on the other.

2. Earlier work

In the literature several illustrations of regulation can be found, some of them 'avant la lettre', but none of these considers the phenomenon systematically along the lines to set forth in this paper. Perhaps the oldest concrete illustration of regulation can be found in Verwey and Overbeek's book.[5] These authors assumed a simple Stern layer and kept y^{o} constant upon overlap. The required reduction of ω^{o} was thought to result from desorption of charge-determining ions. Transport of charges from the surface to the diffuse part of the double layer (spatial regulation) was considered for maintaining electroneutrality. Melville and Smith[6] elaborated this in more detail. Below we shall integrate and refine their approach. There are plenty of illustrations for regulation of the surface charge ω^{o} (planar regulation) in the literature. One of them is that by Bierman,[7] devoted to hetero-interactions. In that work, y^{o} is not a constant but it changes with the distance h separating the two flat surfaces. The occupancy of the surface by charge-determining ions varies upon overlap (ω^{o} becomes $\omega^{o}(h)$), obeying a kind of Langmuir adsorption isotherm. Stern layers are ignored and charge regulation inside the diffuse part is tacitly taken into account, as it is for all other surface regulation models. Interaction between biological surfaces, for which the surface charge is pH-dependent because of its effect on the dissociation of weak surface groups, was the incentive for a paper by Ninham and Parsegian.[8] Stern layers are not considered but the influence of the valency of the counter-cation was emphasized, in view of the important role of Ca^{22} in biological systems. Several other publications deal with extensions and/or reviews,[9-20] where further references can be found. These papers have in common that they treat ω^{o} regulation in terms of a site-binding model. Differences between them refer to the definition of the surface charge-forming mechanism (one - or two - p*K* model(s) to describe the acidity/basicity and, for the two-p*K* models, the way in which these p*K*'s are defined), in the accounting for specific adsorption (triple layer or other ways of positioning the charges) and in the mathematical sophistication (linearization or not of the Poisson-Boltzmann equation, using or not using charge density functionals). Explicit consideration of Stern layers is absent or only present in a rudimentary form. For instance, Healy and White[13] did include specific adsorption but considered a zeroth order Stern layer. Behrens and Borkovec[18] included an embryonic Stern layer of zero thickness whereas Usui[14] used an approach more primitive than ours because he did not discriminate between y^{i} and y^{d}. Other recent elaborations also ignore Stern layers.[21-24] Perhaps the most concrete incorporation of a Stern layer in a planar charge regulation model is in the appendix of the Reiner-Radke review.[16] The absence of a concrete Stern layer in several of the site-binding models is often partly compensated by considering specific adsorption and/or a triple layer model, but the spatial distribution is not always clear. In some models, the Stern layer has a non-zero thickness. In others, distinction is made between y^{o} and a Nernst potential, y^{N}, thought to be located at different positions. Generally, surface site binding models are very suitable to account for experimental $\omega^{o}(\mathrm{pH})$ curves but it is more difficult to predict electrokinetic potentials because $\omega^{ek} - \omega^{d}$ is computed as a small difference between two larger quantities (ω^{o} and ω^{i}) and because the model does not include any view concerning the slip process. However, recently this process became much clearer, thanks to molecular dynamics simulations.[25-26] For all fluids in contact with hard surfaces the molecular density distribution $\psi(x)$ (where x is the direction perpendicular to the surface) shows one big and a few minor oscillations. This ordering is caused by the repulsive part of the molecular pair interaction energy. The viscosity of the fluid in this adjacent layer is obtainable from the time-correlation of the pertaining pressure tensors components; it is anisotropic and much higher than the bulk viscosity. Hence, macroscopically this layer behaves as if it were stagnant. There is no way of telling whether the layer beyond this first density maximum is fully mobile (i.e. having bulk fluidity) or whether the viscosity also drops in an oscillating mode. However, the pragmatic presumption is to account for this stagnancy in terms of a step function. In practice this is carried out by introducing a slip plane, separating the fully mobile and fully stagnant parts of the fluid. In this way, the notion of a 'slip plane' gets a physical meaning even though we cannot locate it exactly because in fact this plane has a certain width. However, the accompanying inference is that the slip plane is most likely very close (or identical, by practical means) to the oHp, because all ions inside the stagnant layer find themselves in a liquid with a structure deviating from that in the bulk fluid, which gives rise to a non-zero non-electrical contribution to the Gibbs energy of adsorption. In passing, it may be noted that the notion of a sharp oHp and, for that matter, all other planes that may be identified in the compact part of the double layer, also are abstractions from reality. The conclusion of all of this motivates our choice to equate ω^{d} and ω^{ek} and use this information to derive ω^{i}. A further consequence is that the position of the slip plane, being determined by the fluid structure, is fixed. For fitting ′ -potentials some site-binding models require the position of the slip plane to depend on the electrolyte concentration; apparently such models are inadequate.

Below we shall often use the term *regulation capacity (RC)*. Qualitatively, a high regulation capacity means that charges easily adjust to new situations i.e. without substantial potential changes, and conversely for low regulation capacity. High capacities imply low potentials. Quantitatively, for the spatial part (transport from the diffuse to the Stern layer and from the Stern layer to the surface) the regulation (capacity) is entirely determined by the three electrical capacitances C^{d}, C_1^{i} and C_2^{i}, denoting the capacitance of the diffuse part of the double layer, the inner and outer Helmholtz layer capacitances, respectively. On the other hand, for the surface charge regulation and for regulation of ω^{i}, if any, the regulation (capacity) is partly of an electric, partly of a chemical nature. Therefore, regulation capacities have generally a chemical and an electric contribution. The former is determined by the parameters characterizing the specific adsorption propensity of ions, such as Gibbs energy of adsorption, numbers of sites available and the magnitude of the charge carried at the surface. Taken over double layers as a whole, the extremes of infinitely high and infinitely low regulation capacity correspond to the cases of interaction at constant (surface) potential and constant (surface) charge, respectively. Some of the older theories distinguishing between 'constant charge' and 'constant potential' interaction were elaborated for the diffuse part of the double layer only. Although these theories [27-28] have played their roles in the progress of our understanding they are useless for practice because conditions where, upon interaction, ω^{d} or y^{d} remain constant are virtually absent, as we shall see later.

Application of regulation models is in the first place found in the domain of particle interaction and its variants. This will be done in the present paper, where in section 4 we shall also elaborate the case of two particles with different double layers and/or regulation capacities (hetero-interaction). Applications include double layer polarization in electrokinetics of which a recent elaboration was given by Keh and Ding.[29] They considered regulation in terms of the Carnie-Chan model[15] for interacting polarized particles. We shall not consider this here.

3. Homo-interaction

3.1. Summary of the basic equations

For homo-interaction, the electrical contribution $M(h)$ to the disjoining pressure can generally be written as[30]

$$M(h) | \ 2c_{\mathrm{s}}RT\Big[\cosh\big(zy^{\mathrm{m}}(h)\big)\,4\,1\Big] \tag{2}$$

where c_{s} is the concentration of the (*z*, *z*) electrolyte and y^{m} is the mid-way potential. As for isothermal reversible interaction the forces are conservative, eq 2 may be integrated to give the corresponding Gibbs energy

$$G(h) | \ 4\int_{\leftarrow}^{h} M(h')\mathrm{d}h' \tag{3}$$

where h' is the distance varying from infinity to *h*. As an aside, for a purely diffuse double layer, it is also possible to derive the Gibbs energy $G(h | \ \leftarrow)$ using Verwey and Overbeek's equation

$$G(\leftarrow) | \ 4\int_{0}^{\ldots^{\mathrm{o}}} \omega^{\mathrm{o'}}\mathrm{d}\ldots^{\mathrm{o'}} \tag{4}$$

where $\omega^{\mathrm{o'}}$ and $\ldots^{\mathrm{o'}}$ are the surface charge and surface potential during the charging process. Equation 4 contains an electrical and a chemical contribution, the latter resulting from the binding of charge-determining ions on the surface. In the more general case considered here there is also a chemical contribution originating from specific ion binding at the iHp. In that case,[4]

$$G(\leftarrow) | \ 4\frac{\left(\omega^{\mathrm{o}}\right)^{2}}{2C_{1}^{\mathrm{i}}}\,4\,\frac{\left(\omega^{\mathrm{d}}\right)^{2}}{2C_{2}^{\mathrm{i}}}\,2\int_{0}^{\ldots^{\mathrm{d}}} \omega^{\mathrm{d'}}\mathrm{d}\ldots^{\mathrm{d'}} \tag{5}$$

In the present analysis, we choose the disjoining pressure route to find the Gibbs energy of interaction. Equation 2 requires the functionality $y^{\mathrm{m}}\left(y^{\mathrm{d}}\right)$. For a flat and purely diffuse double layer the relation between y^{m} and y^{d} is rigorously known and described in terms of elliptic integrals. As we want analytical expressions, we shall use

$$y^{\mathrm{m}} \mid \frac{y^{\mathrm{d}}}{\cosh(\rho h/2)} \tag{6}$$

where ρ is the reciprocal Debye length. Verwey and Overbeek[31] already showed that eq 6 is an excellent approximation given the values of $y^{\mathrm{d}} - y^{\mathrm{ek}}$ under conditions of incipient coagulation. The charge in the diffuse part of the double layer changes with h according to the rigorous expression

$$\omega^{\mathrm{d}}(h) \mid \operatorname{sign}\left(4\, y^{\mathrm{d}}\right)\frac{2Fc_{\mathrm{s}}z}{\rho}\sqrt{2\left\{\left|\cosh\left(zy^{\mathrm{d}}(h)\right)4\cosh\left(zy^{\mathrm{m}}(h)\right)\right|\right\}} \tag{7}$$

which immediately follows from integration of the non-linear Poisson-Boltzmann equation over the half space, using Gauss' law to convert field strengths $\left(\mathrm{d}y/\mathrm{d}x\big|_{x\mid 0}\right)$ into surface charge densities. From now on, x is the direction perpendicular to the surface and counted from the oHp of surface 1, as indicated in Figure 1. The spatial derivative of the potential $\left(\mathrm{d}y/\mathrm{d}x\right)$ changes sign after passing the minimum located at $x \mid h/2$. The charge balance (eq 1) can, in this symmetrical case, be subdivided into two contributions

$$\omega_1^{\mathrm{o}}(h)\,2\,\omega_1^{\mathrm{i}}(h)\,2\,\omega_1^{\mathrm{d}}(h) \mid 0 \tag{8a}$$

$$\omega_2^{\mathrm{o}}(h)\,2\,\omega_2^{\mathrm{i}}(h)\,2\,\omega_2^{\mathrm{d}}(h) \mid 0 \tag{8b}$$

Generally, all three charges depend on h but we may of course consider special cases, like interaction at fixed surface charge, in which ω^{o} is a constant. For the left particle the potential drop over the inner double layer part obeys

$$y^{\mathrm{i}}(h) \mid y^{\mathrm{o}}(h)\,4\,\frac{F\omega^{\mathrm{o}}(h)}{RTC_1^{\mathrm{i}}} \tag{9}$$

Its counterpart for particle 2 is readily formulated. As the inner layer is charge-free and since we consider its dielectric constant independent of the potential, the differential and integral capacitances are equal. Similarly, for the outer Helmholtz layer

$$y^{\mathrm{d}}(h) \mid y^{\mathrm{i}}(h)\,4\,\frac{F\left[\omega^{\mathrm{o}}(h)\,2\,\omega^{\mathrm{i}}(h)\right]}{RTC_2^{\mathrm{i}}} \mid y^{\mathrm{i}}(h)\,2\,\frac{F\omega^{\mathrm{d}}(h)}{RTC_2^{\mathrm{i}}} \tag{10}$$

In Figure 1, a schematic picture of the left particle of the interacting pair is given indicating the different charged planes involved in the regulation mechanisms. Although the two capacitances

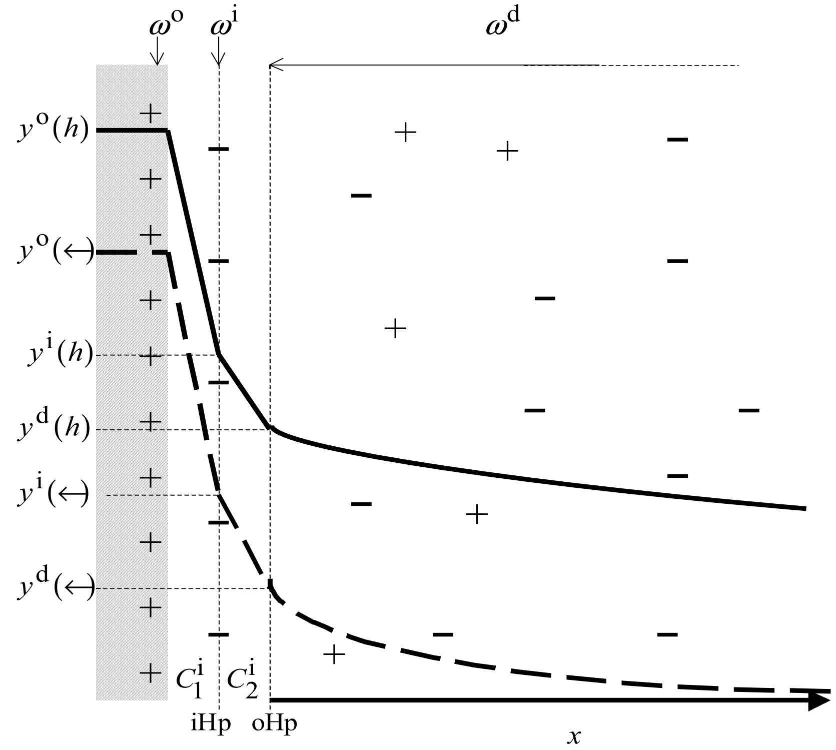

Figure 1. Identification of the various planes and potentials for (homo-) interaction between Gouy-Stern layers at constant surface charge at infinite – – and finite —— separation distance *h*, which stands for the distance between the two oHp's. Constancy of ω^{o} implies that the slope $\mathrm{d}y / \mathrm{d}x$ in the inner Helmholtz layer is independent of *h*. Only the left particle (1) is drawn; the situation for particle (2) is symmetrical.

C_1^{i} and C_2^{i} are constant (independent of *h*), the total capacitance of the Stern layer is variable since this capacitance also depends on ω^{i}, which is function of *h*.[32]

For the specific adsorption isotherm of ions of type i at the iHp, we choose the Frumkin-Fowler-Guggenheim (FFG) equation in the form

$$\omega^{i}(h) \mid \frac{z_i e N_s^{i} x_i K_i \exp\left(4 z_i y^{i}(h)\right)}{1\,2\; x_i K_i \exp\left(4 z_i y^{i}(h)\right)} \tag{11}$$

We consider only one type of ion (valency z_i) at that plane. N_s^{i} is the number of adsorption sites per unit area, x_i is their mole fraction and

$$K_i \mid \exp\left(4 \div_{\mathrm{ads}} G_{\mathrm{m,i}} / RT\right) \tag{12}$$

or, equivalently

$$\mathrm{p}K_i \mid 0.43 \div_{\mathrm{ads}} G_{\mathrm{m,i}} / RT \tag{13}$$

where $\div_{\mathrm{ads}} G_{\mathrm{m,i}}$ is the molar Gibbs energy of specific adsorption for the ion i. In eq 11, the non-specific electrical part is accounted for by the factor $\exp\left(4 z_i y^{i}(h)\right)$.

For systems of constant surface charge (latices with strong surface groups, ionic micelles, clay, etc) ω^{o} is a fixed parameter and eqs 1-3, 6-13 suffice to describe regulation. Relaxing this condition implies the need to include surface charge regulation. At the surface, we do not have to include specific ion contributions because these phenomena are already accounted for by specific adsorption at the iHp. Taking H^{2} and OH^{4} as the charge-determining ions, which can react at a hydroxyl surface with adsorption sites denoted as ROH, we have the following equilibria

$$\mathrm{ROH} \Diamond \;\; \mathrm{RO}^{4}\; 2\; \mathrm{H}^{2} \qquad K_{\mathrm{a}} \mid \frac{\left[\mathrm{RO}^{4}\right]}{\left[\mathrm{ROH}\right]} x^{\mathrm{s}}_{\mathrm{H}^{+}} \tag{14a}$$

$$\mathrm{ROH} + \mathrm{H_2O} \Diamond \;\; \mathrm{ROH}_2^{+}\; 2\; \mathrm{OH}^{\quad 4} \qquad K_{\mathrm{b}} \mid \frac{\left[\mathrm{ROH}_2^{+}\right] K_{\mathrm{w}}}{\left[\mathrm{ROH}\right] x^{\mathrm{s}}_{\mathrm{H}^{+}}} \tag{14b}$$

where $x^{\mathrm{s}}_{\mathrm{H}^{+}}$ is the mole fraction of H^{2} at the surface, and the square brackets indicate surface concentrations as number of moles or functional groups per unit area. The surface charge is defined by

$$\omega^{\mathrm{o}}\; \Sigma F\left(\left[\mathrm{ROH}_2^{2}\right] 4 \left[\mathrm{RO}^{4}\right]\right) \tag{15}$$

We note that in eqs 14 all K's are dimensionless. Some authors prefer other conventions, in some of which the K's are not dimensionless. The relation to the pH can be found from

$$x^{\mathrm{s}}_{\mathrm{H}^{2}} \mid x_{\mathrm{H}^{2}} \exp\left(4\, y^{\mathrm{o}}\right) \tag{16}$$

$$x_{\mathrm{H}^{2}} \mid V_{\mathrm{m}} \exp\left(42.303\mathrm{pH}\right) \tag{17}$$

where V_{m} is the molar volume of water, needed to correct for the dimensional problem incurred in the usual definition of pH as $4\log c_{\mathrm{H}^{+}}$, requiring the logarithm of a quantity having a dimension.

For two surfaces in interaction, from eqs 14-16, writing explicitly the dependence of y^{o} on h, one obtains

$$\omega^{\mathrm{o}}(h) \mid F\left[\mathrm{ROH}\right] \left\{ \frac{K_{\mathrm{b}} x_{\mathrm{H}^{2}} \exp\left(4\, y^{\mathrm{o}}(h)\right)}{K_{\mathrm{w}}} 4 \frac{K_{\mathrm{a}} \exp\left(y^{\mathrm{o}}(h)\right)}{x_{\mathrm{H}^{2}}} \right\} \tag{18}$$

At the point of zero charge (p.z.c.), $\omega^{\mathrm{o}} \mid 0$, $x_{\mathrm{H}^{2}} \mid x^{\mathrm{o}}_{\mathrm{H}^{2}}$, $\mathrm{pH} \mid \mathrm{pH}^{\mathrm{o}}$ and $y^{\mathrm{o}} \mid 0$ (i.e. the reference for the potential as it occurs in eq 16). Hence,

$$x^{\mathrm{o}}_{\mathrm{H}^{2}} \mid \left(\frac{K_{\mathrm{a}} K_{\mathrm{w}}}{K_{\mathrm{b}}}\right)^{1/2} \tag{19}$$

Regulation

It is convenient to introduce the (dimensionless) Nernst potential y^{N} through

$$y^{\mathrm{N}} = -2.303\left(\mathrm{pH} - \mathrm{pH}^{\mathrm{o}}\right) \tag{20}$$

so that

$$x_{\mathrm{H}^+} = x^{\mathrm{o}}_{\mathrm{H}^+} \exp\left[-2.303\left(\mathrm{pH} - \mathrm{pH}^{\mathrm{o}}\right)\right] = x^{\mathrm{o}}_{\mathrm{H}^+} \exp\left(y^{\mathrm{N}}\right) \tag{21}$$

We note that eq 20 does not specify the position (on the *x*-axis) where the potential is y^{N}. Substituting eqs 19-21 in eq 18 leads to

$$\omega^{\mathrm{o}}(h) = 2F[\mathrm{ROH}]\left(\frac{K_{\mathrm{a}}K_{\mathrm{b}}}{K_{\mathrm{w}}}\right)^{1/2} \sinh\left[y^{\mathrm{N}} - y^{\mathrm{o}}(h)\right] \tag{22}$$

This equation can be extended in several ways. In the following, we will consider the situation where the number of surface sites per unit area is finite and equal to $N_{\mathrm{s}}^{\mathrm{o}}$ ($N_{\mathrm{s}}^{\mathrm{o}} \varnothing N_{\mathrm{s}}^{\mathrm{i}}$) in which case eq 22 changes into[10, 13, 15, 16]

$$\omega^{\mathrm{o}}(h) = 2FN_{\mathrm{s}}^{\mathrm{o}} \frac{\left(\frac{K_{\mathrm{a}}K_{\mathrm{b}}}{K_{\mathrm{w}}}\right)^{1/2} \sinh\left[y^{\mathrm{N}} - y^{\mathrm{o}}(h)\right]}{1 + 2\left(\frac{K_{\mathrm{a}}K_{\mathrm{b}}}{K_{\mathrm{w}}}\right)^{1/2} \cosh\left[y^{\mathrm{N}} - y^{\mathrm{o}}(h)\right]} \tag{23}$$

It is noted that the factor $\left(K_{\mathrm{a}}K_{\mathrm{b}}\right)^{1/2}$ acts as chemical capacity factor. In the limit where $\left(K_{\mathrm{a}}K_{\mathrm{b}}\right)^{1/2}$ is not too high, the larger this product is, the higher the surface charge at a given potential or, for that matter, the less sensitive the potentials are to changes in the charge. High values of this factor imply a high regulation capacity.

Given regulation parameters (pH or surface charge, p*K*'s, number of adsorption sites, capacitances, c_{s}), consistent solution of the system of non-linear equations 2, 3, 6-13, 23 was found for every separation distance *h* using numerical Newton-Raphson procedure.

3.2. Homo-interactions: illustrations

The literature contains many experimental data on the electric contribution to the disjoining pressure $M(h)$. Over the past decades such experiments mostly involve Atomic Force Microscopy (AFM) or force apparatus. From the accessible part of the total $M(h)$ curve the Lifshits-van der Waals part and short-distance liquid structure-mediated forces can be subtracted. What is remaining is often identified as $M_{\mathrm{el}}(h)$ which is often analyzed in terms of familiar equations from diffuse double layer theory. Mostly it is investigated what fits better: interaction 'at constant potential' or 'at constant charge'. Obviously, such a procedure only yields y^{d} and

ω^{d}, but not y^{o} or ω^{o}. For lack of better, some authors talk of ‘effective potentials’. In reality, regulation of the two double layers determines how y^{d} and ω^{d} depend on *h*, which dictates the conditions under which these parameters may be independent of *h*. However, on closer inspection, it is not at all likely that upon overlap y^{d} or ω^{d} remain independent of *h*. To analyze that, let us first consider situations in which the real surface charge is fixed (mica plates, poly(styrene sulfonate) latices, NaDS micelles, etc). Figure 2a shows how $\omega^{d}(h)$ becomes less negative when ρh decreases. Eventually, for $h \Downarrow 0$, $\omega^{d}(h) \Downarrow 0$. The difference between ω^{o} (as indicated on the figure) and $\omega^{d}(h)$ comes on the account of $\omega^{i}(h)$, which, in the case of chemical regulation by adsorption of anions, becomes more negative upon decreasing the distance *h*. For $h \Downarrow 0$, $\omega^{i}(h) \Downarrow 4\omega^{o}$. In Figure 2b, the corresponding changes in the four potentials are given for a given ω^{o}. All increase with decreasing ρh. It is noted that, upon reduction of ρh, first y^{m} increases towards y^{d} and later the two approach y^{i}, which is growing as well. The extents of all these changes depend on the regulation capacity of the Stern layer, which we have fixed in this figure by keeping C_1^{i}, C_2^{i} and pK_{i} constant. To illustrate the influence of this capacity, similar

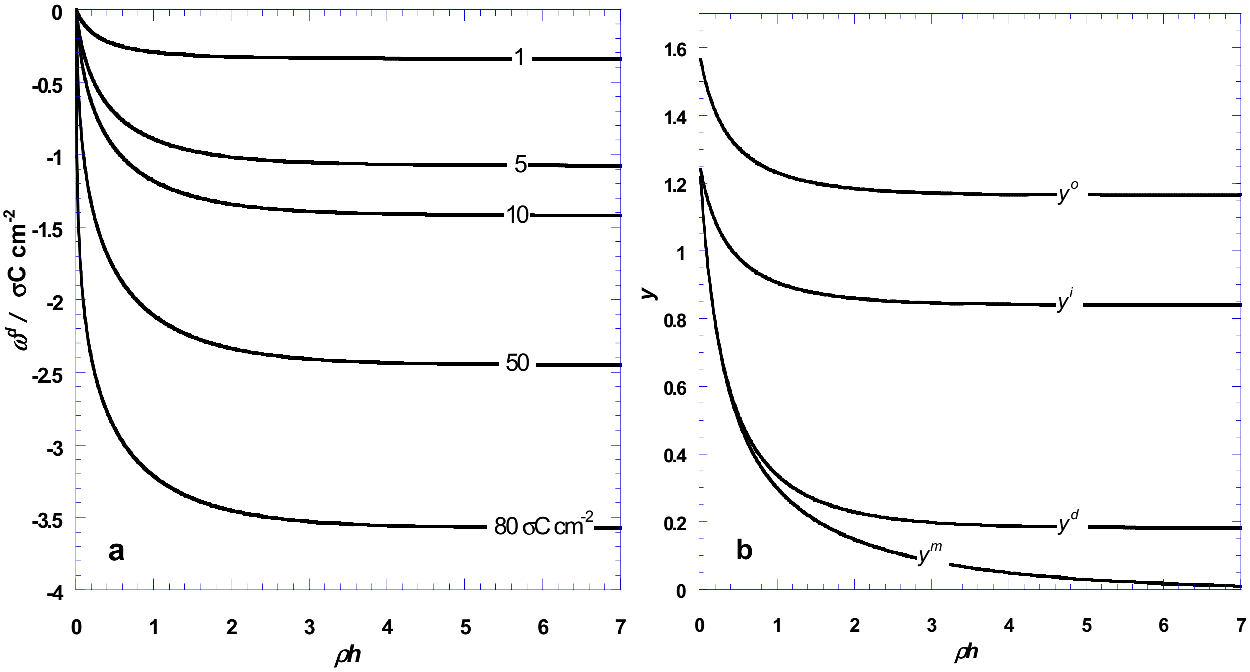

Figure 2. Potential regulation across a Gouy-Stern layer. Constant surface charge ω^{o} (indicated). Parameters: $C_1^{i} \mid 120$ σF cm^{-2}, $C_2^{i} \mid 20$ σF cm^{-2}, $N_s^{i} \mid 5\Delta 10^{14}$ sites cm^{-2}, $K_{i} \mid 2$, electrolyte concentration 10^{-1} M, monovalent symmetrical electrolyte ($\rho^{41} \mid 0.96$ nm). Specific adsorption of anions is considered. Panel a: distance dependency of the diffuse charge for various ω^{o} (as specified). Panel b: the same for the four potentials at $\omega^{o} \mid 1$ σC cm^{-2}.

graphs are given in Figure 3 for a much higher Stern layer regulating capacity, which is varied via the capacitance C_2^{i}. The higher the latter, the more charges are allowed to specifically adsorb at the iHp at a given potential drop over the Stern layer, and hence the earlier regulation sets in upon overlap. This results in potential and charge changes (with respect to the situation at $h \Downarrow \leftarrow$(no overlap)) which already occur at higher ρh. In the currently analyzed case, no influence of the capacitance C_1^{i} on the regulation capacity is noted since the surface charge is maintained constant. Under none of the selected conditions constancy of ω^{d} or y^{d} is observed. Closest to constancy is $\omega^{\mathrm{d}}(h)$ in Figure 3a at low C_2^{i}, but this is trivial because in this case the Stern-layer carries almost no additional charge upon decrease of h.

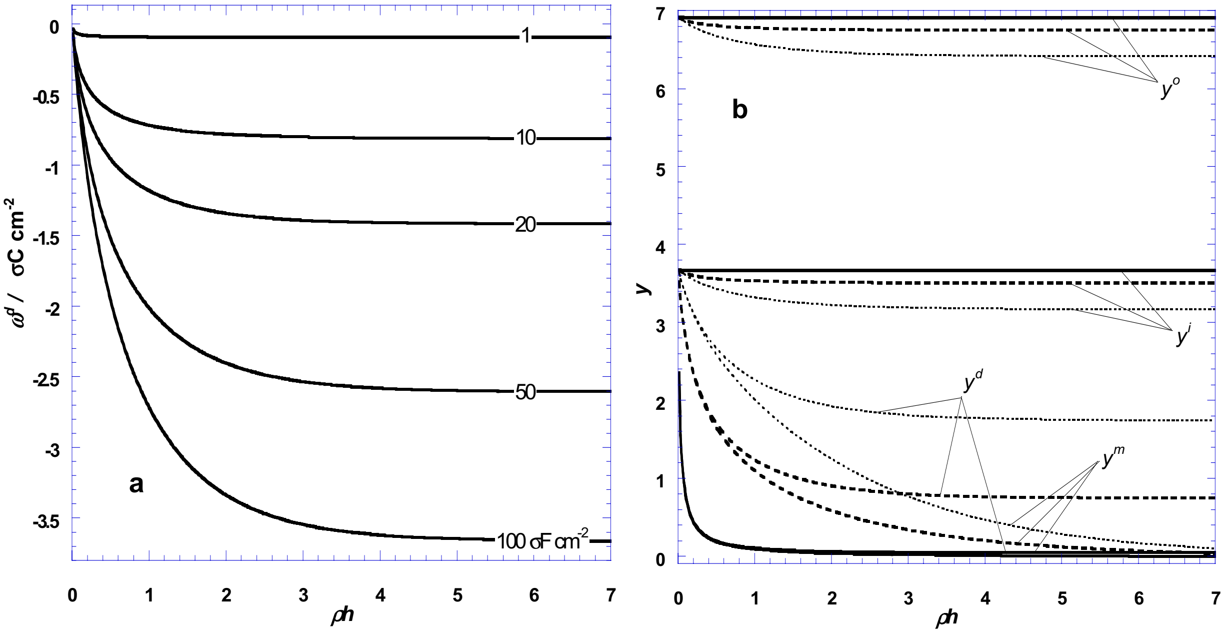

Figure 3. Potential regulation across a Gouy-Stern layer. Constant surface charge ω^{o} | 10 σC cm^{-2}. Same parameters as in Figure 2 except for C_2^{i} (as specified). Panel a: distance dependency of the diffuse charge for various C_2^{i}. Panel b: the same for the four potentials at C_2^{i} | 1 σF cm^{-2} ——, C_2^{i} | 20 σF cm^{-2} – – –, C_2^{i} | 100 σF cm^{-2} …….

In Figure 4a, Gibbs energies of interaction are drawn for the conditions of Figure 2a. The trends are as intuitively expected. The repulsion between the double layers increases with increasing surface charge. Figure 4b illustrates the influence of the regulating capacity of the inner layer as controlled by C_2^{i}. According to eq 10, a higher C_2^{i} results in a smaller difference between the potentials $y^{\mathrm{i}}(h)$ and $y^{\mathrm{d}}(h)$ (see Figure 3), which implies that a larger potential change is left for the diffuse part, provided the other parameters remain constant. Consequently, the repulsion becomes stronger. The features of the disjoining pressure (not shown) are similar to those of $G(h)$.

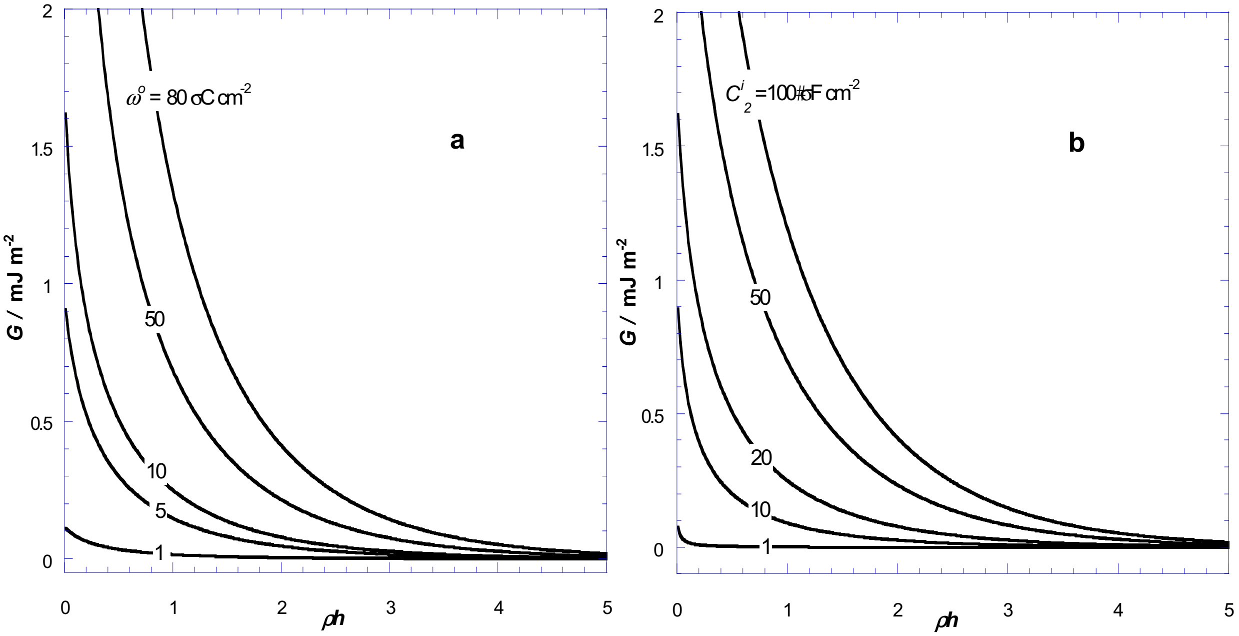

Figure 4. Gibbs energies of interaction, corresponding to Figure 2a (panel a) and Figure 3a (panel b).

The regulation capacity of the Stern layer can also be modified through variation of the specific adsorption of counterions (anions in our example). Figure 5 illustrates this. Here we keep ω^{o} and $N_{\mathrm{s}}^{\mathrm{i}}$ constant but vary the specific adsorption energy via K_{i}, see eq 12. With increasing K_{i}, $G(h)$ first decreases (because an increased fraction of the surface charge is compensated in the Stern layer) to pass through a minimum at $K_{\mathrm{i}} - 100$ (where $\omega^{\mathrm{o}} \mid 4\omega^{\mathrm{i}}$), beyond which $G(h)$ increases again because now superequivalent adsorption takes place. What we encounter here is the well-known phenomenon which is often called ‘charge-reversal’. To be more exact, it is a sign reversal of the net charge surface charge plus adsorbed charge, or otherwise stated, a reversal of the (diffuse) potential, and hence of ′ , at *constant* surface charge. This reversal also occurs for the potential y^{m} (not shown).

The following features refer to interaction at constant surface potential. It is not certain whether this condition is ever met in real systems. The classical argument is that for fully reversible interfaces the chemical potentials of charge-determining ions remain constant because they are identical to those in the solution, which are fixed.[33] AgI sols are the traditional paradigms, but for many oxides the same reasoning may be given. The underlying process requires desorption of charge-determining ions from the particle surfaces in order to reduce ω^{o} upon approach of the particles. However, it is much more likely that this desorption, plus the required lateral diffusion out of the narrow gap between the particles is much slower than reduction of $\left|\omega^{\mathrm{o}}\,2\,\omega^{\mathrm{i}}\right|$ by counterion enrichment in the inner part of the Stern layer.[34] Nevertheless, because such a type of interaction condition is often presumed-if only for the diffuse part- we give in Figures 6 and 7 the counterparts of Figures 2 and 4. Upon overlap the diffuse charge goes to zero, but the specifically adsorbed counterions remain in place and for $\rho h \Downarrow 0$, mostly ω^{i} is responsible for the compensation of ω^{o}. The extent to which this happens depends on C_1^{i} and K_{i}. Under no conditions are constant ω^{d}'s or y^{d}'s observed. Between $y^{\mathrm{i}}(h)$, $y^{\mathrm{m}}(h)$ and $y^{\mathrm{d}}(h)$ in Figures 2b and 6b, there are quantitative differences. The dependence of $G(h)$ on y^{o} (Figure 7a) is according to expectation, also with respect to the influence of the regulation capacity (Figure 7b). We see that $G(h)$ increases with C_1^{i}. The reason for this trend is that high C_1^{i}'s keep $y^{\mathrm{i}}(h)$ high, which, at given C_2^{i}, keeps $y^{\mathrm{d}}(h)$ high. The Gibbs energy for

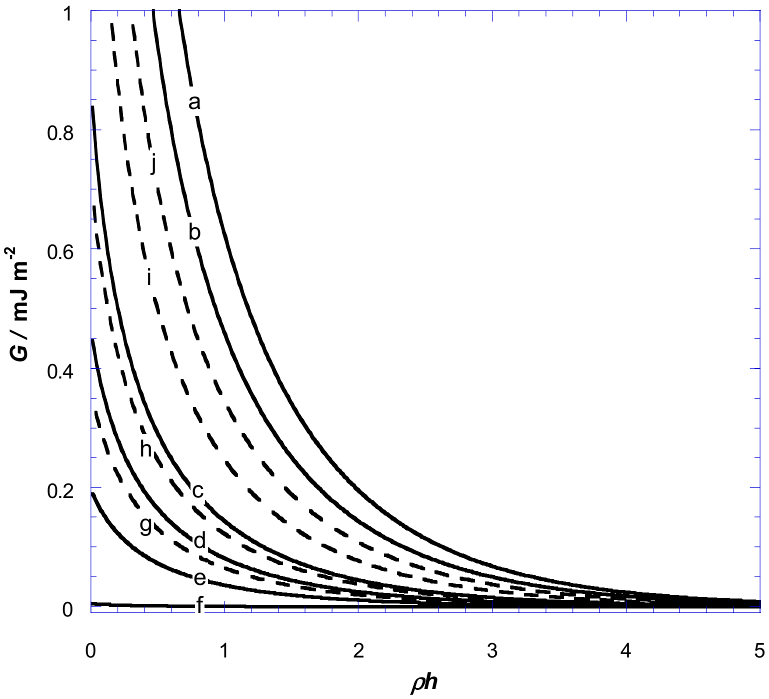

Figure 5. Charge and potential regulation across a Gouy-Stern layer. Given is the interaction Gibbs energy as a function of the specific adsorption Gibbs energy at various K_{i} | (K_{anion}). The surface charge ω^{o} is constant (10 σC cm^{-2}). The other parameters are the same as in Figure 2. K_{i} | 0.2 (a), 0.5 (b), 5 (c), 10 (d), 20 (e), 100 (f), 500 (g), 10^3 (h), 3Δ10^3 (i), 5Δ10^3 (j). The dashed curves correspond to the situation of superequivalent adsorption.

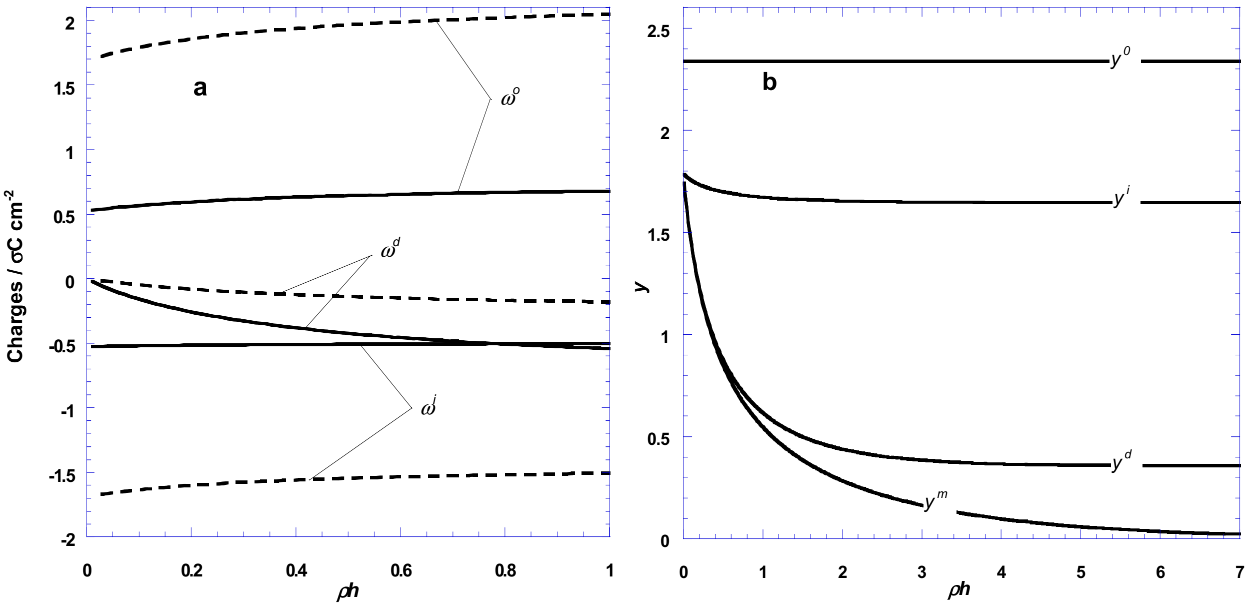

Figure 6. Charge and potential regulation across a Gouy-Stern layer at fixed surface potential. Parameters as in Figure 2. Panel a: dependence of the various charges on the separation distance at …^{o} | 20 mV—— and …^{o} | 60 mV – – . Panel b: the same for the four potentials (…^{o} | 60 mV).

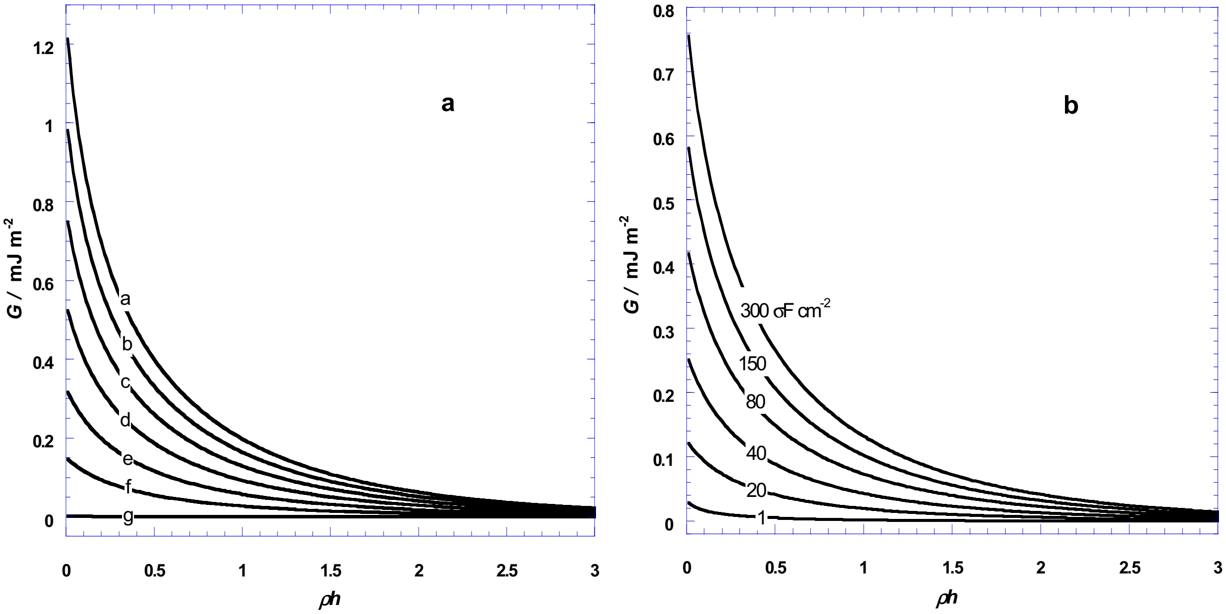

Figure 7. Gibbs energy of interaction at fixed surface potential for Gouy-Stern layers. Panel a: influence of the surface potential, all other parameters fixed as in Figure 2. …^{o} | 140 mV (a), 120 mV (b), 100 mV (c), 80 mV (d), 60 mV (e), 40 mV (f) and 0 mV (g). Panel b: influence of the capacitance C_1^{i} (indicated) at …^{o} | 80 mV.

interaction at constant y^{o} may be compared with that at constant ω^{o}. Although the differences depend on the Stern layer regulation capacity, the trend is that interaction at fixed ω^{o} is stronger. For purely diffuse double layers, this was also found,[28] but for other reasons. For instance, for oxides in 10^{-1} M (1-1) electrolyte a surface charge of 10 σC cm^{-2} (Figure 4a) corresponds to surface potentials of about 120 mV (Figure 7a).

As a final illustration of this category, Figure 8 gives an example of $G(h)$ curves for surface charge regulation as given by eqs 14 at a fixed Stern layer regulation capacity. The choice of K_{a} and K_{b} fixes pH$^{\text{o}}$. The interaction Gibbs energy is zero at pH$^{\text{o}}$ and increases with $\left|\text{pH}\, 4\ \text{pH}^{\text{o}}\right|$. By introducing specific ion adsorption at the iHp, these curves become asymmetric with respect to pH$^{\text{o}}$ owing to a shift of the pH at which the net charge $\omega^{\text{o}}\ 2\ \omega^{\text{i}}$ at $h \Downarrow\ \leftarrow$is zero (Figure 9).

One of the conclusions of this section is that interaction 'at constant potential' or 'at constant charge' does not apply to diffuse double layers. The frequently reported agreement with one of these limits generally means that the experimental data were not sufficiently sensitive to assess the underlying subtleties of the regulation processes. Detailed interpretations on the basis of such observations must therefore be considered with some suspicion.

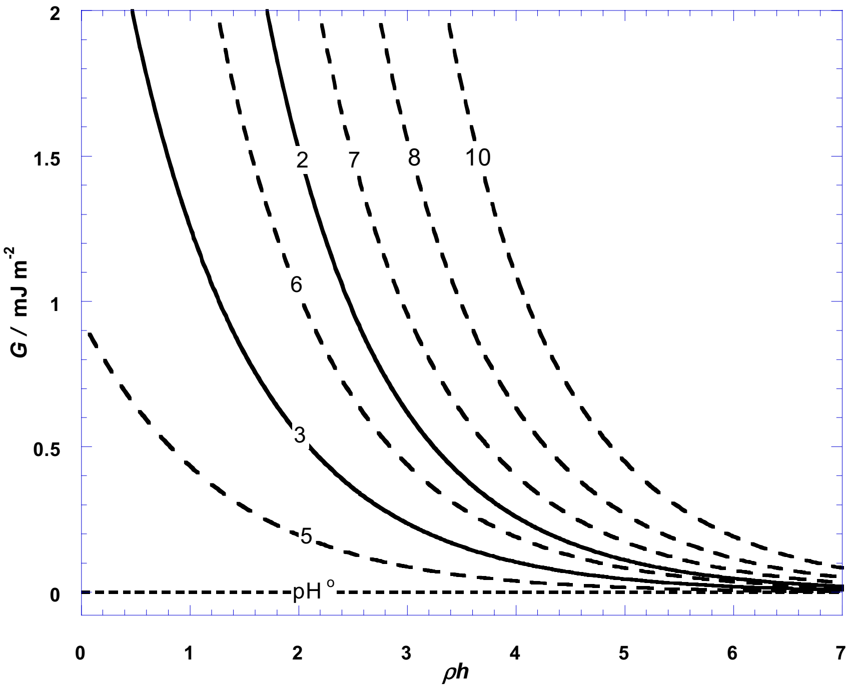

Figure 8. Influence of surface charge regulation at given Stern layer regulation values. Given is the Gibbs energy interaction. Parameter values: C_1^{i} | 120 σF cm^{-2}, N_{s}^{o} | $5\Delta10^{14}$ cm^{-2}, K_{a} | 10^{41}, K_{b} | $10^{46.5}$ (pH$^{\text{o}}$ | 4.26), c_{s} | 10^{41} M (absence of ions specific adsorption). The pH is indicated.

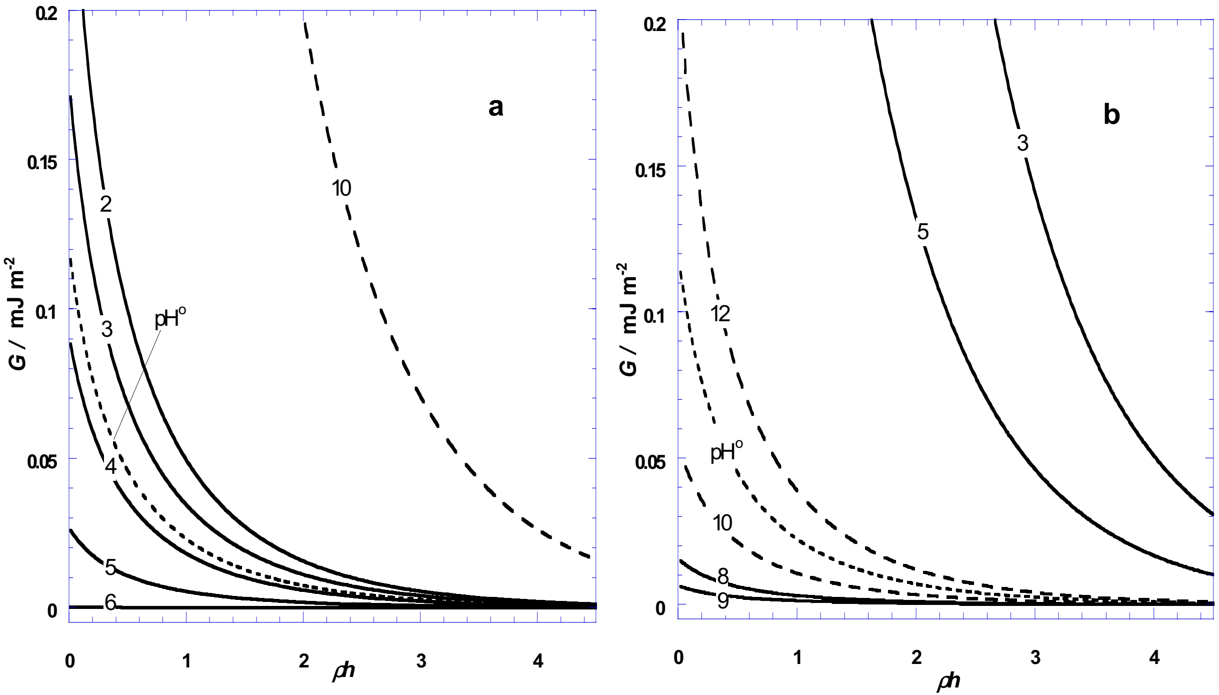

Figure 9. Combination of surface- and iHp- charge regulation. Parameter values: C_1^{i} | 120 σF cm^{-2}, C_2^{i} | 20 σF cm^{-2}, $N_{\mathrm{s}}^{\mathrm{o}}$ | $N_{\mathrm{s}}^{\mathrm{i}}$ | 5Δ10^{14} cm^{-2}, K_{a} | 10^{45}, K_{b} | 10$^{44.5}$ (pH$^{\mathrm{o}}$ | 7.26),K_{i} | 70. Panel a: specific adsorption of anions (z_{i} | 41). Panel b: specific adsorption of cations (z_{i} | 21). The pH is indicated.

4. Hetero-interaction

By 'hetero-interaction' we shall understand all those cases where the two overlapping double layers are different in *any* respect, i.e. including the situation where the two surface charges and -potentials are identical but the two regulation capacities are different. As compared with homo-interaction, the physically new feature is that upon close approach under certain conditions one of the two double layers (the 'stronger' one, 'stronger' having the meaning of 'higher surface charge', 'higher surface potential' or lower regulation capacity) may cause surface charge (and/or potential) reversal in the other (the 'weaker' one), leading to attraction even if at large separations the two surfaces repel each other. Qualitatively, this phenomenon is not new: it can for instance be found in publications by Derjaguin[35] and Hogg et al.[36] The extent to which this induction takes place depends again on the two regulation capacities: the lower the regulation capacity of the 'stronger' double layer, the better it can induce a reverse charge (potential) in the second particle. Figure 10 shows possible potential-distance trends and at the same time defines our nomenclature.

4.1. Theory

Mathematically, the starting equation 2 has to be generalized to

$$M(h) \mid 2c_{\mathrm{s}}RT\left[\cosh\left(zy(h)\right) 4\, 1\right] 4\, \frac{\kappa_0\kappa_{\mathrm{r}}}{2}\left(\frac{RT}{F}\right)^2\left(\frac{\mathrm{d}y(h)}{\mathrm{d}x}\right)^2 \qquad (24)$$

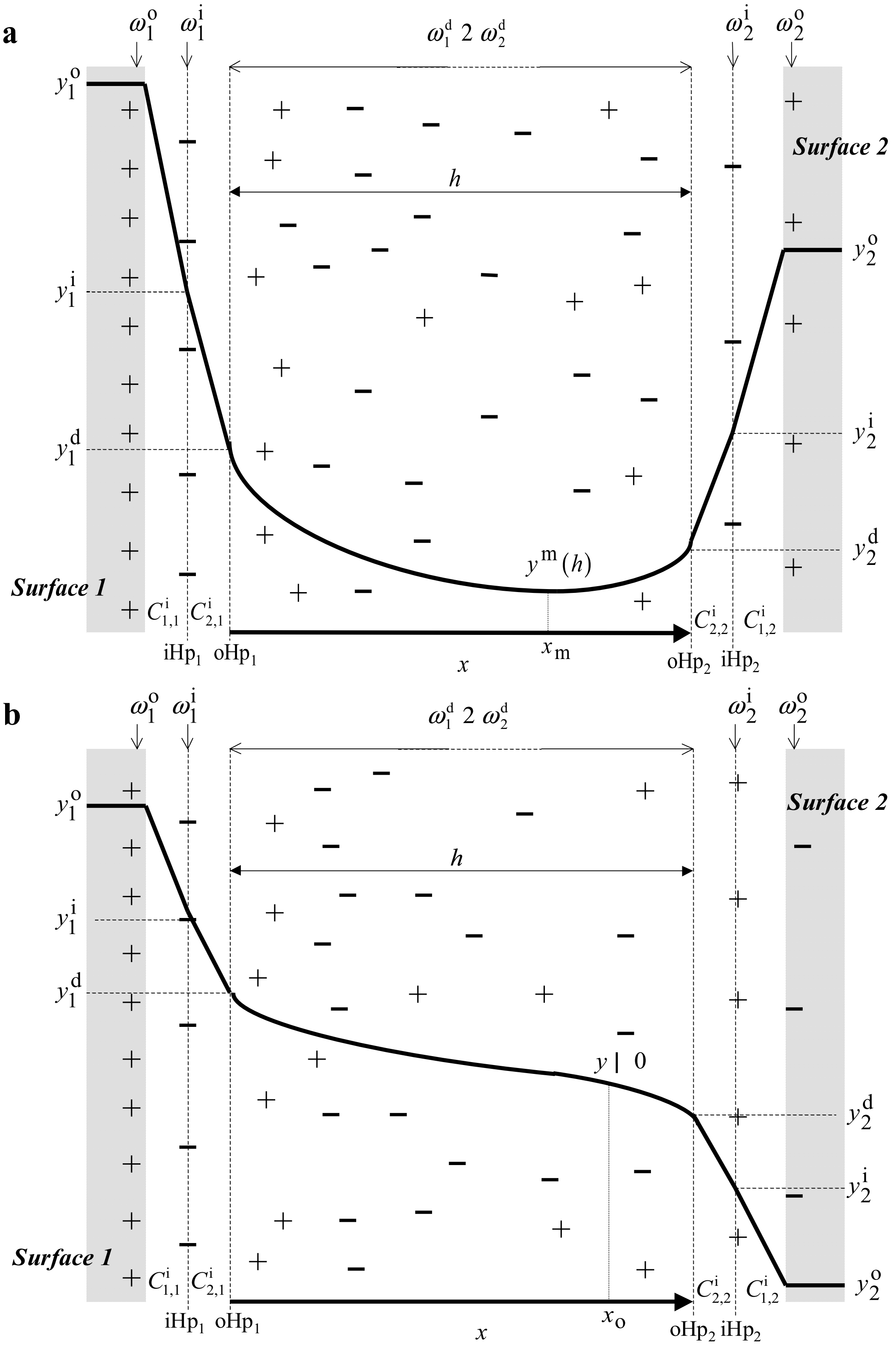
a
ω1o ω1i
ω1d = ω2d
ω2i ω2o
y1o
y1i
y1d
h
Surface 2
y2o
y2i
y2d
ym(h)
Surface 1
C1,1i C2,1i
C2,2i C1,2i
iHp1 oHp1
x
xm
oHp2 iHp2
b
ω1o ω1i
ω1d = ω2d
ω2i ω2o
y1o
y1i
y1d
h
Surface 2
y = 0
y2d
y2i
y2o
Surface 1
C1,1i C2,1i
C2,2i C1,2i
iHp1 oHp1
x
xo
oHp2 iHp2

Figure 10. Hetero-interaction between flat plates. Schematic picture of potential- and charge distributions. (a) Overlap at high regulation capacity with a potential distribution exhibiting a minimum positioned at $x = x_\mathrm{m}$, and (b) without a minimum. In the latter situation, the potential is zero at a certain value of x, called x_o (which depends on h). The picture is not to scale; in practice, mostly $h \gg d$, where d is the Stern layer thickness.

where the first and second term on the r.h.s. are the osmotic part and the Maxwell stress, which both contribute to the disjoining pressure. For homo-interactions, we applied eq 24 to the minimum in the $y(x)$ curve, where the Maxwell stress vanishes so that eq 24 reduces to eq 2. This stress can be evaluated from Poisson-Boltzmann theory except for an integration constant C

$$\left[\frac{\mathrm{d}y(h)}{\mathrm{d}(\rho \mathrm{x})}\right]^2 \,|\, \frac{2}{z^2}\left[\cosh\left(zy(h)\right)\right] 2\, C \tag{25}$$

Consequently,

$$M(h) \,|\, 42c_{\mathrm{s}}RT\left[C(h)\, 2\, 1\right] \tag{26}$$

This equation is deceptively simple but general. It applies to potential distributions with or without a minimum, but theory is required to obtain $C(h)$. Several literature examples are known where this is elaborated for purely diffuse double layers[7, 10, 15, 37-39] under various conditions. Now we generalize the analysis to interaction between Gouy-Stern layers.

A way to find $C(h)$ is by relating the field strengths at $x \,|\, 0$ and $x \,|\, h$ to the corresponding diffuse charges $\omega_1^{\mathrm{d}}(h)$ and $\omega_2^{\mathrm{d}}(h)$ using Gauss' law and by combining the results with eq 25. The calculation leads to

$$C(h) \,|\, \frac{z^2}{2\rho^2}\left(\frac{F\omega_1^{\mathrm{d}}(h)}{\kappa_0\kappa_{\mathrm{r}}RT}\right)^2 4\cosh\left(zy_1^{\mathrm{d}}(h)\right) \,|\, \frac{z^2}{2\rho^2}\left(\frac{F\omega_2^{\mathrm{d}}(h)}{\kappa_0\kappa_{\mathrm{r}}RT}\right)^2 4\cosh\left(zy_2^{\mathrm{d}}(h)\right) \tag{27a,b}$$

In the limit of low potentials, the cosh functions in eqs 24 and 27 may be replaced by their first order Taylor expansions. In the following, for the sake of illustration, the analytical relations between the charges/potentials ω_1^{d}, ω_2^{d}, y_1^{d} and y_2^{d} are given for the linearized Poisson-Boltzmann equation, which applies for low till moderate y^{d} potentials, a condition which is often met experimentally, especially under conditions of coagulation. The potential distribution can be computed by taking either the diffuse charges or the potentials at the oHp's as boundary conditions. These two quantities both depend on h in a way dictated by the type of regulation mechanism (see section 4.2). In terms of y_1^{d} and y_2^{d}, the results are

$$\omega_1^{\mathrm{d}}(h) \,|\, \frac{\kappa_0\kappa_{\mathrm{r}}RT\rho}{F}B^{(\ldots)}(h) \tag{28}$$

$$\omega_2^{\mathrm{d}}(h) \,|\, 4\frac{\kappa_0\kappa_{\mathrm{r}}RT\rho}{F}\left[A^{(\ldots)}(h)\sinh(\rho h)\, 2\, B^{(\ldots)}(h)\cosh(\rho h)\right] \tag{29}$$

with

$$A^{(\ldots)}(h) \mid y_1^{\mathrm{d}}(h) \tag{30}$$

$$B^{(\ldots)}(h) \mid \frac{y_2^{\mathrm{d}}(h) \, 4 \, y_1^{\mathrm{d}}(h)\cosh(\rho h)}{\sinh(\rho h)} \tag{31}$$

If the boundary conditions are written in terms of the diffuse charges, the analysis yields

$$y_1^{\mathrm{d}}(h) \mid A^{(\omega)}(h) \tag{32}$$

$$y_2^{\mathrm{d}}(h) \mid A^{(\omega)}(h)\cosh(\rho h) \, 2 \, B^{(\omega)}(h)\sinh(\rho h) \tag{33}$$

with

$$A^{(\omega)}(h) \mid 4 \frac{F}{\kappa_0 \kappa_{\mathrm{r}} RT\rho}\left[\omega_2^{\mathrm{d}}(h)\operatorname{cosech}(\rho h) \, 2 \, \omega_1^{\mathrm{d}}(h)\coth(\rho h)\right] \tag{34}$$

and

$$B^{(\omega)}(h) \mid \frac{F\omega_1^{\mathrm{d}}(h)}{\kappa_0 \kappa_{\mathrm{r}} RT\rho} \tag{35}$$

Rearranging eqs 28-31 and 32-35, one may write the diffuse charges $\omega_{1,2}^{\mathrm{d}}(h)$ and the potentials $y_{1,2}^{\mathrm{d}}(h)$ as

$$\left[\omega_{1,2}^{\mathrm{d}}(h) \, 4 \, \omega_{1,2}^{\mathrm{d}}(\leftarrow)\right] / \, \omega_{1,2}^{\mathrm{d}}(\leftarrow) \mid \coth(\rho h) \, 4 \left[y_{2,1}^{\mathrm{d}}(h) / \, y_{1,2}^{\mathrm{d}}(h)\right]\operatorname{cosech}(\rho h) \, 4 \, 1 \tag{36}$$

$$\left[y_{1,2}^{\mathrm{d}}(h) \, 4 \, y_{1,2}^{\mathrm{d}}(\leftarrow)\right] / \, y_{1,2}^{\mathrm{d}}(\leftarrow) \mid \coth(\rho h) \, 2 \left[\omega_{2,1}^{\mathrm{d}}(h) / \, \omega_{1,2}^{\mathrm{d}}(h)\right]\operatorname{cosech}(\rho h) \, 4 \, 1 \tag{37),}$$

respectively. This pair of equations accounts for the propensity of the interacting Gouy-Stern layers for charge and/or potential reversals with respect to the situations at infinite separation (isolated double layers). In eqs 36-37, the term $\coth(\rho h)$ dominates at large *h* (weak interaction). The coefficients of the cosech terms account for the extents of induction and they are determined by the regulation capacities of the two double layers. Similar expressions can also be derived for mixed boundary conditions (constant potential y_1^{d} and constant charge ω_2^{d}, etc). On the basis of mere diffuse double layer theory, it is impossible to discriminate between the various options of repulsion and attraction because the sign of M (eq 26) is sensitive to the extent of constancy of ω_1^{d}, ω_2^{d}, y_1^{d} and y_2^{d}, which is determined by the two primary capacities. The next step consists then in finding expressions for the various y^{d}'s and ω^{d}'s in terms of the Stern layers. Otherwise stated, we need to extend eqs 9-11 and 23 to the case of two different Stern layers. The results are

$$y_1^{\mathrm{i}}(h) \mid y_1^{\mathrm{d}}(h) \, 4 \, \frac{\kappa_0 \kappa_{\mathrm{r}} \rho}{C_{2,1}^{\mathrm{i}}} B^{(\ldots)}(h) \tag{38}$$

$$y_2^{\mathrm{i}}(h) \mid y_2^{\mathrm{d}}(h) \, 2 \, \frac{\kappa_0 \kappa_{\mathrm{r}} \rho}{C_{2,2}^{\mathrm{i}}}\left[A^{(\ldots)}(h)\sinh(\rho h) \, 2 \, B^{(\ldots)}(h)\cosh(\rho h)\right] \tag{39}$$

$$\omega_1^{\mathrm{d}}(h) = \frac{RTC_{2,1}^{\mathrm{i}}}{F}\left[y_1^{\mathrm{d}}(h) - y_1^{\mathrm{i}}(h)\right] \quad \omega_2^{\mathrm{d}}(h) = \frac{RTC_{2,2}^{\mathrm{i}}}{F}\left[y_2^{\mathrm{d}}(h) - y_2^{\mathrm{i}}(h)\right] \tag{40a,b}$$

$$y_1^{\mathrm{o}}(h) = y_1^{\mathrm{i}}(h) + \frac{F\omega_1^{\mathrm{o}}(h)}{RTC_{1,1}^{\mathrm{i}}} \quad y_2^{\mathrm{o}}(h) = y_2^{\mathrm{i}}(h) + \frac{F\omega_2^{\mathrm{o}}(h)}{RTC_{1,2}^{\mathrm{i}}} \tag{41a,b}$$

$$\omega_{1,2}^{\mathrm{o}}(h) = 2FN_{\mathrm{s}_{1,2}}^{\mathrm{o}} \frac{\left(\dfrac{K_{\mathrm{a}_{1,2}}K_{\mathrm{b}_{1,2}}}{K_{\mathrm{W}}}\right)^{1/2}\sinh\left[y_{1,2}^{\mathrm{N}} - y_{1,2}^{\mathrm{o}}(h)\right]}{1+2\left(\dfrac{K_{\mathrm{a}_{1,2}}K_{\mathrm{b}_{1,2}}}{K_{\mathrm{W}}}\right)^{1/2}\cosh\left[y_{1,2}^{\mathrm{N}} - y_{1,2}^{\mathrm{o}}(h)\right]} \tag{42}$$

$$\omega_{1,2}^{\mathrm{i}}(h) = \frac{z_{\mathrm{i}}eN_{\mathrm{s}_{1,2}}^{\mathrm{i}}x_{\mathrm{i}_{1,2}}K_{\mathrm{i}_{1,2}}\exp\left(-z_{\mathrm{i}}y_{1,2}^{\mathrm{i}}(h)\right)}{1+x_{\mathrm{i}_{1,2}}K_{\mathrm{i}_{1,2}}\exp\left(-z_{\mathrm{i}}y_{1,2}^{\mathrm{i}}(h)\right)} \tag{43}$$

$A^{(\ldots)}(h)$ and $B^{(\ldots)}(h)$ remain given by eqs 30 and 31, respectively. The definitions of the parameters $y_{1,2}^{\mathrm{N}}$, $K_{1,2}^{\mathrm{i}}$, $N_{\mathrm{s}_{1,2}}^{\mathrm{o}}$, $N_{\mathrm{s}_{1,2}}^{\mathrm{i}}$, $x_{\mathrm{i}_{1,2}}$ and $\mathrm{pH}_{1,2}^{\mathrm{o}}$ are similar to those for homo-interaction. The main difference with homo-interaction is that splitting of the general electroneutrality condition (1) into its two constituents (8a) and (8b) is no longer allowed. With hetero-interaction, situations may occur where, say $\omega_1^{\mathrm{o}}(h) + \omega_1^{\mathrm{i}}(h) + \omega_1^{\mathrm{d}}(h) \neq 0$ provided the sum of all charges on double layer 2 is equal in size but positive in sign. Models for hetero-interactions which include the electroneutrality condition as written in (8a,b) are necessarily valid only for weak double layers overlap, which corresponds to separation distances h where charge regulation is not critical in determining the interaction Gibbs energy. One can show that the set of eqs 3, 26, 27a, 30, 31, 38-43 can be rewritten in terms of the two unknowns $y_1^{\mathrm{d}}(h)$ and $y_2^{\mathrm{d}}(h)$, only. Consistent solution therefore requires two linearly independent equations. One of them is provided by the electroneutrality condition (1) and the other by the relation (27b).

The essential elements for the description of hetero-interaction are, as explicitly described in section 4.1, the concomitant occurrence of electrical and chemical regulations for the two interacting Gouy-Stern double layers. These were numerically implemented in a mean field lattice theory which was developed in our department by Scheutjens and Fleer and which has shown to be valuable for adsorbed polymers and polyelectrolytes.[40-43] In our modification, the space between the two surfaces is divided into a number of plan parallel thin layers of thickness ι. The number of layers ι can be chosen at will; ι is of the order 0.3 nm. In each layer the embedded water molecules and ions are laterally distributed; the nature of this distribution was shown not to be crucial. Each layer consists of cells interacting with all neighboring cells through chemical and electric forces. The mean field principle enters in that in each layer charges and potentials are smeared-out. The mean field analysis is performed in the more general context of the non-linearized Poisson Boltzmann equation. The three contributions to the total interaction Gibbs energy are (i) the electric energy, (ii) the Gibbs free energy change due to chemical ad- and de-sorption of ions at the surface and at the iHp and (iii) the effect of entropy loss or gain.[16] The total interaction Gibbs energy was iteratively computed for every separation distance h. One can show by means of the Euler-Lagrange equation[43,44] that this energy, if calculated from the self consistent potential and charge distributions as governed by the Poisson Boltzmann equation, actually corresponds to the minimum energy searched. In the model, charge and permittivities have to be assigned to each layer. The charges are assumed to sit half-way each layer (Figure 11). Permittivities can jump discretely from one layer to the next. When the potentials are known in each layer, the charge distribution follows from Gauss' law and the potentials are updated till self consistency is reached. This model is not entirely identical to the classical picture of a Stern layer depicted in Figure 10 because there the jumps in permittivity are assumed to coincide with the charged planes (iHp and oHp). This classical picture is physically not necessarily more realistic because the value of the dielectric permittivity is to a large extent determined by the structure of the water-water and water-surface interactions, and only to a lesser extent by the presence of ions. In our analysis, we represent the Stern layer for each interface by two lattice layers, one containing the surface charge ω^{o}, the other the specifically adsorbed charge ω^{i}. To each of these, a different (smeared-out) permittivity is assigned. Starting from the third layer, no specific adsorption occurs and κ_{r} becomes 78, as in pure water. This part corresponds to the diffuse double layer.

Numerical results were first obtained for the limiting cases of interactions at constant potentials[36] and constant charges[45] and were successfully compared, within the Debye-Hückel (DH) regime, with the corresponding available analytical expressions. Results for homo- and hetero- interactions (and compatible with the DH approximation in the diffuse part of the double layer) also well match those expected on the basis of the analytical models of section 3 and 4 (not shown).

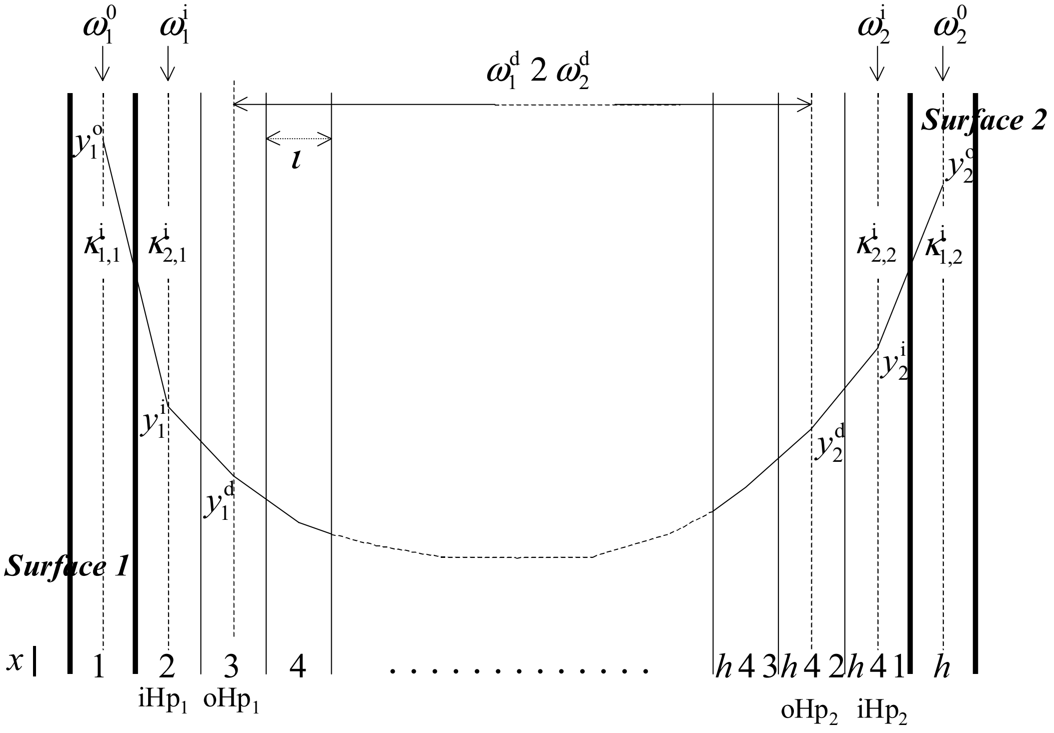
ω_1^0
ω_1^i
$\omega_1^d\ 2\ \omega_2^d$
ω_2^i
ω_2^0
Surface 2
y_1^o
ι
y_2^o
$\kappa_{1,1}^i$
$\kappa_{2,1}^i$
$\kappa_{2,2}^i$
$\kappa_{1,2}^i$
y_2^i
y_1^i
y_2^d
y_1^d
Surface 1
x |
1
2
3
4
. . . .
h 4 3
h 4 2
h 4 1
h
iHp_1
oHp_1
oHp_2
iHp_2

Figure 11. Schematic view of the lattice used for the computations based on a mean-field theory. Numbering of the adjacent layers of thickness ι is done for the situation where the surface charges $\omega_{1,2}^o$ are regulated (i.e., pH-dependent). For the case of constant $\omega_{1,2}^o$, the variable x as mentioned in the figure becomes x + 1. This figure is a discrete pendant of the continuous model as pictured in Figure 10. By choice, surface 2 approaches surface 1 (decreasing h), the latter remains at the position x | 1 (or 0) upon interaction.

4.2. Hetero-interactions: illustrations. 1- No Stern layers

In order to remain close to physical reality, we mimick the interaction between two different oxides. We first ignore specific adsorption. For double layer 1 (left), $\mathrm{p}K_{\mathrm{a}_1}$ | 6, $\mathrm{p}K_{\mathrm{b}_1}$ | 10 (pH_1^o | 5); for double layer 2 (right), $\mathrm{p}K_{\mathrm{a}_2}$ | 8, $\mathrm{p}K_{\mathrm{b}_2}$ | 6 (pH_2^o | 8). At large distances repulsion ensues for $\mathrm{pH} \{ 5$ and $\mathrm{pH} \} 8$, whereas in the window $5 < \mathrm{pH} \{ 8$, the long distance interaction is attractive. The surface charge densities $\omega_{1,2}^o$ are determined by the fraction of surface sites that is dissociated (negatively and/or positively), as in eq 15. The maximum surface charges attainable $eN_{\mathrm{s}_{1,2}}^o(\max)$ are in the lattice model determined by the cross section of each cell and corresponds to about 170 σC cm^{-2}, which is about tenfold higher than met in practice. Later, we shall consider surfaces for which only a fraction $\chi_{1,2}^o$ of $N_{\mathrm{s}_{1,2}}^o(\max)$ is available, with $\chi_{1,2}^o$ defined as

$$\chi_{1,2}^o \mid N_{\mathrm{s}_{1,2}}^o / N_{\mathrm{s}_{1,2}}^o(\max) \tag{44}$$

so that $\omega^{\mathrm{o}}_{1,2}(\max) \,|\, e\chi^{\mathrm{o}}_{1,2}N^{\mathrm{o}}_{\mathrm{s}1,2}(\max)$. These maxima require extreme pH's to be reached; in fact, for oxides, $\omega^{\mathrm{o}}_{1,2}$ are always lower than $\omega^{\mathrm{o}}_{1,2}(\max)$. The charge plays a dual role, viz. not only as a source for the potential, but also as a parameter determining the regulation capacities of the surface charge layer. Figures 12-14 gives first results for the charge and potential distributions for different separations at different pH's. At pH $|$ 3, for long distance, ω^{o}_{2} is more positive than ω^{o}_{1} because for surface 2 the pH is more to the left of the pzc than for surface 1. Both surface charges are largely compensated by the diffuse charge in the layer adjacent to the surface layer (see the hatched areas, Figure 12a). Half-way the two surfaces, there is almost no excess charge; there the potential is near-zero (panel b), implying that the largest distance covered is essentially infinite ($h \,\}\}\, \rho^{41}$). Upon approach, ω^{o}_{2} remains virtually constant except for a slight decrease for $x \,\{\, 3\iota$. At the same time, ω^{o}_{1} decreases: it even becomes slightly negative for short separations. This induced charge reversal has two causes: partly it originates from the strong electric field of the proximate surface 2, partly it has an entropic origin; since double layer 1 carries fewer charges, it has a larger regulation capacity. Similar observations can be made for the potentials. Because of the large regulation capacity of double layer 1, y^{o}_{1} hardly changes but y^{d}_{1} does, as a consequence of the charge accumulation at $x \,|\, 2\iota$, when the two 'diffuse' parts coincide. Figure 13 gives similar pictures for pH $|$ 5, which corresponds to particle 1 being uncharged. At large separations, $\omega^{\mathrm{o}}_{1} \,|\, 0$, but it becomes negative upon approach of particle 2. This is caused by induction from particle 2. At the same time, ω^{o}_{2} starts from a positive value which is less positive than at pH $|$ 3 because we are now closer to $\mathrm{pH}^{\mathrm{o}}_{2}$. The potential profile has no minimum. At large *x*, it starts horizontally from surface 1, becoming steeper upon approach. Upon this, y^{o}_{1} remains almost constant at zero, but y^{d}_{1} increases, to coincide eventually with y^{d}_{2} at the closest distance attainable. The notable observation is that in this situation ω^{o}_{2} increases somewhat. Phenomenologically, this means that the nearby particle 1 with its now negative ω^{o}_{1} acts as a capacitance booster for particle 2. Similar observations for a pH somewhat lower than 5 (not shown) can be made. The only difference is that the potential profile presents at large separations a minimum, which upon approach gradually disappears in tandem with the sign reversal of ω^{o}_{1}. The boosting effect, as mentioned for pH = 5, is for these pH 's not so pronounced since surface 1 carries at large separations a charge of the same sign as surface 2. At pH $|$ 6 (Figure 14), particle 1 is now originally negatively charged, particle 2 (less) positively charged. A certain asymmetry is now observed: upon approach, ω^{o}_{1} becomes more negative, ω^{o}_{2} more positive. Each surface

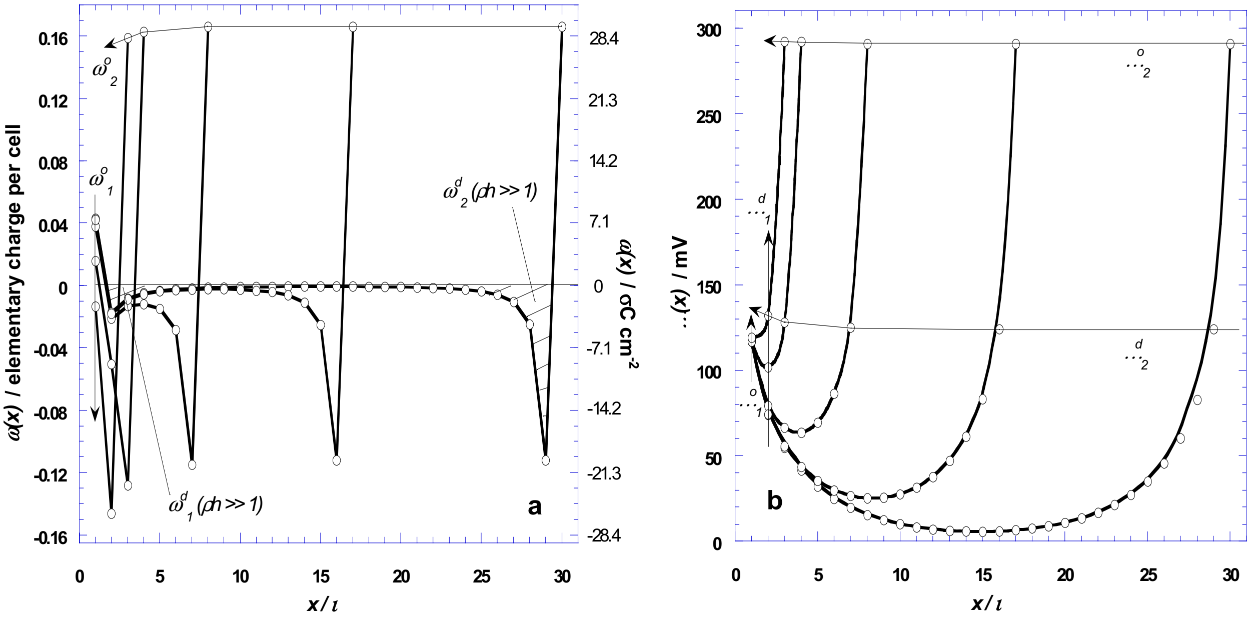

Figure 12. Hetero-interactions between two flat oxide layers, of which the surface charges are regulated across purely diffuse counterlayers. Left, surface 1, pzc_1 | 5; Right, surface 2, pzc_2 | 8; dielectric permittivities of the surface charge carrying layers κ_1^{i} | κ_2^{i} | 40, in all others 78. pH | 3, $\chi_{1,2}^{\mathrm{o}}$ | 1, c_{s} | 0.056 M. Panel a: Charge distribution; panel b: potential distribution.

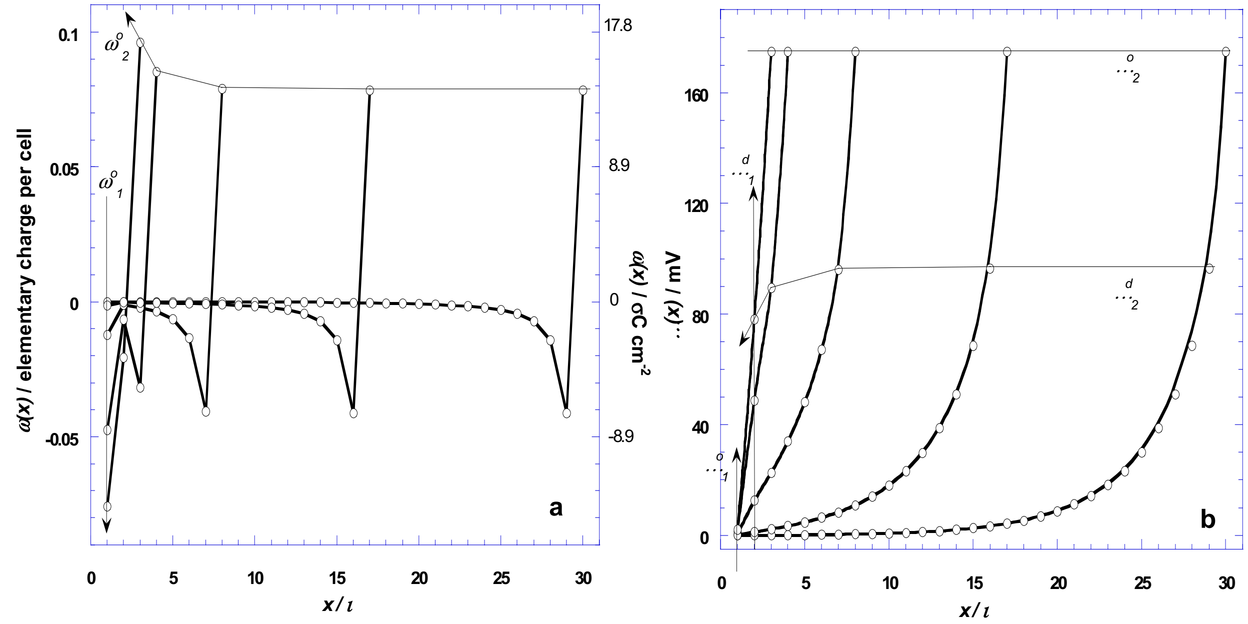

Figure 13. Situation as in Figure 12, but at pH | pzc_1.

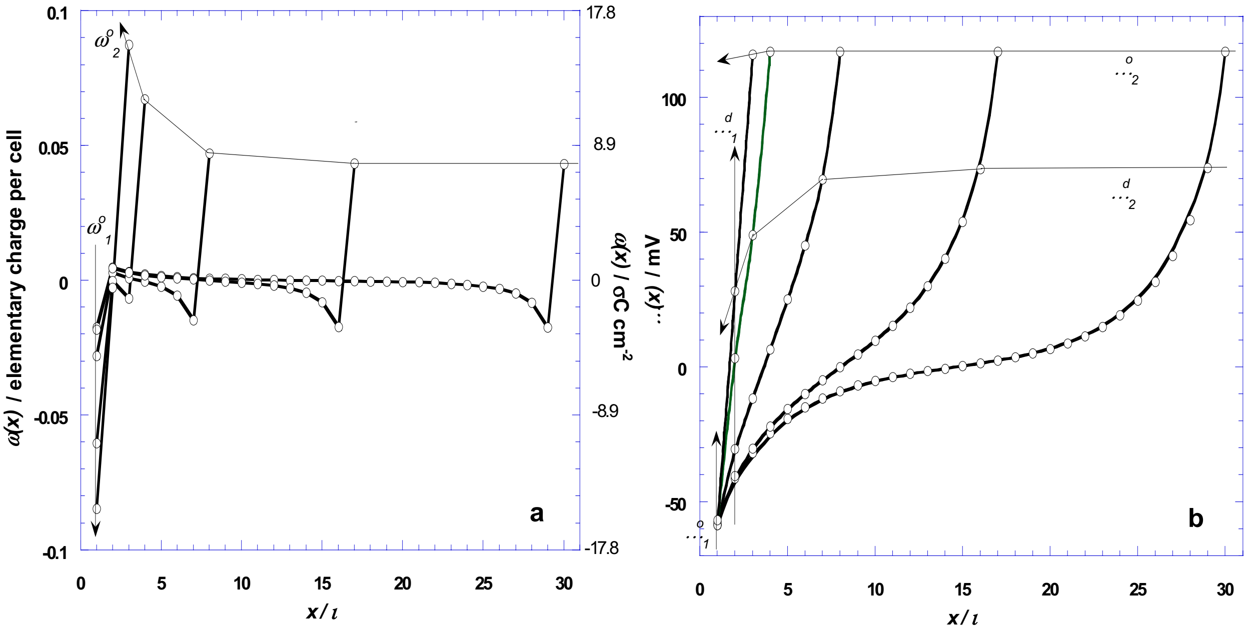

Figure 14. Situation as in Figure 12, but at pH | 6.

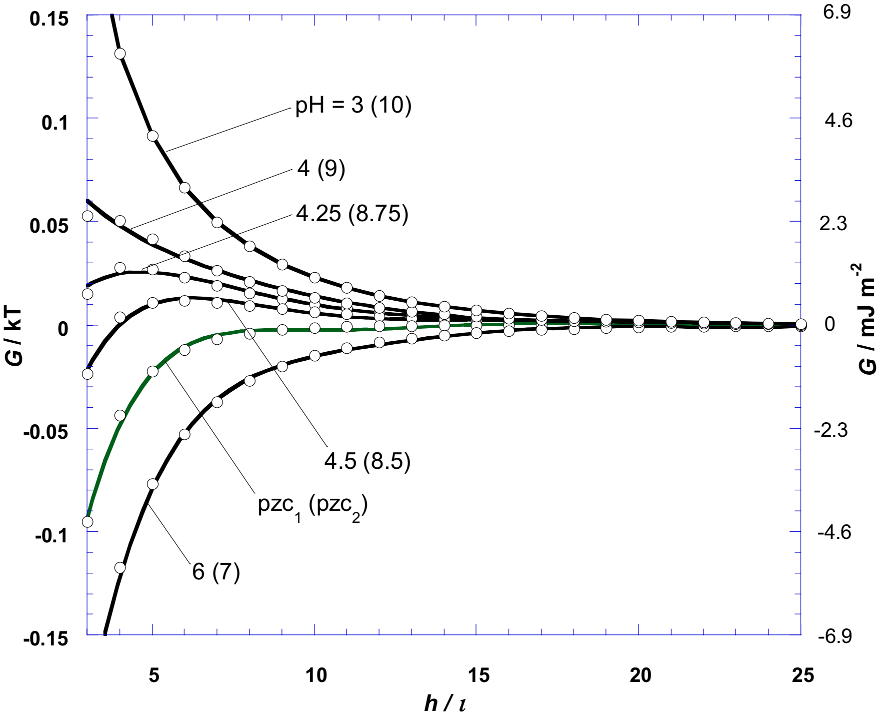

Figure 15. Interaction Gibbs energy for different pH's (indicated). For symmetry reasons, each curve refers to two pH's, pH_1 and pH_2, verifying pzc_1 4 pH_1 | pH_2 4 pzc_2 with pH_1 { pzc_1 and pH_2 } pzc_2. Other model parameters: as in Figure 12.

acquires a higher capacitance caused by the closeness of the other. The surface potentials do not change markedly, but the diffuse potentials do: y_2^{d} becomes less positive, y_1^{d} less negative and even changes sign ($\mathrm{pH} \mid 6$ is closer to $\mathrm{pH}_1^{\mathrm{o}}$ than to $\mathrm{pH}_2^{\mathrm{o}}$) till in the final situation $y_1^{\mathrm{d}} \mid y_2^{\mathrm{d}}$, of course. Similar figures can be drawn for other pH's with the situations at pH 8 and 10 being symmetrical to those at pH 5 and 3, respectively. In Figure 15, we give the Gibbs energy-separation curves for the situations commented above. The transition between overall repulsion and attraction upon increase of pH is in line with the characteristic charge-potential distributions of Figures 12-14.

The surface charge is not only determined by pH (Figures 12-15) but also by $\chi_{1,2}^{\mathrm{o}}$ as given by eq 44. The availability of sites also contributes to the regulation capacity. For $\chi_1^{\mathrm{o}} \mid \chi_2^{\mathrm{o}} \mid 0.05$, charges and potentials become, as expected, lower than for $\chi_1^{\mathrm{o}} \mid \chi_2^{\mathrm{o}} \mid 1$ and the qualitative trends do not change (not shown). Figure 16 illustrates the effects of $\chi_{1,2}^{\mathrm{o}}$ on the Gibbs energy of interaction; it may be compared with the curves for $\chi_1^{\mathrm{o}} \mid \chi_2^{\mathrm{o}} \mid 1$. No qualitatively new features emerge. In all cases, lowering of $\chi_{1,2}^{\mathrm{o}}$ reduces both attraction and repulsion. For $\mathrm{pH} \mid 4.5$, where G is partly negative and partly positive the transition takes place at a separation (panel b) which becomes shorter at lower $\chi_{1,2}^{\mathrm{o}}$. At this point, G is a maximum and $M \mid 0$. The maximum disappears for low $\chi_{1,2}^{\mathrm{o}}$, i.e. low regulation capacities. The Gibbs energies $G^{(\omega)}$ and $G^{(\ldots)}$, corresponding to the limiting interactions 'at constant charge' and 'at constant potential' respectively were computed for $\chi_{1,2}^{\mathrm{o}} \mid 0.05$. For $G^{(\omega)}$ and $G^{(\ldots)}$, we have the well-known analytical expressions derived by Hogg et al. (HHF)[36] and Usui[45] in the Debye-Hückel approximation

$$G^{(\ldots)} \mid \frac{\kappa_0 \kappa_{\mathrm{r}} \rho (RT)^2}{F^2} \left[\left\{ \left(y_1^{\mathrm{d}}(\leftarrow) \right)^2 2 \left(y_2^{\mathrm{d}}(\leftarrow) \right)^2 \right\} \left(1\,4 \coth(\rho h) \right) 2\; 2 y_1^{\mathrm{d}}(\leftarrow) y_2^{\mathrm{d}}(\leftarrow) \operatorname{cosech}(\rho h) \right] \tag{45}$$

$$G^{(\omega)} \mid \frac{\kappa_0 \kappa_{\mathrm{r}} \rho (RT)^2}{F^2} \left[\left\{ \left(y_1^{\mathrm{d}}(\leftarrow) \right)^2 2 \left(y_2^{\mathrm{d}}(\leftarrow) \right)^2 \right\} \left(\coth(\rho h)\, 4\, 1 \right) 2\; 2 y_1^{\mathrm{d}}(\leftarrow) y_2^{\mathrm{d}}(\leftarrow) \operatorname{cosech}(\rho h) \right] \tag{46}$$,

respectively. In these equations, '$\ldots$ constant' and 'ω constant' mean in reality 'y^{d} constant' and 'ω^{d} constant' because this pair was derived for purely diffuse double layers. However, it now transpires that the constancy of y^{d} and ω^{d}, underlying the applicability of (45) and (46), is an unlikely phenomenon, merging with the rigorous numerical results being met for weak overlap of

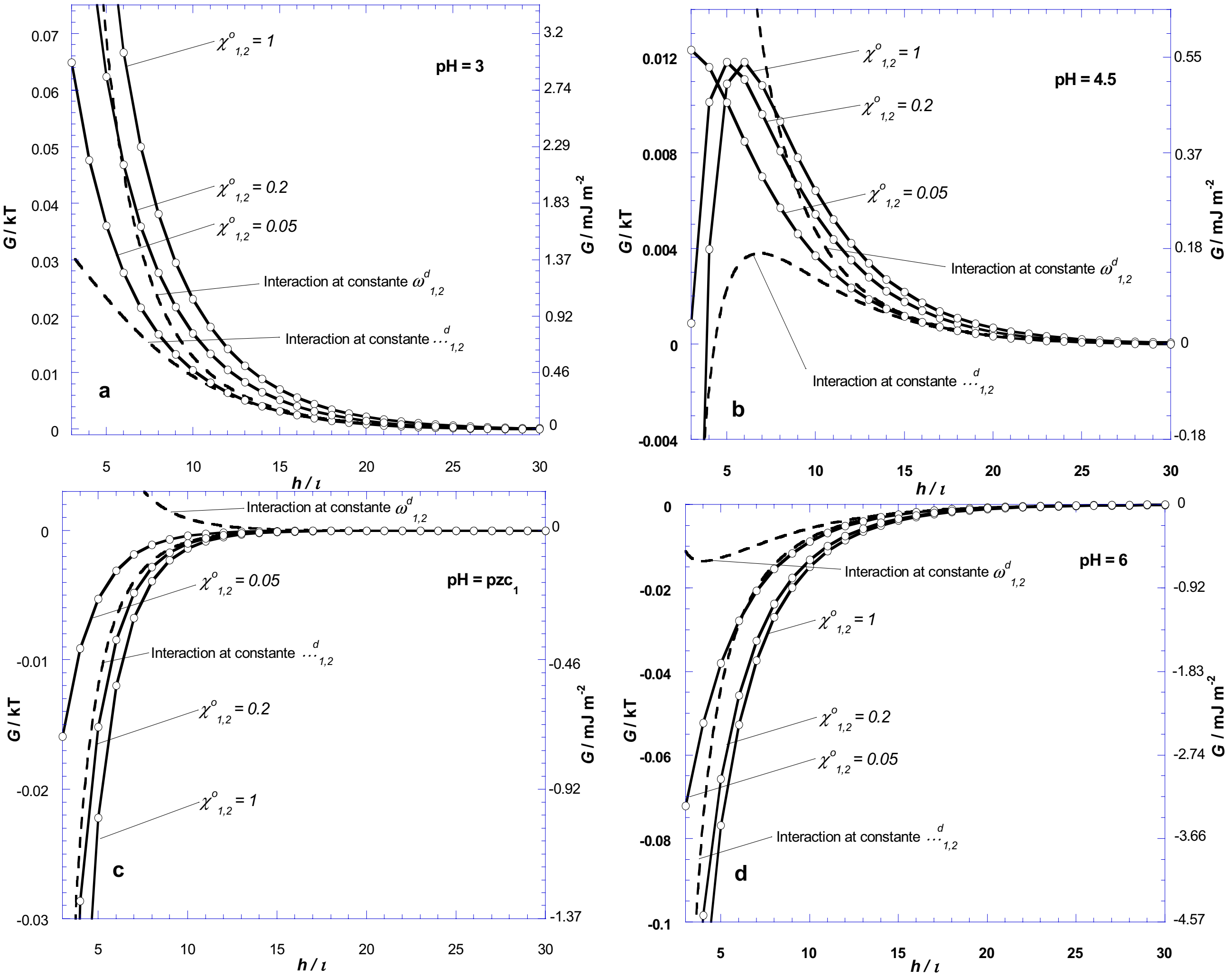

Figure 16. Influence of the number of surface sites $\chi_1^{\mathrm{o}} \mid \chi_2^{\mathrm{o}}$ (indicated). The pH is also given. Otherwise, as in Figure 12. In dashed lines, the electrostatic parts of the DLVO curves calculated at constant (diffuse) potentials and constant (diffuse) charges for $\chi_1^{\mathrm{o}} \mid \chi_2^{\mathrm{o}} \mid 0.05$ are given for comparison purposes.

the double layers. Only under special circumstances is this limit approached in reality. Thereby, it is noted that, although ω_1^{o} (or ω_2^{o}) remains more or less constant, the *distribution* of the countercharge changes substantially.

In Figure 17 we give the first illustrations of interaction between two oxidic surfaces for which not only the pzc's but also the total number of surface sites (expressed in terms of $\chi^{\mathrm{o}}_{1,2}$) is different. This pair of figures may be compared with Figures 12a,b $(\mathrm{pH} \mid 3)$. The first quantitative difference is that for the charges (Figure 17a) and potentials (Figure 17b) the absolute values are less than for $\chi_1^{\mathrm{o}} \mid \chi_2^{\mathrm{o}} \mid 1$. Qualitatively, surface 2 is now unable to change the sign of double layer 1; in fact, upon approach ω_2^{o} reduces more strongly than for $\chi_2^{\mathrm{o}} \mid 1$. The physical reason is that RC$_2$ is higher than that for $\chi_2^{\mathrm{o}} | 1$ (surface 2 has now less adsorption sites available and therefore double layer 2 is weaker). This is essentially an entropic feature. It is also reflected in the potentials: y_2^{o} and y_2^{d} increase more upon reduction of h than for $\chi_1^{\mathrm{o}} | \chi_2^{\mathrm{o}} | 1$. These trends become more pronounced for very low sites coverage ($\chi_2^{\mathrm{o}} | 1\%$, not shown).

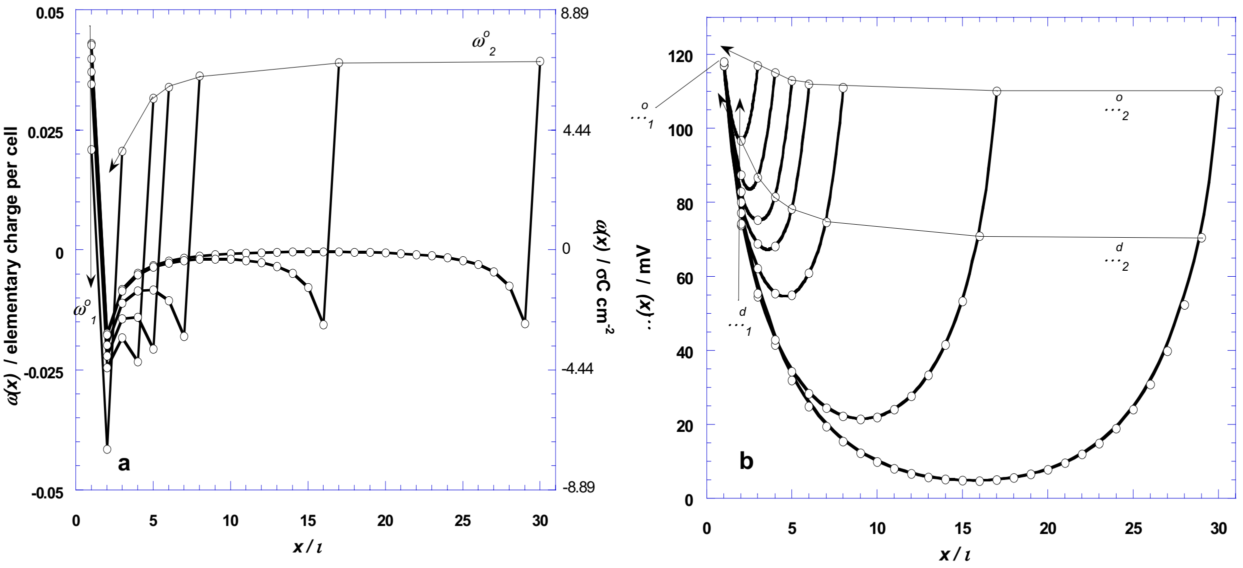

Figure 17. As for Figure 12 (pH | 3), but with $\chi_2^{\mathrm{o}} | 0.10$ ($\chi_1^{\mathrm{o}} | 1$).

The regulation of the surface charges at pH | 8.5, $\chi_1^{\mathrm{o}} | 1$ and $\chi_2^{\mathrm{o}} | 0.1$ are presented in Figure 18a. The pendant for the potentials is shown in Figure 18b. At this pH, surface 1 is strongly negative, surface 2 very weakly so, the latter surface has fewer sites available. Upon approach, ω_2^{o} reverses sign at $h - 10\iota$ and then becomes increasingly positive by induction from surface 1. At the same time, ω_1^{o} does not change much (lower regulation capacity) but on closer inspection it passes through a shallow maximum. First, ω_1^{o} becomes slightly less negative because of the repulsion of particle 2, but when the particles come very close, the increase of the capacitance allows surface 1 to adsorb (a few) more (negative) charges. The potential distributions $y_1^{\mathrm{o}}(h)$ and $y_1^{\mathrm{d}}(h)$ illustrate the same. The trends of Figure 18 are even more marked when $\chi_2^{\mathrm{o}} | 0.01$ (not shown). Then surface 2 behaves as if it is virtually uncharged, so that a situation arises that is almost symmetrical of Figure 13.

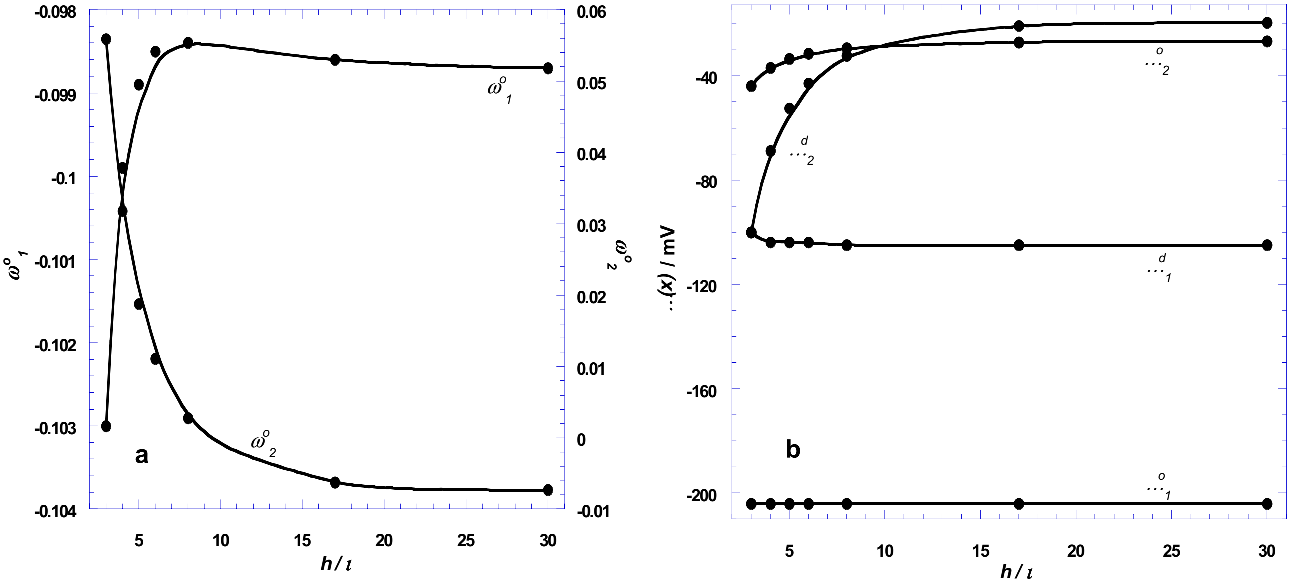

Figure 18. Similar situation as in Figure 17, but at pH | 8.5. For the sake of readability, the distributions of the characteristic charges (in elementary charges per unit cell) and potentials (in mV) as a function of *h* are given. The curves are only guide to the eyes.

The profile changes at different pH's and χ^{o}'s make themselves felt in the Gibbs energy of interaction, of which we now give some illustrations. Generally speaking, $G(h)$ reflects the two surface charges $\omega_1^{\mathrm{o}}(h)$ and $\omega_2^{\mathrm{o}}(h)$ and the distribution of the countercharge between the surfaces which, in turn, are governed by the two regulation capacities, and which have electrical and chemical components (via the pK's). Because of the multiparameter dependence, it is not always easy to relate $G(h)$ in a simple way to these parameters. Figure 19 collects some results. Panel a (pH | 3, 10) shows repulsion over the entire range between surfaces that are positively or negatively charged. For χ_2^{o} | 1, the curves for pH | 3 and 10 coincide, but for χ_2^{o} | 0.1 or 0.01 the symmetry is essentially lost because pH and χ_2^{o} determine ω_2^{o} in a different way. Panel b represents the situation where one of the surfaces is so close to its pzc that reversal of charge can occur, leading to attraction at short distance although far apart the two particles have the same charge sign. As in panel a, for χ_1^{o} | χ_2^{o} | 1 $G(h)$ is symmetrical between pH | 4.5 and 8.5. The change of sign is in this case only determined by the pH influence on ω_1^{o} and ω_2^{o}. For the asymmetrical case (χ_1^{o} ∏χ_2^{o}) the influence of the available sites comes on top of it. When χ_2^{o} | 0.01, the stronger double layer 1 prevails, rendering $G(h)$ repulsive over the entire range. Panel c gives curves for interactions for which one of the pair is uncharged. Attraction prevails. Deviations from symmetry are again observed; $G(h)$ becoming low, or even slightly positive, only when $\chi_2^{\rm o}$ is very low. Panel d is similar but by choice of pH between the two pzc's attraction is much stronger than in panel c.

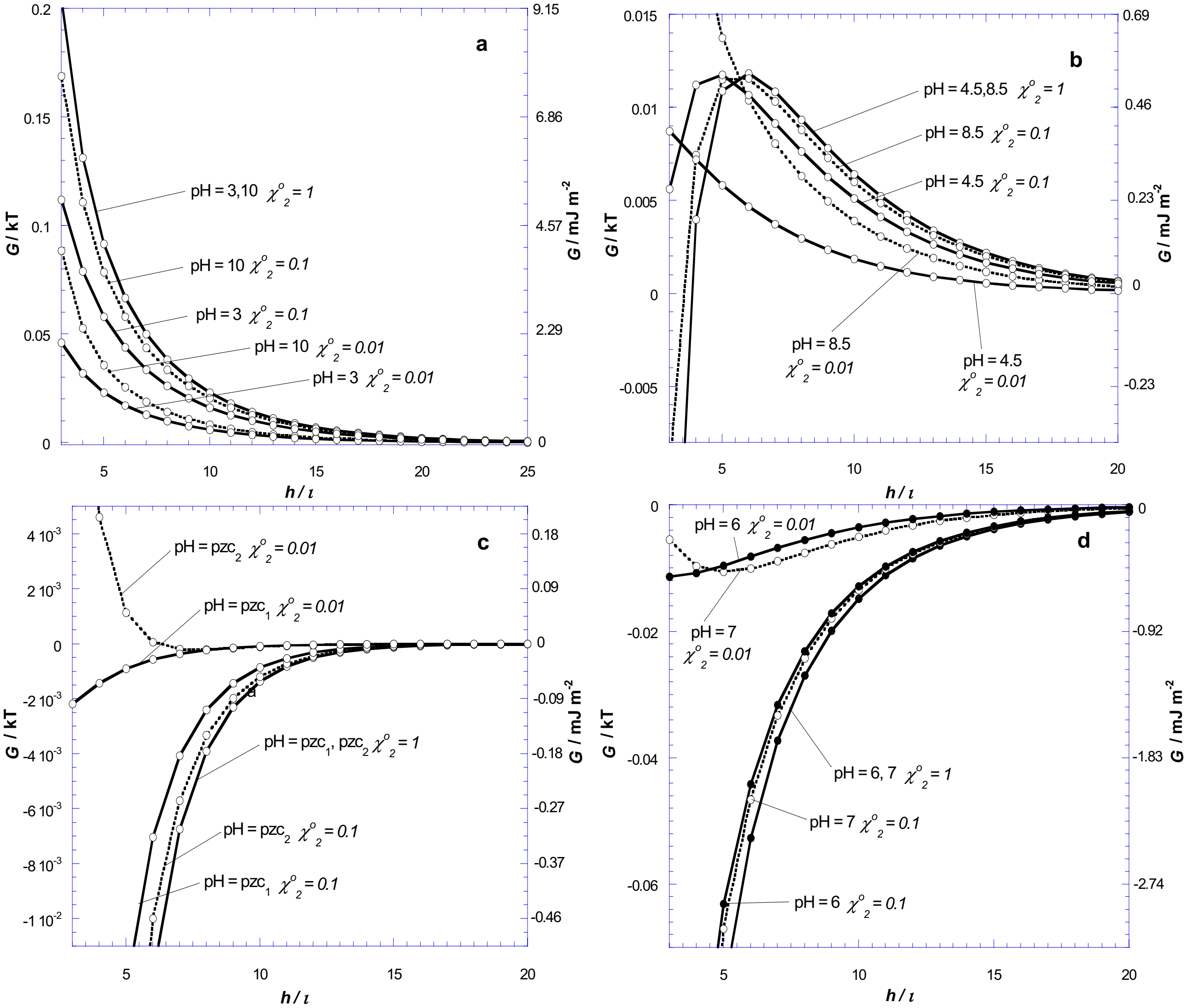

Figure 19. Gibbs energy interaction at various values of pH and $\chi_2^{\rm o}$ for the oxides defined in Figure 12. Throughout, $\chi_1^{\rm o} \mid 1$.

The influence of the indifferent electrolyte concentration $c_{\rm s}$ can be studied via its effect on the absolute value of $\omega_1^{\rm o}(h \mid \leftarrow)$ and $\omega_2^{\rm o}(h \mid \leftarrow)$ at given pH and via its influence on the potential distribution. In Figure 20 we compare the profiles at $\lambda \mid 10^{42}$ and $\lambda \mid 10^{44}$ (λ is the volume fraction defined as $\lambda \mid c_{\rm s} / V_{\rm m}$). For $\lambda \mid 10^{44}$, less charge can built up as compared to the situation at $\lambda \mid 10^{42}$; this difference is also reflected in the sign of ${\rm d}\omega_2^{\rm o} / {\rm d}h$ for low separations. The potential minimum, clearly visible for $\lambda \mid 10^{42}$, disappears at $\lambda \mid 10^{44}$. $c_{\rm s}$ not only tunes the range of electrostatic interaction but also the regulation capacities of the approaching surfaces, via the influence of indifferent electrolyte on the surface charges. The effect on the Gibbs energy of interaction is visible in Figure 21. These trends more or less conform with intuition.

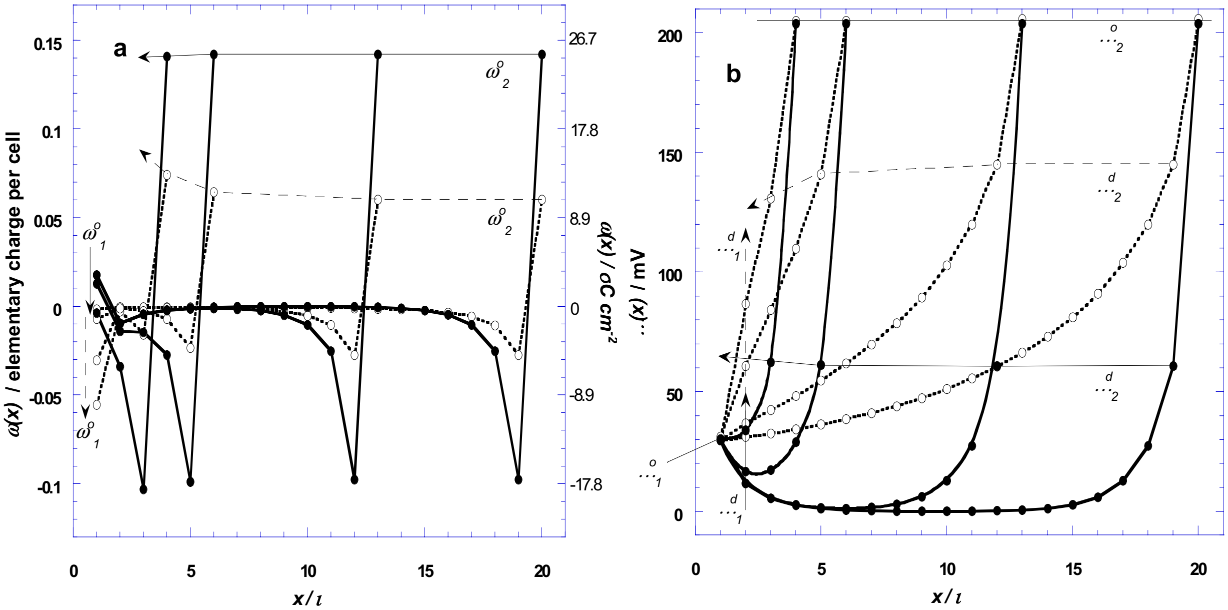

Figure 20. Charge and potential profiles for the double layer of Figure 12 at c_s | 0.56M (———) and c_s | 5.56 mM (·········), pH | 4.5. The profiles are shown for $h\,\Omega 20\iota$, distance which approximately corresponds to the sign reversal of $\omega_1^{\rm o}$ for λ | 10^{44}.

We also investigated the effect of the dielectric permittivities in the two non-diffuse parts, $\kappa_1^{\rm i}$ and $\kappa_2^{\rm i}$. Results are not shown, but the general trend is that lowering of $\kappa_1^{\rm i}$ and $\kappa_2^{\rm i}$ implies lowering of the corresponding first layer capacitances and, hence, of the regulation capacities. For instance, for $\kappa_1^{\rm i}$ | 40, reduction of $\kappa_2^{\rm i}$ from 40 to 10 at pH | 4.5 or 8.5 and $\chi_1^{\rm o}$ | $\chi_2^{\rm o}$ | 1 has no effect on G for h } 6ι but makes G less attractive at shorter distances. The parameters $\kappa_1^{\rm i}$ and $\kappa_2^{\rm i}$ tune the sizes of the surface charges and accordingly the amplitude of the charges/potentials regulations and of the corresponding interaction(s).

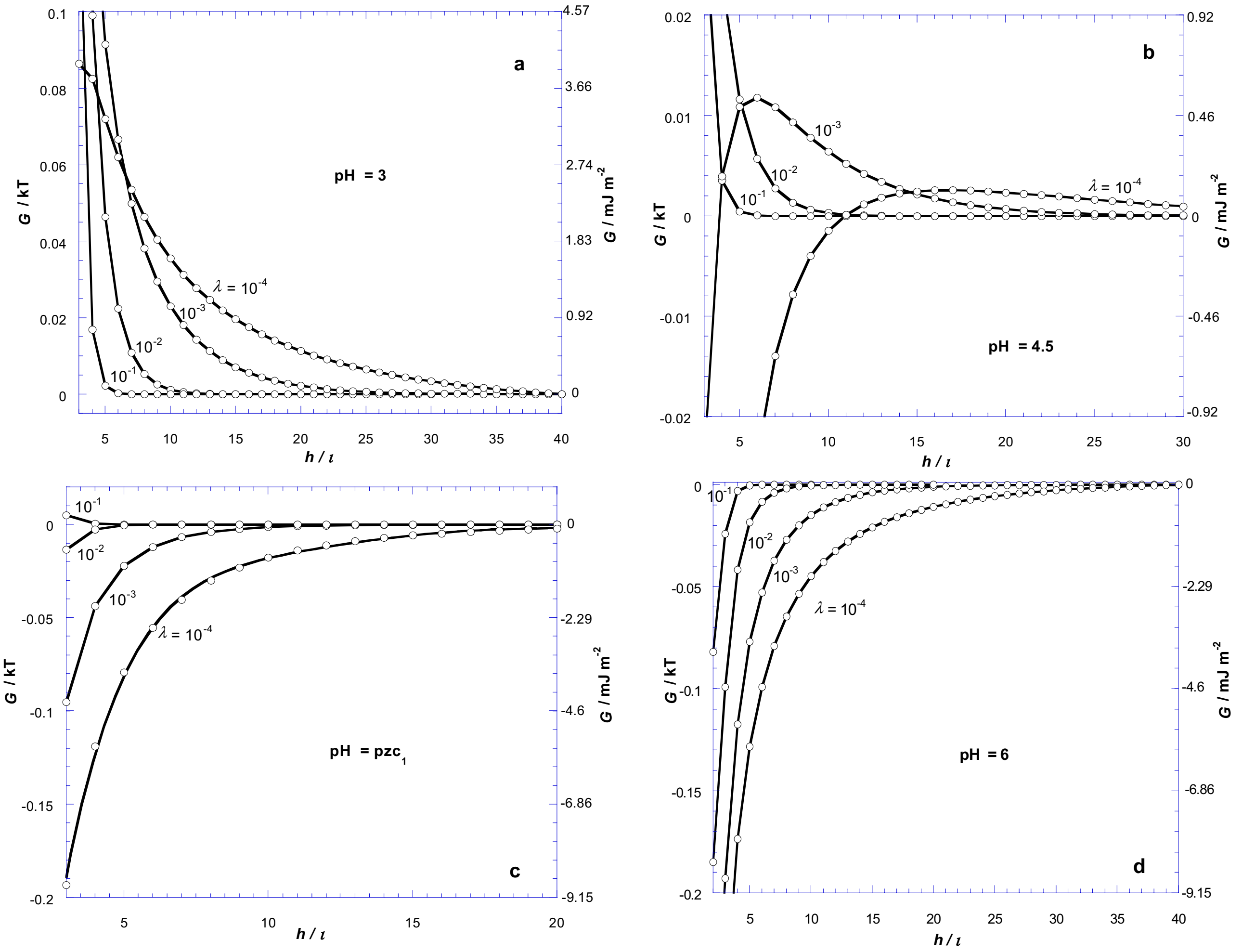

Figure 21. Electrolyte concentration influence on the interaction Gibbs energy. In this figure, c_s is indicated in terms of the volume fraction $\lambda \equiv c_s / 55.55$. Panel b refers to the profiles of Figure 20, panels a, c and d reflect the same double layers but at different pH's (indicated).

4.2. Hetero-interactions: illustrations. 2- Presence of Stern layers

The introduction of Stern layer takes us closer to reality but it also leads to a plethora of new situations, of which we shall select some illustrative cases. In the following, we define the fraction of sites available for specific adsorption as

$$\chi_{1,2}^{i} \equiv N_{s1,2}^{i} / N_{s1,2}^{i}(\max) \tag{47}$$

which is the equivalent of eq 44.

In Figure 22, the two surface charges are kept fixed in order to highlight the consequences of specific adsorption. The model is representative for two latex surfaces with different number (chemically identical) charged sites. In panel a, ω_1^{o} and ω_2^{o} remain fixed at the indicated values. The hatched area gives the countercharge of double layers 1 and 2. The parts of

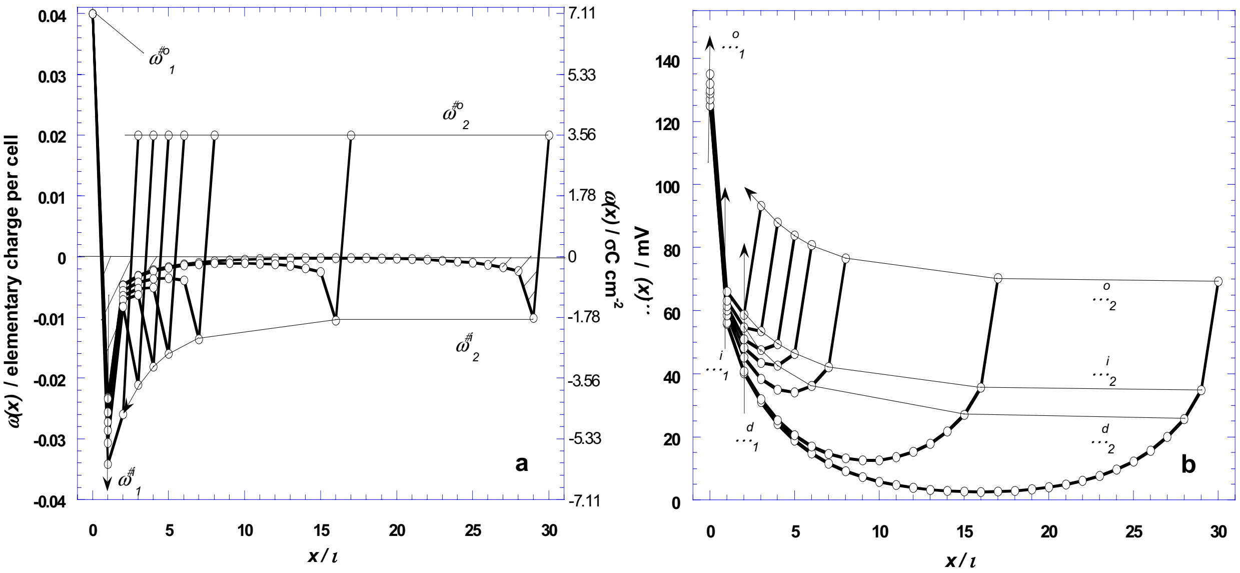

Figure 22. Charge and potential profiles for the interaction between two model surfaces; influence of specific adsorption on hetero-interactions. ω_1^{o} | 0.04, ω_2^{o} | 0.02 elementary charges per unit cell (fixed). $\div_{\mathrm{ads}}G_{\mathrm{m,i}1,2}$ | $4kT$ (anion adsorption), λ | 10^{43}. $\kappa_{1,1}^{\mathrm{i}}$ | $\kappa_{1,2}^{\mathrm{i}}$ | 20, $\kappa_{2,1}^{\mathrm{i}}$ | $\kappa_{2,2}^{\mathrm{i}}$ | 50, $\chi_{1,2}^{\mathrm{i}}$ | 1.

the two countercharges that are in the two Stern layers, ω_1^{i} and ω_2^{i}, are indicated. Upon approach of the two surfaces, ω_2^{i} becomes more negative; anion adsorption in the Stern layer of surface 2 is promoted by the presence of the strong double layer 1. By the same token, ω_1^{i} also becomes more negative but to a lesser extent than ω_2^{i} does because double layer 2 has the larger RC. The ensuing potential profiles (panel b) all increase but y_1^{o} and y_1^{i} do so also to a lesser extent than y_2^{o} and y_2^{i}.

Figure 23 gives profiles for the interaction between a stronger positive and a weaker negative surfaces. As surface 2 is negatively charged, the anions now become co-ions; they are negatively adsorbed. However, upon sufficiently close approach of surface 1, this negative adsorption becomes positive. At the same time, ω_1^{i} becomes slightly less negative because of the attraction exerted by surface 2. The trends in the respective potentials (panel b) are similar: upon approach, all y_1's decrease and y_2's become less negative to change sign at sufficiently low h. Hereby y_2^{d} is the first to change, followed by y_2^{i} and y_2^{o}, in this order, as intuitively expected. As before, the changes in the y_2's are stronger than in the y_1's.

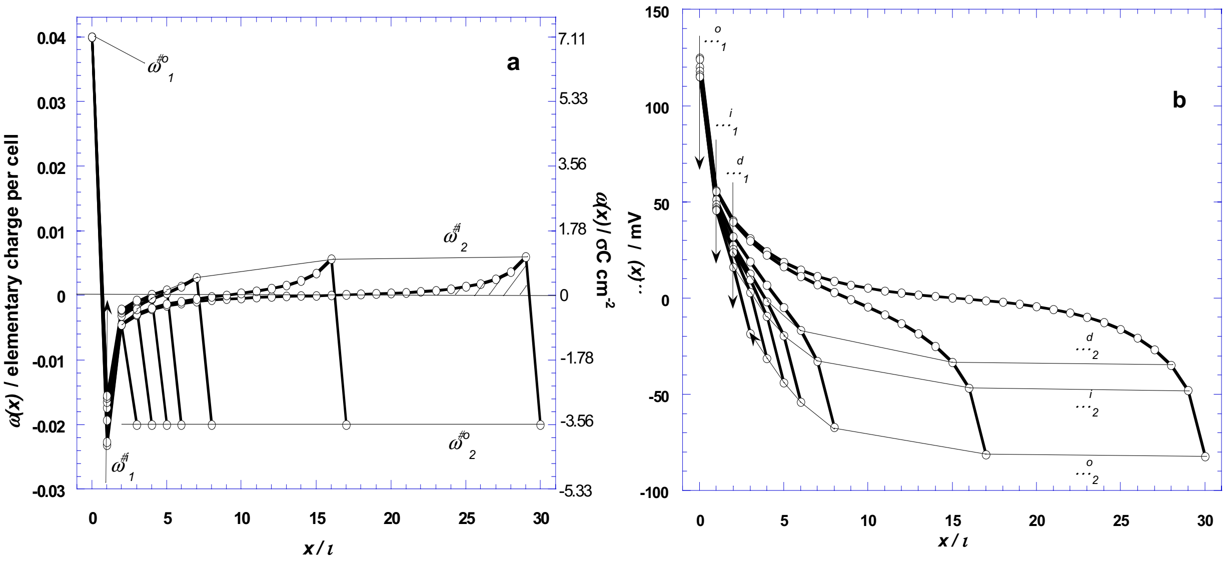

Figure 23. Similar to Figure 22, but with $\omega_1^{\rm o}$ | 0.04, $\omega_2^{\rm o}$ | 40.02 elementary charges per unit cell.

In situations where one of the surface charge is zero, as in Figure 24, there may still be a low but finite $\omega_2^{\rm i}$ because the nature of $\div_{\rm ads}G_{\rm m,i}$ includes the preference of the ion for the surface over that of the solvent (water). Approach of surface 2 to surface 1 increases this excess adsorption. The strong countercharge $\omega_1^{\rm i}$ becomes a bit more negative; eventually, the countercharge $\omega_1^{\rm i}$ | $\omega_2^{\rm i}$ is sandwiched between the two solid surfaces and equals $4\omega_1^{\rm o}$. The corresponding changes in the characteristics potentials is given in panel b. The choice of $\omega_2^{\rm o}$ | 0 imposes that $y_2^{\rm o}$ | $y_2^{\rm i}$ (see eq 41b). The systematic increase of the potentials is consistent with the trends of panel a. Particularly, as in Figures 22 and 23, regulation of the surface potentials and of the potentials at the iHp occur in the same way so as to satisfy the imposed conditions $\mathrm{d}\omega_{1,2}^{\rm o}/\mathrm{d}h$ | 0.

Figure 25 gives the Gibbs energy of interaction in the presence of specific anion adsorption for fixed $\omega_1^{\rm o}$ and various values of $\omega_2^{\rm o}$ (constant with respect to *h*). The gradual transition from attraction to repulsion with increasing $\omega_2^{\rm o}$ is as expected: the charges on the two surfaces are the primary sources for interaction, of which the strength is modulated by the (positive or negative) adsorption of anions. In this figure, no extrema appear, but they are predicted at intermediate values of $\div_{\rm ads}G_{\rm m,i_{1,2}}$, see Figure 26. Referring to this latter figure, strong specific adsorption promotes attraction, mainly because $\omega_2^{\rm o}\,2\,\omega_2^{\rm i}$ becomes very negative. In panels a and b, weak specific adsorption leads to overall repulsion. In the middle range, there are $\div_{\rm ads}G_{\rm m,i_2}$ values for which attraction (repulsion) at larger distance is outweighed by repulsion (attraction) at short distances. In panel c, specific adsorption takes place on surface 2, which is negatively charged. It enhances the attraction but from a certain value of $÷_{\text{ads}}G_{\text{m,i}_2}$, the interaction Gibbs energy becomes independent of $÷_{\text{ads}}G_{\text{m,i}_2}$ since the surface potential is in that case too negative to allow any further anions adsorption (the electrostatics is unfavorable).

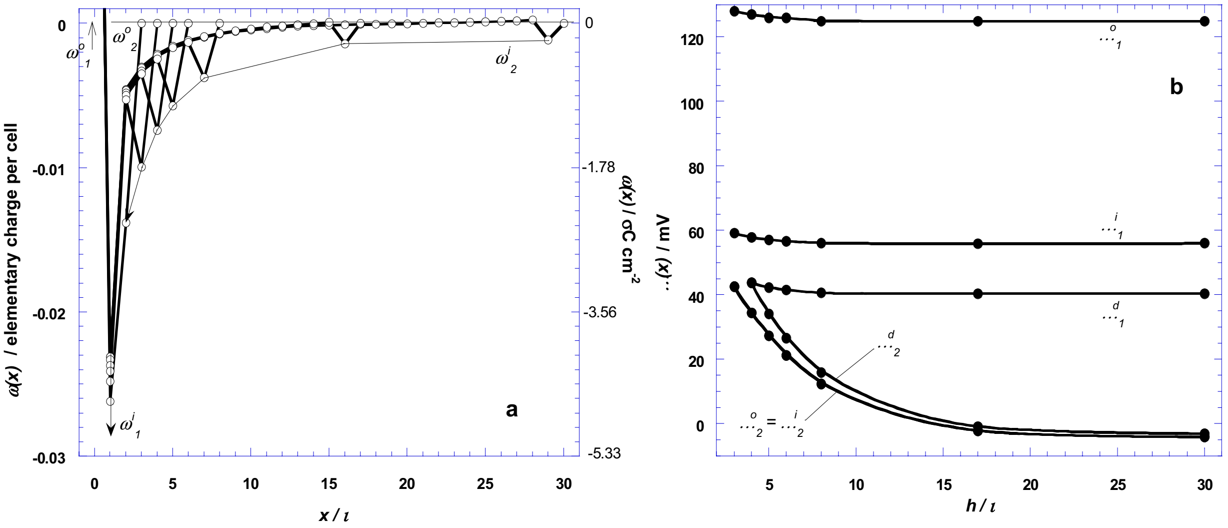

Figure 24. As in Figure 22, but with ω_1^{o} | 0.04, ω_2^{o} | 0 elementary charges per unit cell.

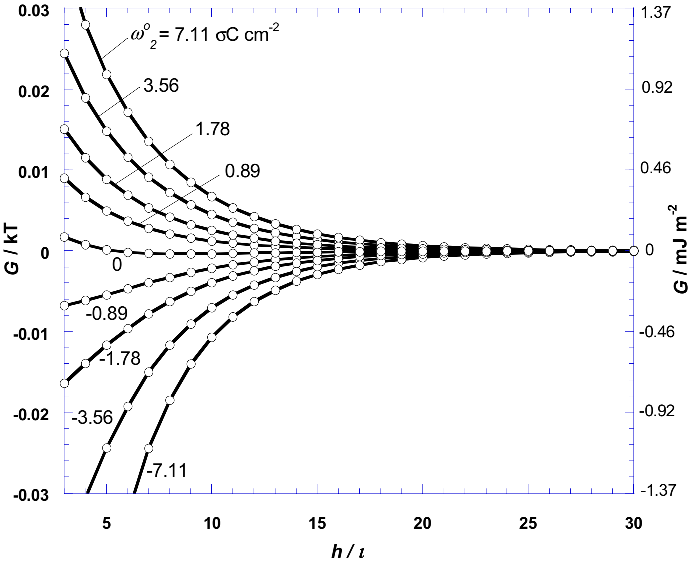

Figure 25. Gibbs energy of interaction corresponding to the profiles of Figures 22-24 and a few others. Throughout, ω_1^{o} | 0.04 elementary charges per unit cell (7.11 σC cm^{-2}). The value for the surface charge ω_2^{o} is indicated in σC cm^{-2}.

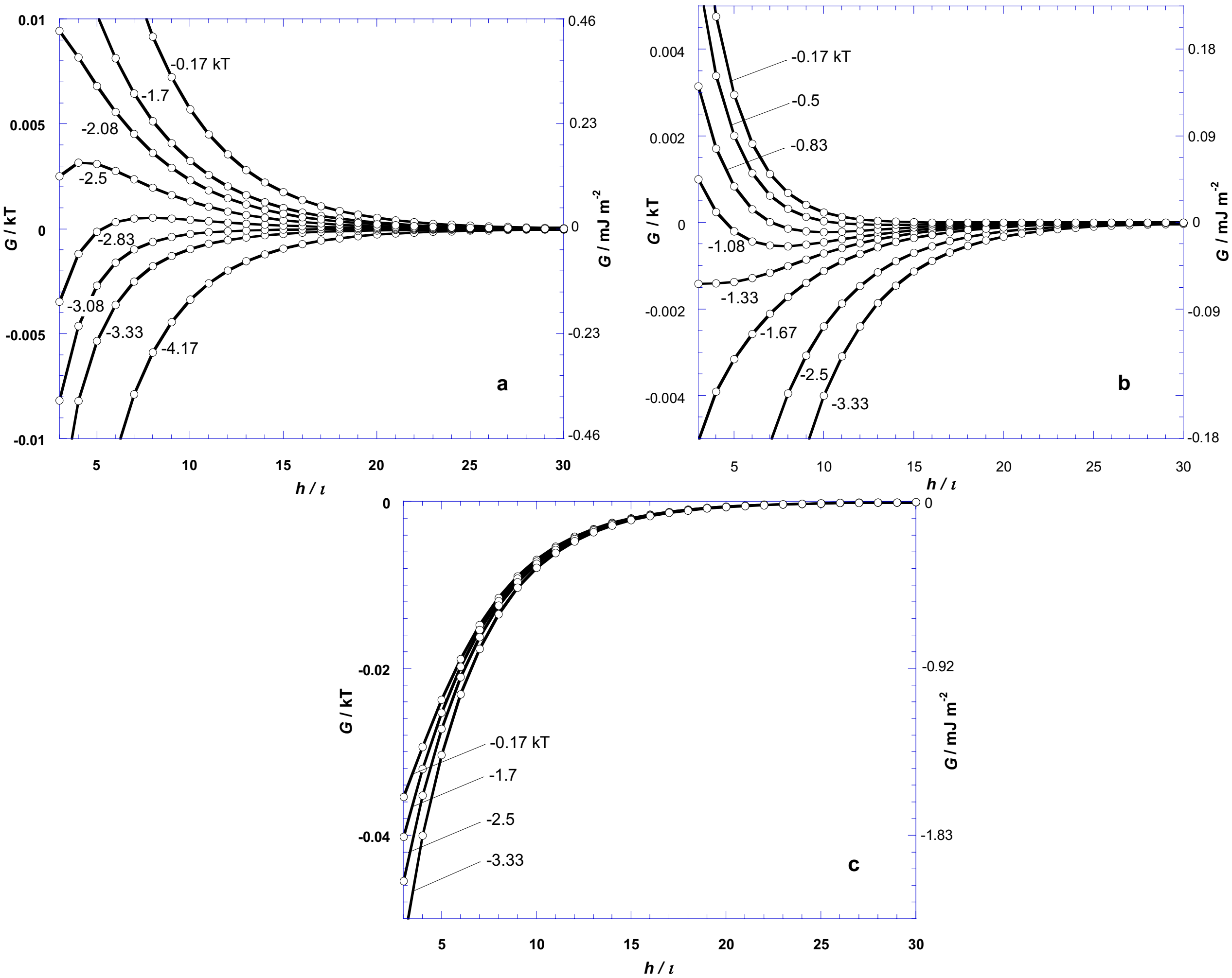

Figure 26. Interaction Gibbs energy for various values of $\div_{\mathrm{ads}}G_{\mathrm{m,i_2}}$, as indicated in kT units, and at fixed surface charges. Throughout, $\div_{\mathrm{ads}}G_{\mathrm{m,i_1}}$ | $4kT$. Panel a: ω_1^{o} | 7.11 σC cm^{-2} and ω_2^{o} | 3.56 σC cm^{-2}; panel b: ω_1^{o} | 7.11 σC cm^{-2} and ω_2^{o} | 0 σC cm^{-2}; panel c: ω_1^{o} | 7.11 σC cm^{-2} and ω_2^{o} | 43.56 σC cm^{-2}. Other parameters as in Figure 22.

Figure 27 illustrates the influence of the indifferent electrolyte concentration. In panel b, surface 2 is uncharged but because of the relatively strong specific anion adsorption it behaves effectively as negative. Zeta-potential measurements would confirm that. Anionic surfactant adsorption on uncharged (say polymeric) surfaces would be representative. At long distance and low c_{s}, attraction between the surfaces prevails (surface 1, including its Stern layer, carries a positive charge) but at shorter distance the interaction becomes repulsive because of the strong anion adsorption on both surfaces. With increasing c_{s}, the minimum deepens and is displaced to lower distances, to disappear for $\lambda \varnothing 2.5 \Delta 10^{43}$. When both surfaces carry a charge of the same sign (Figure 27a), the long-distance interaction is repulsive. At short distance, attraction sets in, resulting from the 'sticking' influence of the anions captured between the two proximate positive surfaces. The maximum in the curve is suppressed by electrolyte addition. In Figure 27c, interaction curves are given for the case where the surface charges are of opposite sign. The results conform to intuition (tuning of the range where electrostatics plays a role). In Figure 27, the curves pertaining to $\lambda \mid 10^{41}$ are repulsive. The Debye length is, in that particular case, so low ($\rho^{41} - 0.43\iota$) that the interaction is not governed by the spatially confined regulation of the charges and potentials but primarily determined by the repulsion between the dielectrics formed by the two Stern layers. It is noted from Figure 27 that for purely electrostatic reasons interaction curves can be obtained that traditionally are interpreted as the sum of the effect of double layer repulsion and Van der Waals attraction, albeit with far too simple double layer models. By va-

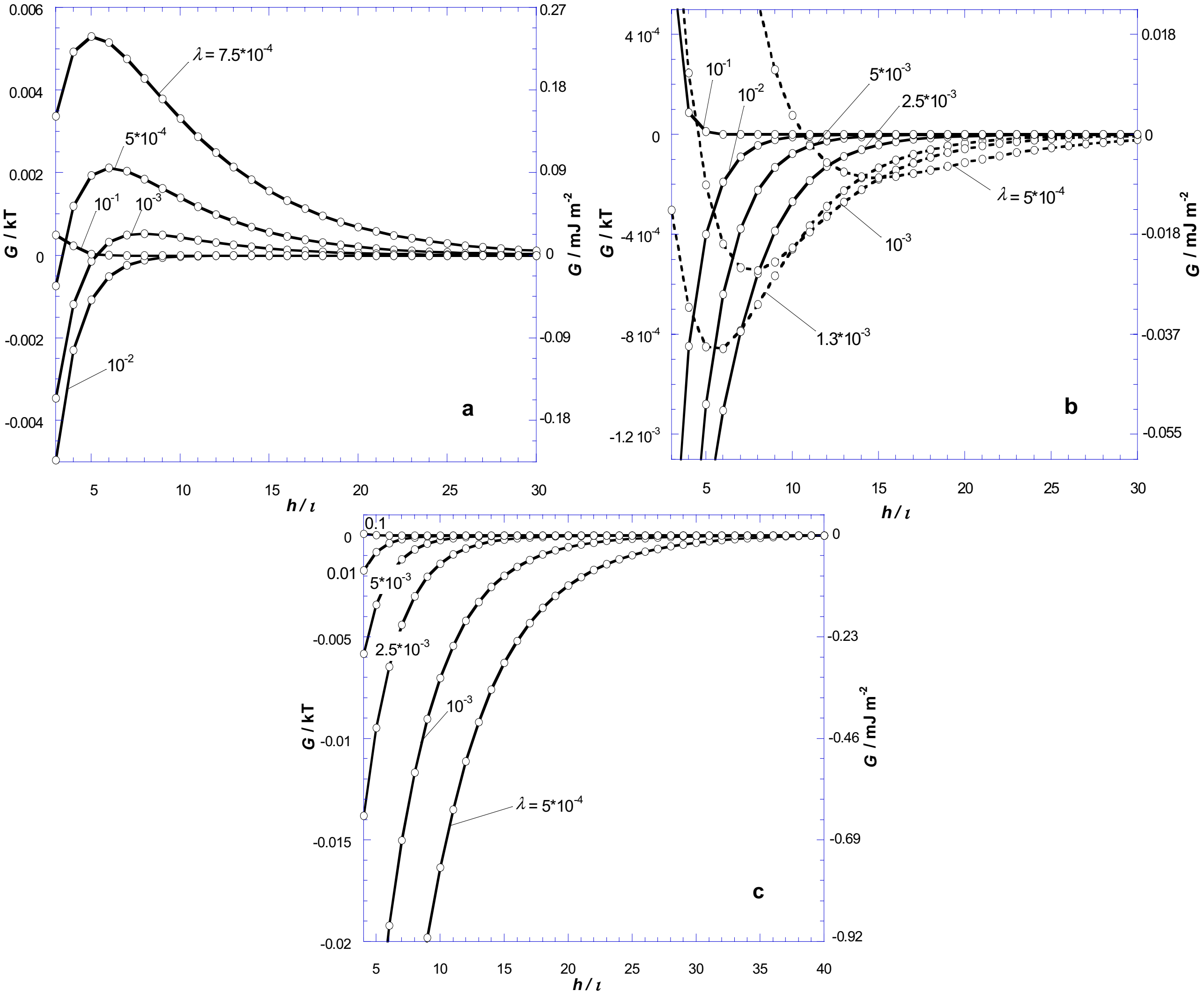

Figure 27. Interaction Gibbs energy for different electrolyte concentrations, expressed in terms of $\lambda \mid c_s / 55.55$. Panel a: $\omega_1^o \mid 7.11$ σC cm^{-2}, $\omega_2^o \mid 3.56$ σC cm^{-2}, $\div_{\text{ads}} G_{\text{m,i}_1} \mid 41$ *kT*, $\div_{\text{ads}} G_{\text{m,i}_2} \mid 42.83$ *kT*; panel b: $\omega_1^o \mid 7.11$ σC cm^{-2}, $\omega_2^o \mid 0$ σC cm^{-2}, $\div_{\text{ads}} G_{\text{m,i}_1} \mid 41$ *kT*, $\div_{\text{ads}} G_{\text{m,i}_2} \mid 41.08$ *kT*; panel c: $\omega_1^o \mid 7.11$ σC cm^{-2}, $\omega_2^o \mid 43.56$ σC cm^{-2}, $\div_{\text{ads}} G_{\text{m,i}_1} \mid \div_{\text{ads}} G_{\text{m,i}_2} \mid 41$ *kT*. Otherwise as in Figure 22.

rying the parameters the model can be extended *ad infinitum*, which we shall not do here. For instance, changing of the variable $\chi_{1,2}^{\mathrm{i}}$, which determines the number of sites available for specific adsorption, would qualitatively yield interaction curves comparable to the ones obtained when tuning $\div_{\mathrm{ads}} G_{\mathrm{m,i}_{1,2}}$ (see eq 43). Rather we shall give some illustrations for which $\omega_{1,2}^{\mathrm{o}}$ are not fixed but depend on pH, c_{s} and $\div_{\mathrm{ads}} G_{\mathrm{m,i}_{1,2}}$.

In Figure 28, the potential and charge distributions are given for pH | 3 and different adsorption parameters $\div_{\mathrm{ads}} G_{\mathrm{m,i}_1}$ and $\div_{\mathrm{ads}} G_{\mathrm{m,i}_2}$ for surfaces 1 and 2, respectively. Because of

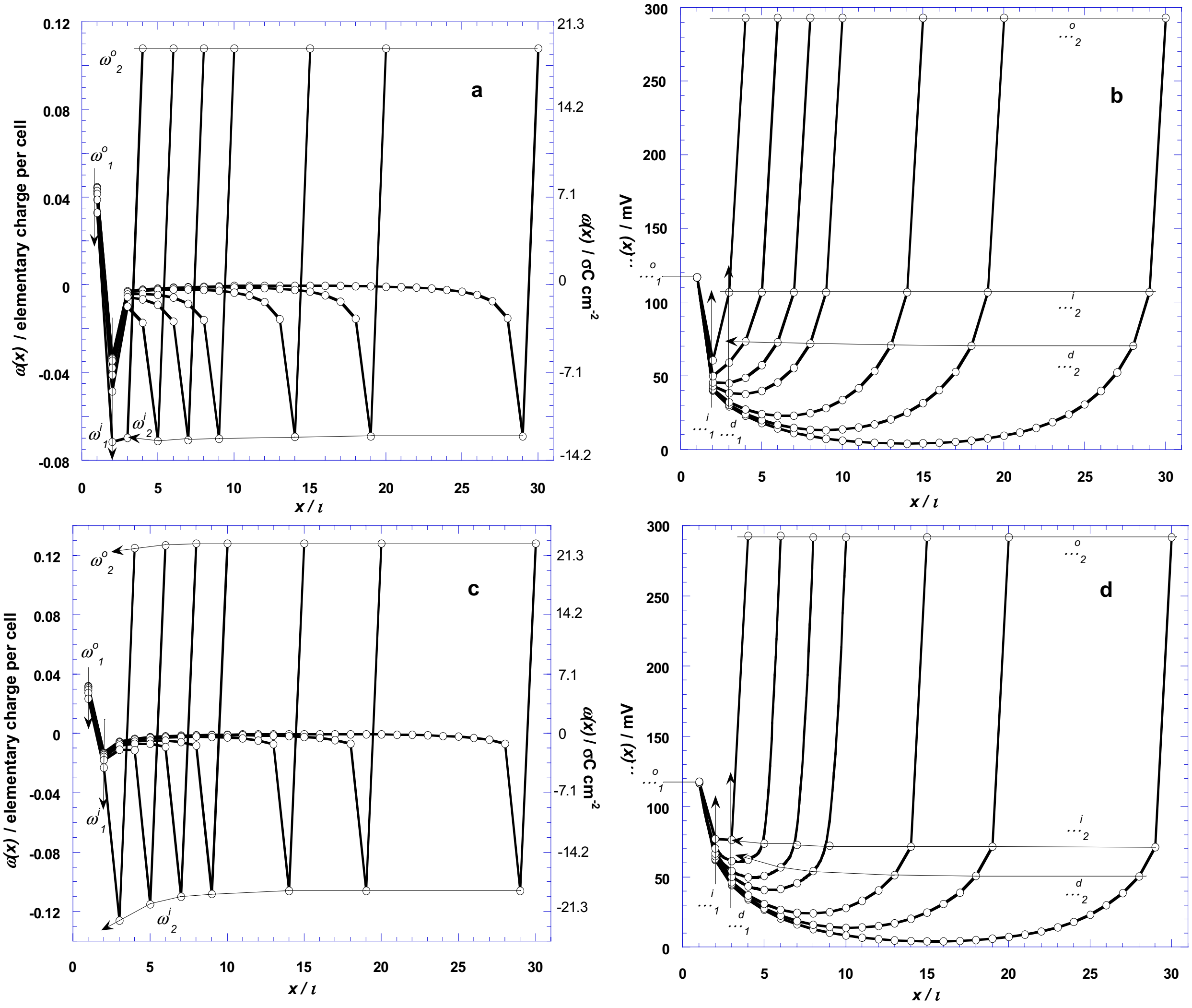

Figure 28. Hetero-interactions between two flat oxide layers, of which the surface charges are regulated across diffuse and Stern counterlayers. Left, surface 1, pzc$_1$ | 5; Right, surface 2, pzc$_2$ | 8; dielectric permittivities $\kappa_{1,1}^{\mathrm{i}} \mid \kappa_{1,2}^{\mathrm{i}} \mid 20$, $\kappa_{2,1}^{\mathrm{i}} \mid \kappa_{2,2}^{\mathrm{i}} \mid 50$, in all others 78. pH | 3, $\chi_{1,2}^{\mathrm{o}} \mid \chi_{1,2}^{\mathrm{i}} = 1$, $\lambda \mid 10^{43}$. Panels a and b: $\div_{\mathrm{ads}} G_{\mathrm{m,i}_1} \mid 42$ *kT*, $\div_{\mathrm{ads}} G_{\mathrm{m,i}_2} \mid 40.17$ *kT*. Panels c and d: $\div_{\mathrm{ads}} G_{\mathrm{m,i}_1} \mid 40.17$ *kT*, $\div_{\mathrm{ads}} G_{\mathrm{m,i}_2} \mid 42$ *kT*.

the choice for $\mathrm{pH}_1^{\mathrm{o}}$ and $\mathrm{pH}_2^{\mathrm{o}}$, $\omega_1^{\mathrm{o}}(\leftarrow)\,\{\,\omega_2^{\mathrm{o}}(\leftarrow)$. For $\div_{\mathrm{ads}}G_{\mathrm{m,i}_2}\ \{\{\ \div_{\mathrm{ads}}G_{\mathrm{m,i}_1}$ (in size) (panels a and b), regulation predominantly takes place at the interface 1. The charges and potentials for surface 2 remain constant and even at low *h* hardly vary. As a result of the respective magnitudes of the two surface charges and the adsorption Gibbs energies, the regulation capacity for surface 1 is higher than that for surface 2. $\omega_1^{\mathrm{i}}(h)$ decreases with *h* because of the increasing anion adsorption as favored by the proximity of the strong double layer 2 (increase of the potential $y_1^{\mathrm{i}}(h)$). The potential $y_1^{\mathrm{o}}(h)$ remains constant, which is possible only upon decrease of the surface charge $\omega_1^{\mathrm{o}}(h)$. For $\div_{\mathrm{ads}}G_{\mathrm{m,i}_2}\ \}\}\ \div_{\mathrm{ads}}G_{\mathrm{m,i}_1}$ (panels c and d), regulation of interface 1 still occurs but to a lesser extent than in the previous situation and is mainly enhanced by the proximity of the strong double layer 2. The new feature is that interface 2, though stronger than interface 1 in terms of the magnitude of the surface charge (or surface potential), is now regulated to an extend determined by the choices made for $\div_{\mathrm{ads}}G_{\mathrm{m,i}_2}$. Owing to the repulsion exerted by surface 1, $\omega_2^{\mathrm{o}}(h)$ decreases as well as $\omega_2^{\mathrm{i}}(h)$. These trends are also reflected in the potential distributions. In Figure 29, similar situations are examined for $\mathrm{pH} \,|\, \mathrm{pzc}_1$. The surface charges are lower in magnitude with respect to the situation at $\mathrm{pH} \,|\, 3$. For $\div_{\mathrm{ads}}G_{\mathrm{m,i}_2}\ \{\{\ \div_{\mathrm{ads}}G_{\mathrm{m,i}_1}$ (panels a and b), $\omega_1^{\mathrm{o}}(h)$ decreases as in Figure 28a and now changes sign upon approach of surface 2. This concomitantly magnifies the regulation capacity of interface 2 of which the surface charge $\omega_2^{\mathrm{o}}(h)$ now increases. The vicinity of the strongly positively charged surface 2 (high electric fields) induces adsorption of anions on surface 1 even if the latter is negatively charged. We are in the typical situation of induction, which leads to attraction. The surface potentials $y_{1,2}^{\mathrm{o}}$ do not markedly change, contrary to the diffuse potentials and the potentials at the iHp: y_1^{d} (y_2^{d}) and y_1^{i} (y_2^{i}) increase (decrease) till $y_1^{\mathrm{i}} \Downarrow y_2^{\mathrm{i}}$ and $y_1^{\mathrm{d}} \Downarrow y_2^{\mathrm{d}}$ in the limit $h \Downarrow 0$ (Figure 29b). For $\div_{\mathrm{ads}}G_{\mathrm{m,i}_2}\ \}\}\ \div_{\mathrm{ads}}G_{\mathrm{m,i}_1}$ (panels c and d), the same trends are observed but since specific adsorption now occurs to a lesser extent on surface 1, the boosting effect for the regulation capacities of the two surfaces is less pronounced. Similar comments hold for the case $\mathrm{pH} \,|\, 6$ ($\omega_1^{\mathrm{o}}(\leftarrow)\,\{\,0$) (not shown). Interaction Gibbs energies are given in Figure 30 for the three pH's discussed before. The results are consistent with the potential and charge regulations of Figures 28-29 (cases $\div_{\mathrm{ads}}G_{\mathrm{m,i}_2} \prod \div_{\mathrm{ads}}G_{\mathrm{m,i}_1}$). When both surface charges are negative ($\mathrm{pH}\,\}\,\mathrm{pH}_2^{\mathrm{o}}$, not shown), upon increase of $\div_{\mathrm{ads}}G_{\mathrm{m,i}_1}$ and/or $\div_{\mathrm{ads}}G_{\mathrm{m,i}_2}$, adsorption of anions is at some point limited by the unfavorable electrostatics, as already discussed before. This is reflected by repulsive interaction curves, which become independent of the Gibbs adsorption energies.

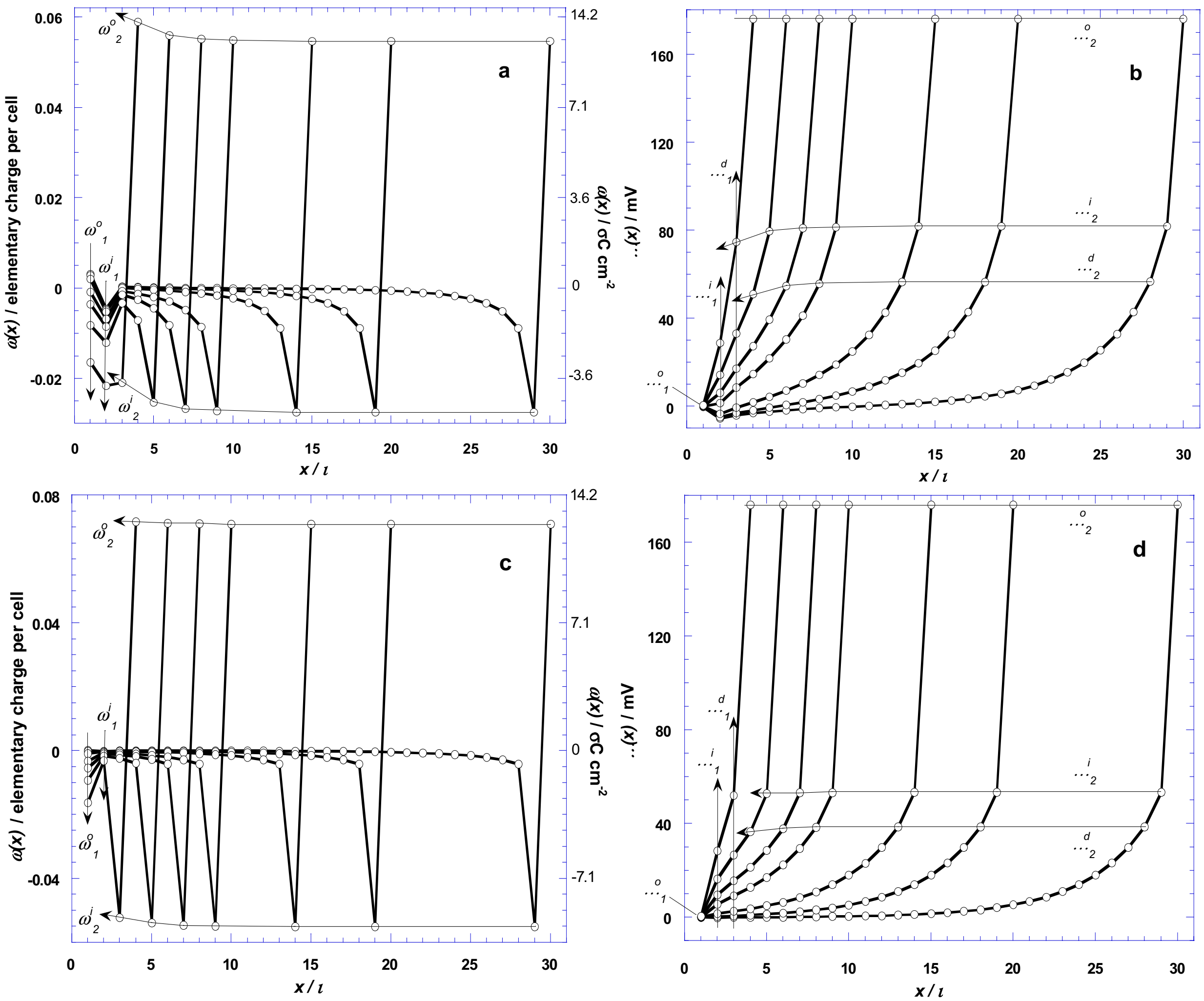

Figure 29. As in Figure 28, but at pH | pzc$_1$.

Finally, the effect of the dielectric permittivities of the Stern layers on the regulation behavior for both surfaces is analyzed. In Figure 31, the potential and charge distributions are given for pH | 3 at two different $\kappa^{\mathrm{i}}_{1,1}$ | $\kappa^{\mathrm{i}}_{1,2}$, the other parameters are kept constant. When increasing $\kappa^{\mathrm{i}}_{1,1}$ | $\kappa^{\mathrm{i}}_{1,2}$, one increases the magnitude of the surface charges, the regulation capacities and subsequently, the charges at the iHp's. The diffuse potentials and Stern potentials follow the same trend. The interaction becomes more repulsive (not shown) over the whole *h* range. Similar effect occurs upon variation of $\kappa^{\mathrm{i}}_{2,1}$ | $\kappa^{\mathrm{i}}_{2,2}$ (not shown). The same kind of analysis can be carried out for other pH's. The corresponding interaction Gibbs energies are tuned as according to the changing in surface charges and in RC's caused by the dielectric permittivities. For instance, at pH | 6, attraction would be enhanced by increasing $\kappa^{\mathrm{i}}_{2,1}$ | $\kappa^{\mathrm{i}}_{2,2}$ and/or $\kappa^{\mathrm{i}}_{1,1}$ | $\kappa^{\mathrm{i}}_{1,2}$.

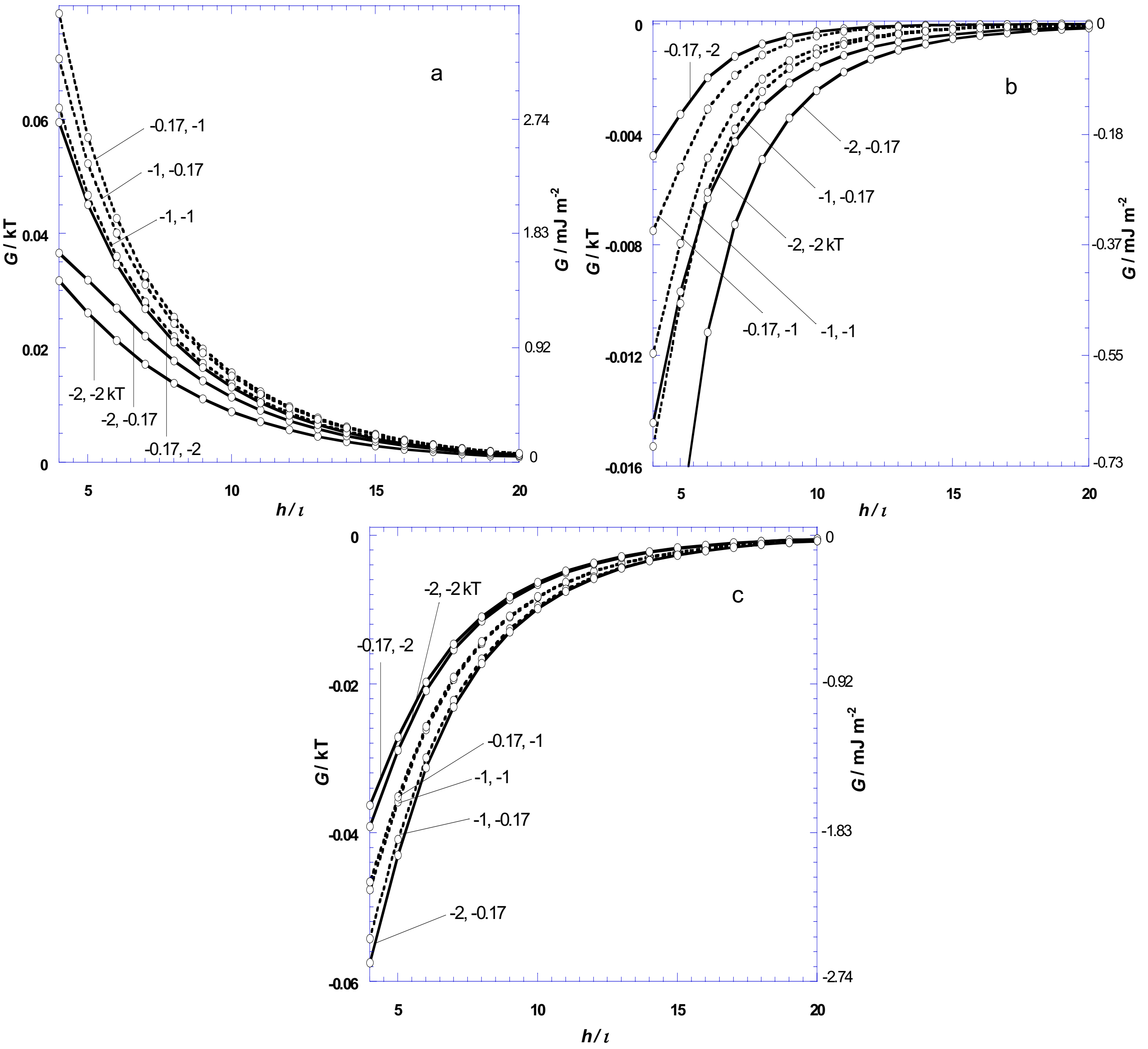

Figure 30. Interaction Gibbs energy at pH | 3 (a), pH | pzc$_1$ (b) and pH | 6 (c) for different sets of $\div_{\mathrm{ads}}G_{\mathrm{m,i_1}}$, $\div_{\mathrm{ads}}G_{\mathrm{m,i_2}}$ as indicated in *kT*. Other parameters as in Figure 28.

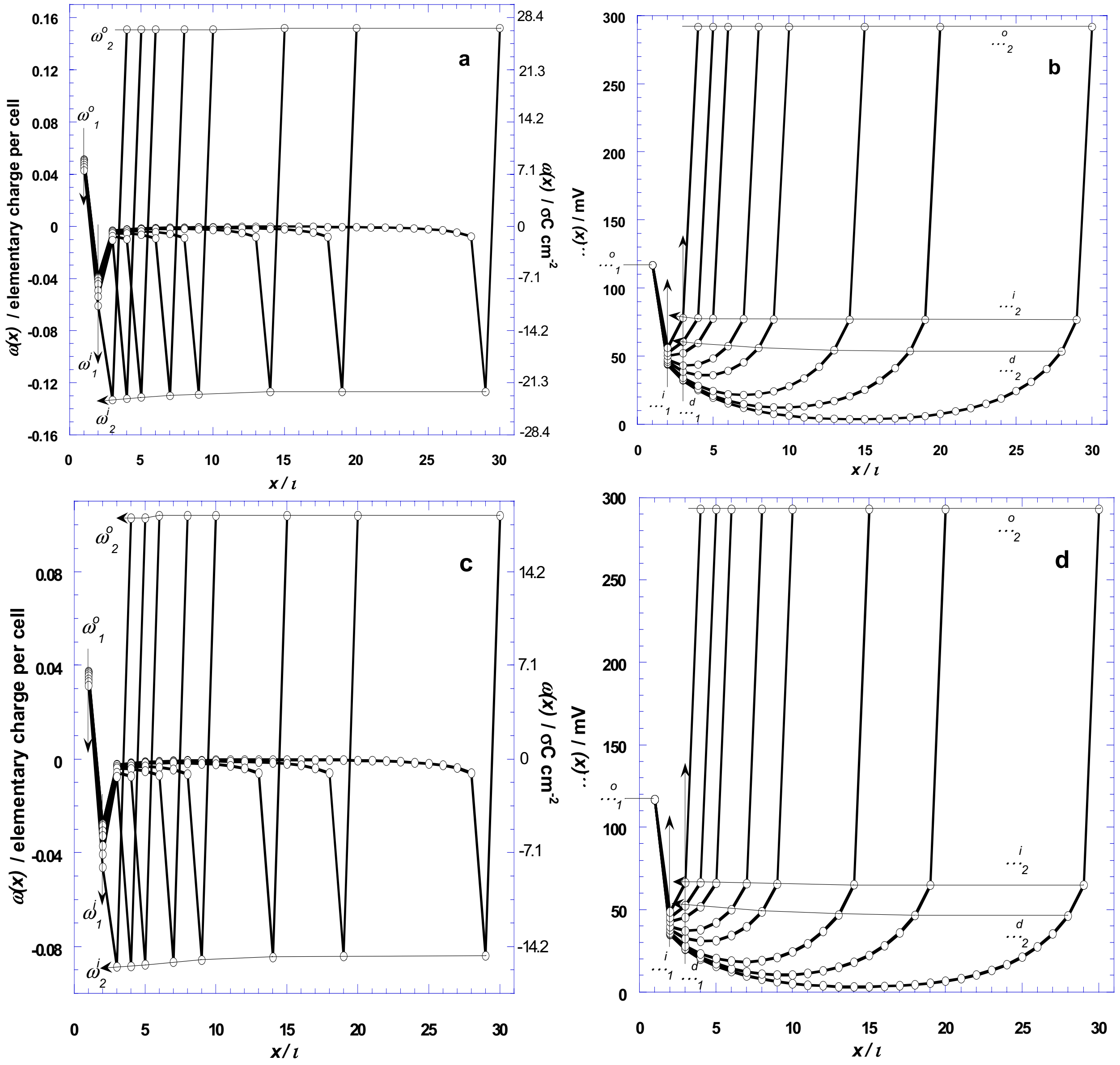

Figure 31. Potential and charge distributions at pH | 3 and $\kappa^{\text{i}}_{1,1}$ | $\kappa^{\text{i}}_{1,2}$ | 35 (panels a and b), $\kappa^{\text{i}}_{1,1}$ | $\kappa^{\text{i}}_{1,2}$ | 5 (panels c and d). Other parameters: $\div_{\text{ads}}G_{\text{m,i}_{1,2}}$ | 42 kT, $\kappa^{\text{i}}_{2,1}$ | $\kappa^{\text{i}}_{2,2}$ | 50 (in the diffuse layer κ | 78), $\chi^{\text{o}}_{1,2}$ | $\chi^{\text{i}}_{1,2} = 1$, λ | 10^{43} .

5. Conclusions

The main purpose of this paper is to give a comprehensive elaboration of regulation upon double layer interaction. A model is used which is sufficiently complete to quantify all physical phenomena with a restricted number of parameters. To achieve this, electric double layers are treated on the Gouy-Stern level, which has the following features (i) specific adsorption is accounted for at the inner Helmholtz plane, (ii) surface charge regulation is allowed at the solid surface, (iii) a fixed slip plane separates the Stern layer from the diffuse part. In this way the positions of ions which contribute to the *chemical* part of the regulation are fixed. The concomitant *electrical* contributions are accounted for in terms of three capacitances, viz. those of the inner and outer Helmholtz layer and that of the diffuse double layer part.

The combined action of the chemical and electrical contributions to regulation defines the *regulation capacity* (RC) of a double layer. Other conditions being equal, the higher this capacity, the more charge it can adsorb without significant increase of the potential. The electrical part of the RC is determined by the three mentioned capacities, the chemical part by the number of adsorption sites available and the molar Gibbs energies of ions adsorbing on the surface (charge-determining ions) and/or at the inner Helmholtz plane (specifically adsorbing ions).

Our approach offers an improvement of existing models. For instance, models containing besides the layer with surface charge (ω^{o}) only diffuse layers are inadequate since most of the regulation takes place in Stern layer and systems for which ω^{d} or $\ldots^{d}$ remain constant are virtually absent. Site-binding models of surface groups all suffer from the deficiency that they do not specify the slip process, and hence, do not predict ´. Moreover, in many advanced site-binding models specific adsorption is accounted for without offering a clear picture of the potential decay in the inner layer. For the diffuse part the linearized Poisson-Boltzmann equation is used (in the frame of homo-interactions), which is often allowed because ω^{d} and $\ldots^{d}$ are generally sufficiently low, as judged by electrokinetic measurements. There is no need for applying more advanced models for this part. Neither do we feel the need for invoking more detailed pictures of the inner-layer because in real systems features like surface roughness on a molecular scale render this practically useless. Our model is restricted to hard surfaces and to equilibrium, i.e. the assumption is made that during particle encounter all regulation processes can relax. Another restriction is that of flat surfaces only, but extension to, say, spherical surfaces is trivial: the Stern part remains essentially unchanged (ρd {{ 1, if *d* is the thickness of the Stern layer) and for the diffuse part the linearized Poisson-Boltzmann equation can be used, for instance in the Derjaguin approximation. A special feature is that hetero-interaction is discussed in detail. For a number of situations, we could analyze the distance dependence of various charges and potentials and the ensuing effect on the Gibbs energy of interaction and disjoining pressure. In this way reversal of the sign of the interaction with decreasing distance by induction was quantified. It follows that in hetero-interaction, the sometimes observed transition from long-range repulsion to short-range attraction can be explained without considering Van der Waals forces. For instance, AFM studies[46,47] sometimes reveal unexpected signs (and sign reversals) in the interactions occurring between dissimilar or presumably identical interfaces which cannot be understood using DLVO theory with fixed ω^{d} or $\ldots^{d}$ only. In principle our analysis offers the elements to account for such observations. Besides pair interaction in AFM or force apparatus measuring conditions, elaboration of our model to heterocoagulation in sols is a prospective application.

We are aware of the fact that the generality of our theory at the same time creates a psychological quandary: experience has shown that many interaction problems can be (fairly) well described with the oversimplified model of fixed $\ldots^{\mathrm{d}}$ or fixed ω^{d}, with $\ldots^{\mathrm{d}} - \prime$ and a fixed Hamaker constant. Given the simplicity of such models, there is often no need to subject the data to more advanced analyses, although we have shown that there is ample reason to do so. The caveat is that the Hamaker constants obtained from such simple models must be considered with reservation,[48] both because of the occurrence of regulation and the difference of range between the repulsive electric and attractive Van der Waals forces (twice the Stern layer thickness). These phenomena tend to overestimate the Hamaker constant. This matter deserves elaboration.

One of the greatest problems ahead is accounting for the non-ideality of the surfaces. In particular, recent 1D-modellings of AFM,[49,50] ion adsorption[51] and electrokinetic[52] data and recent adhesion force measurements[46] underscore the necessity of taking into account the rugosity of the surfaces in order to explain the low value of the calculated apparent (effective) number of sites compared to that expected on the basis of full coverage of the surface. Hence, improvement of the model presented in this paper would be incorporation of rugosity, or, for that matter, the exact surface geometry of the interacting systems. Such an approach, especially relevant for the analysis of AFM measurements, requires investigation of local double layer overlap, replacing the assumption of smeared-out double layers. This analysis is under study.[53]

For conducting amphifunctional interfaces,[49,50] with double layer properties that are governed by the coupling of electronic and ionic surface-charging processes, regulation may also involve the electronic charge. Such electronic regulation depends on the (regulation) capacity of the charge-free layer located between the bare surface of the conducting material and the plane of the ionic countercharge and on the standard potentials and reversibility of the redox reactions involved. This would be another extension of our model.

Acknowledgement

The authors appreciate useful help from Dr. H. P. van Leeuwen in constructing the paper.

Glossary of Symbols

Some recurring symbols

$C(h)$	Parameter as defined in eq 25
C_1^{i}	Capacitance of the inner Helmholtz layer (section 3)

Regulation

C_2^{i}	Capacitance of the outer Helmholtz layer (section 3)
C^{d}	Capacitance of the diffuse layer
c_{s}	Electrolyte concentration
$G(h)$	Gibbs energy of interaction
h	Distance between the oHp's (sections 3 and 4.1) or number of layers used for the numerical computations (section 4.2)
iHp	Inner Helmholtz plane
K_{a}, K_{b}	Equilibrium constants of (14a) and (14b), respectively
K_{i}	Constant describing the specific adsorption of ion i at the iHp
$N_{\mathrm{s}}^{\mathrm{o}}$	Number of adsorption sites (per unit area) for charge-determining ions
$N_{\mathrm{s}}^{\mathrm{i}}$	Number of adsorption sites (per unit area) for specifically adsorbing ions
oHp	Outer Helmholtz plane
RC	Regulation capacity
x	Position in the diffuse layer counted from the left oHp (sections 3 and 4.1) or from the surface (section 4.2)
x_{i}	Mole fraction of ion i
y^{o}	Dimensionless surface potential ($\mid F\ldots^{\mathrm{o}} / RT$)
y^{i}	Dimensionless iHp potential ($\mid F\ldots^{\mathrm{i}} / RT$)
y^{d}	Dimensionless diffuse layer potential ($\mid F\ldots^{\mathrm{d}} / RT$)
z_{i}	Valency of ion i
ι	Thickness of a layer (section 4.2)
$\div_{\mathrm{ads}}G_{\mathrm{m,i}}$	Adsorption energy of ion i at the iHp
κ	Dielectric constant
λ	Volume fraction of electrolyte $(\lambda \mid c_{\mathrm{s}} / 55.55)$
ω^{o}	Surface charge density
ω^{i}	Surface charge density at the iHp
ω^{d}	Charge density of the diffuse layer ($-\omega^{\mathrm{ek}}$)
$M(h)$	Disjoining pressure
χ^{i}	Fraction of the total number of sites available for specific adsorption (section 4.2)
χ^{o}	Fraction of the total number of sites available for adsorption of charge determining ions (section 4.2)

Superscripts and subscripts

$(\ldots)$ superscript at ‘constant potential’

(ω) superscript at ‘constant charge’

1,2 subscript refers to double layers 1 (left) and 2 (right), respectively. In the combination of two subscripts (sections 3 and 4) in the writing of capacitances and dielectric constants (section 4), the first refers to the type of layer, the second to the particle: for instance $C^{\mathrm{i}}_{1,2}$ is inner layer capacitance of double layer 2.

References

(1) Gouy, G. *Compt. Rend.* **1909**, *149*, 654; *J. Phys.* **1910**, *9* (4), 457; *Ann. Phys.* **1917**, *7* (9), 129.

(2) Chapman, D. L. *Phil. Mag.* **1913**, *25* (6), 475.

(3) Stern, O. *Z. Elektrochem.* **1924**, *30*, 508.

(4) For a detailed review, see Lyklema, J. in *Fundamentals of Interface and Colloid Science*; Academic Press, 1995; Vol II, Chapter 3, *Electric Double Layers*.

(5) Verwey, E. J. W.; Overbeek, J. Th. G. in *Theory of the Stability of Lyophobic Colloids. The Interaction of Sol Particles having an Electric Double Layer*, Elsevier 1948, section VII.5. (Also available as a Dover reprint 2000).

(6) Melville, J. B.; Smith, A. L. *J. Chem Soc. Faraday Trans. (I)* **1974**, *70*, 1550.

(7) Bierman, A. *J. Colloid Interface Sci.* **1955**, *10*, 231.

(8) Ninham, B. W.; Parsegian, V. A. *J. Theor. Biol.* **1971**, *31*, 405.

(9) Chan, D.; Perram, J. W.; White, L. R.; Healy, T. W. *J. Chem. Soc. Faraday Trans. (I)* **1975**, *71*, 1046.

(10) Chan, D.; Healy, T. W.; White, L. R. *J. Chem. Soc. Faraday Trans. (I)* **1976**, *72*, 2844.

(11) Healy, T. W. *Pure Appl. Chem.* **1980**, *52*, 1207.

(12) Metcalfe, I. M.; Healy, T. W. *Faraday Discuss. Chem. Soc.* **1990**, *90*, 335.

(13) Healy, T. W.; White, L. R. *Adv. Colloid Interface Sci.* **1978**, *9*, 303.

(14) Usui, S. *J. Colloid Interface Sci.* **1984**, *97*, 247.

(15) Carnie, S. L.; Chan, D. Y. C. *J. Colloid Interface Sci.* **1993**, *161*, 260.

(16) Reiner, E. S.; Radke, C. J. *Adv. Colloid Interface Sci.* **1993**, *47*, 59.

(17) Ettelaie, R.; Buscall, R. *Adv. Colloid Interface Sci.* **1995**, *61*, 131.

(18) Behrens, S. H.; Borkovec, M. *J. Phys. Chem. B* **1999**, *103*, 2918.

(19) Borkovec, M., Jonsson, B.; Koper, G. J. M. in *Surface and Colloid Sci.* **2001**, Matijevic E., Ed., *16*, 99.

(20) Prieve, D. C. ; Ruckenstein, E. *J. Theor. Biol.* **1976**, *56*, 205.

(21) Biesheuvel, P. M. *Langmuir* **2001**, *17*, 3553 and *ibid.* **2001**, *17*, 3557.

(22) Guerin, M.; Seaman, J. *J. Colloid Interface Sci.* **2002**, *250*, 492.

(23) Dan, N. *Langmuir* **2002**, *18*, 3524.

(24) Lee, E.; Tong, T. S.; Chih, M. H.; Hsu, J. P. *J. Colloid Interface Sci.* **2002**, *257*, 109.

(25) Lyklema, J.; Rovillard, S.; De Coninck, J. L. *Langmuir* **1998**, *14*, 5659.

(26) Lyklema, J. *The Role of Surface Conduction in the Development of Electrokinetics* in *Interfacial Electrokinetics and Electrophoresis*, A. V. Delgado, Edition, Marcel Dekker, 2002, Chapter 3.

(27) Frens, G.; PhD Thesis, Utrecht, The Netherlands, 1968.

(28) Honig, E. P.; Mul, P. M. *J. Colloid Interface Sci.* **1971**, *36*, 258.

(29) Keh, H. J.; Ding, J. M. *Langmuir* **2002**, *18*, 4572.

(30) See Ref (5), section V.3.

(31) See Ref (4), section 3.6c.

(32) See Ref (5), section V.2.

(33) Verwey, E. J. W.; Ph.D. Thesis, Utrecht, The Netherlands, 1934.

(34) Lyklema, J.; Van Leeuwen, H. P.; Minor, M. *Adv. Colloid Interface Sci.* **1999**, *83*, 33.

(35) Derjaguin, B. V. *Discuss. Faraday Soc.* **1954**, *18*, 85.

(36) Hogg, R.; Healy, T. W.; Fuersteneau, D. W. *Trans. Faraday Soc.* **1966**, *62*, 1638.

(37) Devereux, O. F.; De Bruyn, P. L. *Interaction of Plane-Parallel Double Layers.* 1963, MIT Press.

(38) Ohshima, H. *Colloid Polym. Sci.* **1974**, *252*, 257 and *ibid.* **1975**, *253*, 150.

(39) Cormack, Mc.; Carnie, S. L.; Chan, D. Y. C. *J. Colloid Interface Sci.* **1995**, *169*, 177.

(40) Scheutjens, J. M. H. M.; Fleer, G. J. *J. Phys. Chem.* **1979**, *83*, 1619.

(41) Hurter, P. N.; Scheutjens, J. M. H. M.; Hatton, T. A. *Macromolecules* **1993**, *26*, 5592.

(42) Leermakers, F. A. M.; van der Schoot, P. P. A. M.; Scheutjens, J. M. H. M.; Lyklema, J. in *The Equilibrium Structure of Micelles*, K. L. Mittal, Editor, Plenum Press, 1989, Volume 7 *Surfactant in Solutions*.

(43) Van Male, J.; PhD Thesis, Wageningen University, the Netherlands, 2003.

(44) Arfken, G. in *Mathematical Methods for Physicists*, third Edition, Academic Press, London, 1985.

(45) Usui, S. *J. Colloid Interface Sci.* **1973**, *44*, 107.

(46) Giesbers, M.; PhD Thesis, Wageningen University, the Netherlands, 2001.

(47) Giesbers, M.; Kleijn, J. M.; Cohen Stuart, M. A. *J. Colloid Interface Sci.* **2002**, *252*, 138.

(48) Meurk, A.; Luckham, P. F.; Bergström, L. *Langmuir* **1997**, *13*, 3896.

(49) Barten, D.; Kleijn, J. M.; Duval, J.; Van Leeuwen, H. P.; Lyklema, J.; Cohen Stuart, M. A. *Langmuir* **2003**, *19*, 1133 (chapter 3 of this thesis).

(50) Duval, J.; Lyklema, J.; Kleijn, J. M.; Van Leeuwen, H. P. *Langmuir* **2001**, *17*, 7573 (chapter 2 of this thesis).

(51) Duval, J.; Kleijn, J. M.; Lyklema, J.; Van Leeuwen, H. P. *J. Electroanal. Chem.* **2002**, *532*, 337 (chapter 4 of this thesis).

(52) Duval, J.; Huijs G. K.; Threels, W. F.; Lyklema, J.; Van Leeuwen, H. P. *J. Colloid Interface Sci.* **2003**, *260*, 95 (chapter 6 of this thesis).

(53) Duval, J.; Leermakers, F. A. M.; Van Leeuwen, H. P. Submitted to *Langmuir* (chapter 11 of this thesis).

Electrostatic Interactions between Double Layers: Influence of Surface Roughness, Regulation and Chemical Heterogeneities[1]

J. F. L. Duval, F. A. M. Leermakers, H. P. van Leeuwen
Department of Physical Chemistry and Colloid Science, Wageningen University,
Dreijenplein 6, 6703 HB Wageningen, The Netherlands.

Abstract. Electrostatic interactions between two surfaces as measured by Atomic Force Microscopy (AFM) are usually analyzed in terms of DLVO theory. The discrepancies often observed between the experimental and theoretical behavior are usually ascribed to the occurrence of *chemical regulation* processes and/or to the presence of surface *chemical* or *morphological heterogeneities* (roughness). In this paper, a two-gradient mean-field lattice analysis is elaborated to quantifying double layer interactions between non-planar surfaces. It allows for the implementation of the aforementioned sources of deviation from DLVO predictions. Two types of ion-surface interaction ensure the adjustment of charges and potentials upon double layer overlap, i.e. specific ionic adsorption at the surfaces and/or the presence of charge-determining ions for the surfaces considered. Upon double layer overlap, charges and potentials are adjusted via re-equilibrium of the different ion adsorption processes. Roughness is modelled by grafting asperities on supporting planar surfaces, with their respective positions, shapes and chemical properties being assigned at will. Local potential and charge distributions are derived by numerically solving the non-linear Poisson-Boltzmann equation under the boundary conditions imposed by the surface profiles and regulation mechanism chosen. A number of characteristic situations are briefly discussed. It is shown how the surface irregularities are reflected in the Gibbs energy of interaction.

---

[1] Submitted for publication in *Langmuir*

Interaction between heterogeneous surfaces

1. Introduction

Accurate knowledge of the interactions between two surfaces is a mandatory prerequisite for understanding a variety of colloidal and interfacial phenomena, such as heterocoagulation, particle deposition, electrosorption or rheological behavior. Classically, the Gibbs energy of interaction between two charged colloidal particles is described by means of the DLVO theory.[1,2] This theory is widely regarded as a cornerstone for understanding colloidal systems and forces on the molecular scale and for predicting macroscopic properties of colloidal dispersions. It reconciles long-range electrostatic double layer interaction[3,4] and short-range Lifshitz-Van der Waals interaction.[5,6] The classical DLVO theory is based on the assumption that the Lifshitz-Van der Waals component can be superimposed on the electrostatic contribution to the pair interaction (superposition approximation). Furthermore it is taken that the interacting surfaces are perfectly smooth and that their surface charge densities are uniform, that is, independent of position. Within these assumptions, the double layer properties are smeared-out along the surface: the potential and charge distributions develop according to one spatial variable, i.e. the dimension perpendicular to the surfaces. As such, the electrostatic part of the DLVO theory can be considered as a self-consistent field approach. However, real colloidal systems generally contain some degree of nonuniformity, in the form of surface roughness and/or chemical heterogeneities. The applicability of the DLVO theory for such systems is questionable, as indicated by various experimental data, which fail to match theoretical prediction. Representative illustrations of the inadequacy of the DLVO theory are provided by surface force/atomic force microscopy measurements,[7-9] particle deposition experiments[10-13] and coagulation kinetics analyses.[14,15]

In an effort to account for the discrepancies between theory and experiment, many attempts were made to modify the existing theory so as to include roughness effects or chemical heterogeneities and to evaluate the corresponding van der Waals and electrostatic interactions. The current paper focuses on the importance of surface nonuniformities in determining interaction forces between two surfaces. In the framework of this context, we shall be interested in the computation of the electrostatic contribution of the total interaction curve. This latter component is sensitive to both surface roughness and chemical heterogeneities. Till now, these two types of nonuniformities have been studied independently. Stankovich *et al.*[16] analyzed the interactions between ideally spherical particles with periodic or random non-uniform surface potentials. The use of the linear Poisson-Boltzmann equation allowed the decoupling of the interactions between uniform and non-uniform components of the surface potential and the (analytical) calculation of the torque and force that particles in a doublet exert on one another. Other types of surface potential/charge distributions were investigated and the reader is referred to the paper of Stankovich *et al.* where further references are given. These studies, particularly relevant in the field of heterocoagulation, focus on nonuniform surface potential and/or charge distributions for which experimental evidence is absent. In the past decade, studies of interactions between rough surfaces have become numerous. They may be classified according to the realistic character of the roughness considered. Common approaches consist in generating geometrically regular asperities,[13,17-21] either conic, hemispheric, spherical, cylindrical or sinusoidal, on one or both surfaces. To compute the corresponding electric double layer interaction energy, solution of the Poisson-Boltzmann (PB) equation is required. It is obtained for the geometries chosen following procedures differing by their degree of mathematical sophistication. Linearization of the PB equation, application of the linear superposition theorem,[22] employment of rigorous numerical schemes such as boundary element,[23] finite element[24,25] or finite differences[26,27] illustrate the variety of tools commonly adopted. A simple alternative is the use of the Derjaguin approximation (DA).[28,29] It relates the interaction per unit area between two flat parallel planes to the corresponding interaction between curved surfaces. This technique is known to be valid only when the principal radius of curvature of the asperities is well above the separation distance and the range of the interactions. Recent extension of the DA has been proposed by Bhattacharjee *et al.*, under the name of surface element integration technique (SEI).[30,31] This technique involves the integration of the corresponding interaction between two flat plates over the exact geometry of the rough surfaces. Contrary to the DA, it is capable of treating both concave and convex asperities and can be applied to very small asperities. Newly developed methods for the generation of roughness have led to a considerable breakthrough in the effort to mimick the real topology of colloids. The use of the fractal approach,[32,33] the possibility of generating asperities randomly distributed on a surface[13,17-21,34] or matching the shape of a colloid by means of a combination of flat and triangular surface elements[35] illustrate the development towards approaching the actual form of surface roughness.

However, despite this variety of techniques and their various degrees of rigor with respect to roughness integration, all these analyses have in common that the boundary conditions adopted for solving the PB equation refer to the very restrictive constant potential or constant charge conditions. In reality, intermediate situations are more likely to occur and this has recently been underlined for the interaction between one-dimensional double layers.[36] Besides, as already mentioned, methods that allow for the concomitant effects of chemical heterogeneities and surface roughness have not been reported so far. Of course, real surfaces will likely contain both of these nonuniformities, as the surface charge on a protrusion could be different from that of the surrounding surface. As mentioned by Walz in a review on the effects of surface heterogeneities on colloid forces,[13] models accounting for both factors are still needed. To come closer to reality, we here propose a two-gradient mean-field lattice analysis to evaluate electrostatic interactions between regulating electric double layers at rough surfaces containing chemical heterogeneities. Though the numerical scheme we use here has become popular in many research fields dealing with wetting phenomena, adsorption of polymers, surfactants or polyelectrolytes at interfaces, its applicability for the colloid stability issue and for understanding electrostatic interactions between heterogeneous surfaces is new.

2. Method of calculation

All the results presented in this paper were obtained using a computer program, called ‘sfbox’, developed on the basis of the Scheutjens-Fleer theory[37] and recently extended and generalized by Van Male.[38] Considering the wide spectrum of problems that can be delt with, complete description of the numerical scheme in the program is beyond the scope of the current paper. Interested readers are referred to [38] for that purpose. Instead, we shall give a comprehensive description of the problem by first writing the basic electrostatic equations and boundary conditions in their continuous forms and then sketching the general discretization procedure adopted and its useful character for generating topologic and chemical nonuniformities at the surfaces. Transient effects will not be tackled here, only electric double layers at equilibrium are considered.

2.1. Continuous description: potential and charge distributions, Gibbs energy of interaction

Two parallel, flat planes are separated by a distance *h*, as specified in Figure 1. The properties (either electrostatic or topological) of the left and right surfaces will be denoted with the subscript $\mathrm{j} \mid 1$ and $\mathrm{j} \mid 2$, respectively. The asperities placed on top of the flat surfaces define the roughness profiles, which can be described by the analytical expressions

$$y \mid y_1(x) \quad y \mid h\,2\,\bullet_2(x) \mid y_2(x) \tag{1}$$

for the coordinate system (x,y) as indicated in Figure 1. The surfaces are supposed to be uniform in the *z*-direction so that the problem can be described by the two spatial dimensions *x* and *y* only. The so-generated infinite ridges on surfaces 1 and 2 are parallel. At a given separation distance *h*, the electrostatic potential distribution $..(x,y,h)$ between the surfaces is described by the PB equation

$$\kappa_0 \subseteq\!.\left[\kappa_r(x,y)\overset{u}{\subseteq}..(x,y,h)\right] \mid 4\,\psi(x,y,h) \tag{2}$$

where κ_0 is the dielectric permittivity of vacuum, $\kappa_r(x,y)$ the relative permittivity at the position (x,y), and $\psi(x,y,h)$ the charge (per unit volume) at the position (x,y) and separation *h*. $\psi(x,y,h)$ is given by

$$\psi(x,y,h) \mid F \underset{\mathrm{i}}{\text{——}} z_\mathrm{i} c_\mathrm{i}^{\leftarrow} \exp\left[4 z_\mathrm{i} F ..(x,y,h) / RT\right] \tag{3}$$

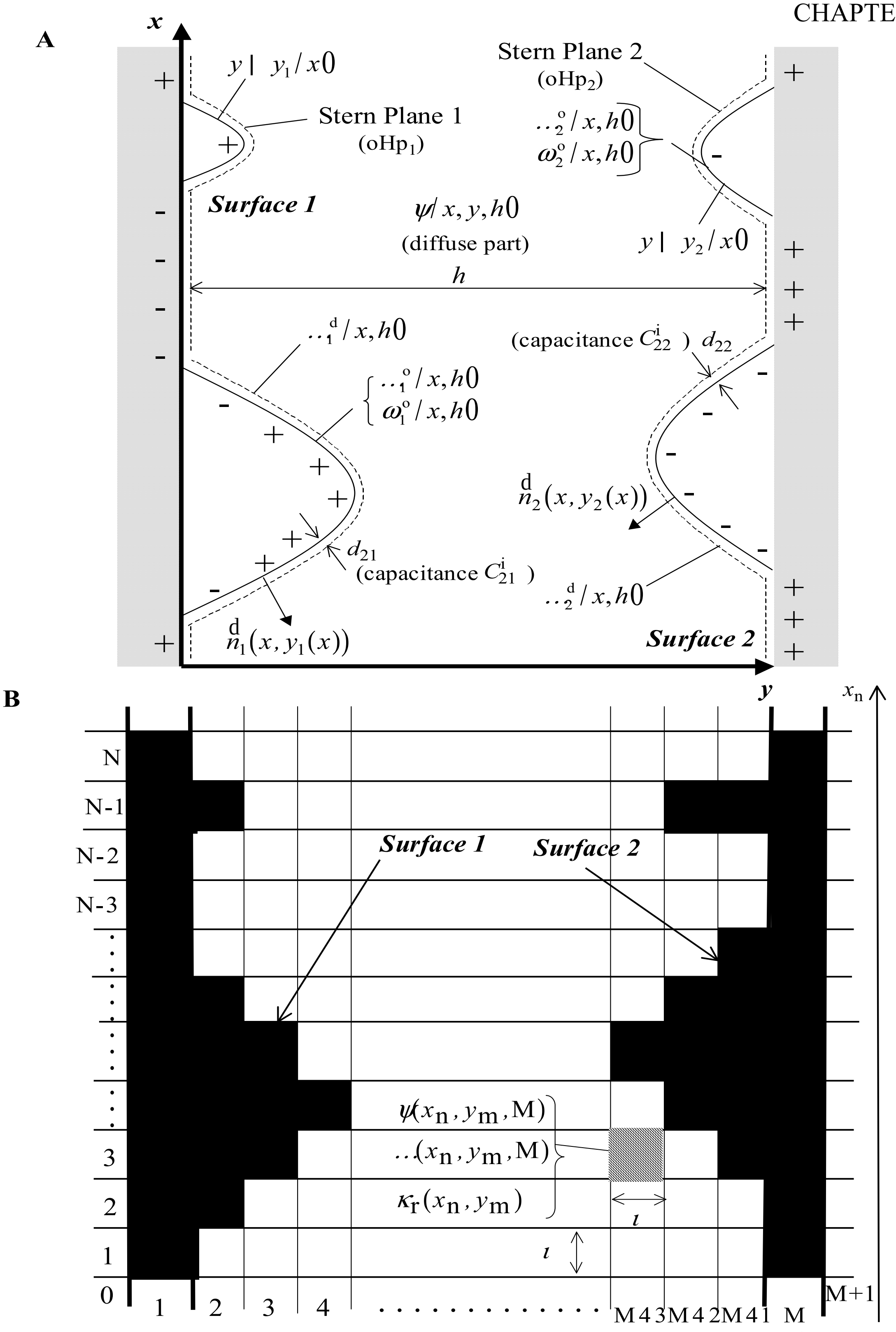
A
x
y | y1/x0
Stern Plane 1
(oHp1)
Stern Plane 2
(oHp2)
..°2/x,h0
ω°2/x,h0
Surface 1
ψ/x,y,h0
(diffuse part)
y | y2/x0
h
..d1/x,h0
(capacitance Ci22) d22
..°1/x,h0
ω°1/x,h0
nd2(x, y2(x))
d21
(capacitance Ci21)
..d2/x,h0
nd1(x, y1(x))
Surface 2
y
B
xn
N
N-1
N-2
N-3
3
2
1
0
Surface 1
Surface 2
ψ(xn, ym, M)
..(xn, ym, M)
κr(xn, ym)
ι
1
2
3
4
M43
M42
M41
M
M+1
ym

Figure 1. Hetero-interaction between rough surfaces. (A) Continuous description (section 2.1) for the case where the regulation of the surface charges occurs across the diffuse part of the double layers and the inner Helmholtz layer. (B) Discrete representation (section 2.2) within a two-gradient mean-field lattice analysis. The inner and outer Helmholtz layers adjacent to the surface located at $/x_{\mathrm{n}},y_{\mathrm{m}}0$ may be modeled by specifying the dielectric permittivities of the cells $/x_{\mathrm{n}},y_{\mathrm{m}}0$ and $/x_{\mathrm{n}},y_{\mathrm{m}}\,2\,1($, respectively.

with R the gas constant, F the Faraday and T the temperature. The index i refers to the ionic species i of valency z_{i} and bulk concentration $c_{\mathrm{i}}^{\leftarrow}$ (i.e. the concentration at infinite separation). The surface charge, denoted as $\omega^{\mathrm{o}}_{\mathrm{j}}(x,h)$, at a separation distance h and position $\left(x,y_{\mathrm{j}}(x)\right)$, is related to the electric potential by the Gauss relation

$$\omega^{\mathrm{o}}_{\mathrm{j}}(x,h) \mid 4\kappa_0 \overset{\mathrm{u}}{\subseteq}\left[\kappa_{\mathrm{r}}(x,y)..(x,y,h)\right].\overset{\mathrm{d}}{n}_{\mathrm{j}}\Big|_{y\mid y_{\mathrm{j}}(x)} \tag{4}$$

where $\overset{\mathrm{u}}{n}_{\mathrm{j}}$ is the unit normal vector to the surface j of which the components $n_{x_{\mathrm{j}}}$ and $n_{y_{\mathrm{j}}}$ are written

$$n_{x_{\mathrm{j}}} \mid 4\varsigma_{\mathrm{j}} \frac{1}{\left(1 2 \dfrac{\mathrm{d}y_{\mathrm{j}}(x)}{\mathrm{d}x}\right)^{1/2}} \frac{\mathrm{d}y_{\mathrm{j}}(x)}{\mathrm{d}x} \qquad n_{y_{\mathrm{j}}} \mid \varsigma_{\mathrm{j}} \frac{1}{\left(1 2 \dfrac{\mathrm{d}y_{\mathrm{j}}(x)}{\mathrm{d}x}\right)^{1/2}} \tag{5}$$

with $\varsigma_1 \mid 21$ and $\varsigma_2 \mid 41$. We note that eq 4 tacitly implies that the electric field in the solid phase corresponding to surface j is zero. There is a plethora of choices for expressing the boundary conditions required to solve eq 2. These may exclusively concern the surface potentials $..^{\mathrm{o}}_{\mathrm{j}}(x,h) \mid ..\left(x,y_{\mathrm{j}}(x),h\right)$ or the surface charges $\omega^{\mathrm{o}}_{\mathrm{j}}(x,h)$. Mixed boundary conditions may be more realistic for certain types of hetero-interactions. The surface potentials and/or charges may be taken constant with respect to h, uniform or actually depending on the position x. In that latter case, the assignment of a spatial surface distribution allows for the presence of chemical heterogeneities on top of surface roughness. In reality, there is no way of telling *a priori* if, upon interaction, the conditions of constant surface potential/surface charge are satisfied.

A more general analysis therefore calls for the inclusion of regulation mechanisms accounting for the adjustment of the potentials and/or charges upon double layer overlap. To that purpose, the occurrence of adsorption equilibria at the surfaces must be notified. In a previous analysis,[36] the issue of regulation of electric double layers at uniform charged colloids was revisited and generalized. To explicitly account for the ionic specificity, the double layers were described on the Gouy-Stern level. Provided that the characteristic length of the asperities introduced is larger than the distances from the surface d_{kj} (k $\mid$ 1 refers to the inner Helmholtz layer and k $\mid$ 2 to the outer Helmholtz layer, see Figure 1), the Stern layer is assumed to follow the contour of the roughness profile. Relaxing the condition of fixed surface charge, we consider surface charge regulation as it occurs between two interacting hydroxyl surfaces with adsorption sites denoted as ROH. The charge determining ions H^{2} and OH^{4} can react at the surfaces following the equilibria

$$\mathrm{ROH} \lozenge \quad \mathrm{RO}^4\ 2\ \mathrm{H}^2 \qquad K_{\mathrm{a}_\mathrm{j}}(x) \mid \frac{\left[\mathrm{RO}^4\right]}{\left[\mathrm{ROH}\right]}\chi^{\mathrm{s}}_{\mathrm{H}^+} \tag{6a}$$

$$\mathrm{ROH} + \mathrm{H_2O} \lozenge \quad \mathrm{ROH}_2^+\ 2\ \mathrm{OH}^4 \qquad K_{\mathrm{b}_\mathrm{j}}(x) \mid \frac{\left[\mathrm{ROH}_2^+\right]K_\mathrm{W}}{\left[\mathrm{ROH}\right]\chi^{\mathrm{s}}_{\mathrm{H}^+}} \tag{6b}$$

where $\chi^{\mathrm{s}}_{\mathrm{H}^+}$ is the mole fraction of H^2 at the surfaces, K_W the dissociation constant of water and the square brackets indicate surface concentrations given as moles of functional groups per unit surface area. To represent the situation of nonuniform charge distribution at the surfaces, we allow the reactions constants $K_{\mathrm{a}_\mathrm{j}}$ and $K_{\mathrm{b}_\mathrm{j}}$ to depend on the position *x*. Following the notation used in [36], all (local) *K*'s (including K_W) written in eq 6 are dimensionless. $\omega_\mathrm{j}^\mathrm{o}(x,h)$ is then related to the surface potential $\ldots_\mathrm{j}^\mathrm{o}(x,h)$ by an adsorption isotherm of the type

$$\omega_\mathrm{j}^\mathrm{o}(x,h) \mid 2FN^\mathrm{o}_{\mathrm{s}_\mathrm{j}}(x)\frac{\left(\frac{K_{\mathrm{a}_\mathrm{j}}(x)K_{\mathrm{b}_\mathrm{j}}(x)}{K_\mathrm{W}}\right)^{1/2}\sinh\left\{\frac{F}{RT}\left[\ldots_\mathrm{j}^\mathrm{N}(x)\,4\,\ldots_\mathrm{j}^\mathrm{o}(x,h)\right]\right\}}{1\,2\,2\left(\frac{K_{\mathrm{a}_\mathrm{j}}(x)K_{\mathrm{b}_\mathrm{j}}(x)}{K_\mathrm{W}}\right)^{1/2}\cosh\left\{\frac{F}{RT}\left[\ldots_\mathrm{j}^\mathrm{N}(x)\,4\,\ldots_\mathrm{j}^\mathrm{o}(x,h)\right]\right\}} \tag{7}$$

$N^\mathrm{o}_{\mathrm{s}_\mathrm{j}}(x)$ are the local densities of adsorption sites per unit area for surface j and the potentials $\ldots_\mathrm{j}^\mathrm{N}(x)$ are defined by

$$\ldots_\mathrm{j}^\mathrm{N}(x) \mid 42.303\left(\mathrm{pH}\,4\,\mathrm{pH}_\mathrm{j}^\mathrm{o}(x)\right) \tag{8}$$

with the local point of zero charge $\mathrm{pH}_\mathrm{j}^\mathrm{o}(x)$ for surface j given by

$$\mathrm{pH}_\mathrm{j}^\mathrm{o}\,/\,x0 = \frac{1}{2}/\,\mathrm{p}K_{\mathrm{a}_\mathrm{j}}\,/\,x0\,2\ \mathrm{p}K_\mathrm{W}\ 4\ \mathrm{p}K_{\mathrm{b}_\mathrm{j}}\,/\,x0(\tag{9}$$

In case of specific adsorption of ions onto the surfaces, the resulting local adsorbed charges, denoted as $\omega_\mathrm{j}^\mathrm{i}(x,h)$, are assumed to be related to the potentials $\ldots_\mathrm{j}^\mathrm{i}$ at the iHp by the Frumkin-Fowler-Guggenheim (FFG) equation in the form

$$\omega_\mathrm{j}^\mathrm{i}(x,h) \mid \frac{z_\mathrm{i}eN^\mathrm{i}_{\mathrm{s}_\mathrm{j}}(x)\chi_\mathrm{i}K_{\mathrm{i}_\mathrm{j}}\exp\left(4\,\frac{z_\mathrm{i}F}{RT}\ldots_\mathrm{j}^\mathrm{i}(x,h)\right)}{1\,2\,\chi_\mathrm{i}K_{\mathrm{i}_\mathrm{j}}\exp\left(4\,\frac{z_\mathrm{i}F}{RT}\ldots_\mathrm{j}^\mathrm{i}(x,h)\right)} \tag{10}$$

Interaction between heterogeneous surfaces

We consider only one type of ion (valency z_i) at the iHp of which the mole fraction in the solution is χ_i. $N^\mathrm{i}_{\mathrm{s}_\mathrm{j}}(x)$ is the local number of adsorption sites per unit area for ion i on surface j, and

$$K_{\mathrm{i}_\mathrm{j}} = \exp\left(-\Delta_\mathrm{ads}G_{\mathrm{m,i}_\mathrm{j}}/RT\right) \tag{11}$$

where $\Delta_\mathrm{ads}G_{\mathrm{m,i}_\mathrm{j}}$ is the molar Gibbs energy of specific adsorption for ion i at surface j. We consider that for the different patches along the surfaces, $\Delta_\mathrm{ads}G_{\mathrm{m,i}_\mathrm{j}}$ is the same and thus is independent of x. The local electrostatic contributions to the ionic adsorption are included in the exponential function. The charge density $\rho(x,y,h)$ in the diffuse part follows directly from the potential distribution, as expressed by Gauss' law. The pair of interfaces as a whole is electroneutral so that for every h we have the relation

$$\iint_{xy}\rho(x,y,h)\mathrm{d}x\mathrm{d}y+\sum_\mathrm{j}\left\{\int_{\mathrm{Surface}_\mathrm{j}}\sigma^\mathrm{o}_\mathrm{j}(x,y_\mathrm{j}(x),h)\mathrm{d}x+\int_{\mathrm{iHp}_\mathrm{j}}\sigma^\mathrm{i}_\mathrm{j}(x,y_\mathrm{j}(x)+d_{1\mathrm{j}},h)\mathrm{d}x\right\}=0 \tag{12}$$

where we have eliminated the distance of normalization in the z-direction. The set of non-linear equations 1-12 must be solved consistently so as to derive the anisotropic potential and charge distributions. Once that is done, the electrostatic interaction energy can be evaluated from the charging energy for both surfaces. These are functions of h and position x. We shall denote them as $\Delta G_\mathrm{j}(x,h)$, where the symbol Δ refers to the difference with respect to the reference state, i.e. the uncharged surface. $\Delta G_\mathrm{j}(x,h)$, counted per unit area, contains a chemical contribution, as resulting from the surface charge regulation and/or the specific adsorption of ions at the iHp, and an electrostatic contribution. Rewriting the result for isolated double layers,[39] we have

$$\Delta G_\mathrm{j}(x,h)=-\frac{\left(\sigma^\mathrm{o}_\mathrm{j}(x,h)\right)^2}{2C^\mathrm{i}_{1\mathrm{j}}}-\frac{\left(\sigma^\mathrm{i}_\mathrm{j}(x,h)\right)^2}{2C^\mathrm{i}_{2\mathrm{j}}}-\int_\infty^h\frac{\partial\left(\sigma^\mathrm{d}_\mathrm{j}(x,h)\psi^\mathrm{d}_\mathrm{j}(x,h)\right)}{\partial h}\mathrm{d}h \tag{13}$$

where the diffuse charges $\sigma^\mathrm{d}_\mathrm{j}$ are given by Gauss' law

$$\sigma^\mathrm{d}_\mathrm{j}(x,h)=-\varepsilon_0\vec{\nabla}\left[\varepsilon_\mathrm{r}(x,y)\psi(x,y,h)\right].\vec{n}_\mathrm{j}\Big|_{y=y_\mathrm{j}(x)+d_{2\mathrm{j}}} \tag{14}$$

$C^\mathrm{i}_{\mathrm{kj}}$ are the capacitances of the inner and outer Helmholtz layers as defined by the corresponding d_{kj} and the relative dielectric permittivities $\varepsilon_\mathrm{r}(x,y)$ taken constant in these layers. $\psi^\mathrm{d}_\mathrm{j}(x,h)$ in eq 13 refers to the potential at the oHp. The total electrostatic interaction energy G is then obtained by integration of eq 13 over the exact surface geometries after subtracting the charging energy of the isolated electric double layers (i.e., at $h\rightarrow\infty$)

$$G(h) \mid \underset{\mathrm{j}}{—}\frac{1}{A_{\mathrm{j}}}\left\{\iint\limits_{y \mid y_{\mathrm{j}}(x)}\left[\div G_{\mathrm{j}}(x,h)\,4\,\div G_{\mathrm{j}}(x,h \Downarrow\ \leftarrow)\right]\mathrm{d}x\mathrm{d}y\right\} \tag{15}$$

with A_{j} the total area of surface j. At this point of the analysis, it is useful to emphasize that the use of the DA[28,29] and the SEI technique[30,31] for estimating G is mainly motivated by the existence of analytical expressions for the interaction Gibbs energy at constant surface potential or constant surface charge between flat parallel planes. However, in the more general situation of interaction between regulating 1D-double layers, no (general) analytical equation has been formulated so far. Therefore, to account for these cases, DA and SEI methods, putting aside the limitations they necessarily imply, should be combined with numerical integration of eqs 1-12 in the flat geometry. More specifically, as far as SEI is concerned, the authors emphasize its suitability for the constant potential case but are more elusive about its feasibility for the other interaction situations.[40] In that respect, the self-consistent-field theory we use allows a higher degree of flexibility since it enables solving eqs 1-15 for any geometries and regulating boundary conditions as expressed by eq 1 and eqs 7 and 10, respectively.

2.2. Self-consistent-field lattice theory

Electrostatics. In this section, we describe the problem previously sketched as it is tackled within a self-consistent-field scheme based on the theory of Scheutjens and Fleer.[37] In the numerical evaluation of the theory, the space between the two surfaces is confined in a two-dimensional lattice of size $\mathrm{N} \Delta \mathrm{M}$. N and M represent the number of plane-parallel thin layers of thickness ι (0.3 nm) in the x and y directions, respectively (Figure 1). The charges and potentials are smeared-out in the z-direction. We describe here the situation of a flat lattice but cylindrical or spherical geometries are also possible.[38] The layers are filled with solvent molecules and (hydrated) ions of which the spatial distribution is governed by the Boltzmann statistics. The volume fraction of ion i at the position (x,y) is denoted as $\pi_{\mathrm{i}}(x,y)$. All sites have equal volume ι^3. Unlike the PB theory which considers point charges, the ions are given here a finite size. It is done by describing the local potential as the sum of the potential as defined within the PB theory and a potential, which can be seen as the isothermal work which must be performed (in the incompressible limit) to carry a unit with volume ι^3 from a position infinite to a position corresponding to a cell (x,y). Each site interacts with all neighboring sites through chemical and electric forces. The mean field principle enters in that an ion interacts with the local average of all other ions, instead of interacting with other ions taken individually. The discretisation of the PB equation is done using a capacitor model.[41] Within this model, the charges are assumed to be located on the planes in the center thus forming a multiplate capacitor of the same geometry as the lattice. The space can therefore be viewed as the succession of M Stern layers, with relative dielectric permittivities $\kappa_{\mathrm{r}}(x,y)$ being assigned at will. The positions are then readily obtained from the relations

$$\mathrm{n} \subset [0,\mathrm{N}]: \qquad x_{\mathrm{n}} \mid \mathrm{n}\iota\, 2\frac{1}{2} \tag{16}$$

$$\mathrm{m} \subset [0,\mathrm{M}]: \qquad y_{\mathrm{m}} \mid \mathrm{m}\iota\, 2\frac{1}{2} \tag{17}$$

The discretised form taken by the PB equation is

$$\begin{gathered}\bar{\kappa}_{\mathrm{r}}(x_{\mathrm{n}},y_{\mathrm{m}})..(x_{\mathrm{n}},y_{\mathrm{m}}) \mid 2\frac{\psi(x_{\mathrm{n}},y_{\mathrm{m}})}{\kappa_0} 2\left[\kappa_{\mathrm{r}}(x_{\mathrm{n}},y_{\mathrm{m}}\,2\,1)\,2\,\kappa_{\mathrm{r}}(x_{\mathrm{n}},y_{\mathrm{m}})\right]..(x_{\mathrm{n}},y_{\mathrm{m}}\,2\,1) \\ 2\left[\kappa_{\mathrm{r}}(x_{\mathrm{n}},y_{\mathrm{m}})\,2\,\kappa_{\mathrm{r}}(x_{\mathrm{n}},y_{\mathrm{m}}\,4\,1)\right]..(x_{\mathrm{n}},y_{\mathrm{m}}\,4\,1)\,2\left[\kappa_{\mathrm{r}}(x_{\mathrm{n}}\,2\,1,y_{\mathrm{m}})\,2\,\kappa_{\mathrm{r}}(x_{\mathrm{n}},y_{\mathrm{m}})\right]..(x_{\mathrm{n}}\,2\,1,y_{\mathrm{m}}) \\ 2\left[\kappa_{\mathrm{r}}(x_{\mathrm{n}},y_{\mathrm{m}})\,2\,\kappa_{\mathrm{r}}(x_{\mathrm{n}}\,4\,1,y_{\mathrm{m}})\right]..(x_{\mathrm{n}}\,4\,1,y_{\mathrm{m}})\end{gathered} \tag{18}$$

with the quantity $\bar{\kappa}_{\mathrm{r}}(x_{\mathrm{n}},y_{\mathrm{m}})$ defined by

$$\bar{\kappa}_{\mathrm{r}}(x_{\mathrm{n}},y_{\mathrm{m}}) \mid \kappa_{\mathrm{r}}(x_{\mathrm{n}},y_{\mathrm{m}}\,2\,1)\,2\,\kappa_{\mathrm{r}}(x_{\mathrm{n}},y_{\mathrm{m}}\,4\,1)\,2\,\kappa_{\mathrm{r}}(x_{\mathrm{n}}\,2\,1,y_{\mathrm{m}})\,2\,\kappa_{\mathrm{r}}(x_{\mathrm{n}}\,4\,1,y_{\mathrm{m}})\,2\,4\kappa_{\mathrm{r}}(x_{\mathrm{n}},y_{\mathrm{m}}) \tag{19}$$

The local charge density $\psi(x_{\mathrm{n}},y_{\mathrm{m}})$ is related to the ion volume fractions by

$$\psi(x_{\mathrm{n}},y_{\mathrm{m}}) \mid \frac{1}{\iota^3}\underset{\mathrm{i}}{\text{—}}\, e z_{\mathrm{i}}\pi_{\mathrm{i}}(x_{\mathrm{n}},y_{\mathrm{m}}) \tag{20}$$

and the electrostatic interaction energy (in $k_{\mathrm{B}}T$ per unit area) by

$$G_{\mathrm{el}} \mid \frac{F}{2k_{\mathrm{B}}T\iota^2}\underset{\mathrm{n}}{\text{—}}\underset{\mathrm{m}}{\text{—}}..(x_{\mathrm{n}},y_{\mathrm{m}})\underset{\mathrm{i}}{\text{—}}\, z_{\mathrm{i}}\pi_{\mathrm{i}}(x_{\mathrm{n}},y_{\mathrm{m}}) \tag{21}$$

where k_{B} is the Boltzman constant.

Reaction equilibria at the surfaces and/or at the iHp's. A possibility offered by the 'sfbox' program is the implementation of reaction equilibria at the surfaces, e.g. the specification of protonation and complexation reactions. For a given position x_{n} along the surface j, we can write such reactions in a concise form as follows

$$\underset{\mathrm{q}}{\text{—}}\,\Upsilon_{\mathrm{q}}^{x_{\mathrm{n}},\mathrm{j}} S_{\mathrm{q}}^{x_{\mathrm{n}},\mathrm{j}} \mid 0 \tag{22}$$

where *S* refers to both reactants and products. The index q denotes the species q involved in the reaction and the $\Upsilon_{\mathrm{q}}^{x_{\mathrm{n}},\mathrm{j}}$ are the stoichiometric coefficients. We follow the convention $\Upsilon_{\mathrm{q}}^{x_{\mathrm{n}},\mathrm{j}} \} 0$ for q product and conversely for the reactant. The associated thermodynamic constant $K_{\mathrm{j}}(x_{\mathrm{n}})$ is related to the bulk volume fractions $\pi_{\mathrm{q}}^{\leftarrow}$ of the species q by

$$\ln\left(K_{\mathrm{j}}(x_{\mathrm{n}})\right) \,|\, \underset{\mathrm{q}}{\text{——}}\Upsilon_{\mathrm{q}}^{x_{\mathrm{n}},\mathrm{j}}\ln\left(\nu_{\mathrm{q}}\pi_{\mathrm{q}}^{\leftarrow}\right) \tag{23}$$

with ν_{q} the activity coefficient of q. At constant temperature, the local adsorption Gibbs energy at surface j, denoted as $G_{\mathrm{j}}(x_{\mathrm{n}})_{\mathrm{chem}}$ (in $k_{\mathrm{B}}T$ per unit area), and corresponding to the equilibrium (22) is given by

$$G_{\mathrm{j}}(x_{\mathrm{n}})_{\mathrm{chem}} \,|\, 4\frac{1}{k_{\mathrm{B}}T}\underset{\mathrm{q}}{\text{——}}B_{\mathrm{q}}^{\mathrm{j}}(x_{\mathrm{n}})\sigma_{\mathrm{q}} \tag{24}$$

where $B_{\mathrm{q}}^{\mathrm{j}}(x_{\mathrm{n}})$ is the amount (moles) per unit area of adsorbed species q at the position x_{n} on surface j and σ_{q} the chemical potential of q given by

$$\sigma_{\mathrm{q}} \,|\, k_{\mathrm{B}}T\ln\left(\nu_{\mathrm{q}}\pi_{\mathrm{q}}^{\leftarrow}\right) \tag{25}$$

Equation (24) can be rearranged using the relation valid at thermodynamic equilibrium

$$\underset{\mathrm{q}}{\text{——}}\Upsilon_{\mathrm{q}}^{x_{\mathrm{n}},\mathrm{j}}\sigma_{\mathrm{q}} \,|\, 0 \tag{26}$$

and the mass balance relation (the total number of adsorption sites is constant). $B_{\mathrm{q}}^{\mathrm{j}}(x_{\mathrm{n}})$ is related to the local charge density by

$$\omega_{\mathrm{j}}^{\mathrm{o,i}}(x_{\mathrm{n}}) \,|\, F\underset{\mathrm{q}}{\text{——}}z_{\mathrm{q}}B_{\mathrm{q}}^{\mathrm{j}}(x_{\mathrm{n}}) \tag{27}$$

where the superscript o holds for (protonation) reactions taking place at the surface and the superscript i for (complexation) reactions at the iHp. We note in passing that the adsorption isotherms as written in eqs 7 and 10 may be obtained by writing the condition stating that, at equilibrium, the electrochemical potential of the free ions in the bulk solution is equal to that of the corresponding ions bound at the surface.

Using the appropriate boundary conditions (constant charge, constant potential or boundary regulation conditions) for different separation distance *h*, i.e. different M, the potential distribution $..(x_{\mathrm{n}},y_{\mathrm{m}})$, the charge density $\psi(x_{\mathrm{n}},y_{\mathrm{m}})$ and volume fraction $\pi_{\mathrm{i,q}}(x_{\mathrm{n}},y_{\mathrm{m}})$ are computed in an iterative scheme where the potential is taken as variable and updated till a self-consistent solution is obtained. Electrostatic mirrors placed at the layers 0 and M+1 ensure the condition of zero-electric field at these coordinates and the condition of electroneutrality for the pair of colloids, i.e. the relation $\underset{\mathrm{n}\ \ \mathrm{m}}{\text{———}}\psi(x_{\mathrm{n}},y_{\mathrm{m}}) \,|\, 0$. Then the total interaction energy *G* at a given M is yielded by

$$G(\mathrm{M}) \,|\, G_{\mathrm{el}}(\mathrm{M})\,2\underset{\mathrm{j}\ \ \mathrm{n}}{\text{———}}G_{\mathrm{j}}(x_{\mathrm{n}},\mathrm{M})_{\mathrm{chem}} \tag{28}$$

which is the pendant of eq 15.

Generation of the surface roughness. The surface profile is assigned following what we call a 'lego' type procedure. More specifically, the positions (n,m) along the surface to be modeled are 'frozen', meaning that the corresponding sites will effectively act as solid substrate. These sites are inaccessible for molecules (ions, water). The chemical and electrostatics characteristics of these (p*K* values, adsorption energies, number of sites, surface charges and κ_r values) may differ from the ones chosen for the flat surface on top of which the asperities are grafted. An example is given in Figure 1. The asperities may be of the type 'protusion' or 'depression', i.e. convex or concave, respectively. One or both surfaces may contain asperities.

3. Results and discussion

The 'sfbox' program was first tested for a number of 1D-interaction situations where analytical expressions, generally given in the Debye-Hückel (DH) approximation,[36] are available. Good agreement was found in the three geometries (flat, cylindrical, spherical) for the separation range effectively corresponding to the DH regime (not shown). Results including charge/potential regulations in the conditions of constant surface potential/charge were also successfully compared to those expected on the basis of the expressions given by Hogg *et al*[42] and Usui.[43] Considering the multi-parameter nature of the issue presented in the previous section, the variety of situations that can be envisaged is virtually infinite. We shall here focus on a few characteristic examples, which clearly highlight the paramount importance of roughness and chemical nonuniformities in determining electrostatic interaction energy.

As a starting point, we analyze the interaction between a flat plate $(\mathrm{j}\,|\,2)$ and a flat surface $(\mathrm{j}\,|\,1)$ on which a bar of height h_a and width ι is positioned. Figure 2 shows the results for different h_a and different bulk volume fractions $\pi_{\overset{\leftarrow}{\mathrm{b}}}$ of a 1:1 electrolyte. The surface charges are kept constant upon interaction and the charge density carried by the asperity, denoted as $\omega_{\mathrm{a}_1}^{\mathrm{o}}$, is the same as the one carried by its supporting plane, denoted as $\omega_{\mathrm{s}_1}^{\mathrm{o}}$. In the following, all the charge densities ω of interest will be given in elementary charge per unit cell (0.01 elementary charge per unit cell = 1.78 μC cm^{-2}). Variation in $\pi_{\overset{\leftarrow}{\mathrm{b}}}$ allows for tuning the range of electrostatic double layer (EDL) interaction expressed in terms of the Debye length ρ^{41}. In the framework of the Debye-Hückel regime, ρ^{41} is read from the slope of the plot $\log(G)$ versus $\log(h)$. For ρh_a {{ 1 (low $\pi_{\overset{\leftarrow}{\mathrm{b}}}$), the roughness of the left surface is 'unseen', or otherwise stated, screened by the range of EDL interaction. The resulting interaction curve is essentially the same as that between two flat surfaces. For $\rho h_{\mathrm{a}} - 1$ or $\rho h_{\mathrm{a}} \} 1$ (high $\pi_{\mathrm{b}}^{\leftarrow}$), the spatial detail of the surface profile, that is, the characteristic size of the asperity, becomes comparable to or even overrules the range of EDL interaction. Upon increasing $\pi_{\mathrm{b}}^{\leftarrow}$, this is materialized by a splitting of the interaction curves calculated for different h_{a}. At given $\pi_{\mathrm{b}}^{\leftarrow}$, the larger h_{a}, the stronger the repulsion (the surface charges $\omega_{\mathrm{j}}^{\mathrm{o}}$ have the same sign). At given h_{a}, the larger $\pi_{\mathrm{b}}^{\leftarrow}$ the less the repulsion because of the screening effect of the counterions. The numerical results may be compared with those expected on the basis of the scaling technique proposed by Derjaguin (Derjaguin approximation, DA). We mention however that this latter is not expected to fit the results since the surface geometry considered here is not 'smooth'. The comparison is only relevant in the sense that it clearly highlights the origin of the descrepancies between the numerical and DA approaches. For the simple geometry of surface roughness chosen, we have

$$G_{\mathrm{DA}}\left(h_{\mathrm{a}},\mathrm{M}\right) | \ \frac{\mathrm{N}\,4\,1}{\mathrm{N}} G^{(\mathrm{flat})}(\mathrm{M})\, 2\, \frac{1}{\mathrm{N}} G^{(\mathrm{flat})}\left(\mathrm{M}\,4\,h_{\mathrm{a}}\,/\,\iota\right) \qquad (29)$$

where the superscript '(flat)' is read as 'the interaction energy between flat parallel plates (without any asperity)'. For high ρh corresponding to weak overlap of the EDL, the DA well predicts the computed G but underestimates G for low ρh and high ρh_{a} (Figure 2). In these regi-

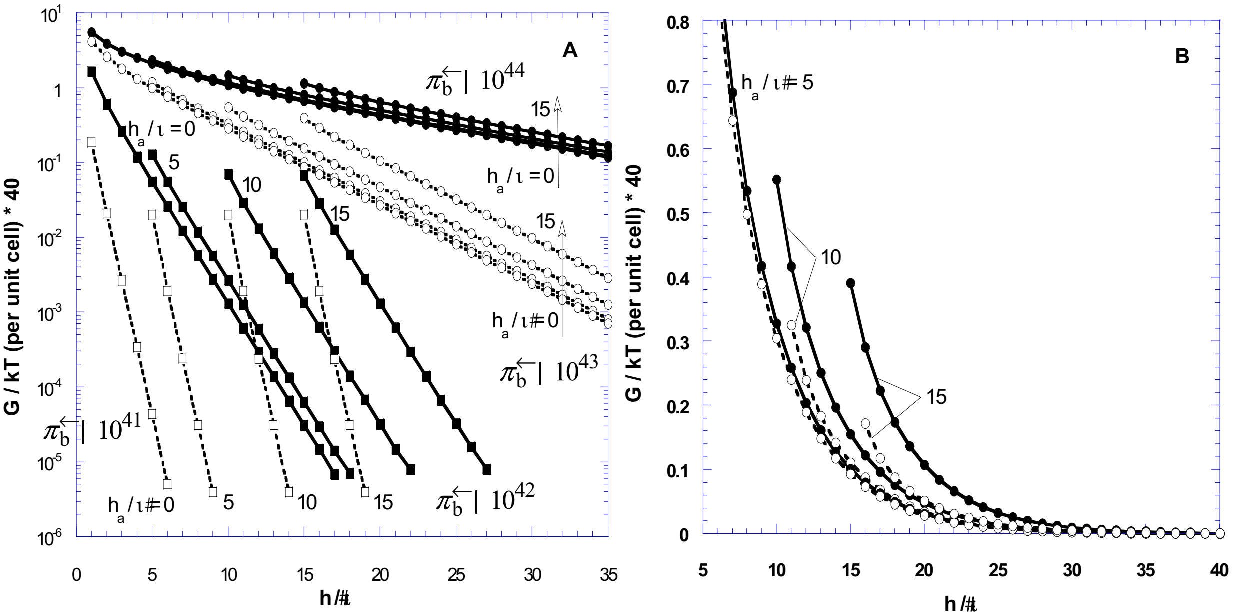

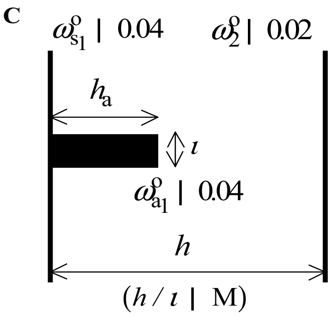
C
$\omega_{\mathrm{s1}}^{\mathrm{o}} | 0.04$
$\omega_{2}^{\mathrm{o}} | 0.02$
h_{a}
ι
$\omega_{\mathrm{a1}}^{\mathrm{o}} | 0.04$
h
$(h/\iota \ | \ \mathrm{M})$

Figure 2. (A) Interaction Gibbs energy corresponding to the situation depicted in the scheme panel (C). In panel (B), the numerical results (full lines) are compared to the predictions based on the DA approximation (dashed lines) for $\pi_{\mathrm{b}}^{\leftarrow} | \ 10^{43}$ ($\rho^{41}/\iota - 4.3$). No Stern layers are explicitly considered ($\kappa/\text{Stern}0|$ $\kappa/\text{diffuse part}0|$ 78).

mes, the interactions between elements of the surfaces that do not face each other contribute for an overall repulsion that is not taken into account by the DA scaling technique. Similar results are obtained when increasing the width of the asperity at given ρh_a.

In the next case, the charge density carried by the asperity differs in size and sign from that (positive) at the surface where it is grafted (Figure 3). Besides, we choose $\omega_2^o \} 0$. As intuitively expected, when increasing ρh_a the interaction then progressively changes from repulsion to attraction. For high ρh_a, the sign and magnitude of the interaction are predominantly determined by the chemical properties of the asperity and of course by those of the opposed surface $j | 2$.

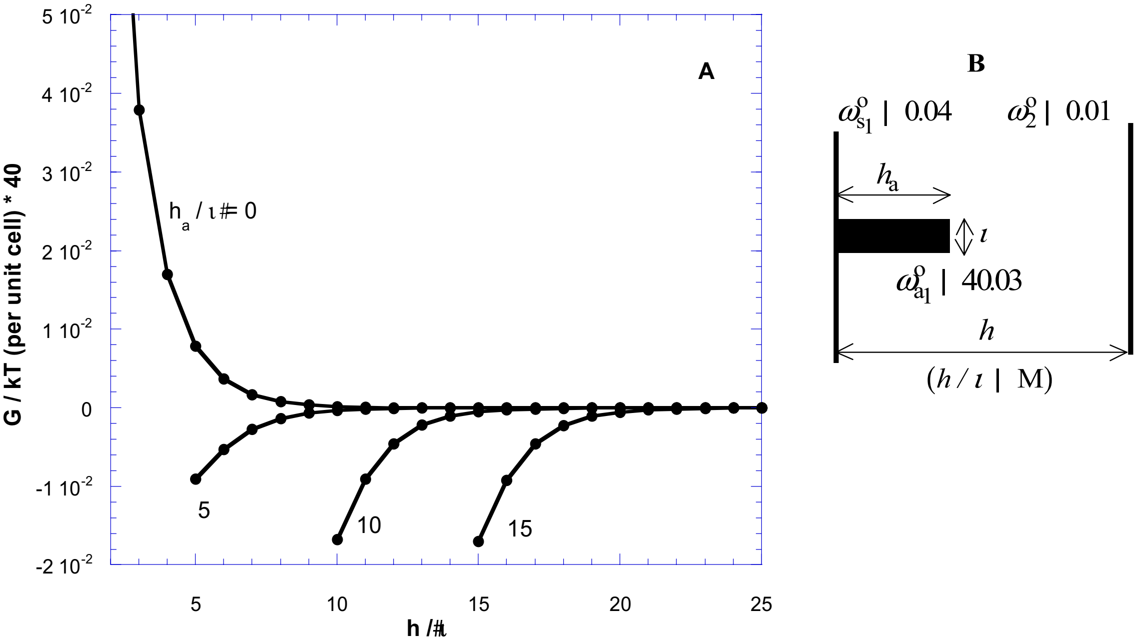

Figure 3. (A) Interaction Gibbs energy corresponding to the situation depicted in the scheme panel (B) for $\pi_b^{\leftarrow} | 10^{42}$. No Stern layers are explicitly considered ($\kappa/\text{Stern}\,0| \ \kappa/\text{diffuse part}\,0| \ 78$).

In Figure 4, two protrusions of the same height h_a are placed on the left surface $(j | 1)$. For the sake of convenience, we shall denote the surface charge densities of the asperities as $\omega_{a_{1,2}}^o$. We have arbitrarily chosen $\omega_{a_{1,2}}^o | 2\omega_{s_1}^o$. The respective positions of the two asperities are changed by varying their separation distance ^ in the *x*-direction. In order to highlight the eventual effects of ^ on *G*, h_a was chosen such that $\rho h_a \} 1$. For the simplistic configuration chosen, the dependence of *G* on ^ is not very pronounced but still the results are illustrative of the electrostatic anisotropy developed in the *x*-direction. To qualitatively understand the results, one may reason in terms of the quantity ρ^. We emphasize however that the scaling distance ρ^{41}

along the *x*-direction is arbitrary since this latter primarily indicates the extent of the EDL in the *y*-direction. The physically relevant Debye length, $\rho 1^{41}$, is actually function of *x*. For the sake of illustration, we present in the Appendix a way to derive the functionality $\rho 1^{41}(x)$ in the cases where $h_{\mathrm{a}} / \wedge \{ 1$. Getting back to Figure 4 and keeping in mind the previous point, it is clear that $\wedge$ does not affect *G* for large ρh, as intuitively expected. At lower ρh, provided that the double-layers in between the two asperities (in the *x*-direction) do not overlap ($\rho\wedge \}\} 1$), *G* remains independent of $\wedge$ (high $\pi_{\mathrm{b}}^{\leftarrow}$). In the other case, weak overlap of the EDL along the rough surface ($\rho\wedge \}\} 1$) leads to a slight additional repulsion in the overall interaction curve and strong overlap ($\rho\wedge \{\{ 1$) to an attractive contribution. In this latter situation, the local electrostatic repulsion between the asperities is completely screened and therefore not reflected in *G*. If increasing the absolute magnitude of the charge on the two asperities, these effects are magnified. The DA approximation can not predict any dependence of *G* on $\wedge$ since the corresponding scaling of the interaction energy between flat plates is done according to the *y*-direction only.

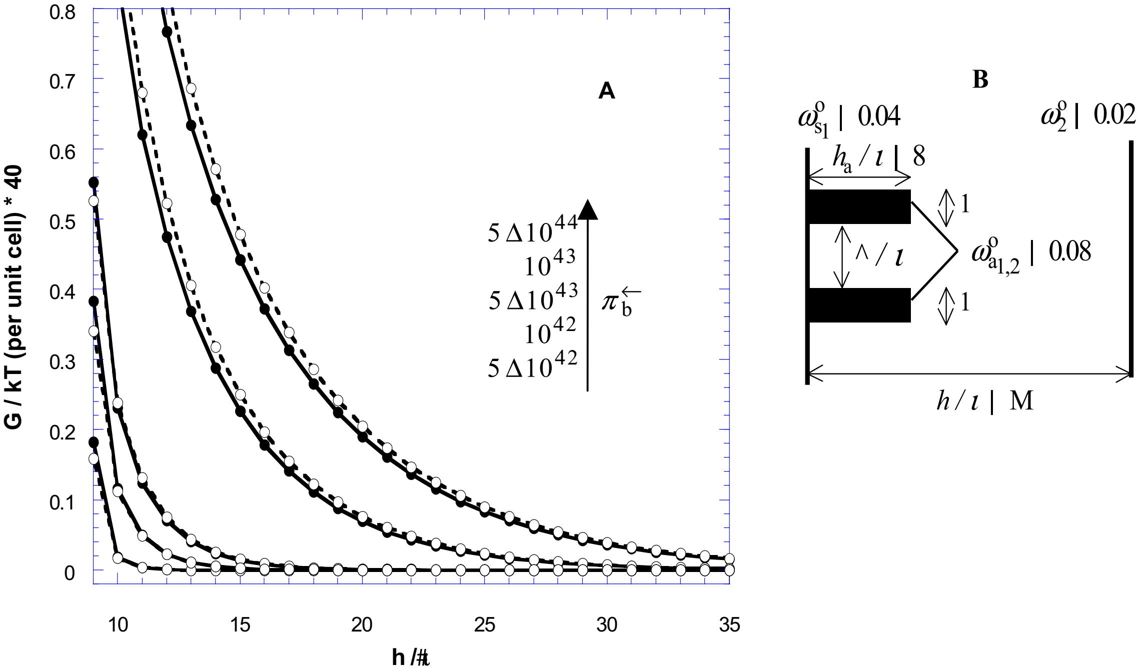

Figure 4. (A) Interaction Gibbs energy corresponding to the situation depicted in the scheme panel (B). The full and dashed lines stand for $\wedge/\iota \mid 1$ and $\wedge/\iota \mid 30$, respectively. The bulk volume fraction of 1:1 electrolyte is indicated. In this picture, the dielectric permittivity κ_{r} in the outer Helmholtz layers is set to 20, otherwise 78.

In Figure 5, we analyse the situation where $\omega_{\mathrm{a}_1}^{\mathrm{o}} \mid 4\omega_{\mathrm{a}_2}^{\mathrm{o}} (\} 0)$ and $\rho\wedge \}\} 1$ (same h_{a} for the two asperities and $\rho h_{\mathrm{a}} \} 1$). The total charge carried by the rough surface is kept constant (in the example given, $\omega_{\mathrm{a}_1}^{\mathrm{o}}\ 2\ \omega_{\mathrm{a}_2}^{\mathrm{o}}\ 2\ \omega_{\mathrm{s}_1}^{\mathrm{o}} \mid 0$). The results are given for different $\omega_{\mathrm{a}_1}^{\mathrm{o}}$ and $\pi_{\mathrm{b}}^{\leftarrow} \mid 5\Delta 10^{43}$.

Contrary to first intuition, the overall interaction actually depends on $\omega^{o}_{a_1}$, the interaction becoming repulsive upon increase of $\omega^{o}_{a_1}$. The results can be qualitatively understood by means of the DA approximation, which is now written

$$G_{DA}\left(\omega^{o}_{a_{1,2}}, M\right) | \ \frac{N\,4\,2}{N} G^{(\text{flat})}(M)\,2\,\frac{1}{N} G^{(\text{flat})}\left(\omega^{o}_{a_1}, M\,4\,h_a / \iota\right) 2\,\frac{1}{N} G^{(\text{flat})}\left(\omega^{o}_{a_2}, M\,4\,h_a / \iota\right) \quad (30)$$

where the two last terms in the r.h.s. of eq 30 stand for the energy of interaction between a flat plate carrying the charge $\omega^{o}_{a_1}$ (or $\omega^{o}_{a_2}$) and a flat plate carrying the charge ω^{o}_{2}. The sign and magnitude of the overall interaction results from the asymmetry of the interactions between the asperities taken separately and the surface $j\,|\,2$. For the example given, the DA approximation qualitatively yields the same results as those obtained by the numerical analysis and quantitatively we have $G_{DA} \} G$. For $\omega^{o}_{2}\,|\,0$, changing in the charge $\omega^{o}_{a_1}\,|\,4\omega^{o}_{a_2}$ carried by the protrusions would affect the local distribution of the countercharge but not the total Gibbs energy of interaction.

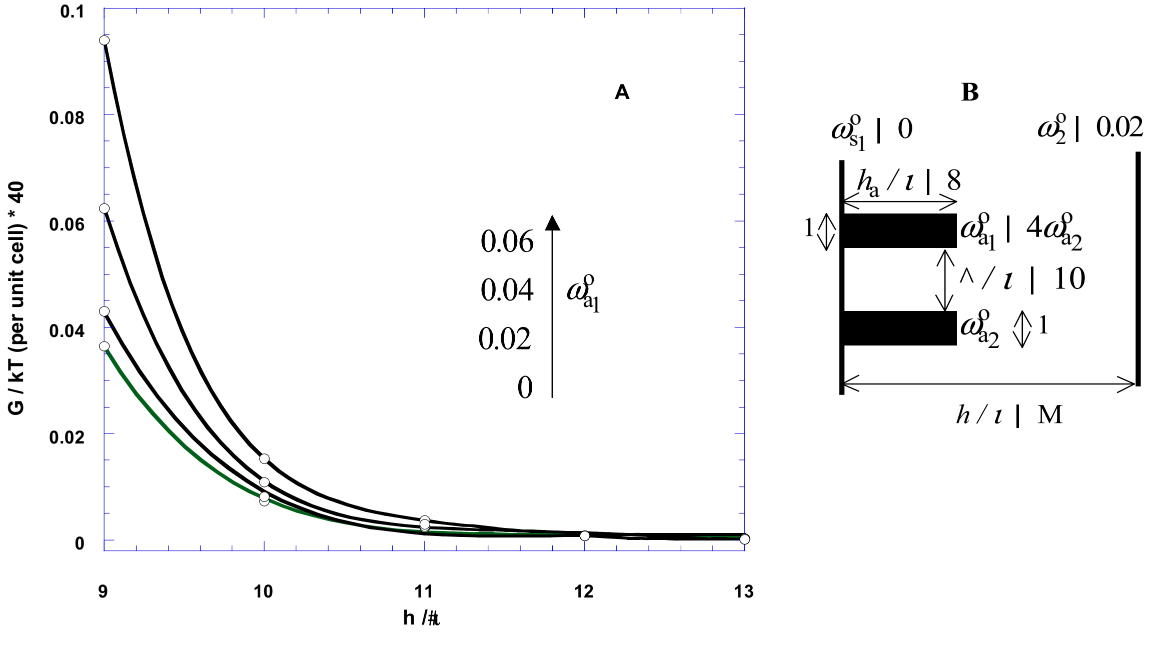

Figure 5. (A) Interaction Gibbs energy corresponding to the situation depicted in the scheme panel (B). The charges carried by the asperities are indicated. In this picture, the dielectric permittivity κ_r in the outer Helmholtz layers is set to 20 (otherwise 78). $\pi^{\leftarrow}_{b}\,|\,5\Delta10^{43}$.

In Figure 6, specific interaction of anions with both surfaces is taken into account. The characteristics of the inner and outer Helmholtz layers as well as the molar Gibbs energies of adsorption are specified. Upon increase of the asperity size, the interaction gradually changes from repulsion to attraction. The total adsorbed charge at the iHp$_1$ which comes into play for the determination of *G* is given by the summation of the local adsorbed charges along the contour of surface 1. For low ρh_a, this charge does not suffice to reverse the sign of the total charge carried by surface 1, so that repulsion ensues ($\omega_2^{o} \} 0$). When increasing ρh_a, the electric and chemical properties of the asperity prevail in the determination of *G* (see Figure 2) so that, roughly speaking, the only charge distribution in the vicinity of the asperity, or otherwise stated, the local regulation features at the asperity become of importance. The total effective (apparent) charge carried by surface 1 decreases and now superequivalent adsorption occurs, thus leading to attraction.

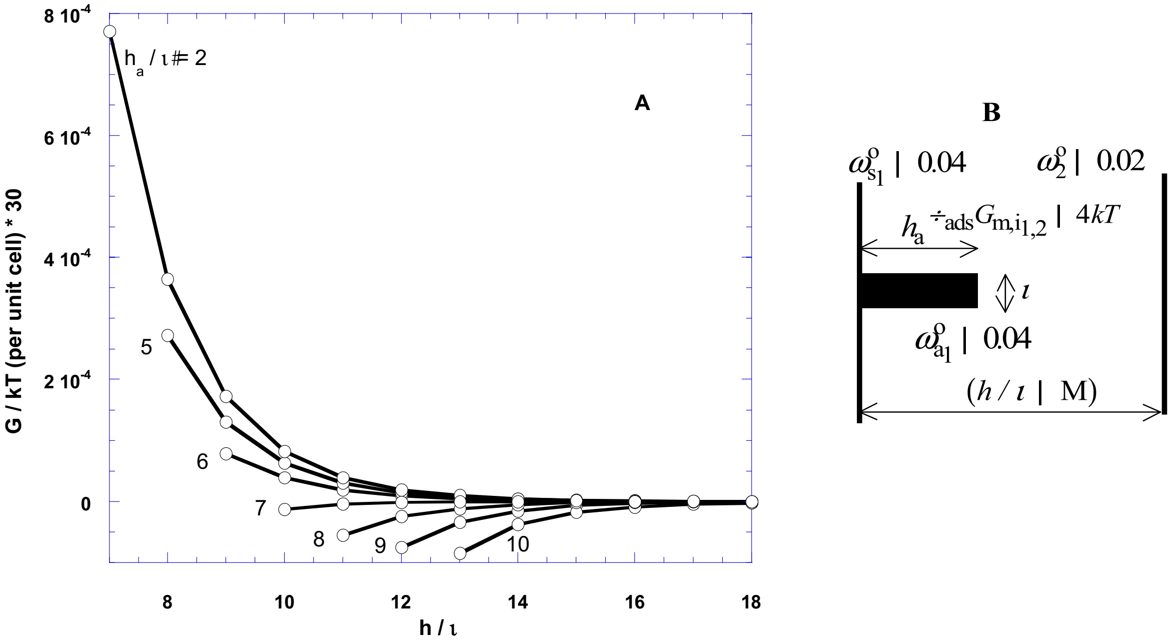

Figure 6. (A) Interaction Gibbs energy corresponding to the situation depicted in the scheme panel (B). $\pi_{\mathrm{b}}^{\leftarrow}$ | 10^{42}. For both surfaces, the dielectric permittivities κ_{r} in the inner and outer Helmholtz layers are set to 20 and 50, respectively. In the diffuse part, κ_{r} | 78. Specific adsorption of anions on both surfaces is considered.

In Figure 7, interaction curves are given for different combinations of $\omega_{\mathrm{a}_1}^{\mathrm{o}}$, $\omega_{\mathrm{s}_1}^{\mathrm{o}}$, $\div_{\mathrm{ads}} G_{\mathrm{m,i}_{1,2}}$ and various values of ρh_{a}. The results, qualitatively in line with intuition, again illustrate the possibility of sign reversal of the overall interaction as the result of the presence of morphological/chemical heterogeneities.

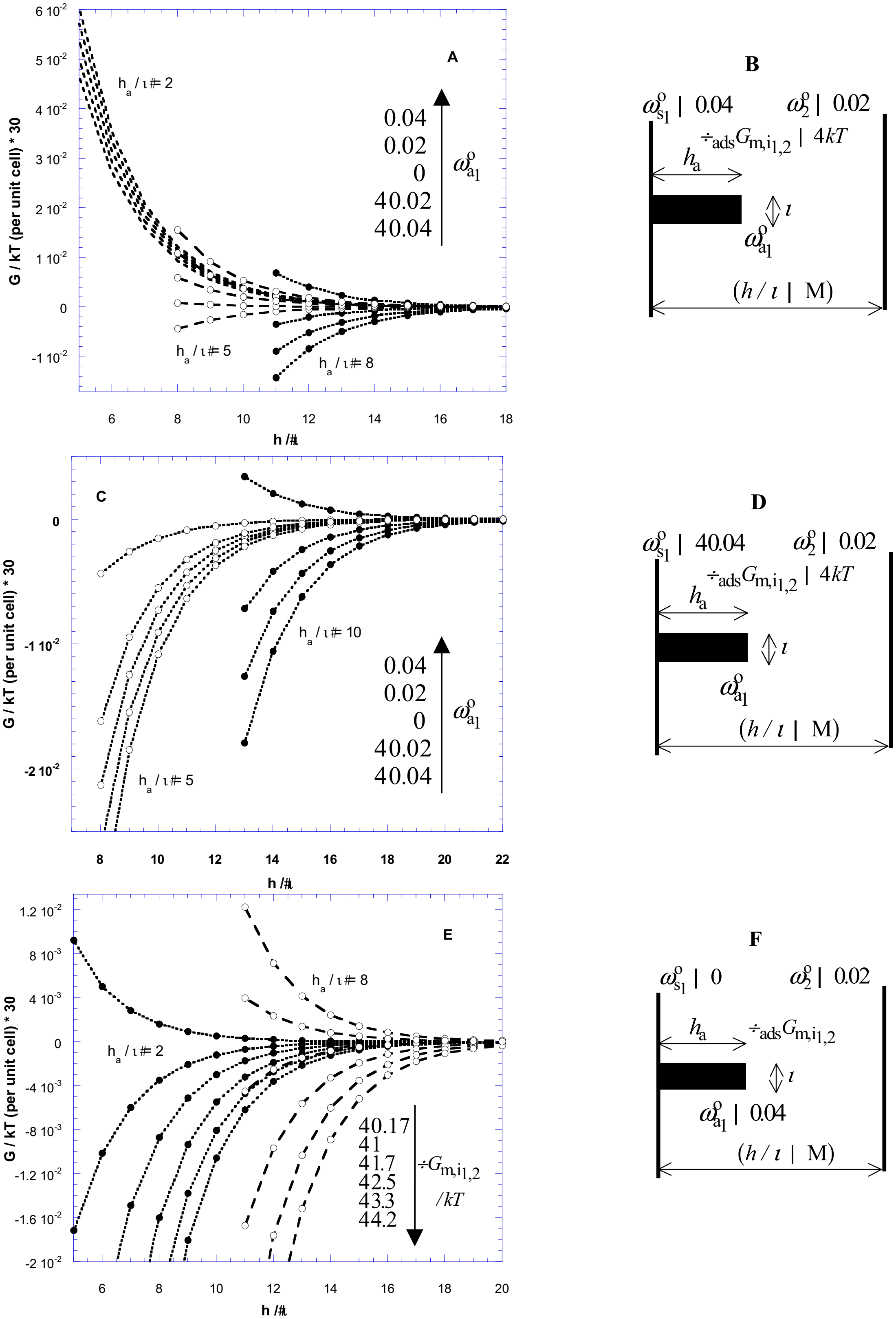

Figure 7. Interaction Gibbs energy computed for different topological/chemical heterogeneities (indicated) located at surface 1. The schemes in panels B, D and F refer to the set of curves of panels A, C and E, respectively. $\pi_{\mathrm{b}}^{\leftarrow} \mid 5\Delta10^{43}$. For both surfaces, the dielectric permittivities κ_{r} in the inner and outer Helmholtz layers are set to 20 and 50, respectively. In the diffuse part, $\kappa_{\mathrm{r}} \mid 78$. Specific adsorption of anions on both surfaces is considered.

Next, we analyze the situation where both surfaces contain an asperity, the sizes of these being identical. The charge carried by the asperity positioned at surface j| 2, denoted as $\omega_{\mathrm{a}}^{\mathrm{o,j|\ 2}}$, is varied in magnitude as well as in sign compared to that of the asperity at surface j| 1 ($\omega_{\mathrm{a}}^{\mathrm{o,j|\ 1}}$ chosen positive). The spatial shift between the protrusions is denoted as •. For high *h*, *G* is independent of • for reasons already mentioned. At lower *h*, for $\omega_{\mathrm{a}}^{\mathrm{o,j|\ 1}}\omega_{\mathrm{a}}^{\mathrm{o,j|\ 2}}$ } 0, the results presented in Figure 8 indicate that for a given separation distance, the energy of interaction increases when decreasing • and increasing $\omega_{\mathrm{a}}^{\mathrm{o,j|\ 2}}$. The repulsive energy is maximum when the two protrusions are in line (•| 0). For $\omega_{\mathrm{a}}^{\mathrm{o,j|\ 1}}\omega_{\mathrm{a}}^{\mathrm{o,j|\ 2}}$ { 0, decrease of • alters *G* both in amplitude and sign because of the increasing contribution of the attractive bar-bar interaction. Upon increase of •, the interaction energy tends to a constant value as the result of the diminishing of the extension of the double layers overlap in the direction given by the extremities of the two asperities. The conclusions pertaining to the effect of • on *G* are in line with those derived by Tsao[44] for electrostatic interactions between two corrugated surfaces. In this paper, the interaction energy is computed using a perturbation theory valid for smooth corrugation and only the case of uniformly charged surfaces is examined.

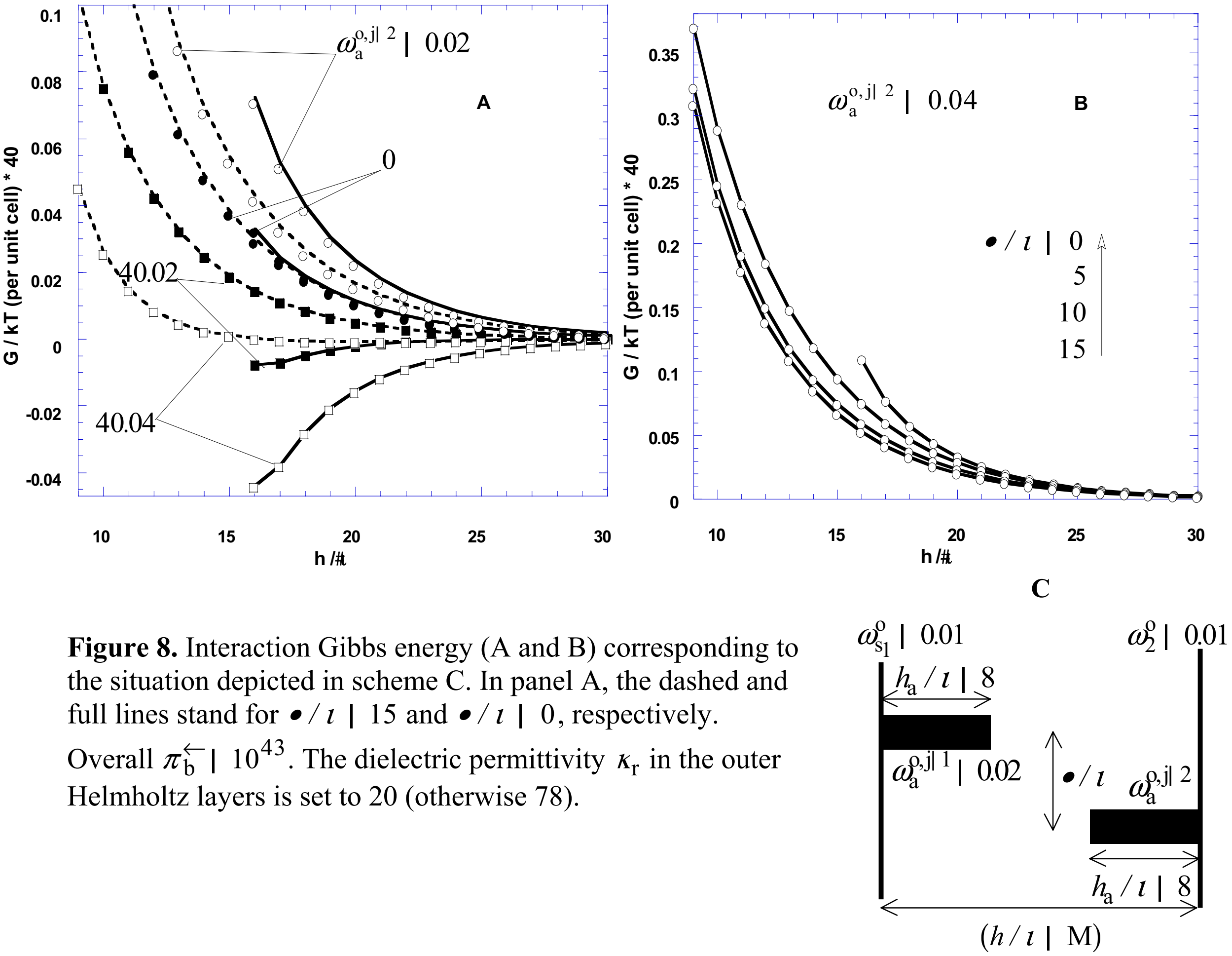

Figure 8. Interaction Gibbs energy (A and B) corresponding to the situation depicted in scheme C. In panel A, the dashed and full lines stand for • / ɩ | 15 and • / ɩ | 0, respectively. Overall $\pi_{\mathrm{b}}^{\leftarrow}$ | 10^{43}. The dielectric permittivity κ_{r} in the outer Helmholtz layers is set to 20 (otherwise 78).

As a final example, we compute the interaction energy between two plates of which the surface charges are determined by the charge determining ions H^+ present in the solution (equilibria 6a,b). Surface $(j \mid 2)$ is flat and surface $(j \mid 1)$ contains a protusion of height h_a. Figure 9 shows the results for different h_a and different pH's. By choice of the p*K*'s, we have $pH^o_{j=1} \mid 4.5$ and $pH^o_{j=2} \mid 8.5$. The results for $h_a \mid 0$ have already been discussed in detail in ref. [36]. Upon increase of h_a, the repulsion $(pH \mid 3{,}10)$ or the attraction $(pH \mid 6,\ pH^o_{j=1})$ increases at given *h*. For the case where induction takes place $(pH \mid 4.4)$, the transition long-range repulsion/short-range attraction occurs at longer separation distance. The 2D-morphology as introduced for the

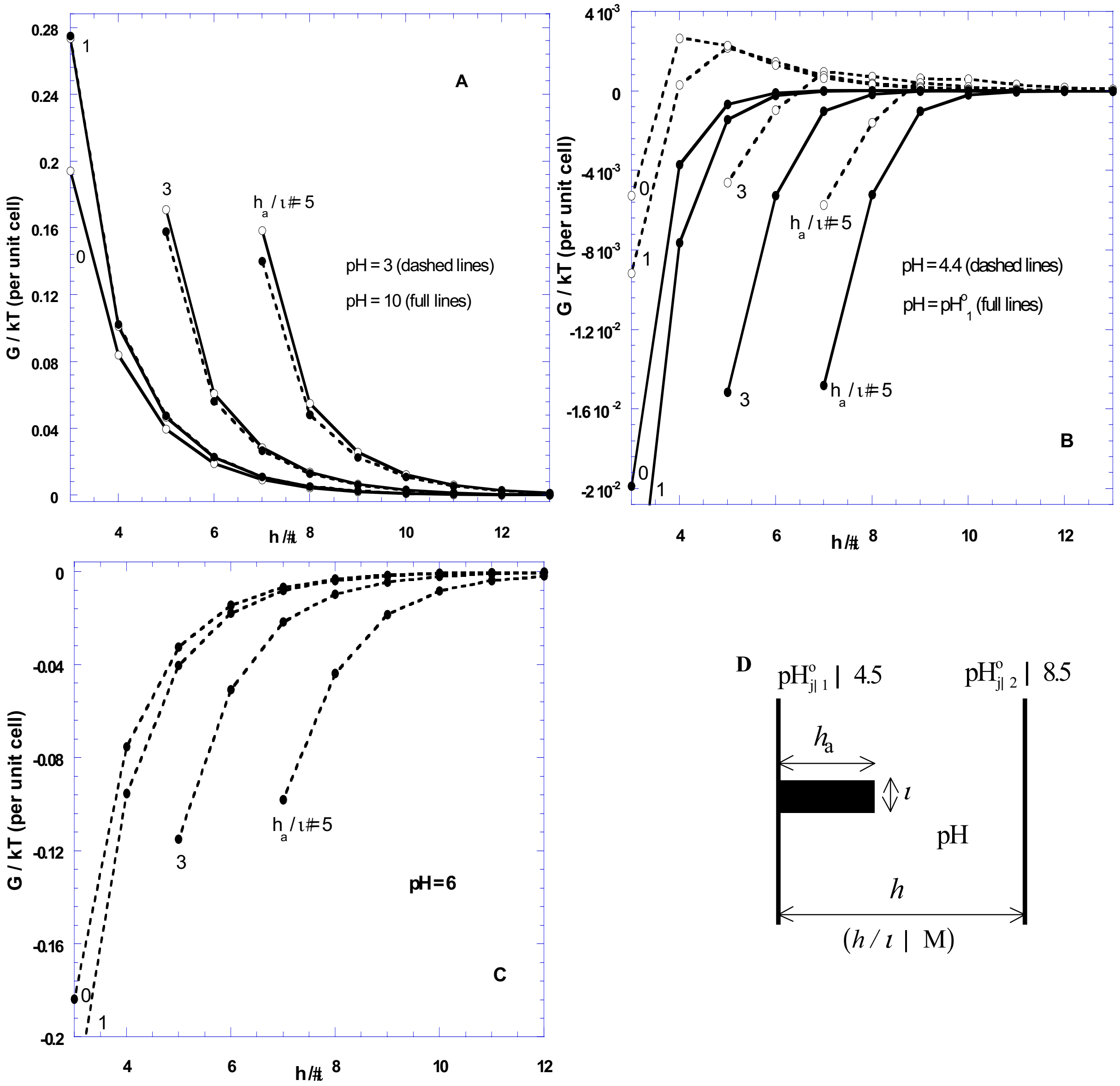

Figure 9. Interaction Gibbs energy (A-C) corresponding to the situation depicted in the scheme panel (D). The results are shown for different pH's and h_a, as indicated. $\pi_b^{\leftarrow} \mid 10^{42}$. The dielectric permittivity κ_r in the outer Helmholtz layers is set to 40 (otherwise 78).

left surface generates a loss of the symmetry of *G* with respect to the pH's, denoted pH_1 and pH_2, and verifying $\mathrm{pH}_1 \; 4 \; \mathrm{pH}^{\mathrm{o}}_{\mathrm{j|}\,1} \mid \mathrm{pH}^{\mathrm{o}}_{\mathrm{j|}\,2} \; 4 \; \mathrm{pH}_2$ (see panel A). The trends constitute the pendant of the results discussed in Figure 2 for the constant surface charge situation.

4. Conclusions

The electrostatic contribution to the Gibbs energy of interaction between heterogeneous surfaces has been evaluated for simple geometrical models and various boundary conditions. These are pertaining to the surface charges carried by the asperities and by the planar surfaces on which they are grafted. The analysis presented is far from being exhaustive since multiple combinations of asperity distributions and charge density distributions can be imagined and computed. The few examples presented illustrate the variety of interaction situations that can be handled by the theoretical formalism described. To our knowledge, the method of calculation outlined in this paper is the first that offers the possibility to concomitantly account for the effects of surface roughness and non-uniform surface charge density. On top of that, various regulation mechanisms as originating from the presence of specific interactions of ions from the background electrolyte with the surfaces can be introduced. The examples in this study clearly highlight the dramatic effects of surface heterogeneities on the Gibbs energy of interaction, both in sign and magnitude.

We recognize that the surface profile that is generated with the lego-procedure described may be, for certain practical situations, restrictive since the ensuing anisotropy is two-dimensional only. A challenge remains the development of a methodology which allows mimicking of three-dimensional patterns and still accounts for the chemical and electrical components of the regulation of the double layers at the same level as the 2D-analysis presented in this paper.

Appendix

In this appendix, a general expression is given for the electrostatic potential distribution $\ldots/x',y'($ in the diffuse part of the double layer at an isolated surface of which the profile is described by the spatial functionality $y' \mid y_1/x'($ (section A1). $/x',y'($ are the spatial variables and, for mathematical convenience, $/x,y($ are dimensionless variables (see below). For the sake of simplicity, the constant (surface) potential condition is chosen but the analysis can also be performed for the constant charge case and extended, in a very elegant way, to the situation of interaction between two charged rough surfaces or between charged flat and rough surface (section A2).[1] The development proposed constitutes an extension of the work by Tsao[44] because the Taylor expansion we derive here for $\ldots(x,y)$ is valid for smoothly as well as moderately roughed surfaces (see below).

A1. Solution of the linearized Poisson-Boltzmann equation for a rough surface: use of the perturbation theory and calculation of $\rho 1^{41}(x)$. For a two dimensional problem, the linearized PB equation with homogeneous dielectric permittivity is written

$$\frac{\in^2 \ldots(x',y')}{\in x'^2} 2 \frac{\in^2 \ldots(x',y')}{\in y'^2} | \rho^2 \ldots(x',y') \qquad \text{(A1)}$$

One can scale the y'-axis and the x'-axis as followed

$$y | \rho y' \quad \text{(A2)} \quad ; \quad x | \rho x' h_a / \wedge \quad \text{(A3)}$$

with h_a the characteristic height of the asperities and $\wedge$ the typical correlation length characterizing the distribution of the protrusions along the surface (see Figure 4B). x and y are from now on dimensionless quantities. Equation A1 is then rewritten

$$\varsigma \frac{\in^2 \ldots/x,y0}{\in x^2} 2 \frac{\in^2 \ldots/x,y0}{\in y^2} | \ldots/x,y0 \qquad \text{(A4)}$$

with

$$\varsigma | /h_a/\wedge 0^2 \qquad \text{(A5)}$$

Provided that $\varsigma \{ 1$, the potential $\ldots(x,y)$ may be expanded as follows

$$\ldots/x,y0 | \ldots_0/x,y0 2 \overset{\leftarrow}{\underset{n|1}{-}} \ldots_n/x,y0\varsigma^n \qquad \text{(A6)}$$

$\ldots_0(x,y)$ is the first order term of the Taylor development and is simply given by

$$\ldots_0(x,y) | A_0(x)\exp(4y) \qquad \text{(A7)}$$

with

$$A_0(x) | \ldots^o \exp(y_1(x)) \qquad \text{(A8)}$$

$\ldots^o$ is the surface potential defined by $\ldots(x, y | y_1(x)) | \ldots^o$, with $y_1(x) | \rho y_1'(x)$. One can easily show that the terms of order $O/\varsigma^n 0_{n \varnothing 1}$ are given by the recursive differential equation

$$\frac{\in^2 \ldots_n(x,y)}{\in y^2} 4 \ldots_n(x,y) | 4 \frac{\in^2 \ldots_{n\text{-}1}(x,y)}{\in x^2} \qquad \text{(A9)}$$

The boundary condition associated with eq A9 is

$n \varnothing 1 \qquad \ldots_n(x, y | y_1(x)) | 0 \qquad$ (A10)

---

[1] Detailed derivation of the results presented in this appendix will be provided in "supporting information" of the forthcoming publication of chapter 11

Selecting the solution verifying $\Phi(x, y \to -\infty) \to 0$, the terms Φ_n may be written in the form

$$n \geq 1 \qquad \Phi_n(x,y) = \left(A_n(x) + \sum_{k=1}^{n} B_{k,n}(x) y^k \right) \exp(-y) \tag{A11}$$

Condition (A10) yields the general relationship which exists between the unknown spatial functions $A_n(x)$ and $B_{k,n}(x)$ to be determined

$$A_n(x) = -\sum_{k=1}^{n} B_{k,n}(x) \left(y_1(x) \right)^k \tag{A12}$$

After substitution of eq A11 in eq A9 and identification of the coefficients $B_{k,n}(x)$ of the polynome in *y*, one finds the recursion formulas allowing the calculation of the $B_{k,n}(x)$ and, subsequently of the $A_n(x)$ (eq A12). The mathematical analysis is straightforward but tedious.

The results are:

$$B_{n,n}(x) = \frac{1}{2^n n!} \frac{\partial^{2n} A_0(x)}{\partial x^{2n}} \tag{A13}$$

$$B_{n-1,n}(x) = \frac{n}{2} B_{n,n}(x) + \sum_{i=1,n\geq 4}^{n-3} \frac{(n-i)!}{2^{i+1}(n-1)!} \frac{\partial^{2i} B_{n-i,n-i}(x)}{\partial x^{2i}} + \frac{1}{2^{n-2}(n-1)!} \frac{\partial^{2(n-2)} B_{1,2}(x)}{\partial x^{2(n-2)}} \tag{A14}$$

$$B_{n-2,n}(x) = \frac{n-1}{2} B_{n-1,n}(x) + \sum_{i=1,n\geq 5}^{n-4} \frac{(n-i-1)!}{2^{i+1}(n-2)!} \frac{\partial^{2i} B_{n-i-1,n-i}(x)}{\partial x^{2i}} + \frac{1}{2^{n-3}(n-2)!} \frac{\partial^{2(n-3)} B_{1,3}(x)}{\partial x^{2(n-3)}} \tag{A15}$$

…

$$B_{n-j,n}(x) = \frac{n-j+1}{2} B_{n-j+1,n}(x) + \sum_{i=1,n\geq j+3}^{n-j-2} \frac{(n-i-j+1)!}{2^{i+1}(n-j)!} \frac{\partial^{2i} B_{n-i-j+1,n-i}(x)}{\partial x^{2i}} + \frac{1}{2^{n-j-1}(n-j)!} \frac{\partial^{2(n-j-1)} B_{1,j+1}(x)}{\partial x^{2(n-j-1)}} \tag{A16}$$

…

$$B_{2,n}(x) = \frac{3}{2} B_{3,n}(x) + \frac{1}{2.2!} \frac{\partial^2 B_{1,n-1}(x)}{\partial x^2} \tag{A17}$$

$$B_{1,n}(x) = B_{2,n}(x) + \frac{1}{2} \frac{\partial^2 A_{n-1}(x)}{\partial x^2} \tag{A18}$$

For a given ς, calculation of the $A_n(x)$ and $B_{k,n}(x)$ is then iteratively performed up to the order n$_o$ verifying

$$\forall (x,y), \qquad \Phi_{n_o}(x,y) / \Phi_{n_o - 1}(x,y) \ll 1 \tag{A19}$$

The potential distribution is then completely determined

$$\psi(x,y) = \psi^o \exp(y_1(x) - y) + \sum_{k=1}^{n_o\geq 1}\sum_{m=1}^{k} B_{m,k}(x)\left[y^m - (y_1(x))^m\right]\varsigma^k \exp(-y) \qquad \text{(A20)}$$

The dependence of $\rho 1^{-1}$ (written in its dimensionless form, see eq A2) on the position *x* is then readily obtained from eq A20

$$\psi^o(e) = \psi^o \exp\left(y_1(x) - \rho 1^{-1}\right) + \sum_{k=1}^{n_o\geq 1}\sum_{m=1}^{k} B_{m,k}(x)\left\{\left(\rho 1^{-1}\right)^m - (y_1(x))^m\right\}\varsigma^k \exp\left(-\rho 1^{-1}\right) \qquad \text{(A21)}$$

A2. Application for the situation of interaction between two rough surfaces. We now consider the interaction between two surfaces denoted 1 (left surface) and 2 (right surface) and defined by the profiles $y = y_1(x)$ and $y = y_2(x)$, respectively. As in eq A5, we define ς_1 and ς_2 by

$$\varsigma_{1,2} = \left(h_{a_{1,2}}/\lambda_{1,2}\right)^2 \qquad \text{(A22)}$$

with $h_{a_{1,2}}$ and $\lambda_{1,2}$ the characteristic heights and correlation lengths of the asperities on surfaces 1 and 2. We treat the case $\varsigma_1 = \varsigma_2 = \tilde{\varsigma}$. Equations A3-A6 remain valid after replacing ς by $\tilde{\varsigma}(\ll 1)$. The first order term $\psi_0(x,y)$ is written

$$\psi_0(x,y) = C_0(x)\cosh(y) + D_0(x)\sinh(y) \qquad \text{(A23)}$$

$C_0(x)$ and $D_0(x)$ are calculated from the boundary conditions $\psi_0(x,y = y_{1,2}(x)) = \psi^o_{1,2}$, with $\psi^o_{1,2}$ the potential at surface 1 and 2. One obtains

$$C_0(x) = \frac{\psi_2^o \sinh(y_1) - \psi_1^o \sinh(y_2)}{\sinh(y_1 - y_2)} \quad \text{(A24)} \quad ; \quad D_0(x) = \frac{\psi_1^o \cosh(y_2) - \psi_2^o \cosh(y_1)}{\sinh(y_1 - y_2)} \quad \text{(A25)}$$

The terms $\psi_n(x,y)_{n\geq 1}$ verify eq A9 and may be written in the general form

$$\psi_n(x,y) = C_n(x)\cosh(y) + D_n(x)\sinh(y) + \sum_{k=1}^{n} E_{k,n}(x)y^k\cosh(y) + \sum_{k=1}^{n} F_{k,n}(x)y^k\sinh(y) \qquad \text{(A 26)}$$

The functions $C_n(x)$ and $D_n(x)$ are related to the unknown $E_{k,n}(x)$ and $F_{k,n}(x)$ via the conditions $\psi_n(x,y = y_{1,2}(x)) = 0$, which yields

$$C_n(x) = \frac{1}{\sinh(y_1 - y_2)}\left\{\sum_{k=1}^{n} E_{k,n}(x)\left[y_1^k \sinh(y_2)\cosh(y_1) - y_2^k \sinh(y_1)\cosh(y_2)\right]\right.$$
$$\left. + \sinh(y_2)\sinh(y_1)\sum_{k=1}^{n} F_{k,n}(x)\left[y_1^k - y_2^k\right]\right\} \qquad \text{(A27)}$$

$$D_{\mathrm{n}}(x) = \frac{1}{\sinh(y_2 - y_1)}\left\{\sum_{\mathrm{k}=1}^{\mathrm{n}} F_{\mathrm{k,n}}(x)\left[y_1^{\mathrm{k}}\sinh(y_1)\cosh(y_2) - y_2^{\mathrm{k}}\sinh(y_2)\cosh(y_1)\right] + \cosh(y_2)\cosh(y_1)\sum_{\mathrm{k}=1}^{\mathrm{n}} E_{\mathrm{k,n}}(x)\left[y_1^{\mathrm{k}} - y_2^{\mathrm{k}}\right]\right\} \qquad \text{(A28)}$$

To obtain the $E_{\mathrm{k,n}}(x)$ and $F_{\mathrm{k,n}}(x)$, one can rewrite the expression A26 for the potential in terms of $\exp(y)$ and $\exp(-y)$ so as to return to a treatment similar to the one presented in section A1. One then easily shows that the recursion formulae (A13-A18) allow computation of the $E_{\mathrm{k,n}}(x)$ and $F_{\mathrm{k,n}}(x)$ via the simple transformations

$$B_{\mathrm{k,n}}(x) = \frac{1}{2}\left(E_{\mathrm{k,n}}(x) - F_{\mathrm{k,n}}(x)\right) \quad \text{and} \quad A_{\mathrm{n}}(x) = C_{\mathrm{n}}(x) - D_{\mathrm{n}}(x) \qquad \text{(A29a,b)}$$

$$y = -y \quad ; \quad B_{\mathrm{k,n}}(x) = \frac{1}{2}\left(E_{\mathrm{k,n}}(x) + F_{\mathrm{k,n}}(x)\right) \quad \text{and} \quad A_{\mathrm{n}}(x) = C_{\mathrm{n}}(x) + D_{\mathrm{n}}(x) \qquad \text{(A30a,b,c)}$$

The potential distribution (eq A26) is found after solving the system of eqs (A24-A25, A27-A30) up to the order n_o verifying A19.

References

(1) Verwey, E. J. W. and Overbeek, J. Th. G. in *Theory of Stability of Lyophobic Colloids*, Elsevier, Amsterdam, 1948.

(2) Derjaguin, B. V. and Landau, L. *Acta Physicochim. URSS* **1941**, *14*, 633.

(3) Russel, W. B.; Saville, D. A. and Schowalter, W. R. in *Colloidal Dispersions*, Cambridge University Press, Cambridge, 1989.

(4) Israelachvili, J. N. in *Intermolecular and Surface Forces*, 2nd Edition, Academic Press, London, 1992.

(5) Lifshitz, E. M. Z. *Eksp. Teor. Fiz.* **1955**, *29*, 44.

(6) Hamaker, H. C. *Physica* **1937**, *4*, 1058.

(7) Tsao, Y.-H.; Yang, S. X.; Evans, D. F. and Wennerström, H. *Langmuir* **1991**, *7*, 3154.

(8) Tsao, Y.-H.; Evans, D. F. and Wennerström, H. *Science* **1993**, *262*, 547.

(9) Tsao, Y.-H.; Evans, D. F. and Wennerström, H. *Langmuir* **1993**, *9*, 779.

(10) Marshall, J. K. and Kitchener, J. A. *J. Colloid Interface. Sci.* **1966**, *22*, 342.

(11) Hull, M. and Kitchener, J. A. *Trans. Faraday. Soc.* **1969**, *65*, 3093.

(12) Elimelech, M.; Gregory, J.; Jia, X. and Williams, R. A. in *Particle Deposition and Aggregation: Measurement, Modeling and Simulation*, Butterworth, Oxford, 1995.

(13) Walz, J. *Adv. Colloid Interface Sci.* **1998**, *74*, 119.

(14) Kihira, H.; Ryde, N. and Matijevic, E. *J. Chem. Soc. Faraday. Trans.* **1992**, *88 (16)*, 2379.

(15) Vreeker, R.; Kuin, A. J.; den Boer, D. C.; Hoekstra, L. L. and Agterof, W. G. M., *J. Colloid Interface. Sci.* **1992**, *154*, 138.

(16) Stankovich, J. and Carnie, S. L. *J. Colloid Interface. Sci.* **1999**, *216*, 329.

(17) Elimelech, M. and O'Melia, C. R. *Langmuir* **1990**, *6*, 1153.

(18) Herman, M. C. and Papadopoulos, K. D. *J. Colloid Interface. Sci.* **1990**, *136*, 385.

(19) Herman, M. C. and Papadopoulos, K. D. *J. Colloid Interface. Sci.* **1991**, *142*, 331.

(20) Suresh, L. and Walz, J. *J. Colloid Interface. Sci.* **1996**, *183*, 199.

(21) Suresh, L. and Walz, J. *J. Colloid Interface. Sci.* **1997**, *196*, 177.

(22) Sader, J. E. and Lenhoff A. M. *J. Colloid Interface. Sci.* **1998**, *201*, 233.

(23) Grant, M. L. and Saville, D. A. *J. Colloid Interface. Sci.* **1995**, *171*, 35.

(24) Chan, B. K. C. and Chan, D. Y. C. *J. Colloid Interface. Sci.* **1983**, *92*, 281.

(25) Stankovich, J. and Carnie, S. L. *Langmuir* **1996**, *12*, 1453.

(26) Hoskin, N. *Philos. Trans. R. Soc. London* **1956**, *248*, 433.

(27) Hoskin, N. and Levine, S. *Philos. Trans. R. Soc. London* **1956**, *248*, 449.

(28) White, L. R. *J. Colloid Interface. Sci.* **1983**, *95*, 286.

(29) Derjaguin, B. V. *Kolloid Z.* **1934**, *69*, 155.

(30) Bhattachrjee, S.; Ko, C.-H. and Elimelech, M. *Langmuir* **1998**, *14*, 3365.

(31) Hoek, E. M. V.; Bhattachrjee, S. and Elimelech, M. *Langmuir* **2003**, *19*, 4836.

(32) Shulepov, S. Y. and Frens, G. *J. Colloid Interface. Sci.* **1995**, *170*, 44.

(33) Shulepov, S. Y. and Frens, G. *J. Colloid Interface. Sci.* **1996**, *182*, 388.

(34) Czarnecki, J. *Adv. Colloid Interface Sci.* **1986**, *24*, 283.

(35) Sun, N. and Walz, J. Y. *J. Colloid Interface. Sci.* **2001**, *234*, 90.

(36) Lyklema, J. and Duval, J. To be submitted (chapter 10 of this thesis).

(37) Scheutjens, J. M. H. M. and Fleer, G. J. *J. Phys. Chem.* **1979**, *83*, 1619.

(38) Van Male, J.; PhD thesis, Wageningen University, the Netherlands, 2003.

(39) Lyklema, J. in *Fundamentals of Interface and Colloid Science*, Academic Press, 1995, Vol II, Chapter 3.

(40) Bhattachrjee, S. and Elimelech, M. *J. Colloid Interface. Sci.* **1997**, *193*, 273.

(41) Barneveld, P. A.; Hesselink, D. E.; Leermakers, F. A. M; Lyklema, J. and Scheutjens, J. M. H. M. *Langmuir* **1994**, *10*, 1084.

(42) Hogg, R.; Healy, T. W. and Fuersteneau, D. W. *Trans. Faraday Soc.* **1966**, *62*, 1638.

(43) Usui, S. *J. Colloid Interface Sci.* **1973**, *44*, 107.

(44) Tsao, H.-K. *J. Colloid Interface. Sci.* **1999**, *216*, 370.

CHAPTER 12

CONCLUSIONS, PERSPECTIVES

The present study largely focuses on the equilibrium properties of electric double layers in conducting colloidal systems. Their interfacial characteristics are generally determined by the concomitant occurrence of electronic and ionic charging processes. As such, the resulting double layers combine the reversible en polarizable features as met for purely insulating and conducting colloids, respectively. The double layer can be polarized by means of a potential externally applied across the interface. If no electron transfer occurs between the solid and liquid solution phases, the double layer is said to be completely polarized; in the other case, faradaic depolarization takes place. A fundamental parameter characterizing such amphifunctional colloids is the potential at the slip plane located in the vicinity of the particle surface, the so-called electrokinetic potential or zeta-potential (′ -potential). This parameter is a useful indicator of the charge carried by the surface and allows the prediction of a number of interfacial phenomena, e.g. stability against coagulation, sedimentation kinetics, particle-particle or particle-electrode interactions under various conditions (for instance under application of external electric fields), to mention just a few of them. The ′ -potential of colloids may experimentally be determined by electrokinetic methods. The movement of charged colloidal particles in an external electric field is termed electrophoresis. When the charged solid surface is fixed, the electric field causes a movement of the liquid called electroosmosis. Forcing a liquid through a capillary or porous plug induces an electric potential difference called the streaming potential.

The work reported in this thesis combines theoretical and experimental investigations of the double layer properties of model amphifunctional substrates, such as gold and aluminum. The experimental analysis is essentially based on the streaming potential technique. The electrokinetic response is studied for various bulk solution compositions in the absence or presence of faradaic processes at the interface. Typically in electrochemistry, electron transfer between the solution and the conducting solid phase is effected by external application of a potential difference across the interface. In this work, the processes and circumstances under which such electron transfer can occur without the need for any applied potential difference are investigated. The analysis leads to the development of new concepts concerning bipolar electrochemistry and bipolar electrode kinetics in the specific context of electrokinetics of conducting surfaces. The streaming potential measurements are analyzed in terms of the electrochemical characteristics of the electron transfer under the experimental conditions of interest. Accordingly, theories are elaborated for converting the electrokinetic data into ′-potentials. The ensuing results are compared with predictions based on double layer models developed for describing the interfacial properties of oxidized metals polarized by an externally applied electric field and/or as the result of the presence of an electroactive couple in the solution. These models are further used to quantitatively interpret double layer potentials derived from atomic force microscopy measurements performed on metallic and semiconducting substrates polarized via an external source.

In **chapter 2**, a theoretical model is proposed to capture the basic double layer properties of amphifunctional substrates, such as partly oxidized metallic surfaces. Emphasis is placed on the dependencies of the ′-potential, the isoelectric point, the open-circuit potential and the potential of zero-surface charge on the solution pH and the potential difference applied across the interface. In **chapter 3**, AFM results obtained for gold electrodes subjected to an external potential are analyzed in terms of the amphifunctional model previously presented. This analysis highlights the importance of including surface roughness for the interpretation of double layer potentials as derived from measured force/separation distance curves. The possibility of specific interaction of ions other than the charge determining ones with amphifunctional substrates is considered in detail in **chapter 4**. Experimental data referring to the adsorption behavior of sulfate and phosphate anions onto a TiO_2 surface as a function of pH and applied potential are re-examined and interpreted after extending the amphifunctional model to the case of semiconducting oxides. **Chapter 5** describes the bipolar behavior of flat aluminum surfaces placed in a thin-layer cell, subjected to an electric field applied in the solution parallel to the surfaces. It is shown that above a certain value of the total potential drop across the cell, electron transfer occurs at the metallic surfaces in a direction perpendicular to that of the electric field set in solution. A first-order analytical model is proposed for computing the total faradaic current flowing in the cell from monopolar voltammetric data. Assuming that the electric field remains constant in the solution, use of those data indeed allows straightforward derivation of the spatial distribution of the faradaic current density along the surfaces. The integration of the latter over the relevant surface area yields the overall bipolar faradaic current, as reflected in the measured conductivity curves. In **chapter 6**, the role of faradaic depolarization in the electrokinetics of conducting surfaces is extensively discussed. It is demonstrated that electron transfer reactions may be induced by applying a pressure drop along the cell thus forcing the electrolyte solution to flow tangentially with respect to the electrodic surfaces. This mechanism is shown to be effective providing that the interface exhibits reversible or quasi-reversible electrochemical characteristics. The analysis is supported by experimental data obtained on gold and aluminum in the presence or absence of the redox couple $\mathrm{Fe(CN)}_6^{34} / \mathrm{Fe(CN)}_6^{44}$. The classical Helmholtz-Smoluchowski (H-

S) equation is inadequate for interpreting streaming potential measurements under conditions of faradaic depolarization. Extension of the H-S equation requires computation of the bipolar faradaic current as a function of bulk solution composition, applied pressure and the resulting streaming potential. For the sake of illustration, this is done by analyzing the pressure dependence of the bipolar current assuming that the potential decay in the solution is linear. In **chapter 7**, the distribution of the lateral electric field in the thin-layer cell, as tightly coupled to that of the transversal faradaic current density, is rigorously tackled for the two limiting cases of bipolar electrodic behavior, i.e. totally irreversible electron transfer and Nernstian (diffusion limited) electrodics. The analysis is carried out for the situation where the driving electric field for faradaic depolarization is externally applied in the solution. For both cases investigated, the theoretical calculations are successfully compared with experimental data. Deviation of the potential distribution from linearity is shown to be substantial for reversible bipolar faradaic processes, even at relatively low applied fields. In **chapter 8**, numerical evaluation of the bipolar current, as resulting from the confined hydrodynamic flow of an electrolyte solution containing a reversible redox couple, is carried out. As in chapter 7, the analysis integrates the interplay between conduction and faradaic processes taking place in the bulk solution and the bulk solid substrate. The electron transfer is now limited by convective diffusion of the electroactive compounds to/from the conducting surfaces. Following this analysis, the characteristic features of streaming potential/pressure plots under conditions of reversible faradaic depolarization are derived. On the basis of the theory developed in chapter 8, an attempt is made in **chapter 9** to derive the ′ -potentials of the interfacial system gold/($\mathrm{Fe(CN)}_6^{34}$ / $\mathrm{Fe(CN)}_6^{44}$, KNO_3) electrolyte solution from the electrokinetic data reported in chapter 6. The inadequacy of the theory is attributed to a subtle spatial distribution of the reversibility of the electron transfer reaction along the bipolar surface. This is inferred by comparing cyclic voltammetric data under convective conditions and electrolyte compositions approaching those met in electrokinetic experiments with the current density distribution computed under the very demanding condition that the faradaic processes are fully reversible, irrespective of the local convective diffusion situation. Semi-quantitative analysis of the data is performed within the limit of high-applied pressures where the electron transfer is predominantly limited by the electron transfer kinetics. The resulting ′ -potentials compare well with those obtained for gold surfaces in the absence of faradaic depolarization. In **chapter 10**, sets of analytical equations and a numerical method are proposed to account for the regulation phenomena that occur during encounter of two charged surfaces (homo- and hetero-interaction). The interacting double layers are described on the Gouy-Stern level, which allows explicit consideration of the chemical and electric components of the regulation processes. For a number of interaction situations considered, the analysis highlights the narrow link between the spatial potential/charge distributions and the resulting electrostatic contribution of the total Gibbs energy of interaction. In **chapter 11**, it is shown how the numerical approach adopted in the previous chapter allows simultaneous implementation of the three sources of deviation from DLVO predictions for electrostatic interaction between two colloids, namely (i) the occurrence of regulation phenomena, as examined in chapter 10 for one-dimensional surfaces and the presence of (ii) chemical and (iii) topological surface heterogeneities. Several illustrative examples are provided.

The theory for the potential and charge regulations upon interaction of two colloids, as presented in chapters 10 and 11, may serve to achieve better interpretation of AFM force measurements. Comparison with available experimental data is the incentive of a paper currently in preparation. The possibility of using this theory for describing the influence of electrostatic interactions on the adsorption behavior of immunoglobulin G at negatively charged silica and positively charged amine-functionalised silica[1] is under study. Description of the secondary electroviscous effect[2] integrating the possiblity of double layer regulation is also in preparation. Chapters 2, 4 and 10 offer the theoretical elements required to account for electronic charge regulation upon encounter of two colloids, one (or both) of them exhibiting conducting properties. Experimentally, it would be interesting to analyse by AFM the force curves for such systems in the presence of well controlled faradaic reactions (by means of redox-active species).

A novel and fundamental issue addressed in this thesis concerns the intimate coupling between electrokinetic and electrode kinetic properties of interfacial systems of the type conducting substrate⁄aqueous electrolyte solution (chapters 2-9). A number of important aspects are discussed and the underlying analyses open the way for further investigations and prospective developments and applications. Some of those are outlined below.

In chapter 9, the streaming-potential data are analyzed after deriving the overall bipolar current in the asymptotic limit of high-pressure where the electron transfer reaction is thought to be mainly limited by electron transfer kinetics. A rigorous theoretical evaluation of the bipolar faradaic current which integrates the spatial distribution of the kinetic and reversible (convective-diffusion limited) components of the local faradaic current density (quasi-reversible bipolar process) is still needed. This analysis, which should further take into account the interrelation between conduction and electronic processes as underlined in chapter 7, is currently underway.

The common basis for the collapse of streaming potential of metals in electroactive electrolyte or, for that matter, the enhancement of electrophoretic mobility of conducting particles (‘superfast electrophoresis') is the occurrence of bipolar faradaic depolarization. The work discussed here offers new perspectives to achieve better theoretical description of the superfast electrophoretic effect, which so far has mainly been considered in connection with electrophoresis of ion-exchanger particles submitted to high applied external fields. The parallel which exists between superfast electrophoresis for conducting particles and ion-exchanger particles is of the same nature as the one between the collapse of streaming-potential for conducting 'hard' surfaces and 'soft' surfaces, like ionic-conducting gel phases.[3]

As an extension of the work reported in this thesis, one could conceive faradaic depolarization of semi-conducting surfaces in the context of electrokinetics as driven by tangential hydrodynamics *and* photoexcitation of the solid phase.

For the electrokinetic measurements reported, the typical size of the spacing between the bipolar surfaces placed in the thin-layer cell allows the decoupling of the transversal potential distribution inherent to double layer formation and the lateral potential distribution resulting from the hydrodynamic flow for the determination of the overall bipolar faradaic current. In view of the development of small-integrated devices such as micro- and nano- reactors, an exciting challenge remains the experimental and theoretical investigations of the regime where such decoupling is lost, i.e. the regime where cell dimension and double layer thickness are no longer extremely different. To that purpose, one can think of using recently developed microslit electrokinetic set-up,[4] which is currently tested in our laboratory. This set-up offers the possibility of measuring streaming potential, streaming current and conductivity curves for a wide range of channel sizes.

The electrokinetic study presented deepens the insight into the interfacial properties of conducting surfaces under various chemical and electrochemical conditions. As mentioned in chapter 1, such knowledge is of importance for the understanding and optimization of electrophoretic deposition processes in aqueous systems. In the longer term, other concrete applications of this knowledge can be imagined, for instance in the field of micro- or even nano-technology. Often regarded as components of 'the new industrial revolution', these technologies deal with matter in its most elemental form, i.e. atoms and molecules, as computers break down data into their most basic binary representation. These advanced technologies are multidisciplinary in the sense that they integrate numerous fundamental aspects related to scientific fields of different origins, such as optics, hydrodynamics, electrokinetics and electrochemistry. Paradigms are the micro total analysis systems (σ-TAS), also called lab-on-a-chip,[5] or micro-reactors. For the sake of illustration, in the following, a short description is presented for the basic processes occurring in σ-TAS systems, highlighting the fundamental physicochemical features inherent to these micro/nano-sized devices and the relevancy of the results in the current thesis for the comprehension of electrochemistry which is steadily integrated in small areas and at higher speeds in conjunction with hydrodynamics.

The σ-TAS was originally conceived as the miniaturization of chemical analysis systems to act as sensors for automated sample measurement in research laboratory, factory or field locations. A σ-TAS usually looks like a planar device in which or on which chemical processes are being performed to go from reactants to products or from sample to analysis. σ-TAS are based on either microfluidics or microarrays. The former is the equivalent of printed circuit board (PCB) in microelectronics, routing fluid paths in a planar format and reducing the plumbing and tubing demands of conventional auto-analyzer systems in the same way as the PCB reduces the need for complex wiring. In the latter, the sample or reagent is immobilized in large arrays on a plate and fluids are flushed over the surface. Roughly speaking, the processes taking place inside σ-TAS are (i) the injection of the fluid mixture to be analyzed (ii) the transport of the fluid in the channel by electroosmosis/electrophoresis or by applying pressure drops (iii) the separation of the fluid components by various methods such as electrophoresis, chromatography, etc (iv) the reaction (chemical and/or electrochemical) and finally (v) the detection. The past decade has seen the merging of electrochemical methods for detecting electroactive compounds in σ-TAS. These methods do not suffer from size limitations contrary to optical techniques. Furthermore, reducing the size of spherical/hemispherical microelectrodes generates benefits in the sense that the development of diffusion layers for such geometries is accomplished in very short time. A (very) schematic representation of a σ-TAS functioning with electrochemical detection is given in Figure 1A. One of the great problems ahead related to the use of electrochemical detection for analyzing electrophoretically or hydrodynamically driven species is the possible interference between the electric field required for the detection (V_2) and the electric field applied or electrokinetically generated for the transport process (V_1). A classical solution consists in the use of high electrolyte concentration in the chamber so as to maintain a low resistance such minimizing eventual cross-talk between the different fields involved. The price of such a solution is that it diminishes the performance of the migration process (longer time scale).

In Figure 1B, an alternative detection principle for electrokinetically driven fluids is proposed. This method offers the advantage that the imposed hydrodynamics induces electric fields, which simultaneously serve for both transport and detection phases. The trick relies on the partial coating of the channel wall(s) with metallic compounds. The 'bipolar sensor' thus generated may be connected to a system of electrodes which allows measurement of the total electric field along the bipolar surface (this field is determined by the streaming potential of the metallic coating considered) and the bipolar current. Detection is mostly considered from a purely analytical point of view: a calibration line relating the measured quantity with the concentration of the compound of interest is first established and then comparison with data collected for unknown samples is performed. Rare are the physicochemical integrations of the detection data. With the method proposed, reaction kinetics and/or mass transport properties of the reactants may be directly derived from the analysis of 3-dimensional plots: induced field/applied pressure/bipolar current (chapter 8). Performing successive metallic coatings of different sizes along the channel wall(s) and at different separation distances (arrays of bipolar sensors) may also render possible spatial electrochemical separation of the compounds. Use of a single bipolar sensor might also achieve this providing that details of the spatial distribution of the faradaic current at the bipolar surface are assessable.

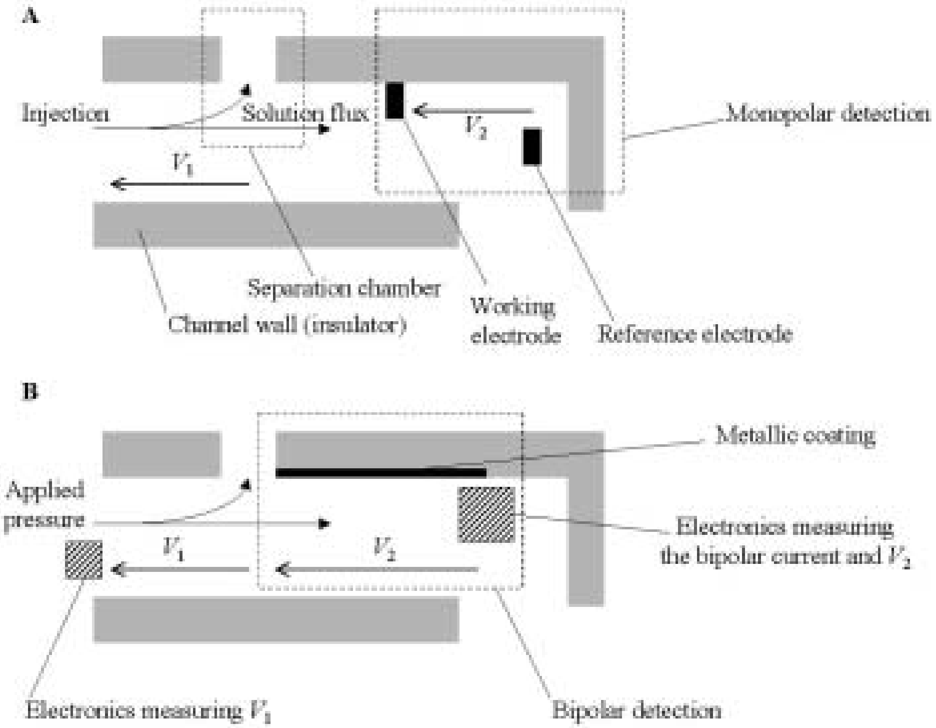
A
Injection
Solution flux
V_2
V_1
Monopolar detection
Separation chamber
Channel wall (insulator)
Working electrode
Reference electrode
B
Metallic coating
Applied pressure
V_1
V_2
Electronics measuring the bipolar current and V_2
Electronics measuring V_1
Bipolar detection

Figure 1. (A) Representation of a σ-TAS device working according to the principle of capillary electrophoresis or electrokinetically driven fluid (corresponding to imposed and induced field V_1, respectively) with (monopolar) electrochemical detection (imposed V_2). In panel (B), a similar device is sketched except that the electric fields V_1 and V_2 required for transport and detection are both now electrokinetically generated.

References

(1) Bremer, M. G. E. G., PhD thesis, Wageningen University (The Netherlands), Chapter 2 (2001).

(2) Russel, W. B. *J. Colloid Interface Sci.* **55(3)**, 590 (1976).

(3) Ohshima, H. *Adv. Colloid Interface Sci.* **62**, 189, (1995).

(4) Werner, C.; Körber, H.; Zimmermann, R.; Dukhin, S.; Jacobasch, H.-J. *J. Colloid Interface Sci.* **208**, 329 (1992).

(5) Drexler, K. E. in ‘Engines of Creation: the Coming Era of Nanotechnology’, Anchor Books, 1986.

SAMENVATTING

In dit proefschrift worden de evenwichtseigenschapen van elektrische dubbellagen (EDL) aan geleidende oppervlakken bestudeerd. Die zijn bepaald door de koppeling van elektronische en ionische ladingsprocessen. Zulke amfifunctionele dubbellagen combineren de reversibele eigenschappen van EDL zoals zij aan niet-geleidende oppervlakken ontstaan, met het polariseerbare karakter van EDL aan pure metalen. De EDL kan gepolariseerd worden door een aangelegd potentiaalverschil tussen de vastefase en de vloeistoffase aan het grensvlak, zoals gebruikelijk in de elektrochemie. Als elektronuitwisseling tussen oplossing en oppervlak optreedt, ontstaat een faradayse stroom die door het uitwendige circuit loopt: faradayse depolarizatie van de EDL vindt plaats.

Een belangrijke EDL parameter is de potentiaal in het vlak waar de afschuifsnelheid nul is, de zogenoemde zeta-potentiaal (′-potentiaal). Deze potentiaal kan beschouwd worden als de effectieve elektrische potentiaal van het kolloïd, en is een maat voor de hoeveelheid lading aan het oppervlak. Die lading speelt een belangrijke rol in de wisselwerking tussen kolloïdale deeltjes in een dispersie of tussen een elektrode en een deeltje. De ′-potentiaal kan worden gemeten met behulp van elektrokinetische methoden. De beweging van geladen kolloïdale deeltjes in een aangelegd elektrisch veld wordt elektroforese genoemd. Als het geladen oppervlak gefixeerd is, veroorzaakt het veld een beweging van de vloeistoffase, dit is elektro-osmose. Als de vloeistoffase door een capillair wordt geperst, onstaat er een potentiaalverschil tussen de uiteinden van het capillair, de stromingspotentiaal.

Het werk in dit proefschrift betreft theoretische en experimentele analyse van de karakteristieken van EDL die aan amfifunctionele oppervlakken ontstaan. Goud en aluminium zijn illustratieve voorbeelden. Het elektrokinetische gedrag van die systemen wordt geanalyseerd voor verschillende oplossingssamenstellingen in de aanwezigheid of afwezigheid van faradayse processen. Het is onderzocht hoe en onder welke omstandigheden elektronuitwisseling ontstaat zonder dat een potentiaal aan het grensvlak hoeft aangelegd te worden. Die analyse leidt tot het begrip van bipolaire elektrochemie en bipolaire elektrodekinetiek in de specifieke context van electrokinetische verschijnselen aan amfifunctionele oppervlakken. De stromingspotentiaalmetingen zijn geïnterpreteerd rekening houdend met de bipolaire elektrochemische karakteristieken van de elektron overdrachts reactie onder de hydrodynamische omstandigheden van de experimenten. Theorieën zijn ontwikkeld om de gemeten stromingspotentiaal in de ´-potentiaal om te rekenen. De experimentele resultaten worden vergeleken met voorspellingen die gebaseerd zijn op dubbellaagmodellen ontwikkeld voor de grensvlakstructuur aan gedeeltelijk geoxideerde metaaloppervlakken gepolariseerd door een extern veld en/of als gevolg van de aanwezigheid van redoxactive stoffen in de oplossing. Die modellen zijn verder gebruikt voor de interpretatie van dubbellaagpotentialen zoals bepaald met AFM metingen aan metalen en halfgeleiders gepolariseerd door een externe bron. Een ander aspect dat in dit proefschrift wordt bekeken heeft betrekking op heterointeractie, of, anders gezegd, de wisselwerking tussen geladen oppervlakken waarvan de elektrische en chemische eigenschappen verschillen. De daarvoor ontwikkelde theorie is een uitbreiding en aanvulling op bestaande theoretische benaderingen. Zowel met regulatiefenomenen als met fysische en chemische oppervlakteheterogeniteiten wordt rekening gehouden.

LIST OF PULICATIONS

∉ Nature of the Magnetic Ground State in the A_1C_{60} series
Coulon, C.; Duval, J.; Lavergne, C.; Barra, A.L. and Penicaud, A. *J. Phys. IV France* **2000**, *10*.

∉ Electrophoretic Deposition: A Quantitative Model for Particle Deposition and Binder Formation from Alcohol-Based Suspensions
De Beer, E.; Duval, J. and Meulenkamp, E.A. *J. Colloid Interface Sci.* **2000**, *222*, 117.

∉ Bipolar Electrode Behaviour of the Aluminium Surface in a Lateral Electric Field (Chapter 5)
Duval, J.; Kleijn, J.M. and van Leeuwen, H.P. *J. Electroanal. Chem.* **2001**, *505*, 1.

∉ Amphifunctionally Electrified Interfaces: Coupling of Electronic and Ionic Surface-Charging Processes (Chapter 2)
Duval, J.; Lyklema, J.; Kleijn, J.M. and van Leeuwen, H.P. *Langmuir* **2001**, *17*, 7573.

∉ Double Layers at Amphifunctionally Electrified Interfaces in the Presence of Electrolytes Containing Specifically Adsorbing Ions (Chapter 4)
Duval, J.; Kleijn, J.M.; Lyklema, J. and van Leeuwen, H.P. *J. Electroanal. Chem.* **2002**, *532*, 337.

∉ The Double Layer of a Gold Electrode Probed by AFM Force Measurements (Chapter 3)
Barten, D.; Kleijn, J.M.; Duval, J.; van Leeuwen, H.P.; Lyklema, J. and Cohen Stuart, M.A. *Langmuir* **2003**, *19*, 1133.

∉ Faradaic Depolarization in the Electrokinetics of the Metal / Electrolyte Solution Interface (Chapter 6)
Duval, J.; Huijs G.K.; Threels, W.F.; Lyklema, J. and van Leeuwen, H.P. *J. Colloid Interface Sci.* **2003**, *260 (1)*, 95.

∉ Coupling of Lateral Electric Field and Transversal Faradaic Processes at the Conductor / Electrolyte Solution Interface (Chapter 7)
Duval, J.; Minor, M.; Cecilia, J. and van Leeuwen, H.P. *J. Phys. Chem. B* **2003**, *107 (17)*, 4143.

∉ Rigorous Analysis of Reversible Faradaic Depolarization Processes in the Electrokinetics of the Metal / Electrolyte Solution Interface (Chapter 8)
Duval, J.; van Leeuwen, H.P.; Cecilia, J. and Galceran, J. *J. Phys. Chem. B* **2003**, *107 (28)*, 6782.

∉ Electrokinetics of the Amphifunctional Metal / Electrolyte Solution Interface in the Presence of a Redox Couple (Chapter 9)
Duval, J. *J. Colloid Interface Sci.*, in press, **2003**.

∉ Interaction between Electric Double layers: Regulation. Its Chemical and Electrostatic Aspects (Chapter 10)
Lyklema, J. and Duval, J. To be submitted.

∉ Electrostatic Interactions between Double Layers: Influence of Surface Roughness, Regulation and Chemical Heterogeneities (Chapter 11)
Duval, J.F.L.; Leermakers, F.A.M. and van Leeuwen, H.P. Submitted to *Langmuir*.

- Electrostatic Interactions between IgG Molecules and a Charged Sorbent Surface
  Bremer, M; Duval, J.; Norde, W. and Lyklema, J. To be submitted to *Colloids and Surfaces, A: Physicochem. and Eng. Asp.*

- Quasi-Reversible Faradaic Depolarization in the Electrokinetics of the Metal / Electrolyte Solution Interface
  Duval, J.F.L. and van Leeuwen, H.P. In preparation.

CURRICULUM VITAE

Jérôme Duval was born the 6th August 1976 in Domfront, a small village in Normandy (France). In 1994, he obtained the Baccalauréat C (specialities Mathematics, Physics and Chemistry) with distinction ('mention Très Bien'). He then entered 'Les Classes Préparatoires aux Grandes Ecoles Scientifiques', one of the most selective graduate programs in the French education system. In the framework of this program, he successfully followed the courses 'Mathématiques Supérieures' (1994-1995) and 'Mathématiques Spéciales (option P')' (1995-1996) in Caen. In september 1996, he entered 'L'Ecole Nationale Supérieure de Chimie et Physique de Bordeaux', where he graduated with excellence in june 1999 as physico-chemist engineer (dux of the class). His final year undergraduate training period (6 months) was undertaken in the Philips Research Laboratories in Eindhoven, the Netherlands. There he studied the fundamental aspects of electrophoretic deposition process of LaB_6 colloids onto conducting substrates. He then followed the post-graduate program 'Le Diplôme d'Etudes Approfondies (DEA), Chimie-Physique de la Matière et de l'Environnement' of University Bordeaux I, graduating with distinction ('mention Bien', dux of the class) in 1999. Within that program, he carried out a training period (4 months) in the Centre de Recherche Paul Pascal (CRPP, CNRS laboratory) in Bordeaux (France) where he investigated the electronic and magnetic properties of alkali-doped fulleride materials. From september 1999 till september 2003, he was attached to the Physical Chemistry and Colloid Science Laboratory of Wageningen University (the Netherlands) as a PhD student. This thesis, the subject of which was part of a joint project with Philips Research Eindhoven, is the result of that work. During his PhD studies, he gave many oral presentations in the Netherlands and abroad, namely at the International Symposia on Electrokinetic Phenomena in Dresden (Germany, october 2000), in Cracow (Poland, august 2002) and in the framework of the XVI European Chemistry at Interfaces Conference in Vladimir (Russia, may 2003).

DANKWOORD

Het proefschrift dat u net heeft gelezen (of gedeeltelijk of helemaal niet) is eindelijk af. Als fransman, heb ik toch die vier jaar overleefd (nee, ik ga niet klagen over het eten, het weer en de rare Nederlandse gewoontes die ik heb meegemaakt) … Maar, zoals u al weet, zo erg was het niet, maar juist het tegenovergestelde! Ik kan nu wel beweren dat er fransen zijn die helemaal naar hun zin in Nederland kunnen hebben. Ik was, ben en zal altijd een van die zijn. Mijn verblijf was een heel leerzame ervaring in allerlei aspecten, zowel personeerlijk als wetenschapelijk. Dit was mede mogelijk gemaakt door de heel bijzondere sfeer in de groep en van sommige bijzondere mensen die mij hebben gesteund, aangemoedigd en begeleid in goede zoals in slechte tijden.

Ten eerste wil ik de mensen noemen, zonder wie dit proefschrift nooit tot stand was gekomen.

Herman, er valt zoveel te zeggen over onze samenwerking dat ik eigenlijk niet weet waar ik beginnen moet. Je was altijd (tijdens de werkuren, ‘s avonds laat en in de weekenden) bereid om mijn vragen te beantwoorden en om duidelijke perspectieven aan mijn werk te geven. Jouw expertise in elektrochemie en elektrode kinetiek heb ik heel veel benut en gewaardeerd. Jouw filosofie van de wetenschap past heel goed bij mij en heel vaak heb ik de indruk gekregen dat jouw rol niet beperkt was als die van supervisor. Als buitenlander, heb ik aan het begin zware momenten gehad om alles op een rij te zetten. Ik was ver weg van huis voor lang en het viel niet mee om eigen herkenningtekens te vinden. Je was (en bent nog steeds) een van de personen die geholpen hebben om mijn verblijf in Wageningen gemakkelijk en aangenaam te maken. Ik kon geen betere supervisor hebben. Bedankt voor alles Hermanus! (toch maar oefenen voor het poolen).

Hans, tu as toujours montré beaucoup d’intérêt pour mon travail de thèse et le chapitre 10 n’en est qu’une illustration. Tu es toujours prêt à partager ton savoir et malgré l’expérience et la connaissance des colloïdes qui sont les tiennes, tu cherches toujours à apprendre de ceux qui à priori ont encore tout à apprendre. Je regrette seulement que les règles concernant l’obtention et la soutenance d’une thèse à Wageningen n’aient pas permis un caractère plus officiel au rôle important que tu as joué dans le cadre de mon travail. “La modestie est au mérite ce que les ombres sont aux tableaux. Elle lui donne de la force et du relief”, Jean de la Bruyère. Tu comprendras certainement ce que je veux dire par là. Merci, Hans.

Josep, Jaume, Joan, I want to thank you for our very productive cooperation (chapters 7 and 8). I enjoyed a lot my two stays in Spain. Josep, many thanks for the medical (and moral) support you provided during my 'strawberry-face time'. Muchas gracias para el aal tem en Lleida!

Mieke, bedankt voor jouw commentaren en correcties van hoofdstukken 2, 4 en 5.

Een student heb ik mogen begeleiden in mijn AIO-schap, Geertje Huijs. Dit was een zeer leerzame periode voor mij. Geertje, veel succes met jouw baan in Nizo.

Wim, dank je voor de elektrochemische and elektrokinetische experimenten dat je voor mij hebt uitgevoerd. Marcel, dank je voor jouw bijdraag in hoofdstuk 7. Ab, dank je voor de goede adviezen over het gebruik van de stromingspotentiaal apparatuur. Raewyn, thanks for the language corrections you brought in chapters 1 and 12. Gert, dank je voor de omslag van het proefschrift.

Naast de mensen die direct bij mijn onderzoek betrokken waren, waren ook anderen (of dezelfden) van Fysko die hebben gezorgd voor een prettige tijd en voor oplossingen aan dagelijkse problemen die ik ben tegengekomen. Die wil ik ook noemen.

Ben, Rhoda, Anneke, Arnold, bedankt voor de gezellige discussies tijdens de koffie-tijd. Ben, Rhoda, de shag dat jullie roken is heerlijk. Sorry voor de aanstekers die ik van jullie onbewust heb meegenomen. Over roken gesproken, ik ben jullie niet vergeten, Joanne (toch maar Frans gaan leren …) en Ab (hup, hup "les Bleus"!). Anneke, sorry voor de puinhoop in mijn kamer. Je hebt het zwaar gehad, ik weet het … Wim, Herman, Ben, jullie hebben mij flink geholpen zodat ik wel van mijn auto legaal in Nederland kan genieten … ik ben jullie daarvoor heel dankbaar. Ronald, Rob, Peter, bedankt voor de computer zaken. Frans, Jos, bedankt voor het helpen met de sfbox. Richard, de gezelligheid in ons kamer kende geen grenzen maar je bent wel van de gestoorde fransman af. Succes met je eigen promotie. Jasper, Wouter, het was geen we day maar wel their day. Volgende keer beter … misschien. Ana, thanks for the spanish lessons en the tour in Granada. Farid, merci pour le bon-temps qu'on a passé ensemble et les parties fanatiques de billard de l'après-boulot. Yoann, pendant ton séjour à Wageningen, nombreuses ont été nos escapades nocturnes et nos (ou plutôt tes) discussions sur l'existence et l'homme en générale. Je garde de cette période un souvenir très particulier et nostalgique. Tom, Lee, your imitation of the frenchy-english is poor. You should really work on it. Luuk, ik ben af en toe naar jou gekomen om wat dingen te vragen en punten te bespreken. Ik moet wel zeggen dat meestal aan het eind van de discussie, had ik vergeten de vraag dat ik oorspronkelijk aan jou had gesteld. Paulo, many thanks for the very nice tour in Faro and neighborhood.

Microsoft, I shall not thank you for the programs you provide (Frans, toch maar een Mac gebruiken …).

Bedankt allemaal voor de dagelijkse Nederlandse lessen. Voor wat betreft de mensen die ik voor een paar maanden heb begeleid om hun Frans te verbeteren, is het feit dat ik weg ga geen excuus om te stoppen met het leren van de taal van Molière.

Hafida, Katka, Rink, Krisztina, Paula, bedankt voor de gezellige tijd en de ontspanning. Nu, heb ik wat tijd om een heerlijke zalm klaar te maken (beloofd!).

Marit, Paulus, Arjen, Ester, Sven, Oma, Janneke, Johan, Lian, Kees, in jullie heb ik vrienden en familie gevonden. Dat is heel kostbaar en ik weet niet hoe ik jullie daarvoor bedanken moet. Olechka, Lica, your smiles and optimism gave me the courage to overcome the difficulties of the past two years. Cʧacʠвʦ. The fisherman shall always find the way to get back to the harbor …

Papa, maman, vous avez toujours été là pour m'aider quelles que soient les circonstances. Je sais que vous avez eu du mal à accepter certaines de mes décisions professionnelles et pourtant vous n'avez cessé de me soutenir dans mes choix. Sans vous, je n'aurais jamais pu atteindre ce que j'ai atteint jusqu'à aujourd'hui. Merci.

Mijn laatste woorden zijn voor jou Wim en voor jou Marijke. Jullie hebben zoveel voor mij gedaan en wij hebben samen zoveel dingen meegemaakt … In de loop van de tijd, hebben wij een heel bijzondere relatie opgebouwd. Dankzij jullie heb ik heel veel geleerd over het leven, over de mensen en over mezelf. Jullie hebben mij als een zoon geaccepteerd en ik zal altijd van jullie als ouders houden. Ik kan niet op papier schrijven wat jullie voor mij betekenen. Marijke, ik mis jou. Van boven, ik hoop dat je trots bent op wat ik in die vier jaar heb bereikt, mede dankzij jou.

Merci à tous, bedankt allemaal,

Jérôme